

JPL PUBLICATION 80-61

Radar Geology: An Assessment

Report of the Radar Geology Workshop

Snowmass, Colorado

July 16-20, 1979

(NASA-CR-163638) RADAR GEOLOGY: AN
ASSESSMENT REPORT OF THE RADAR GEOLOGY
WORKSHOP (Jet Propulsion Lab.) 515 p
HC A22/MF A01

N81-10472
THRU
N81-10496
Unclas

G3/42 29032

September 1, 1980

National Aeronautics and
Space Administration

Jet Propulsion Laboratory
California Institute of Technology
Pasadena, California

REPRODUCED BY
**NATIONAL TECHNICAL
INFORMATION SERVICE**
U.S. DEPARTMENT OF COMMERCE
SPRINGFIELD, VA. 22161

JPL PUBLICATION 80-61

Radar Geology: An Assessment

**Report of the Radar Geology Workshop
Snowmass, Colorado
July 16-20, 1979**

(Color Illustration Reproduced in Black and White)

September 1, 1980

National Aeronautics and
Space Administration

Jet Propulsion Laboratory
California Institute of Technology
Pasadena, California

This publication was prepared by the Jet Propulsion Laboratory, California Institute of Technology, under NASA Contract NAS7-100.

CONTENTS

INTRODUCTION	1
EXECUTIVE SUMMARY AND OVERALL RECOMMENDATIONS	3
TECHNIQUE DEVELOPMENT GROUP RECOMMENDATIONS	6
ENGINEERING AND ENVIRONMENTAL GROUP RECOMMENDATIONS	8
MAPPING GROUP RECOMMENDATIONS	10
EXPLORATION GROUP RECOMMENDATIONS	17
PRESENTED PAPERS	20
OVERVIEW PAPERS	
Historical Sketch - Radar Geology	
H. MacDonald	23
Radar Geology: Technology and Program Overview	
Frank T. Barath	38
TECHNIQUE DEVELOPMENT PAPERS	
Simulation of Orbital Radar Images	
R. S. Saunders, J. C. Holtzman, and Charles Elachi	45
Expression of San Andreas Fault on Seasat Radar Image	
F. F. Sabins, R. Blom, and C. Elachi	64
Analysis of Seasat Orbital Radar Imagery for Geologic Mapping in the Appalachian Valley and Ridge Province, Tennessee-Kentucky- Virginia	
J. P. Ford	75
Radar Imaging of Volcanic Fields and Sand Dune Fields: Implications for VOIR	
C. Elachi, R. Blom, M. Daily, T. Farr, and R. S. Saunders	114
Rock Type Discrimination and Structural Analysis with Landsat and Seasat Data: San Rafael Swell, Utah	
H. E. Stewart, R. Blom, M. Abrams, and M. Daily	151
Terrain-Analysis Procedures for Modeling Radar Backscatter	
Gerald G. Schaber, Richard J. Pike, and Graydon L. Berlin	168
Realistic Earth/Land Radar Models	
Andrew J. Blanchard	200

Some Confusion Factors in Radar Image Interpretation Bruce J. Blanchard	223
Multichannel SAR in Geologic Interpretation: An Appraisal Philip L. Jackson	233
Automatic Shading Correction and Speckle Noise Mapping/Removal Techniques for Radar Image Data Pat S. Chavez, Jr.	251

ENGINEERING/ENVIRONMENT PAPERS

Applications of Radar Imagery to Arctic and Subarctic Problems P. Jan Cannon	265
Radar Detection of Surface Oil Accumulations John E. Estes, Peggy O'Neill, and Michael Wilson	275
Application of SLAR in Nuclear Power Plant Siting: A Case History Barry S. Siegal	293

MAPPING PAPERS

Application of Imaging Radar to Mapping Franz W. Leberl	307
Stereo Radar for Mapping and Interpretation L. Graham	336
A New Look at Togo Through the Eyes of a SLAR Louis F. Dellwig	351

EXPLORATION PAPERS

The Use of Radar and Landsat Data for Mineral and Petroleum Exploration in the Los Andes Region, Venezuela Robert K. Vincent	367
Geological Mapping in the Amazon Jungle - A Challenge to Side- Looking Radar Aderbal C. Correa	385
Side-Looking Airborne Radar Image Interpretation and Geological Mapping: Problems and Results J-Y. Scanvic and E. H. Soubari	417
The Evaluation of 3-cm-Wavelength Radar for Mapping Surface Deposits in the Bristol Lake/Granite Mountain Area, Mohave Desert, California Ray Sugiura and Floyd Sabins	439

Radar, an Optimum Remote Sensing Tool for Detailed Plate Tectonic Analysis and Its Application to Hydrocarbon Exploration (An Example in Irian Jaya, Indonesia) Claude M. Froidevaux	457
Fracture Trace Expression and Analysis in Radar Imagery of Rain Forest (Peru) P.H. A. Martin-Kaye, J. W. Norman, and M. J. Skidmore	502
Appendix A. List of Attendees	508
Appendix B. Program Agenda	511

ABSTRACT

This report contains an assessment of the application of imaging radar to geologic problems in the form of a collection of 24 papers and recommendations for NASA's program in this field. The material was developed in the framework of a Workshop held in Snowmass, Colorado, from 16 through 20 July 1979, under the auspices of the Jet Propulsion Laboratory, California Institute of Technology, with sponsorship of the Resource Observation and Planetary Divisions of NASA.

omit
70
P.23

INTRODUCTION

The launch of a Synthetic Aperture Radar (SAR) on Seasat in the summer of 1978 demonstrated that radar observation of the Earth on a global basis is now feasible. Initial examination of the Seasat radar data has indicated that useful applications of these data could be made to a variety of problems in geology, agriculture, hydrology, and oceanography, as well as to planetary exploration. Wide interest has therefore resulted in the rise of spaceborne radars for these purposes. The basic problem in the furtherance of these applications is centered on the need for a detailed understanding of the electromagnetic interactions of the surface (surface signatures) and the effects of key radar system parameters (resolution, incidence angle, frequency, polarization, etc.) on these interactions. The goal of the ongoing research program is thus directed at understanding these surface interactions and demonstrating optimum radar configurations for the various applications.

In order to define a research program responsive to the needs of the various applications, NASA has undertaken a series of planning exercises and workshops. This workshop was one in the series. These planning exercises have resulted in the initial definition of a NASA Program Plan for Active Microwave Remote Sensing. The plan outlines a systematic theoretical and experimental program addressed to the central issues in the various disciplines. The program encompasses modelling activities and extensive experimental investigations making use of ground and airborne facilities. These studies provide the necessary background for the definition of the next sequence of space flight experiments. The space flight experiments include Spacelab experiments and culminate in free flyer demonstrations. The program utilizes synthetic aperture radar systems of broad flexibility to permit a systematic exploration of optimum radar configurations for the various fields of application.

The field of geology has seen the widest application of radar for both terrestrial and planetary exploration. The prospects of geologic SAR global and planetary mapping are thus particularly exciting. Accordingly, it appeared particularly appropriate to assemble key researchers and users of radar data from the fields of terrestrial and planetary geology in order to assess the current state-of-the-art of radar sensing in geology and to provide recommendations on the needed steps in a radar geology research program.

The Radar Geology Workshop was conducted under the auspices of the Technology and Space Program Development (TSPD) Office at the Jet Propulsion Laboratory with the sponsorship of the Resource Observation and Planetary Divisions of NASA. An organizing committee was appointed to determine the content and format of the Workshop and to prepare a list of invitees. The committee consisted of the following:

Paul Harrison, Chairman	Cities Service Co.	Tulsa OK
Frank Barath, Exec. Secy.	JPL	Pasadena CA
James Taranik	NASA HQ	Washington DC
Louis Dellwig	U. of Kansas	Lawrence KA
John Estes	NASA HQ/	Santa Barbara CA
	U. of California	
Harold Masursky	USGS	Flagstaff AZ

Stephen Saunders
Paul Teleki
Carol Snyder, Logistics

JPL
USGS
JPL

Pasadena CA
Reston VA
Pasadena CA

The Workshop took place in Snowmass, Colorado, from July 16 through July 20, 1979, with 44 attendees. The attendees are listed in Appendix A together with their affiliations and addresses. Appendix B shows the agenda, which was closely followed.

This report presents the recommendations evolving from the Workshop and the papers presented by the participants. These papers were independently reviewed and modified by the authors as required. The output of this Workshop as reflected by this report has provided a major input to the NASA Program Plan for Active Microwave Sensing.

EXECUTIVE SUMMARY
AND
OVERALL RECOMMENDATIONS

The Radar Geology Workshop was organized and structured for the dual purpose of (1) performing an in-depth assessment of the current understanding of the applications of radar imagery in geology and (2) developing recommendations for shaping NASA's future programs in this field. Attendance at the Workshop was by invitation only and generally limited to persons who were knowledgeable and willing to take an active part in the effort.

Activities for the first three days consisted of sequential plenary sessions, organized by general topic, with formal presentations by the participants and a short discussion after each talk. The general topics for consideration were:

Technique Development - relating to general geologic mapping, discrimination from orbit, modeling, and experimental approaches to quantification of image data.

Engineering/Environmental - mapping of specific sites, sea state (oil-on-water), sea ice, vegetation.

Mapping - cartographic products, stereoscopic utilization, multiuse maps, and image characteristics.

Exploration - specific targets or purpose-oriented projects.

This, the technical presentation phase of the meeting, certainly accomplished its intended objective of defining the present state-of-the-art for geological applications of radar data by a wide variety of users. That material, which makes up the bulk of this report, in addition to those few papers which were presented but are not included, is unquestionably the most extensive compilation of practical radar geology prepared to date.

The last two days were the real workshop phase in which the participants gathered in separate working groups according to their topical interest and/or experience. These individual groups concentrated on defining the specific problem areas in their own fields which would be assisted by further research and development. They prepared a set of recommendations with supporting arguments for each point that identified the work which they proposed to be done. Then, with the groups in joint session again, each group chairman presented the recommendations and rationale that had been independently developed. The extensive ensuing discussion of these points further clarified the R & D issues and plainly illustrated that many points of interest are common to the various application topics.

The individual groups' recommendations were correlated and an overview prepared that summarized the identifiable points of needed development:

Coordination and continuity of research efforts. - Much good, pertinent work is being done by different groups (government, universities, and industry) that if properly coordinated and funded would save a lot of duplicated individual effort and provide more rapid progress.

Frequency and polarization effects in target/energy interaction. - The reflectivity signature of natural targets should be quantified as a function of radar wavelength and transmit/receive signal polarity to determine diagnostic interpretation information and possible optimum system parameters.

Geometry. - What are the effects of look direction and depression angle on image interpretability over various terrain types?

Dynamic range of backscatter signal and recording. - What is the expected range of reflected signal intensity from geologic targets and what recording system bandwidths will be necessary to prevent loss of useful information by clipping? What level of calibration (actual and relative) is required for differing geologic applications?

Digital data processing. - This is acknowledged as necessary to preserve dynamic range and system calibration, permit image signature quantification and analysis, facilitate comparison with other types of data by digital rectification, registration, enhancement and information extraction. Hardware should be improved for faster digital data throughput, and existing image processing software surveyed for utilization. New and improved software should be developed.

Collateral instrumentation and data. - Numerous ancillary sets of data are needed to properly support further research, e.g., surface roughness, digital topography, scatterometer data from truck- and helicopter-mounted systems, and aerial photography.

Data identification, archiving and distribution. - A large amount of data (ground truth, spectrometer data, aircraft imagery from several systems, Seasat, etc.) already exists that would be very informative, and ongoing programs collect more data all the time, but this information does not provide the needed coherent data base for research because of unknown system/mission parameters and/or practical inaccessibility.

Education and training. - Many users are unaware of the limitations and unique characteristics of imaging radar systems. A much larger and diverse market potential (user community) could be developed by increased academic research support and workshop-seminars for geological applications of imaging radar data.

This overview was presented to and discussed by the entire group. And, as would be expected, there was good agreement on the technical aspects of each of the points. In view of the widely ranging awareness levels of the individuals and their own area of expertise, assignment of relative importance and priority to these items was not fully accomplished.

There are essentially two groups that comprise the radar geology community: (1) government and academic research, and (2) commercial contractors and users. The former group is looking at long-term (3-7 years) research efforts to resolve many of the questions that remain in the design of an "optimum" orbital radar system. The latter group have been using airborne radar imagery in an operational, or at least quasioperational, mode for more than 10 years and believe that the utility of radar imagery for certain kinds of geologic application has been established. This practical difference in perspective produces conflict only when it comes time to prioritize the efforts to be funded.

Attendant to this philosophical realization on the part of the workshop attendees and their recognition that parallel development paths are viable and even complementary, an overall recommendation was made in consensus and conclusion to the workshop: "Based on the current level of experience and awareness, it is recommended that:

- (1) An* imaging radar system (X-band, 45° look angle, like-polarization) be placed as soon as possible in a Landsat type orbit.
- (2) An increased level of study be funded in the noted areas where further R&D efforts may lead to significant advancement of knowledge and capability.
- (3) An increased level of processing and dissemination of Seasat-1 data be initiated to speed up the evaluation and proof-of-concept testing for the first orbital imaging radar system."

*The underscored words have been added by the Chairman to the original wording for clarity.

TECHNIQUE DEVELOPMENT GROUP RECOMMENDATIONS

This research discipline addresses the quantitative aspect of the analysis of radar images and the specification of system parameters for particular features detection. This activity has a number of aspects:

- (1) Theoretical and experimental research to better understand the interaction of electromagnetic waves with the surface and near subsurface, and to quantify the relative importance of different geophysical parameters, e.g., surface roughness, slope, dielectric constant, moisture content, volumetric inhomogeneities, and surface cover.
- (2) Research to refine the system parameters to optimize detection of specific features. This includes simulation by computer as well as field experiments.
- (3) Research on obtaining better calibration techniques which would allow the extraction of quantitative information.

The specific areas of research recommended by the workshop participants are (not in order of priority):

- (1) Continue backscatter and surface signature research. Expand the work conducted in Death Valley to other regions. Emphasis should be on understanding how the radar backscatter cross-section at different frequencies and polarizations can be used to discriminate and identify different surface units and surface cover type.
- (2) Continue theoretical research to derive simple equations which are consistent with field measurements. This theoretical work will hopefully lead to a good understanding of the interaction of electromagnetic waves with different surfaces. This will be a key element in assessing the necessary combination of different observation geometry, radar frequency and radar signal polarization to be able to achieve a certain discrimination and identification level.
- (3) Develop helicopter-borne radar scatterometer and polarimeter systems covering the spectral region from L-band to K-band. These systems are needed to conduct an experimental program to verify the different theories and determine the extent of their validity.
- (4) Search out presently available Landsat and other image processing techniques that can be utilized in radar research. Many techniques have been very successfully applied for enhancing the extraction of the information in Landsat imagery. Some of these techniques can be directly applicable to radar images. In some cases, some modifications are necessary because of the unique radar observation geometry and the inherent presence of speckle in the SAR images.

- (5) Concentrate the quantitative work in a limited number of well-mapped geologic sites with diverse vegetation cover, roughness scales and climate conditions. The techniques developed in the previous activities should be tested in test sites to verify their accuracy and capability. These sites would then be used as training sites for extending the use of these techniques for large-scale applications using space-borne imaging radar sensors.
- (6) Develop cost-effective simulation techniques for examining the interactive effect of the different variables, i.e., geometry, number of looks, resolution, polarization, and frequency. These techniques could be used as a low-cost approach for a first-level simulation of the effect of these parameters.
- (7) Develop calibration techniques which would allow relative calibration better than 1 dB and absolute calibration better than 3 dB. This calibration capability is necessary for any quantitative analysis of the data and for comparison of data obtained at different times and in different locations. The measurement of image tone variation and the corresponding surface backscatter variation is essential for the development of the capability to monitor surface cover (vegetation, forest cover, etc.) and surface moisture.
- (8) Develop stereo and radargrammetric techniques which are necessary for using radar data for topographic and cartographic applications. Good cartographic fidelity is essential for the use of radar data in conjunction with other types of information as a comprehensive data set to understand the surface properties.

ENGINEERING AND ENVIRONMENTAL GROUP RECOMMENDATIONS

Engineering applications of imaging radar presented at the workshop include a range of topics and use of a variety of radar-image types. Radar imagery was used in a multidisciplinary phased approach to selecting a dam site in highly fractured terrain in northern California (R. Gelnett) and to siting a nuclear power plant in seismically active terrain in the Philippines (B. Siegal). Radar imagery was used to interpret geomorphic processes in Alaska (J. Cannon) and for geologic mapping in the Virginia Piedmont and Coastal Plain (D. Krohn). Surface-oil slicks in the marine environment of the Santa Barbara Channel, California, were detected by means of radar images (J. Estes, et al.). For each land area the radar images were used primarily to define geologic structure. The areas reported are mostly in physiographically rough, inhospitable terrain that is difficult of access for a variety of climatic and/or cultural reasons. The range of radar-image types used in the studies includes Westinghouse K-band real aperture, Motorola S-band real aperture, Goodyear X-band synthetic aperture, JPL L-band synthetic aperture—all acquired from airborne platforms—and spaceborne L-band synthetic aperture imagery acquired from the Seasat satellite.

Many different independently variable factors combine to affect the radar backscatter returned from any given target. Commonly it is not possible to separate and effectively determine the contribution of each factor for purposes of image interpretation. The problem is compounded and cannot be adequately resolved using uncalibrated imaging radar systems. Further problems arise in optical correlation of imagery due to nonlinearity of the transfer function that exists when data are converted from digital tape to signal film, and due to a high level of operator dependence inherent in the optical correlation process. Thus in first priority it is recommended that for further studies and application of radar geology a calibrated imaging-radar be developed having a 3-dB tolerance from end to end of the system. In addition radar data should be digitally correlated.

In the opinion of the Engineering and Environmental Applications Group the important requirements of imaging-radar systems are a wide dynamic range, moderate resolution, a scale that is appropriate to the application, variability of look angle, and controlled look direction. Reasons for the above opinion are as follows. The dynamic range of an imaging radar directly influences the range of information content available for presentation on images. This in turn affects image interpretability. Resolution of radar images for geologic applications should be the best that can be obtained consistent with a reasonable cost of the imaging system. A moderate resolution is in the range of 10-25 m. For synthetic aperture radars the effect of resolution reduction versus speckle reduction should be optimized for maximum image interpretability that is consistent with the scale of the image and the degree of detail desired. As radar backscatter is strongly affected by slope effects at look angles from 0° to 30°, by surface roughness at look angles from 30° to 70°, and by shadowing at look angles from 70° to 90°, it is desirable for maximum flexibility that imaging radar systems have variability of look angle. Controlled look direction is desirable to compensate for effects of radar layover, or radar blindness relative to feature orientation.

Quality, quantity and timeliness of radar image-data are most important to the user community. Especially in the case of dynamic studies, digitally correlated radar data should be processed in real-time or near-real-time. All processed data should contain information specifying the image system parameters, time and date of image acquisition and ground location coordinates in latitude and longitude. The source of all imagery should be specified, and "quick look" imagery should be available for users to determine image quality prior to undertaking any detailed study. Much imaging radar data already exists but is not readily available to the user community. A need exists to establish a clearing center where the occurrence of all types of radar imagery would be tabulated and available to the user community for public inspection.

Research in radar data-registration and rectification should be funded. Automated techniques of pattern, shape- and texture-recognition from radar imagery should be developed. Correlative analyses should be made with other types of geological and geophysical data in rectified digital format. Empirical and mathematical modelling and simulation studies should proceed to determine radar response characteristics.

An important need exists for adequate communication and dialogue to be maintained between the sensor-engineering community and the user community. Users must make their requirements known to engineers, who in turn can make the necessary determinations as to how data-bits are to be transmitted, compressed, etc., to achieve the stated requirements. Research on sensory systems should be directed at stereo-imaging and at determining optimal radar frequencies for use in specific applications. Target responses should be compared using multiple frequencies, polarizations and look angles. For applications purposes now and in the future, studies should be made to determine what requirements exist for repetitive global coverage using a radar satellite, either experimentally or operationally. Attention should be given to the effects of many different types of vegetation cover on radar backscatter, and to responses in X-band and longer-wavelength radars.

A clear need is evident to define and standardize terminology with respect to radar imaging geometry. Terms such as look angle, incidence angle, and depression angle, appear to be poorly understood and differently used. A glossary of terminology commonly used by the radar-image interpreter should be prepared. A need for education and training in radar-image interpretation exists among the user community but details of implementation remain for discussion.

MAPPING GROUP RECOMMENDATIONS

In the present context, mapping is defined in relation to acquiring and presenting geological information in a geometrically accurate map. Mapping represents the task of:

- (1) Creating base maps for thematic presentations.
- (2) Producing planimetric (x,y) locations of features.
- (3) Producing terrain heights (z), slopes and height differences.
- (4) Revising existing maps.

The rectification of images, generation of orthophotographs, production of grid overlays and other preprocessing functions concerning geometric and radiometric image contents can be classified under item (2) above.

These definitions of mapping are a subset of those set forth in a report of the Task Force on Mapping, Charting and Geodesy.¹

A number of broader areas were defined where research needs to be done to investigate applications of radar to mapping. Structuring of such areas for a discussion was found difficult because of the many interrelations that exist between the parameters of a radar system. Mapping applications seem to depend basically on two factors:

- (1) Accuracy.
- (2) Stereo capability.

These factors, in turn, depend on a series of radar system or configuration parameters such as:

- (3) Resolution,
- (4) Incidence angles.
- (5) Synergisms.
- (6) Look direction.
- (7) Frequency/polarization/calibration.

¹Donelson et al. (1973), Report of the Task Force on Mapping, Charting and Geodesy, Office of Management and Budget, Washington, D.C.

In addition, three factors were discussed that bear on the anticipated studies and possible applications:

- (8) Radar inteferometer.
- (9) Type of optimum experiments.
- (10) Possible mapping scales.

The following sections will address each of the above items, stating first a recommendation and then generating a rationale.

1. Accuracy

Recommendation

The mapping accuracy that can be obtained with imaging radar should be investigated. Open questions concern optimum mapping methods and quantitative accuracy models for mapping with single images, stereo pairs and image blocks.

Rationale

For an application, or a prediction of the usefulness, of radar mapping, one needs to define the possible accuracies that can be obtained in a specific configuration: this may vary from case to case. Although there exists a long list of studies dealing with radargrammetry (Leberl, 1979),² the conclusions that can be drawn are rather limited. The studies generally are small in scope and concern random samples of a wide range of feasible parameters. They do not permit valid conclusions to be drawn on the interdependence between accuracy and the important parameters that govern it, such as

Density of ground control points.

Resolution and speckle.

Incidence or look angle.

Antenna stabilization and navigation or orbit accuracy.

Also, the majority of studies only dealt with the basics of radargrammetry, addressing essentially only single images. There has been a definite lack of work to evaluate advanced radargrammetric concepts.

2. Stereo

Recommendation

The physiological aspects of stereo viewing of radar images should be analyzed, and the accuracy of measuring three-dimensional coordinates and of derived quantities such as slope must be studied in function of the various parameters that influence radar stereo.

²Reference herein relate to papers appearing elsewhere in this report.

Rationale

The intersection geometry of radar stereo configurations has been successfully modeled (see Graham, 1979; Leberl, 1979). The physiological limitations of visually perceiving radar stereo models are not well understood; this is essentially caused by the lack of appropriate experimental material. Stereo radar does have importance as an interpretation tool. The parameters that have an effect on its usefulness have been identified in the past; however, the lack of appropriate test imagery thus far has not permitted the study of interdependencies. The following influencing factors can be identified:

Incidence angle of radiation.

Stereo convergence angle.

Dynamic range (similarity in grey tones).

Frequency.

Resolution and speckle.

Exterior orientation stability of sensor (antenna).

Type of terrain or surface.

There exist several measures of quality for stereo:

Vertical exaggeration.

Absolute accuracy of a measured height (z) and/or a planimetric position (x, y).

Accuracy of coordinate differences, of slope, etc.

Height acuity or sensitivity.

The experimental analysis of interdependencies will have to address particularly the limitations of stereo viewing as caused by differences in image tones and textures due to drastically different illumination angles. Thereby, opposite-side stereo with fairly steep look angles should be investigated. Emphasis must be also on preprocessing methods using contrast dodging methods to help improve the image grey tones for stereo. A point of some interest is also the possibility to carry out stereo analyses with images from intersecting flight lines; such configurations typically can occur with orbital data.

3. Spatial Resolution

Recommendation

The tradeoffs between resolution and the following factors must be considered:

Stereo.

Accuracy of identifying features or control points.

Speckle.

Cost.

Rationale

Available studies have been insufficiently broad to deal with the effect of resolution on radar mapping performance. Of particular interest is the identifiability of control points, especially of man-made structures. The same applies to the use of radar for map revision.

4. Incidence Angle

Recommendation

The optimum incidence angles must be defined so that the best possible radar mapping accuracy and feature interpretation capability are obtained.

Rationale

In aircraft radar, the user of images does not have a wide choice of incidence angles. The need for wide coverage leads to a great variation of incidence angles. In satellite radar, the incidence angle is chosen and does not exhibit as wide a variation as in aircraft. However, little evidence exists from the mapping accuracy and stereo point of view to make a responsible choice of an incidence angle. To provide this evidence one needs to carry out experimental work with a variety of incidence angles (look angles off-nadir).

5. Synergisms

Recommendations

Interpretation techniques must be developed to display images from different sensors or from different position, times, etc. These techniques must be evaluated.

Rationale

The interdisciplinary character of remote sensing and the wide range of sensing tools available have led to a consensus that the combined use of different images must be pursued for optimum results of geoscience applications. Optimum methods are presently not defined. Image registration is but one out of many routes to follow. There is no consensus that this registration is satisfactory from a point of view of economy and diagnostic power.

Apart from enhancing the interpretation, data synergisms or combinations of images from different sensors can help in training, study and demonstrations. An important criterion for the value of method of combined image interpretation is the ease with which the interpreter can use it.

6. Look Direction

Recommendation

The optimum look direction and angles between flight lines should be studied for various types of terrain.

Rationale

Studies have been performed on the interrelation between the look direction of a radar, the dominating orientation of surface topographic features, and the success of studying those features with radar (MacDonald, 1979). It is obvious that complete coverage of an area is desired. If terrain is very irregular, then an arrangement of flight lines must be found that results in a complete image of the broken terrain, including mountain slopes and valley bottoms. The optimum arrangement is defined by a combination of look directions and incidence angles for a certain terrain type. Clear conclusions can be drawn about the problem only when experimental work completes the presently only spotty knowledge.

7. Frequency/Polarization/Calibration

Recommendation

Available experimental data should be employed to study the effects of various radar system parameters on accuracy and on feature interpretability (control point identification).

Rationale

There are a number of radar system parameters such as frequency, polarization, and calibration which may have certain effect on the mapping performance. Although a great impact is not expected, there are no studies to confirm or reject this expectation.

8. Radar Interferometer

Recommendation

The available body of knowledge on radar interferometry to measure depression angles to objects should be reviewed and a cost/benefit analysis performed.

Rationale

Radar interferometry was developed in the early radar topographic mapping context to provide an on-line, automatic, 3-dimensional mapping capability. The echo-time measurement provided distance to objects; the interferometer

provided the angle to objects. The concept proved feasible, but performance was, at the time, not satisfactory for the purpose. However, in the context of extra terrestrial satellite radar mapping, and of an increased interest in stereo, a responsible analysis should include consideration of interferometry performance.

9. Type of Experiments

Recommendation

For the study and analysis of radar mapping performances, the following types of data are required:

Aircraft data to study parameters such as look-direction, resolutions, etc.

Satellite data, where short missions such as those with the Space Shuttle suffice.

Simulated data to study effects of incidence angles and look direction.

Radar images must be accompanied by collateral data, in particular by photography, to have a reference against which the radar can be evaluated.

Rationale

The studies that should be done to more fully understand radar performance for mapping cannot all be done with aircraft data. Effects of orbit stability and incidence angles on accuracy and stereo need satellite data and simulated images. The areas for test are not very critical and essentially need only to satisfy certain topographic criteria since accuracy is largely site-independent.

It is important first, to compare sensors to prove the value of radar and, second, to have, in an experimental environment, a source of data with higher performance so that the radar can be evaluated and better understood.

10. Possible Mapping Scales

Recommendation

The possible mapping scales for base maps must be defined on the basis of accuracy and interpretability performance of radar.

Rationale

Though analyses do not exist at present to evaluate the cost-benefit ratio for mapping with radar, the national map accuracy standards as used in the U. S. A. (see for example Leberl, 1979) can serve as one point of reference for geometric accuracy. However, although one may optimistically expect that 1:50,000 mapping would be possible with highest resolution radar taken from a highly stable platform, evidence is scarce to support this hope. This lack is particularly distinct with the quantitative or thematic aspects of mapping. Experiments would be required to evaluate the usefulness of radar for map revision whereby spatial resolution would be a key element. Other mapping methods,

based on aerial or satellite photography, will presumably not be affected by the availability of radar. But radar, through its all-weather capability, may represent a valuable extension of the mapping tools, provided that its capabilities and limitations are well understood in relation to a series of system parameters.

EXPLORATION GROUP RECOMMENDATIONS

The recommendations of the Exploration Group reflect the needs of a user community with a great variance in radar application experience. Some exploration groups have never used radar while many have used aircraft X-band radars for over 15 years. Petroleum exploration companies are paying up to \$8/km² for radar mapping, mostly for data over foreign areas. In tropical areas of the world, where cloud cover is present over most of the year, visible imaging systems are not as useful as radar. A radar system can be flown and data collected through the cloud cover in minimal time. All the commercially available systems now flying are X-band; for this reason industry photogeologists are most experienced at interpretation of low depression angle X-band images. These images are valuable not only because of the structural, land form type information they provide, although this information is most readily interpretable. There have been several studies in tropical areas which show X-band coverage to be particularly sensitive to changes in leaf geometry of different vegetation cover. In many cases these mappable vegetation units corresponded closely with the mapped geologic units. This was extremely useful because in most areas, rather than being able to identify drillable structures, the interpreter is trying to define the limits of a basin and its relationships with nearby igneous rocks and major plate tectonics induced structures. More often than not the photogeologist is identifying areas for further exploration effort, seismic surveys or sedimentation stratigraphy work.

The obvious next step in using radars for exploration for nonrenewable resources is to go beyond the simple qualitative approach, where map unit A is different from map unit B, to the ability to identify the map units from their unique backscatter response. In order to accomplish this we must initiate a research effort over selected test areas which will test depression angles, azimuth angles, resolution, frequency (at least X, C and L), and different polarizations (combinations of horizontal and vertical as well as circular). Using this methodology we should be able to define a system or systems which will best enable us to detect and map the desired geological parameters.

In effect the exploration community makes two basic recommendations: (1) to orbit an X-band system as soon as possible, and (2) develop a research plan to investigate multifrequency, multipolarization systems.

The recommendations were organized into four categories:

User services.

Image acquisition systems.

Image processing systems.

Basic research.

1. User Services. In that the explorationists are generally outside of the government, it was deemed necessary to provide a system whereby data from the different acquisition systems, now experimental and later operational, could be quickly available to this community.

- (1) Data accessibility. All data should be available through a single central agency such as Eros Data Center. It should be staffed and equipped to respond promptly to user inquiries.
- (2) Image format. Film should be the main product for distribution from optical processing systems while both film and computer-compatible tapes should be available of the digitally processed data.
- (3) User's manual. A user's manual such as was produced for Landsat would be very useful, especially if more information pertinent to the image interpreter was included.
- (4) Turnaround time. Rapid turnaround between acquisition and distribution of images is essential for monitoring dynamic phenomena such as sea ice and flooding but not as critical for other applications. It is essential that time between ordering and receiving data should be minimal.
- (5) Coverage. Global coverage is needed with initial priorities assigned to areas that are poorly covered by Landsat because of cloud cover and polar darkness. Repetitive coverage should exist at least seasonally to take advantage of changes in vegetation geometry which take place through the growing season. As much of the land surface is covered by vegetation and studies have shown that this cover is controlled by the underlying soil and rock type, we should maximize our capabilities of mapping vegetation cover.

2. Acquisition Systems. For both experimental and operational work in rock discrimination, which is the core of exploration, orbital acquisition systems are absolutely necessary. Small variation in look angle is necessary and can only be accomplished from an orbital platform. The desired parameters are as follows:

- (1) Wavelength. For research purposes X-, C-, and L-band wavelengths should be extensively studied. Very little data exists with comparable dynamic range and resolution. Available operational systems are at X-band and generally are good quality and resolution, but not comparable with the experimental C- and L-band systems flying on aircraft at this time.
- (2) Depression angle. Constraints inherent in orbital systems will probably have a strong influence over the available range of depression angles. Different angles are optimal for different topographies, and the best system should be variable angle system.
- (3) Polarization. Multiple polarization capability is a must for mapping ground cover effectively.

- (4) Image scale. Larger scale than Landsat, approx. 1:100,000.
- (5) Wide swath. Probably better than 50 km, although tradeoffs probably will be necessary with considerations of resolution and number of looks.
- (6) Spatial resolution. Should be as good or better than the thematic mapper, which is about 30 meters.
- (7) Stereo images. Desirable to enable effective mapping of landforms.
- (8) Dynamic range. Widest possible.
- (9) Altimeter. Desirable.
- (10) Constant and calibrated parameters. Should have good level of repeatability of results.
- (11) Supplemental non-radar images. Required to tie to other systems such as Landsat D for best ability to evaluate an area from an explorationist's standpoint.

3. Image Processing Systems. For considerations of quality of final image as well as its usefulness, special care must be taken in the processing stage to preserve the fidelity inherent in the system. For this reason digital processing is a must for future systems. In the evaluation stage it is recognized that optical processing might need to be used for the bulk of the data. In this case digital processing should be provided for selected areas to maximize information extraction.

4. Basic Research. The most important aspect of our research program should be to systematize our knowledge and understanding of radar backscatter cross section from different geologic and geomorphic surfaces. We must determine if there are characteristic geometries associated with different rock types and then design a radar system and geometry which will best detect and differentiate these characteristics.

Along these same lines we should better understand backscatter response from different vegetation types and the importance of frequency and polarization in leaf and branch geometry.

This research should be carried out in areas where there is extensive ground truth such as the Geosat test areas.

PRESENTED PAPERS

In order to establish a common understanding of the radar geology state-of-the-art, each workshop participant was requested to prepare and present a paper in his area of expertise. These papers were presented and discussed during the first three days of the workshop and constituted the foundation upon which the subsequent program recommendations were based. The presentations followed the sequence shown in Appendix B and are reproduced here in the same order and grouping. Four papers presented at the workshop by H. Masursky, R. Gelnett D. Krohn and B. Roberts are not included due to proprietary information contained therein or other reasons. The papers were independently reviewed for appropriateness and content by at least one person familiar with the subject. Modifications as required were made by the authors and then minor editing was performed by the JPL Documentation Section.

OVERVIEW PAPERS

Historical Sketch - Radar Geology
H. McDonald

Radar Geology: Technology and Program Overview
Frank T. Barath

HISTORICAL SKETCH - RADAR GEOLOGY

H. MacDonald
University of Arkansas
Department of Geology
Fayetteville, Arkansas

I. INTRODUCTION

Paul Harrison, Chairman of the Organizing Committee, requested that the keynote address provide a historical sketch of radar geology. He emphasized the need to reduce a large volume of information into a short review. The intent of my presentation therefore is to summarize briefly "how we got to where we are." Papers presented by the participants of this workshop will provide evidence of where we are, and some indication of the direction radar geology is going in the future.

II. RADAR GEOLOGY BEFORE SIDE-LOOKERS

In the early 1900's the United States and several European countries independently developed Plan Position Indicator (PPI) Radar for military applications. These circularly scanning devices provided a terrain format radiating in a circular fashion from beneath the aircraft. During World War II, radar operational techniques were developed to a high degree; after the war, however, the development of radar technology was somewhat decelerated. Dunlap (1946) was among the first authors to provide high-quality PPI radarscope photographs in the open literature after the war. These relatively high-resolution images of New York City, Washington, D.C. and Nantucket Island off the Massachusetts coast provided an early indication of nonmilitary uses of radar. Lt. H.P. Smith (1948) compared PPI presentations with existing charts of northwestern Greenland and noted that the radar-derived data far exceeded the terrain information from available maps. He submitted his report to the U.S. Geological Survey and subsequently other government agencies began to consider the potential of radar imagery for displaying terrain information (Scheps, 1962).

Among the first unclassified reports and open literature articles suggesting the use of radar images (PPI) for terrain-geologic studies were those of Hoffman (1954, 1958, 1960) and Feder (1957, 1959, 1960a). Hoffman's work related mostly to development of radar imagery interpretation keys, parallel to the recognition elements used in photo interpretation. Feder stressed the potential qualitative and quantitative uses of radar, and suggested that textures of surficial materials as well as subsurface soil and rock composition might be determined through image interpretation. Feder (1960b) completed an M.S. thesis, "Radar Geology," at the University of Buffalo, and although his initial research embraced only images from low-resolution PPI systems, he was one of the primary advocates of the potential application of radar interpretation to geologic investigations. Coincident with the declassification of PPI

radar images in the early 1950's was the development of complex navigational radars and sophisticated components required for the tracking of missiles and satellites. Although the concept of side-looking airborne radar (SLAR) systems had been known in the late 1940's, it was not until the 1950's that system components became available.

III. SLAR SYSTEM DEVELOPMENT

In an attempt to synthesize the history of SLAR development, I have selected for discussion only those systems that have had a relatively significant impact on radar geology. Leberl's (1978) recent informative summary article gives an insight to other geoscience applications of active microwave imaging systems, and Fenner and Sampsel (1977) provide an excellent up-to-date listing of available SLAR systems, regardless of application.

Side-looking radar development is best presented according to the two basic classes of systems: (1) real aperture or noncoherent SLAR and (2) synthetic aperture radar, SAR, which is a coherent airborne radar.

A. Real Aperture SLAR

During the mid to late 1950's Westinghouse, Texas Instruments, Motorola, and Goodyear were the primary developers of real aperture SLAR systems, mainly with Air Force and Army funding. Imagery from such systems as the AN/APQ-56 (Ka-band) and AN/APQ-69 (X-band) provided some of the quality data first examined by geologists in the early 1960's. In 1961 the Army initiated a program to develop and fabricate a one-of-a-kind SLAR imaging system which also incorporated an interferometer to be used for topographic contouring (Fisher, 1975). This Westinghouse Ka-band system (AN/APQ-97) was modified in 1964 to accommodate a cross-polarized channel. The AN/APS-94 (X-band) series of radars remained under the domain of the military until the early 1970's when Grumman Aircraft Corporation, and later Motorola Remote Sensing Inc., refurbished these systems for commercial use.

B. Synthetic Aperture Radars

While SLAR developments were taking place, parallel programs were conducted for synthetic aperture radars (SAR) or coherent SLAR. The early history of SAR is well documented in an article by Sherwin et al., (1962). Fischer (1975) summarized the development programs associated with SAR systems up to 1975, and Leberl (1978) provides a more recent historical review with an international perspective. According to Fischer, the early (1950's-60's) SAR work was carried out primarily by four organizations: Goodyear Aircraft Corporation, Philco Corporation, The Control Systems Laboratory of the University of Illinois, and the Willow Run Laboratories of the University of Michigan. Several experimental SAR systems developed since the late 1950's have provided imagery for geologic investigations. They include the AN/UPD-1 used in the "Project Michigan" effort at the University of Michigan's Willow Run Laboratories developed under the auspices of the U.S. Army Signal Corps, the AN/APS-73 assembled by Goodyear, the Philco-Ford DPD-2, the Naval Research Labs (NRL) four frequency radar, the ERIM test bed system which ultimately provided simultaneous X- and L-band SAR images with two polarizations (Inkster et al., 1979) and the JPL X- and L-band systems (Barath, 1977). The first truly operational (military) SAR system was the Goodyear AN/APQ-102. In early 1971 this X-band imager was modified to become the

resource-oriented GEMS system when Goodyear Aerospace joined with Aero Service Corporation to begin offering a commercial radar imaging service.

Recently the ERIM X-L SAR has been upgraded through a major hardware development program, and is now known as the SAR-580 Facility. This facility is maintained through mutual agreement with the Canada Centre for Remote Sensing (CCRS), INTERA Environmental Consultants Ltd., and the Environmental Research Institute of Michigan (ERIM). An on-board processor and display allow SAR image quality and site coverage verification in real-time; digital data recording and internal calibration references provide unprecedented reliability in quantitative signature measurement programs (Inkster et al., 1979).

The most recent addition to operational SAR systems is a modified AN/APQ-102 X-band system mounted in the NASA WB-57 aircraft at the NASA/Johnson Space Center, Houston, Texas. Implementation of a C-band SAR for operation in the WB-57 has recently been initiated at JSC (Rouse, 1977).

IV. RADAR GEOLOGY AND SIDE-LOOKERS

A. Geoscience Activity Early 1960's

Limited declassification of SLAR imagery in 1959 and the early 1960's allowed the geoscience potential of such systems to be discussed openly in the literature (Leonardo, 1959; Perry, 1960; Claveloux, 1960; Rydstrom, 1961; Fischer, 1963). Early studies conducted by the Autometric Corporation were oriented toward engineering geology investigations, and a report by Bienvenu and Pascucci (1962) summarizes some of the initial phases of applied research using SLAR imagery.

In the summer of 1963, NASA retained Dr. Peter Badgley, a geologist and professor at the Colorado School of Mines, to provide advice on the development of sensors for mapping the lunar surface from orbit (Lintz and Simonett, 1976). Access to many classified military reconnaissance imaging systems convinced Badgley that SLAR imagers had definite applicability for lunar mapping.

In 1964, NASA's Manned Space Science Division initiated its Applications Aircraft Research Program, conceived as an adjunct to the development of sensors for mapping the lunar surface from orbit. The sensors were to be developed for use during the Apollo Program and tested in earth orbit by observing designated terrain features alongside those features being observed as lunar analog test sites. Initially the Applications Aircraft Research Program developed around four major "instrumentation teams," and for the United States, was one of the first attempts to bring together groups of civilian users and instrumentation specialists (Matthews, 1975, p. 22). The radar team (active microwave) was headed by R.K. Moore at the University of Kansas. The direction of the University of Kansas effort was to evaluate geoscience applications of imaging radars, with D.S. Simonett in geography and L.F. Dellwig in geology insuring that applications received emphasis rather than system engineering.

Necessary to the lunar mapping effort was the selection of terrestrial geologic test sites to be used in evaluating both lunar and terrestrial applications of remote sensors. It is interesting to note that some of the radar questions NASA's Manned Space Science Division was trying to answer 15 years ago, are still being addressed today. For example, how accurately can active microwave sensors predict the surface roughness and detailed topography of planetary surfaces (Badgley, 1964)?

One of the first comprehensive unclassified investigations directed solely to terrestrial geologic analysis was "An Evaluation of Geoscience Applications of Side-Looking Airborne Mapping Radar," compiled by the Autometric Facility of the Raytheon Company (Simons and Beccasio, 1964). The authors generally concluded that experienced photogeologists can adapt easily to the use of monoscopic SLAR imagery in making terrain evaluations. Among the many promising fields of application for side-looking airborne radar systems, they cited reconnaissance of natural resources and preliminary economic evaluations in underdeveloped countries as potentially the most rewarding. The SLAR imagery illustrated and annotated in this report originated from the declassified Ka-band, AN/APQ-56 system.

Pierson et al. (1964) provided a general summary of the application of radar imagery to geologic interpretation up to 1964. Although Cameron (1965) did not use SLAR imagery in his study, he reported that radar scope photographs (PPI) of the Gaspé Peninsula revealed linears and patterns suggesting several new geologic features including two unmapped thrust faults cutting across fold trends.

One of the milestones and major accomplishments supporting radar geology in the mid-1960's was the geoscientifically oriented report on SLAR imagery interpretation released by NASA in 1965 (Beatty et al., 1965). This report summarizes the civilian state-of-the-art of radar imagery interpretation at that time, and provides both text and numerous images obtained from a wide variety of SLAR systems. The publication of this report coincidentally with NASA's increasing earth resources involvement provided impetus for a review of security classification procedures for military remote sensors that might have earth resource applications. Declassifications eventually provided geologists access to several military remote sensor systems and data sources.

B. Radar Geology Development, Late 1960's and Early 1970's

During 1965-1966, Westinghouse under contract to NASA and USGS, and with cooperation of the U.S. Army Electronics Command, imaged a large number of SLAR flight lines (about 500,000 km²) in the continental United States. This Ka-band imagery (AN/APQ-97), recorded in the like- and cross-polarized modes, is considered by many geologists to be some of the finest quality SLAR ever produced for civilian use. The imagery was made available to a limited number of institutions including the University of Kansas at Lawrence and the University of California at Berkeley as well as several federal agencies, including the USGS and NASA. Dellwig et al. (1966) published one of the first examples of the Westinghouse imagery and provided an insight to the interpretation of regional geologic features from SLAR systems. Using like- and cross-polarized image comparisons from this same system, Dellwig and Moore (1966) reported on the geologic value of such data in volcanic terrain. During this same time period, Goodyear Aircraft Corporation was conducting investigations on extracting mapping detail from radar presentations, analyzing earth-material radar return intensity for possible applications in lunar surface mapping, and most important, developing a method for interpreting local geology from radar imagery (Rystrom, 1966). Levine et al. (1966) also provided an insight to interpretation of geologic features from radar as well as an excellent discussion of SLAR theory and radargrammetric techniques.

One of the major achievements in radar geology was the completion of Project RAMP, Radar Mapping of Panama, in 1967. The Westinghouse AN/APQ-97 system provided multiple-look SLAP imagery of 17,000 km² in Panama's Darien Province. Among the federal agencies involved in this program were the Corps of Engineers, U.S. Air Force Southern Command, U.S. Army Electronics Command, and the U.S. Army Engineer Topographic Lab. Darien Province was selected as a test site because the major part of the province had never been mapped and the nearly perpetual cloud cover allowed evaluation of performance characteristics of state-of-the-art radar equipment in an operational environment.

Geologic interpretation of the Westinghouse imagery obtained from NASA-supported projects in the continental United States, as well as the Panama imagery, provided several reports during the mid to late 1960's. Unfortunately, during these formative years for radar geology, experimental effort and research support were lacking in certain key areas. For example, radar system calibration was almost nonexistent. Imagery was often provided to interpreters months or even years after it was obtained, and consequently data interpretation could not be supported by collateral observations or measurements. Because of the complex nature of the interaction of microwaves and surface parameters to be measured, results from single frequencies were not adequate. Probably most important from a geologist's point of view, was the fact that quality radar imagery was not generally available to a significant number of scientists. In the majority of cases, geologists were asked to "do what they could" with the data provided. Of necessity, geologists used an empirical method for interpreting radar imagery and developing geologic models. The geologic models devised by these interpreters were not unlike the three-dimensional concept achieved in the field, where outcrop observations provided information for geologic maps of the surface (plan view) and structural cross-sections of the subsurface. Because the radar imagery allowed geologists to analyze systematically the visual pattern elements of terrain (drainage, vegetation, landforms, etc.) for geologic significance, geologic models were often rapidly developed. Model implementation usually provided the geologist with an insight to the three-dimensional geologic environment, i.e., inference about landform type and origin, rock characteristics, and structural complexity (Taranik and Trautwein, 1977).

Because of the total imbalance between funding for data acquisition and funding for data analysis, many geologic investigations were applications-oriented. The empirical method of processing observational information provided satisfactory results in a variety of geologic terrains. Some of the capabilities and limitations defined in these early studies established the framework for radar geologic remote sensing. Summary bibliographies of the early reports are provided by Walters (1968) and Barr (1969, p. 26-36). In the early 1970's evaluation of the Westinghouse imagery and the 1967-1968 vintage Panama imagery was continuing. In addition the ERIM multifrequency system and JPL L-band system were being evaluated for geologic analysis.

Radar bibliographies, including citations on radar geology up to 1975, are available in three different sources: Bryan (1973), Moore et al. (1974) and Dellwig et al. (1975). Sabins (1976) summarizes published geologic interpretations of radar imagery and presents author conclusions in a table format.

V. EVOLUTION OF COMMERCIAL RADAR MAPPING

Although the Westinghouse AN/APQ-97 SLAR had been operated in a commercial mode prior to geologic evaluation of the Project RAMP data, the success of the Panama project during 1967-1968 was the primary stimulus that initiated interest in commercial radar mapping. The early 1970's were especially significant for large-area commercial radar mapping and for radar geology. In late 1971, for example, the entire country of Nicaragua was surveyed by the Westinghouse SLAR for the production of a 47-sheet sequence of 1:100,000-scale mosaics. Subsequent geologic interpretation was carried out by Hunting Geology and Geophysics Ltd. (Martin-Kaye, 1973).

The most impressive radar mapping program ever conducted by any radar system was Aero Service/Goodyear RADAM Project (RADAR of the AMazon). The radar survey started in 1971, and was initially intended to cover only 1.5 million km² of the Amazon Basin. However, eventually the entire country of Brazil was imaged, an area in excess of 8.5 million km². Worthy of note is the fact that a large part of the Brazilian mapping project area is outside the cloud-covered equatorial rain forest. Airborne radar was selected over other sensors because of the distinct advantages to be gained in both time and quality of information available for producing meaningful maps and interpreting data. Significantly, Project RADAM proved to be cost effective; i.e., side-looking radar was less expensive to obtain than aerial photography where considerable standby time would be required to obtain complete-coverage photography (Lintz and Simonett, p. 6, 1976).

Westinghouse terminated commercial operation in 1973, and at about the same time the Grumman Aircraft Corp. entered the commercial radar imaging market for a brief period. In late 1974 Motorola Aerial Remote Sensing Inc. (MARS) initiated SLAR radar mapping service and they along with Aero Service/Goodyear provided radar for geologic mapping in parts of South America, Central America, Southeast Asia, Africa, and of course the United States.

The ERIM-Canada SAR-580 facility has been flown in support of Canada's surveillance requirements program and since July 1978 has collected in excess of 200,000 km² of multichannel imagery (Inkster et al., 1979). Because this service is just being established, its availability and cost are not yet well defined.

VI. NASA ACTIVE MICROWAVE PROGRAMS - 1970's

Despite an encouraging beginning in the mid-1960's, NASA largely ignored the microwave remote sensing field after the approval of ERTS-A (Landsat) in 1967. Until the early 1970's, it was difficult to discern any unified approach to either the design or use of either aircraft or spaceborne radar. The impact of the Landsat success, of course, has been global. Most nations have received selected frames of Landsat imagery and, because of relatively low cost and wide availability, several countries have obtained complete coverage on a global basis. The U.S. Government and the United Nations have both promoted the acquisition and the use of Landsat as an economic tool among developing nations.

Finally in 1973, imaging radars began to attract renewed interest with the conception of Seasat, and in 1974 the Johnson Space Center sponsored the Active Microwave Workshop (Matthews, 1975), which served to launch an accelerated

microwave applications research effort. Many of the recommendations from this workshop were implemented into the NASA program plans at Headquarters level and formed the basis for development of the Objectives of Microwave Earth Observations Remote Sensing Program.

These objectives were refined in a series of events including annual microwave research program reviews at NASA Headquarters. In a follow-up to the 1974 workshop, a Space Program Imaging Radar (SPIR) Study Group under the direction of D.S. Simonett attempted to define space radar applications. The report released by this group (Simonett, 1976) is a review of needs, applications, user support, and empirical research and theoretical studies with imaging radars.

The 1976 Active Microwave Users Workshop (Matthews, 1978) was designed to provide a sharp focus on microwave applications and specific guidelines for developing and implementing a plan to establish the measurement potential of active microwave imaging sensors. The Mineral and Energy Resources and Geologic Applications Group of this workshop addressed the limited understanding of geologic information from multiparameter imaging radars. In addition, this group identified and prioritized the information needs, and designed a very detailed research program which included test sites, ground based and aircraft sensor needs, measurements desired, schedules, and approximate costs. The program plan progressed from the present state of knowledge through the steps necessary to obtain multiparameter space radars for geologic exploration. Also included in the tasks addressed by this group was the design of potential land applications of Seasat data and imaging radar data processing system options.

In 1977 the National Research Council's Committee on Remote Sensing Programs for Earth Resource Surveys completed a review of a proposed Microwave Remote Sensing Program Five Year Technical Plan which was under consideration by the Office of Applications in NASA (Anderson, 1977). Among the Committee's conclusions was that an adequate experimental data base was available to support a single frequency, single polarization radar for geological exploration as a shuttle experiment. The Committee did not feel that an adequate experimental data base was available to support the initial development of a multifrequency, multipolarization radar for soil moisture measurements and vegetation or crop classification purposes. The message for geologists should have been clear. Establish your own geologically dedicated microwave program!

In August of 1977 NASA approved SIR-A, the first phase of the Spaceborne Imaging Radar Program for earth resource sensing (Elachi, 1977). It will consist of reflaying the Seasat-A L-band SAR (with minor modifications) aboard the second Shuttle orbital flight test (OFT-2), now optimistically scheduled for launch in late 1980. The prime objective of the SIR-A experiment is to evaluate the potential and demonstrate the applicability of spaceborne imaging radars as tools for geologic exploration in general, and mineral exploration, petroleum exploration, and fault mapping in particular. Finally, someone has taken the initiative to establish a geologically dedicated radar experiment from space.

At the third Microwave Remote Sensing Symposium/Workshop held in Houston, Texas, December 6-9, 1977, 32 invited presentations gave a concise overview of nearly all of the ongoing NASA-sponsored microwave remote sensing research projects (Rouse, 1977a). A two-day structured workshop followed the symposium to recommend immediate goals and priorities for research in several discipline areas: Water Resources, Vegetation Resources, Geologic Applications, and

Oceanographic Applications and Technology. It was the general consensus of participants that acquisition of orbital active microwave image data is a critical step in developing an effective global remote sensing capability, and support for the development of a multifrequency SIR-B system was acknowledged. The Statement of Goal by the Geologic Applications Panel was, "Develop an adequate data base of aircraft and orbital radar imagery and technology to allow the user community to select the optimum configuration for an operational earth orbital radar system" (Rouse, 1977b).

The primary application area was the identification and mapping of surface structural/tectonic features for energy and resource exploration, refinement of earthquake hazard maps, structural mapping for potential nuclear power plant sites and dam sites. The secondary application area was the identification and mapping of surface materials for improved energy and resource exploration, and for construction and engineering purposes.

In January 1978, the SPIR Study Group released a report on the second phase of its effort. This study, "Active Microwave Applications Research and Development Plan" (Simonett, 1978), also provided guidelines for research on multiparameter radar systems for geologic applications. The 1978 report refined the earlier work by the Study Group (Simonett, 1976), and further emphasized the need for active microwave image measurements from orbital altitudes. During the same time period, the Johnson Space Center and the Jet Propulsion Laboratory jointly proposed a research and development program for a multiparameter active microwave facility on the Shuttle. The facility received the title of Spaceborne Imaging Radar--Phase B and C, denoted SIR B/C. The most recent microwave workshop was held in 1978 for the purpose of reviewing the JSC/JPL proposal (Rouse, 1978). The panel members of the Shuttle Active Microwave Facility Review recommended that:

- (1) Active microwave imagery of economically significant areas of the globe be obtained using the Shuttle.
- (2) SIR-B include an X-band imager with incident angle capability of at least 70°, spatial resolution of 30 m (comparable with Landsat D), "five-look" spatial averaging, and a swath of approximately 50 km.
- (3) Research programs using ground-based and aircraft sensor data be initiated to improve the understanding and the utility of multiparameter active microwave imaging data in geologic applications.
- (4) A geology experiments program using Seasat imaging radar measurements, and expanded SIR-A experiments, be initiated.

VII. RESEARCH IN RADAR GEOLOGY TODAY

Most of the proven benefits to date from radar remote sensing have arisen from geologic interpretation for nonrenewable resources. Despite the apparent success in practicality, radar geologists generally have been unsuccessful in establishing a coordinated experimental program which would provide a scientific basis for exploiting the sensitivity of radar reradiation to various aspects of the geologic environment. Individually, radar geologists have managed to convincingly support radar's practical application, but as a radar geology

community we have failed to emphasize the fact that little research has been devoted to the development of optimum specifications for the radar geology sensor or for optimum strategies for geologic information extraction from radar data. Not surprisingly, advances in applied radar geologic research, i.e., development of techniques that will aid in the mapping of structural/tectonic features, have been spearheaded by the private sector. Examples include Wide Dynamic Range Color Radar, Landsat/Radar Combinations (Graham, 1977), and terrain enhancement techniques (Gelnett, 1977).

During the past five years, though NASA has resumed a lead role in active microwave development by supporting microwave vegetation and soil moisture basic research, experimental effort has been lacking in several specific areas for radar geology. Obviously, ground-based measurements with varying frequency, polarization, and incidence angle in vegetation and soil moisture studies will contribute to the understanding of microwave terrain interaction. However, other basic research is needed - an experimental effort dedicated specifically to recognition of area extensive features common to radar geology has been lacking in a number of areas. Major questions remain unanswered.

1. What Spatial Resolution Should Be Provided for Optimum Data Extraction? At present there is no general agreement or experimentation on the question of required resolution vs a specific radar geology application.

2. What Spectral Regions Are Optimal for Radar Geology? Although certain geologic applications may appear somewhat wavelength-dependent, good multifrequency imagery has been exceedingly scarce. Most fine resolution imaging radars to date operated at approximately 0.8, 3, 25 cm for radar geology. Wavelengths outside this range might be very useful for some terrain environments. In those areas of the world where there are no mappable outcrops and no easily discernible landforms, geomorphic evidence such as drainage, subtle slope change, or vegetation is used in developing geologic models. Maximum sensitivity to vegetation, provided by the shortest wavelength practical, would be useful in such places. Conversely, the loss of sensitivity to some terrain vegetation at longer wavelengths might provide enhancement of topographically expressed large-scale structural features. The development of geologic models for a multispectral approach to geologic exploration to exploit the potential information content of radar backscatter for surface rock discrimination is now receiving attention (Daily et al., 1978).

3. What Can Polarization Diversity Provide the Radar Geologist? Because depolarization of microwave energy is strongly associated with terrain geometry, at a wavelength scale, polarization provides potential in the multispectral approach to radar geology. Blanchard (1977) has recently investigated volumetric effects in the depolarization of electromagnetic waves scattered from rough surfaces, and has shown the existence of a subsurface (volume) depolarization mechanism. Definitive research to establish the best polarization for radar geology is almost totally lacking.

4. What Calibration Accuracy Is Required for Radar Geology? Machine processing with the potential for qualitative analysis of data and use of sophisticated algorithms will require amplitude calibration of radar signal return. In some geologic applications good relative amplitude calibration will suffice, but in others absolute calibration will be of importance.

5. What is the Potential Information Content of Radar Backscatter Data for Rock Type Discrimination? The state of knowledge about use of radar backscatter for geologic mapping, even from relatively flat terrain, is not well defined. In the microwave portion of the spectrum, the chemical nature of the material serves largely to establish the conductivity and the dielectric constant of the substance; however, these parameters do not provide significant spectral response because any fine structure in the reradiation variation is primarily a consequence of the geometric structure of the scatterer. Current research into radar discrimination of surface materials through their diverse size-frequency distribution and radar cross-section is encouraging (Schaber et al., 1976; Daily et al., 1978); however, the regions examined have limited soil moisture and vegetation cover. Although lithologic mapping is not expected to be possible with radar backscatter data by itself, the derived information could complement data from other remote sensors. The key question to be answered in assessing the role of a radar for multispectral geologic applications is whether the terrain scattering properties which are wavelength-dependent are sufficiently systematic and unique to yield reliable classification.

6. What Is the Role of Radar in Multiple Data Source Analysis? Where nature is not so obliging as to provide the desired simplicity and uniformity of "conditions" that would permit the ready application of empirical methods of developing geologic models, interpreting the geologic significance of remote sensor data will depend largely on the interpreter's ability to perform interactive analysis. Machine-aided human analysis necessitates a merge of remote sensor, surface, and geophysical information. This multiple data source approach to geologic remote sensing is now being supported by NASA (Kahle and Stewart, 1977). The role of radar in interactive analysis is yet to be defined.

7. What Is the Role of Radar Image Simulation in Geologic Modeling? There is every reason to believe that geologists will use experimental spacecraft radar imagery (for example, SIR-A) predominantly for structural/tectonic mapping where the enhancement and detection of terrain geometry are of primary concern; however, the ability to model the complex geometrical and scattering phenomena which allow the characteristic terrain expression of geologic features to be faithfully reproduced in an image has not been adequately addressed. Because of the limited number of multiparameter radar systems available for geologically dedicated research programs, definitive studies for optimizing complete radar remote sensing systems and evolving optimum strategies for information extraction from radar data have not been conducted. Radar image simulation (Holtzman, 1978) allows superposition of a wide range of empirical and theoretical scattering cross-sections on digital images of terrain models. Complete parametric (system and terrain) sensitivity analysis could be conducted for each model. Analysis of geologic terrain models by image simulation may be a cost-effective method which allows modeling of terrain and system variation, prediction of results, and definition of optimum sensor parameters.

VIII. CONCLUSIONS

The evolution of radar geology has been most significant during the last three decades. In the 1950's the use of imaging radars was mostly the privilege of the military, but the 1960's were highlighted by the development and declassification of SLAR systems. The introduction of the geologic community to high-quality radar images in the mid-1960's led to the definition of capabilities and limitations and the establishment of a framework for radar geology. The

1970's have been noteworthy because of the availability of commercial SLAR imagers, renewed involvement of NASA in microwave earth resources applications, and of course the approval of the SIR-A experiment.

Radar has an important role in geologic remote sensing from aircraft and satellite. Much research is needed to define optimum specifications for the radar sensor and optimum strategies for information extraction from radar data, even though enough is known now to make a geologically dedicated satellite immediately useful.

Space-derived radar images will become as commonly used in geologic investigations as have Landsat images. However, timely development of this application depends on the general availability of good quality radar images to a significant number of scientists who can learn how best to employ these data, much as geologists learned to use Landsat images. It also depends on the development of the scientific basis for exploiting the sensitivity of radar signals to various aspects of geologic terrain. Currently available radars and radar research programs can provide some insight into these matters, but probably will not suffice to settle the key questions fully. A coordinated experimental program is needed to supply fundamental data for geologically dedicated space systems.

ACKNOWLEDGEMENT

Part of the section of this report, Research in Radar Geology Today, is modeled after a theme provided in an unpublished paper "Multispectral Radar Remote Sensing" by Dr. L.J. Porcello, Environmental Research Institute of Michigan.

ADDENDUM

Although not optimum for terrestrial applications, the Apollo Lunar Sounder Experiment (ALSE) flown on the Apollo 17 mission provided a good test of advanced orbital planetary radar concepts (Matthews, 1975).

REFERENCES

1. Anderson, A. G., ed., 1977, Microwave Remote Sensing from Space for Earth Resource Surveys, Committee on Remote Sensing Programs for Earth Resource Surveys, National Academy of Sciences, Washington, D.C., 139 pages.
2. Badgley, P.C., 1964, The Applications of Remote Sensors in Planetary Exploration: Third Symposium on Remote Sensing of Environment, Proc., Univ. Michigan, Ann Arbor, pp. 9-28.
3. Barath, F.T., 1977, The JPL SAR Program: Microwave Remote Sensing Symposium Proc., NASA/JSC, Houston, Texas, Dec. 1977, pp. 14-15.
4. Barr, D.J., 1969, Use of Side-Looking Airborne Radar Imagery for Engineering Soil Studies: Tech. Rept. 46-TR, Project 4A623501A854, Geographic Sciences Div., U.S. Army Engineer Topographic Lab, Fort Belvoir, Virginia, 156 pages.
5. Beatty, F.D., and Others, 1965, Geoscience Potentials of Side-Looking Radar, Raytheon Autometric Corp., Vol. 1, 99 pages; Vol. 2, 114 pages.
6. Bienvenu, L., and R. Pascucci, 1962, Engineering Geology from Side-Looking Radar Records: Autometric Corporation, Alexandria, Virginia, restricted circulation, 13 pages.
7. Blanchard, A.W., 1977, Volumetric Effects in the Depolarization of Electromagnetic Waves Scattered from Rough Surfaces, Remote Sensing Center Tech. Rept. RSC-83, Texas A&M Univ., College Station, Texas, 190 pages.
8. Bryan, M.L., 1973, Radar Remote Sensing for Geosciences: An Annotated and Tutorial Bibliography, ERIM, Univ. Michigan, Ann Arbor, 298 pages.
9. Cameron, H.L., 1965, Radar as a Surveying Instrument in Hydrology and Geology, Third Symposium on Remote Sensing of Environment, Proc., Univ. Michigan, Ann Arbor, pp. 441-452.
10. Claveloux, B.A., 1960, Sketching Projector for Side-Looking Radar Photography, Photogramm. Engr., Vol. 26, No. 4, pp. 644-646.
11. Dailey, M., C. Elachi, T. Farr, W. Stromberg, S. Williams, and G. Schaber, 1978, Application of Multispectral Radar and LANDSAT Imagery to Geologic Mapping in Death Valley, Jet Propulsion Laboratory Publication 78-19, Pasadena, California, 59 pages.
12. Dellwig, L.F., J.N. Kirk, and R.L. Walters, 1966, The Potential of Low-Resolution Radar Imagery in Regional Geologic Studies, Jour. Geophys. Research, Vol. 71, No. 20, pp. 4995-4998.
13. _____, and R.K. Moore, 1966, The Geologic Value of Simultaneously Produced Like- and Cross-Polarized Radar Imagery, J. Geophys. Res., Vol. 71, pp. 3597-3601.
14. _____, B.C. Hanson, N.E. Hardy, P.L. Hulen, J.R. McCauley and R.K. Moore, 1975, Use of Radar Images in Terrain Analysis: An Annotated Bibliography, U.S. Army Engineer Topograph. Lab, ETL Rept. 0024, Fort Belvoir, Virginia, 318 pages.

15. Dunlap, O.E., 1946, Radar, What It Is and How It Works: Harper and Brothers Publishers, New York, N.Y., 208 pages.
16. Elachi, C., 1977, All-Weather Surface Observation Experiment (SIR-A) on the Shuttle OFT-2 Flight, Proc. Microwave Remote Sensing Symposium, NASA/JSC, Dec., 1977, pp. 118-128.
17. Feder, A.M., 1957, The Application of Radar in Geologic Exploration, Bell Aircraft Corp. Rept., Buffalo, N.Y.
18. _____, 1959, Radar as a Terrain-Analysing Device, Geol. Soc. Amer. Bull., Vol. 70, No. 12, pp. 1804-1805.
19. _____, 1960a, Interpreting Natural Terrain from Radar Displays, Photogramm. Eng., Vol. 26, No. 4, pp. 618-630.
20. _____, 1960b, Radar Geology, M.A. Thesis, Dept. Geol., Univ. of Buffalo, N.Y., 80 pages.
21. Fenner, R.G. and T.K. Sampsel, 1977, Microwave Sensors for Applications Research An Overview, Microwave Remote Sensing Symposium, NASA/JSC, Dec. 1977, Houston, Texas, pp. 268-310.
22. Fischer, W., 1963, An Application of Radar to Geological Interpretation, First Symposium on Remote Sensing of Environment Proc., (Feb. 1962), Univ. Michigan, Ann Arbor, pp. 469-493.
23. _____, 1975, History of Remote Sensing, in Reeves, R.G. ed., Manual of Remote Sensing: Ch. 2, pp. 27-50, Amer. Soc. Photogramm., Falls Church, Virginia.
24. Gelnett, R.H., 1977, The Importance of Look Direction and Depression Angle in Geologic Applications of SLAR, Microwave Remote Sensing Symp. Proc., NASA/JSC, Dec. 1977, pp. 142-154.
25. Graham, L.C., 1977, Synthetic Aperture Radar Geologic Interpretation Techniques, in Microwave Remote Sensing Symposium, NASA/JSC, Dec. 1977, pp. 129-140.
26. Hoffman, P., 1954, Interpretation of Radar Scope Photography, Photogramm. Engr., Vol. 20, No. 3, pp. 406-411.
27. _____, 1958, Photogrammetric Applications of Radar Scope Photographs, Photogramm. Engr., Vol. 24, No. 5, pp. 756-764.
28. _____, 1960, Progress and Problems in Radar Photo Interpretation, Photogramm. Engr., Vol. 26, No. 4, pp. 612-618.
29. Holtzman, J.C., V.S. Frost, J.L. Abbott, and V.H. Kaupp, 1978, Radar Image Simulation, IEEE Trans. Geosci. Electron., Vol. GE-16, No. 4, pp. 296-303.
30. Inkster, D.R., R.K. Raney, and R.F. Rawson, 1979, State of the Art in Airborne Imaging Radar, 13th Int'l Symp. on Remote Sensing of Envir., Univ. Michigan, Ann Arbor, in press, (Abstract in Program Proc., p. 43).

31. Kahle, A.B., and H.E. Stewart, 1977, A Multiple-Data-Source-Approach to Remote Sensing for Mineral Exploration: A Status Report, in Microwave Remote Sensing Symposium, Rouse, J.W. Jr. ed., NASA/JSC, pp. 103-107.
32. Leberl, F., 1978, Current Status and Perspectives of Active Microwave Imaging for Geoscience Application, ITC Journal, pp. 167-190.
33. Leonardo, E.S., 1959, An Application of Photogrammetry to Radar Research Studies, Photogramm. Engr., Vol. 25, No. 3, pp. 376-380.
34. Levine, D., C. Colbert, L.C. Graham, P.H. Crane, and B.B. Scheps, 1966, Combinations of Photogrammetric and Radargrammetric Techniques, in Manual of Photogrammetry, Levine, D., Author-Editor, Vol. II, Ch. XXI, pp. 1003-1048.
35. Lintz, J. Jr., and D.S. Simonett, Eds., 1976, Remote Sensing of Environment, Addison Wesley Pub. Co., Reading, Massachusetts, 649 pages.
36. Martin-Kaye, P.H.A., 1973, Geology of Eastern and Central Nicaragua-Interpretation of Side-Looking Radar Imagery, Amer. Assoc. Petroleum Geologists Bull. (Abstract), Vol. 57, No. 4, p. 792.
37. Matthews, R.E., 1975, Active Microwave Workshop Report, NASA SP-376, NASA/JSC, July 1974, 502 pages.
38. Matthews, R.E., 1978, Active Microwave Users Workshop Report, NASA Conference Publication 2030, NASA/JSC, Aug. 1976, 285 pages.
39. Moore, R.K., L.F. Dellwig, S.K. Parashar, N.E. Hardy and M.A. Soule, 1974, Applications of Imaging Radars, A Bibliography, Remote Sensing Lab Rept. 265-2, Univ. Kansas, Lawrence, Kansas, 237 pages.
40. National Academy of Sciences, 1977, Microwave Remote Sensing from Space for Earth Resource Surveys, National Research Council, Washington, D.C., 141 pages (NASA CR-157891).
41. Perry, W., 1960, Scouting Battlefield of Tomorrow, Electronics, Vol. 33, No. 47, pp. 40-41.
42. Pierson, W.J., B.B. Scheps and D.S. Simonett, 1965, Some Applications of Radar Return Data to the Study of Terrestrial and Oceanic Phenomena, Proc. Third Goddard Memorial Symp. on Scientific Experiments for Manned Orbital Flight, Washington, D.C., pp. 87-137.
43. Rouse, J.W., Jr., ed., 1977a, Microwave Remote Sensing Symposium, NASA/JSC, Houston, Texas, Dec. 1977, 310 pages.
44. _____, 1977b, Microwave Remote Sensing Workshop Report, NASA/JSC, Dec. 1977, 20 pages.
45. _____, 1978, Shuttle Active Microwave Facility Review, NASA Headquarters, Washington, D.C., June 1978, 33 pages.
46. Rydstrom, H.O., 1961, Geological Map of an Area in Southeastern Arizona Prepared from Radar Photography, Goodyear Aerospace Corp., Rept. AAP-13730, 6 pages.

47. _____, 1966, Interpreting Local Geology from Radar Imagery, Fourth Symposium on Remote Sensing of Environment, Proc., Univ. Mich., Ann Arbor, pp. 193-201.
48. Sabins, F.F., 1976, Geologic Applications of Remote Sensing, in Lintz, J. Jr. and D.S. Simonett eds., Remote Sensing of Environment, Addison-Wesley Publishing Co., Reading, Mass., pp. 508-579.
49. Schaber, G.C., G.L. Berlin, and W.E. Brown, Jr., 1976, Variations in Surface Roughness Within Death Valley, California: Geologic Evaluation of 25-cm on Wavelength Radar Images, Geol. Soc. Amer. Bull., Vol. 87, pp. 29-41.
50. Scheps, B.B., 1962, The History of Radar Geology, First Symp. on Remote Sensing of Environ. Proc., Univ. Michigan, Ann Arbor, pp. 79-81.
51. Sherwin, C.W., J.P. Ruina, and R.D. Rawcliffe, 1962, Some Early Developments in Synthetic Aperture Radar Systems, IRE Trans. on Military Electronics, MIL-6, No. 2, pp. 111-115.
52. Simonett, D.S., Ed., 1976, Applications Review for a Space Program Imaging Radar, Santa Barbara Remote Sensing Unit, SBRSU Tech. Rept. 1, Univ. California, Santa Barbara, NASA/JSC Contract NAS 9-14816, 217 pages.
53. _____, 1978, Active Microwave Applications Research and Development Plan, Santa Barbara Remote Sensing Unit, SBRSU Tech. Rept. 2, Univ. California, Santa Barbara, NASA/JSC Contract NAS 9-14816.
54. Simons, J.H. and A.D. Beccasio, 1964, An Evaluation of Geoscience Applications of Side-Looking Airborne Mapping Radar, Autometric Facility, Raytheon Co., 70 pages.
55. Smith, H.P. Jr., 1948, Mapping by Radar - The Procedures and Possibilities of a New and Revolutionary Method of Mapping and Charting: U.S.A.F., Randolph Field, Texas.
56. Taranik, J.V. and C.M. Trautwein, 1977, Integration of Geological Remote Sensing Techniques in Subsurface Analysis, in Subsurface Geology, LeRoy, L.W., D.O. LeRoy, and J.W. Raese, Eds., Colorado School Mines, Boulder, CO, pp. 767-787.
57. Walters, R.L., 1968, Radar Bibliography for Geoscientists, CRES Rept. 61-30, Univ. Kansas, Lawrence, Kansas, 28 pages.

RADAR GEOLOGY: TECHNOLOGY AND PROGRAM OVERVIEW

Frank T. Barath

Jet Propulsion Laboratory
California Institute of Technology
Pasadena, California 91103

ABSTRACT

This paper presents a brief overview of the state-of-the-art of active microwave remote sensors (altimeters, scatterometers and imagers) used in geologic applications, and summarizes the ongoing radar geology activities within NASA, government agencies, industry, universities and foreign organizations. Also outlined are NASA's present plans for radar geology research and development and space flight missions.

I. INTRODUCTION

In the preceding paper H. MacDonald has traced in detail the evolution of the utilization of radars for geologic applications. It is evident that a certain level of understanding has already been achieved, particularly in the application of imaging radar data to the petroleum exploration problem. The first steps have also been taken to extend radar techniques to space with the Seasat radar altimeter, scatterometer and synthetic aperture imager, and the Shuttle Imaging Radar, indicating that the field is maturing rapidly. It is timely, therefore, to summarize the technology state-of-the-art, to review the ongoing activities, and to present NASA's planned space flight projects.

II. TECHNOLOGY STATE-OF-THE-ART

A. Altimeters

As the name indicates, altimeters measure the distance between the vehicle carrying the altimeter device and the ground directly below. Radar altimeters transmit either pulsed or frequency-modulated RF signals and obtain distance by measuring the elapsed time between pulse transmission and echo reception, or the difference in frequency between transmitted and received echo signal. This can be accomplished either from aircraft or from spacecraft, the technique needing only minor modifications between the two types of vehicles to account for the greater altitude of the spacecraft.

Two types of information of interest to geologists can be derived from altimeters. The first is terrain profile, obtained as the vehicle carrying the radar translates over the terrain. This yields gross geomorphology, and in the case of spacecraft where very long traverses are easily obtained, it permits a determination of the geoid with great precision. The second type of information obtainable is surface radar reflectivity, which is a measure of the complex physical (i.e., roughness) and electromagnetic (i.e., dielectric constant) properties of the reflecting surface as integrated over the footprint of the altimeter. So far, the exploitation of these types of terrain information by the geologic community has been rather limited although research is underway at several institutions as will be described later.

The Seasat spacecraft altimeter is representative of the present-day capability. This is a system that operates at a frequency of 13.9 GHz (about 2 cm wavelength), has a parabolic antenna 80 cm in diameter, and achieves from a 790-km orbit a 7-cm altitude measurement precision over a 2-km-diameter footprint.

B. Scatterometers

Scatterometers are designed to obtain with high accuracy reflectivity data as a function of angle of incidence. This is obtained by either scanning the beam of what essentially is a calibrated altimeter, or by building a system with a fan beam. In the former case, the angular dependency information is gathered by stepping the beam sequentially; in the latter case, the echo from larger angles arrives later in time than echos from smaller angles, thus permitting separation.

Scatterometers can be built to be used on the ground, i.e., mounted on "cherry-pickers," on aircraft, and on spacecraft, with only minor design differences driven by the instrument-terrain distance. The information of interest to geologists that can be obtained from scatterometer data is similar to that derivable from altimeters, with two important differences: scatterometers are optimized for accurately measuring surface reflectivity, and the angular dependence of the reflectivity is obtained. These factors combine to make scatterometers a good research tool with which fundamental radar wave-terrain interaction studies are made.

A good example of present-day capability is the Seasat scatterometer, which operates at 14.6 GHz (about 2 cm wavelength), has four stick-antennas, each 3 m long by about 20 cm wide and is capable of obtaining data at two polarizations on both sides of the spacecraft. Reflectivity data are gathered over a 25-to 55-degree range of angles of incidence from orbit. The absolute accuracy of the data is 2 dB, averaged over a ground resolution element of about 50 km in size.

C. Imagers

Imaging radars provide a two-dimensional display of the radar reflectivity of the terrain under the aircraft or spacecraft carrying the instrument. These instruments carry antennas that generate fan beams which are narrow in the azimuth direction (parallel to the flight path) and wide in the range direction (perpendicular to the flight path). Resolution cells in the range direction are obtained by time-slicing the echo; in the azimuth direction, resolution is obtained by either the actual width of the fan beam ("real aperture" radar) or by the potentially much narrower width of a synthesized fan beam ("synthetic aperture" radar or SAR). Imaging radars to date have all been airborne with

the exception of the Seasat SAR; building such a system for spacecraft operation is a very complex task, and the sizes, weights, powers and funds required are high.

The information of geologic interest in radar imagery is considerable, principally as derived from the study of shapes and patterns. Such morphological information has been used for nearly two decades, mainly for petroleum and mineral exploration in many areas of the world, and considerable work is underway to improve this interpretation capability. Substantial research is also being done to extend the information that can be extracted from radar imagery to compositional and microstructure analysis.

The Seasat Synthetic Aperture Radar represents the present day state-of-the-art. It operates at 1.275 GHz (about 24 cm wavelength), has an unfurlable planar phased array antenna 10 x 2 m in size, and provides a 100-km-wide image swath that has 25 x 25 m resolution elements.

III. ONGOING GEOLOGY-RELATED ACTIVITIES

A. NASA

Under the Supporting Research and Technology (SR&T) Programs, basic radar signature research is being carried out utilizing cherry-picker scatterometers (1 to 18 GHz) and aircraft SARs (L-, C-, and X-band) for data acquisition at the Johnson Space Center (JSC) and the Jet Propulsion Laboratory (JPL). Seasat SAR data reduction and analysis for geologic purposes is also ongoing at JPL, and preparations are being made at JPL for the reduction and analysis of the data from the Shuttle Imaging Radar-A (SIR-A), which is a SAR mission entirely dedicated to geology.

B. Government Agencies

The U. S. Geologic Survey is participating in various aspects of aircraft and Seasat SAR data reduction and analysis and is represented on the SIR-A science team.

C. Industry

Extensive aircraft L- and X-band SAR data gathering, reduction and analysis is under way at ERIM, Goodyear Aircraft, Aero Services, and a number of mineral and petroleum exploration companies.

D. Universities

Cherry-picker scatterometer (1 to 18 GHz) data gathering, reduction and analysis is underway at the University of Kansas and Texas A&M University (TAMU); airborne scatterometer (9.3 GHz) data gathering, reduction and analysis is being performed at the University of Kansas. Airborne SAR data gathering, reduction and analysis is being done at the University of Kansas, the University of Arkansas and the University of California at Santa Barbara. Seasat data analysis is being carried out at several universities including University of Alaska, UCSB, University of Massachusetts, TAMU, University of Arkansas and University of Kansas. The University of Arkansas and University of Kansas are also participating in the SIR-A project.

E. Foreign

Germany is in the process of implementing an X-band (3 cm) SAR system to be flown on Spacelab-1 in 1981. Although this is a limited capability system with very narrow swath width, it will be the first X-band system in space since the L-band Seasat SAR, and could easily be upgraded for later reflights. Scientists from France and Bolivia are participating as Coinvestigators in the SIR-A flight. Canada, France and the UK are participating in the reduction and analysis of Seasat SAR data. Finally, France is in the early planning phases of the SPOT-2 spacecraft which will carry a high-performance X-band SAR in the late 1980s.

IV. PROPOSED NASA ACTIVITIES

In the Research and Development area, NASA's plans are for steadily increasing support for geology application development through cherry-picker scatterometer and aircraft SAR data gathering, reduction and analysis. In addition, substantial investment is planned in the development of SAR sensors and digital processors. This latter item represents a major need for the efficient production of timely and quantitative SAR data in the required volumes at the present time and in the near future.

A number of space flight projects are also in the planning stages, as follows:

SIR experiments in 1982-1985 (L-band and X-band).

Venus Orbiting Imaging Radar (VOIR) flight in 1985 (L-band).

Ice and Climate Experiment (ICEX) wide swath SAR, (X-band) altimeter (13.5 GHz) and scatterometer (14.6 GHz) flight in 1985.

National Oceanic Statellite System (NOSS) altimeter (13.5 GHz) and scatterometer (14.6 GHz) flight in 1985.

Earth Resources SAR (ERSAR) multifrequency imager flight in 1987.

V. CONCLUSION

The increasing awareness of the shortcomings of conventional geologic research and exploration tools, coupled with the improving understanding of the unique capabilities of radar have given impetus to the development and expansion of the role of radar sensors for geologic applications. It is expected that this expansion will continue and will substantially contribute to alleviating the petroleum and mineral crisis in the world.

TECHNIQUE DEVELOPMENT PAPERS

Simulation of Orbital Radar Images

R. S. Saunders, J. C. Holtzman, and Charles Elachi

Expression of San Andreas Fault on Seasat Radar Image

F. F. Sabins, R. Blom, and C. Elachi

Analysis of Seasat Orbital Radar Imagery for Geologic Mapping
in the Appalachian Valley and Ridge Province, Tennessee-Kentucky-
Virginia

J. P. Ford

Radar Imaging of Volcanic Fields and Sand Dune Fields:

Implications for VOIR

C. Elachi, R. Blom, M. Daily, T. Farr, and R. S. Saunders

Rock Type Discrimination and Structural Analysis with Landsat
and Seasat Data: San Rafael Swell, Utah

H. E. Stewart, R. Blom, M. Abrams, and M. Daily

Terrain-Analysis Procedures for Modeling Radar Backscatter

Gerald G. Schaber, Richard J. Pike, and Graydon L. Berlin

Realistic Earth/Land Radar Models

Andrew J. Blanchard

Some Confusion Factors in Radar Image Interpretation

Bruce J. Blanchard

Multichannel SAR in Geologic Interpretation: An Appraisal

Philip L. Jackson

Automatic Shading Correction and Speckle Noise Mapping/Removal
Techniques for Radar Image Data

P. S. Chavez, Jr.

SIMULATION OF ORBITAL RADAR IMAGES

R. S. Saunders

Jet Propulsion Laboratory
California Institute of Technology
Pasadena, California 91103

J. C. Holtzman

University of Kansas
Lawrence, Kansas 66044

Charles Elachi

Jet Propulsion Laboratory
California Institute of Technology
Pasadena, California 91103

ABSTRACT

Many of the questions that arise concerning the operating parameters for spaceborne synthetic aperture imaging radar systems can be addressed in a cost-effective manner by using simulation techniques. This can include use of airborne images, Seasat images, and computer simulation. The first computer simulation of spaceborne radar imagery has been analyzed for system definition studies. Analysis of the simulation indicates that incidence angles as small as 30° are useful for general terrain geomorphologic analysis.

I. INTRODUCTION

The Seasat imaging experiment has demonstrated the feasibility of an orbiting synthetic aperture imaging radar system. The land images contain a wide variety of geologic features (Figure 1) and preliminary analyses indicate that the Seasat images may be a useful geologic mapping tool in certain types of terrain (Elachi, 1980; Ford, 1980; Stewart, 1980) where the relief is low to moderate.

Previous studies have indicated that, for airborne systems, the optimum incidence angle (Figure 2) depends on the terrain (MacDonald and Waite, 1971). Similarly, with stereo, the pair of incidence angles that yields the strongest visual stereo model may depend on the terrain. Opposite side stereo at 45° incidence provides the largest vertical exaggeration, but may only be usable

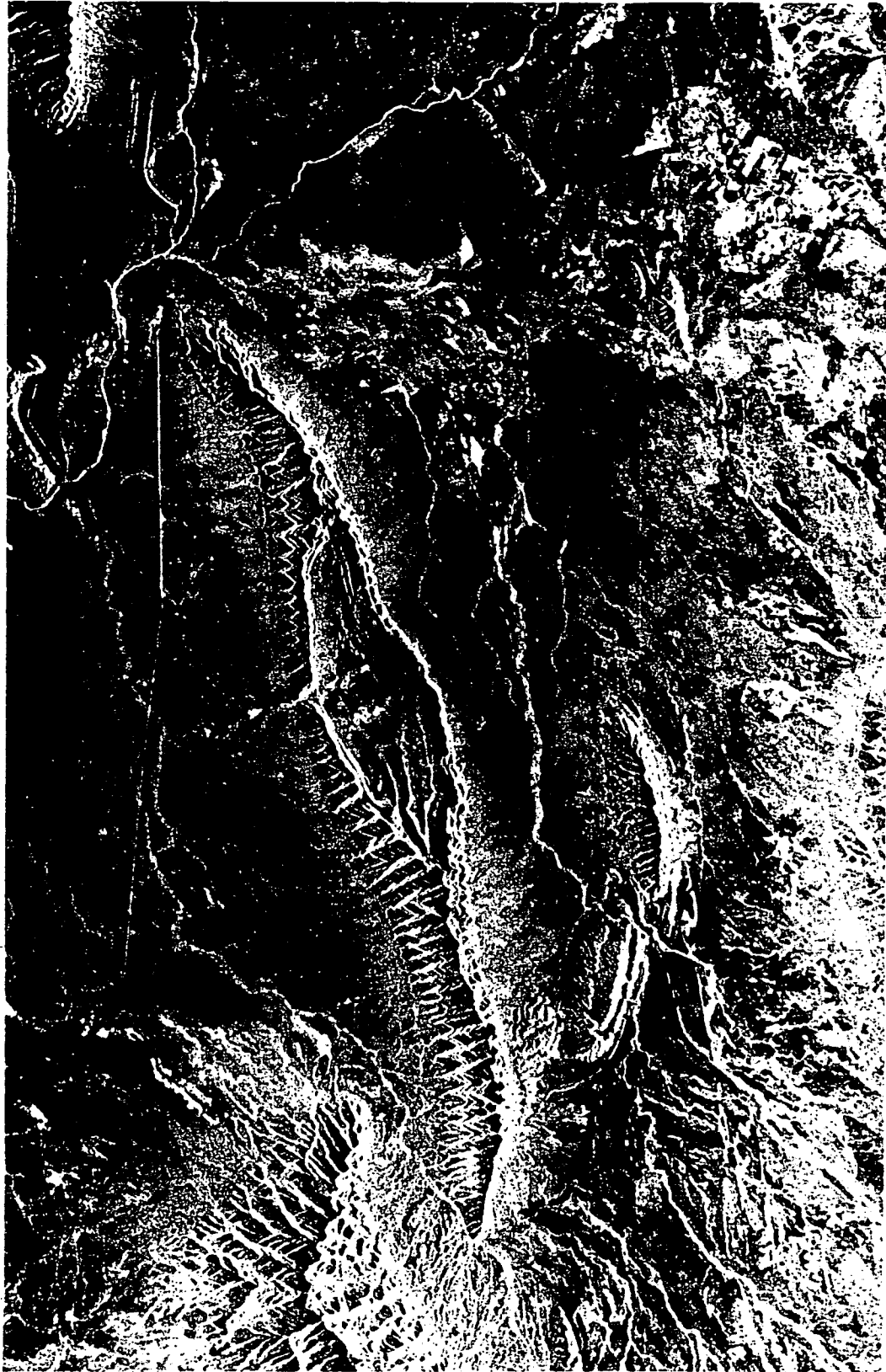


Figure 1. Breached doubly-plunging anticlines in Cretaceous sedimentary rocks west of Obayos, Coah., Mexico, as seen by Seasat imaging radar. The axes of two of the anticlines are oriented near-normal to the radar look-direction (approximately N 70° E). The layered character of the rocks is denoted by flatiron patterns on the northeast-facing flanks of the anticlines. Compression of the southwest-facing flanks is caused by foreshortening due to radar layover.

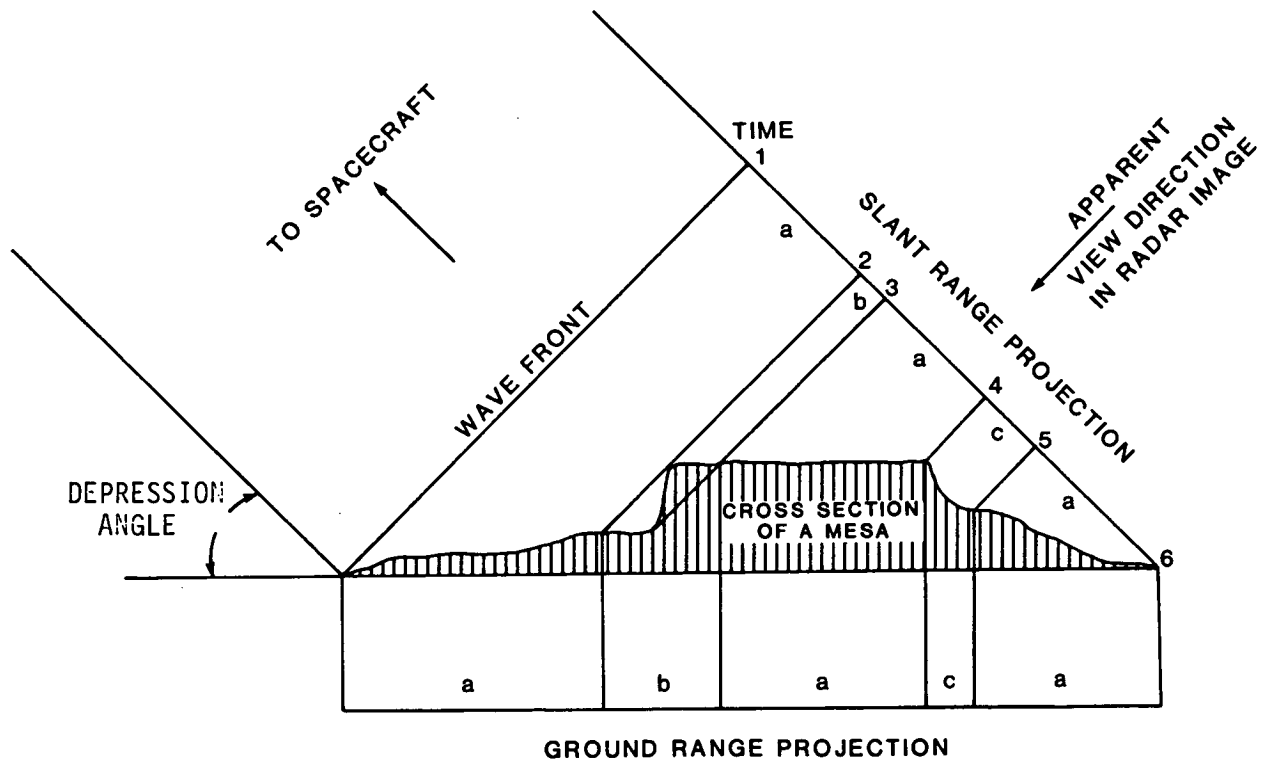


Figure 2. Illustration of layover and shadow. For spaceborne geometry note that there is little change in incidence angle across the scene. The wave front strikes the surface and is reflected back and its intensity recorded as a function of time. Between time 1 and 2, normal image is obtained (a). Between time 2 and 3, the plateau top and the area near the cliff base are at the same range and thus overlap in the image, a condition known as layover (b). No reflection is recorded between time 4 and 5, resulting in radar shadow (c).

in areas of relatively flat terrain. Other pairs may be most useful in mountainous regions.

Three current imaging radar experiments have faced the necessity of defining operating parameters for a spaceborne SAR. These are the Seasat SAR experiment, the Shuttle Imaging Radar (SIR-A) and the Venus Orbiting Imaging Radar (VOIR) SAR Experiment.

The Seasat SAR was designed to image the ocean surface rather than the land, and no consideration was given to the problem of layover (Figure 2) in the land images where the local slopes exceed the incidence angle. Nevertheless Seasat images are useful for studies of land use and structural analysis in moderate to low relief regions (Bryan, 1980; Sabins et al., 1980).

SIR-A was specifically designed to assess the utility of imaging radar as an aid to geologic mapping. It has been generally assumed that the optimum incidence angle for this purpose must be large, certainly large enough to avoid layover, and preferably large enough to provide shadow. This perception apparently arises from experience with airborne SAR images. The only such images available were obtained by systems developed for the military. Although the images taken with extreme (60° - 80°) incidence angle superficially resemble air photos in their maplike appearance and shading, a primary consideration in the design of these systems appears to be a desire to avoid flying close to the enemy positions. Very little high quality radar imagery is available at low incidence angles for comparative studies. The SIR-A team grappled with the question of incidence angle and decided on about 50° as a good compromise for the widest variety of geologic terranes.

The VOIR Science Working Group faced the same problems. In general such problems as wavelength selection, resolution requirements and radiometric quality of the image, although by no means trivial, can be addressed with existing experience. The question of incidence angle for Venus could not be as easily decided. At one extreme, it may be argued that Venus is dominated by modest slopes as seen in the existing Earth-based radar images (Figure 3) and the Pioneer Venus altimetry. The argument is that very low incidence angles provide resolution of small slope changes because of the steepness of the backscatter function in that region (Figure 4). At the other extreme is terrestrial experience suggesting that shadow may be essential to geomorphological analysis, and that high ($>60^{\circ}$) incidence angles are needed. Meanwhile, the radar system analysis demonstrates that high incidence angles for orbital systems can only be obtained with very large (and expensive) antennas and from a practical standpoint the incidence angle cannot exceed 50° by a significant amount. For VOIR a 50° incidence angle was requested by the science investigators and remains the baseline design. From the above, it is clear that uncertainties about the viewing geometry that is best for imaging various terrains dominate the design concerns. Since we have no practical way of obtaining orbital images with varying incidence angles, other approaches have been devised to study this parameter. These involve simulations using airborne and computer-generated images.

In general, airborne images have considerable variation in incidence angle across the swath. To produce images with less variation, multiple close tracks were flown over a region of northern Arizona so that a mosaic could be assembled from small strips with 5° or less variation of incidence angle across them.

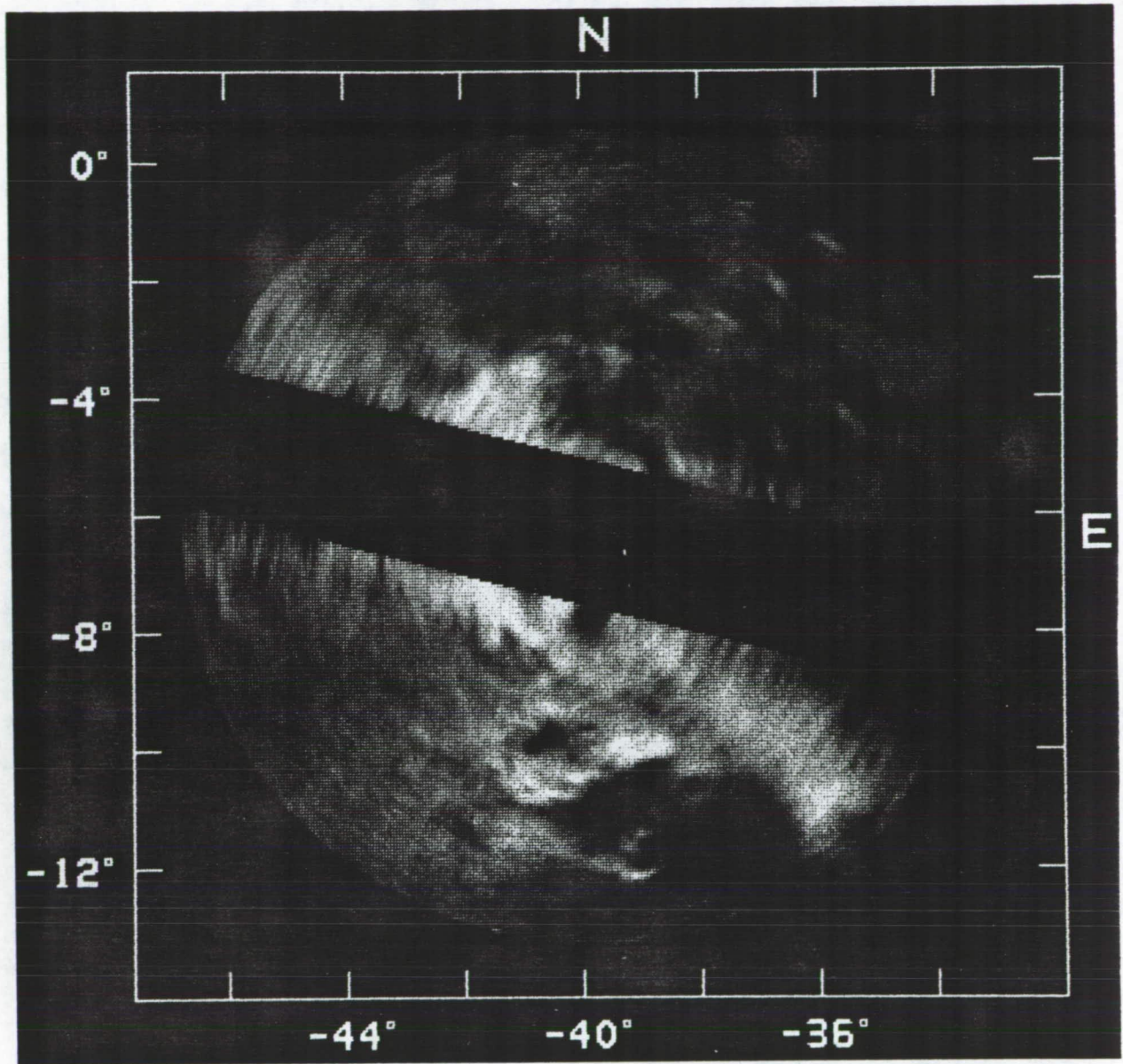


Figure 3. Earth-based radar image of a portion of Venus approximately 1500 km across. The dark band is a region that cannot be unambiguously imaged. This image shows that at incidence angles of 4° to 6° a very small change in slope can be detected. The circular craterlike feature in the lower half has slopes of less than one degree. Image courtesy Raymond Jurgens, JPL.

ORIGINAL PAGE IS
OF POOR QUALITY

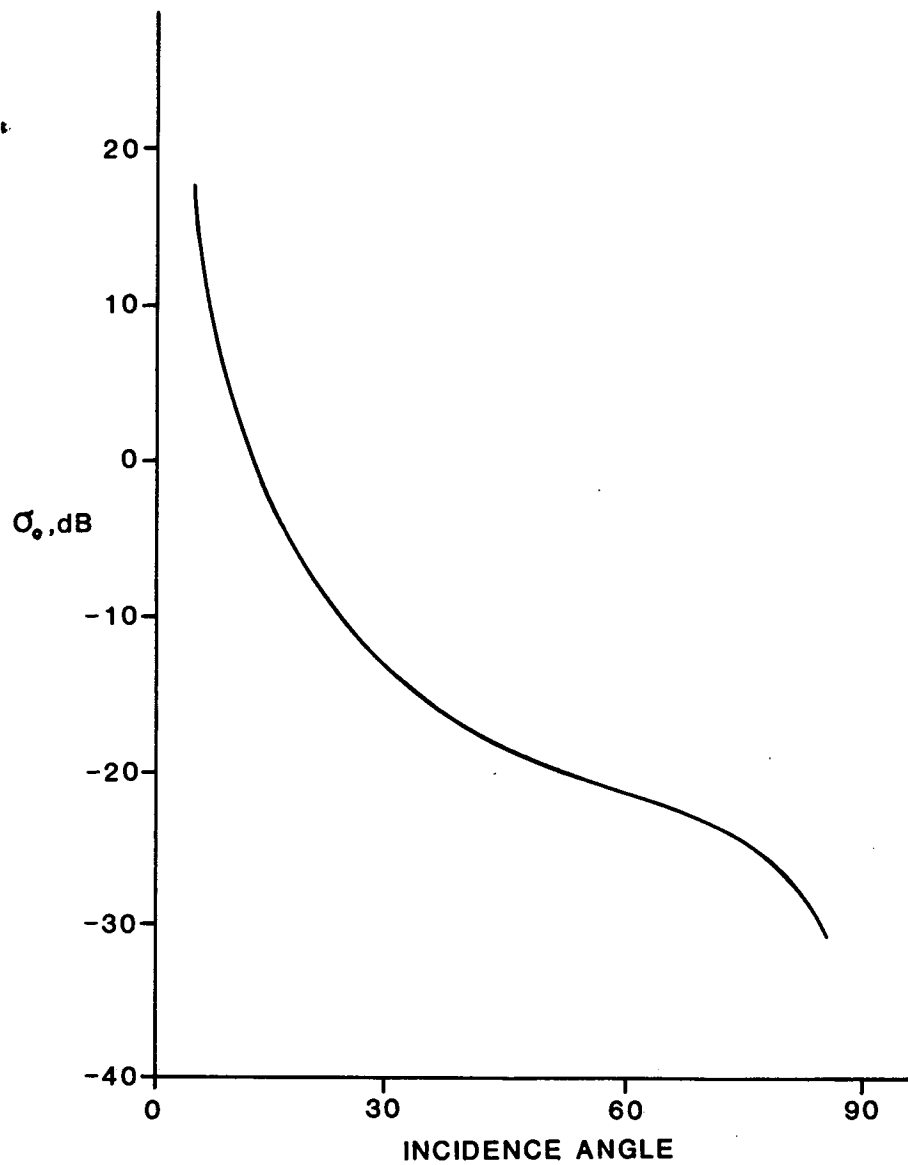


Figure 4. Typical backscatter function for a dry cinder surface of L-band, like-polarized. Note that near zero incidence, the backscatter is most sensitive to small changes in slope.

The other approach is to use computer image simulation to study the effects of varying the incidence angle. In this approach we used the "Point Scattering Model" developed at the University of Kansas (Holtzman et al., 1978).

II. SIMULATION OF ORBITAL GEOMETRY USING AIRBORNE IMAGES

The JPL L-band airborne SAR system was used to simulate orbital geometry. Conventional airborne SAR images typically have a range of incidence angle of more than 10° . For the simulation, a region of northern Arizona that includes part of the Grand Canyon and the San Francisco Mountains was chosen. The flight paths for the image strips were chosen to provide closely overlapping images from several directions. The system can operate in two modes, one that images from nadir (0° incidence) out to 45° and a second that images the area from 40° out to about 60° . An example of the imagery from nadir to 45° is shown in Figure 5. These images were cut into strips having a narrow ($\leq 5^\circ$) band of incidence angle and mosaicked to produce images having incidence angles near 45° and 55° (Figure 6).

III. COMPUTER SIMULATION

Techniques for computer simulation have been developed at the University of Kansas (Holtzman et al., 1978). Applications to date have been in simulation of airborne images. Here we present the first results of computer simulation of spaceborne radar images.

Radar images have been successfully generated by digital computers for geoscience and guidance applications using techniques called the Point Scattering Model (PSM). The PSM provides the flexibility required to efficiently simulate, by digital means, the radar image products of a wide variety of radar systems for diverse target scenes.

The PSM is centered around a closed-system description of the microwave imaging process. This description rigorously treats the closed-system consisting of the radar transmitter and receiver, the ground dielectric properties, the geometric orientation of target features, and the data recording medium. The random nature of this system is also modeled. The process of simulating radar images via the PSM includes acquiring input data about the ground scene, radar system, and vehicular position. Also, an imaging process transfer function must be implemented which implies recognition of resolution cell boundaries. Succeeding algorithms must then relate the backscattered or reflected microwave signals to the synthesized image.

Important in the simulation of radar imagery is establishment of an accurate "ground model" which will be relevant for microwave remote sensors. By appeal to the classical radar equation relating the average radar return power to the transmitted power, and to the target cross section (σ). Alternately, we may model the ground by σ^0 and elevation samples, from which slope information can be derived. These data go into the making, but are not synonymous with the "ground truth data base" (hereafter referred to as data bases) upon which the implementation algorithms operate.

The data base can be in the form of a rectangular matrix (facilitating digital implementation). It represents the sampled version of the ground scene by storing (1) backscatter category (e.g., pasture) and (2) elevation. The distinction between the ground model and the data base is seen to be the use of

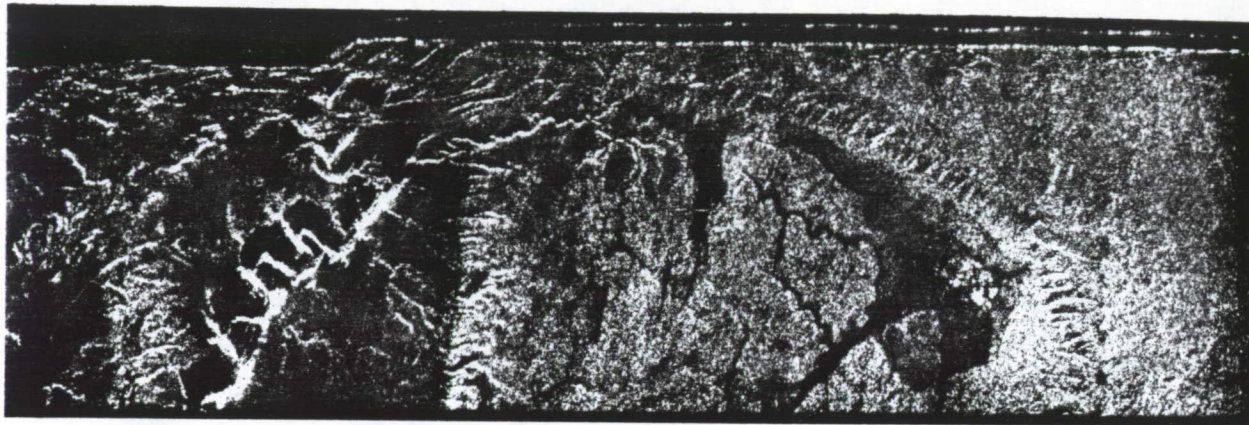


Figure 5. JPL L-band image of nadir out to 45° . Many such strips were used to produce the mosaics of Figure 7. The top of the image is the nadir and is essentially a profile of land surface beneath the aircraft ground track.

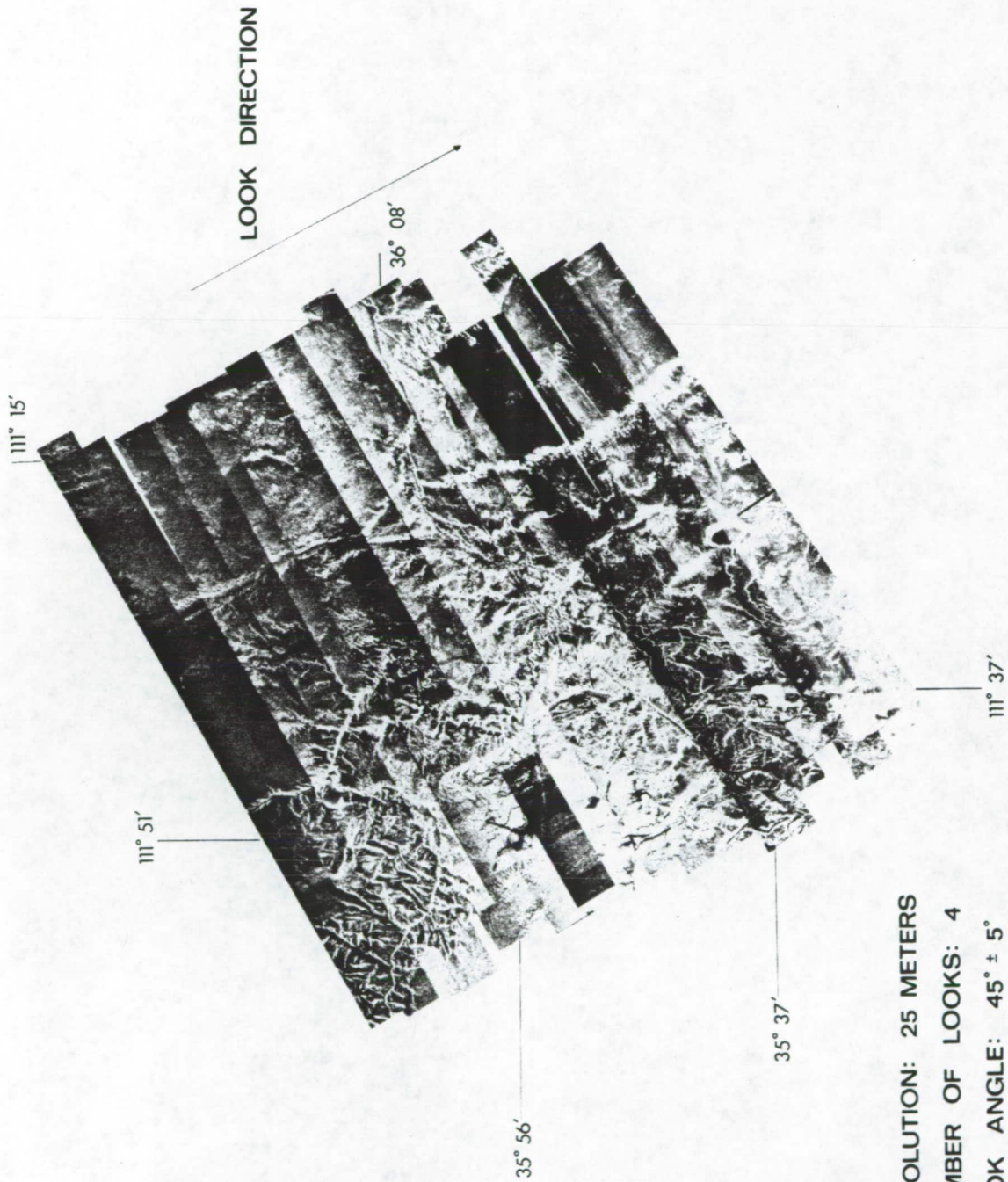
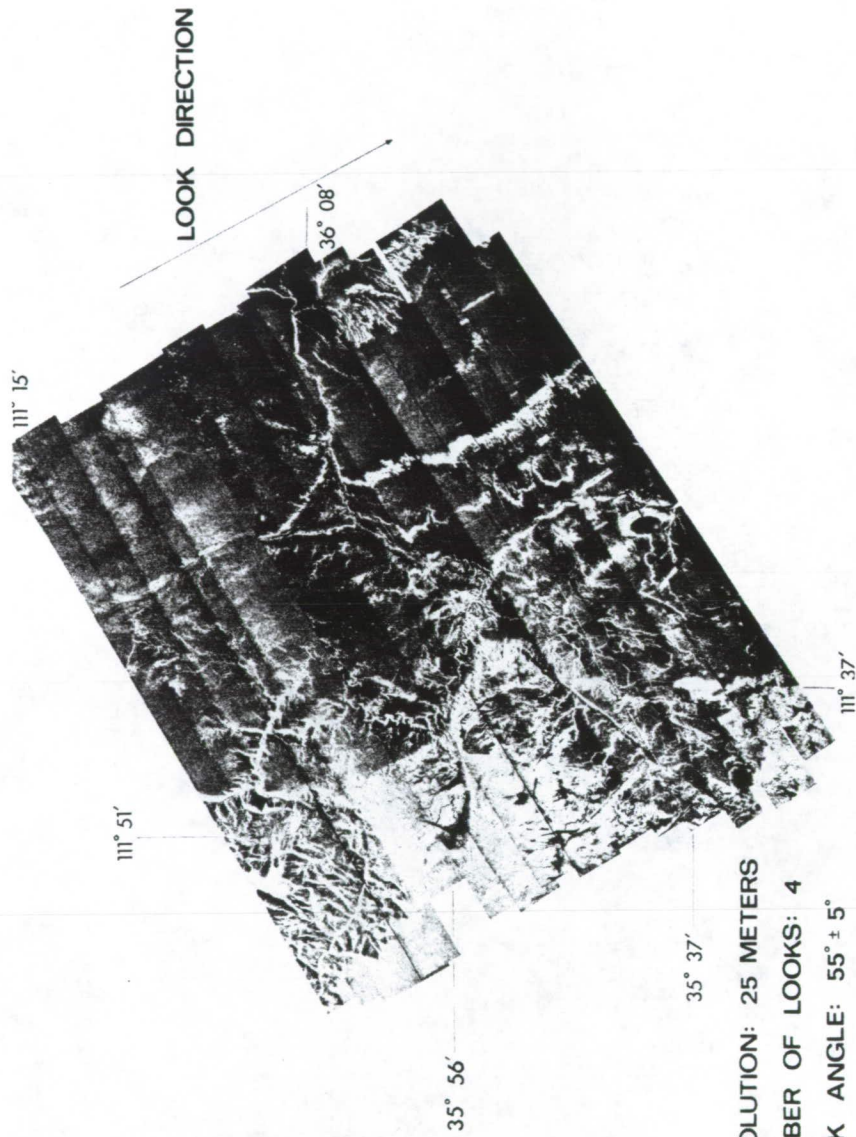


Figure 6. Airborne radar image mosaics obtained at two different look angles, 45° and 55°. The mosaic covers the San Francisco volcanic field and the southern rim of the Grand Canyon.

ORIGINAL PAGE IS
 OF POOR QUALITY



RESOLUTION: 25 METERS
 NUMBER OF LOOKS: 4
 LOOK ANGLE: $55^{\circ} \pm 5^{\circ}$

Figure 6 (contd)

category rather than σ^0 in the data base. This is done because σ^0 is a function not only of the backscattered category, but also the radar incidence angle with respect to the resolution cell, frequency, polarization, etc. Therefore, storing σ^0 in the data base would limit the data base utility to simulations with a fixed radar look direction and incidence angle, etc.

Data bases have been constructed from two sets of source data: available digital elevation tapes and geometrically rectified aerial photography. The purpose of the imagery (which is not suggested to be limited to air photos; infrared and radar imagery can be instrumental) is to allow a photo/radar-interpreter to delineate boundaries of distinct backscatter regions. The interpreter produces an outline map for the target scene, separating different radar scattering (or reflecting) objects. This line drawing is digitized, and the digitized "category" data are oriented properly into a rectangular matrix to be merged with the elevation data matrix.

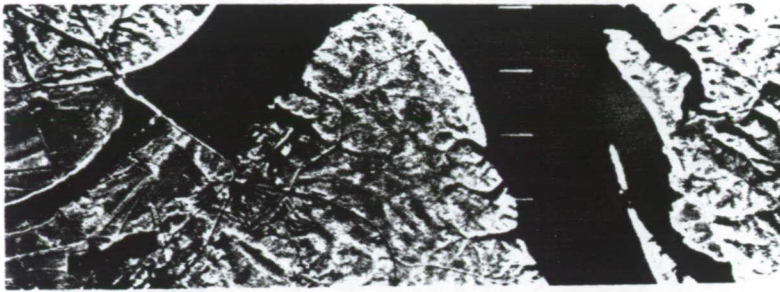
The next step is to calculate the return power from each of the resolution cell areas. For medium resolution radar systems, these areas can be simulated independently. The simplification allowed by ignoring the effect of adjacent cells greatly reduces the computational complexity of the problem. The information of adjacent cells is needed only to calculate the slopes of each cell and to calculate the effects of radar "shadow," "layover," and "fore-shortening." At each cell the local incidence angle is calculated from the radar incidence angle and the local terrain slope at the cell. The category information stored at each cell describes the backscatter target type represented by the area. By use of a curve, fit to empirical or theoretical backscatter data for the category, a σ^0 value for the specific angle of incidence is determined. This information is used to calculate the return power from each resolution cell area by application of the general radar simulation model.

The final step is to produce an output image. The array of return powers calculated in the previous step is converted to relative greytone representing density on photographic film. Each greytone value represents the return from a specific resolution cell area on the ground. The final image product is displayed and then photographed.

This summary of the Point Scattering Model and associated techniques has been presented in order to explain how radar image simulations (for distributed targets) are generated. Simulation results have been compared against actual radar imagery of the test terrain sites, with positive results. For example, Figure 7 illustrated real radar and simulated radar imagery.

For the VOIR space simulation we used the topographic file produced by the Defense Mapping Agency of the Flagstaff (NI 12-2) Quadrangle. The resolution of the data set is 200 feet with 50 foot contour intervals (Figure 8). In the simulation we have an east look direction from an altitude of 300 km. The incidence angles chosen are 23°, 30°, 50°, and 70°. A single class of terrain was used for the entire image: dry soil with a roughness of 2.0 cm RMS height and moisture content of .03 g/cm³. The simulation has a resolution of 61 m along track and 76 m across track at 50° (Figure 9).

The results of the simulation suggest that for this area, an incidence angle of 30° provides full interpretability. Less than 30° introduces layover which complicates the interpretation but greater than about 50° appears in this



APD-10 SAR IMAGE Resolution 10 Feet



SIMULATED RADAR IMAGE Resolution 60 Feet

3.23 miles

3.23 miles



Figure 7. Simulated radar image compared to SAR image of Pickwick Dam site.

ORIGINAL PAGE IS
OF POOR QUALITY

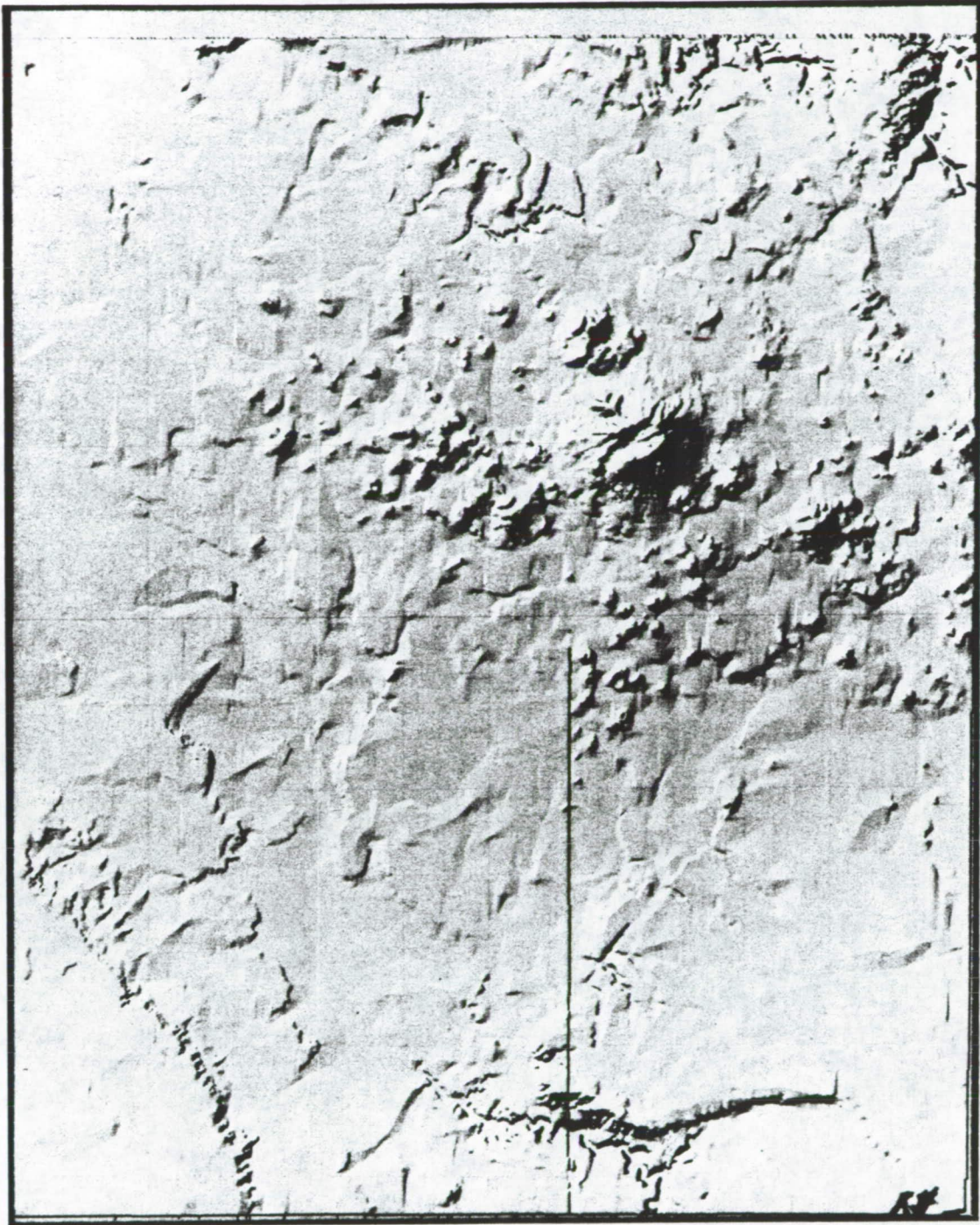


Figure 8. Shaded relief version of the DMA digital topographic data base used in the computer simulations. Image processing was done at the JPL Image Processing Laboratory.

ORIGINAL PAGE IS
OF POOR QUALITY

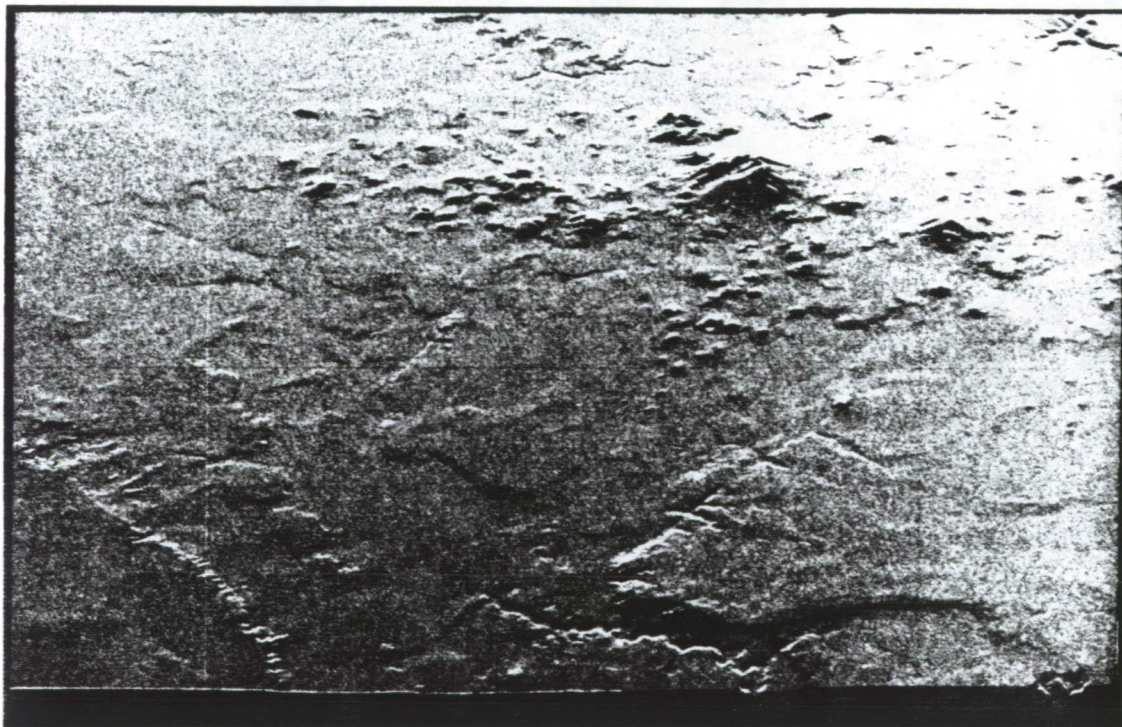
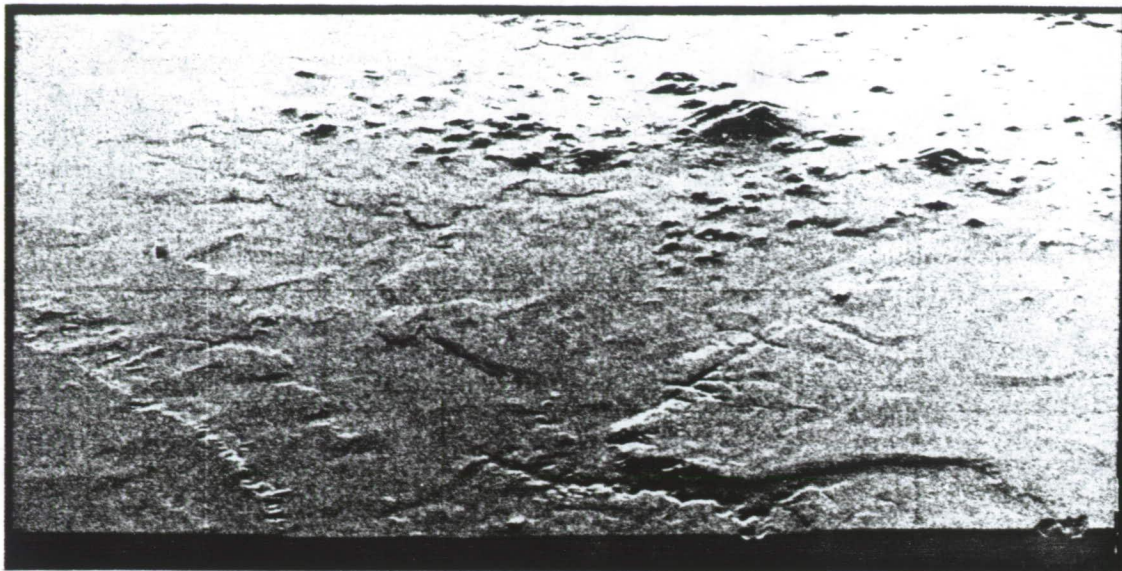


Figure 9. Computer simulation of region north of Flagstaff, Arizona, between the San Francisco Peaks and the Grand Canyon. The simulation illustrates the effect of varying incidence angle. The resolution in each case is 200 feet (60 meters). In all views, south is at the top. (a) through (d) are in slant range projection. Incidence angle is (a, top) 23° (b, bottom) 30° (c, page 59) 50° (d, page 60) 70° . In 9 (e, page 61) the 30° incidence simulation is presented in a ground range projection. Figure 9 (f, page 62) shows the same region in a digitally processed JPL Seasat image which was imaged from a different direction. The digital simulations were done at the Remote Sensing Laboratory of the University of Kansas Center for Research, Inc. Digital to film processing, enhancement, and geometric transformations were done at the JPL Image Processing Laboratory.

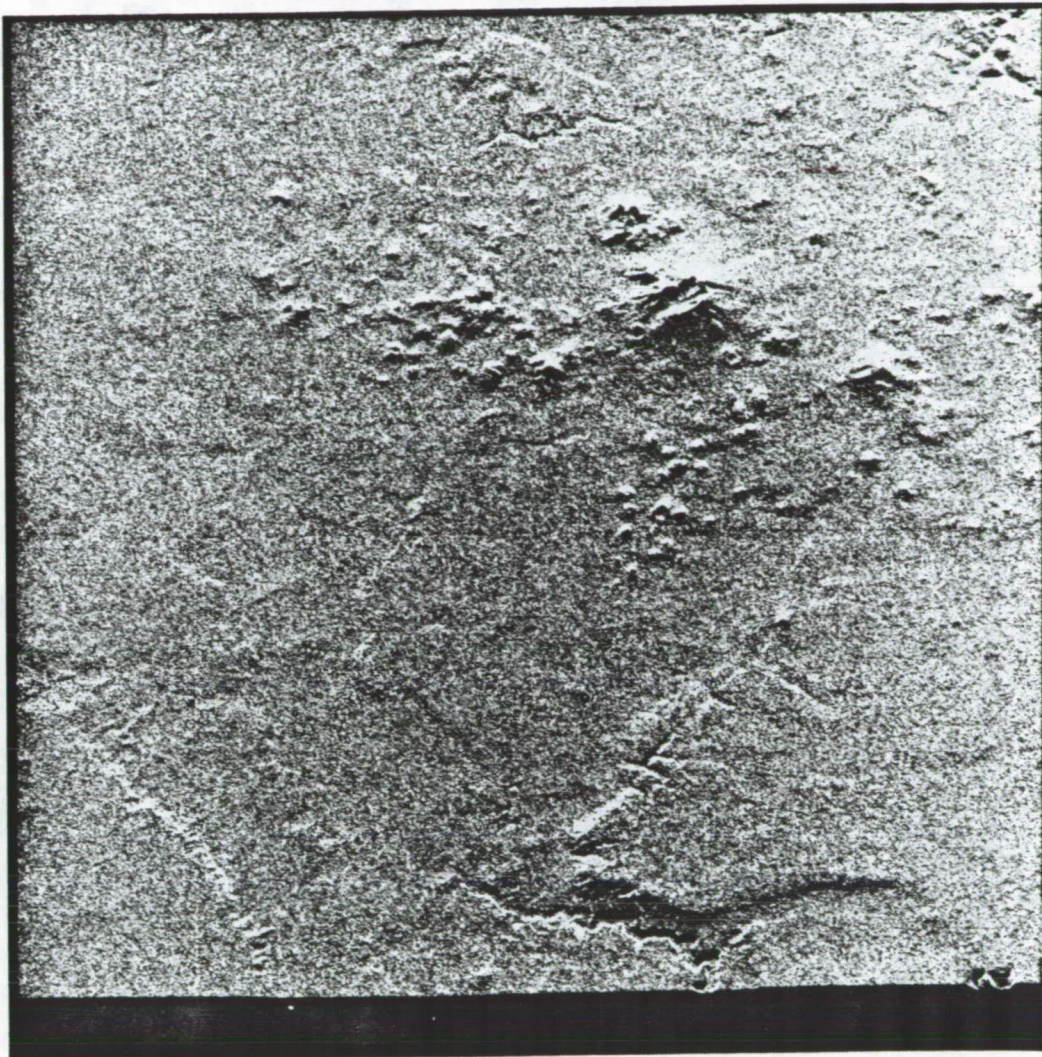


Figure 9 (contd)

ORIGINAL PAGE IS
OF POOR QUALITY

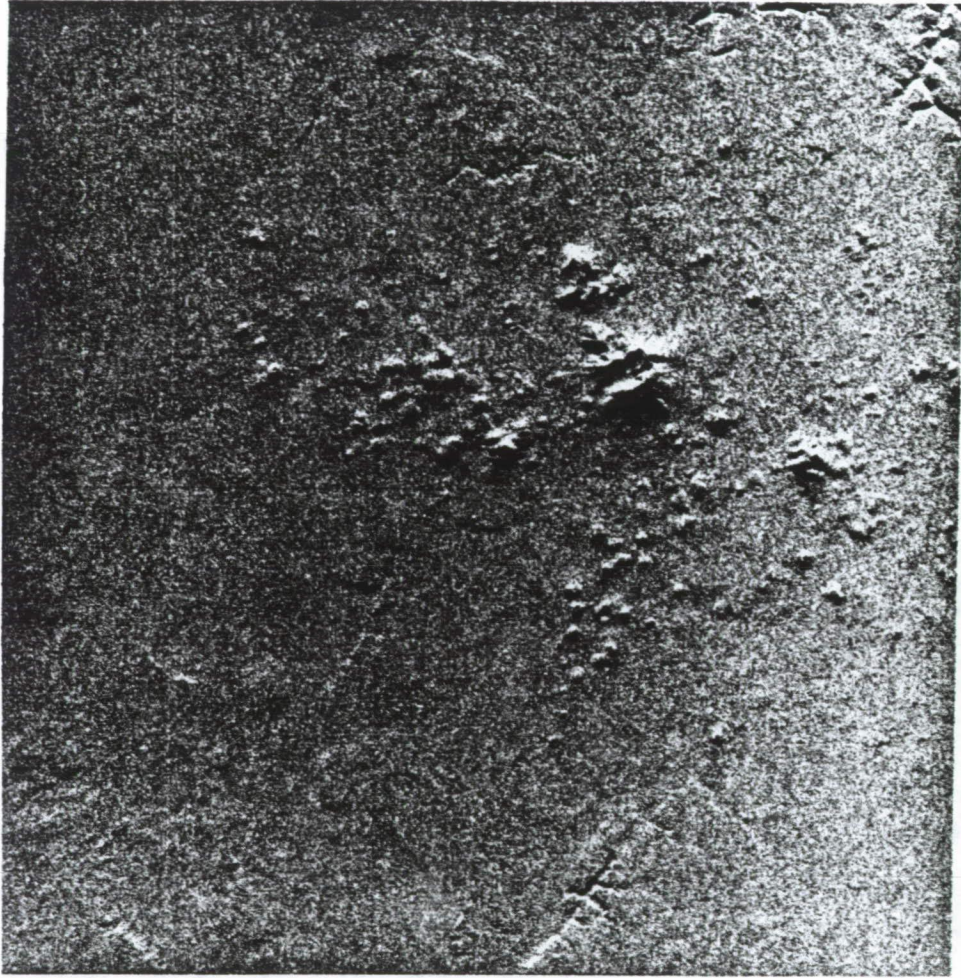


Figure 9 (contd)



Figure 9 (contd)

ORIGINAL PAGE IS
OF POOR QUALITY

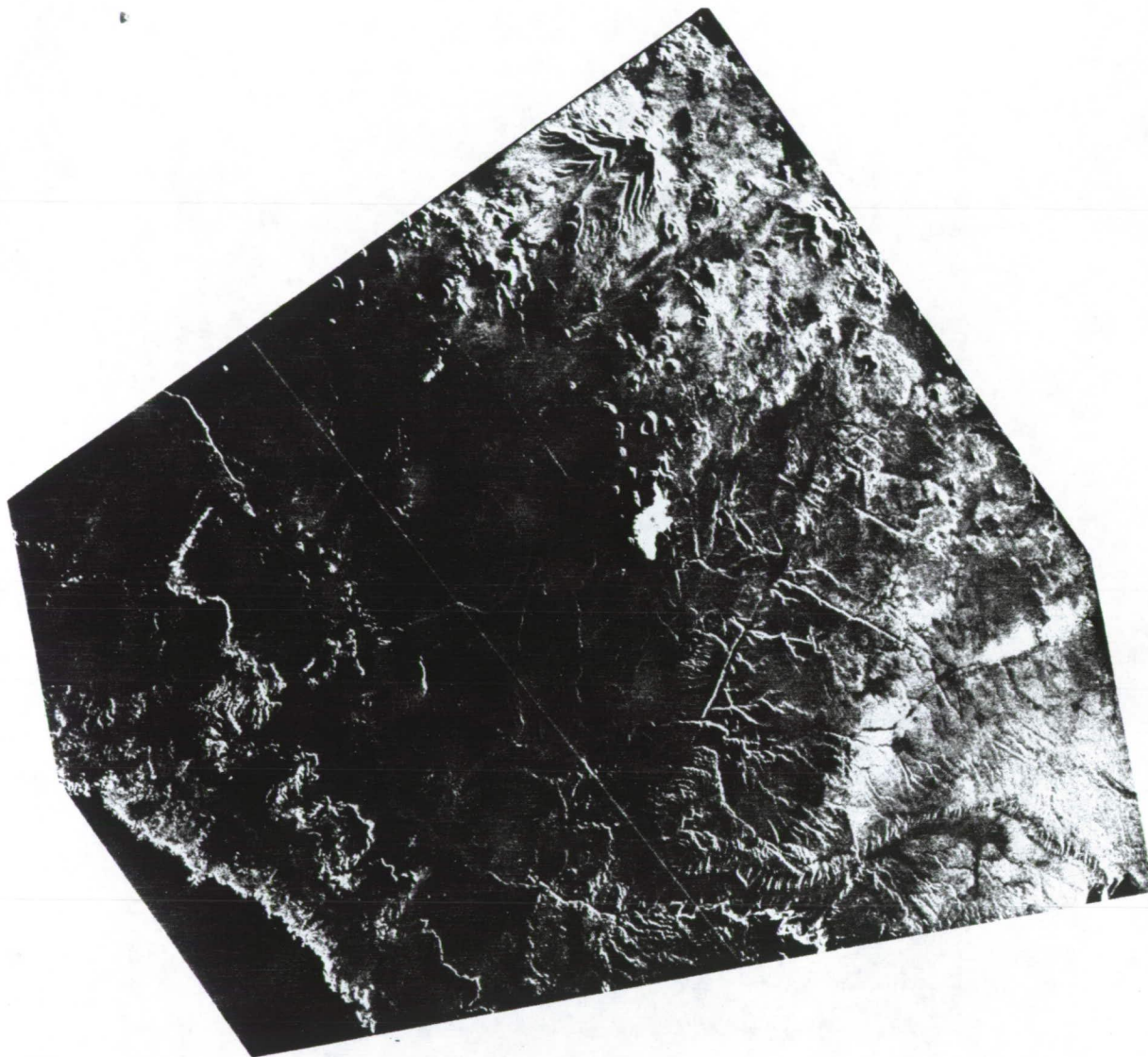


Figure 9 (contd)

ORIGINAL PAGE IS
OF POOR QUALITY

simulation to actually degrade the interpretability. Further simulations in other terrains must be performed to assess the significance of these observations.

REFERENCES

- Bryan, M. L., Radar Study of Vegetated Pediment (submitted to Science).
- Elachi, C., Spaceborne Imaging Radar in Oceanography and Geology, Science, 205, (in press), 1980.
- Ford, J. P., Analysis of Seasat Orbital Radar Imagery for Geologic Mapping in the Appalachian Valley and Ridge Province, Tennessee - Kentucky - Virginia: This Volume.
- Holtzman, J. C., Frost, V. S., Abbott, J. L., and Kaupp, V. H., "Radar Image Simulation," IEEE Trans. on Geoscience Electronics, Vol. GE-16, No. 4, Oct. 1978.
- MacDonald, H. and Waite, W., Optimum Radar Depression Angles for Geological Analysis: Modern Geology, 2, 179-193, 1971.
- Sabins, F. F., Blom, R., and Elachi, C., Expression of San Andreas Fault on Seasat Radar Image: Bull. AAPG, 64, (in press), 1980.
- Stewart, H. E., Blom, R., Abrams, M., and Daily, M., Rock Type Discrimination and Structural Analysis with Landsat and Seasat Data: San Rafael Swell, Utah: This Volume.

EXPRESSION OF SAN ANDREAS FAULT ON SEASAT RADAR IMAGE

F. F. Sabins
Chevron Oil Field Research Company
La Habra, Calif.

R. Blom and C. Elachi
Jet Propulsion Laboratory
Pasadena, Calif.

ABSTRACT

On a Seasat image (23.5-cm wavelength) of the Durmid Hills in southern California, the San Andreas fault is expressed as a prominent southeast-trending tonal lineament that is bright on the southwest side and dark on the northeast side. Field investigation established that the bright signature corresponds to outcrops of the Borrego Formation, which weathers to a rough surface. The dark signature corresponds to sand and silt deposits of Lake Coahuila which are smooth at the wavelength of the Seasat radar. These signatures and field characteristics agree with calculations of the smooth and rough radar criteria. On Landsat and Skylab images of the Durmid Hills, the Borrego and Lake Coahuila surfaces have similar bright tones and the San Andreas fault is not detectable. On a side-looking airborne radar image (0.86-cm wavelength), both the Borrego and Lake Coahuila surfaces appear rough, which results in bright signatures on both sides of the San Andreas fault. Because of this lack of roughness contrast, the fault cannot be distinguished. The wavelength of the Seasat radar system is well suited for mapping geologic features in the Durmid Hills that are obscure on other remote sensing images.

I. BACKGROUND AND OBJECTIVES

On September 14, 1978, the Seasat satellite acquired a strip of L-Band radar imagery (23.5-cm wavelength) that was processed at the Jet Propulsion Laboratory and includes the eastern margin of the Salton Sea in southern California (Figure 1). Examination of the image revealed a prominent tonal lineament in the Durmid Hills and this portion of the image, indicated in Figure 1, was selected for detailed study. The objectives of the study were to (1) determine the cause of the contrasting signatures on opposite sides of the lineament, (2) evaluate the geologic significance of the lineament, and (3) compare the Seasat image with other remote sensing images.

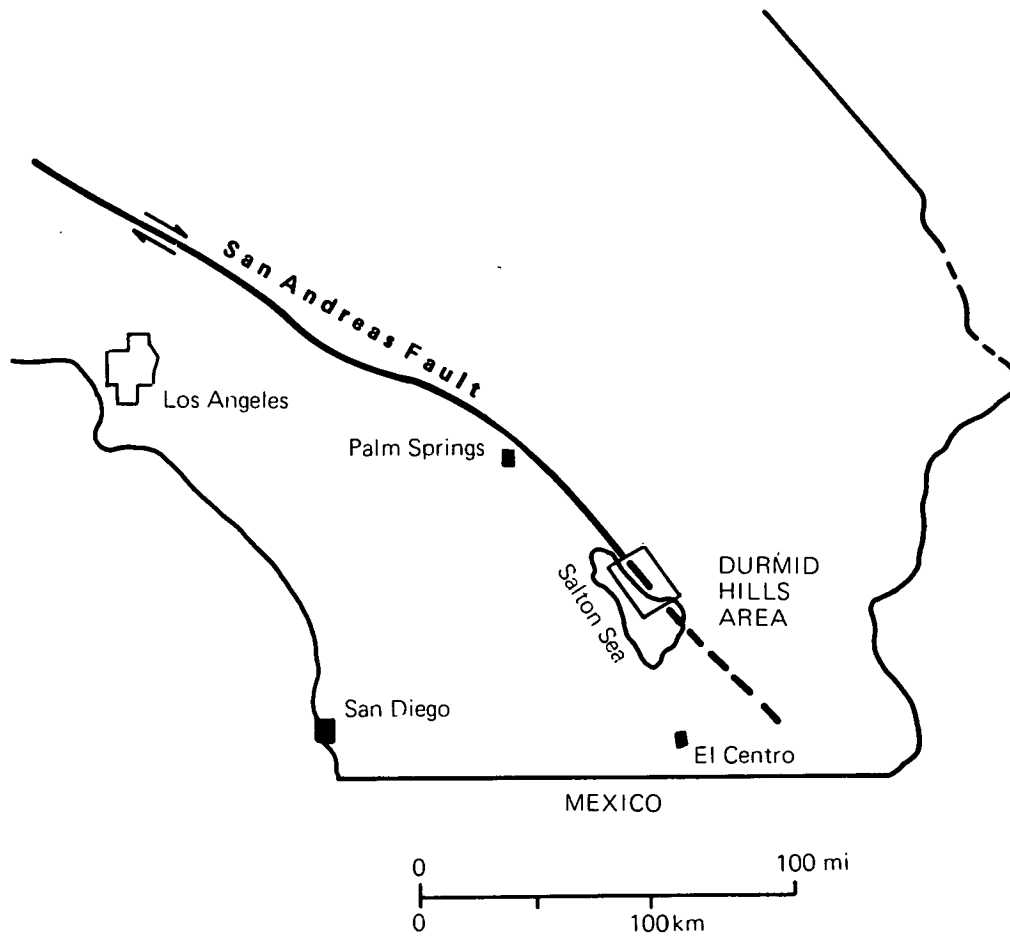


Figure 1. Index map of Southern California showing location of Seasat image of Durmid Hills.

II. SEASAT IMAGE

The Seasat image of the Durmid Hills (Figure 2A) has been greatly enlarged photographically, which accounts for the grainy, or speckled, appearance. The image has not been enhanced by digital processing methods.

A. General Description

The bright signature of the Salton Sea in Figure 2A is caused by the steep depression angle (67° to 73°) of the Seasat radar and the small ripples that prevail on the sea. The bright signature of Bombay Marina at the southeast end of the Durmid Hills (Figure 2B) is caused by the buildings and recreational trailers at this resort community. The prominent bright signature of the unnamed intermittent stream east of Bombay Marina is caused by the concentration of vegetation (mesquite, creosote bush, ironwood, and salt cedar) and gravel and boulders in the channel. The same explanation applies to the bright signature of Salt Creek at the northwest end of the Durmid Hills. The very bright patch at the head of Salt Creek (Figure 2B) is caused by a rough surface crust of salt that has evaporated from saline springs and seeps. The surface roughness is accentuated by a dense growth of rushes and other salt-tolerant vegetation. The medium-to-bright signature along the northeast margin of the image is caused by the gravel of alluvial fans at the foot of the Orocopia Mountains, which are east of the area covered by Figure 2.

The arcuate bright streak in the northeast corner of the image correlates with the west-facing escarpment that was cut by waves along the shore of Lake Coahuila, which occupied the Salton trough during late Pleistocene time. The look direction of the Seasat radar on this orbit was toward the northeast. The Lake Coahuila escarpment faces the look direction which reflects radar energy back to the antenna and produces the bright signature (Sabins, 1978, p. 178).

B. Radar Lineament

On the Seasat image (Figure 2A) a prominent tonal lineament trends southeastward along the crest of the Durmid Hills for a distance of 18 km. The lineament is defined on the image by the straight contact between bright tones on the southwest side and dark tones on the northeast. The lineament correlates with the trace of the San Andreas fault shown on the geologic maps by Jennings (1967) and by Babcock (1974). These maps also show that the bright radar signature on the southwest side of the San Andreas fault corresponds to outcrops of the Borrego Formation and the dark signature to the northeast corresponds to sand and silt deposited in Lake Coahuila. Having established a correlation between the radar lineament and the geologic features, the next step is to determine in the field the properties that cause the different signatures on the Seasat image.

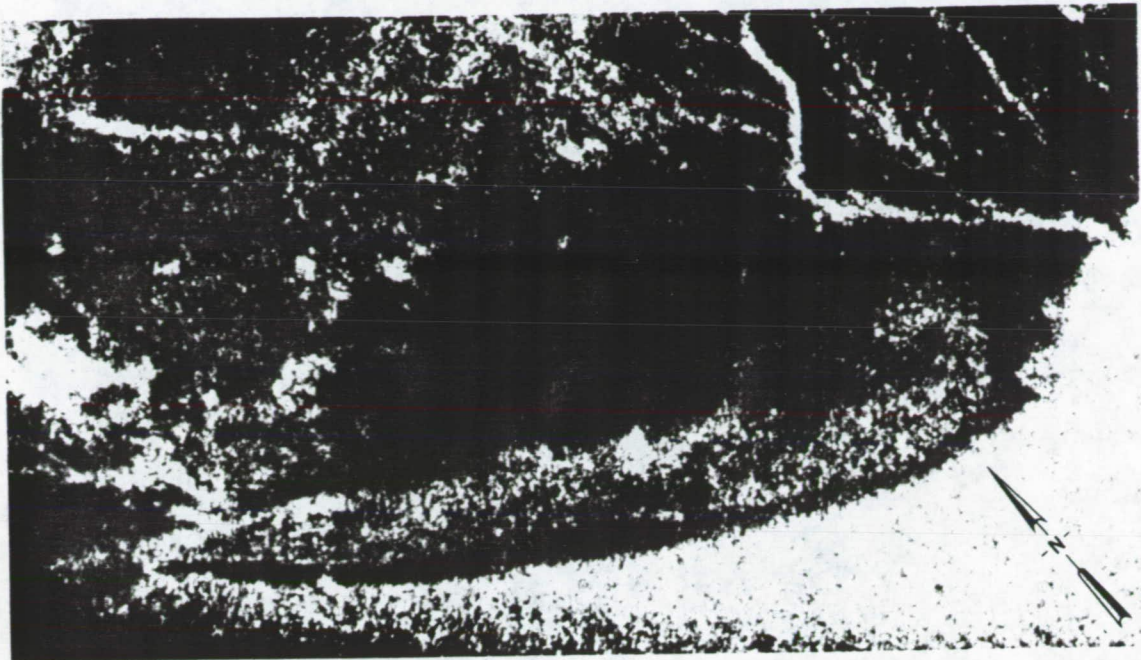
As a guide for the field investigation it is useful to calculate the smooth and rough criteria of Peake and Oliver (1971) which were described by Schaber, Berlin, and Brown (1976) and by Sabins (1978). These criteria are:

Smooth Criterion

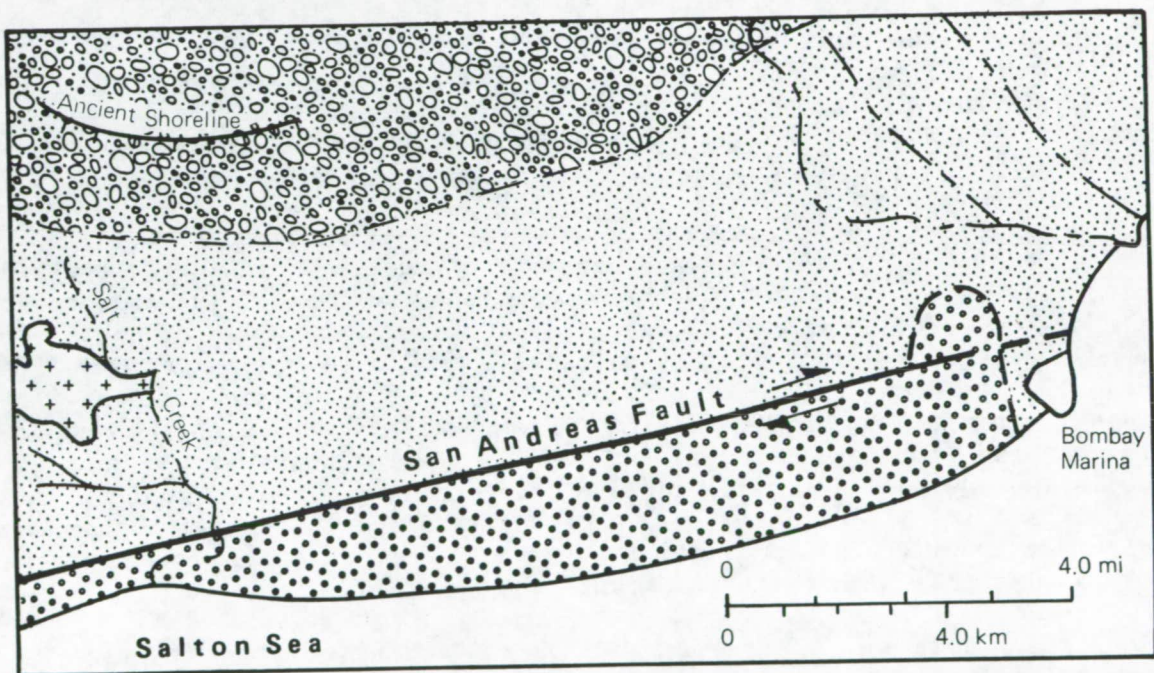
$$h < \frac{\lambda}{25 \sin \gamma}$$

Rough Criterion

$$h > \frac{\lambda}{4.4 \sin \gamma}$$



A. Seasat Radar Image Acquired September 14, 1978
Look Direction is Toward the Northeast.




 ALLUVIAL FAN
 DEPOSITS OF
 SAND AND GRAVEL


 SALT CRUST


 LAKE COAHUILA
 DEPOSITS OF
 SAND AND SILT


 BORREGO FORMATION
 OUTCROPS

B. Interpretation Map

Figure 2. Seasat image and interpretation map.

where

h = the average height of surface irregularities, or surface roughness

λ = the radar wavelength, which is 23.5 cm for Seasat

γ = the depression angle between the horizontal plane and the radar wave incident upon the terrain. For Seasat the average depression angle is 70° .

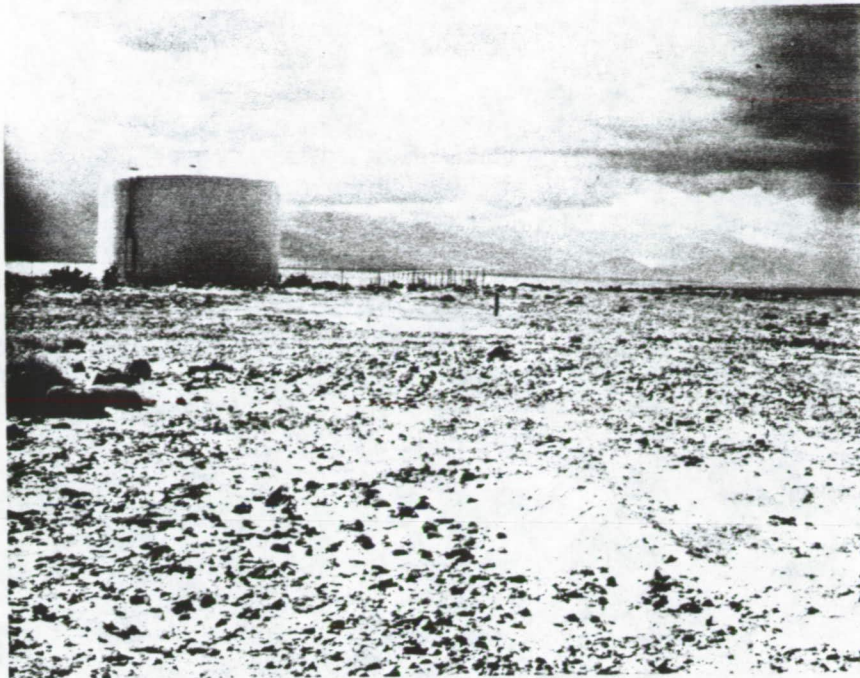
For Seasat the smooth criterion is calculated as 1.0 cm, which means that surfaces with a vertical relief of 1.0 cm or less will appear smooth and have a dark signature. The rough criterion is 5.7 cm, which means that surfaces with a vertical relief of 5.7 cm or more will appear rough and have a bright signature. Surfaces with vertical relief ranging from 1.0 to 5.7 cm will have intermediate signatures. These roughness values are for comparative purposes, because radar returns are influenced by many surface properties in addition to vertical relief. The shape and horizontal spacing of surface features are important but difficult to describe in a quantitative manner. Variations in the complex dielectric constant, principally due to variations in moisture content, may also influence the strength of the radar return (MacDonald and Waite, 1973, p. 149).

C. Field Investigation

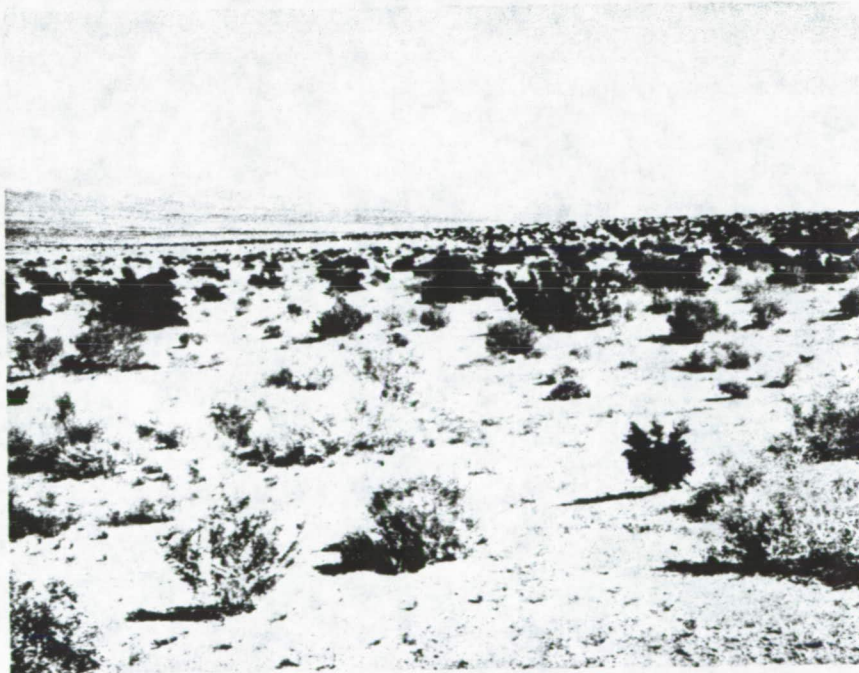
Topographic maps, stereo aerial photographs, and field observations show that the Durmid Hills are a low, southeast-trending ridge with slopes of 2° or less. The maximum elevation is 30 m and the minimum elevation is 70 m below sea level at the shore of the Salton Sea. Vegetation is very scarce in this arid climate.

The Borrego Formation (Pleistocene age) crops out on the southwest side of the San Andreas fault (Figure 2B) and consists of poorly consolidated siltstone with minor beds and concretions of hard, resistant sandstone. The infrequent rains erode the soft siltstone and produce a surface that is littered with fragments and concretions of sandstone that range from gravel to boulders in size (Figure 3A). The local relief of this detritus is well in excess of the 5.7-cm criterion for a rough surface on Seasat images, which agrees with the bright signature of the Borrego outcrop in Figure 2A. The roughness of the Borrego surface is increased by a myriad of closely spaced, steep-walled gullies. The Borrego siltstone is impermeable, which causes rainfall to run off rather than soak into the ground. The combination of high surface runoff and nonresistant bedrock results in a highly dissected surface.

The surface northeast of the San Andreas fault is covered by unconsolidated sand and silt deposited in Lake Coahuila (Figure 2B), which occupied the Salton trough in Pleistocene time. As shown in the photograph of Figure 3B, relief of this surface is less than the 1.0-cm value for the smooth criterion, which accounts for the dark signature on the Seasat image. Gullies are scarce on the Coahuila surface because the permeable sand and silt absorb most of the rainfall. Creosote bush and other desert shrubs are scattered over the Coahuila surface but are too sparse to influence the radar signature.



A. Outcrop of Borrego Formation on Southwest Side of San Andreas Fault. The Boulders and Cobbles Form a Rough Surface That Has a Bright Signature on the Seasat Radar Image.



B. Sand and Silt Deposits of Lake Coahuila on Northeast Side of San Andreas Fault. These Deposits Form a Relatively Smooth Surface That Has a Dark Signature on the Seasat Radar Image.

Figure 3. Outcrop photographs in the Durmid Hills.

The field observations and radar calculations explain the bright and dark signatures on opposing sides of the Seasat lineament that corresponds to the San Andreas fault. In the field the fault trace is relatively obscure and is marked by the contact between Borrego outcrops and the Coahuila surface. In the Durmid Hills the San Andreas fault is not marked by topographic features such as scarps, sag ponds, and pressure ridges. If these features were formed by displacement along the fault, they have later been removed by erosion of the nonresistant rocks. Babcock (1974, Figure 5) mapped outcrops of Borrego Formation on the northeast side of the San Andreas fault, but these are largely mantled by thin deposits of Coahuila sand and silt, which produce a relatively smooth surface.

III. COMPARISON OF IMAGES

It is instructive to compare the Seasat image with images that were acquired by other remote sensing systems. The Landsat and Skylab images (Figure 4) and the aircraft radar image (Figure 5) are reproduced at the same scale as the Seasat image.

A. Landsat Image

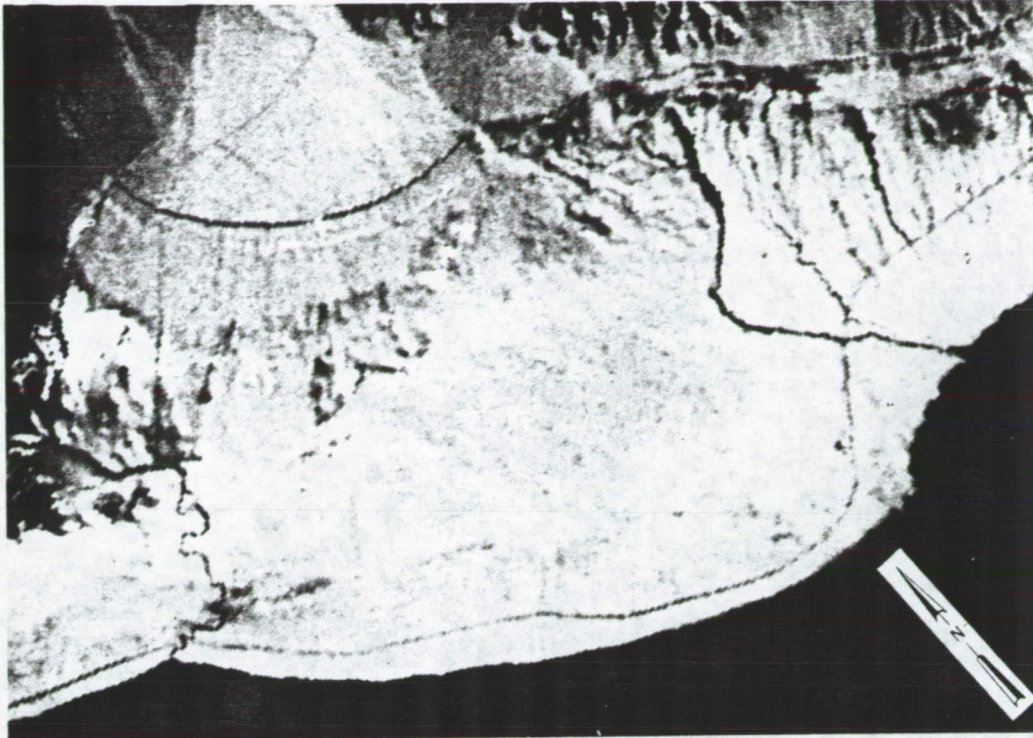
The red image (band 5) of Landsat (Figure 4A) was selected because this band has the maximum tonal contrast in the Durmid Hills area. The image was digitally processed at the EROS Data Center to improve the contrast and spatial detail. Water in the Salton Sea and Coachella Canal has a dark signature, as do the water and vegetation in Salt Creek and the unnamed creek near Bombay Marina. The dark trace parallel with the shoreline is formed by Highway 111 and the Southern Pacific Railroad. On the Landsat image there is no tonal difference between the Borrego and Coahuila surfaces, and the San Andreas fault cannot be recognized. Infrared-color composite Landsat images of Durmid Hills (not illustrated here) were also examined, but no evidence was found of the fault or of the differences in surface materials.

B. Skylab Photograph

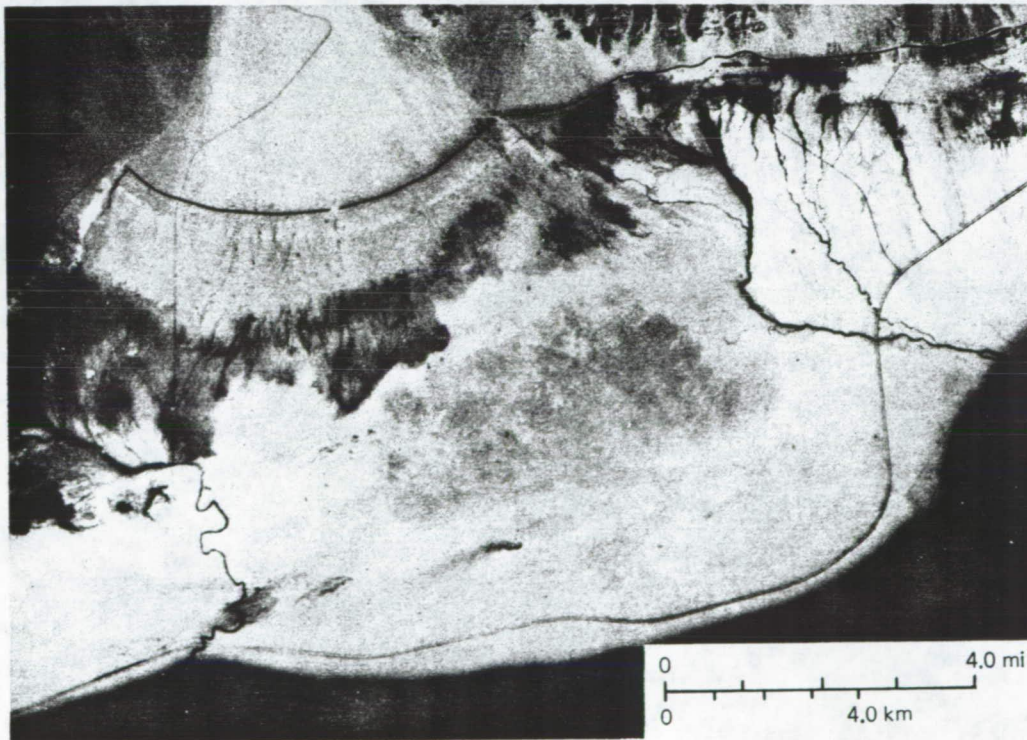
The Skylab earth terrain camera photograph (Figure 4B) was acquired in the reflected infrared band and has a spatial resolution of approximately 15 m in contrast to the 80-m resolution of Landsat images. Aside from the higher resolution of the Skylab photograph, there is little difference in appearance of the two images. The Skylab photograph has no discernible tonal difference between the Borrego and Coahuila surfaces, and the San Andreas fault is not recognizable. There is an area of medium gray tone on the northeast flank of the Durmid Hills, but this is an area of reduced reflectance within the Coahuila surface that is not related to the fault contact.

C. Aircraft Radar Image

The side-looking airborne radar image (Figure 5) was acquired at a wavelength of 0.86 cm and an average depression angle of 45°. For this image the smooth criterion is calculated as 0.05 cm and the rough criterion as 0.28 cm. Most natural surfaces, other than calm water, are rough for these criteria, and this is seen in the overall bright appearance of the image (Figure 5). Even the sands of the Coahuila surface are rough and produce a bright signature that is indistinguishable from the Borrego surface. Because of this lack of tonal contrast, the San Andreas fault cannot be recognized on the short-wavelength radar

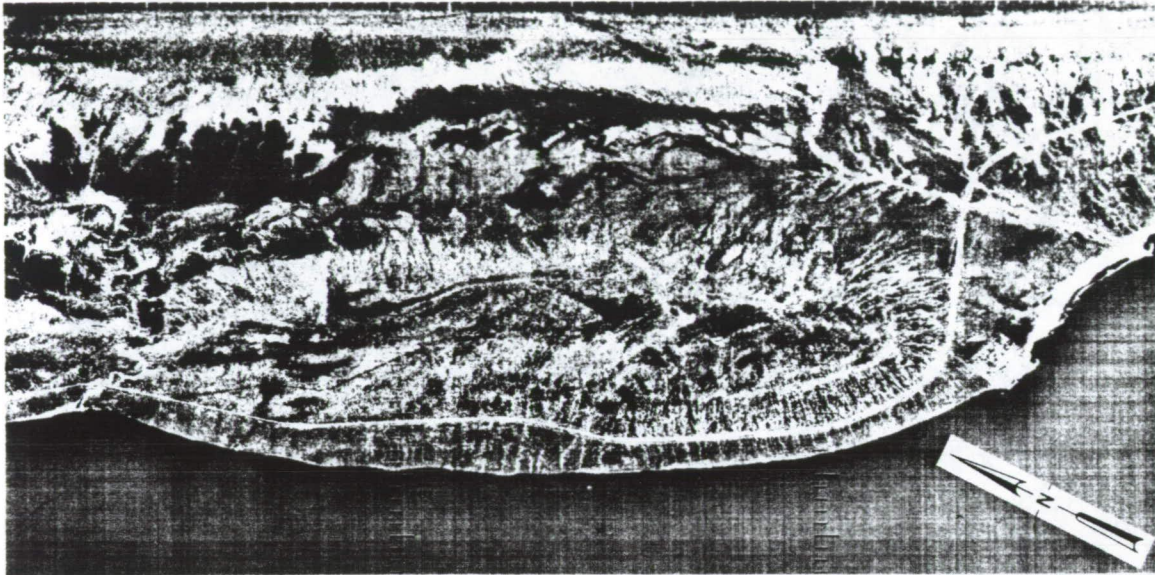


A. Landsat 2066-17384, Band 5 (red). Acquired March 29, 1975 and Digitally Processed at Eros Data Center.



B. Skylab-3 Infrared Black-and-White Photograph Acquired September 10, 1973 With Earth Terrain Camera (S-190B).

Figure 4. Landsat and Skylab images of Durmid Hills.



0 4.0 mi
0 4.0 km

Figure 5. Real aperture side-looking airborne radar image. This Ka-band image (wavelength = 0.86 cm) was acquired in November 1965. Radar look direction is toward the southwest. Image courtesy NASA and U.S. Geological Survey.

image. In the northeastern portion of the image are some patches of fine-grained sediment within the Coahuila deposits that produce dark signatures.

The airborne radar image was acquired at a short wavelength and relatively low flight altitude (approximately 6000 m) which results in a relatively high spatial resolution of approximately 10 m. The high resolution and optimum depression angle enable individual gullies to be recognized on the southwest flank of the Durmid Hills. These gullies are not discernible on any of the other images.

IV. SUMMARY AND CONCLUSIONS

The wavelength of the Seasat radar (23.5 cm) is optimum for producing contrasting image signatures of surface materials juxtaposed along the San Andreas fault in the Durmid Hills. Erosion of the Borrego Formation on the southwest side of the fault produces a surface that appears rough at the Seasat wavelength and has a bright signature on the image. Sand and silt deposits of Lake Coahuila on the northeast side of the fault are relatively smooth and produce a dark signature. The San Andreas fault is clearly expressed on the Seasat image as a southeast-trending tonal lineament that is bright on the southwest side and dark on the northeast. The San Andreas fault is not distinguishable on Landsat and Skylab images of the Durmid Hills because the Borrego Formation and the Coahuila deposits have a relatively high albedo and do not produce contrasting signatures at these visible and photographic infrared wavelengths. An airborne radar image was acquired at a very short wavelength; therefore, both the Borrego Formation and the Coahuila deposits appear rough. As a result, on the airborne radar image the signatures are bright on both sides of the fault and there is no tonal contrast.

The geologic cause for the juxtaposition of the Borrego Formation and Lake Coahuila deposits along the San Andreas fault has not been determined. The two most probably hypotheses are: (1) in Coahuila time the fault formed a topographic scarp that restricted deposition of Coahuila sediments to the northeast side of the fault, or, (2) in post-Coahuila time, uplift of the southwest side of the fault resulted in erosion of Coahuila deposits and exposure of Borrego outcrops on that side of the fault.

In summary, although the Seasat radar system was designed for oceanographic applications, it does have a capability for geologic mapping in suitable terrain. These Seasat observations suggest that geologically useful information will be obtained from future orbital radar missions, such as the Space-Imaging Radar (SIR-A) Mission of Space Shuttle.

REFERENCES

- Babcock, E. A., 1974, Geology of the northeast margin of the Salton trough, Salton Sea, California: Geological Society of America Bulletin, v.85, pp. 321-332.
- Jennings, C. W., compiler, 1967, Salton Sea sheet: Geologic Map of California, 1:250,000 scale, California Division of Mines and Geology, Sacramento.
- MacDonald, H. C., and W. P. Waite, 1973, Imaging radars provide terrain texture and roughness parameters in semiarid environments: Modern Geology, v. 4, p. 145-158.

Peake, W. H., and T. L. Oliver, 1971, The response of terrestrial surfaces at microwave frequencies: Ohio State University Electroscience Lab., 2440-7, Tech. Rep. AFAL-TR-70-301, Columbus, Ohio.

Sabins, F. F., 1978, Remote sensing — principles and interpretation: W. H. Freeman and Co., San Francisco.

Schaber, G. G., G. L. Berlin, and W. E. Brown, 1976, Variations in surface roughness within Death Valley, California — geologic evaluation of 25-cm-wavelength radar images: Geological Society of America Bulletin, v.87, pp. 24-41.

ANALYSIS OF SEASAT ORBITAL RADAR IMAGERY FOR GEOLOGIC MAPPING IN THE
APPALACHIAN VALLEY AND RIDGE PROVINCE, TENNESSEE-KENTUCKY-VIRGINIA

J. P. Ford
Jet Propulsion Laboratory
California Institute of Technology
Pasadena, California

ABSTRACT

Seasat orbital imaging radar shows a high sensitivity to terrain-surface features in the Appalachian Valley and Ridge province. In an area of very little rock exposure, with extensive forest cover and leaf canopy, topographic mapping from the SAR imagery provides an effective basis for small-scale lithologic and structural interpretation. Extensive geomorphic lineaments that correlate with mapped faults from published sources, and numerous uncorrelated lineaments less than 10 km long are widespread on the imagery. The extensive lineaments are perceived and mapped about equally from Landsat MSS imagery, but larger numbers of the short lineaments are mapped from the SAR and their preferred orientations are more clearly revealed. The close coincidence of some of the uncorrelated lineaments with geophysical trends in the basement, the alignments with known structural features, and the orthogonal relationship of certain lineaments suggest areas for further geological investigation.

The high image-contrast that facilitates lineament perception and highlights topography on the SAR images reflects the high sensitivity of the Seasat radar to change in terrain slope in the Appalachian Valley and Ridge area. Both the Seasat SAR and the Landsat MSS sensors suppress lineaments that are oriented at or near the illumination direction of the respective imaging systems. Lineament suppression by the SAR is partly compensated by the dual-look capability of the Seasat system. The advantages of the SAR in highlighting topography and detecting geomorphic lineaments from orbital altitudes are offset to some extent by the layover and geometric distortion introduced in the Seasat imaging geometry. The present study shows that future geologic application of orbital imaging radar for mapping and geologic interpretation demands an imaging geometry that reduces the effects of layover encountered on the Seasat SAR images but retains the topographic enhancement capability of imaging radar systems.

I. INTRODUCTION

The synthetic-aperture radar (SAR) experiment aboard Seasat was designed primarily for imaging ocean-surface conditions and determining the distribution and movement of sea-ice in polar latitudes. The radar was operated at L-band (23.5 cm wavelength) in order to ensure the capability of cloud penetration. It was flown on a satellite in circular near-polar orbit at about 800 km above the Earth. A detailed description of the Seasat SAR experiment with its objectives and rationale is given by Teleki and Ramseier (1978). The purpose of the present study is to analyze Seasat SAR imagery of a land area and determine the potential of this microwave imaging system for geologic mapping.

SAR imagery was selected from portions of three orbits that cover the southern Appalachian Basin in Tennessee, Kentucky and Virginia. The study area occupies approximately 12,000 km² in the Valley and Ridge geomorphic province, and in adjacent margins of the Cumberland Plateau (northward) and Smoky Mountains (southward). The images were optically correlated. The ground tracks of imagery of the three orbits that were used in this study are shown superimposed on a generalized geologic map of the area in Figure 1. As the Seasat SAR is a single right-side-looking system orbiting in a plane inclined to the Earth's axis of rotation, the imagery was acquired from two different look directions. The orientation of the look direction for any given image is determined from the bearing of the spacecraft at the time of image acquisition. Special attention is given here to the area of the Valley and Ridge province from 35° 40' to 36° 55' N latitude and from 83° 00' to 84° 20' W longitude. This area is covered by imagery acquired looking N67.5° E (Figure 2; ascending pass) and looking N67.5° W (Figure 3; descending pass). No Seasat imagery exists looking N67.5° W (Figure 3; descending pass). No Seasat imagery exists looking N67.5° W for the area in Figure 2 that is not covered in Figure 3.

Previous applications of radar remote-sensing for structural interpretation in the southern Appalachians have been reported by Elder et al. (1974) and Johnston et al. (1975). Their imagery was acquired by aircraft using the AN/APQ-97 system. This is real-aperture radar that operates at much shorter wavelength (0.8 cm, at K-band) and has superior resolution to the L-band SAR system aboard Seasat. Studies by the above-mentioned authors show that fault and joint systems identified by lineaments and linear patterns in the K-band radar imagery were verified by surface observations and that two examples of prominent lineaments proved to be previously unrecognized faults. They also cautioned that not all lineaments seen on the imagery are structural in origin and that laboratory interpretations should be field-checked.

The use and application of Seasat SAR images for geologic mapping purposes are described in this study, and compared with Landsat multispectral scanner (MSS) imagery and with aerial photography. The SAR imagery is originally at a scale of 1:500,000. Photographic enlargement by a factor of 2 provides the best image-size for visual analysis. Valleys, ridges and mountains appear strongly contrasted on the SAR images because of changes in radar energy returned from their respective surfaces. Fine details of drainage networks are selectively revealed and the varied topography of the area produces distinctive textures and tones on the images.

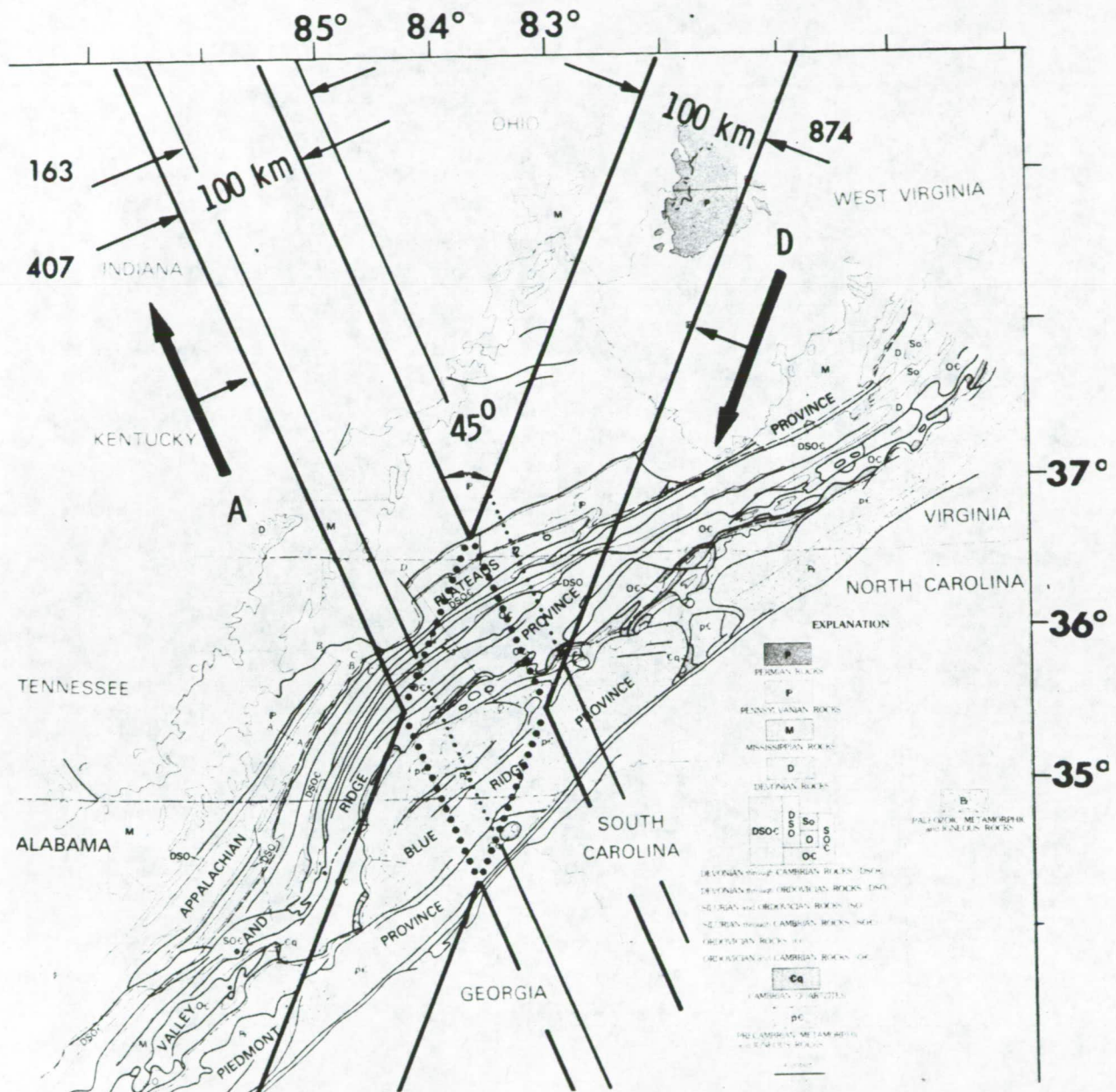


Figure 1. Ground tracks of Seasat SAR imagery looking N 67.5° E (A), and N 67.5° W (D) superimposed on generalized geologic map (from Harris and Milici, 1977). Area of the present study is confined within latitudes 35°40' N to 36°55' N and longitudes 83°00' W to 84°20' W. Numerals against the ground tracks are to identify specific satellite revolutions.



Figure 2. Seasat SAR mosaic of imagery from revolutions 407 and 163. Look direction is N 67.5° E. Satellite is in ascending pass.

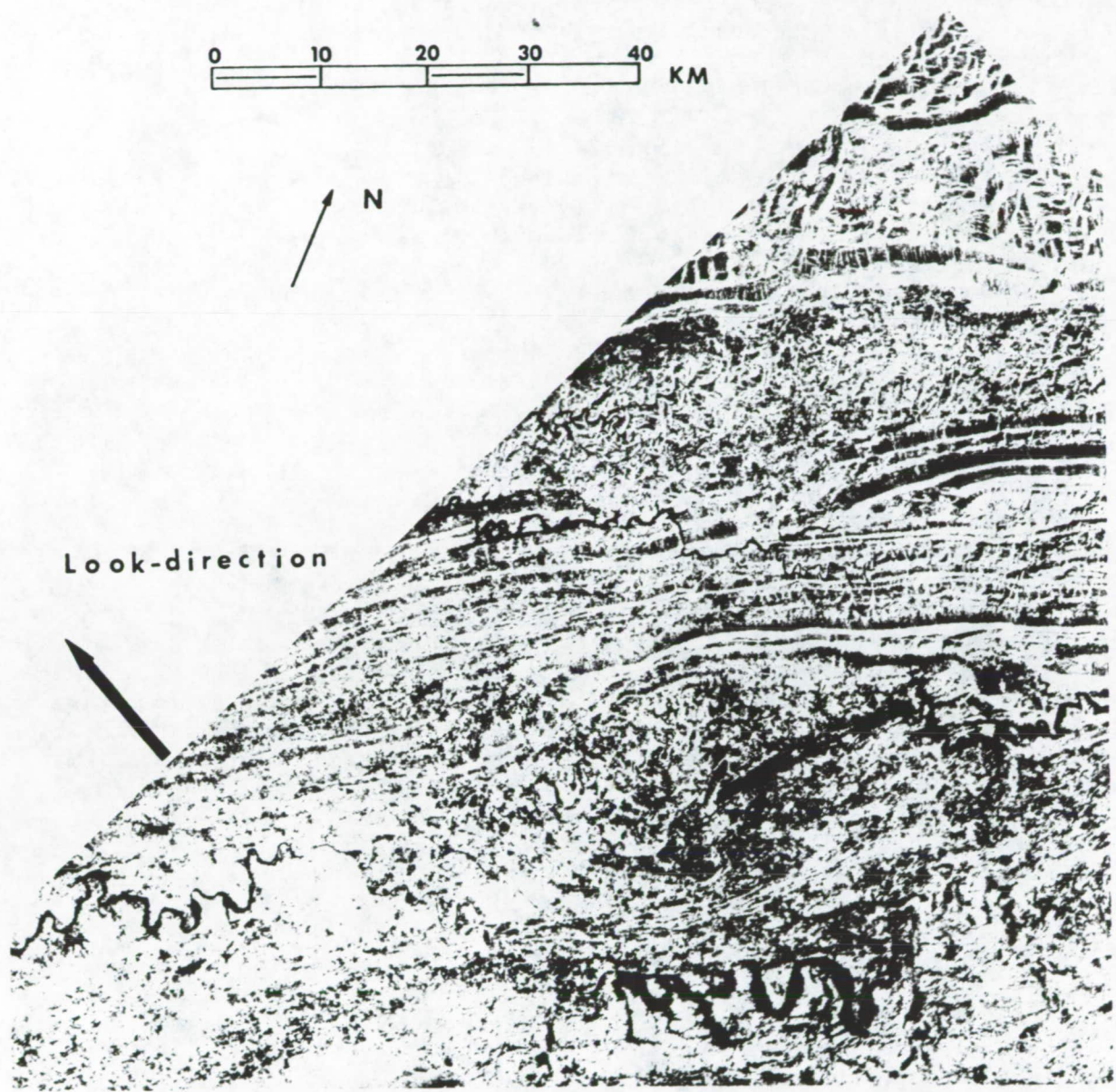


Figure 3. Seasat SAR mosaic of imagery from revolution 874. Look direction is N 67.5°W. Satellite is in descending pass.

ORIGINAL PAGE IS
OF POOR QUALITY

II. LITHOLOGIC MAPPING

Bedrock in the southern Appalachians is deeply weathered and covered by a nearly continuous regolith of variable thickness up to about 30m. Depth to bedrock varies with slope and type of underlying lithology (Harris and Kellberg, 1972). Transported regolith commonly integrates with residual mantle, especially at and near the base of ridges (Hadley and Goldsmith, 1963; King, 1964). Outcrops are limited to stream sections, highway cuts and quarries, steep slopes, and small local bedrock pinnacles that project to the surface. The surface area of rock outcrop as seen by the Seasat imaging radar is therefore virtually negligible.

The Seasat SAR imagery was acquired in summer 1978. Except for cities and other cultural features the southern Appalachians are entirely vegetation-covered at that season of the year. Major valleys are cultivated or grass-covered. Ridges and mountains, which are blanketed with mixed deciduous and coniferous forest, are covered by a thick leaf-canopy. The valleys have level to gently undulating surfaces, with slopes that are generally less than 7°. The ridges and mountains have steep slopes, commonly from 20° - 30° up to maximum of about 40°. The shape of the leaf-canopy surface over the steep slopes appears to reflect the general shape of the underlying terrain surface. Lithology cannot be seen or directly identified from the SAR images (Figures 2, 3). The potential for lithologic mapping from the images is therefore limited to interpretation from the patterns of topography or vegetation.

Five distinctive image textures are discriminated from the SAR images (Figures 2, 3) and mapped in Figure 4. Each mapped image texture is characterized by a representative image area equivalent to about 7 km square. At this scale each textural unit mapped is relatively independent of the local brightness variations in the two images that result from differences in the radar look-direction. The textures on the images are discriminated on the basis of image granularity, definition, and contrast. Granularity refers to the clustering of gray levels, and ranges from coarse to fine. Definition is the degree to which gray levels can be discriminated on the images. It ranges from high to low. Contrast refers to the range of gray levels present. It extends from few widely spaced levels of gray that give high contrast to numerous closely spaced levels of gray that result in low contrast. On a scale of high, medium, and low, none of the mapped image textures have a low contrast. Table 1 shows that each mapped image texture displays a unique combination of the above characteristics.

The features of each image texture listed in Table 1 provide a measure of the Seasat SAR backscatter from the vegetation cover on the level-to-sloping terrain in the study area. The SAR images (Figures 2, 3) and the image texture map (Figure 4) were compared with U. S. Geological Survey topographic maps, with Landsat MSS images, and with aerial photography. A mosaic was made from overlapping aerial photographs at a scale of 1:120,000. About 40 photographs were necessary to cover the SAR image-area common to Figures 2 and 3. Vegetation and topography were field checked. A strong correlation between topography and the SAR image textures mapped in Figure 4 was observed.

In many areas of the Valley and Ridge province both reconnaissance and detailed geologic mapping are facilitated by studying topography (Swingle, 1973). In order to compare the close correlation between SAR image texture and topography with the underlying lithology, detailed comparisons of the data were made using existing state geologic maps (Tennessee: Halden, et al., 1966. Virginia:

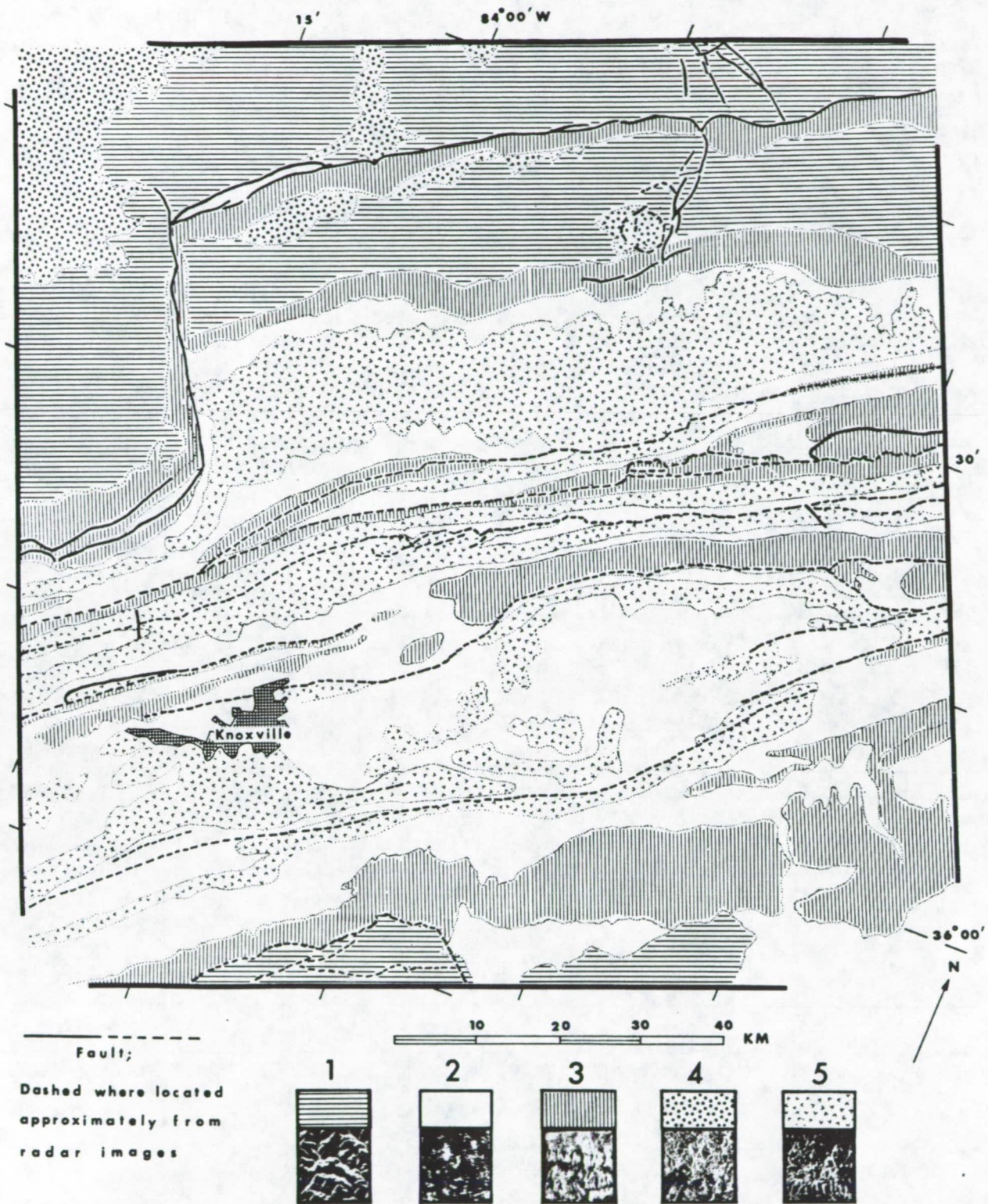


Figure 4. Image-texture map drawn from Seasat SAR images (Figures 2, 3). Characteristics of image-texture units 1-5 are listed in Table 1. Faults (from published sources) are correlated with extensive lineaments on the SAR imagery.

Calver and Hobbs, 1963), numerous Geologic Quadrangle maps and Miscellaneous Investigations maps in the Tennessee-Kentucky-Virginia tri-state area published by the U.S. Geological Survey or by the Tennessee Division of Geology respectively, and relevant published literature (e.g., Harris and Milici, 1977; Milici, 1973).

Details of the topography, vegetation cover, underlying lithology, and stratigraphy relevant to each mapped image texture (Figure 4) are summarized in Table 2. Maturely dissected mountains with high relief (texture 1) are held up by thick clastic sequences that include coal-bearing rocks in the Cumberland Plateau, and by quartzite, shale and conglomerate in the marginal portion of the Smoky Mountains. Maturely dissected rolling hills in the Cumberland Plateau (texture 4) have lower relief than the adjacent mountains. They are underlain by the same clastic sequences, from which the upper section has been stripped by erosion. Level to gently undulating valleys (texture 2) are extensively formed on clay-shale and on limestone. Elogated mountain slopes and ridge slopes, prominent cliffs and hogbacks (texture 3) tend to be steep and scalloped in profile. They are formed mostly on associations of shale with siltstone, sandstone, or calcareous sandstone. Rolling undulating knobby hills in the elongated ridges (texture 5) are mostly underlain by dolomite or cherty dolomite.

In comparing the image texture map (Figure 4) with the geologic maps referenced above it is evident that the varied topography which is expressed by the five image textures serves to discriminate five underlying bedrock associations. Each broad class of topography reflects the differential resistance to erosion of the underlying bedrock. By contrast there is very little correlation between image texture and vegetation cover, and no correlation with lithologic or stratigraphic units. Mixed deciduous and coniferous leaf-canopy blankets the area covered by four of the five different image textures. None of the image textures corresponds with a specific lithologic or stratigraphic unit.

Comparison with Landsat MSS imagery and aerial photography of the same area shows potential for discriminating resistant and weak lithologic associations from the latter forms of imagery by interpreting image textures as described above. Figure 5 is an example of a contrast-enhanced Landsat MSS image (band 6) of the study area. Topography is less strongly contrasted on the MSS image than on the SAR images. Topography on aerial mapping photography appears in very

Table 1. Summary of granularity, definition, and contrast for each of five image-texture units mapped in Figure 4

Texture	Granularity	Definition	Contrast
1	Coarse	High	High
2	Fine	Low	High
3	Fine	High; closely spaced, sub-parallel, linear orientations; or finely granular	Medium
4	Fine	High	Medium
5	Medium	Medium; linear to curvilinear orientations	High

Table 2. Correlation of mapped image units (1-5) with topography, vegetation cover, underlying lithology and stratigraphic units

Image Texture	Topography	Vegetation	Lithology	Stratigraphic Units
1	Maturely dissected mountains; steep slopes up to 40°; relief up to 700 m.	Mixed forest, deciduous and coniferous.	North: Interbedded sandstone, shale siltstone, coal; ss. in massive beds up to 10 m thick. South: Quartzite, quartz-pebble conglomerate, interbedded shale, ss., conglom.	<u>Pennsylvanian</u> : Upper Breathitt Grp. (USGS); equiv. Vowell Mtn. Fm., Redoak Mtn. Fm, Graves Gap Fm., of Tenn. usage). <u>Cambrian</u> : Hesse Ss., Cochran Conglomerate. <u>Precambrian</u> : Sandsuck Fm.
2	Level to gently undulating valley floors; slopes mostly less than 7°; relief up to 80 m, mostly less than 40 m.	Cultivation and grass land, few clusters of deciduous trees on small hills and knolls.	Shale and interbedded limestone clay-shale, interbedded siltstone, some dolomite.	<u>Ordovician</u> : Chickamauga Grp. excluding Tellico Sandstone and Holston Ls. <u>Cambrian</u> : Conasauga Grp. (shales)
3	Elongated mountain slopes, ridge slopes, prominent cliffs, hogbacks; steep mostly 30° ±5°; relief up to 120 m except along Cumberland Mtn. where it reaches 300 m.	Mixed forest, deciduous and coniferous.	Interbedded conglomerate, sandstone, shale, coal; massive sandstone; shaly limestone; shale with interbedded siltstone and sandstone; calcareous sandstone.	<u>Pennsylvanian</u> : Lee Fm. (USGS: equiv. Crab Orchard Mtns. Grp. of Tenn. usage), Gizzard Grp. (Tenn. usage). <u>Mississippian</u> : Grainger Fm. <u>Silurian</u> : Clinch Sandstone <u>Ordovician</u> : Sequatchie Fm., Juniata Fm., Tellico Sandstone <u>Cambrian</u> : Rome Formation.

Table 2. Correlation of mapped image units (1-5) with topography, vegetation cover, underlying lithology and stratigraphic units (continued)

Image Texture	Topography	Vegetation	Lithology	Stratigraphic Units
4	Rolling hills, maturely dissected; moderate slopes; relief up to 180 m.	Mixed forest, deciduous and coniferous.	Interbedded sandstone, shale, siltstone, coal; ss. massive. Thick-bedded up to 12 m, locally cliff-forming.	<u>Pennsylvanian</u> : Lower Breathitt Grp., Upper Lee Fm. (USGS, equiv. Indian Bluff Fm., Slatestone Fm., Crooked Fork Grp., of Tenn. usage).
5	Rolling, undulating hills in places forming knobby elongated ridges, maturely dissected; slopes up to 30° relief up to 120 m.	Mixed forest, deciduous and coniferous.	Dolomite and cherty dolomite; dense crystalline limestone and interbedded shale.	<u>Ordovician</u> : Holston Ls., Knox Grp. including Newala Fm., Longview and Chepultepec dolomites. <u>Cambrian</u> : Copper Ridge Dolomite (Basal Knox Grp.); Conasauga Grp., (limestones).

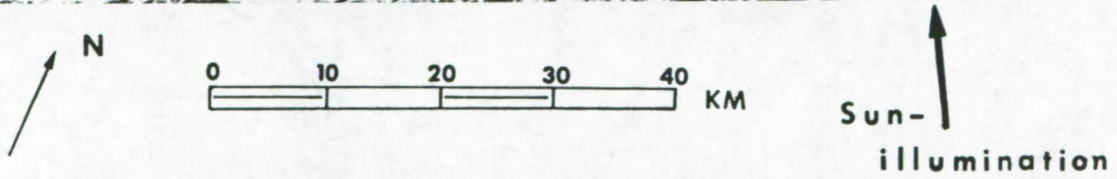


Figure 5. Landsat MSS subsene of area covered by Seasat SAR in Figure 2. Image is contrast-enhanced. Sun illumination direction is N 30° W (AZ 150), elevation angle is 26°. (Scene ID: 1858-15303, Sevierville, Tennessee, Band 6, Nov. 28, 1974).

ORIGINAL PAGE IS
OF POOR QUALITY

great detail, as likewise do vegetation, patterns of land utilization, and other cultural features. This wealth of detail tends nevertheless to obscure the regional topographic patterns seen on small scale imagery acquired from orbital altitudes.

III. DRAINAGE MAPPING

Drainage of the Valley and Ridge province is structurally controlled and forms a characteristic regional trellis pattern. Major streams meander in the strike valleys, and in many places pass through a ridge gap to the next adjacent major valley. Geomorphic lineaments are emphasized by the alignment of drainage courses and low gaps in the intervening ridges. Ridge slopes are extensively dissected by small tributary streams whose respective orientations lie at various angles across the ridge-trends (Figure 6). Major streams that are wider than an image resolution element (about 50 m) act as specular reflectors and appear black on the imagery. Positions of smaller streams and tributaries are revealed more by multiple reflections from their respective banks and associated vegetation than from water that is present in them.

The Cumberland Plateau is maturely dissected and shows a dendritic drainage pattern. Extended linear and curvilinear elements of the regional pattern are highlighted on the SAR imagery by the layover of steep slopes in the area.

The large reservoirs of the Tennessee Valley Authority appear mostly in black on the imagery. Gradational changes in shades of gray obscure the water-land interface in places, and the position of the lakeshore is not everywhere clear around the margins of Cherokee and Douglas Lakes. Field checks show that an abrupt transition exists from water to land. Therefore, it is not clear whether the gradational changes in shades of gray represent turbulent water, marsh, or other conditions that relate to characteristics of the radar imaging system. The Seasat SAR system is insensitive to small linear drainage features of low relief that are oriented at, or are near-parallel to the radar look-direction.

IV. STRUCTURAL MAPPING

Structurally the Valley and Ridge province is dominated by thrust faults that flatten at depth to form low-angle bedding-plane thrusts, and by folds unconnected with the basement. Figure 7 is a simplified structural sketch map and cross-section that shows the major folds and faults in the area. The Cumberland Plateau is underlain by relatively undeformed gently dipping strata. The Pine Mountain thrust has carried a thin plate of rocks northwestward over the Cumberland Plateau for a distance estimated at about 6.4 km (Harris and Milici, 1977). The basement surface dips evenly southeastward. Estimates of depth to basement in the study area range from about 3 km at the north end of the Jacksboro fault to over 5 km southeast of Douglas Lake. Basement structures and lithology have been inferred from magnetic and gravitational data (Watkins, 1962, 1964). The topographic trend in the Valley and Ridge province is parallel to the structural strike. The terrain in the study area is divided by major thrust faults into 7 northeast-trending thrust slices, with strata folded and faulted in a more or less regular fashion. West of a line between Morristown, Tn., and Middlesboro, Ky., the structural strike is about N 50° E. East of that line the strike trends N 60° E.

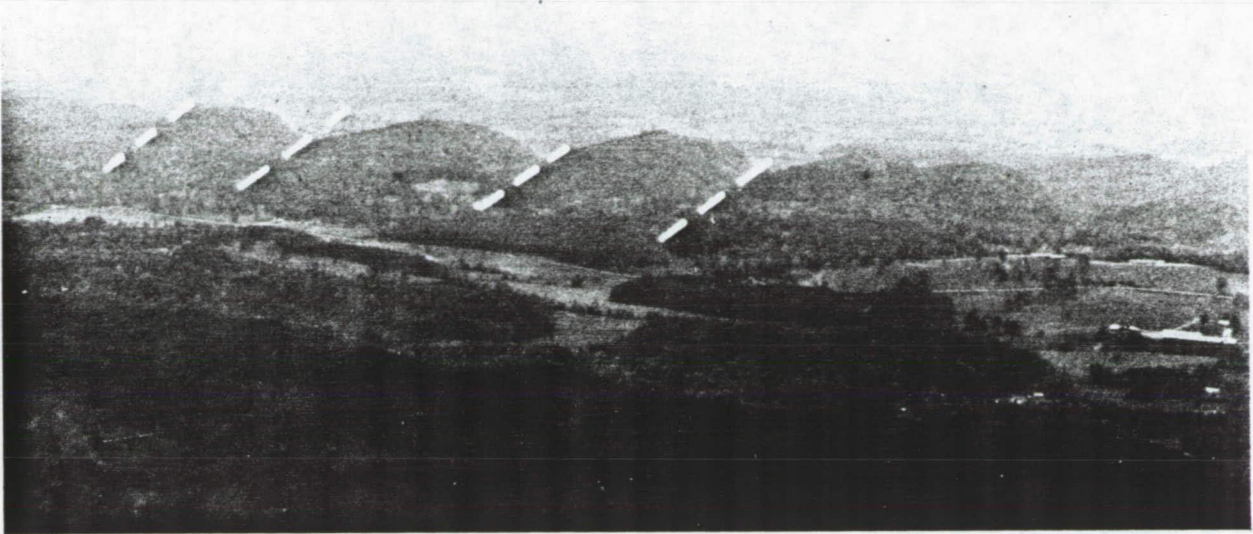


Figure 6. Valley and Ridge topography, looking north from Chilhowee Mountain, Tennessee, showing pronounced symmetrical repetition of small tributary valleys (marked by dashed lines) forming wind gaps in Tellico Sandstone. Photo date: May 1979.

ORIGINAL PAGE IS
OF POOR QUALITY

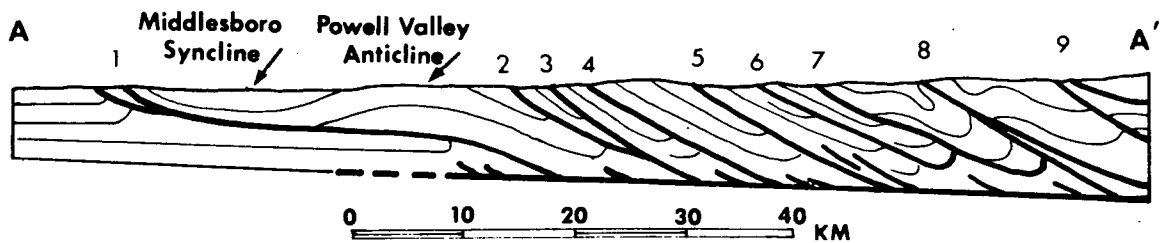
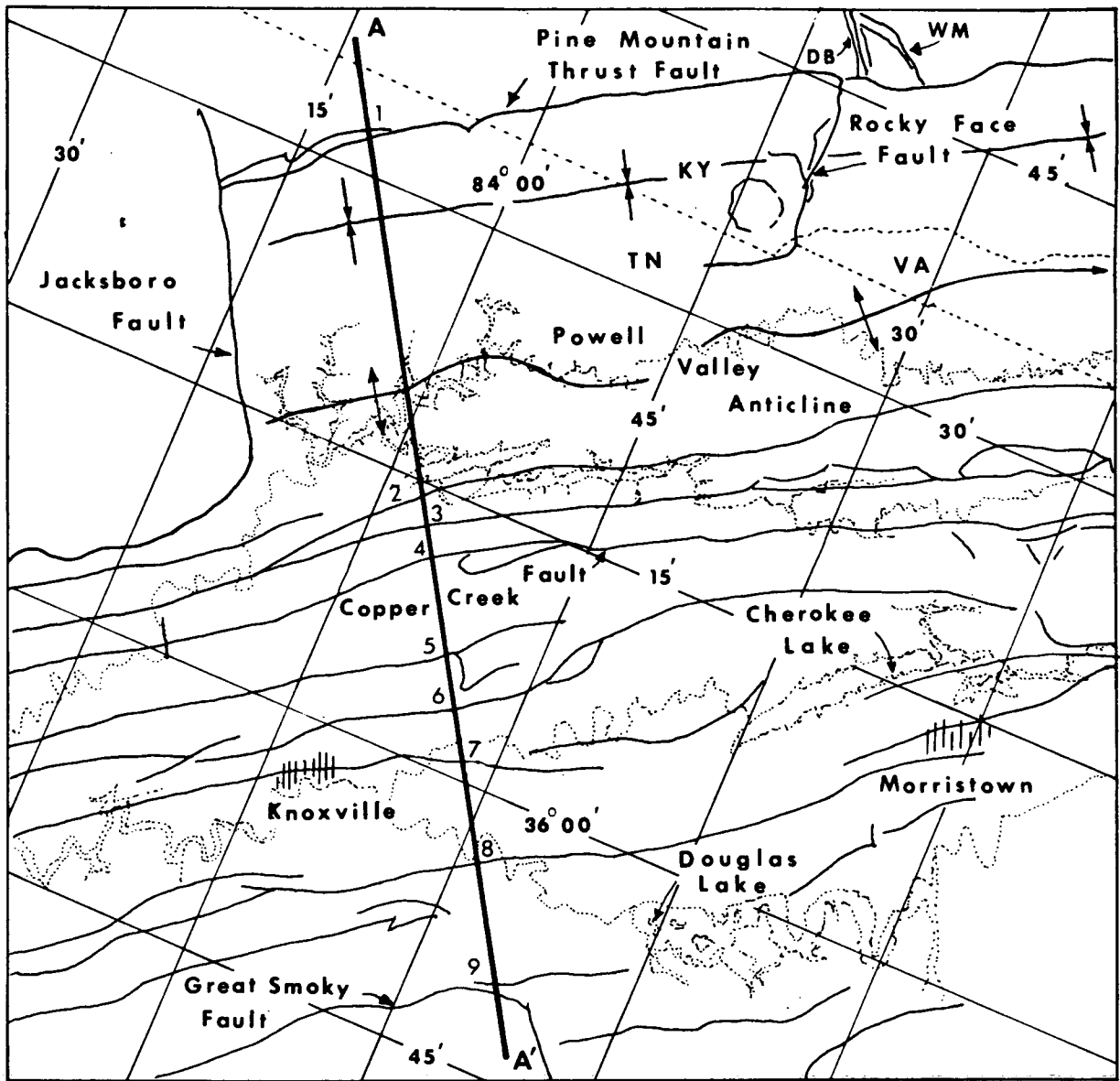


Figure 7. Simplified structural sketch map and cross-section of study area showing major folds and faults (after Harris and Milici, 1977). Numbered faults are: (1) Pine Mountain, (2) Wallen Valley, (3) Clinchport, (4) Copper Creek, (5) Beaver Valley, (6) Saltville, (7) Knoxville, (8) Dumplin Valley, (9) Guess Creek/Great Smoky. WM = White Mountain fault zone, DB = Dorton Branch fault zone, m = Middlesboro Basin.

Structural mapping in the southern Appalachians from Seasat SAR imagery is feasible where the structures can be inferred from the geomorphology. Major faults appear on the SAR imagery (Figures 2, 3) as extensive lineaments. The Jacksboro, Pine Mountain and Rocky Face faults are among the more notable examples. Curvilinear changes in image texture (Figure 4) denote the Middlesboro Basin faults. Repetition of the distinctive topography in the successive parallel to sub-parallel ridges or valleys denotes repetition of the underlying lithologies by faulting. Corresponding repetition of distinctive image texture on the SAR images enables the position of most mapped thrust faults to be located approximately (cf. Figures 4, 7). Offset ridges and abruptly terminated ridges typically indicate some type of faulting even though the fault may not be exposed. The offsets or abrupt terminations mapped from the SAR imagery appear in the form of abrupt linear changes in image tone or texture.

A "nose" to some of the parallel ridges and valleys on the imagery suggests some plunging fold structures. Uncertainty concerning the dip-direction of the folded strata generally precludes identification of the fold-type from the imagery. An exception can be seen on the original of Figure 3. A faint banding is evident along the southeast-facing scarp slope of Cumberland Mountain, and along the northwest-facing scarp slope of Pine Mountain, in the area 5-10 km east of Rocky Face. The banding is suggestive of ledge-forming strata that produce slope-change on the respective scarps. The slope-change is discriminated by the SAR. The respective scarp slopes are sub-parallel and face away from each other. The dip slopes face toward each other. The synclinal structure of the Middlesboro Syncline is thus evident from the SAR imagery (see cross-section, Figure 7).

Structural mapping can be performed from Landsat MSS imagery (Figure 5), though as already noted topography appears less pronounced than on the Seasat SAR images. Detailed structural mapping can be more easily performed from aerial photography. Stereoscopic coverage, which is available on most mapping photography, enables measurements of dip, strike, and relief to be made that are generally not possible with existing Seasat SAR or Landsat MSS images. However, the scale of stereo pairs is very much larger than that which either of the orbital systems can provide, whereas stereo photography at a regional scale is not available.

V. LINEAMENT MAPPING

Lineament maps (Figures 8, 9) were made from the SAR imagery (Figures 2, 3) and compared with a lineament map (Figure 10) that was made from a selected Landsat MSS image (Figure 5). Landsat RBV imagery of the area was examined but available images provide insufficient cover for comparison. An aerial photo-mosaic was used to verify the geomorphic nature of the lineaments that were mapped. Artifacts and linear features of cultural origin are omitted from the lineament maps. Differences observed between the maps relate significantly to imaging-system characteristics of the Seasat SAR and the Landsat MSS respectively.

The Seasat SAR is an active microwave sensor with a fixed beam that is inclined at a low angle off nadir. The Landsat MSS is a sun-synchronous passive sensor that measures reflections of sunlight in four spectral bands (Nos. 4-7) in the visible and near-infrared range of the electromagnetic spectrum. Detection of geomorphic lineaments by the Seasat SAR in the study area is governed by the sensitivity of the radar to slope-change. The effect of slope-change on

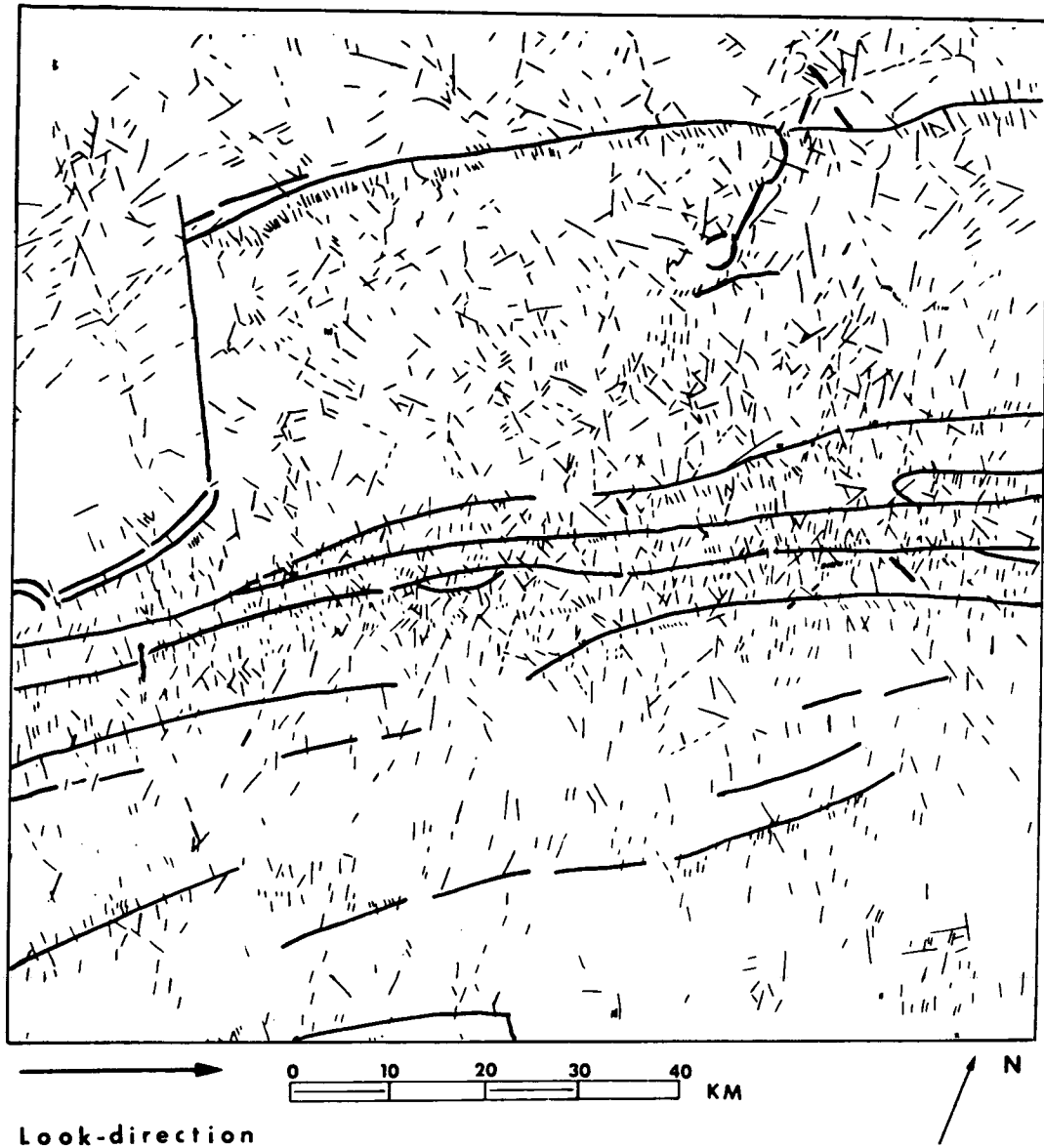


Figure 8. Lineament map made from Seasat SAR image looking N 67.5° E. Lineaments correlated with faults from published sources shown by heavy lines. Uncorrelated lineaments shown by thin lines.

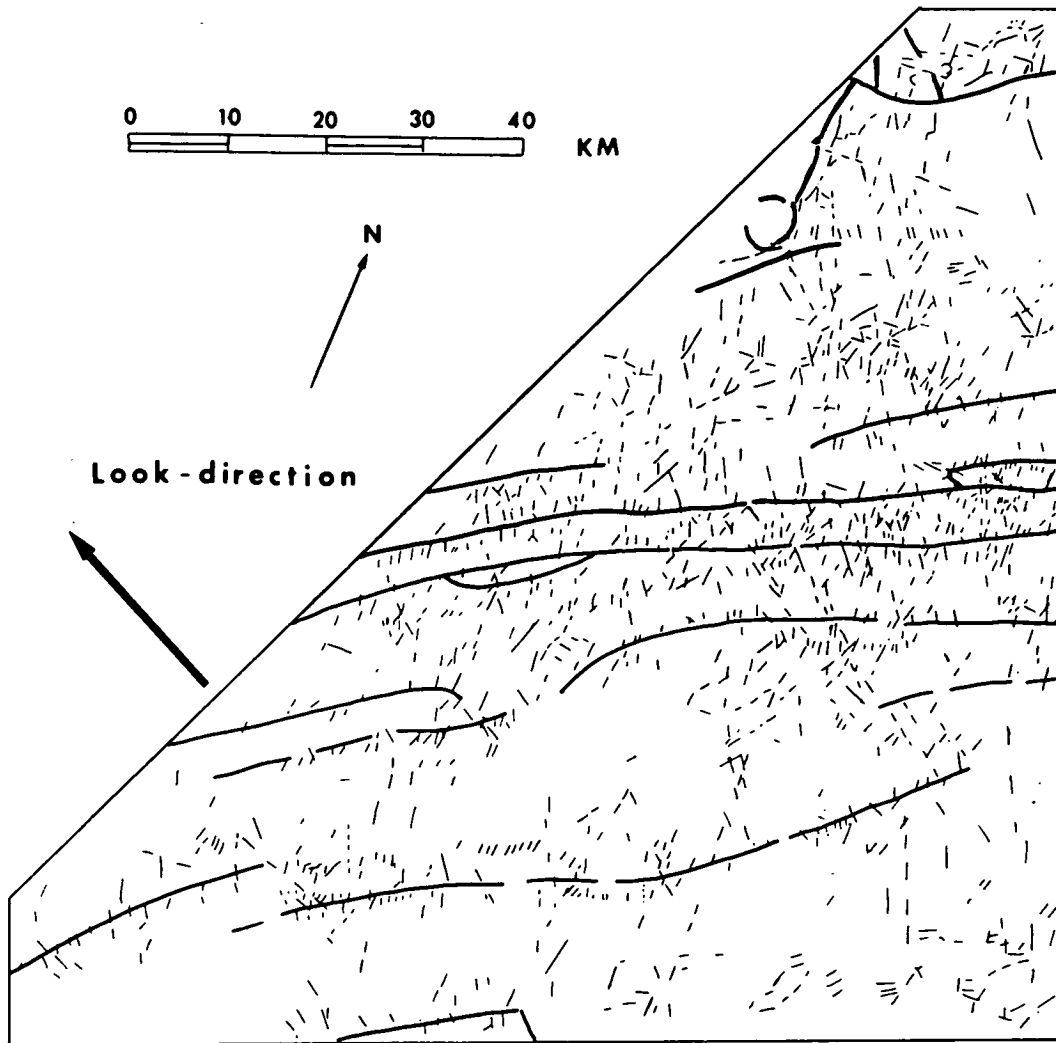


Figure 9. Lineament map made from Seasat SAR image looking N 67.5° W. Lineaments correlated with faults from published sources shown by heavy lines. Uncorrelated lineaments shown by thin lines.

radar backscatter is outlined in Appendix A. Detection of lineaments by the Landsat MSS is governed by shadowing, which in part is determined by the elevation angle and illumination direction of the sun. For topography of low relief the maximum shadowing occurs where the sun elevation is below 30° and features are oriented near-normal to the sun illumination.

In latitudes of the study area Landsat MSS images with suitably low sun-elevation angles are acquired only between November and January. Images that have been processed to produce high contrast are best for maximum preception of lineaments. Inspection of several images shows that the best available MSS scene for mapping geomorphic lineaments (No. 1858-15203, Sevierville, Tennessee) is one that was acquired on November 28, 1974, at a sun elevation of 26° . The direction of illumination of this scene is N 30° W. The highest image contrast of this scene occurs in the infrared spectral bands 6 and 7. The image in Figure 5 was processed from spectral band 6. A suitable high frequency non-directional filter was used to enhance the contrast. Additional cosmetics procedures that were used include the addback of 20% of the original scene to the filtered image so as to reduce harshness, and contrast stretching. The MSS image was enlarged to the same scale as the SAR images.

Lineaments in the study area consist of a few extensive features that are tens of kilometers in length, and many short features that are generally less than 10 km long. The extensive lineaments are formed by long ridges and valleys that parallel the structural strike, and by elongated mountains with local relief up to 400 m. Most of the extensive lineaments correlate with mapped faults. The correlated lineaments on the SAR and MSS images are shown by thick bold lines on the lineament maps (Figures 8, 9, 10). Lineaments less than 10 km long are formed by linear segments of rivers, small valleys and ridge crests, and small drainage channels. Local relief in these short linear features is mostly less than 60 m, but the relief from one end of the lineament to the other varies with the feature. Linear segments of some rivers and valley floors that are a few kilometers in length have an end-to-end relief of 10-20 meters. Some linear drainage channels about 1 km in length are steeply inclined and have an end-to-end relief of about 200 m. The short lineaments are widespread and oriented in a variety of directions throughout the area. They occur in closely spaced near-parallel swarms, and in alignments that extend over distances up to 100 km. The great majority of the short lineaments are uncorrelated geologically though in some instances they probably reflect faulting, jointing or fracturing. The uncorrelated lineaments are shown by thin lines on the lineament maps (Figures 8, 9, 10).

Comparison of the lineament maps (Figures 8, 9, 10) shows that most correlated lineaments mapped from the SAR images (Figures 2, 3) were also mapped from the corresponding MSS image (Figure 5). However, the number of short uncorrelated lineaments mapped from either of the SAR images is greater than the number mapped from the corresponding MSS image by a factor of about 2. The number and average length of uncorrelated lineaments mapped in the area common to the SAR images (Figures 2, 3) and the MSS image (Figure 5) are listed in Table 3.

The orientation of the uncorrelated lineaments is plotted in 5° increments east and west of north in the form of histograms (Figure 11 A-C). Measurements are at the center point of each 5° cell. The number of lineaments in each cell is plotted on the vertical axis of the histograms. Measurement accuracy is within $\pm 2.5^\circ$.

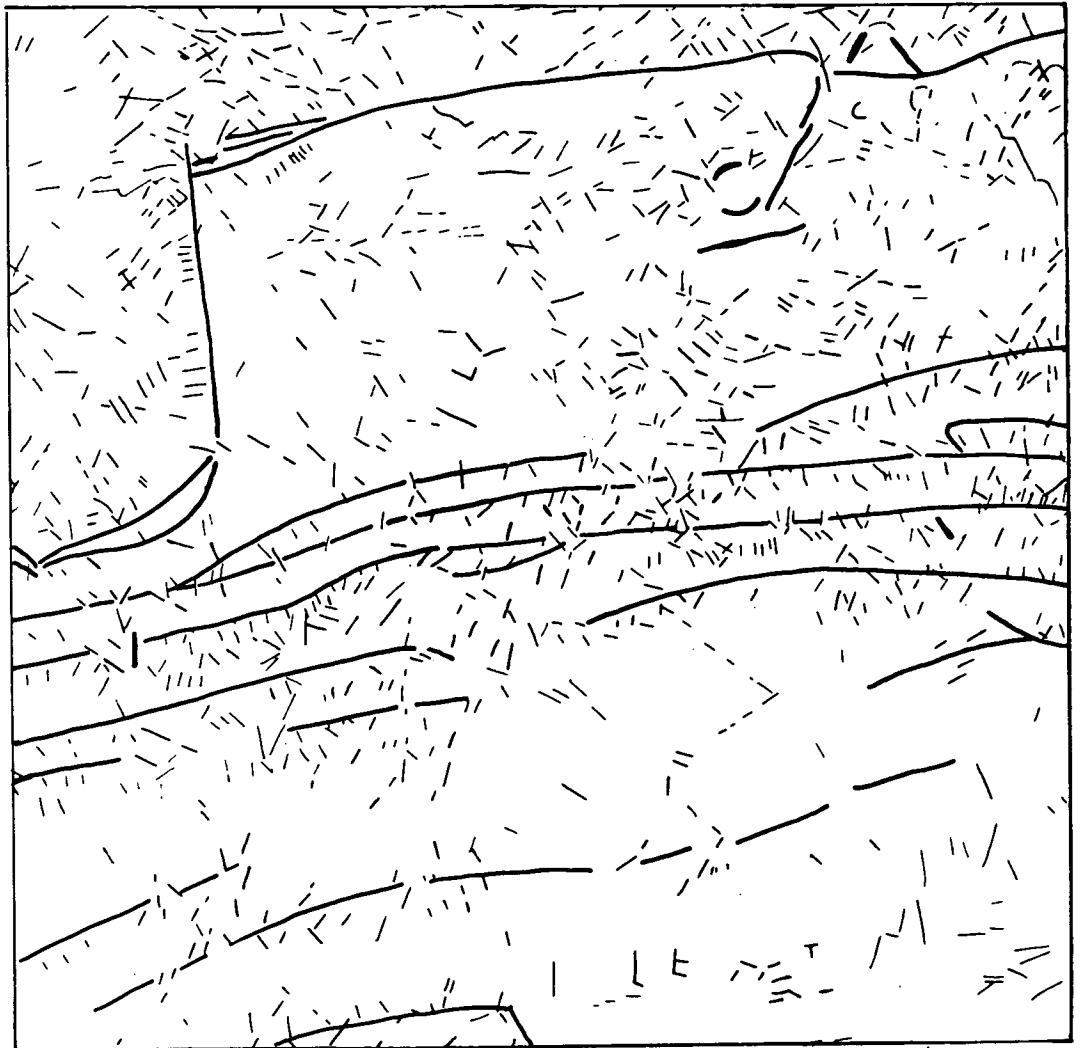


Figure 10. Lineament map made from Landsat MSS image. (Figure 5). Lineaments correlated with faults from published sources shown by heavy lines. Uncorrelated lineaments shown by thin lines.

ORIGINAL PAGE IS
OF POOR QUALITY

Table 3. Number and average length of short, uncorrelated lineaments mapped from the area common to Seasat SAR and Landsat MSS images of Figures 2, 3 and 5, listing respective histograms In Figure 11

Image Area Mapped	Number of lineaments	Average length	Histogram (Figure 11)
SAR Looking N 67.5° E common to SAR looking N. 67.5° W (Figure 2 area common to Figure 3)	1323	1.19 km	A
SAR looking N 67.5° W (Figure 3)	1156	1.03 km	B
Landsat common to SAR looking N 67.5° W (Figure 5 area common to Figure 3)	654	1.34 km	C

To account for the differences in lineament detection the SAR lineament maps (Figures 8, 9) were each registered to the MSS lineament map (Figure 10). Each lineament map contains a number of short lineaments that are missing on the coregistered map. Figure 12 shows lineaments on the MSS map (Figure 10) that do not appear on the SAR map looking N 67.5° E (Figure 8). Figure 13 shows lineaments on the MSS map that do not appear on the SAR map looking N 67.5° W (Figure 9). The lineaments on both Figures 12 and 13 are mostly oriented within $\pm 15^\circ$ of the respective radar look-direction. Comparison of Figures 11 A-C shows that a larger number of lineaments were mapped from the MSS imagery than from the SAR imagery for lineament orientations close or parallel to the radar look-direction. In registering the SAR lineament maps to each other (Figures 8, 9) it is also evident that lineaments mapped from either one of the SAR images whose orientation is close or parallel to the radar look-direction of the complementary SAR image are suppressed on that image. Thus it appears that the Seasat SAR tends to suppress certain lineaments depending upon their orientation. The overall effect of the lineament suppression is diminished where the dual-look coverage of the system is available.

Figure 14 shows lineaments on the SAR map looking N 67.5° E (Figure 8) that do not appear on the MSS map (Figure 10). The majority of these lineaments are oriented within $\pm 15^\circ$ of the sun illumination-direction (N 30° W) in the Landsat scene. Figures 11 A-C show that significantly larger numbers of lineaments were mapped from the SAR imagery in both the radar look-directions than from the MSS imagery for lineament orientations close to the direction of the sun's illumination. Comparing Figure 14 with the SAR image looking N 67.5° E (Figure 2) shows that the lineaments not mapped from the MSS imagery include closely spaced swarms that are individually less than 2 km in length. Evidently in this case the Landsat MSS suppresses short lineaments whose orientation is close or parallel to the illumination direction of the sun.

From the foregoing observations it appears that under certain conditions geomorphic lineaments are suppressed on both the Seasat SAR and the Landsat MSS images. Both types of sensor show a low sensitivity to topography that is oriented at or near-parallel to the direction of the scene illumination. Figure 15 depicts the relationship between the direction of scene illumination and the zone of lineament suppression for each of the SAR images (Figures 2, 3) and the MSS image (Figure 5). In Figure 15A the SAR sensor is looking N 67.5° W

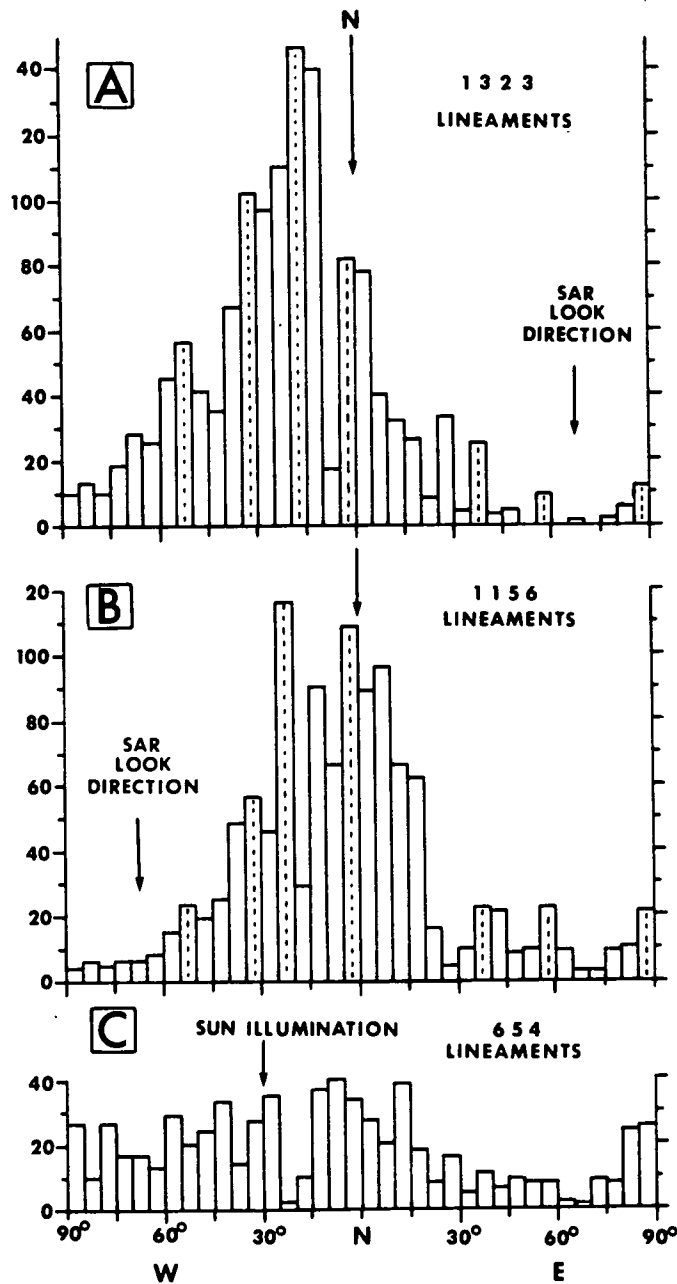


Figure 11. Histograms of uncorrelated lineaments mapped in Figures 8-10 from SAR and MSS images. Orientation is plotted at center of 5° cells measured in increments east and west of north. Number of lineaments mapped is plotted on vertical axis. (A) SAR looking N 67.5° E common to SAR looking N 67.5° W, (B) SAR looking N 67.5° W, (C) MSS common to SAR looking N 67.5° W. Corresponding frequency maxima in (A) and (B) are marked by dashed lines.

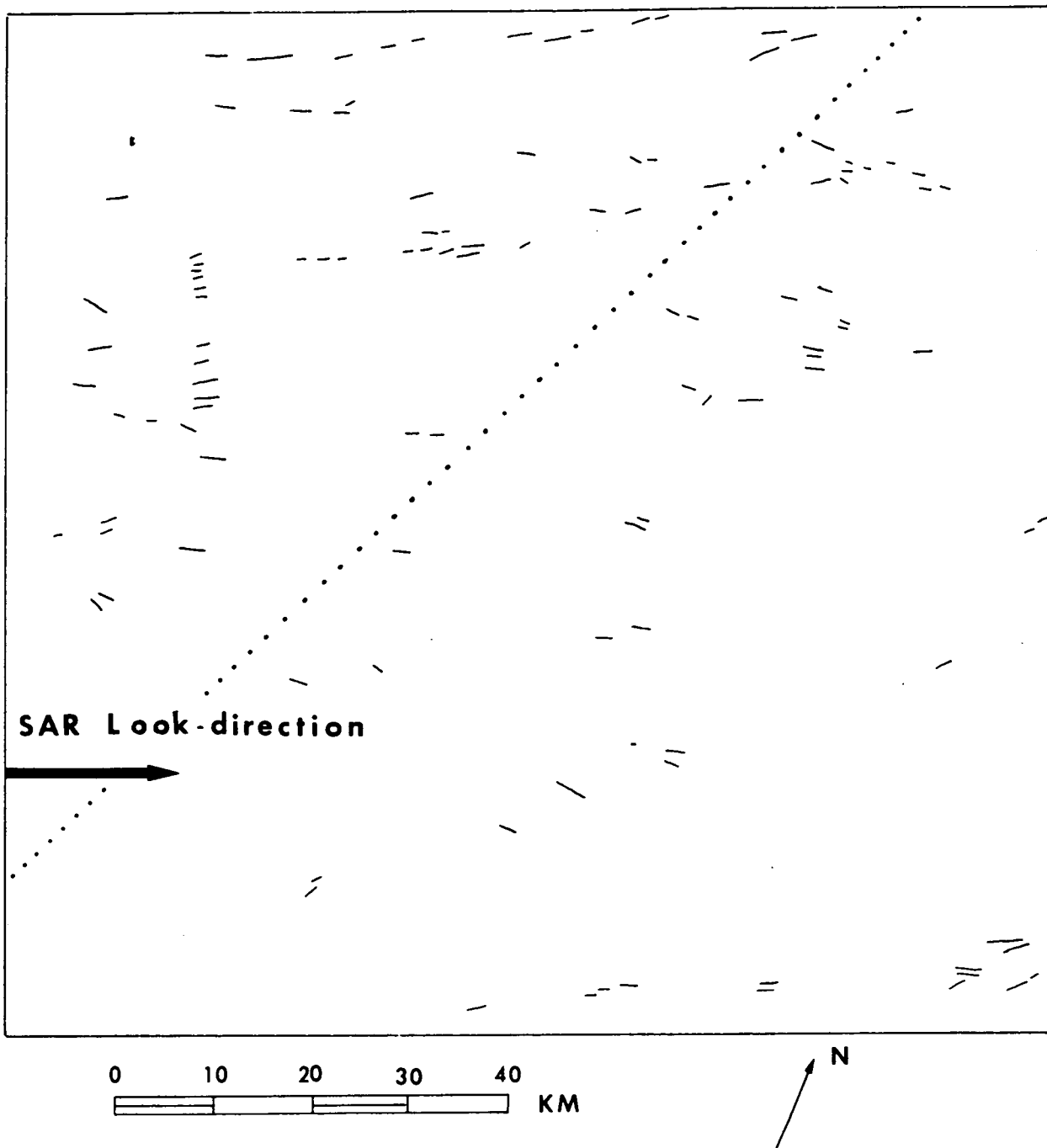


Figure 12. Lineaments on MSS map (Figure 10) that do not appear on SAR map looking N 67.5° E (Figure 8). Most lineaments are within $\pm 15^\circ$ of SAR look-direction shown above. Area south of dotted line is common to SAR looking N 67.5° W.

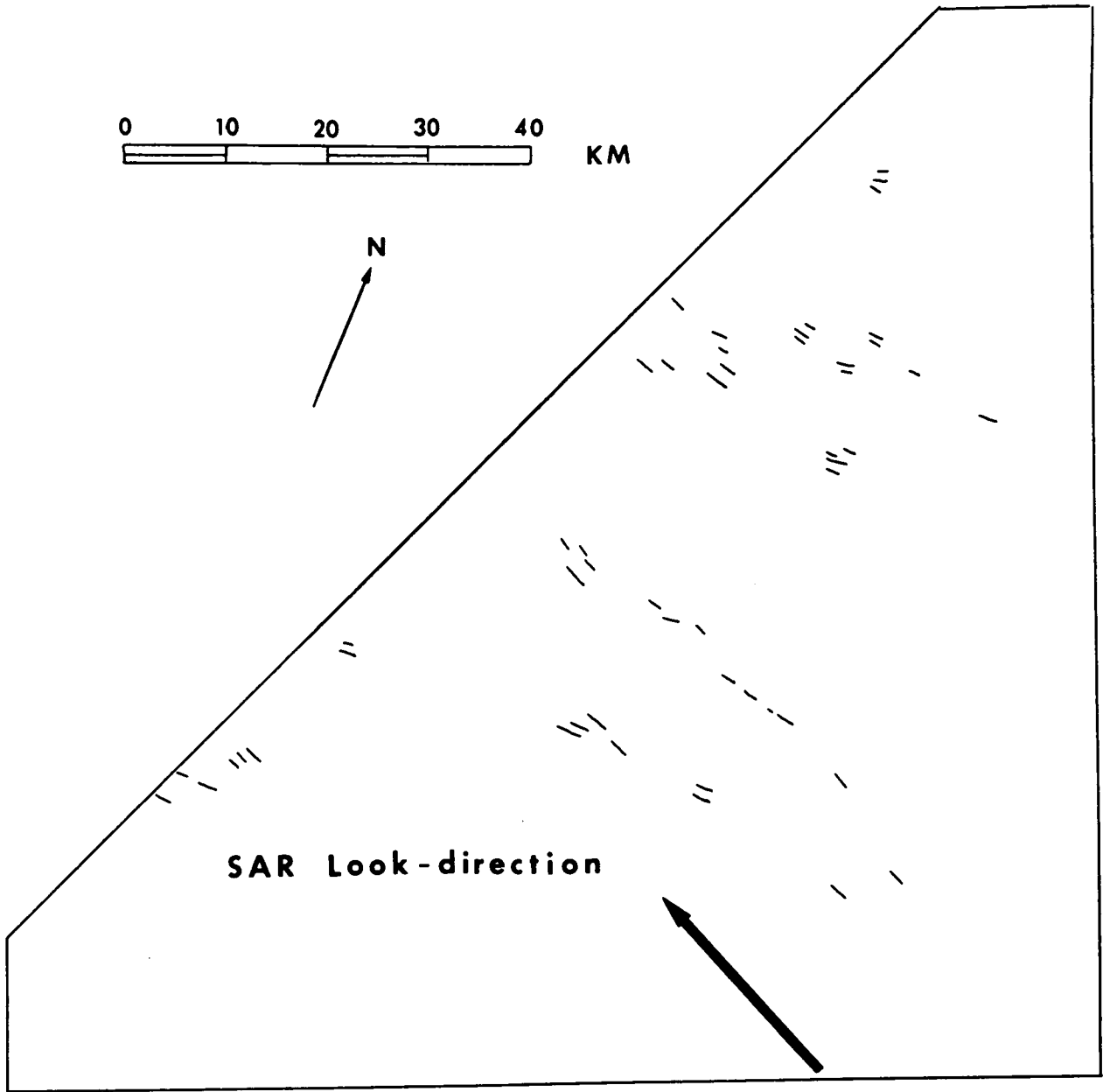


Figure 13. Lineaments on MSS map (Figure 10) that do not appear on SAR map looking N 67.5° W (Figure 9). Most lineaments are within $\pm 15^\circ$ of SAR look-direction shown above.

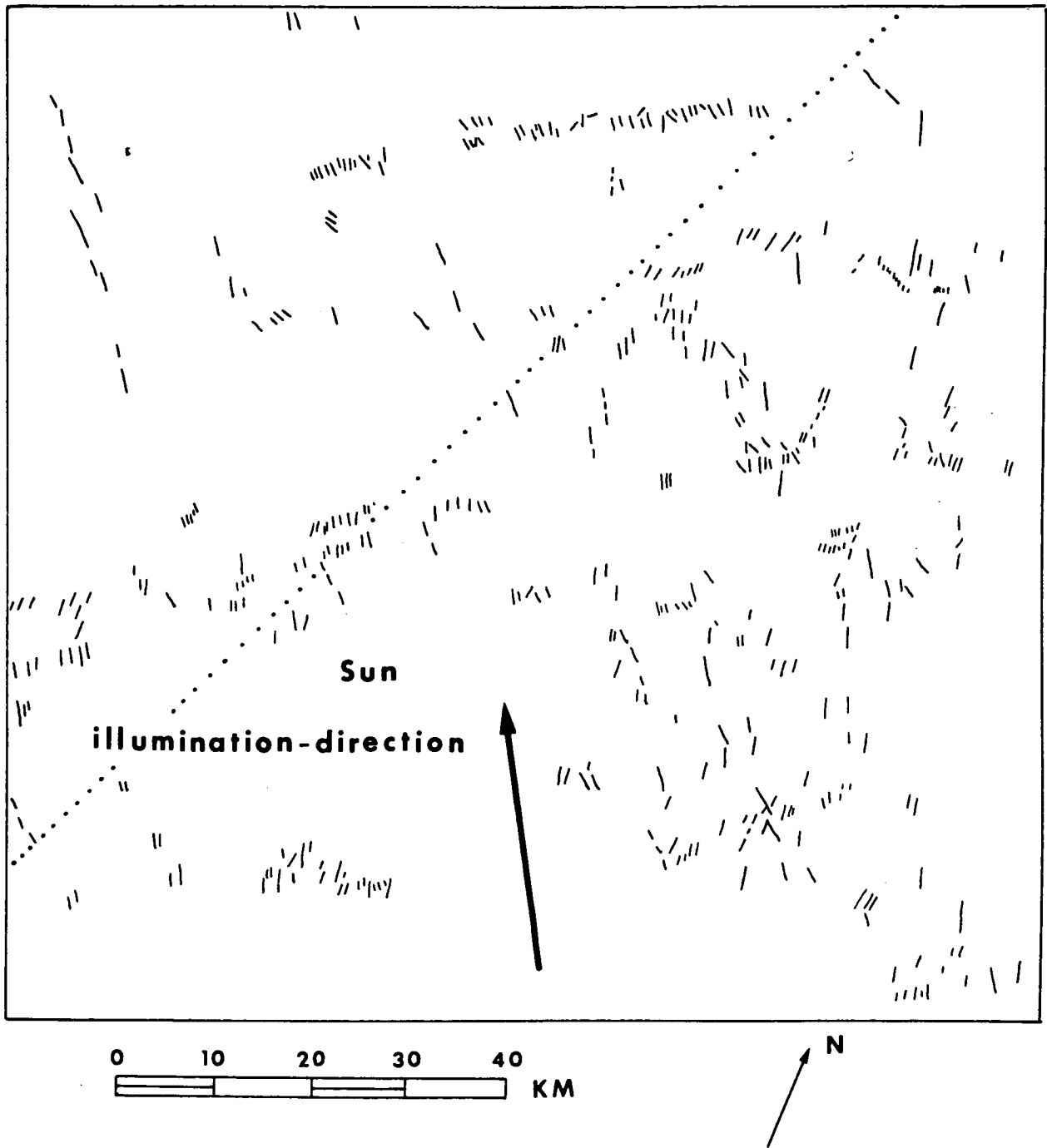


Figure 14. Lineaments on SAR map looking N 67.5° E (Figure 8) that do not appear on MSS map (Figure 10). Most lineaments are within $\pm 15^\circ$ of sun illumination-direction shown above. Area south of dotted line is common to SAR looking N 67.5° W.

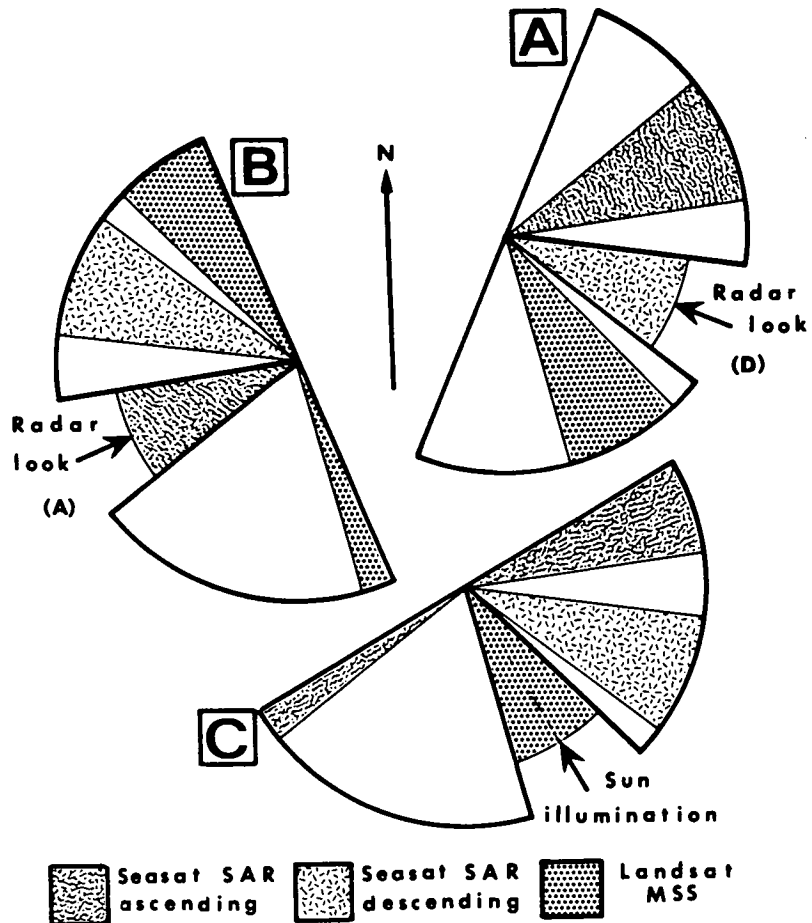


Figure 15. Directions of scene illumination with respective arcs of lineament suppression indented, (A) SAR looking N 67.5° W, (B) SAR looking N 67.5° E, (C) MSS. The arc of lineament suppression for a given scene illumination falls within the zone of lineament detection for the other two scene illuminations.

ORIGINAL PAGE IS
OF POOR QUALITY

(descending). In Figure 15B the SAR sensor is looking N 67.5° E (ascending). In Figure 15C the MSS scene is illuminated in a direction N 30° W. For each of the three directions of scene illumination lineaments are detected by the respective sensors for all orientations outside the zones marked by indented arcs. Each indented arc represents a 30° zone in which lineament suppression occurs. The arc of lineament suppression for a given scene illumination (as in Figure 15A) falls within the zone of lineament detection for the other two scene illuminations (as in Figures 15B, C).

Lineaments suppressed by the SAR looking N 67.5° W are detected by the SAR looking N 67.5° E. Lineaments suppressed by the MSS are detected in both SAR look-directions. Lineaments suppressed in either of the SAR look-directions are detected by the MSS. These observations reveal a complementary relationship between Seasat SAR imagery and Landsat MSS imagery for mapping linear topographic features.

The photograph in Figure 16 was taken looking down the axis of a small linear valley that is typical of the uncorrelated lineaments. The valley slopes are mostly forest-covered, with abrupt changes of slope occurring at the base and top. Evidently the SAR is more sensitive to such features than the MSS. The strong local image contrast that highlights geomorphic lineaments on the SAR images represents abrupt change in radar backscatter. At the low inclination of the Seasat SAR beam off nadir the radar backscatter is strongly affected by change of slope (see Appendix A for details). Strong slope changes across linear topography are common in the study area.

VI. LINEAMENT ANALYSIS

The short uncorrelated lineaments mapped from the SAR images (Figures 8, 9) and the MSS image (Figure 10) were examined for frequency of orientation and for aerial distribution, and were compared with the orientation and aerial distribution of the major lineaments that are geologically correlated with mapped faults. The approximate orientation of the major correlated lineaments is N-S (Rocky Face fault), N 30° W (Jacksboro fault), and N 50° E - N 60° E (Pine Mountain fault and other thrust faults parallel to regional strike).

The histograms of the uncorrelated lineaments in the area common to both SAR look-directions (Figures 11A,B) show a number of peaks on the vertical axis that are flanked by substantial reductions on both sides. This suggests the presence of several maxima in the orientation of the lineaments. A well-defined maximum is at N 17.5° W for the SAR looking N 67.5° E, and N 22.5° W for the SAR looking N 67.5° W. This probably represents a single maximum, based on the observations that follow. This maximum is clearly not evident on the corresponding MSS histogram (Figure 11C).

The lineament orientations mapped from the SAR imagery that have maximum frequency range from N 15° W - N 25° W on the histograms (Figures 11A,B). The lineaments appear mostly to represent features less than 2 km long that occur in closely spaced swarms. The SAR images show that they are distributed along the flanks of ridges and mountains from the Pine Mountain thrust southward to and beyond Lake Douglas (see Figure 7 for the above locations). Aerial photographs show that these lineaments mostly represent drainage gullies down the flanks of ridges and elongated mountains, or wind gaps and some water gaps across ridges.

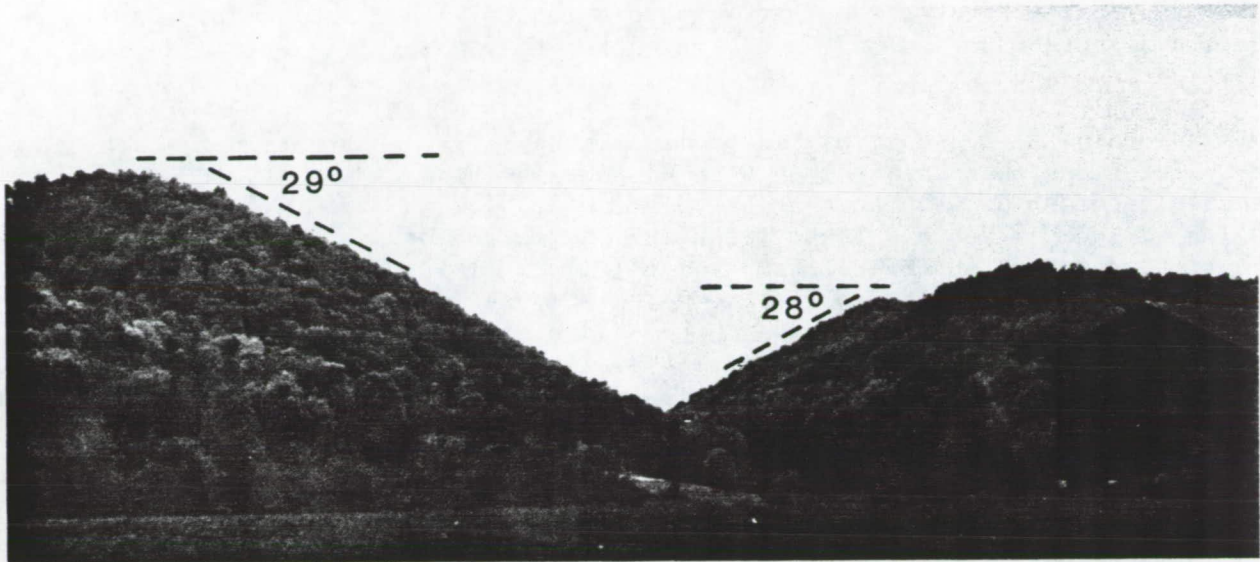


Figure 16. Hamilton Gap, looking down axial trace of Booker Hollow, Tennessee, seen from Raccoon Valley, south of Norris Lake. Hollow forms small segment of N-S alignment of lineaments. Slopes are forest-covered, with abrupt slope-change at base and top. Photo date: May 1979.

ORIGINAL PAGE IS
OF POOR QUALITY

Comparison of Figures 11A and 11B shows that the maximum frequency measurement for each SAR look-direction is nearer to that direction relative to the maximum frequency measurement in the other SAR look-direction. At the low inclination of the Seasat SAR beam off nadir, slopes that are greater than about 20° are displaced toward the look-direction due to radar layover. Lineaments that are highlighted due to layover may therefore be geometrically distorted toward the radar look-direction. This suggests that the difference in the orientation of the maxima of the two SAR look-directions may be due to distortion introduced in the imaging system. In contrast to this the lineaments in the sector from $N 15^\circ W - N 25^\circ W$ are almost all suppressed on the MSS imagery. This is probably because the features are oriented within 15° of the sun-illumination direction in the MSS scene, which results in insufficient shadowing for their perception.

Subordinate frequency maxima of lineaments in the area common to both SAR look-directions that coincide on both histograms (Figures 11A, B) occur in decreasing order of abundance at $N 2.5^\circ W$, $N 32.5^\circ W$, $N 52.5^\circ W$, $N 37.5^\circ E$, $N 57.5^\circ E$ and $N 87.5^\circ E$. These frequency maxima are not strongly supported by the histogram from the MSS lineament map (Figure 11C). The much lower amplitude variation between adjacent 5° cells on the MSS histogram inhibits clear recognition of the frequency maxima seen on the SAR histograms. Further analysis of the frequency maxima interpreted from the SAR histograms is therefore made in conjunction with the aerial distribution of the lineaments represented in each maximum.

Lineaments at and near-parallel to the frequency maximum at $N 2.5^\circ W$ are concentrated in the central and eastern part of the study area. Short aligned and en echelon valley segments up to 3 km long parallel the Rocky Face fault and extend far north and south of its surface trace. A linear magnetic gradient in the basement underlies the Rocky Face fault and extends southward across the Powell Valley anticline (Watkins, 1964). A northerly trend of magnetic and gravitational anomalies in the basement extending through eastern Kentucky southward toward the latitude of Knoxville, Tennessee, was observed, and interpreted by Watkins (1962, 1963, 1964) as reflecting a pre-Appalachian structural grain in the basement. The close coincidence of surficial lineaments mapped from the Seasat SAR images may reflect the sub-surface structural grain. However, the structural characteristics of the rocks associated with the lineaments at the surface are not known. Examination of the MSS image (Figure 5) and lineaments map (Figure 10) shows the presence also of some of the lineaments mapped from the SAR images that are parallel to, or aligned south of Rocky Face fault.

The frequency maximum oriented at $N 32.5^\circ W$ corresponds closely with the orientation of the Jacksboro fault. The lineaments consist of segments up to 3 km long that are aligned in the area adjacent to and south of the Jacksboro fault. They include such notable geomorphic features as linear segments of major rivers southeast and southwest of Knoxville, Tennessee, aligned water gaps across successive ridges, and the abrupt linear truncation of Beaver Ridge. Parallel structural alignment exists at the surface where the Great Smoky fault is inflected to the southeast, and in the Dorton Branch fault zone (see Figure 7 for locations).

The Jacksboro fault is a tear fault that has associated gravity and magnetic discontinuities in the basement. On these grounds Watkins (1964) suggested that a basement fault underlies the surface trace of the Jacksboro fault and

appears to extend further to the southeast. Some lineaments mapped from the SAR and the MSS images coincide with this postulated extension of the basement fault. The orientation of the lineaments is near-normal to the regional strike. They may represent fracture traces associated with the compressive stresses that gave rise to the Jacksboro fault. However the mapped lineaments are geomorphic features whose structural control is mostly not known.

The lineaments with a frequency maximum at N 52.5° W occur in the north central and northeast part of the area, from the Pine Mountain thrust southward to Cherokee Lake. Most of the lineaments were mapped from the SAR image looking N 67.5° E. The lineaments are clear on the MSS imagery, but they are suppressed on the SAR image looking N 67.5° W. The orientation of the features relative to the radar look-direction produces insufficient change in radar backscatter for their detection. The lineaments consist notably of segments of tributary valleys to the Powell River in the region of the Powell Valley anticline. The only mapped faults that are similarly oriented are in Kentucky, in the White Mountain fault zone, especially where the faults terminate against the Pine Mountain thrust fault (Figure 7).

Only small numbers of lineaments are mapped from the SAR and MSS images in the three other frequency maxima shown on the histograms (Figures 11A,B), but their distribution and orientation are notable. Lineaments oriented about N 37.5° E occur in the same general area of the Pine Mountain thrust sheet and the Powell Valley anticline as those that are oriented about N 52.5° W. The two sets are normal to each other. Lineaments oriented about N 87.5° E occur in the vicinity of Rocky Face fault, and southward in the Powell Valley anticline in association with lineaments that are oriented about N 2.5° W. The two sets are also normal to each other. Lineaments oriented about 57.5° E represent small valleys south and east Douglas Lake that occur in the Tellico Sandstone. These lineaments parallel the regional strike, which as noted above is normal or near-normal to the lineaments that parallel the Jacksboro fault. Lineaments that parallel the regional strike tend to be suppressed on the SAR imagery looking N 67.5° E.

The frequency maxima of lineament orientations noted from the histograms of the SAR lineament maps are summarized below in Table 4, and compared with previously reported orientations of joints from Knox County, Tennessee (Harris, 1972). Knox County is situated in the southwest portion of the imaged area entirely within the Valley and Ridge province. The data reported by Harris consist of joint measurements by Dale (1924) combined with measurements of all major stream patterns in Knox County. The observations reported here do not conflict with Harris (1972) though neither data set is considered to be exhaustive. No other published studies of joint orientations or fracture traces in the area are available for comparison with the data from the SAR lineament maps.

The orientation of significant numbers of short uncorrelated lineaments and their distribution relative to known structural features in the Valley and Ridge province has been determined from Seasat SAR imagery. Larger number of short lineaments are mapped from the SAR than are perceptible from Landsat MSS imagery, and preferred orientations are more clearly revealed. However, the orientation of short lineaments that have significant topographic relief from one end of the lineament to the other is substantially distorted due to layover, and geometry of the Seasat SAR beam. The most notable geometric distortion

Table 4. Frequency maxima of lineament orientations from Seasat SAR imagery compared with orientation of joint sets previously reported from Knox County, Tennessee

Frequency maximum from Figures 11A, B.	Structural relationship of uncorrelated lineaments observed in this study	Orientation of joint sets in Knox County, TN., from Harris, 1972.
N 17.5° W - N 22.5° W	Small erosional features not parallel or normal to any known structure	N 19° W - N 38° W
N 2.5° W	Parallel to Rocky Face fault; coincide with geophysical trend in basement	N 7° E - N 11° W
N 87.5° E	Normal to above trend	N 78° E - N 90° E
N 32.5° W	Parallel to Jacksboro fault; coincide with geophysical trend in basement	N 19° W - N 38° W
N 57.5° E	Normal to above trend; generally parallel to regional strike	N 50° E - N 65° E
N 52.5° W	Features with no clear structural relationship	N 50° W - N 63° W
N 37.5° E	Normal to above trend	N 23° E - N 35° E

occurs in the orientation of linear drainage features that flank the major ridges, as seen by comparing the SAR images in the two different look-directions (Figure 2,3). The orientation of lineament alignments is more reliable and potentially of greater geologic significance than the orientation of single short lineaments.

The geologic significance of the lineament orientations revealed by the SAR demands further study and explanation. While no structural information is evident from the clusters of short lineaments, extended alignments of lineaments require investigation. The close coincidence of some uncorrelated lineaments with geophysical trends in the basement, the alignment with known structural features, and the orthogonal relationship of certain lineaments shown by this small-scale reconnaissance mapping from Seasat SAR imagery indicate a need for further field work. Further studies may show that certain lineaments are related to zones of fracture porosity. Recognition of this would aid in exploration for oil and gas in the area. The potential for favorable fracture-porosity traps in the Pine Mountain thrust sheet has previously been reported by Harris (1976). It is known that production from existing gas wells in the area is substantially greater where the wells coincide with the intersection of major lineaments. Other applications of the SAR imagery exist in localizing areas for further detailed study of the Appalachian structural pattern.

VII. CONCLUSION

Geologic mapping using orbital Seasat SAR imagery is feasible in the Appalachian Valley and Ridge province, where the radar system is highly sensitive to the terrain-surface features. In an area of very little rock exposure, with extensive forest cover and leaf canopy, topographic mapping from the SAR imagery provides an effective basis for lithologic and structural interpretation. Linear segments of erosional topography are strongly highlighted on the SAR imagery. Most of the extensive lineaments correlate with previously mapped faults. Short uncorrelated lineaments are widespread. Some are aligned in close coincidence with mapped faults or with subsurface geophysical trends. Others appear to represent erosional features that show no structural relationship. Analysis of the Seasat SAR images provides a basis for planning more detailed field investigations of geologic structure.

The wide image ground-track of the orbital SAR is admirably suited to regional geologic reconnaissance mapping at a relatively small scale. The high image contrast on the SAR images that results from variations in terrain slope is directly attributable to the low incidence-angle of the radar beam at sloping surfaces which face the radar and the high sensitivity of the radar to any change in that incidence angle in the range from 0° - 30° . This highlights the topographic texture and the short segments of linear topography in the study area more than is possible on the enhanced Landsat MSS image chosen for comparison. The low incidence-angle of the Seasat SAR beam also produces strong geometric distortion and loss of geologic information due to layover. The MSS image presents no distortion to compare with the destructive effect of layover on the Seasat SAR images. A remedy for this defect of the Seasat SAR with respect to imaging land surfaces is an orbital imaging radar system with a much higher incidence-angle. Linear geomorphic features would be enhanced by radar shadowing, rather than by radar sensitivity to change of slope, and layover would be reduced or eliminated. However, a variable depression-angle at the SAR antenna is necessary if a high incidence-angle is desired for terrain with a wide range of slope.

Both the Seasat SAR and the Landsat MSS sensors tend to suppress lineaments that are oriented at or near the illumination direction of each of the respective imaging systems. The SAR system is probably more prone to this than the MSS system. The effect of lineament suppression by the Seasat SAR is partly compensated by the dual-look capability of the system.

The L-band wavelength used on the Seasat SAR penetrates clouds and, in common with all imaging radars, it can be successfully operated both day or night at any time of the year. The MSS on Landsat cannot penetrate cloud or be operated at night. It is operated in a sun-synchronous mode. It is dependent on the sun elevation and the terrain orientation to highlight features of low relief by the shadowing effect of the sun's illumination. This restricts effective mapping of landforms to a portion of the year when low sun elevation prevails. At mid-latitudes such a condition coincides with a season of much cloud and/or snow-cover, which could delay the acquisition of usable imagery.

APPENDIX A

RELATIONS BETWEEN SEASAT SAR IMAGING GEOMETRY, TERRAIN SURFACE CHARACTERISTICS, AND RADAR BACKSCATTER

The strong local image-contrast that highlights topography on the Seasat SAR images represents abrupt change in the radar backscatter. The abrupt change results from interaction of the radar-system properties with the terrain properties. At any given wavelength and polarization the most important radar variables that affect the backscatter are the radar look-direction, the look angle off nadir (complement of the depression angle), and the incidence angle. Equally important terrain variables are the orientation and slope of the surface and its roughness and dielectric constant. In general, the interrelation of these two sets of variables governs the amount of transmitted energy that is returned to a SAR antenna as backscatter.

At the time that SAR images used in this study were acquired, the roughness and the dielectric constant of the widespread leaf canopy over the sloping terrain surface were relatively uniform, but the steepness and orientation of the slopes vary widely. Thus in assessing backscatter variations on the SAR images in the area covered by this report it is necessary to identify the relationship between the radar imaging geometry and the terrain orientation and slope and to determine the backscatter from leaf canopy as a function of that imaging geometry.

Figure 17 is a perspective diagram that shows the relationship between radar imaging geometry and terrain orientation and slope. For an Earth-orbiting SAR, as on Seasat, it is convenient to measure the inclination of the radar beam from a line that joins the satellite to the Earth's center. This line is in a vertical plane relative to the Earth's surface, and the angle of inclination is the look angle off nadir (γ in Figure 17). If the inclination of an imaging radar beam is measured from the horizontal plane relative to the Earth's surface, as is commonly the case with airborne imaging-radar platforms, it is termed the depression angle (not shown on Figure 17). The look angle off nadir and the depression angle are complementary terms. The incidence angle (θ in Figure 17) is the angle between the incident radar beam and the plane that contains the normal to the true slope at the ground surface. The term "incidence angle" is sometimes used to designate the off-nadir look angle defined above. This results in confusion and misunderstanding. The look angle is generally fixed, or it may be controlled at the radar antenna. The incidence angle varies in accordance with the local terrain slope. The look angle and the incidence angle are equal only in the special case where the terrain surface is level, and the SAR imagery is not noticeably affected by the Earth's curvature. In the case of Seasat the SAR incidence angle to level terrain surfaces ranges from about $20^\circ - 27^\circ$ outward across the image ground-track. It is not equal to the look angle at the antenna, which is centered at 20.5° .

The slope orientation-angle (ϕ in Figure 17) is measured in the horizontal plane relative to the radar look-direction; $\phi=0^\circ$ when the slope is oriented parallel to the radar look-direction. The apparent slope angle of a surface seen by the radar is less than the true slope (α_{ap}, α_t in Figure 17) for all orientations of $\phi < 90^\circ$.

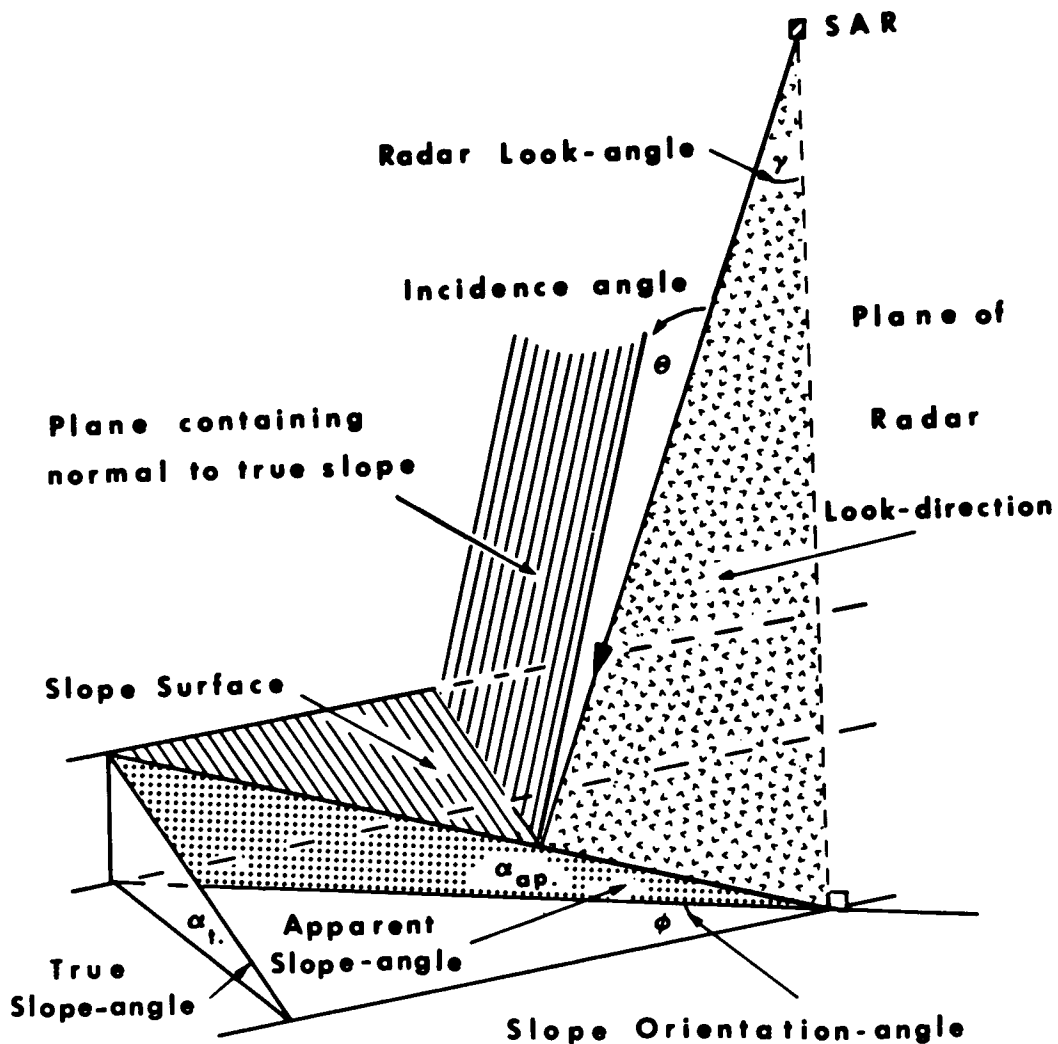


Figure 17. Perspective diagram showing relationship between radar look-angle off nadir γ , incidence angle θ , and slope orientation ϕ measured in horizontal plane relative to radar look-direction. Apparent slope α_{ap} seen by radar is less than true slope α_t for all orientations of $\phi < 90^\circ$.

ORIGINAL PAGE IS
OF POOR QUALITY

Where the incidence angle θ is 0° or less at sloping surfaces which face toward the imaging radar, referred to as foreslopes, layover occurs on the imagery. Where the incidence angle is 90° or greater at sloping surfaces which face away from the radar, referred to as backslopes, shadowing occurs on the imagery. The result in both cases is loss of surface information on the radar image. In the Valley and Ridge area of this report, layover occurs for slopes of 20° or more in the near range and 27° or more in the far range. However, many foreslopes that are steeper than $20^\circ - 27^\circ$ are not laid over on the imagery because they are sufficiently oblique to the plane of the radar look-direction that the incidence angle is less than the layover threshold value. Shadowing occurs where a backslope is steeper than the depression angle; effectively about $63^\circ - 70^\circ$ for Seasat SAR. As almost no slope in the study area even approaches 60° , none of the backslopes in either of the look directions is in radar shadow. Thus an important property of the Seasat imaging system relative to the Valley and Ridge terrain is the low incidence angle of the radar beam to the foreslopes and the high incidence angle to the backslopes.

Ament, et al. (1959) and Bush, et al. (1976) have measured the radar backscatter as a function of incidence angle for mixed deciduous and coniferous forest in New Jersey and for deciduous hardwood forest in Kansas, respectively. They used horizontal parallel-polarized L-band radar at a frequency close to the Seasat SAR frequency. Their results are reproduced in Figure 18. From their experiments it appears that for sloping leaf-canopy a small change of incidence angle in the range of $0^\circ - 30^\circ$ results in a large change in power reflectivity, up to 0.5 dB per degree. If these results are applied to the present study it is apparent that the ability of the Seasat SAR images to highlight topography is largely a function of the radar sensitivity to local change of incidence angle. In turn this results from local change in steepness and/or orientation of the terrain slope. The relationship between the incidence angle θ and the look angle γ , the true slope α_t and the slope orientation ϕ relative to the radar look direction Figure 17 is given by:

$$\cos \theta = \cos \gamma \cos \alpha_t + \sin \gamma \sin \alpha_t \sin \phi$$

Using this formula and a Seasat look-angle value of $\gamma = 20^\circ$, incidence angle was plotted against slope orientation for a series of true-slope values of $\pm 10^\circ$, $\pm 20^\circ$, $\pm 30^\circ$, $\pm 40^\circ$, that correspond to the range of most slopes in the study area. The curves are plotted in Figure 19, where α represents true slope; positive signifying foreslope and negative signifying backslope.

Following are the important observations revealed by the curves:

- (1) The change of incidence angle $\Delta \theta$ decreases for any given change of foreslope $\Delta \alpha_t$ at a slope orientation less than normal (90°) to the radar look-direction.
- (2) The incidence angle θ increases as the orientation of any foreslope α_t approaches the look direction (0°).
- (3) The incidence to backslopes is relatively high. The angle increases as the backslope orientation approaches the normal to the look direction.

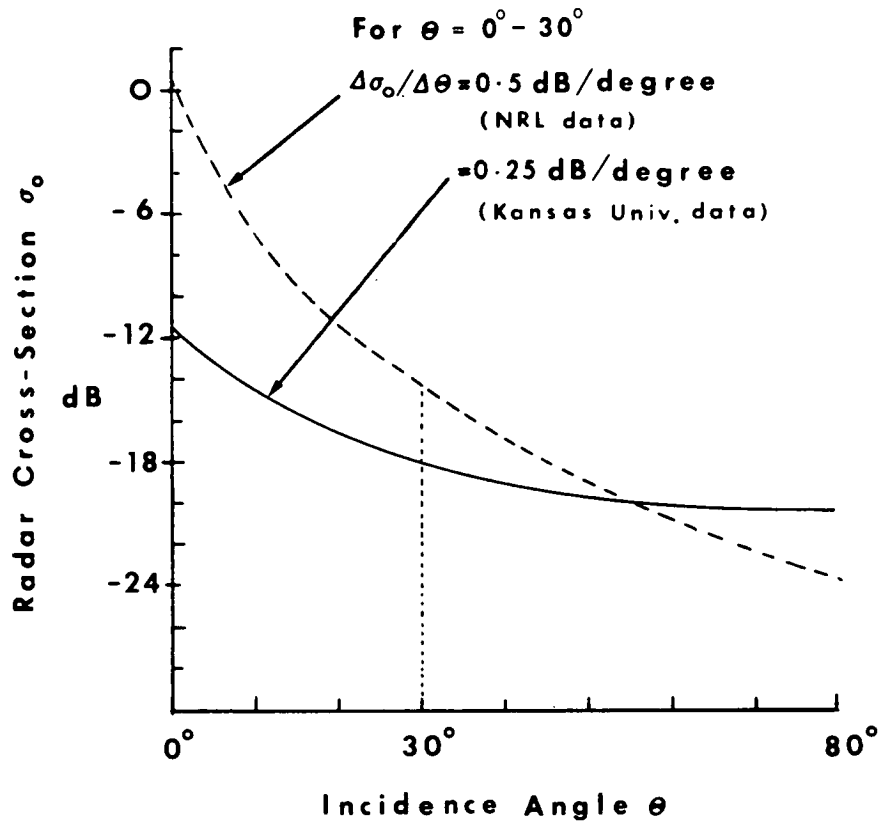


Figure 18. Effect of change in incidence angle $\Delta\theta$, on change in radar backscatter cross-section $\Delta\sigma_0$ from leaf canopy at L-band. NRL data from Ament, et al. (1959). Kansas University data from Bush, et al. (1976).

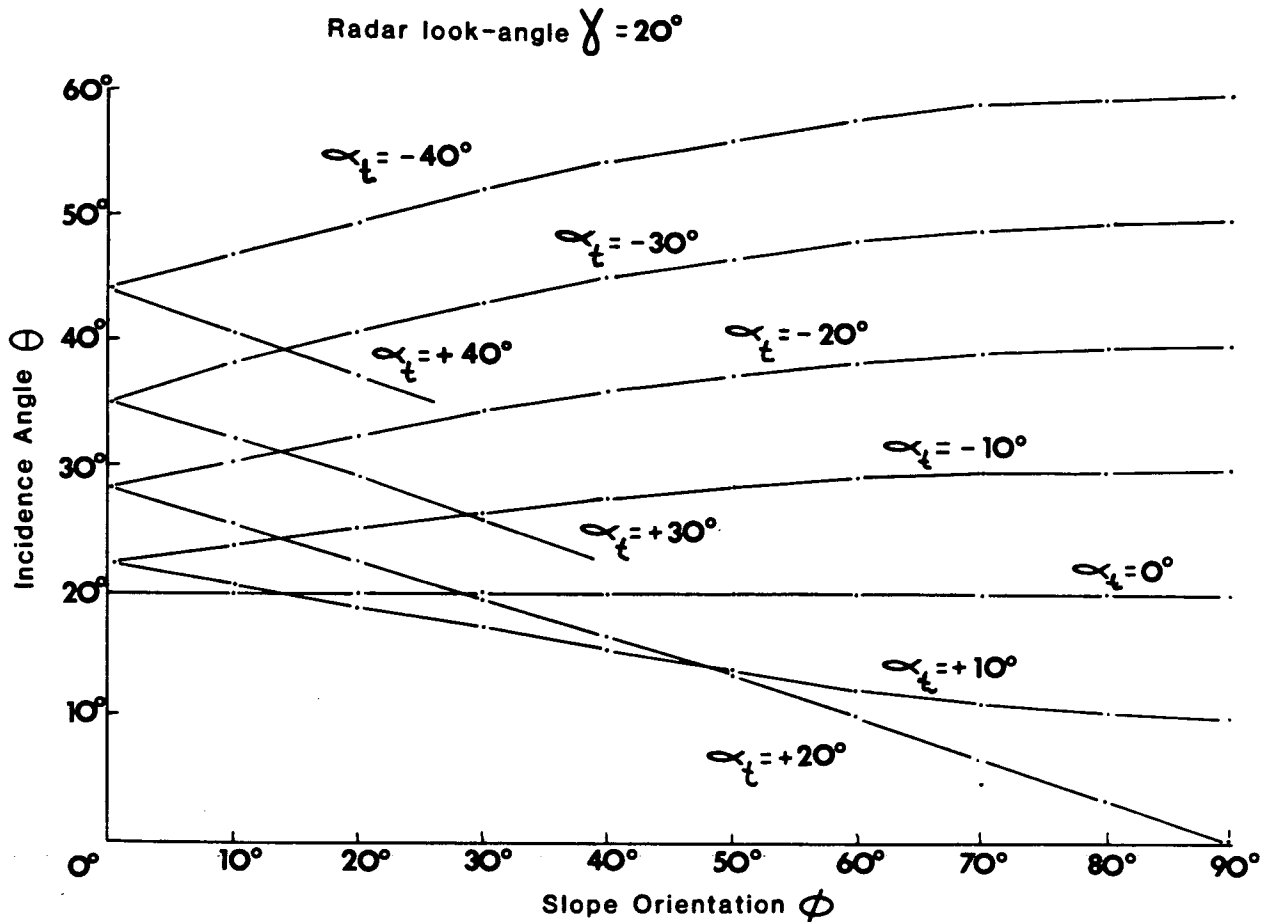


Figure 19. Incidence angle θ plotted against slope orientation ϕ for true slope values α_t at a Seasat look-angle = 20° . Positive α_t signifies foreslope; negative α_t signifies backslope.

- (4) Slopes that are steeper than the radar look-angle are not laid over at oblique orientations to the look direction.

The significance of these observations relative to the radar backscatter can be determined by inspection of Figure 18. In the range of incidence from $0^\circ - 30^\circ$ a reduced change of incidence angle $\Delta \theta$ will substantially reduce the resultant change in backscatter $\Delta \sigma_0$, shown as radar cross-section in Figure 18. This is tantamount to reducing the specific imaging-system feature which has been shown to be mostly responsible for highlighting topography on the SAR imagery.

The radar backscatter σ_0 from leaf canopy decreases as the incidence angle θ increases. For incidence values greater than 30° a change of incidence angle produces little change of backscatter. Figure 19 shows that high incidence angles occur for all steep backslopes and for steep foreslopes that are oriented close to the look direction. Under such conditions a significant slope change and equivalent change in incidence angle has little effect on the backscatter and probably will not be noticeable on the SAR imagery. Thus the orientation of slopes relative to the radar look-direction strongly influences the extent to which a change of incidence angle is capable of significantly changing the radar backscatter.

ACKNOWLEDGEMENT

The research described in this paper was carried out at the Jet Propulsion Laboratory, California Institute of Technology, under NASA Contract No. NAS 7-100.

REFERENCES

- Ament, W., F. MacDonald and R. Shrewbridge, 1959, Radar terrain reflections for several polarizations and frequencies: Trans. 1959 Symposium on radar return, Pt. 2, May 11-12, 1959, University of New Mexico. N.O.T.S. TP 2339, U.S. Naval Ordnance Test Station, China Lake, California.
- Bush, T., F. Ulaby, T. Metzler and H. Stilles, 1976, Seasonal variations of the microwave scattering properties of the deciduous trees as measured in 1-18 Ghz spectral range: U. of Kansas Rept. RSL 177-60.
- Calver, James L., and C.R.B. Hobbs, Jr., (eds.), 1963, Geologic map of Virginia: Virginia Div. Min. Resources, Charlottesville, Virginia.
- Dale, T. N., 1924, Constitution and adaptation of the Holston Marble in east Tennessee: in Tenn. Div. Geol., Bull. 28, pt. 2, p. 87-160.
- Elder, C. H., P. W. Jeran and D. A. Keck, 1974, Geologic structure analysis using radar imagery of the coal mining area of Buchanan County, Virginia: U.S. Bur. Mines, Rept. Inv. 7869, 29 p.
- Hadley, J. B., and R. Goldsmith, 1963, Geology of the eastern Great Smoky Mountains, North Carolina and Tennessee: U. S. Geol. Survey, Prof. Paper 349-B, 118 p.
- Haldeman, W. D., et al., 1966, Geologic map of Tennessee: Ten. Div. Geol., Nashville, Tennessee.
- Harris, Leonard D., 1972, Structure map of Knox County, Tennessee: U.S. Geol. Survey, Miscellaneous Investigations Map I-767D.
- _____, 1976, Thin-skinned tectonics and potential hydrocarbon traps illustrated by a seismic profile in the Valley and Ridge province of Tennessee: U.S. Geol. Survey, Jour. Research, V. 4, No. 4, p. 379-386.
- _____, and John M. Kellberg, 1972, Overburden related to type of bedrock and engineering characteristics of the bedrock, Knox County, Tennessee: U.S. Geol. Survey, Miscellaneous Investigations Map I-767J.
- _____, and Robert C. Milici, 1977, Characteristics of thin-skinned style deformation in the southern Appalachians, and potential hydrocarbon traps: U.S. Geol. Survey, Prof. Paper 1018, 40 p.
- Johnston, J. E., R. L. Miller and K. J. Englund, 1975, Applications of remote sensing to structural interpretation in the southern Appalachians: U.S. Geol. Survey, Jour. Research, V. 3, No. 3, pp. 285-293.
- King, P. B., 1964, Geology of the central Great Smoky Mountains, Tennessee: U.S. Geol. Survey, Prof. Paper 349-C, 148 p.
- Milici, Robert C., 1973, The stratigraphy of Knox County, Tennessee: in Tenn. Div. Geol., Bull. 70, p. 9-24.

REFERENCES (continued)

- Swingle, George D., 1973, Structural geology of Knox County, Tennessee: in Tenn. Div. Geol., Bull. 70, p. 63-73.
- Teleki, P. G., and R. O. Ramseier, 1978, The Seasat-A synthetic-aperture radar experiment: Proc. Int. Soc. for Photogrammetry, Commission VII, July 3-7, 1978, Freiburg, Germany.
- Watkins, J. S., 1962, Precambrian basement structure and lithology inferred from aeromagnetic and gravity data in eastern Tennessee and southern Kentucky: U.S. Geol. Survey, Prof. Paper 450-C, p. C25-C28.
- _____, 1963, Simple Bouguer gravity map of Kentucky: U.S. Geol. Survey, Geophysical Investigations Map GP-421.
- _____, 1964, Regional geologic implications of the gravity and magnetic fields of a part of eastern Tennessee and southern Kentucky: U.S. Geol. Survey, Prof. Paper 516-A, p. A1-A17.

**RADAR IMAGING OF VOLCANIC FIELDS AND SAND DUNE FIELDS:
 IMPLICATIONS FOR VOIR***

C. Elachi, R. Blom, M. Daily, T. Farr, and R. S. Saunders

Earth and Space Science Division
 Jet Propulsion Laboratory
 Pasadena, California

ABSTRACT

A number of volcanic fields and sand dune fields in the western part of North America have been studied using aircraft and Seasat SAR images and Landsat images. The objective of the study was to assess the capability of radars with different characteristics (i.e., frequency, polarization and look-angles) to identify and map different volcanic features, lava flows and sand dune types. It was concluded that (1) volcanic features which have a relatively large topographic expression (i.e., cinder cones, collapse craters, calderas, etc.) are easily identified; (2) lava flows of different ages can be identified, particularly on the L-band images; and (3) sand dunes are clearly observed and their extent and large-scale geometric characteristics determined, provided the proper imaging geometry exists.

I. INTRODUCTION

Airborne imaging radars have been used, over the last decade, as a major source of information for geologic mapping in regions of the world where heavy vegetation and extensive cloud cover limit the usefulness of visible and IR sensors. Radar has, in fact, provided the only practical geological reconnaissance exploration technique in those regions of the world that are almost perpetually cloud covered. Many countries in the equatorial regions, such as Brazil, Nigeria, Togo and Indonesia, have conducted large-scale radar mapping programs and obtained accurate maps of vast areas that were formerly almost unknown and largely unmapped (e.g., MacDonald, 1969). Imaging radars have also been used over cloud-free regions to obtain complementary information to optical imaging sensors by providing surface reflectivity data in a different region of the electromagnetic spectrum (Schaber et al., 1976; Daily et al., 1978a,b,c).

The launch and successful operation of the L-band SAR on Seasat was a major step in demonstrating the capability of synoptic and large areal mapping using spaceborne SARs. Preliminary analysis of the Seasat-A SAR image indicates the potential for this to be a major remote sensing tool which would complement Landsat for the monitoring and assessment of Earth resources.

The cloud penetration capability of the SAR makes this sensor the only tool that can be used to map the surface of Venus. NASA is presently planning a VOIR (Venus Orbiting Imaging Radar) mission to provide global mapping of the Venusian surface with a resolution of a few hundred meters, with limited targetable mapping capability at a higher resolution (~50 meters).

In order to be able to define the desirable characteristics of the VOIR radar, such as frequency, polarization and viewing geometry, research is ongoing to understand the radar signature of a number of geologic terrains which might be encountered on Venus.

In this paper, we report on some aspects of our activities as related to the study of volcanic fields and sand fields using airborne and Seasat SAR data. The different remote sensing systems used in this study are described in Table 1. The locations of the sites under study are indicated in Figure 1. In Section II we give a brief overview of radar backscatter theories which are directly relevant to this work. In Section III we discuss the radar, photographic and ground observations of the different volcanic fields under study and provide an explanation of the radar signature observed. Section IV will address the different sand dune fields studied. Section V summarizes our results and provides recommendations for future research.

II. OVERVIEW OF RADAR SCATTERING THEORIES AS APPLIED TO GEOLOGIC SURFACES

In order to interpret radar images, the geologist used two different types of information: (a) geometric patterns such as lineaments, texture, contacts, shapes, etc., in a way similar to what is done in the interpretation of visible and IR photography, and (b) the radar backscatter (or image tone) of specific features to derive information on the macrorelief (such as slope) and subresolution microrelief (roughness) structure of the surface.

The radar backscatter from geologic surfaces (scattering from vegetated surfaces is not discussed here) is dependent on the following surface parameters: (a) surface slope, (b) surface roughness at the scale of the wavelength, (c) dielectric constant of surface material, and (d) subsurface inhomogeneities, particularly in very dry regions.

For surfaces where there are plane smooth facets which are many radar wavelengths in dimension (such as slip faces of dunes or blocky lava), quasispecular backscatter is usually dominant. In this case, most of the backscattered radar energy comes from facets which are oriented perpendicular to the incident wave vector. This type of backscatter is usually relatively strong because all of the energy is conserved in the reflected and transmitted directions (very little scattered in other directions). This type of scattering is usually encountered while imaging at small incidence angles (of up to about 30 degrees from the vertical). However in the case of block lava flows, specular return can occur at even higher incidence angles because lava block facets can be encountered at nearly all angles. Another important factor is that single and double specular backscattering does not depolarize electromagnetic waves. Thus, this type of scattering is important in the interpretation of like-polarized images. Also, it should be pointed out that specular scattering is not dependent upon the radar frequency as long as the surface is smooth relative to the observing radar wavelength.

Table 1. Remote sensing systems

Type ^a	Band	Polarizations	Wavelength (cm)	Organization	Resolution (m)	Altitude (km)	Incidence Angle	h (cm)
RAR	K	HH, HV	0.86	Westinghouse Aerospace	15	Not Available	65°	0.2
SAR	X	HH	3	Goodyear Aerospace	12 3 (Amboy)	10	65°	0.8
SAR	L	HH, HV	25	JPL	25	10	40°	4
Sea- sat- A	L	HH	23.5	JPL/NASA	30	800	20°	3.2

^a RAR - Real Aperture Radar;

SAR - Synthetic Aperture Radar.

^b Incidence angle = 90 - depression angle.

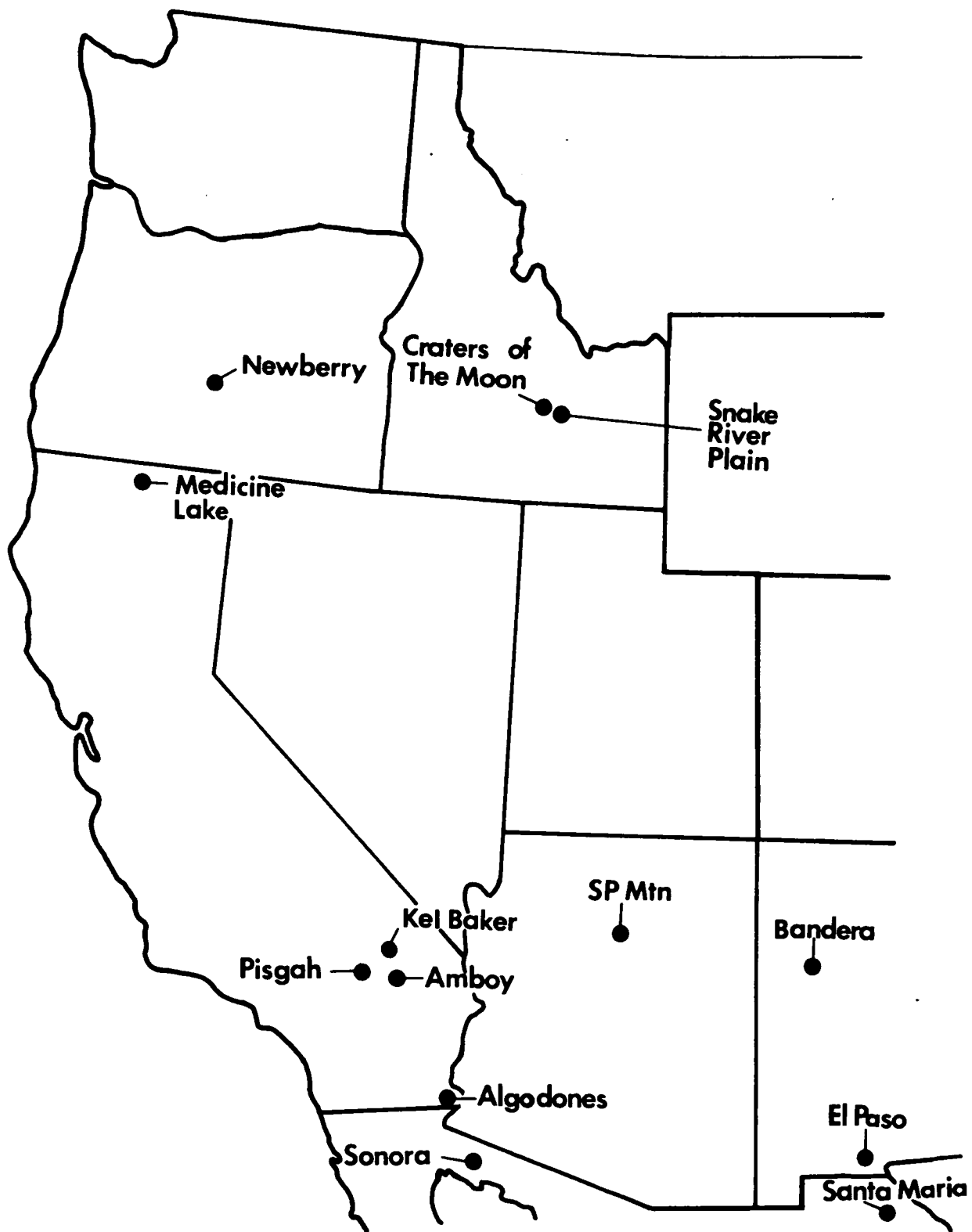


Figure 1. Map of western United States showing locations of study areas.

In the case of slightly rough surfaces, the like-polarized backscatter cross-section σ_L is proportional to the surface spectral roughness density $W(k)$ at the spatial wavelength Λ_b , which satisfies the Bragg condition (Beckmann and Spizzichino, 1963); i.e.,

$$\Lambda_b = (\lambda/2 \sin \theta)$$

and

$$\sigma_d \sim W(K_b)$$

where $K_b = 2\pi/\Lambda_b$, λ is the radar wavelength, and θ is the incidence angle. This type of scattering is dominated by the presence of roughness at the scale of the Bragg resonant wavelength. Thus, the brightness in the like-polarized radar image is a direct indication of the surface roughness at the scale close to the radar wavelength. For instance, in a radar image taken at 25-cm wavelength lava flows will look much brighter than alluvium or desert pavement, because they are much rougher on the scale of 25 cm. However, the brightness difference will be less in the case of X-band radar images because most geologic surfaces are rough at the scale of a few centimeters, to which X-band radar backscatter is most sensitive.

The cross-polarized backscatter cross-section σ_i is related to the integral of $W(k)$. Thus, it is sensitive to the overall roughness of the surface with a well-defined weighting function (Valenzuela, 1967). This is a result of the fact that cross-polarization is due to multiple scattering. Thus, a relatively recent aa lava flow is expected to have large σ_i at L-band because it is very rough at all scales, from a few millimeters to many tens of centimeters; its σ_d will also be large. However, a pahoehoe flow or an eroded aa flow will still have a large σ_d , but appreciably smaller σ_c because most of the roughness is in the range of a few tens of centimeters.

The above discussion is based on theoretical modeling, which is mathematically correct only in the case of slightly rough surfaces (i.e., where rms (root mean square) height is less than $\lambda/8 \sin \theta$ (see Schaber et al., 1976). For very rough surfaces, no accurate models exist. Scattering is most likely affected by the resonant Bragg scattering discussed above as well as by the presence of cavities and sharp slope discontinuities. However, we have found that in the case of the lava flows under study, the general behavior of the radar backscatter is almost always consistent with the discussions in the previous paragraphs.

Cross-polarization is also high in the case of volume scattering (Janza, 1975). In the case of dry, unvegetated regions, the electromagnetic signal will penetrate a few wavelengths below the surface and will scatter from volume inhomogeneities. However, this mechanism is not well understood and experimental field verification is very difficult.

Finally, radar backscatter is dependent on the dielectric constant of the surface material. In arid regions, this effect is usually small, relative to the effects of the roughness or slope. Most surface materials have dielectric constants ranging from about 3 (in the case of sand) to about 9 (for most rocks). This variation leads to a variation in the power reflection coefficient of about 2 (i.e., 3 dB). In comparison, backscatter variations of more than 10 dB are commonly encountered due to roughness or slope variations.

Another type of scattering which sometimes plays an important role is the Rayleigh scattering from bodies of finite shape such as pebbles and rocks (Ruck et al., 1970). The backscatterer cross-section increases as

$$\sigma \sim (d/\lambda)^4$$

for $d \ll \lambda$, where d is the size of the rock. For $d \gg \lambda$, the backscatter cross section tends to be equal to the geometric cross-section of the body.

III. VOLCANIC FIELDS

Almost all volcanic features which are larger than a few resolution elements, such as cinder cones, flow shapes, squeeze ups, flow contacts, collapse craters, calderas, etc., can be easily recognized on the radar images. These features are identifiable because they are usually reflected in a change of the local slope (topography) or change in the surface roughness (microrelief at the scale of the radar wavelength), and they have characteristic geomorphic expressions.

The radar backscatter from lava flows is dominated by the surface roughness. Thus, we would expect that

- (1) L-band (25-cm wavelength) radar images would show more brightness variation than X-band (3-cm wavelength) and shorter wavelength radar images, thus allowing better recognition of lava flows. Obviously, the reflectivity variation by itself does not identify a lava flow. Usually, a combination of reflectivity variation and geometric shape allows the identification of a lava flow.
- (2) Recent lava flows would have a higher reflectivity than older flows because they are less eroded (i.e., rougher).
- (3) Cross-polarized radar images would be more helpful in discrimination of different types of flows.
- (4) Volcanic features such as cinder cones and collapse craters, where the slope effect (i.e., topography) is important, should be equally recognizable independent of the frequency of the imaging radar.
- (5) At small incidence angles (less than 30 degrees from vertical), the quasispecular return is usually dominant relative to the diffuse return from surface roughness. This will still allow delineation of rough lava flows. However, it will be harder to discriminate between flows where there is limited variation in roughness due to erosion. Larger incidence angles provide better sensitivity to change in surface roughness.

Qualitative analysis of images from the volcanic fields which were studied has supported the above expectations. Following is a discussion of the specific sites studied. The results of the studies on SP lava flow (Arizona) and Askja Caldera flow in Iceland have been reported elsewhere (Schaber et al., 1979; Malin et al., 1978; Evans, 1978).

IV. OBSERVATIONS

A. Pisgah Crater and Lava Field

Pisgah Crater and lava field are located about 60 km east of Barstow in the Mojave Desert of California (Figure 1). The lava field is about 23 km long, more than 6 km wide, and has an area of 80 km². Pisgah Crater is a cinder cone nearly 100 m high and 488 m in diameter at the base. Lavic lake, a playa about 3.5 km in diameter, lies at the southeast end of the lava field.

Pisgah lava field formed in three eruptive phases which were distinguished on the basis of phenocryst textures (Wise, 1966). Each phase resulted in the formation of a cinder cone. The first two cones are nearly eroded away and the most recent is presently being mined for cinders. The first- and second-phase flows were more voluminous than the third. The first flow is pahoehoe, now broken up. The second flow is predominantly aa and the third is pahoehoe with numerous pressure ridges, lava tubes, and tumuli. Wind-blown material has accumulated in pockets on the pahoehoe surfaces. Figure 2a is a geologic map of Pisgah lava field from Wise (1966).

Pisgah lava field was imaged by all the sensors listed in Table 1 (Figures 2, 3, and 4). The dominantly pahoehoe units (first and third eruptive units) and the aa lava of the second phase of eruption are distinguishable on LHV (L-band, horizontal transmit, vertical receive) and KHV radar images. The aa-pahoehoe contact can barely be discerned in the LHH image and cannot be seen in the XHH and KHV images. The first and third flow units cannot be separated on any of the images. In LHV, the second unit is brighter than its surroundings. This effect was suggested by Sabins (1978, p. 399), and is similar to the effect noted for SP lava flow by Schaber et al. (1979). In the KHV image, the aa flows are darker than the surrounding pahoehoe, while in the KHH image, the lava field has a uniform reflectivity. Dellwig and Moore (1966) and Mc Cauley (1972) explained high KHH returns from blocky surfaces by single reflection from properly oriented block facets. Thus, the aa of the second phase appears to be blocky at K-band (0.86-cm wavelength) and rough at L-band (25-cm wavelength). The second unit can also be separated from the first and third units in the Landsat image (Figure 4a). The second unit is darker at visible and near infrared wavelengths partly because of shadowing in the rough aa lavas.

Discrimination between aa and pahoehoe lavas is also possible in the Seasat-A (LHH) image (Figure 4b). The aa areas to the east and southeast of Pisgah Crater are slightly brighter than the surrounding pahoehoe, as in the LHH image acquired by aircraft (Figure 3c). An area of hummocky pahoehoe west of Pisgah Crater is also bright in the Seasat-A image. This is probably caused by the low slope angles of the hummocks furnishing normal specular reflection at the small incidence angle of Seasat-A (20°) and not at the larger incidence angles characteristic of the aircraft images.

The sand-covered western tongue of pahoehoe is difficult to separate from its surroundings in K-band images, but X- and L-band clearly show the flow boundaries. This implies either that only the smallest scale (<1 cm) surface roughness has been masked by the wind-blown sediment or that longer wavelengths are able to penetrate the sediments. Aeolian material visibly masks portions of the flow in the Landsat image (Figure 4a).



Figure 2. Pisgah lava field. a) Geologic map modified from Wise (1966). b) Goodyear XHH image acquired before 1970. Illumination is from lower left. Orientation and scale is the same as in a). c) Contact of phase one lava with alluvium. Flow front is 2-3 m high. The surface is broken up pahoehoe. Ground photo 3-10, located shown in a). d) Contact between second phase aa (left) and third phase pahoehoe (right). Ground photo 2-13, location shown in a).

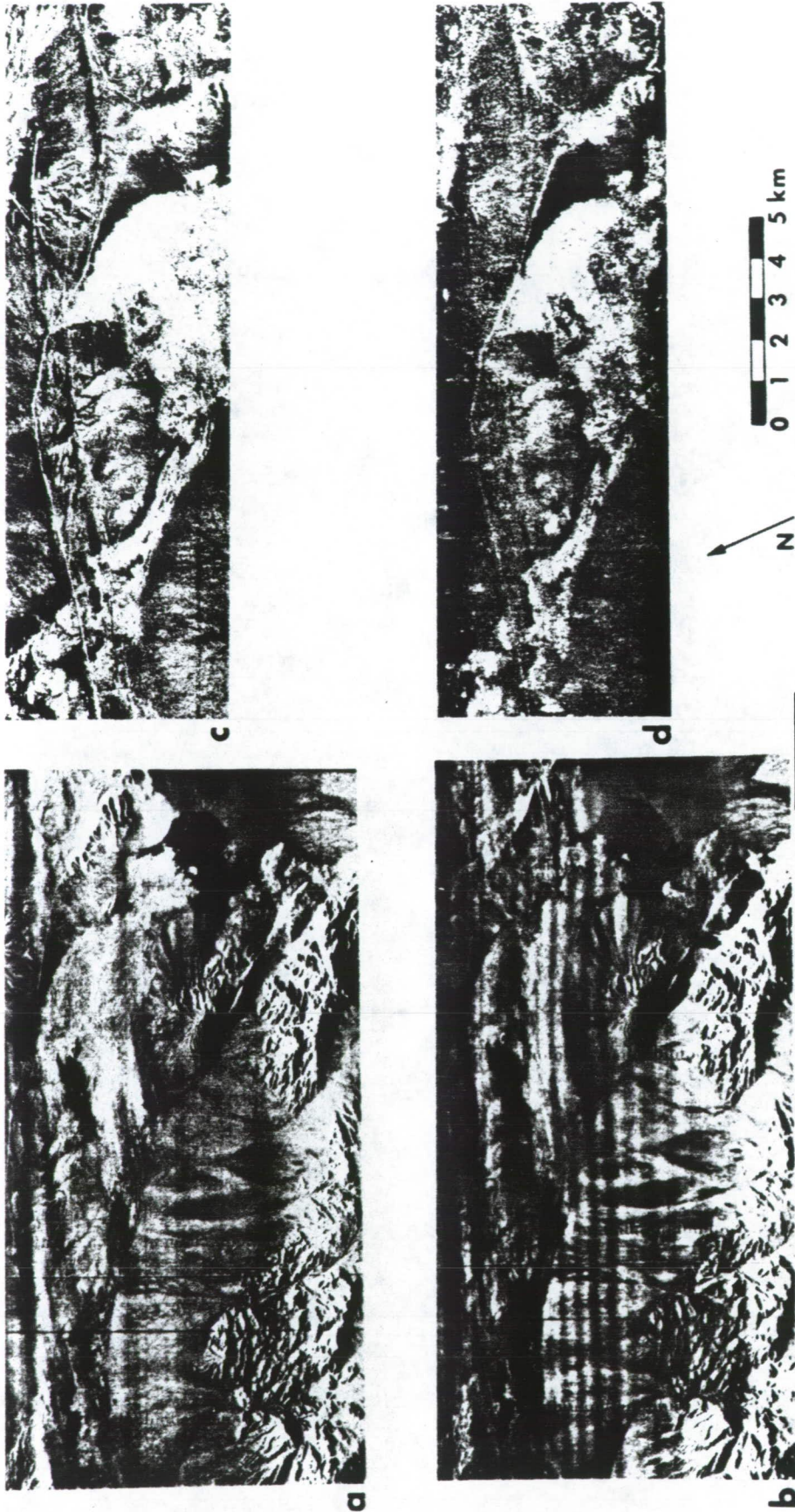
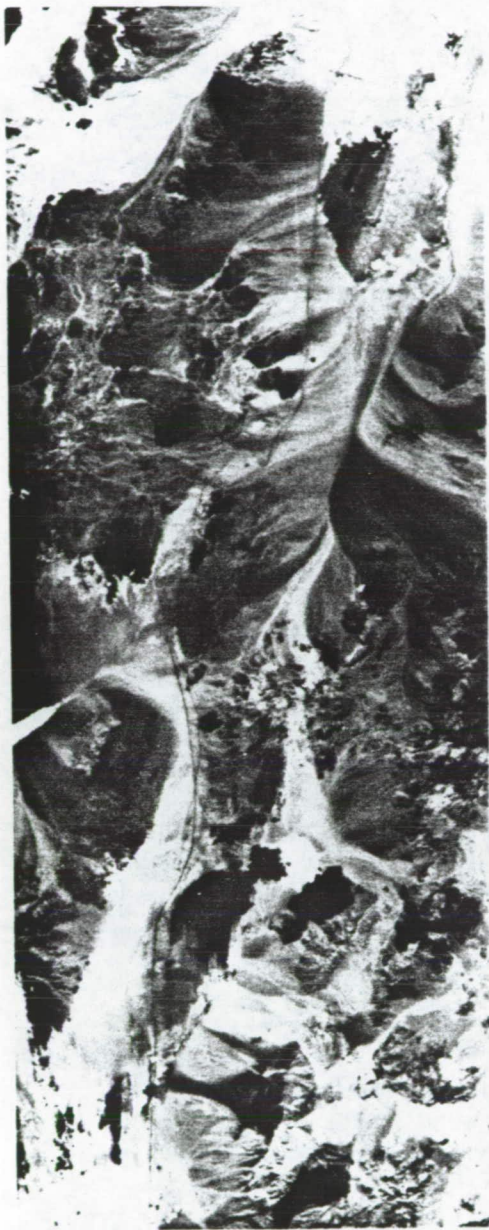


Figure 3. Pisgah lava field. a) Westinghouse KHH image acquired in 1965. Illumination from top. b) Westinghouse KHV image acquired in 1965. Illumination from top. c) JPL LHH image of northern half of field acquired 3 May 1978. Illumination from top. d) JPL LHV image of northern half of field acquired in May 1978. Illumination from top.



a

LANDSAT



b

SEASAT (OP)

10 KM

Figure 4. Pisgah and Amboy lava fields. a) Part of Landsat frame 5474-17002, band 7 showing Pisgah lava field (left) and Amboy lava field (lower right). Acquired 5 August 1976. b) Digitally correlated Seasat-A SAR image covering same area as a). Illumination from lower left. Revolution 882, 27 Aug. 1978.

ORIGINAL PAGE IS
OF POOR QUALITY

The cinder cone of Pisgah Crater is clearly delineated on the K- and X-band images because of their small depression angles and the resulting shadows, and on the Seasat-A image because, at the small incidence angle, surface slope change leads to a large tonal change in the image. It is barely discernible on the aircraft L-band image.

B. Amboy Crater and Lava Field

Amboy Crater and lava field are located 130 km east of Barstow in the Mojave Desert of California (Figure 1). The lava field is nearly circular, about 10 km in diameter, and has an area of about 70 km². Amboy Crater is an undissected, composite cinder cone 75 m in height and about 460 m in diameter at its base. The lava field is mostly composed of undifferentiated flows of degassed pahoehoe that form a hummocky terrain. Surface relief ranges from 2 to 5 m. The oldest flows are platform units that contain collapse depressions up to 10 m in diameter and several meters deep. Younger platform units are isolated areas of uniform, relatively flat basalt that were probably not disturbed while cooling. Vent lavas are exposed at the presumed location of a main vent for the lava field. They form plateaus of relatively dense pahoehoe about 10 m high. The vent plateaus have some collapse depressions and are generally ringed by fractures (Figures 5a, b), indicating subsidence either by draining back into the vents or through production of secondary flows. In addition to the collapsed features, there are several piles of boulders 1 to 4 m high that have been interpreted to be explosive features (Parker, 1963; Greeley and Iversen, 1978). Most low lying areas and hollows in the lava field are filled with aeolian deposits as much as 1 m thick. A few prominent sediment-free streaks trail downwind from such topographic features as the cinder cone and vent plateaus.

XHH, LHH, LHV and Seasat-A radar data were available for Amboy Crater and lava field (Table 1, Figures 4b and 6). The X-band image has sufficient resolution for recognition of many geomorphic types within the flow. The vent lavas and some of the remnant platform units that have relatively smooth desert pavement surfaces are prominent. The undifferentiated flows are very irregular, as the many shadows and bright radar returns indicate. Amboy Crater can be seen in the images because the large incidence angle of the X-band system accentuates topographic features.

The large subsidence fractures around the peripheries of the vent areas are visible in the X-band image as dark lines, because aeolian material has filled the fractures leaving smooth floor. The collapse depressions stand out as circular areas with dark centers for the same reason. The chaotic piles of boulders on the main vent plateau are visible as bright point returns.

Although the L-band images have a lower resolution than the X-band image, the vent lavas and remnant platform units are visible. Subsidence features and the chaotic piles of boulders are not visible on the L-band images because of their lower resolution. The morphology of Amboy Crater is reasonably well delineated, though shadowing is decreased because of the lower incidence angle of the L-band systems. Image layover is particularly noticeable in the Seasat-A images and Landsat image. The oldest platform unit on the east side of the flow, however, is not obvious on any of the images and appears to be buried by the alluvial material of Bristol Lake.

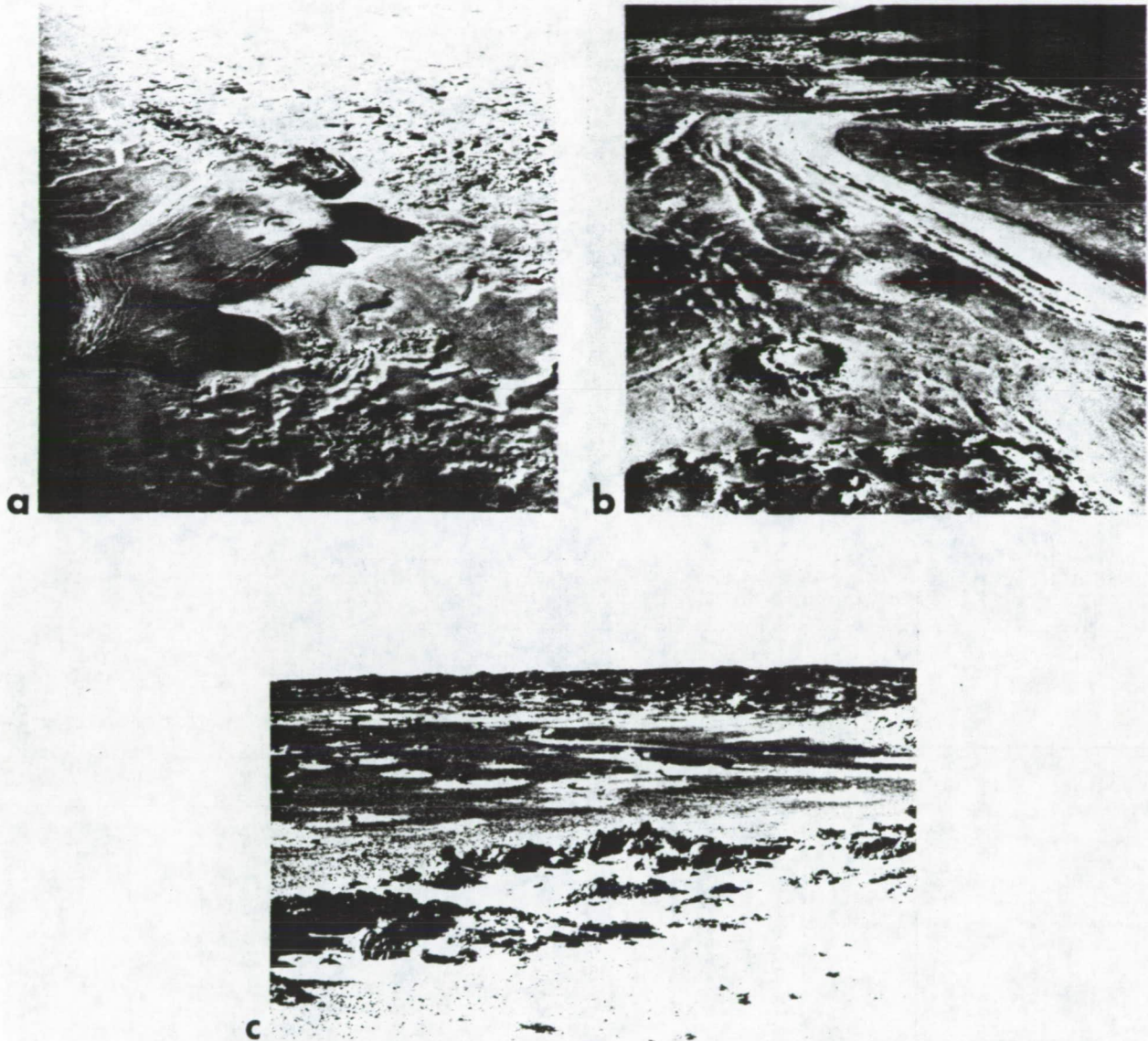


Figure 5. Amboy lava field. a) Aerial view south of vent plateau near center of lava field. Lava knobs and subsidence features visible on the plateau. The irregular surface of the rest of Amboy lava field is also visible. Photo by J. Iversen from Greeley and Iversen from Greeley and Iversen (1978). b) Aerial view northeast of vent plateau in a). Aeolian material partly fills subsidence features. Photo by R. Greeley. c) Ground photo of remnant platform unit on northeast side of Amboy Crater. Area has smooth desert pavement surface.

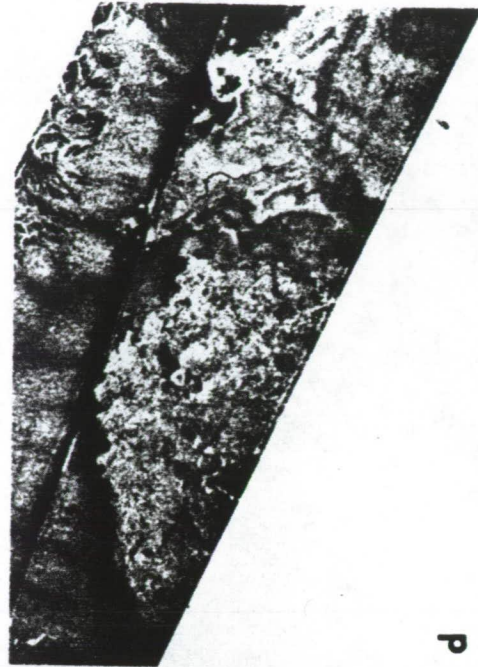
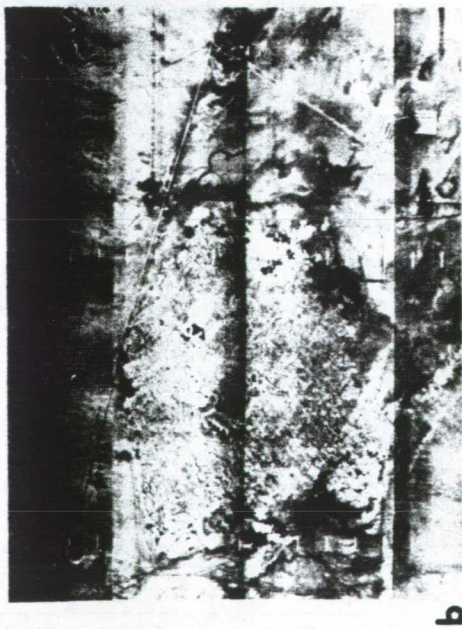
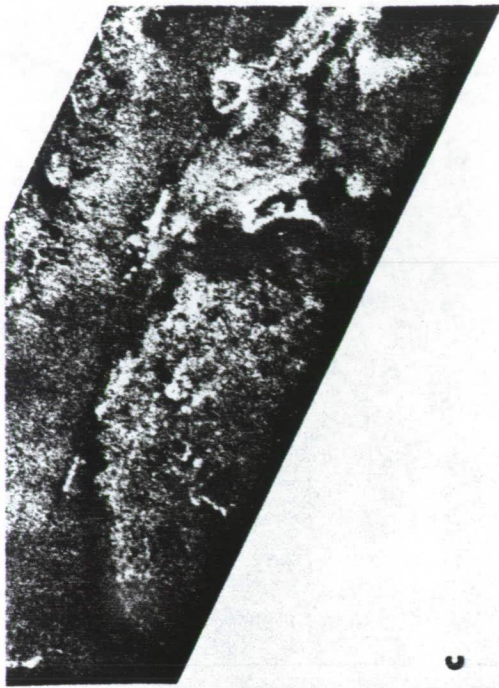
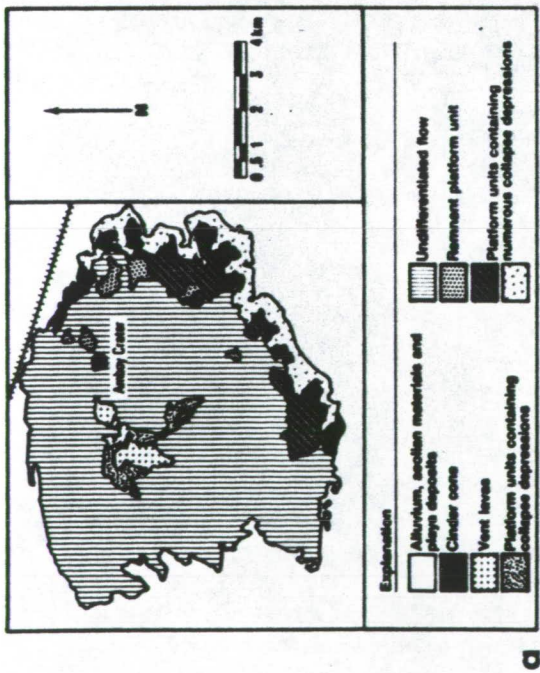


Figure 6. Amboy lava field. a) Geologic map simplified from Hatheway (1971). Units on right side of explanation are older than units on left. b) Goodyear XHH image acquired 19 Jul. 1976. Illumination from top. c) JPL LHV image acquired 3 May 1978. Illumination from upper right. d) JPL LHH image acquired 3 May 1978. Illumination from upper right.

The aeolian material masking portions of Amboy lava field is clearly shown in the Landsat image by the lighter tone of the lava field as compared to Pisgah lava field (Figure 4a). The sediment-free wind shadows are also easily identified as dark streaks trailing southeastward from topographic obstacles. These areas are visible on the radar images as slightly brighter returns because the surface roughness is less attenuated.

C. Kel-Baker Volcanic Field

The Kel-Baker Volcanic Field is an area of some two dozen cinder cones and associated basaltic lava flows about 145 km east of Barstow, between Kelso and Baker in the Mojave Desert of California (Figure 1). The flows are as much as 15 m thick and cover an area of more than 75 km². Most of the flows rest upon a pediment formed on the Cretaceous Teutonia quartz monzonite. Elsewhere the flows overlie alluvium or Precambrian gneiss. The flows and cinder cones range in age from Pliocene to Recent, some possibly as young as a few thousand years. The older flows are weathered, eroded, and partially vegetated. The most recent flows and cinder cones preserve a rough hummocky aa lava surface. No soil or vegetation has been established on these flows (Figure 7) (Barca, 1965).

The flows are much more easily separated on the L-band images than on the X-band image (Figure 8). Reflectivity contrasts between the flows and their surrounding alluvium are larger at L-band and nonexistent at X-band. There is an increase in LHH brightness with decreasing age of the flows.

The only way the flows can be distinguished in the X-band image is by specular reflection and shadowing at their flow fronts. This effect is also seen in the L-band images as most of the field was imaged at a large incidence angle. Similarly, the cinder cones of the field show up well in both LHH and XHH image.

The youngest flow in the southern part of the field (Figure 7b) is the brightest in the L-band images. It is much brighter than the alluvium and the older flows in LHV, whereas it is only slightly brighter than the other lava flows in LHH. The high cross-polarized return is probably caused by multiple scattering from the very rough surface of the young flow. The older flows are weathered and eroded (Figure 7d), providing a relatively low cross-polarized return. Alluvium and desert pavement areas are very smooth and therefore dark on both polarizations.

D. Medicine Lake Highland

Medicine Lake Highland is about 55 km east of Mount Shasta and south of Lava Beds National Monument in northern California (Figure 1.) The highland begins at an elevation of about 1500 m and rises to an elevation of almost 2400 m. It has an area of about 50 km² and a basal diameter of 35 km. It is surrounded by an elliptical rampart of cinder cones and domes, the highest of which is Mount Hoffman, at 2418 m. The highland is forested, except on the most recent lava flows. Medicine Lake Highland is the remnant of a shield volcano on the east boundary of the Cascade Range. The central portion collapsed to form a caldera, and ring fractures around the periphery of the caldera became the sites of eruptions of viscous andesitic lavas, which built the rampart of cones that enclose the caldera. In most recent times, dacites, rhyodacites, and rhyolites erupted on the rampart and on the floor of the caldera. At about the same time, basalt flows erupted on the flanks of the volcano. The flows of Lava Beds National

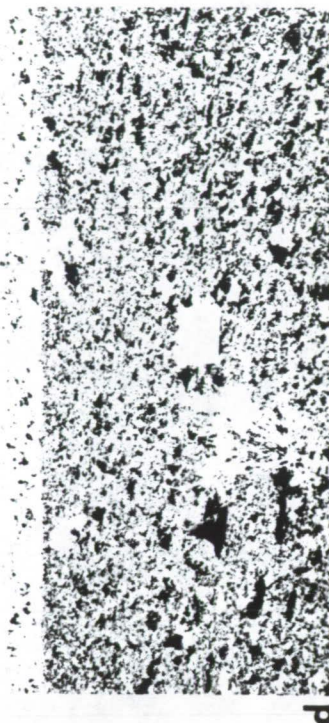
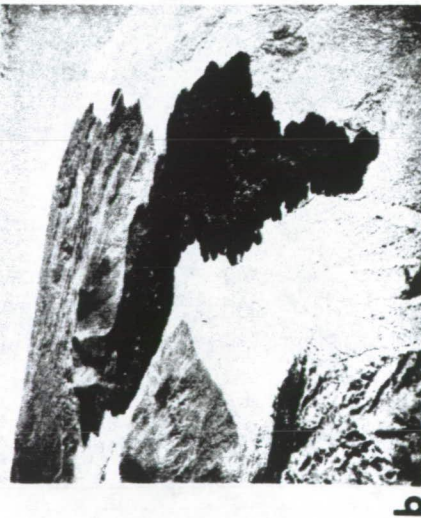
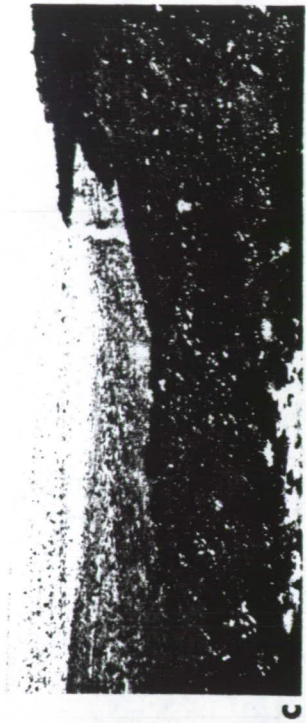
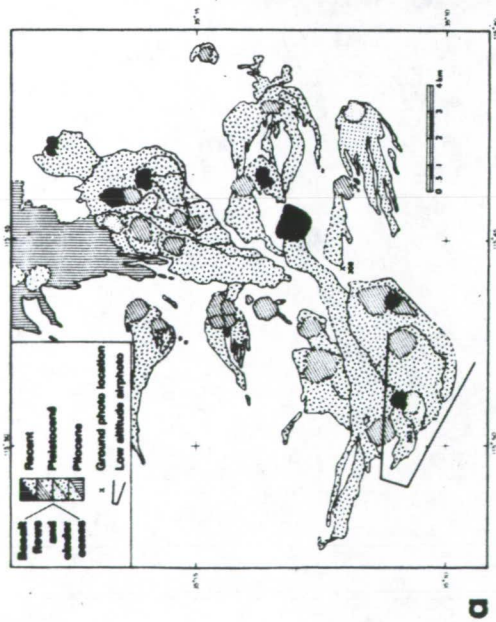


Figure 7. Kel-Baker volcanic field. a) Preliminary geologic map by W. Wise (unpublished; written communication, 1978). b) Low altitude air photo of the youngest flow, in the southwest corner of the field. View east photo by R. Greeley. c) Ground photo showing rough aa surface of youngest flow in foreground, dark desert pavement surface derived from older flow in middle ground, and light colored vegetated alluvial surface beyond. Photo number 303. d) Surface of older flow to northeast of youngest flow. Surface is sparsely vegetated cobbles pavement. Chalkboard is 20 cm square. Photo number 308.

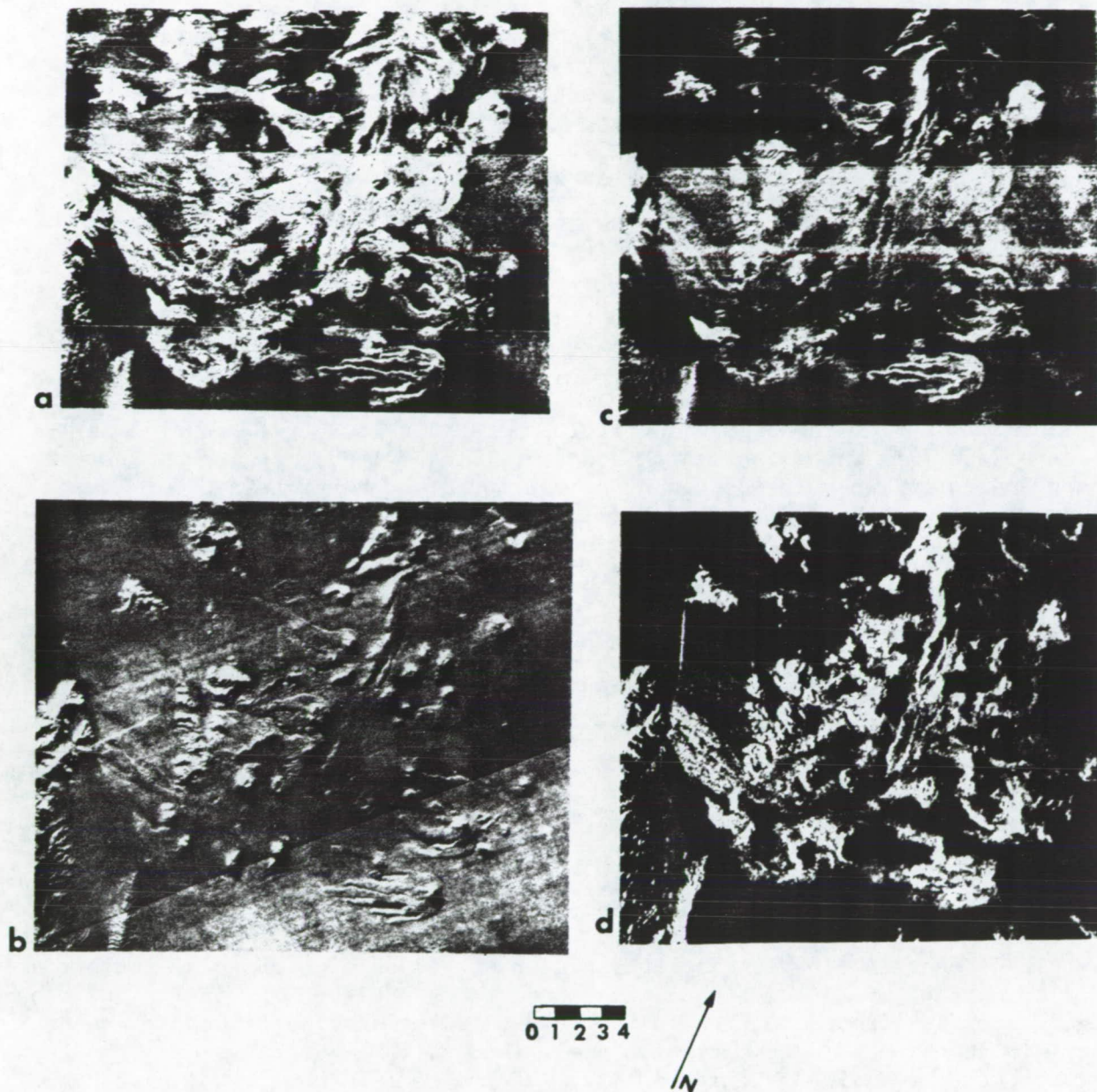


Figure 8. Kel-Baker volcanic field. a) JPL LHH mosaic obtained 30 Aug. 1977. Illumination from top. b) Goodyear XHH image acquired before 1970. Illumination from upper left. c) JPL LHV mosaic obtained 30 Aug. 1977. Illumination from top. d) Optically correlated Seasat-A SAR image acquired 14 Sept. 1978 (Rev. 1140). Illumination from left.

ORIGINAL PAGE IS
OF POOR QUALITY

Monument to the north and Burnt Lava Flow to the south are examples of these parasitic flows. Numerous cinder cones also formed at this time (Anderson, 1941).

Three of the Recent flows were studied in detail: Glass Mountain Flow, Medicine Lake Flow, and Burnt Lava Flow (Figure 9d). Glass Mountain Flow is a composite flow including an early phase of explosive cone building followed by extrusion of stony dacite and rhyolite obsidian. The western extension of the flow partially covered the earlier Hoffman dacite. Most of the composite flow is rhyolite obsidian with a pumiceous surface and glassy interior. A second, much smaller rhyolite obsidian flow erupted later and formed high flow fronts distinct from the earlier composite flow. The surface of this flow is also pumiceous to scoriaceous. The final stage of activity was marked by the rise of a dome of rhyolitic glass, the surface of which is partly pumiceous and covered with glassy spines (Anderson, 1941).

Medicine Lake Flow is a small dacite flow (about 2.5 km² in area) north of Medicine Lake. The flow has high (15 to 45 m) lobate flow fronts and an irregular, blocky surface (Figure 10b,c) with enough ash-filled pockets to support a sparse tree growth.

Burnt Lava Flow is composed of at least three units: (1) oxidized aa, (2) pahoehoe, and (3) aa and fragmented pahoehoe (Finch, 1933). Aa lavas are the most prevalent. Two main sources have been found for Burnt Lava Flow: the cinder cone called High Hole Crater (Figure 9d) and a linear fissure on the north end of the flow (Anderson, 1941). Several older cinder cones have been surrounded by Burnt Lava Flow. These cinder cones are more eroded and forested than High Hole Crater. The surface of Burnt Lava Flow is practically devoid of vegetation (Figure 10a).

Burnt Lava Flow shows up as a light tone in all the radar images because of its rough, unvegetated aa surface. The contrast between the flow and the surrounding coniferous forest is greater at L-band than at X-band. A probable explanation for this contrast difference is that the top of the forest canopy is rougher to X-band and scatters nearly as much energy as the lava flow. Forest clear cuts, visible on the L-band images as dark areas, indicate that the forest has a reasonably high return at L-band, but not as high as the return from the aa flow. The clear cuts are not visible on the X-band image; however, it is not known whether they existed at the time the X-band data were obtained.

Glass Mountain Flow is distinguished on the basis of high radar reflectivity and flow morphology on the L-band images and topographic expression in the X-band image. The flow fronts related to the several flows at Glass Mountain can be discriminated by the large incidence angle used by the X-band system. The rhyolite obsidian, the composite rhyolite-dacite, and the Hoffman dacite all have high (~30 m) flow fronts. In addition, the Hoffman dacite has a concentric flow-ridge structure visible on the X-band image. The rhyolite obsidian flow front is also visible on the L-band images. No reflectivity differences are apparent between the flows in the X-band image. The Hoffman dacite, however, is distinguishable from the glass flow in both L-band images because of the different tone: ash and forest cover on this flow appear to affect L-band more than X-band.

The high flow fronts of Medicine Lake Flow are visible in both X- and L-band images. The flow is at a larger incidence angle than Glass Mountain on the L-band images, and topographic effects are therefore much greater. Reflectivity of the flow at X-band is only slightly greater than the surrounding forest. The flow is clearly delineated by the shadow of the flow front in the far range. In the LHH

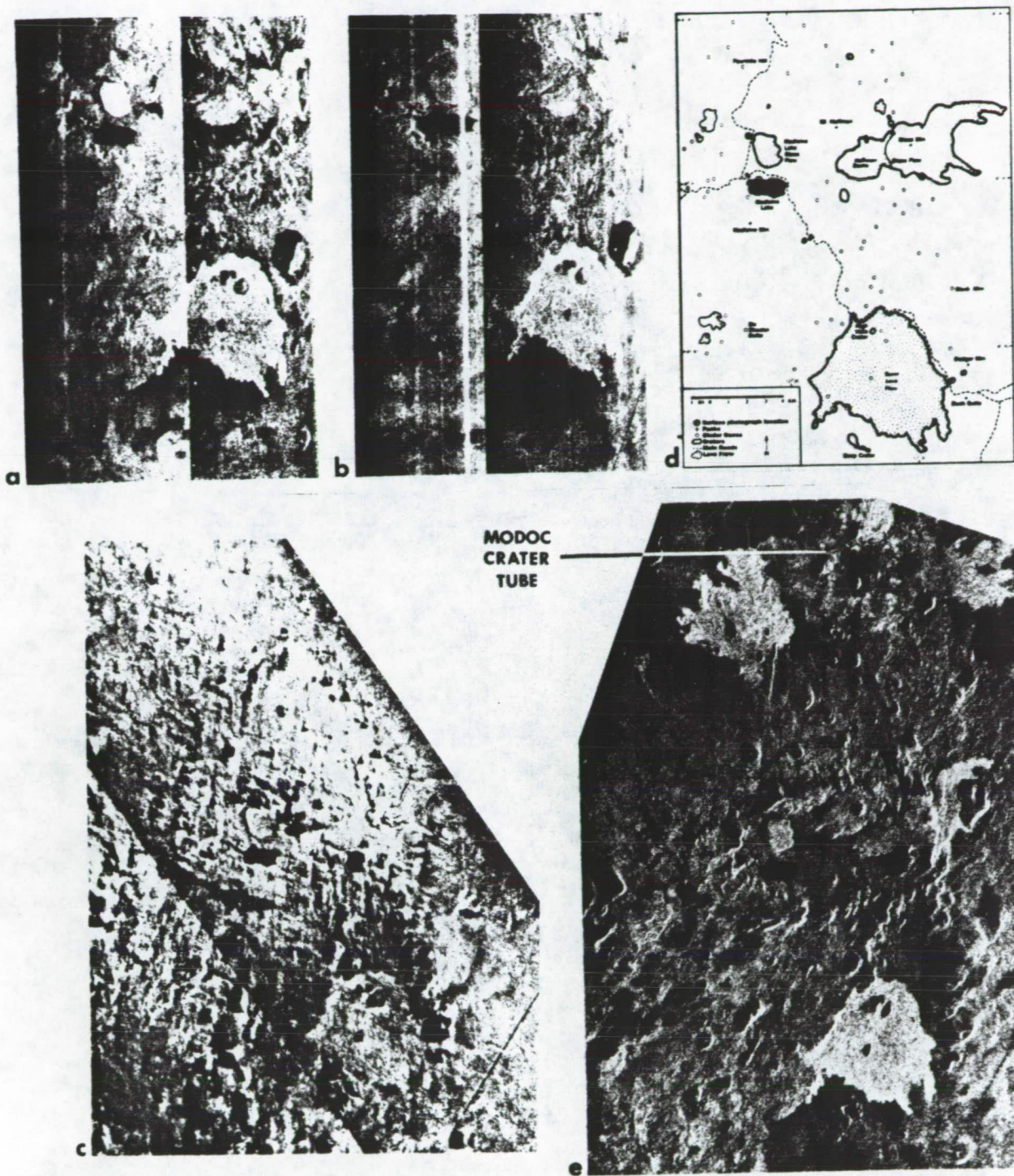


Figure 9. Medicine Lake Highland. a) JPL LHH image acquired 6 Sept. 1977. Dark checkerboard south of and dark area northeast of Burnt Lava Flow are clear cuts. Illumination from right. b) JPL LHV image acquired 6 Sept. 1977. Illumination from right. c) Goodyear XHH image acquired before 1979. Illumination from upper right, d) Location map showing major lava flows and cinder cones. e) Digitally correlated Seasat-A SAR image acquired 3 Oct. 1978. (Ref. 1406). Area shown is larger than a, b, c, and d. Bright areas at top are flows in Lava Beds National Monument. Modoc Crater Lava Tube is indicated.

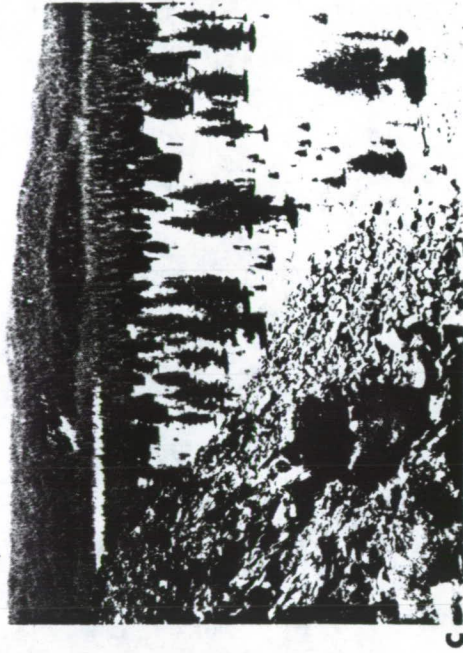
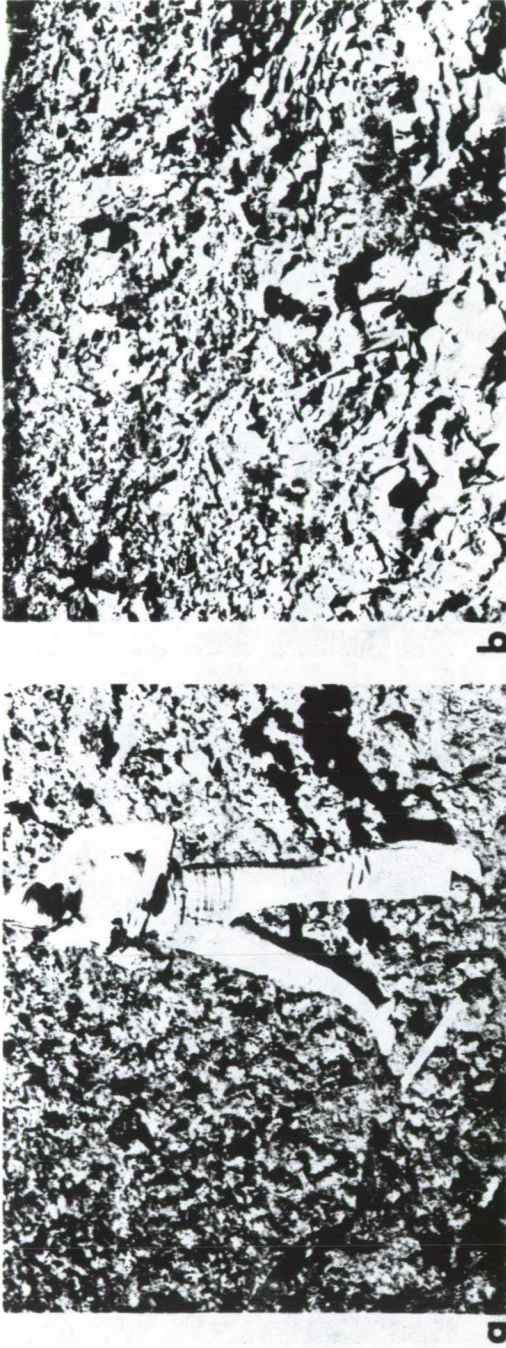


Figure 10. Medicine Lake Highland. a) Surface of Burnt Lava Flow. Note craggy, jumbled texture. b) Surface of Medicine Lake Flow. Note faceted blocks as large as 2 m across. The surface of glass Mountain Flow is slightly more craggy. c) View south from location of b). Flow front of Medicine Lake Flow is on left smooth, ash covered plain on right. Medicine Lake is in left background.

image, the entire flow is very bright, whereas it is dark in the LHV image. This effect could be explained by the large, extremely angular faceted blocks that make up this surface (Figure 10b). These blocks give specular reflections that do not depolarize the radar signal, as discussed earlier. The area west of the flow edge, that is dark on the L-band images, consists of a relatively smooth, treeless, ash-covered plain (Figure 10c). The area is only slightly darker than the flow on the X-band image.

Other geomorphic features of interest in the Medicine Lake Highland include cinder cones and lava tubes. Cinder cones are easily visible on the X-band image. Its high resolution and small depression angle emphasize topographic features. Some details are hidden in shadow, but the morphology of cones and summit craters is usually well presented. High Hole Crater on Burnt Lava Flow is a good example. Cinder cones can be seen in the aircraft L-band images, but their morphology is more difficult to interpret because lower resolution and small incidence angles produce few shadows. However, in the extreme case of the Seasat-A radar, the cinder cones are clearly visible because of near specular return from the cones' surface inclined toward the radar. A few cinder cones appear in the far range of the L-band images and sections of several lava tubes have been identified. The lava tubes appear as bright curvilinear features, probably caused by collapsed sections of roof. Modoc Crater Tube (Hatheway, 1971) is indicated in Figure 9e.

E. Eastern Snake River Plain

Volcanic rocks of the eastern Snake River Plain lie in a northeast-trending structural depression in southeastern Idaho (Figure 1). Most of the approximately 30,000 km² of the eastern plain is covered by Quaternary basalt and lesser amounts of alluvial sand and gravel. Russell (1902) described the eastern plain as constructed by vast floods of extremely fluid basalt that poured in all directions from many local vents, thus building a broad, nearly level plain, still relatively little dissected. Igneous rock types in the area are dominantly olivine tholeiites with a few plugs of more silicic rock.

Only dual polarization L-band (LHH and LHV) and Seasat-A images were available for the Snake River Plain. Radar returns from its volcanic units can be broadly classified as weak from Pleistocene lavas (Qb₄, Qb₃ and Qb₂ in Figure 11d) and strong but more variable from Recent flows (Qb₁). Volcanic units older than Qb₁ return very little radar energy because of their smooth surfaces. The Pleistocene volcanic units (Qb₂₋₄) are covered by loess and, in some places, by soil derived from weathering of the basalt in situ. Vegetation consists of only sparse growth of sage and grass. This thin cover of plants appears to be the only reflector of radar energy on the otherwise featureless older units. This effect is demonstrated at F (Figure 11c), where a cleared field has a distinctly lower radar brightness than its surroundings. Note that the vegetation effect is most pronounced on the LHV image. The northern portion of the eastern Snake River Plain contains many young pahoehoe and aa lava flows. They are typically unweathered and free of mantling loess. The oldest Pleistocene flows have surface deposits of loess and cinders from subsequent eruptions. The strongest radar scatters are outcrops of fresh aa whose locations are shown in Figure 11d. The aa units are exceptionally bright on the cross-polarized image, a consequence of multiple reflections from the craggy, jumbled surface.

Figure 11b is a Seasat-A radar image of the western part of the eastern Snake River Plain. The brightnesses of the various units are generally similar

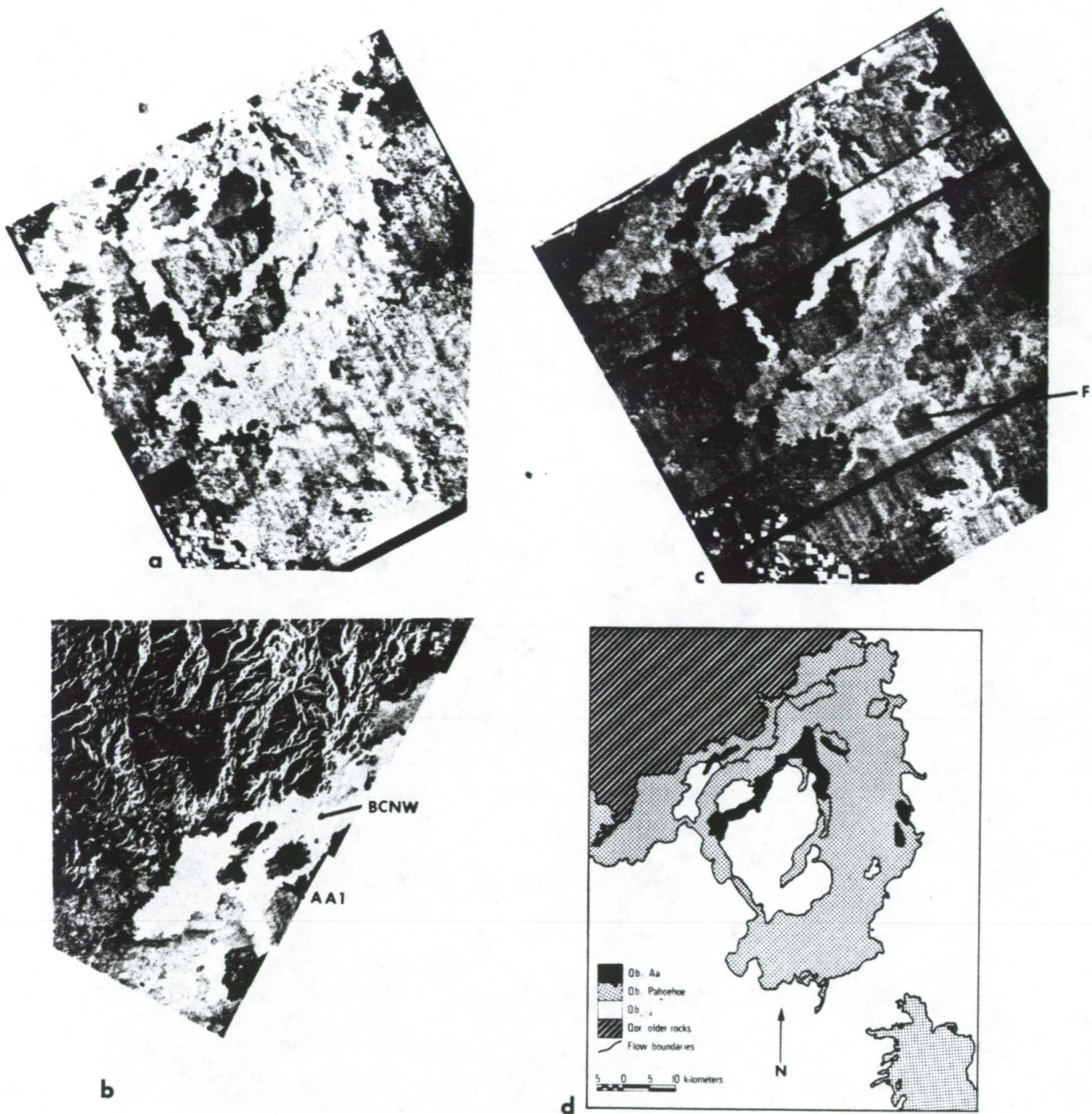


Figure 11. Eastern Snake River Plain. a) JPL LHH mosaic acquired 25 Aug. 1977 and 6 Sept. 1977. Illumination from upper left and lower right. b) Digitally correlated Seasat-A SAR image of north-west part of eastern Snake River Plain. Note brightness differences for BCNW and AA1 flows in a). c) JPL LHV mosaic acquired 25 Aug. 1977 and 6 Sept. 1977. Illumination from upper left and lower right. d) Geologic map simplified from La Point, 1977.

on the aircraft and satellite images except for the Big Crater North West (BCNW) pahoehoe flow for which the effect of incidence angle variation is particularly noticeable. The LHH aircraft image taken at $\theta = 45^\circ$ displays considerable mottling on the BCNW flow and distinct contrast with a nearby brighter aa flow (AA1). On the Seasat image taken at $\theta = 20^\circ$, the mottling is not present and the BCNW flow actually appears brighter than AA1. Figure 12 provides, in sketch form, an explanation for this effect. The backscatter cross section σ as a function of incidence angle is much flatter for the very rough aa than for the pahoehoe of the BCNW flow. This is similar to the effect noted earlier for the hummocky pahoehoe of Pisgah lava field.

Other geomorphic features seen in the radar images include buttes, lava lakes, and lava tubes. Most of the buttes and lava lakes have a bright peripheral contour caused by collapse of their walls. Several can be seen on the west side of Figure 11a and c. Lava tubes appear as bright, curvilinear features as in Medicine Lake Highland. Part of Bear Trap Lava Tube may be seen outside the eastern corner of the cleared field at F in Figures 11a and c.

F. Newberry Volcanic Field

Newberry volcano is located about 40 km south of Bend, Oregon. The volcanic activity that built the prehistoric shield volcano probably began during the Pliocene (Peterson et al., 1965). The early flows from the volcano were basalt followed by thick sheets of rhyolite and basaltic ash. After the volcano reached its maximum size, successive eruptions of basaltic lavas resulted in the collapse of the summit. Postcaldera explosive eruptions alternated with quiet outflow to form a variety of landforms. Parasitic cinder cones, which are mostly confined to the north and south slopes of the shield, are well-preserved. All of the cones are composed of scoriaceous bombs, lapilli and basaltic cinders. Most of the area around the caldera is forest covered. The summit caldera and cinder cones are clearly visible on the Seasat SAR image (Figure 13), for the most part because of their topography. The bright region around the caldera is mostly due to the forest cover. The flows within the caldera are not distinguishable.

A zone of faults and fissures, called the Northwest Rift, runs about N 30° W from the caldera wall. Eight separate basaltic aa flows have been erupted from this rift zone. All of the flows have radiocarbon ages between 5800 ± 100 and 6380 ± 130 years (Chitwood, 1977). On the Seasat images, these flows are clearly visible as bright units to the upper left of Figure 13.

A large basaltic pahoehoe lava flow of questionable Holocene age has been mapped east of China Hat (Peterson et al., 1976). The flow is thickly covered with pumice from Holocene explosive eruptions from within Newberry Volcano. The pumice cover on the flow supports a pine forest; however, ropy surfaces, tumuli and primary flow surfaces are preserved at the northern terminus. China Hat is visible on the Seasat image because of its topographic expression; however, the different flow units are not clearly visible because of the vegetation cover.

The Devil's Garden is located near the center of the High Lava Plains approximately 80 km southeast of Bend. The plains form a hummocky, undulating upland region that is underlain by a thick section of Cenozoic volcanic rocks. Most of the surface shows little or no erosion (Peterson et al., 1965). The oldest rocks exposed are Pliocene andesites, dacites, and glassy rhyolites. However,

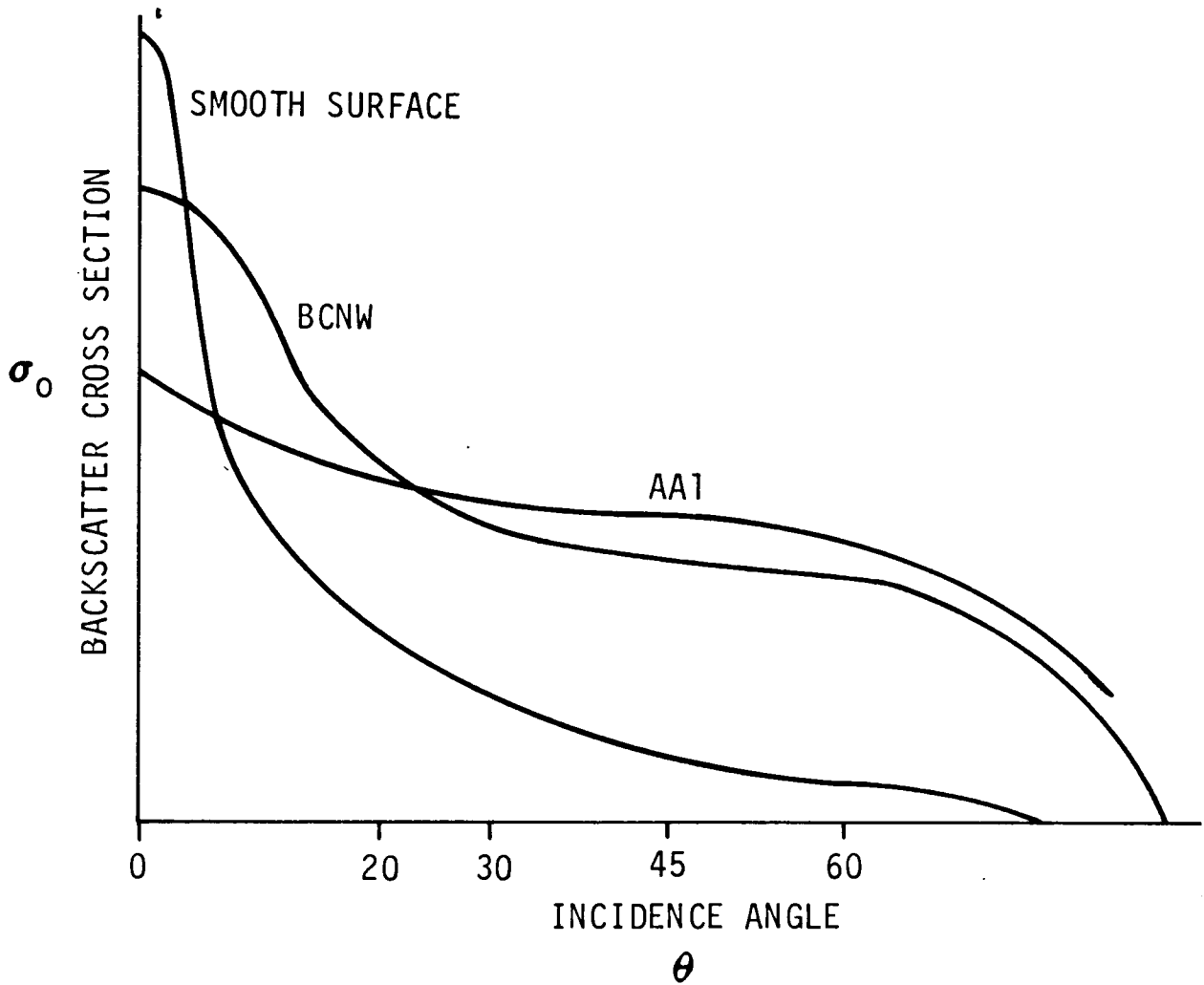
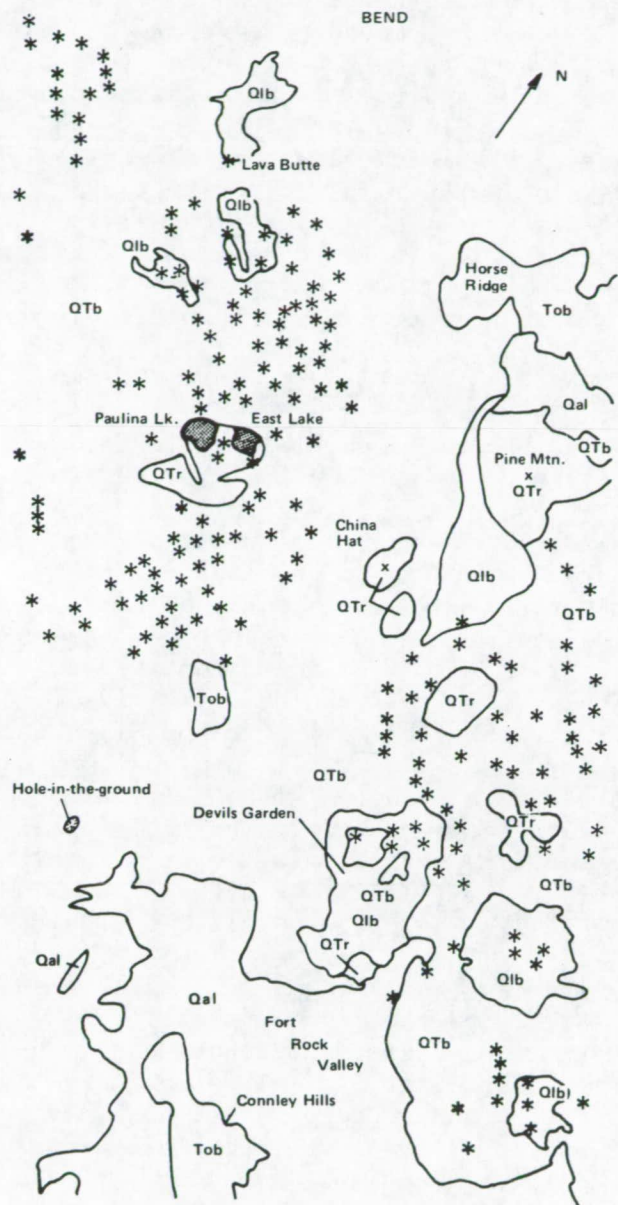


Figure 12. Schematic backscatter curves for three different surfaces showing backscatter cross section, σ_0 , as a function of incidence angle θ . Note that $\sigma_0(\text{AA1}) < \sigma_0(\text{BCNW})$ for $\theta = 20$ whereas $\sigma_0(\text{AA1}) > \sigma_0(\text{BCNW})$ for $\theta = 45^\circ$.



SEASAT (OP)

10km



*Cinder cones

Qal : unconsolidated alluvial, dune and other deposits

Qlb : youngest flows of scoriaceous, olivine and basalt

QTb: flows and pyroclastic deposits of basaltic to rhyolitic composition

QTr: rhyolite and dacite flows, breccia and domes

Tob: basaltic and andesitic flows and tuffs (generalized from geologic map of Oregon)

Figure 13. Seasat-A SAR image and a simplified geologic map of the Newberry volcanic field region, Oregon.

basaltic eruptions predominated at the close of the Pliocene and continued through the Pleistocene. The Devil's Garden Lava Field is made of thin pahoehoe flows from numerous vents in the prehistoric Holocene. The lava originated from fissure vents in the north and northeast part of the Devil's Garden and spread to the south, surrounding several rounded hills of older rocks. The pahoehoe surfaces are pockmarked by depressions of various sizes and shapes caused by collapsing lava tubes. Where resistance to spreading of the lavas was too great, the crust swelled upward into low, rounded, cracked-open domes or tumuli which resulted in jumbled slabs and sheets of lava (Peterson et al., 1965). This flow shows as a very bright region on the Seasat SAR image. Some ashy soil and pumice fragments overlying the Devil's Garden indicate that it is older than the Mt. Mazama eruption (6600 years). The lava surface north of Devil's Garden has been blanketed by pumice from eruptions of Mt. Mazama and Newberry Volcano. Because of its smooth surface, it shows relatively dark on the Seasat image.

G. Bandera Lava Field

The Bandera Lava Field is located on the Continental Divide in Valencia County, southwest of Grants, New Mexico. The field is composed of olivine basalts and several cinder cones from Pleistocene in age to as young as a few hundred years covering an area of about 640 km². The rim of the largest cinder cone, Bandera Crater, is at an elevation of about 2700 m. Many of the flows originate from cinder cones which form the northeast extension of a large Tertiary volcanic field located to the southwest of Bandera Lava Field. The surfaces of the lava flows are mostly pahoehoe except for some aa and block lava units. Aa lava generally results from localized fissure eruptions and spatter cones related to faulting. Several well-developed lava tubes are found in the pahoehoe units. Some structural control is indicated by alignment of cinder cones and lineaments observed on air photos at an orientation of N 40° E. Eleven basalt units were mapped in the northwestern part of the field on the basis of stratigraphic position, freshness, relative relief, albedo, vegetative cover and soil development (Hatheway, 1971). Figure 14 shows a generalized geologic map of Bandera Lava Field. The eleven Pleistocene units have been grouped together as one unit.

The Seasat SAR image in Figure 14 shows the southwestern part of Bandera Lava Field and the adjacent Tertiary lava field. The morphology of the smallest cinder cones is easily distinguished (e.g., El Calderon: 500 m in diameter at its base). In addition, all late Tertiary lava flows can be distinguished from Pleistocene and younger flows, possibly because of soil and vegetation development on the older flows. The Pleistocene units of Bandera Lava Field cannot be mapped in the Seasat SAR image.

V. SAND DUNE FIELDS

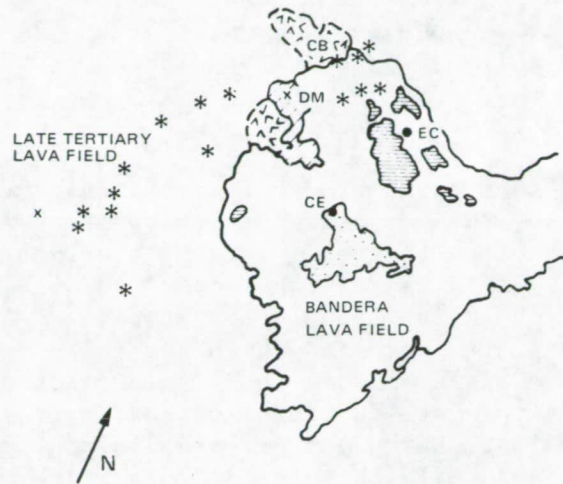
For each of the sand dune fields which were studied, the areal extent, general pattern and geometric organization of the fields was easily recognized on the radar images. This includes (1) the differentiation between sand sheets or stringers and sand dunes, (2) areal extent and boundaries of the sand fields, and (3) the large-scale dune types which compose each dune field. Dune features which are smaller than a few resolution elements cannot be readily discerned.



10 KM

SEASAT (OP)

- * CINDER CONES
- DM DEER MTN BASALTIC DOME AND FLOWS
- CB CERRO BANDERA AND EARLIER FLOWS
- CE CERRO ENCIERO AND FLOWS
- UNDIFFERENTIATED SEDIMENTARY ROCKS



GENERALIZED GEOLOGIC MAP (from Hatheway, 1971)

Figure 14. Seasat-A SAR image and a simplified geologic map of the Bandera Flow, New Mexico

ORIGINAL PAGE IS
OF POOR QUALITY

The radar backscatter from sand dunes is dominated by the specular return from the dunes' slip faces, which have slopes of less than 34° . Thus, sand dunes should show better on images with small incidence angles (less than 34° from vertical) versus intermediate incidence angles (34° to 56°). This was pointed out by Brown and Saunders (1978) in their analysis of airborne radar images of the Algodones Dunes (see Figure 15). Preliminary analysis of the radar images of some sand fields in the U.S. and Mexico is presented in this section.

A. Algodones Dunes, California

The Algodones Dunes are in southeastern California near the Arizona and Mexican borders. These dunes are among the largest active dunes in the United States. A large volume of literature is available on the dunes and surrounding areas (McKee and Breed, 1976; Smith, 1978). Cutts and Smith (1973) and Breed (1977) discuss the resemblance of the Algodones Dunes to the Hellespontus Dunes on Mars.

Large-scale aeolian features in the main dune field include giant crescent dunes at the southern end, parallel dunes on the west side and complex coalesced domical dunes in the center of the field. To the west of the dunes proper, are extensive sand sheets and stringers.

Figure 16 shows a sketch map of the prominent features, a Seasat SAR image and a Landsat image of the Algodones sand field. Figure 17 is a blowup of the Seasat image of the northern part of the field (digitally processed). A comparison of the Seasat and Landsat images shows that all the various aeolian features visible on the Landsat image are recognizable on the radar image. The giant crescent dunes are characterized by a high density of bright points, which correspond to specular radar returns from numerous dune faces. Interdune flats are gravel deposits which are quite smooth. The parallel dunes on the west side are visible because their slip faces are parallel to the path of the satellite; thus they are favorably oriented for specularly reflecting the radar signal. The long, dark area (Figures 15 and 16) east of the main axis of the dunes in the northern half corresponds to a ridge of dunes which has a steep slope facing away from the radar look direction. Thus, the return is very low because the effective incidence angle is large, eliminating the possibility of specular return.

B. Sonora Dunes, Mexico

The Sonora Dunes are in northern Mexico southeast of the Algodones Dunes. They exhibit a considerable variety of aeolian features. McKee and Breed (1976) and McKee et al. (1977) have studied the Skylab and Landsat images of these dunes and present data on the wind regime.

Landsat and Seasat images of the Sonora Dunes are shown in Figure 18. Major features which are visible on both images include chains of star dunes in the northwest, giant crescent dunes in the east and a region of parallel wavy dunes, sand sheets and stringers on the west and south. The Pinacate volcanic field starts on the right edge of the Seasat image.

The sand dunes' features are observed on the radar image due to the variation in the density of bright specular returns. Each specular return most likely corresponds to a favorably oriented face of a small dune which is part of the giant dune. The chain of star dunes and the intradune flats are

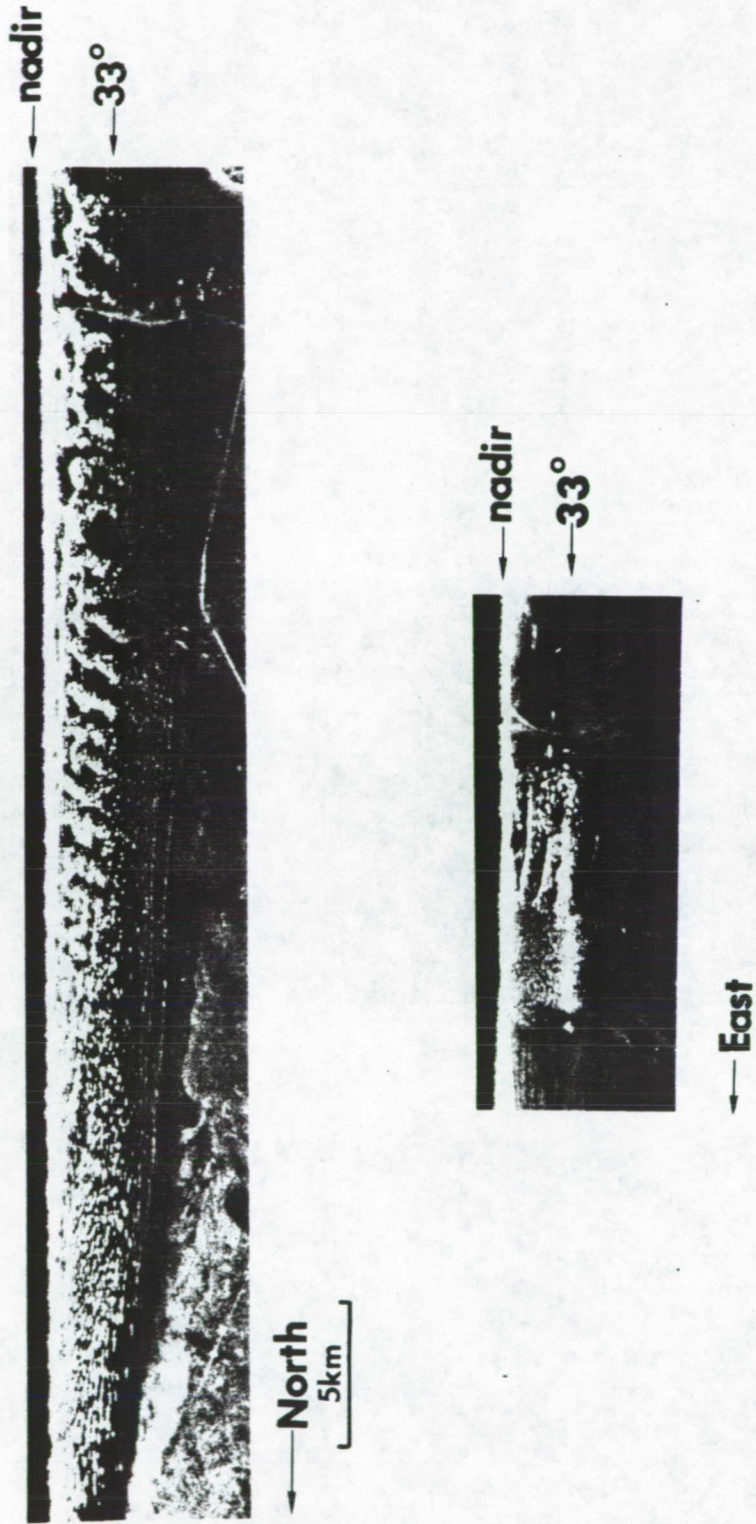
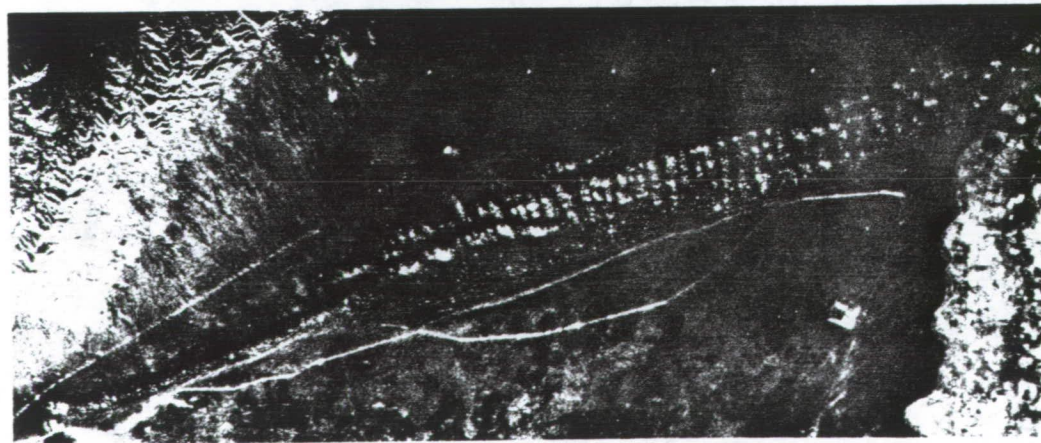
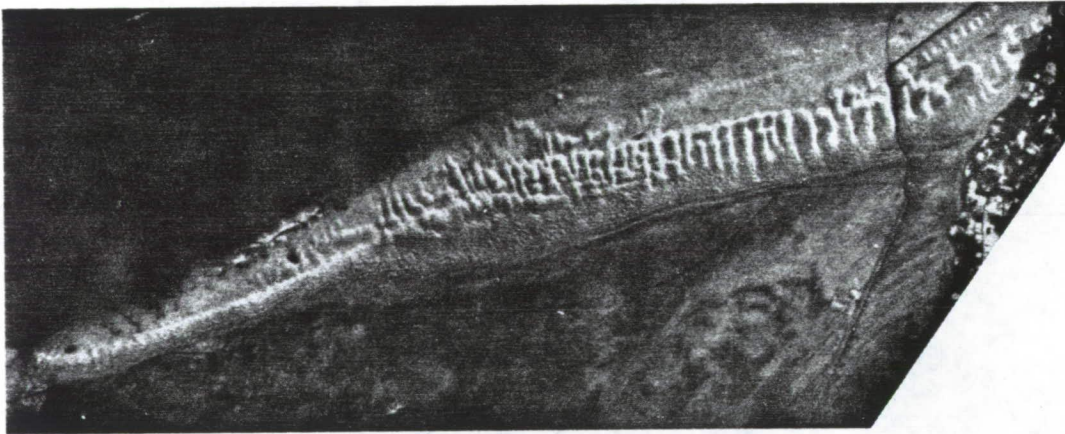


Figure 15. Airborne L-band HH radar image of the Algodones Dunes. The upper image was taken during a flight along the long axis of the dune field. The lower image was taken across the dune field. Note the presence of specular returns at incidence angles less than 33°, a sharp increase in brightness around 33°, and a quick cutoff at larger angles.

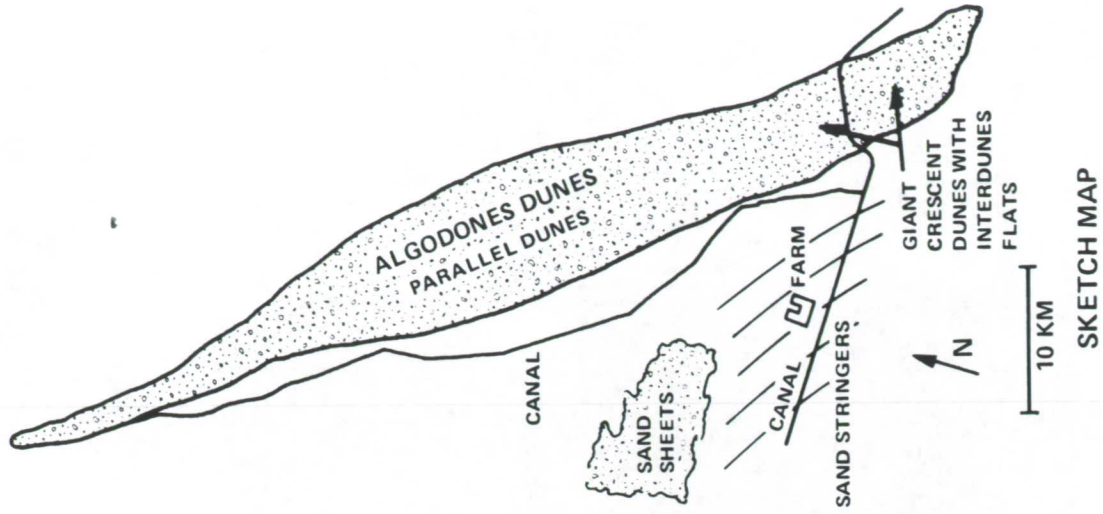
ORIGINAL PAGE IS
OF POOR QUALITY



SEASAT (OP)

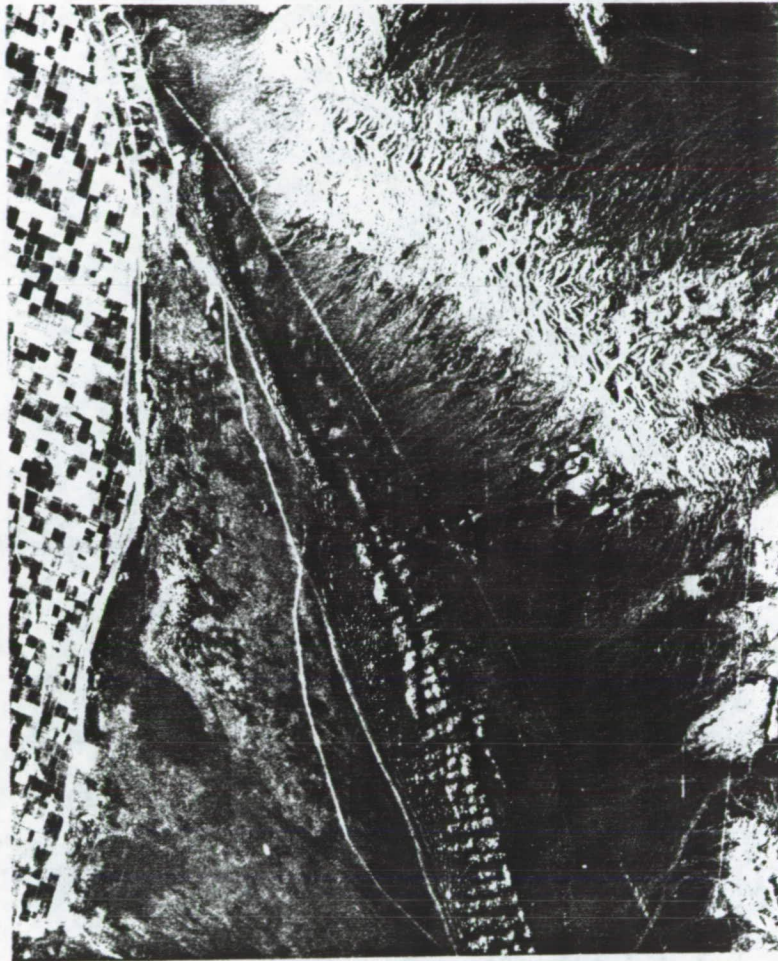


LANDSAT (ENHANCED)



SKETCH MAP

Figure 16. Seasat-A SAR and Landsat images of the Algodones Dunes field. On the right is a sketch map of some of the most prominent features.



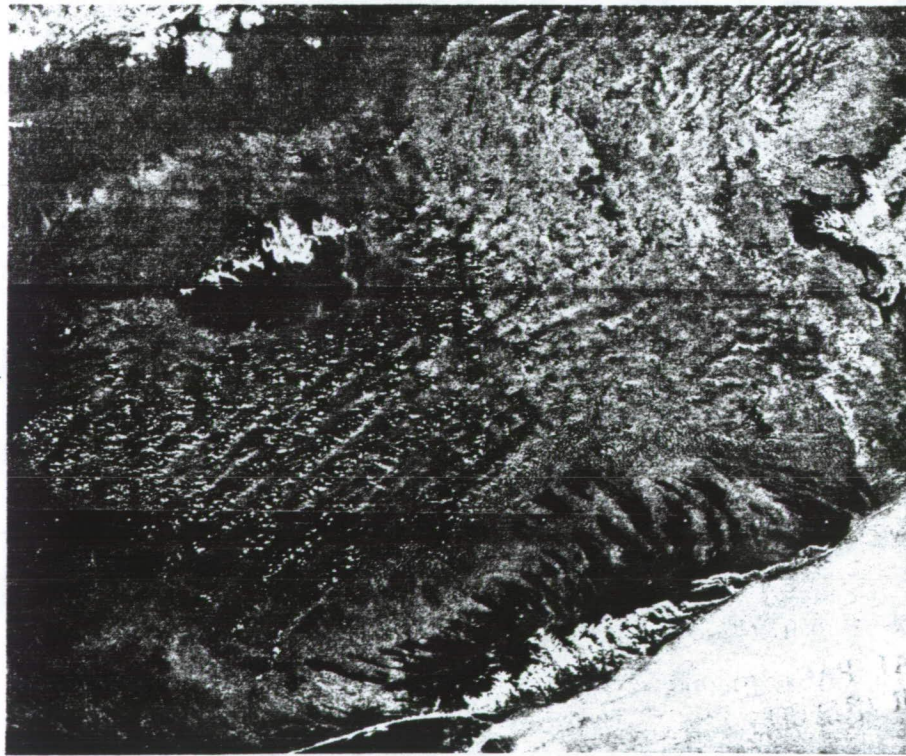
10km

Seasat SAR (DP)

Figure 17. Blowup of the Seasat-A SAR image of the northern section of the Algodones field. This image has been digitally processed with a 25 m resolution.

ORIGINAL PAGE IS
OF POOR QUALITY

CHAINS OF STAR DUNES



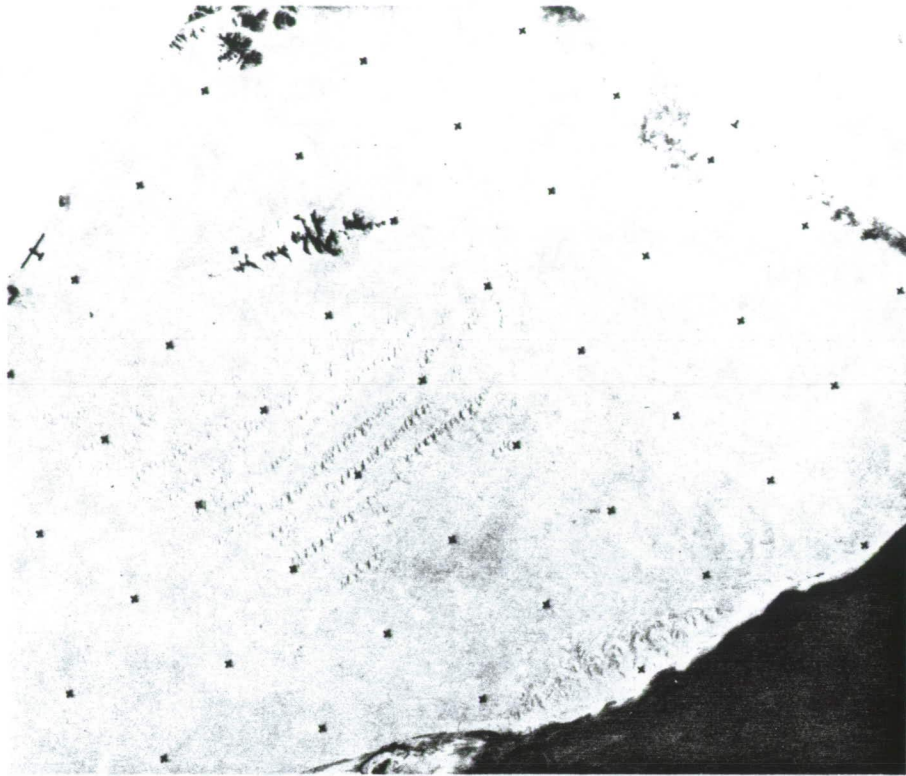
SAND SHEETS AND STRINGERS
SEASAT (OP)

10 KM

N

DELTA OF
COLORADO
RIVER

GIANT
CRESCENT
DUNES



LANDSAT (ENHANCED)

Figure 18. Seasat-A SAR and Landsat images of the Sonora desert dunes, Mexico.

clearly visible. However, it is difficult to recognize from the radar image that these are star dunes. The addition of an image with a different illumination direction would give sufficient information to infer the dune type.

C. Santa Maria Sand Dunes

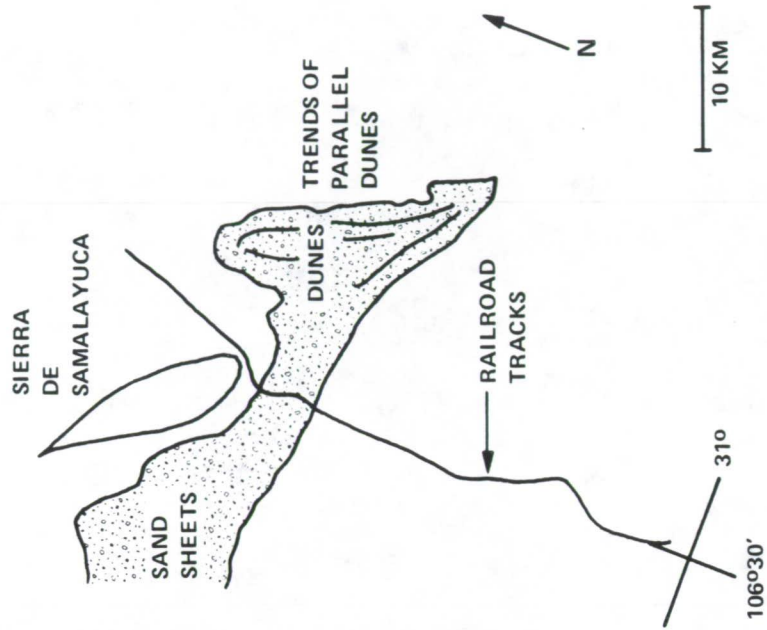
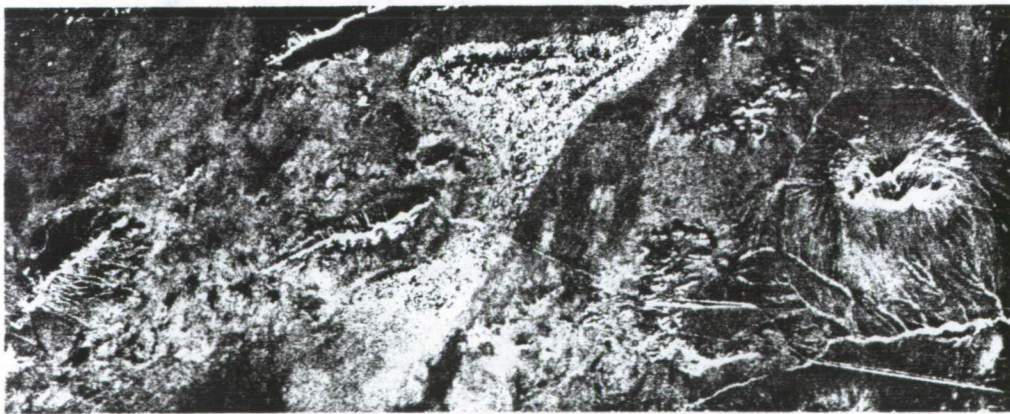
The deserts of northern Mexico contain numerous small dune fields. Figure 19 shows a Seasat SAR image of a dune field near Santa Maria and Samalayuca just south of El Paso (Texas). This image is interesting because of the very high density of specular returns relative to the other Seasat images of sand dunes. This is most likely an indication of a large number of small dunes of the parallel wavy type with slip faces favorably oriented. Note also the presence of relatively high dune ridges with the corresponding dark area away from the direction of illumination. This is the same effect observed in the Algodones region.

VI. CONCLUSIONS AND RECOMMENDATIONS

Based on the limited number of sites which have been studied we can make some preliminary conclusions. In the case of volcanic fields:

- (1) Volcanic features which have a relatively large topographic expression and characteristic geomorphology (cinder cones, calderas, collapse craters, etc.) are easily recognized on radar images independently of the frequency or polarization of the radar sensor. The look-angle is also not critical, except that small look-angles would lead to distortions and, in the extreme case, fold over.
- (2) The identification of lava flows and differentiation between flows of different ages is best done with an L-band system (vs X- or K-band). This is simply a result of the fact that in the case of X- and K-band systems the wavelength is so small that almost all flows, as well as most surrounding terrains, look very rough to the radar.
- (3) In the L-band case, it seems that the cross-polarized channel (LHV) is more sensitive than the direct polarized channel (LHH) of different lava flows.
- (4) In the L-band case, younger flows are always brighter than older flows.
- (5) The use of multiple frequency and multiple polarization will help in the possibility of determining the type of flow, such as aa vs pahoehoe vs blocky.
- (6) For small look-angles (i.e., 20°), the interpretation of the image is harder than for large look-angles. This is due to the fact that at around 20° both quasispecular and diffuse scattering play major roles and their relative contributions cannot be determined. At large incidence angles, the diffuse component is dominant, which allows delineation of flows based on their roughness, which seems to be a very effective identifying parameter.

In the case of sand dune fields:



SEASAT (OP)

SKETCH MAP

Figure 19. Seasat-A SAR image of a sand dune field near Santa Maria in Mexico, just south of El Paso.

- (1) Most of the features of sand dune fields (such as areal cover and geometric organization) can be determined.
- (2) Differentiation between straight parallel dunes, wavy parallel dunes and sand sheets or stringers is possible. However, identification of distributed dune features such as barchans or star dunes requires that they subtend several resolution elements (~ 10) to be identifiable.
- (3) It seems that small look-angles (less than 34°) might be necessary to clearly observe sand dune fields.
- (4) The effect of polarization was not studied. However, the cross-polarized return should be practically nonexistent because of the specular nature of the scattering.

Based on these observations, the following preliminary recommendations can be made for VOIR:

- (1) L-band is a preferred frequency. This choice is also required to avoid excessive atmospheric absorption.
- (2) Direct polarization is preferred. The addition of a cross-polarized channel is useful, particularly for identifying the types of lava flows.
- (3) A variable look-angle is highly desirable. The range should extend from about 20° to as large as possible, preferably more than 56° .

The above conclusions and recommendations were based on a limited set of data. Appreciably more work is still needed to further our capability of identifying and mapping lava flows and sand dune types. These recommendations based on terrestrial studies should be complemented by the results of investigations into the erosional mechanisms and weathering patterns which might be expected on Venus.

REFERENCES

- Anderson, C. A., Volcanic History of Glass Mountain, Northern California, *Am. Jour. Sci.*, 26, 485-506, 1933.
- Anderson, C. A., Volcanoes of the Medicine Lake Highland, California, *Univ. of California Pub. in Geol. Sci.* 25, 344-422, 1941.
- Barca, R. A., Geology of the Northern Part of Old Dad Mountain Quadrangle, San Bernardino Co., California, *Calif. Div. Mines Geol. Map Sheet 7*, 1965.
- Beckman, P., and Spizzichino, A. M., *Electromagnetic Scattering from Rough Surfaces*, Pergamon Press, London, 1963.
- Breed, C. S., Terrestrial Analogs of the Hellespontus Dunes, Mars, *Icarus*, 30, 326-340, 1977.
- Brown, W. E., and Saunders, R. S., Radar Backscatter from Sand Dunes, *NASA Tech. Memo 79729*, 137-139, 1978.
- Chesterman, C. W., Age of the Obsidian Flow at Glass Mountain, Siskiyou Co., California, *Am. Jour. Sci.*, 253, 418-424, 1955.
- Chitwood, L. A., Jensen, R. A., and Groh, E. A., The Age of Lava Butte, The Ore Bin, 39, 157-164, 1977.
- Cutts, J. A., and Smith R. S. U., Eolian Deposits and Dunes on Mars, *J. Geophys. Res.*, 78, p. 4139-4154, 1973.
- Daily, M., Elachi, C., Farr, T., Stromberg, W., Williams, S., and Schaber, G., Application of Multispectral Radar and Landsat Imagery to Geologic Mapping in Death Valley, *NASA-Jet Propulsion Lab. Pub. 78-19*, 1978a.
- Daily, M., Elachi, C., Farr, T., and Schaber, G., Discrimination of Geologic Units in Death Valley Using Dual Frequency and Polarization Imaging Radar Data, *Geophys. Res. Letters*, 5, p. 889-892, 1978b.
- Daily, M., Farr, T., Elachi, C., and Schaber, G., Geologic Interpretation of Multipolarization Radar/Landsat Digital Composite Image in Death Valley, California, *Photogram. Eng. Rem. Sensing*, 45, 1109-1116, 1978c.
- Dellwig, L. F., An Evaluation of Multifrequency Radar Imagery of the Pisgah Carter Area, California, *Modern Geol.*, 1, 65-73, 1969.
- Dellwig, L. F., and Moore, R. K., The Geologic Value of Simultaneously Produced Like and Cross-Polarized Radar Imagery, *Jour. Geoph. Res.*, 71, 3597-3601, 1966.
- Evans, D. L., Radar Observations of a Volcanic Terrain, Askja Caldera, Iceland, *NASA-Jet Propulsion Lab Pub. 78-81*, 42 pp. 1978.
- Finch, R. H., Burnt Lava Flow in Northern California, *Seit, Vulk.* 15, 180-183, 1933.

- Greeley, R., and King, J. S., Ed., Volcanism of the Eastern Snake River Plain, Idaho: A Comparative Planetary Geology Guidebook. Pub. by Office of Planetary Geology, NASA, 308 pp. 1977.
- Greeley, R., and Iversen, J. D., Field Guide to Amboy Lava Flow, San Bernardino Co., California, in Aeolian Features of Southern California: A Comparative Planetary Geology Guidebook, Pub. by Office of Planetary Geology, NASA, 1978.
- Hatheway, A., Lava Tubes and Collapse Depressions, Unpub. Ph.D. Thesis, Univ. of Arizona, 1971.
- Janza, F. J., Interaction Mechanisms, Chapter 4 in Manual of Remote Sensing, R. G. Reeves Ed., Amer. Soc. of Photogram., 1975.
- La Point, P. J. I., Preliminary Photogeologic Map of the Eastern Snake River Plain, Idaho, USGS Misc. Field Studies Map MF-850, 1977.
- Lefebvre, R. H., Mapping in Craters of the Moon Volcanic Field, Idaho, with Landsat (ERTS) Images. Proc. of Tenth Int'l. Symp. on Rem. Sensing of Env., 951-963, 1976.
- MacDonald, G. A., Geology of the Cascade Range and Modoc Plateau, Calif. Div. Mines Geol. Bull. 190: 65-96, 1966.
- MacDonald, H. C., Geologic Evaluation of Radar Imagery from the Darien Province, Panama, Modern Geology, 1, 1-63, 1969.
- Malin, M. C., Evans, D. L., and Elachi, C., Imaging Radar Observations of Askja Caldera, Iceland, Geoph. Res. Letters. 5, 931-933, 1978.
- McCauley, J. R., Surface Configuration as an Explanation for Lithology Related Cross-Polarization Radar Image Anomalies, Univ. of Kansas Center for Research, Inc., Tech. Rept. 177-36, 54 pp., 1972.
- McKee, E. D., and Breed, C. S., Sand Seas of the World, in ERTS-1, A New Window on Our Planet, USGS Prof. Paper 929, 1976.
- McKee, E. D., Breed, C. S., and Fryberg, S. G., Desert Sand Seas, in Skylab Explores the Earth, NASA SP-380, 5-48, 1977.
- Parker, R. B., Recent Volcanism at Amboy Crater, San Bernardino Co., California, Calif. Div. Mines Geol., Spec. Rept. 76, 23 pp., 1963.
- Peterson, N. V., Groh, E. A., Taylor, E. M., and Stensland, D. E., Geology and Mineral Resources of Deschutes County, Oregon, State of Oregon Dept. of Geology and Mineral Industries Bulletin 89, 66 pp. 1976.
- Peterson, N. V., Groh, E. A., Newhouse, C. J., State of Oregon Lunar Geological Field Conference Guidebook, State of Oregon Dept. of Geology and Mineral Industries Bulletin 57, 51 pp., 1965.
- Russell, I. C., Geology and Water Resources of the Snake River Plain of Idaho, USGS Bull. 199, 192 pp., 1902.

- Ruck, G. T., Editor, Radar Cross-Section Handbook, Plenum Press, N.Y., 1970.
- Sabins, F. F., Jr., Remote Sensing, Principles and Interpretation, W. H., Freeman and Co., San Francisco, 426 pp., 1978.
- Schaber, G. G., Berlin, G. L., and Brown, W. E., Jr., Variations in Surface Roughness Within Death Valley, California, Geologic Evaluation of 25 cm Wavelength Radar Images, Geol. Soc. Am. Bull. 87, 29-41, 1976.
- Schaber, G. G., Elachi, C., and Farr, T., Remote Sensing Data of SP Mountain and SP Lava Flow in North Central Arizona, Remote Sensing of the Environment, in press, 1979.
- Valenzuela, G. R., Depolarization of EM Waves by Slightly Rough Surfaces, IEEE Trans. Ant. and Prop., AP-15, p. 552, 1967.
- Wise, W. S., Geologic Map of the Pisgah and Sunshine Cone Lava Fields, NASA Tech. Letter NASA-11, 1966.
- Wise, W. S., Preliminary Geologic Map of Kel-Baker Volcanic Field, unpublished, personal communication, 1978.

ACKNOWLEDGEMENT

The authors acknowledge the constructive comments and help from their colleagues at JPL, in particular Dr. J. Ford and Ms. D. Evans. The effort on volcanic field mapping with radar was conducted in conjunction with efforts at USGS in Flagstaff (G. Schaber).

The research described in this paper was carried out by the Jet Propulsion Laboratory, California Institute of Technology, under NASA Contract No. NAS7-100.

ROCK TYPE DISCRIMINATION AND STRUCTURAL ANALYSIS
WITH LANDSAT AND SEASAT DATA:
SAN RAFAEL SWELL, UTAH

H. E. Stewart, R. Blom, M. Abrams, and M. Daily

Jet Propulsion Laboratory
California Institute of Technology
Pasadena, California

ABSTRACT

The San Rafael Swell, (located in southeastern Utah), is a breached asymmetric anticline composed of a variety of sedimentary rock types. Landsat multispectral and Seasat radar imagery are being investigated to determine the structural and lithologic information they contain. Various image enhancement techniques including principal components, color ratio compositing and low pass filtering of the Landsat image have been used to enhance lithologic and structural features. The Seasat digitally correlated image has been median value filtered to remove image speckle and experiments with color density slicing show improved lithologic discrimination through the color display.

The enhanced Landsat images, with information available in four spectral bands, allow good discrimination of the rock units. The Seasat image, with only one wavelength (25 cm) and polarization available, allows differentiation of fine grained rock units from coarse grained units. The Seasat resolution of about 35m improves the discrimination capability of this sensor. Because of the complementary nature of the radar image, which is sensitive to surface roughness, and the Landsat image, which indicates surface composition, the images from these two sensors are being registered and the contribution of each can then be evaluated for rock discrimination.

Structural interpretations of images from the two sensors also show complementary effects. Comparison shows that the Seasat images' superior resolution and sensitivity to slopes and surface roughness allows recognition of features not seen on the Landsat image.

I. INTRODUCTION

The purpose of this study is to evaluate satellite synthetic aperture radar (SAR) images for geologic purposes. The benchmark to which the SAR images are

compared is Landsat, used both for structural and lithologic interpretations. Control for the geologic analysis is provided by Hawley (1968), Johnson (1957), and by our own field work.

II. GEOLOGY

The San Rafael Swell is a large asymmetric anticline located in Emery County, Utah. Rocks ranging in age from Pennsylvanian to Cretaceous outcrop in the area. The Swell is a breached structural feature. The central region (Figure 1) is underlain by Permian and Triassic age rocks; the outer region is underlain by Triassic and Jurassic age rocks; younger strata of Jurassic and Cretaceous age ring the structure.

The oldest rocks, of Pennsylvanian and Permian age, are exposed in deep canyons and consist of the Elephant Canyon formation and the Hermosa formation. Younger strata in the central zone are more widely exposed and consist of the Coconino Sandstone and Kaibab Limestone of Permian age and the Moenkopi and Chinle formations of Triassic age. In the outer zone the units exposed are the Wingate Sandstone, Kayenta formation, and Navajo formation of Triassic and Jurassic age. Ringing the swell are exposures of the Carmel formation, the Entrada Sandstone, the Curtis formation, the Summerville formation, and the Morrison formation of Jurassic age, the Cedar Mountain formation, the Dakota Sandstone, and the Mancos Shale of Cretaceous age.

The rocks of the swell were folded in early Tertiary time into a large asymmetric doubly plunging anticline (Hawley et al., 1968). The major axis of the fold trends north-northeast to east-northeast. Dips of 2° - 5° are prevalent on the west flank of the anticline. To the east, the dip gradually increases before abruptly steepening to vertical in a monoclinical fold, with moderately to steeply dipping beds.

The sedimentary rocks are cut by numerous high angle faults, with both normal and reverse displacements. Faulting probably started about the time of folding but continued later into the Tertiary (Hawley, *ibid*).

III. COMPUTER PROCESSING OF LANDSAT DATA

A Landsat-1 scene of the San Rafael Swell was obtained on computer-compatible tapes (Scene No. 1068-17364, September 29, 1972). JPL's Image Processing Laboratory produced color ratio composite, principal component, and subtractive low pass filter images for analysis and interpretation.

The ratio composite (Figure 2) was produced from three images. Each was made by ratioing two bands, pixel by pixel, and then applying a linear contrast stretch to each of the three ratio pictures. A color composite was created by standard three-color reconstruction; ratios 4/5, 5/6, and 6/7 are displayed as blue, green and red, respectively. The ratioing process exaggerates subtle color differences between units and, to the first order, removes the effects of brightness differences due to topography (Rowan et al., 1975).

The principal components image (Figure 3) was created by applying the Karhunen-Loeve transformation to the data. This process transforms the data to new variables which are linear combinations of the original variables (bands 4, 5, 6, 7). The new variables are orthogonal, hence, uncorrelated. Three of the four

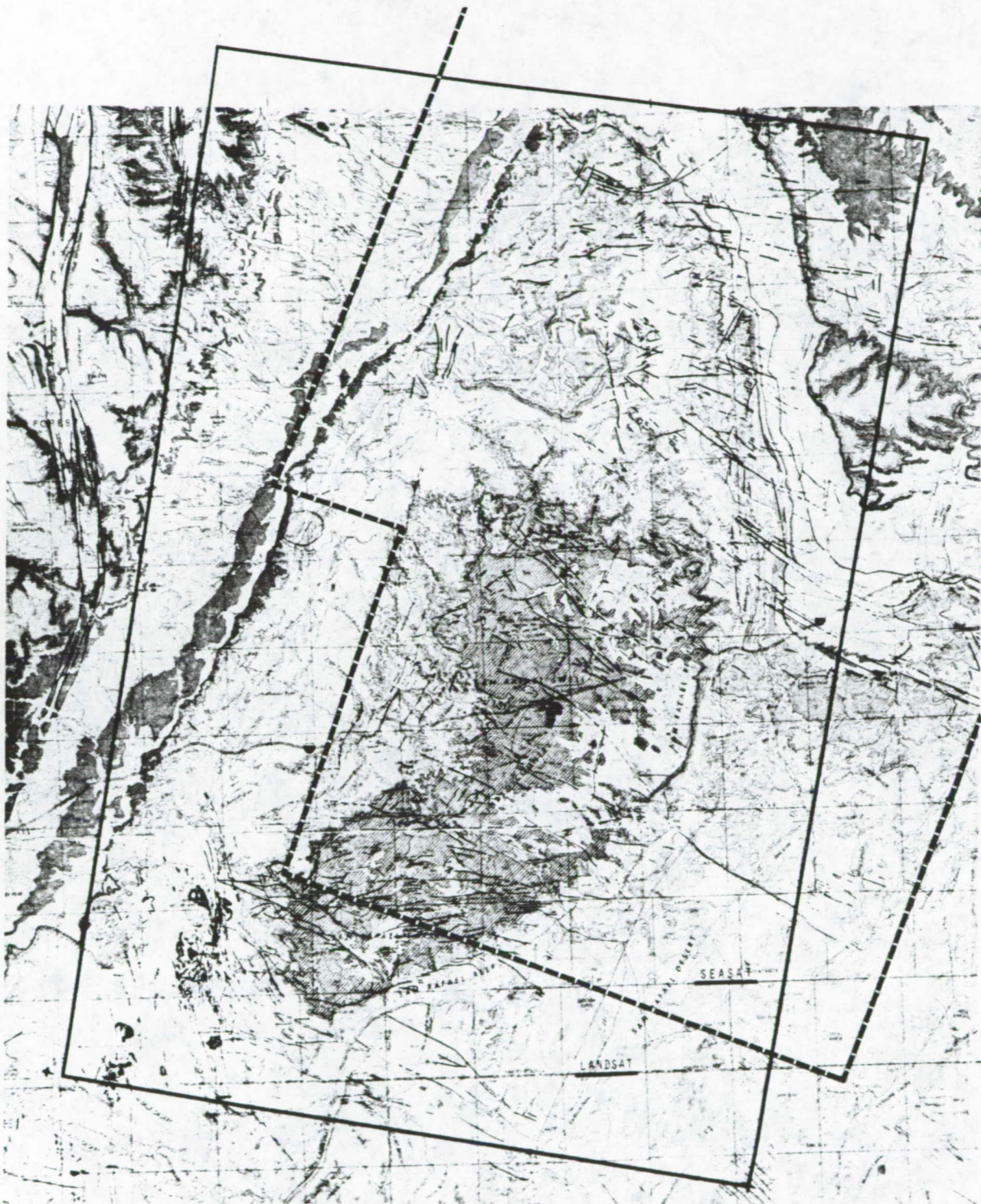


Figure 1. Geologic map of the San Rafael Swell, Utah, showing outlines of Landsat (black) and Seasat (dashed) coverage.

ORIGINAL PAGE IS
OF POOR QUALITY

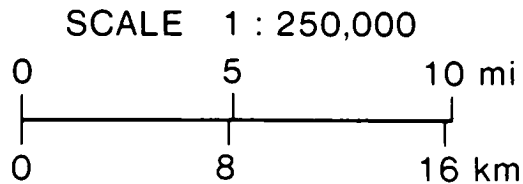
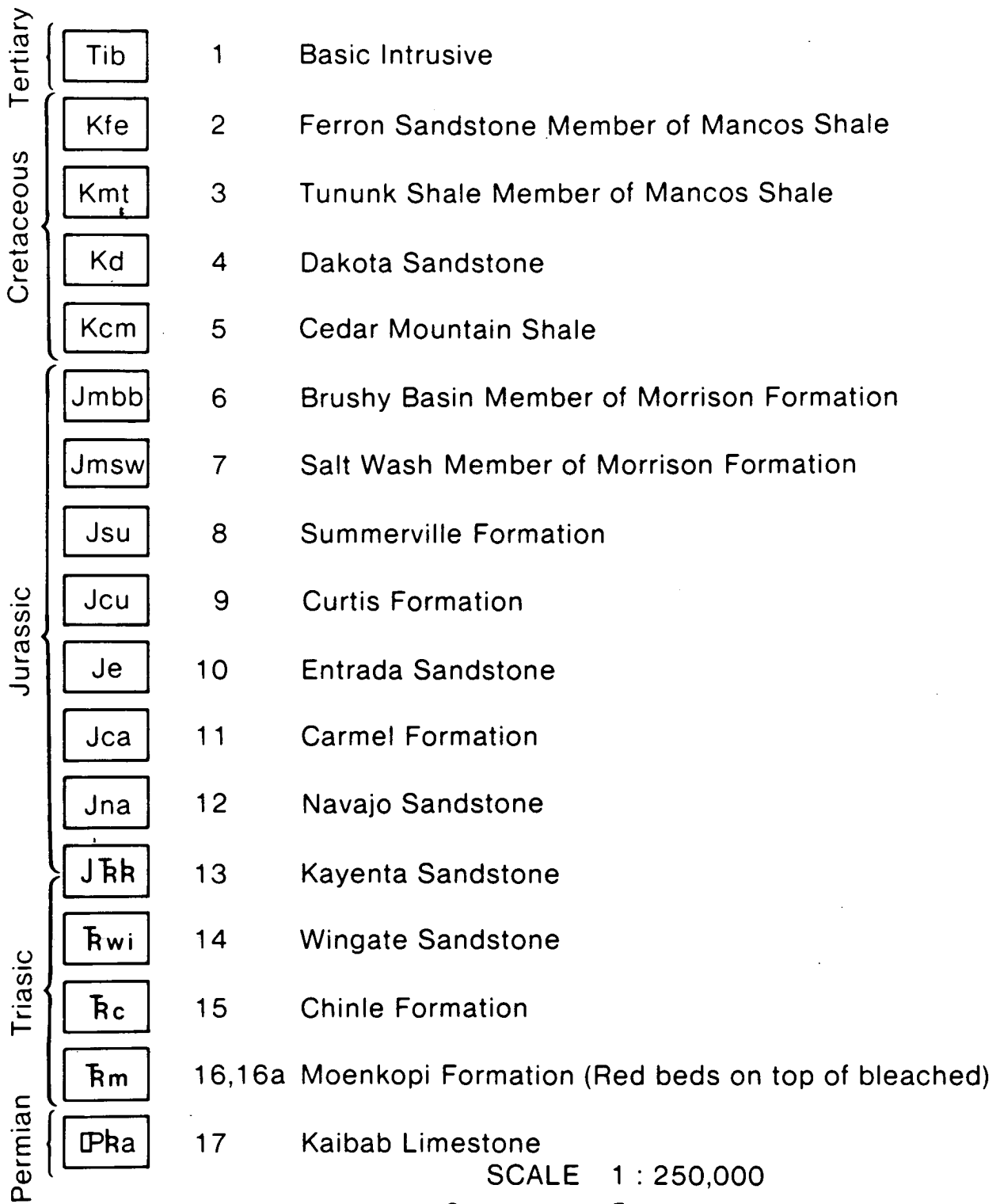


Figure 1 (cont'd). Legend for geologic map. Numbers refer to lithologic interpretations in later illustrations.



Figure 2. Landsat color ratio composite with lithologic interpretation. Ratios 4/5, 5/6, 6/7 displayed as blue, green and red.



Figure 3. Landsat principal components composite.

new variables were contrast stretched, and components 1, 2, and 3 are displayed as blue, green, and red, respectively. The main advantages of this type of processing are removal of interband correlation and compression of four channels of data to three, the fourth principal component containing mostly noise. The scene variance tends to be concentrated into fewer new variables that still contain all of the original variability of the bands (Blodget et al., 1978).

The filtered image (Figure 4) was produced by applying the following transformation to band 7:

$$\text{OUT} = 1.2 \text{ IN} - (25 \times 25)^2 \text{ IN} + 100$$

where OUT is the output picture, IN is the input picture, $(25 \times 25)^2$ is a low-pass convolution box filter of 25 by 25 element size, applied twice sequentially to the input, and 100 is an additive constant to rescale the data. The size of the filter was chosen after producing images using several different size boxes ranging from 25 by 25 to 101 by 101. This type of filter is equivalent to a high-pass filter. The filter was applied twice to reduce the artifacts introduced by convolution box filtering (Gillespie, in press).

IV. DIGITAL CORRELATION

The Seasat image of the San Rafael Swell was digitally correlated at the Jet Propulsion Laboratory. Digital correlation performs the signal processing of an optical correlator mathematically, with the advantage of eliminating the artifacts contributed by optical hardware and film processing. Digital correlation also preserves more of the dynamic range of the imaging system. The Seasat imaging radar system has a dynamic range for distributed targets of about 20 dB which, upon correlation, has a potential dynamic range of about 60 dB for point targets. Digital correlation allows about 40 dB to be recorded on the computer output tape. Since film has a dynamic range of about 20 dB, not all the data can be displayed at once as an image. Image processing techniques can display on film the desired portions of the dynamic range from the digitally correlated tape. This same procedure can be done optically through recorrelation of the data on the optical correlator. The major disadvantage to digital correlation is that it requires substantial computer time. The digital correlation of a 100 x 100 km area on the JPL system requires 9-1/2 hours, as compared to a few minutes for the equivalent area optically processed. However, the problem of absolute calibration of radar backscatter remains because the analog spacecraft-to-ground data link is uncalibrated, there are STC (sensitivity time control) positioning errors, and there are residual attitude control errors. The shift of the STC also causes some degradation by improper positioning of the analog-to-digital quantization window.

The digital processing scheme consists of recording each returned radar pulse on digital tape with 5-bit quantization. These data are transferred to computer-compatible tapes by truncating to 4-bit accuracy. Experiments have shown that this truncation does not seriously affect image quality. The data are processed in sections which are read off the tape by a general-purpose computer and stored on disk for processing. The processing is accomplished in the frequency domain using a special-purpose fast Fourier transform peripheral device. A discussion of the mathematics of digital correlation can be found in Kirk (1975). The individually correlated segments of the image are processed or conversion to film. The final image represents a 100 x 100 km area with pixels



1068-17364 7 IR2 29SEP72 SAN RAFAEL SWELL
N38-54/W111-13 HDG190 SUN EL42 AZ145 PRC121 SCALE 79.94M/PXL
DS4
F2 1.2*IN1-IN2+100.0 - STRETCH 78- 155

TPL PIC ID 79/04/06/055327 REA/SR204X
JPL IMAGE PROCESSING LABORATORY

Figure 4. Landsat band 7, subtractive low pass filtered with structural interpretation.

representing 18 m in range and 16 m in azimuth on the ground. The image is processed to 4 looks and the effective resolution is about 35 meters.

V. IMAGE PROCESSING

The digitally correlated San Rafael Swell Seasat image is undergoing extensive processing at the Image Processing Laboratory at JPL. The goals of this processing effort are to extract and display as much structural and lithologic information as possible. Use of the digitally correlated Seasat imagery allows access to nearly the full dynamic range of the imaging system, hence, far greater sensitivity.

To produce images of the entire San Rafael Swell, two 100 x 100 km areas were digitally correlated and then registered. Because of the unwieldy size of the resultant data set (8000 by 6000 pixels), it was elected to resample the picture with a 3 x 3 average value filter. This reduced the number of pixels by a factor of 9, smoothed the inherent speckle, and greatly increased computational speed of later processing. Although this reduced the resolution, the tradeoff was considered worthwhile. Selected areas of interest can also be processed at full resolution for detailed analysis.

Although resampling the picture with a 3 x 3 average value filter smoothed the speckle somewhat, it was determined that the remaining speckle was detrimental to further image processing. Our experiments have shown that applying a median value filter can be highly effective in removing speckle while causing minimal image degradation (Blom, in prep.). Median value filtering is a nonlinear ad hoc procedure which is effective in removing discrete noise while maintaining boundaries and causing minimal influence on the surrounding areas (Pratt, 1978). The filter operates by determining the median DN value of the pixels in the specified window size and replacing the center pixel DN value with compared median value. The variance contributed by speckle is thus largely removed. The San Rafael Swell image was processed with a median value filter with a 5 x 5 box size. The resulting image is both pleasing to the eye and amenable to further processing techniques such as pattern recognition and automatic classification. In order to increase visual discriminability of geologic units and features, a technique of color encoding DN values is being evaluated with the radar data. Briefly, the technique consists of operating in hue, saturation, and intensity space and then setting intensity and saturation to a constant value while letting color be a function of the DN value. Since the human eye is more sensitive to subtle color changes than subtle gray level changes, the procedure makes interpretation easier if the color ranges for various DN's are judiciously chosen. Also, a greater portion of the dynamic range inherent in the digital radar data can be visually interpreted in color. Our experiments to date indicate that visual separation of sandstone and shales is greatly improved and that some structural features are enhanced. Other color encoding schemes and display techniques are being explored, directed by determination of the ranges of DN values occupied by various geologic units of interest.

In order to exploit the complementary effects of radar and Landsat¹ imagery, the digital Seasat image and a Landsat image of the San Rafael Swell are being registered. The procedure consists of rotating and sizing the images to one another and finding common tie points. The relative value of the radar data and of each of the various Landsat channels can then be evaluated for rock discrimination by principal components analysis by determining the contribution of each channel to

each principal component. Linear discriminant analysis, a supervised classification procedure, will also be used to assess the relative value of the radar data and each of the Landsat channels for rock discrimination. Images generated by these two procedures will be compared and analyzed for rock discrimination purposes.

VI. INTERPRETATION

A. Lithology

A ratio composite (Figure 2), consisting of 4/5, 5/6, 6/7 displayed as blue, green, and red, respectively, allowed effective differentiation of the sandstone from the shale units. This variability, observable on the Landsat ratio composite, is strongly controlled by variations in the amount and oxidation state of iron in the surface and by vegetation cover. Looking specifically at the Beckwith Plateau area, the Mancos shale is easily separable from the Ferron sandstone which forms its base. Both units are sparsely vegetated and the sandstone has a greater radiance in the four Landsat bands. The topographic expression of the sandstone is more rugged than the shales.

The principal component image (Figure 3) enhances the boundaries between some of the more subtly different sandy shale and shale units. As with Landsat, the variables controlling sensor response are fixed such that the lithologic units can be traced almost completely around the uplift.

The Seasat image with lithologic overlay (Figure 5) allows additional lithologic units to be differentiated. With a radar cell size of about 35 meters, the image has twice the resolution of Landsat, and this added detail in surface texture is of great help in differentiating some subtly different units. In the Beckwith Plateau area, this texture is mostly defined by differences in drainage density and vegetation cover.

It should be noticed that there is a marked decrease in dynamic range and resultant number of gray levels as we go further out in range. This is in part due to natural falloff in S/N but is aggravated by the STC error and the analog-to-digital conversion step. For this reason the interpretation was most successful in near swath.

The brightness of the individual resolution cells is related to backscatter energy return from the surface. The parameters primarily responsible for this return are slope, surface roughness, incidence angle, polarization, frequency and complex dielectric constant (MacDonald et al., 1967).

The Seasat SAR system's dynamic range is low, corresponding at best to 6 gray levels. This best-case situation for determining small variations in surface texture is in topographically flat areas in the near range. For this reason, the more subtle variations in lithologic units are not seen. Due to the overwhelming effects of slope, very little information pertaining to surface texture or dielectric properties is detectable. In dealing with an SAR image with a look angle of 20.5° , any surfaces with a larger slope angle are going to be geometrically distorted due to layover. Since the angle of repose for loose materials is greater than 20.5° , one would expect to see considerable distortion in mountainous terrain. This is seen in the northeast part of the study area.



Figure 5. Digitally correlated Seasat image with lithologic interpretation.

ORIGINAL PAGE IS
OF POOR QUALITY

Although the incidence angle of the Seasat-A SAR is not optimal for scattering from geological surfaces, we may still use theoretical studies as a guide to predict radar response of different surface types. Qualitatively, radar backscatter (HH) from a surface shows an increasing dependence on electrical properties and a decreasing dependence on surface roughness as incidence angle steepens. In geological materials, variations in electrical properties are dominated by moisture content. Within the L-band, the relative dielectric constant (ϵ) varies from approximately 3 to 9. Since the backscatter cross-section σ^0 varies as

$$\frac{\epsilon-1}{\epsilon+1}^2, \text{ then } \sigma^0 \text{ varies as } \frac{3-1}{3+1}^2 = .07 \text{ to } \frac{9-1}{9+1}^2 = .25,$$

a range of less than 6 dB. This is small compared to the 30-dB variation in σ^0 for roughness variations.

Mathematical descriptions of scattering by rough surfaces are exceedingly difficult. Nevertheless, an approximate description of the scattering properties of a surface can be obtained by use of Rayleigh and Bragg scattering equations convolved with functions representing the statistical properties of surface features. The simplest such function is a lognormal size distribution common to many sediments. For such simple models, the size range 3-7 cm (mean) yields the steepest change in σ^0 at L-band frequency (Figure 6).

B. Structure

In both the Landsat band 7 filter image and the Seasat image, the overall structure of the swell is obvious. Many of the linears mapped on the Landsat and Seasat correspond to mapped faults. The Landsat linears are mappable due essentially to shadowing denoting a low area along the feature. The Seasat linears are bright features corresponding to scarps showing higher energy return due to slope. A few linears on the Seasat such as feature A on Figure 7 show a difference in material made visible by different radar signal returns on either side of the feature. Though it would be expected that scarps orthogonal to the look direction would be selectively enhanced in the radar, the observation is that linears corresponding to mapped faults are visible even though many approach angular relationships parallel to look direction.

By using a digital color sliced image (Figure 8), it is possible to extend linear feature A-A' beyond that possible in either the Landsat or Seasat black and white images.

VII. FUTURE DIRECTIONS

Future SAR sensors may differ from Seasat in one or more of three parameters: incidence angle, frequency, and polarization.

Incidence angles will probably be less steep, thereby increasing the influence of surface roughness upon backscatter. Comparison of two images acquired at different incidence angles gives two points on the σ^0 vs θ (incidence angle) curves. Figure 9 shows schematic curves for two volcanic units (AAL and BCNW) whose relative backscatter cross-sections reverse in going from Seasat (~ 20°) to aircraft (45°) imaging geometries.

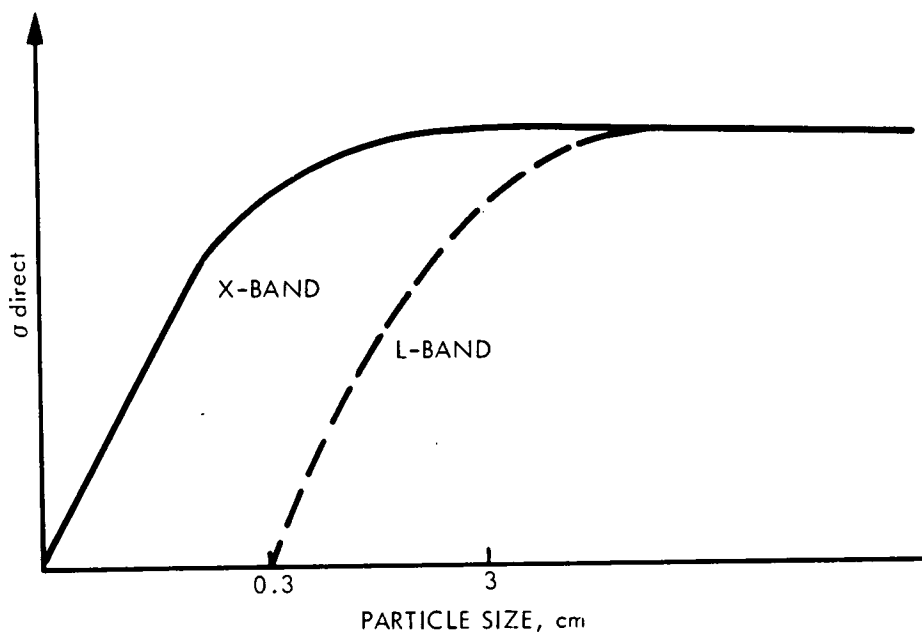


Figure 6. Sketch of the behavior of the mean backscatter cross-section from particles at X-band and L-band.



Figure 7. Seasat structural interpretation.

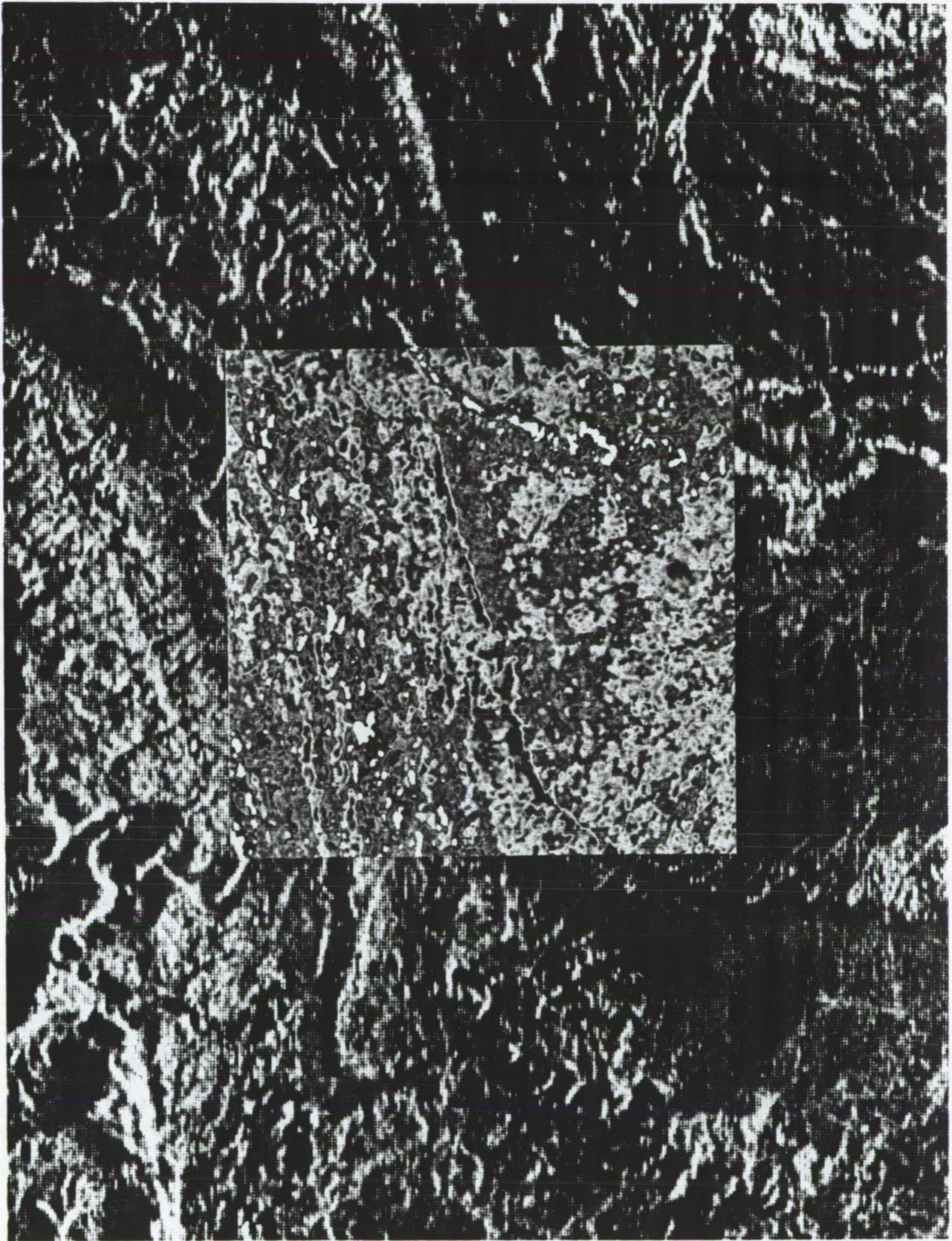


Figure 8. Color sliced Seasat data inserted into black-and-white.

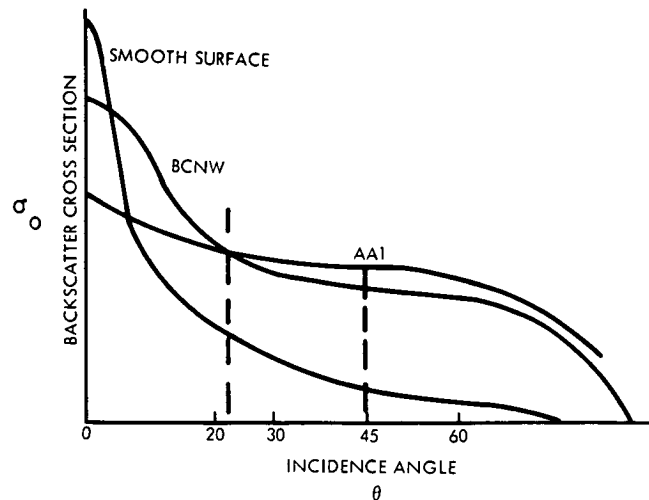


Figure 9. Backscatter cross section vs incidence angle for two volcanic units and a smooth surface.

Frequencies should include C- and X-band, bands for which large variations in backscatter occur at smaller surface roughness scales than for L-band. Multi-frequency radar data can, for many surfaces, provide information on the size variation of surface materials.

Polarization effects are very difficult to model, but multipolarization is easier to implement from a hardware point of view, requiring only a second antenna rather than an entire second radar system for dual-frequency capability. For some geological environments (e.g., Death Valley), the addition of a second polarization provides more information than does a second frequency (Daily et al., 1978).

REFERENCES

- Blodget, H. W., F. J. Gunther, and M. H. Podwysocki, "Discrimination of Rock Classes and Alteration Products in Southwestern Saudi Arabia with Computer-Enhanced Landsat Data," NASA Technical Paper 1327, NASA Scientific and Technical Information Office, Washington, D.C., October 1978.
- Daily, M., C. Elachi, T. Farr, W. Stromberg, S. Williams, G. Schaber, "Application of Multispectral Radar and Landsat Imagery to Geologic Mapping in Death Valley," Jet Propulsion Laboratory Publication 78-19, Pasadena, Calif., 1978.
- Gillespie, A. R., "Directional Fabrics Introduced by Digital Filtering of Images," Proceedings of the Second Annual New Basement Tectonics Conference, in press.

- Hawley, C. C., R. C. Robeck, and H. C. Dyer, "Geology, Altered Rocks and Ore Deposits of the San Rafael Swell, Emery County, Utah," U.S. Geological Survey Bulletin 1239, 1968.
- Johnson, H. S., Jr., Uranium resources of the San Rafael District, Emery County, Utah - a Regional Synthesis, U.S. Geo. Survey Bull. 1046-D 37-54, 1957.
- Kirk, J. C., "A Discussion of Digital Processing in Synthetic Aperture Radar," IEEE Transactions of Aerospace and Electronic Systems, Vol. AES-11, No. 3, 1975, pp. 326-337.
- MacDonald, H. C., P. A. Brennan, and L. F. Dellwig, "Geologic Evaluation by Radar of NASA Sedimentary Test Site," IEEE Transactions of Geoscience Electronics, Vol. GE-5, No. 3, 1967, 72-79.
- Pratt, W. K., Digital Image Processing, John Wiley and Sons, New York, NY, 1978, pp. 330-334.
- Rowan, L. C., P. H. Wetlaufer, A. F. H. Goetz, F. C. Billingsley, and J. H. Stewart, "Discrimination of Rock Types and Detection of Hydrothermally Altered Areas in South-Central Nevada by the use of Computer-Enhanced ERTS Images," U.S. Geological Survey Professional Paper 883, Washington, D.C., 1974.

ACKNOWLEDGEMENTS

This paper is the result of research carried out at the Jet Propulsion Laboratory, California Institute of Technology, under Contract NAS7-100 sponsored by the National Aeronautics and Space Administration.

TERRAIN-ANALYSIS PROCEDURES FOR
MODELING RADAR BACKSCATTER

Gerald G. Schaber and Graydon L. Berlin

U.S. Geological Survey
Flagstaff, ArizonaRichard J. Pike
U.S. Geological Survey
Menlo Park, California

ABSTRACT

The collection and analysis of detailed information on the surface of natural terrain are important aspects of radar-backscattering modeling. Radar is especially sensitive to surface-relief changes in the millimeter-to-decimeter scale for conventional K-band (~1-cm wavelength) to L-band (~25-cm wavelength) radar systems. Surface roughness statistics that characterize these changes in detail have been generated by a comprehensive set of seven programmed calculations for radar-backscatter modeling from sets of field measurements. The seven programs are (1) formatting of data in readable form for subsequent topographic analysis program, (2) relief analysis, (3) power spectral analysis, (4) power spectrum plots, (5) slope angle between slope reversals, (6) slope angle against slope interval plots, and (7) base length slope angle and curvature. This complete Fortran IV software package, "Terrain Analysis," is here described for the first time and is available through the senior author. The software package was originally developed a decade ago for investigations of lunar morphology and surface trafficability for the Apollo Lunar Roving Vehicle.

I. INTRODUCTION

Radar backscatter has been shown to be especially sensitive to changes in geometry that are responsible for the transition from primarily diffuse backscatter (bright radar image tone) to Rayleigh scattering (dark image tone). For example, McDonald and Waite (1973) showed that at K-band (0.86-cm wavelength) this transition takes place between 0.1- and 0.3-cm mean relief at 10° to 80° incidence angles; it is applicable only to very smooth playa and alluvial fans in desert regions. Schaber, Berlin, and Brown (1976), describing the L-band (25-cm wavelength) radar behavior in Death Valley, California, showed that this same transition between radar-bright (diffuse backscatter) and radar-dark (Rayleigh scattering) image tone takes place at a mean relief between 4 cm and 7 cm for moderate incidence angles 35°-45°. Many unvegetated terrain surfaces

have variations in microrelief that bridge this roughness range; thus such terrains can be easily discriminated from adjacent smoother or rougher surfaces by L-band (and longer wavelength) radar systems (see Sabins, 1978).

Proper collection and analysis of detailed data on surface geometry are essential to any research on radar backscatter modeling. The procedures for accomplishing these tasks have not been well defined in the open literature, nor have the data requirements for specific radar frequencies and terrain types been identified. In this paper we describe procedures developed to obtain both raw measured and surface-roughness statistics for radar backscatter modeling. We also describe for the first time a comprehensive and highly flexible software package for terrain analysis. This set of computer programs originally was developed in trafficability studies for the Apollo Lunar Roving Vehicle and investigations of lunar surface geometry (Rozema, 1969; Pike, 1978; U.S. Geological Survey, 1970).

II. GENERATION OF MICRORELIEF PROFILES

A. Surface Profiles from a Templet

Field measurement of terrain microrelief can be accomplished inexpensively and with satisfactory results using a templet that accurately reflects the topographic variations of a surface over the length of the device (Figure 1). The templet fabricated for evaluation during radar backscatter research in Death Valley (Schaber, Berlin, and Brown, 1976) was made of solid aluminum stock and consisted of 65 moveable rectangular rods capable of measuring maximum relief of approximately one meter over a horizontal distance of one-half meter. The device was moved horizontally to acquire longer profile base-lengths for later statistical analysis. Applicability of such a templet depends on the level of resolution required for calculations of specific roughness statistics; for example, this device cannot record potentially important millimeter-scale relief (high-frequency component) of the topography.

The experimental templet has two distinct advantages: (1) many terrain profiles can be measured cheaply, and (2) fairly high resolution (1.0-cm horizontal by 0.5-cm vertical) can be maintained. Disadvantages include (1) difficulty in transporting the heavy device long distances on foot across adverse terrains, and (2) inability to obtain millimeter-scale relief statistics. Comparison of profiles derived from the templet and from conventional stereophotogrammetric techniques will be made at the end of the next section.

B. Surface Profiles from Stereo Photographs

High-resolution (± 1 -mm horizontal and vertical) surface profiles can be obtained by photogrammetric reduction of high-quality large format (e.g., 70-mm metric camera) photographs taken in overlap and convergent stereo from several meters above the ground surface (Figure 2). A conventional 60-mm focal-length lens results in profiles approximately one meter long. Calibration of the lens at the measurement distance is required for high precision and ultimate resolution (< 1 mm). Longer profile lengths can be obtained simply by increasing the camera-to-ground distance, but photogrammetric resolution will be reduced. Photogrammetric reduction of the stereo image data requires an analytical stereoplotter that can accommodate different viewing geometries. A baseline level is established in the model by placing two "leveled" meter sticks orthogonally in the field of view. Horizontal scale is determined from the meter sticks, and vertical scale and exaggeration are computed in the stereoplotter from camera parameters and viewing geometry.



Figure 1. Aluminum templet used to record surface relief, shown in moderately rough saltpan in Death Valley, California. Templet approximately 1.2 m high by 0.5 m wide. A level is built into top crossbar for proper orientation; handles were included for ease in carrying; weight about 65 pounds. Profile shown on templet is left half of those shown in Figure 3.

ORIGINAL PAGE IS
OF POOR QUALITY

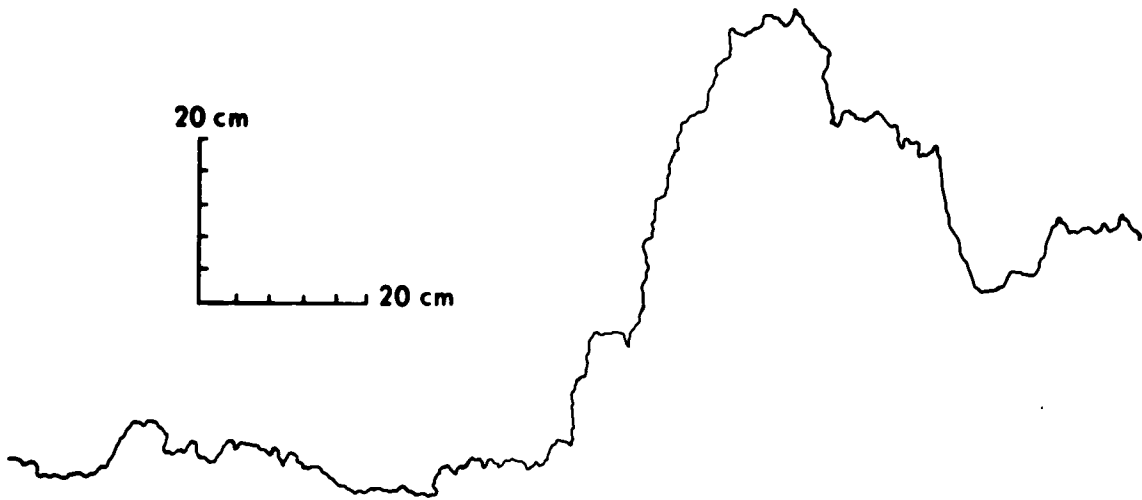


Figure 2. Example of topographic profile obtained by photogrammetric reduction of metric-camera (70 mm) stereopair photographs. Profile was digitized at 3-mm equivalent ground interval and used as input for the Terrain Analysis program, the output of which is in Appendix A.

A continuous high-resolution (± 1 mm) topographic profile is recorded in orthogonal directions across the stereo model. A contour map of the entire model could also be produced at a contour interval of 1 to 2 mm; however, a contour map from many stereo models would be prohibitively expensive. If a 1-m^2 area of terrain within a stereo model has homogeneous roughness in all directions, as is true of most microterrain surfaces, then orthogonal topographic profiles are sufficient for representative statistics on roughness.

In Figure 3 we directly compare topographic profiles derived from the templet described above and the analytical stereoplotter technique. Note the close similarity between the two profiles but the evident loss of high-frequency (millimeter-scale) relief in the templet results.

III. TERRAIN ANALYSIS

Parametric description of natural topography, for practical applications (e.g., radar-backscatter modeling) as well as more academic objectives (Pike, 1963; Pike and Rozema, 1975), is a bewilderingly complex subject. Research in this area, which commonly is referred to (not always correctly) as "terrain analysis," embraces aspects as diverse as theoretical topology, numerical taxonomy, and tactical military operations. The resulting literature is vast and it is difficult to keep up with current developments. For a glimpse of the general problem and some recent keys to the literature, see Speight (1974), Pike and Rozema (1975), Speight (1977), and Pike (1978). Many studies in terrain analysis are parochial and often are undertaken to develop a classification scheme for a highly specific set of circumstances. We emphasize that none of these systems have universal applicability in terrain analysis, despite occasional authors' claims to this impossible achievement. Accordingly, the descriptive statistics that we have applied to microterrain for modeling radar backscatter likewise constitute only one way to address the general problem: abstracting the geometry of natural landscapes. The application to radar tends to restrict descriptive variables to those expressing surface roughness rather than other, more exotic characteristics of the terrain (Pike, 1978; Pike and Rozema, 1975). Moreover, the statistical description of topography at one-millimeter resolution represents application of terrain analysis to one extreme of the scale with which there is little experience on the part of earth scientists. And finally, the statistics are computed from a linear profile, not from an areal sample design (e.g., Grender, 1967; Day, 1979). Some of our subroutines have been converted to accept areal data (elevations at grid intersections), but we have not applied the results to radar work. Thus we were pleasantly surprised to find that our specialized requirements for computation were met so handily by an off-the-shelf package of software nearly a decade old. Although the package described here does not fulfill every need of our radar work, its present usefulness testifies to the flexibility built into the system of description. Undoubtedly this software will meet the requirements of other terrain analysts as well.

IV. COMPUTATION OF ROUGHNESS STATISTICS

The topographic profile shown in Figure 2 was digitized at a 3-mm equivalent ground interval, and the resulting elevations were used to calculate parameters of surface roughness. Roughness statistics were generated by the Terrain Analysis program developed by the U.S. Geological Survey under NASA funding for trafficability analysis for the Apollo Lunar Roving Vehicle and in incidental studies of lunar morphology (Pike and Rozema, 1975; Pike, 1978; U.S. Geological Survey, 1979).

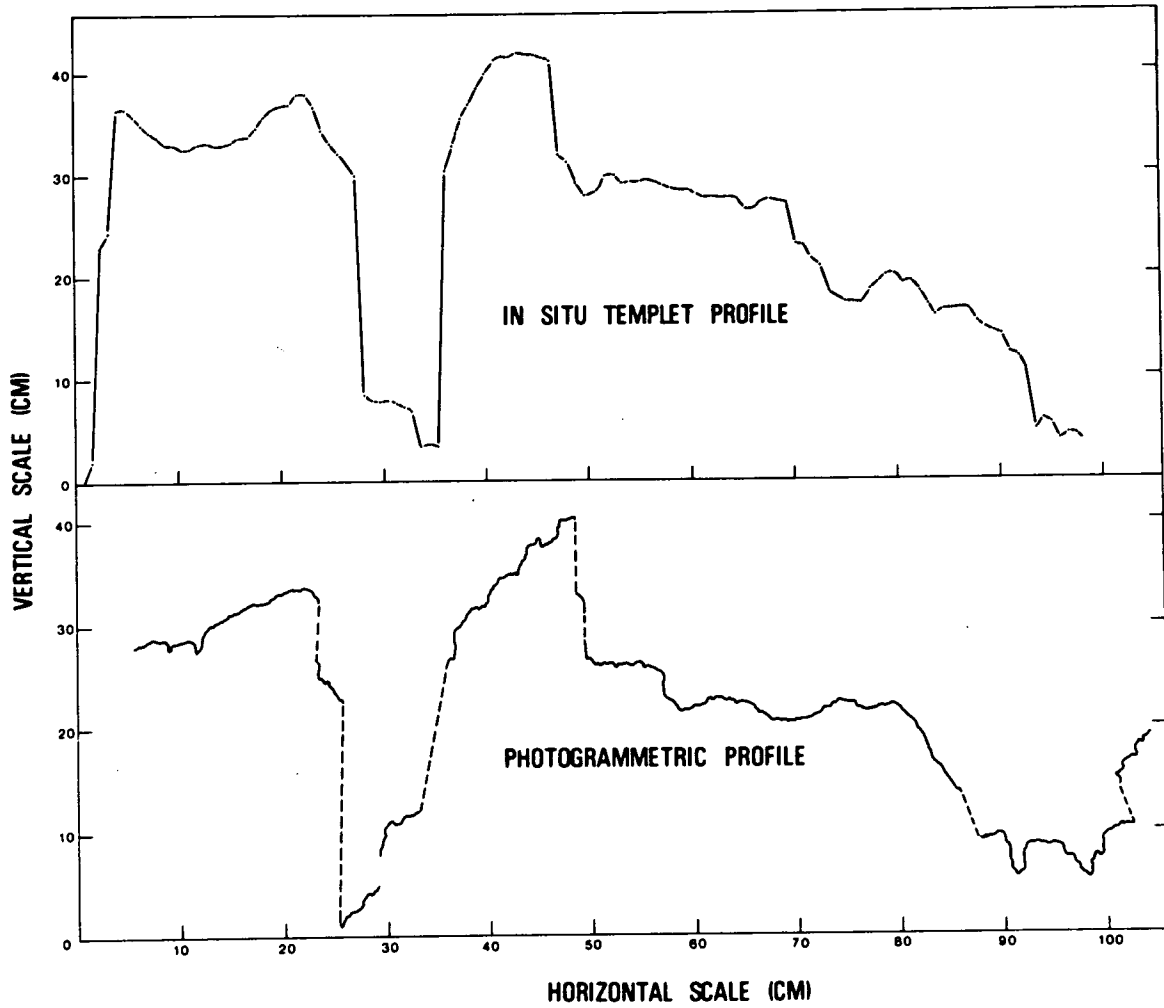


Figure 3. Topographic profiles obtained by templet device and by photogrammetric reduction of stereo photomodels. Profiles include that shown in Figure 1 and an additional ≈ 0.5 m to the right.

This software package, only recently published (Schaber, Pike and Berlin, 1979), was conceived by R. J. Pike, who coordinated the overall effort. The individuals who did the actual programming and were responsible for the seemingly endless refinements demanded by the two senior authors are S. E. Wilson, R. H. Godson, D. K. McMacken, G. I. Selner, J. E. Crawforth, Eric Eliason, J. J. Stapleton, and Loretta Barcus of the U.S. Geological Survey and W. J. Rozema of Northern Arizona University (Flagstaff, Arizona).

The Terrain Analysis software, written in Fortran IV language, consists of seven integrated data analysis and plotting routines. The program furnished nearly 100 individual pieces of graphical and tabular data that describe four major aspects of topographic geometry: (1) relative relief, hypsometry, topographic grain; (2) power (variance) spectral density of relief; (3) slope angle between slope reversals; and (4) baselength slope angle and curvature. A sample output from the Terrain Analysis program, including the plotting subroutine products, is given in Appendix A. Input data were elevation values derived from the profile in Figure 2.

The Terrain Analysis program is well documented, and because so many statistical parameters are calculated, only those topographic descriptions that may be unfamiliar to the general reader will be described below. Those seeking more information on the software or its statistical computations should contact the authors or refer to Schaber, Pike and Berlin (1979).

Duplicate computer tapes (9 track-800 bpi) are available in either ASCII or EBCDIC at no cost by sending a new blank tape and the sender's return address to the senior author at:

U.S. Geological Survey
Branch of Astrogeologic Studies
2255 North Gemini Drive
Flagstaff, Arizona 86001

Program 1. This initial program of the Terrain Analysis software simply formats the input data in readable form for subsequent analysis. Input consists of topographic elevations, measured at a constant horizontal increment ('delta-L') along a continuous profile.

Program 2 - Relief Analysis. This part of the Terrain Analysis program provides comprehensive data on the statistical variation of topographic elevations along a profile. The output includes relief, mean elevation, variance, standard deviation, and other standard statistical parameters of elevation such as skewness, kurtosis, elevation-relief ratio (E.R.), hypsometric integral (H) (Pike and Wilson, 1971), and topographic grain (Wood and Snell, 1960). This portion of the program also tabulates the frequency and cumulative percent frequency of elevations within class intervals, so that histograms may be constructed. Ten of these parameters are recalculated from decreasing sample sizes (N), at lengthening sampling intervals (I). This practice reveals the minimum sample size from which stable statistics can be calculated from each data set. In the example given in Appendix A, no fewer than 23 elevations should be used for the calculations.

Hypsometric analysis is valuable in radar backscatter analysis because it gives a quantitative assessment for the proportion of surface area within a unit volume that can readily contribute to radar backscatter and the proportion that

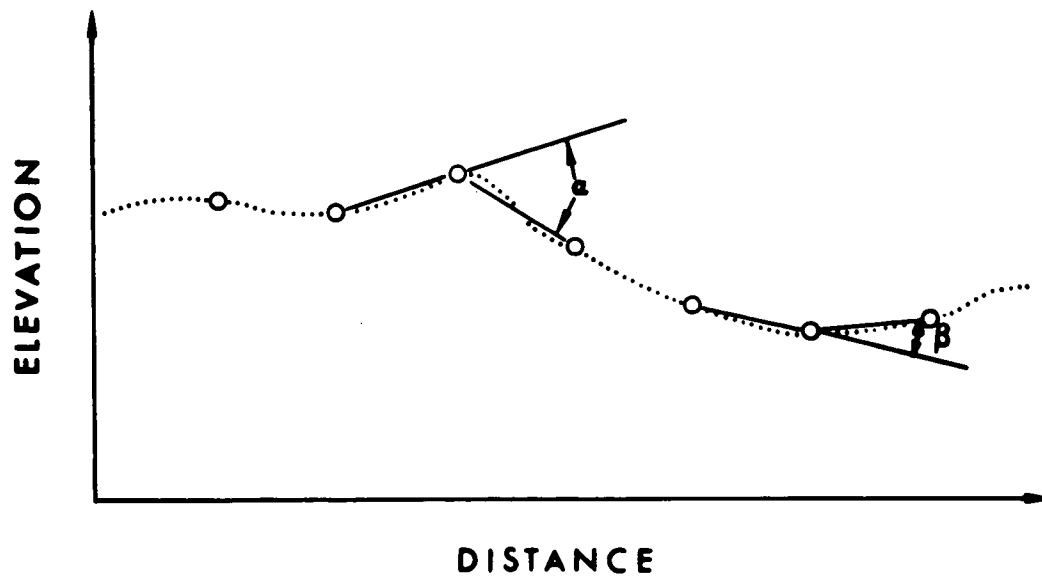


Figure 4. Diagrammatic representation of slope curvature along a profile. Dots show ground surface. Circles are sample elevations measured at a constant horizontal increment (ΔL). Positive curvature shown by α ; negative curvature shown by β .

would behave quasispectrally to the radar. Hypsometry is the distribution of ground surface area, or horizontal cross-sectional area of a ground surface, with respect to relief or elevation (Strahler, 1952). Wood and Snell (1960) and Pike (1963) have shown that topographic samples may resemble one another with respect to local relief, average slope, or other geometric aspects, and yet may vary appreciably in appearance as demonstrated by different values of elevation-relief ratio (E.R.):

$$E.R. = \frac{\text{mean elevation} - \text{minimum elevation}}{\text{maximum relief}}$$

which was shown by Pike and Wilson (1971) to be equivalent to the hypsometric integral (H), or the proportionate area below the hypsometric function curve. The derivation of the hypsometric function is beyond the scope of this paper but has been well documented by Strahler (1952) and Pike and Wilson (1971). Simply defined, the hypsometric function is the proportion of the total surface area of a unit terrain surface containing elevations greater than a measured elevation. A surface that has exactly equal proportions of its area above and below the mean height value would have a hypsometric integral equal to 0.5.

Topographic grain needs to be determined before computing statistics on roughness or any other aspect of terrain geometry. If the profile obtained by either the templet or photogrammetric technique is of insufficient length to contain most of the relief elements, or is unnecessarily long, then statistical errors will enter the calculations for modeling radar backscatter. Topographic grain of a terrain is essentially the minimum area or linear sample distance on a surface that contains most of the important relief structure (Wood and Snell, 1960). If the size of a progressively larger, nested interval along the horizontal axis of a profile is plotted against the maximum relief within the intervals, relief increases rapidly to a point and then levels off. The sampling interval size corresponding to the point at which relief inflects is the "topographic grain." Most of the topographic characteristics of the sample region will thus be contained within an interval of this size (See Appendix A).

Program 3 - Power Spectral Analysis. The analysis of relief variance is of significant importance for radar backscatter modeling, as shown by Peake (1959), Valenzuela (1967), and Barrick (1972), who made use of the covariance spectrum of relief in various perturbations of the Bragg-Rice scattering models. W. E. Brown, Jr., and G. G. Schaber (work in progress) have found that covariance spectra obtained by the photogrammetric and statistical analysis technique described above can be used with a Bragg-Rice scattering model to correctly predict radar cross-section values for saltpan and gravels within Death Valley.

This power spectral density (PSD) subprogram computes the various frequency components of the relief (Rozema, 1969). Power spectral or time series analysis examines the frequency content of topographic or surface-roughness profiles. For natural terrain surfaces, most profiles are statistically random functions that can only be represented by the continuous variance spectrum. Elevation amplitudes that contribute to variability of a random isotopic surface above its mean height value thus are associated with a continuum of wavelengths. Separating a random profile into wavelength bands yields the spectral density of the relief variance, which is given as the square of the amplitude per unit bandwidth of the contributing wavelength bands (Pike and Rozema, 1975). This value is the power spectral density (PSD).

The variance spectral density program used in this study derives the autocovariance function and the Fourier transform of the autocovariance function that is the spectral density function of the variance and vice versa (Pike and Rozema, 1975). Autocorrelation of relief data enhances any periodicities that may be present in the topographic profile.

The "variance" or power spectral density graphs are sloping lines representing continuous functions of topographic (spatial) wavelengths (see Appendix A). Because the greatest relief within a surface profile (natural terrain) is generally associated with the longer wavelengths, the spectral density decreases rapidly with decreasing terrain wavelengths. The slopes of the PSD curves describe a relation between the relief content of the long and short features (Bryson and Dutton, 1967). An overall slope of -3 is thought to indicate a "uniformity" of topographic slope for all relief features in the sample area, regardless of their size (Bekker, 1969). A slope less steep than -3 indicates that small topographic features (high frequency) are rougher than large (low frequency) features. Likewise, a spectrum slope steeper than -3 suggests more rough, coarse-grained features and less smooth, fine-grained relief forms.

Digital bandpass filtering of the very low frequency data in the surface profiles is performed prior to calculation of the PSD functions. This operation is included because a long-term trend in the profiles affects the PSD function in two ways: (1) it may result in a nonstationary profile, that is, a profile whose statistical properties are affected by a change in origin; and (2) because the amplitude of the profile associated with the low frequency of a long trend would likely be relatively large, enough power would be contributed by the low frequency to obscure that contributed by higher frequencies (Rozema, 1969).

Program 4 - Power Spectrum Plots. This subroutine plots the elevation variance of relief as frequency (cycles per mm) vs power spectral density (mm^2 per cycle per mm). Conversion of the PSD values to m^2 per cycle per m involved multiplying each frequency value by 10^3 . Pike and Rozema (1975) have shown that PSD values are interchangeable with variance [amplitude², per wave number (units²)], in the same fashion: frequency (in cycles per unit) is interchangeable with wave number (units⁻¹). Immediately following the PSD plot, in Appendix A, a least squares regression line fit equation is given for the PSD data in addition to the total variance of the integrated spectrum.

Program 5 - Slope Angle Between Slope Reversals. There are innumerable ways to characterize topographic slope. One of them is to identify terrain segments that occur between reversals in slope direction along a profile. Both the length and steepness of the slope are variables. Radar backscatter power is strongly dependent on the number of reflecting facets on the target area at moderate to high angles of incidence. This program can furnish quantitative data on such facets, which are the areas between two adjacent slope reversals. Every reversal of slope from the input topographic profile is listed, as are the slope angle and slope length between these reversals. Also given are the three steepest and the three longest slopes, and the number of slope reversals per meter. A regression line is computed for slope length and slope angle.

Program 6 - Slope Angle Against Slope Interval Plots. This subroutine plots each slope length against its slope angle on semilog scale. The computer-printed graph is an approximation and may differ slightly from the actual values. Where more than nine values occupy the same position, a letter symbol code is printed

indicating the number of points at that location. The steepest slope angle printed out is 20 degrees. This value is too low a cutoff for microterrain applications, where the slopes are very steep. This graph is only of minor value in its present format.

Program 7 - Base Length Slope Angle and Curvature. This subprogram is exceptionally comprehensive and flexible, and yields a large amount of information on surface roughness. Two parameters, slope angle and the angle of slope curvature, are computed for different values of the unit cell, or base length (ΔL). Slope angle at the smallest ΔL , the input sampling interval, is simply the slope of the line connecting any two adjacent sample elevations. Curvature is the angle subtended by three adjacent elevations along the traverse (Figure 4). Calculations start with a horizontal sampling interval (ΔL) of X-mm (3.0 mm in the example shown in Appendix A). The subroutine then calculates algebraic and absolute values of statistics for both slope angle and the angle of curvature, including minimum, maximum, mean, variance, standard deviation, skewness, kurtosis and median. Absolute values are unsigned. Algebraic values are positive (slopes facing the end of the profile and convex curvature, Figure 4), and negative (slopes facing the opposite direction and concave curvatures, Figure 4). Algebraic frequency distributions are symmetric about the zero values and often approach the Gaussian ideal. Absolute distributions approach the "half-normal" model (Elandt, 1961) and are skewed strongly to the right. Slopes and curvatures calculated by both conventions are necessary and complement one another.

The dispersion coefficient (algebraic standard deviation divided by absolute mean) is analogous to the usual coefficient of variation (Croxtton et al., 1967, p. 198), and is an excellent measure of relative dispersion. The "Elandt coefficient" (informal name by Pike, 1978), defined as absolute mean divided by absolute standard deviation (Elandt, 1961), can be used as a rapid initial test for the "half-normality" of an absolute slope frequency distribution (see Pike, 1978, pp. 14-15).

Following a listing of the number of negative and positive values of slope and curvature (and their ratios) are tabulations of algebraic and absolute frequency-distribution statistics. These are intended for histograms and other graphic output. The percent (10 to 90) dispersion of the algebraic values is also listed, in addition to the results of a chi-square test for the normality of the algebraic frequency distribution of both slope and curvature. Regression line-fits are calculated relating cumulative percent frequency and slope angle and cumulative percent frequency and percent mean slope. Similar regression equations are given for the curvature statistics. These equations enable the histograms to be roughly expressed by only two parameters, slope and coefficient of the fit.

The ΔL value (sampling interval) is then doubled (for example, from 3.0 mm to 6.0 mm) and all calculations are rerun. This stepping of the ΔL value continues until the desired upper limit of sampling interval is reached or until too few cases remain to calculate good statistics. The final calculations in the program are linear regression fits relating ΔL to mean absolute slope and curvature for all iterations. This valuable equation can be used to assess the relation of slope and curvature angles for a specific terrain at various fractions (or multiples) of radar wavelength scales (where ΔL is equated to roughness sampling-interval of the radar).

V. POSSIBLE PROGRAM IMPROVEMENTS

The Terrain Analysis software has been found to be almost ideal for radar backscatter modeling studies of fine-scale relief, and can be used with topographic information derived from either in situ templates or photogrammetric reduction of stereo photographs. Experience with this software, however, has indicated the need for at least four additional computations and plotting subroutines of significance to radar backscatter modeling: (1) height correlation coefficient autocorrelation, or statistical association between various pairs of elevations along a profile; (2) probability density function for surface elevation; (3) probability density function for surface slopes (Pike and Rozema, 1975; Barrick, (1970); and (4) root mean square (rms) slopes and curvatures for all base lengths. These additional programs and subroutines could simply be added to the existing Terrain Analysis software with minimal effort and expense. Autocorrelation of surface heights already is performed as part of the PSD computations (Program 3) and merely needs to be printed out. The information on relief and slope necessary for calculating their probability density functions is available in Programs 2 and 7. Only the rms calculations will require writing an entire new subprogram.

ACKNOWLEDGEMENTS

The research described in this paper was funded by the National Aeronautics and Space Administration under various contracts to the U.S. Geological Survey. The Terrain Analysis software package, developed from 1968 to 1970 under terrain analysis and trafficability projects, was supported under NASA contracts W12,388 and W13,276. Development of terrain analysis procedures specifically for radar backscatter modeling was supported by NASA under contracts W13,130 and W13,709. The authors acknowledge the excellent support of the U.S. Geological Survey Photogrammetry Section of the Branch of Astrogeologic Studies (Flagstaff, Az), especially the fine work of Raymond Jordan and Loretta Barcus.

REFERENCES

- Barrick, D. E., 1970, Unacceptable height correlation coefficients and the quasi-specular components in rough surface scattering: *Radio Science*, v. 5, no. 4, p. 647-654.
- _____, 1972, First order theory and analysis of MF/HF/VHF scatter from the sea: *IEEE Trans. Ant. and Prop.*, v. 20, p. 2-10.
- Bekker, M. G., 1969, Introduction to terrain-vehicle systems: Ann Arbor, University of Michigan Press, pp. 158-378.
- Bryson, R. A., and Dutton, J. A., 1967, The variance spectra of certain natural series, in Garrison, W. L., and Marble, D. F., eds., *Quantitative Geography, Part II: Physical and Cartographic Topics*: Evanston, Illinois, Northwestern University Press, pp. 1-24.
- Croxton, F. E., Cowden, D. J., and Klein, S., 1967, *Applied general statistics*, Prentice-Hall, Englewood Cliffs, N.J. (3rd edition), 745 pages.
- Day, M. J., 1979, Surface roughness as a discriminator of tropical karst styles: *Z. Geomorph.*, v. 32, pp. 1-8.

- Elandt, R. C., 1961, The folded normal distribution: two methods of estimating parameters from moments: *Technometrics*, v. 3, no. 4, pp. 551-562.
- Greender, C. C., 1976, Topo III, A Fortran program for terrain analysis: *Computers and Geoscience*, v. 32, pp. 195-209.
- McDonald, H. C., and Waite, W. P., 1973, Imaging radars provide terrain texture and roughness parameters in semi-arid environments: *Modern Geology*, v. 4, p. 145-158.
- Peake, W. H., 1959, Theory of radar return from terrain: *IRE National Convention Record*, v. 7, pt. 1, pp. 27-41.
- Pike, R. J., 1963, Landform regions of southern New England - quantitative delimitation: M. A. Thesis, Clark University, Worcester, Mass., 80 pages.
- _____, 1978, Lunar landscale morphometry: U.S. Geological Survey Open-File Report 78-812, 142 pages.
- Pike, R. J., and Rozema, W. J., 1975, Spectral analysis of landforms: *Annals of the Association of American Geographers*, v. 65, no. 4, pp. 499-516.
- Pike, R. J., and Wilson, S. E., 1971, Elevation-relief ratio, hypsometric integral, and geomorphic area-altitude analysis: *Geological Society of America Bulletin*, v. 82, pp. 1079-1084.
- Rozema, W. J., 1969, The use of spectral analysis in describing lunar surface roughness: U.S. Geological Survey Professional Paper 650-D, pp. 180-188.
- Sabins, F. F., Jr., 1978, *Remote Sensing: Principles and Interpretation*: San Francisco, W. H. Freeman, 426 pages.
- Schaber, G. G., Berlin, G. L., and Brown, W. E., Jr., 1976, Variations in surface roughness within Death Valley, California: Geologic evaluation of 25-cm wavelength radar images: *Geological Society of America Bulletin*, v. 87, pp. 29-41.
- Schaber, G. G., Pike, R. J. and Berlin, G. L., 1979, Terrain-Analysis Procedures for Modeling Radar Backscatter, U.S. Geological Survey Open-File Report, 79-1088, 67 pages.
- Speight, J. G. 1974, A parametric approach to landform regions: *Special Publication No. 7*, The Institute of British Geographers, pp. 213-230.
- _____, 1977, Landform pattern description from aerial photographs: *Photogrammetria*, v. 32, pp. 161-182.
- Strahler, A. N., 1952, Hypsometric (area-altitude) analysis of erosional topography: *Geological Society of America Bulletin*, v. 63, pp. 1117-1142.
- U.S. Geological Survey, 1970, Topographic data analysis system, Administrative Report: Computer Center Division, Flagstaff, Arizona, 100 pages.

Valenzuela G. R. 1967, Depolarization of radar waves by slightly rough surfaces, IEEE Trans. Ant. and Prop., v. AP-15, no. 4, pp. 552-557.

Wood, W. F., and Snell, J. B., 1960, A quantitative system for classifying landforms: U.S. Army Natick Laboratory Technical Report EP-124, Natick, Mass., 80 pages.

APPENDIX A

Included in this Appendix is a sample output from the Terrain Analysis software package described in the text. The profile shown in Figure 1 was digitized at a 3 mm-equivalent ground spacing and these data used as input to the Terrain Analysis program. All linear values are in millimeters and all angles in degrees. Brief descriptions of the tabular and graphical output data are included in the text. *Delta-L is the sampling interval of the profile in millimeters. **Maximum, minimum and mean values listed under relief analysis (first page of output) are arbitrary elevation values (in millimeters) used in establishing the coordinate system for the stereo model. For brevity, results for only the first two of seven iterations of the base length subroutine are shown.

OUTPUT FROM
PROGRAM 2

R E L I E F A N A L Y S I S

MODEL 2 OH X-DIR RERUN 02-13-78
PROFILE NO. 1

DELTA L = 3.000 HMS

BELOW ARE SOME DESCRIPTIVE PARAMETERS
FROM MELEVATIONS, EVERY I-TH SAMPLE ELEVATION

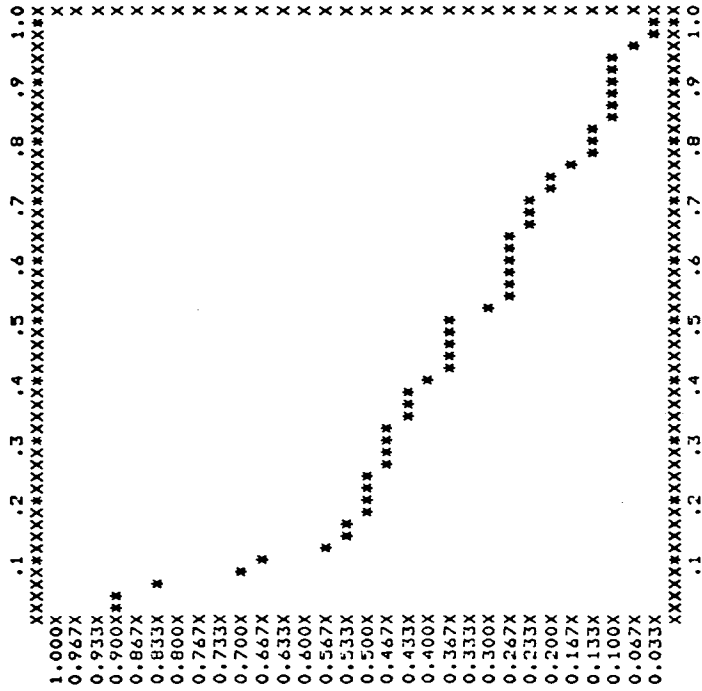
I	N	MINIMUM	MAXIMUM	RELIEF	MEAN	VARIANCE	STD.DEV.	SKEWNESS	KURTOSIS	E.R. 1	E.R. 2
1	454	885.200	1451.900	566.700	1085.246	32655.94	180.7095	0.6281	-1.0332	0.3530	0.3530
2	227	885.200	1451.900	566.700	1084.935	32725.73	181.0407	0.6329	-1.0301	0.3525	0.3525
4	114	885.300	1451.900	566.600	1085.100	32899.87	181.3832	0.6416	-1.0164	0.3527	0.3527
10	46	885.200	1451.900	566.700	1084.250	33677.67	183.5148	0.6648	-0.9674	0.3512	0.3512
20	23	887.000	1451.900	564.900	1082.874	34228.09	185.0084	0.7004	-0.8960	0.3467	0.3488
50	10	892.500	1426.100	533.600	1080.160	32793.67	181.0902	0.9588	-0.1745	0.3517	0.3440

E.R. 1 IS CALCULATED FROM EACH SAMPLE OF N POINTS AND IS THE RATIO
(MEAN - HMIN)/(HMAX - HMIN)

E.R. 2 IS THE SAME RATIO, BUT CALCULATED USING THE TOTAL SAMPLE'S HMAX AND HMIN.

CLASS	CLASS BOUNDARIES	FREQ.	CUM. PERCENT
1	885.200 904.090	40.	8.81
2	904.090 922.980	46.	18.94
3	922.980 941.870	69.	34.14
4	941.870 960.760	52.	45.59
5	960.760 979.650	9.	47.58
6	979.650 998.540	11.	50.00
7	998.540 1017.430	4.	50.88
8	1017.430 1036.320	4.	51.76
9	1036.320 1055.209	0.	51.76
10	1055.209 1074.100	17.	55.51
11	1074.100 1092.990	5.	56.61
12	1092.990 1111.879	10.	58.81
13	1111.879 1130.770	20.	63.22
14	1130.770 1149.660	4.	64.10
15	1149.660 1168.550	4.	64.98
16	1168.550 1187.439	36.	72.91
17	1187.439 1206.330	7.	74.45
18	1206.330 1225.220	2.	74.89
19	1225.220 1244.109	4.	75.77
20	1244.109 1263.000	2.	76.21
21	1263.000 1281.890	11.	78.63
22	1281.890 1300.779	9.	80.62
23	1300.779 1319.669	14.	83.70
24	1319.669 1338.560	24.	88.97
25	1338.560 1357.450	3.	89.65
26	1357.450 1376.339	3.	90.31
27	1376.339 1395.229	3.	90.97
28	1395.229 1414.120	8.	92.73
29	1414.120 1433.009	14.	95.81
30	1433.009 1451.899	19.	100.00

FOLLOWING IS A GRAPH OF THE HYPSONETRIC FUNCTION,
 G(R)=PROPORTION OF AREA LYING ABOVE HMIN*RELIEF.
 ON THE HORIZONTAL AXIS IS R, THE PROPORTION-OF-RELIEF VARIABLE.
 ON THE VERTICAL AXIS IS CUMULATIVE PROPORTION OF SAMPLE POINTS,
 BOTH GRAPHED FROM 0.0 TO 1.0



PIKE AND WILSON, 1971, GEOL. SOC. AM. BULL. VOL. 82, 1079-1084.

HYPSONETRIC INTEGRAL= 0.3430

HYPSONETRIC INTEDRAL= 0.3629

AVERAGE HYPSONETRIC INTEGRAL= 0.3530

THE FOLLOWING DATA AND GRAPH GIVE INFORMATION RELATED TO THE TOPOGRAPHIC
 GRAIN OF A SAMPLE AREA. IF THE SIZE OF PROGRESSIVELY LARGER
 NESTED INTERVALS (HORIZONTAL AXIS) OF A PROFILE IS PLOTTED AGAINST THE
 MAXIMUM RELIEF WITHIN THE INTERVAL (VERTICAL AXIS), THE GRAPH INCREASES
 RAPIDLY TO A POINT AND THEN LEVELS OFF. THE INTERVAL_SIZE_OF...

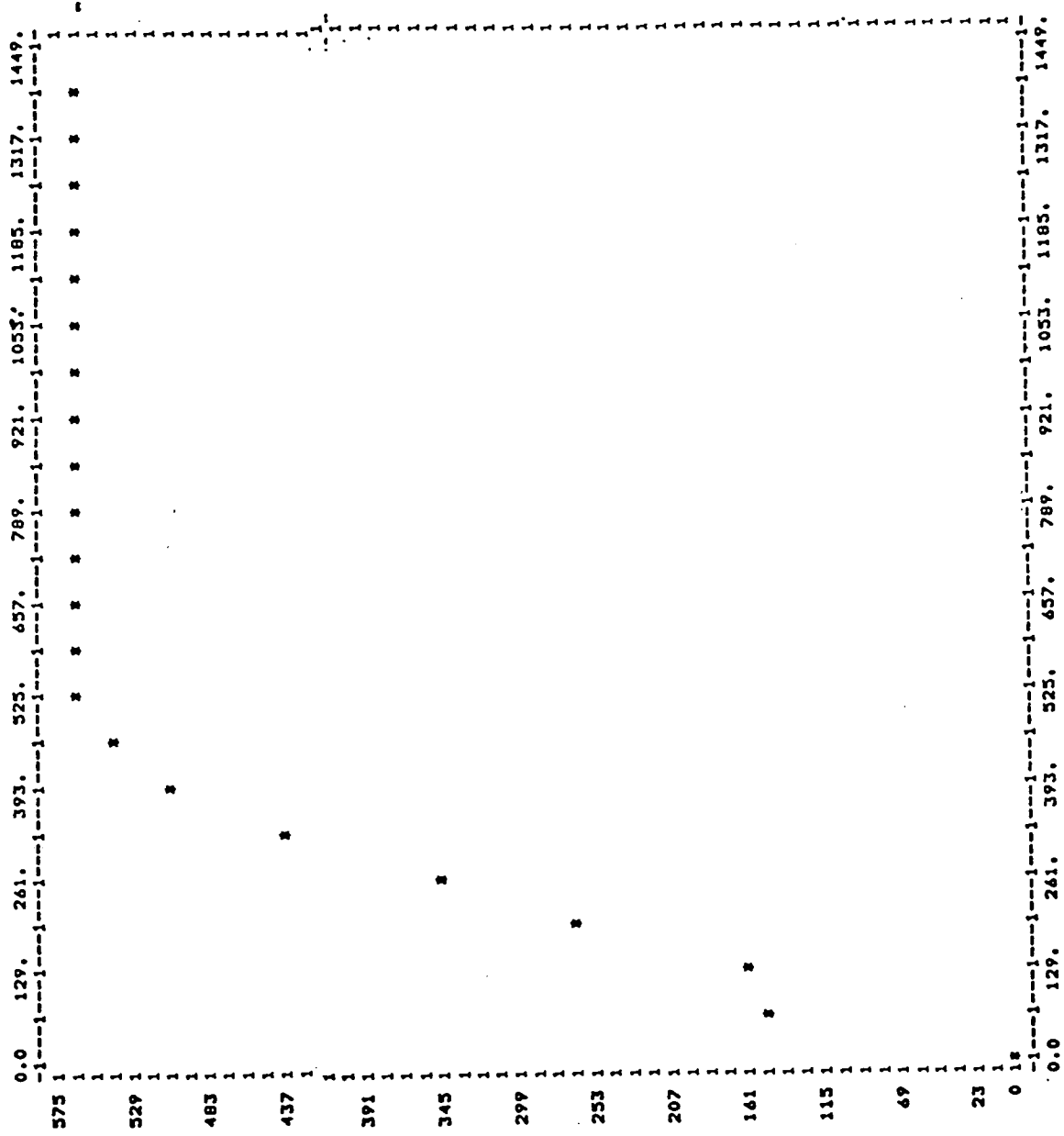
THE POINT AT WHICH THE GRAPH LEVELS OFF IS THE TOPOGRAPHIC GRAIN. MOST OF THE TOPOGRAPHIC CHARACTERISTICS OF THE SAMPLE REGION WILL BE CONTAINED WITHIN AN INTERVAL OF THIS SIZE.

IN THE FOLLOWING DELTA L IS THE DISTANCE BETWEEN SAMPLE POINTS. THE COMPUTER PRINTED GRAPH IS ONLY AN APPROXIMATION AND MAY DIFFER SLIGHTLY FROM THE DATA IN THE TABLES.

DELTA L ■ 3,000 MMS
 SAMPLE SIZE ■ 454 ELEVATIONS
 MINIMUM HEIGHT ■ 885.200 MMS
 MAXIMUM RELIEF ■ 566.700 MMS
 TOPOGRAPHIC GRAIN ■ 591.000 MMS

INTERVAL (MMS)	MAXIMUM RELIEF (MMS)
63.000	146.20
129.000	159.30
195.000	259.90
261.000	348.30
327.000	442.30
393.000	508.00
459.000	544.70
525.000	561.30
591.000	566.70
657.000	566.70
723.000	566.70
789.000	566.70
855.000	566.70
921.000	566.70
987.000	566.70
1053.000	566.70
1119.000	566.70
1185.000	566.70
1251.000	566.70
1317.000	566.70
1383.000	566.70

THE FOLLOWING GRAPH SHOWS THE RELATIONSHIP BETWEEN INTERVAL
 AND THE MAXIMUM RELIEF WITHIN A GIVEN INTERVAL
 -THE HORIZONTAL AXIS LISTS THE INTERVAL IN MMB
 -THE VERTICAL AXIS LISTS THE HEIGHT IN MMS ABOVE MINIMUM ALTITUDE.



OUTPUT FROM
PROGRAM 3

P O W E R S P E C T R U M A N A L Y S I S
ROZEMA, 1969, U.S. GEOL. SURVEY PROF. PAPER 650-D, D180-D189

MODEL 2 OH X-DIR RERUN 02-13-78
PROFILE NUMBER 1 NUMBER OF POINTS IS 454 SAMPLING INTERVAL IS 3.000 MMS
THE PROFILE IS SMOOTHED USING A HIGH-PASS FILTER
(EICHER, USGS COMPUTER DIVISION, PROGRAM NO. W9323)
THE CUT-OFF FREQUENCY IS 0.001468 PARAMETER H = 0.001
THERE ARE 354 POINTS ON WHICH TO COMPUTE PSD

MAXIMUM LAG OF 36

FOR THE FREQUENCY	THE PSD VALUE IS
0.000E-01	1.852E+05
4.630E-03	1.440E+05
9.259E-03	6.945E+04
1.389E-02	2.318E+04
1.852E-02	6.749E+03
2.315E-02	2.861E+03
2.778E-02	2.212E+03
3.241E-02	1.838E+03
3.704E-02	1.427E+03
4.167E-02	1.048E+03
4.630E-02	7.915E+02
5.093E-02	6.464E+02
5.556E-02	5.882E+02
6.019E-02	4.816E+02
6.481E-02	3.380E+02
6.944E-02	2.514E+02
7.407E-02	2.207E+02
7.870E-02	1.975E+02
8.333E-02	1.872E+02
8.796E-02	1.716E+02
9.259E-02	1.420E+02
9.722E-02	1.248E+02
1.019E-01	1.150E+02
1.065E-01	1.145E+02
1.111E-01	1.295E+02
1.157E-01	1.439E+02
1.204E-01	1.496E+02
1.250E-01	1.426E+02
1.296E-01	1.237E+02
1.343E-01	9.961E+01
1.389E-01	8.063E+01
1.435E-01	8.053E+01
1.481E-01	9.724E+01
1.528E-01	1.187E+02
1.574E-01	1.370E+02
1.620E-01	1.312E+02
1.667E-01	1.188E+02

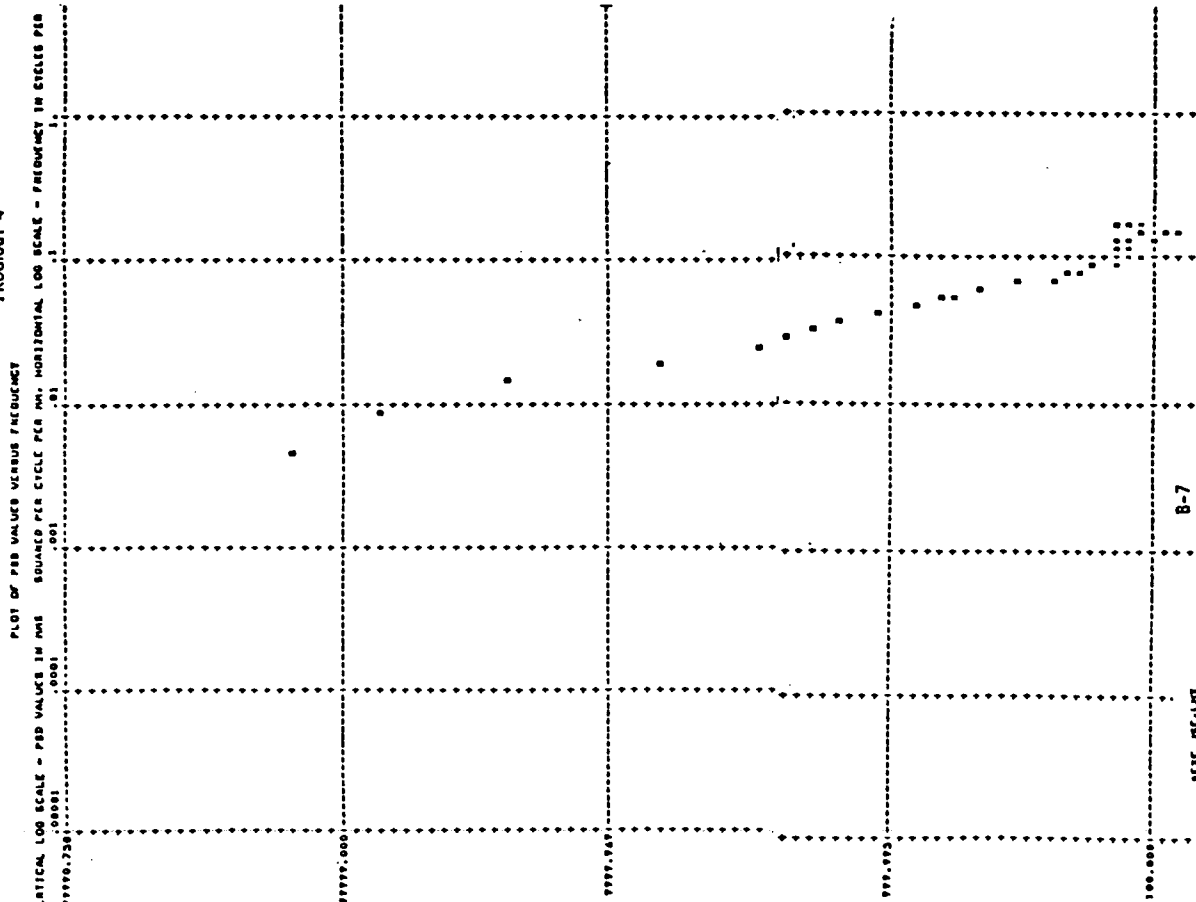
THE RESULTS OF FITTING A REGRESSION LINE OF THE FORM
 $\text{LOG}_{10}(\text{PSD}) = \text{LOG}_{10}(A) + B * \text{LOG}_{10}(\text{FREQ})$, WHERE A = PSD FOR FREQ = 1, ARE AS FOLLOWS:
 $\text{LOG}_{10}(A) = -0.3840$ A = 0.413009048 B = -2.454790115
TOTAL VARIANCE (INTEGRATED SPECTRUM) IS 1.626E+03

OUTPUT FROM
PROGRAM 4

OUTPUT FROM
PROGRAM 4

VERTICAL LOG SCALE - PSD VALUES IN RMS SQUARED PER CYCLE PER MM. HORIZONTAL LOG SCALE - FREQUENCY IN CYCLES PER
 .0001 .001 .01 .1 1

 99999.750 *****



B-7

SECRET

OUTPUT FROM
PROGRAM 5

SLOPE ANGLE BETWEEN SLOPE REVERSALS
MODEL 2 OH X-DIR RERUN 02-13-78

PROFILE NO. 1		DELTA L = 3.000 MMS						
REV NO	SLOPE ANGLE(DEG)	SLOPE LENGTH(MM)	REV NO	SLOPE ANGLE(DEG)	SLOPE LENGTH(MM)	REV NO	SLOPE ANGLE(DEG)	SLOPE LENGTH(MM)
1	8.734	9.160	2	9.462	3.041	3	0.000	3.000
5	0.000	3.000	6	16.698	6.264	7	6.609	6.174
9	9.462	3.041	10	23.426	3.269	11	10.883	18.840
13	24.232	25.130	14	7.520	6.082	15	51.953	63.693
17	34.179	12.012	18	44.096	52.871	19	22.446	9.990
21	33.607	15.279	22	29.560	37.061	23	40.733	37.471
25	14.148	9.351	26	18.887	12.834	27	11.312	3.059
29	37.616	8.438	30	48.803	21.612	31	30.186	14.650
33	11.263	6.131	34	29.854	64.035	35	32.429	3.270
37	29.517	6.899	38	12.071	6.177	39	13.120	6.164
41	9.462	3.041	42	9.462	3.041	43	20.904	6.592
45	14.932	3.105	46	10.365	6.107	47	10.365	6.107
49	1.906	3.002	50	3.813	3.007	51	41.103	44.436
53	26.766	28.723	54	26.822	14.774	55	34.795	7.458
57	18.873	19.295	58	33.731	15.221	59	3.813	3.007
61	7.597	3.037	62	13.949	6.204	63	30.984	51.066
65	55.429	86.051	66	5.711	3.015	67	61.807	55.336
69	37.400	3.780	70	32.329	7.104	71	30.904	10.892
73	61.015	181.770	74	32.346	3.551	75	60.701	109.585
77	52.891	118.047	78	23.892	9.862	79	23.901	7.043
81	46.176	26.796	82	19.181	6.374	83	3.818	3.007
85	51.683	20.903	86	56.182	155.964	87	33.405	24.853
89	44.689	23.350	90	40.842	58.480	91	49.012	15.526
93	30.968	3.499	94	53.560	19.188	95	32.346	3.551
97	43.609	8.484	98	64.149	178.206	99	0.000	3.000
101	33.690	7.211	102	33.018	7.157	103	16.698	3.132
105	41.021	29.299	106	27.525	23.883	107	59.082	82.264
109	15.120	18.720	110	21.348	19.588	111	61.424	12.629
113	37.764	22.769						

THE FIRST STEEPEST SLOPE IS 178.21 MMS AT 64.15 DEGREES

THE SECOND STEEPEST SLOPE IS 55.34 MMS AT 61.81 DEGREES

THE THIRD STEEPEST SLOPE IS 12.63 MMS AT 61.42 DEGREES

THE FIRST LONGEST SLOPE IS 181.77 MMS AT 61.02 DEGREES

THE SECOND LONGEST SLOPE IS 178.21 MMS AT 64.15 DEGREES

THE THIRD LONGEST SLOPE IS 155.96 MMS AT 56.18 DEGREES

THE NUMBER OF SLOPE REVERSALS PER METER = 83.1494

THE FOLLOWING GRAPHS PLOT EACH SLOPE LENGTH AGAINST ITS SLOPE ANGLE ON SEMI-LOG SCALE. THE COMPUTER-PRINTED GRAPH IS AN APPROXIMATION AND MAY DIFFER SLIGHTLY FROM THE ACTUAL VALUES. WHERE MORE THAN NINE VALUES OCCUPY THE SAME POSITION, THE SYMBOL PRINTED MAYBE INTERPRETED AS FOLLOWS

SYMBOL NO. OF VALUES

A	10
B	11
C	12
D	13
E	14
F	15
G	16
H	17
I	18
J	19
K	20
L	21
M	22
N	23
O	24
P	25
Q	26
R	27
S	28
T	29
U	30
V	31
W	32
X	33
Y	34
Z	35 AND OVER

THE RESULTS OF FITTING A REGRESSION LINE OF THE FORM

$$\text{LOG}_{10}(\text{SLOPE LENGTH}) = \text{LOG}_{10}(A) + (\text{SLOPE ANGLE}) * \text{LOG}_{10}(B)$$

ARE AS FOLLOWS:

$$\begin{aligned} \text{LOG}_{10}(A) &= 0.4810 & \text{LOG}_{10}(B) &= 0.0202 \\ A &= 3.0269 & B &= 1.0477 \end{aligned}$$

9EXE JSF,LM1

OUTPUT FROM
PROGRAM 7

DATA FROM BASE LENGTH SLOPE ANGLE AND CURVATURE PROGRAM

DATA SET IDENTIFICATION

MODEL 2 OH X-DIR RERUN 02-13-78 NUMBER OF PROFILES = 1 TYPE OF DATA = URV

SLOPE STATISTICS

PROFILE NUMBER = 1 DELTA L = 3.00 MMS NUMBER OF SLOPES OR CURVATURES = 453

ALGEBRAIC STATISTICS

MINIMUM	MAXIMUM	MEAN	VARIANCE	ST DEVIATION	SKEWNESS	KURTOSIS	MEDIAN
-87.29547	87.84738	3.03776	1796.36279	42.38351	0.01421	-0.98158	1.91101

ABSOLUTE STATISTICS

MINIMUM	MAXIMUM	MEAN	VARIANCE	ST DEVIATION	SKEWNESS	KURTOSIS	MEDIAN	DISP. COEFF.	ELANDT COEFF.
0.00000	87.84738	36.41495	476.62927	21.83184	0.37277	-0.84876	33.69020	1.16390	1.66797

NUMBER OF NEGATIVE VALUES = 221
 NUMBER OF POSITIVE VALUES = 229
 RATIO OF NEGATIVE VALUES TO TOTAL = 0.488

RATIO OF POSITIVE VALUES TO TOTAL = 0.506
 NUMBER OF REVERSALS PER METER OF TRAVERSE = 83.1494

ALGEBRAIC VALUES

CLASS	CLASS BOUNDARIES	FREQ.	CUM. PERCENT FREQ.
1	-87.295 TO -69.781	13.0	0.0287
2	-69.781 TO -52.267	36.0	0.1082
3	-52.267 TO -34.753	41.0	0.1987
4	-34.753 TO -17.238	73.0	0.3598
5	-17.238 TO 0.276	61.0	0.4945
6	0.276 TO 17.790	54.0	0.6137
7	17.790 TO 35.305	51.0	0.7263
8	35.305 TO 52.819	52.0	0.8411
9	52.819 TO 70.333	53.0	0.9581
10	70.333 TO 87.847	19.0	1.0000

CUM. PERCENT FREQ. CUM. FREQ. SLOPE ANGLE

0.010	4.53	-82.5361
0.020	9.06	-78.7016
0.030	22.65	-66.3025
0.100	45.30	-53.1303
0.150	67.95	-40.9156
0.200	90.60	-34.2103
0.300	135.90	-23.5917
0.400	181.20	-14.9324
0.500	226.50	1.9087
0.600	271.80	14.9323
0.700	317.10	30.9649
0.800	362.40	46.3030
0.850	385.05	53.1640
0.900	407.70	59.3055
0.950	430.35	69.2900
0.980	443.94	77.8397
0.990	448.47	82.3736
1.000	453.00	87.8474

10 PERCENT TO 90 PERCENT DISPERSION OF THE ALGEBRAIC VALUES = 100.30112

PERCENTILE VALUES FOR 7 DEGREES OF FREEDOM FOR THE CHI-SQUARE DISTRIBUTION

.995	.99	.95	.90	.75	.50	.25	.10	.05
20.3	18.5	16.0	14.1	12.0	9.0	6.4	4.3	2.8
								2.2

CHI-SQUARE = 34.96

ABSOLUTE VALUES

CUM. PERCENT FREQ.	CUM. FREQ.	SLOPE ANGLE	PERCENT OF MEAN SLOPE
1.000	453.00	0.0000	0.000
0.900	407.70	9.4623	0.260
0.800	362.40	14.9324	0.410
0.700	317.10	20.1343	0.553
0.600	271.80	28.0704	0.771
0.500	226.50	33.6902	0.925
0.400	181.20	40.9135	1.124
0.300	135.90	50.1954	1.378
0.200	90.60	56.8894	1.562
0.150	67.95	61.8221	1.698
0.100	45.30	67.1806	1.845
0.050	22.65	75.6096	2.076
0.020	9.06	81.5155	2.239
0.010	4.53	84.2736	2.314
0.005	2.27	86.0974	2.364
0.002	0.91	87.2955	2.397
0.001	0.45	87.2955	2.397

THE RESULTS OF FITTING A REGRESSION LINE OF THE FORM:
 $\text{LOG}_{10}(\text{CUM. PERCENT FREQ.}) = \text{LOG}_{10}(A) + B * (\text{SLOPE ANGLE})$ ARE AS FOLLOWS:
 $\text{LOG}_{10}(A) = 0.5154$ $A = 3.2768$ $B = -0.0294$

THE RESULTS OF FITTING A REGRESSION LINE OF THE FORM:
 $\text{LOG}_{10}(\text{CUM. PERCENT FREQ.}) = \text{LOG}_{10}(A) + B * (\text{PERCENT OF MEAN SLOPE})$ ARE AS FOLLOWS:
 $\text{LOG}_{10}(A) = 0.5154$ $A = 3.2768$ $B = -1.0705$

C U R V A T U R E S T A T I S T I C S

PROFILE NUMBER = 1 DELTA L = 3.00 MMS NUMBER OF SLOPES OR CURVATURES = 452

ALGEBRAIC STATISTICS

MINIMUM	MAXIMUM	MEAN	VARIANCE	ST DEVIATION	SKWENESS	KURTOSIS	MEDIAN
-149.44556	131.74463	0.12164	1165.64453	34.14154	-0.10424	2.43628	0.16063

ABSOLUTE STATISTICS

MINIMUM	MAXIMUM	MEAN	VARIANCE	ST DEVIATION	SKWENESS	KURTOSIS	MEDIAN	DISP. COEFF.	ELANDT COEFF.
0.00000	149.44556	24.24335	576.61646	24.01284	1.88206	4.35075	17.99183	1.40828	1.00960

NUMBER OF NEGATIVE VALUES = 215
 NUMBER OF POSITIVE VALUES = 230
 RATIO OF NEGATIVE VALUES TO TOTAL = 0.476
 RATIO OF POSITIVE VALUES TO TOTAL = 0.509
 NUMBER OF REVERSALS PER METER OF TRAVERSE = 176.2536

ALGEBRAIC VALUES

CLASS	CLASS BOUNDARIES	FREQ.	CUM. PERCENT FREQ.
1	*49.446 TO *21.327	1.0	0.0022

2	*21.327 TO -93.208	4.0	0.0111
3	-93.208 TO -65.089	11.0	0.0354
4	-65.089 TO -36.969	33.0	0.1084
5	-36.969 TO -10.850	102.0	0.3341
6	-10.850 TO 19.269	196.0	0.7677
7	19.269 TO 47.388	75.0	0.9336
8	47.388 TO 75.507	19.0	0.9757
9	75.507 TO 103.626	6.0	0.9889
10	103.626 TO 131.745	5.0	1.0000

CUM. PERCENT FREQ. CUM. FREQ. SLOPE ANGLE

0.010	4.52	-102.4371
0.020	9.04	-81.1298
0.050	22.60	-56.7936
0.100	45.20	-40.8179
0.150	67.80	-29.7705
0.200	90.40	-22.9107
0.300	135.60	-10.8095
0.400	180.80	-4.7661
0.500	226.00	0.0044
0.600	271.20	7.0535
0.700	316.40	13.6935
0.800	361.60	22.1815
0.850	384.20	28.2733
0.900	406.80	34.8890
0.950	429.40	51.3592
0.980	442.96	77.5254
0.990	447.48	98.6255
1.000	452.00	131.7446

10 PERCENT TO 90 PERCENT DISPERSION OF THE ALGEBRAIC VALUES = 64.65945

PERCENTILE VALUES FOR 7 DEGREES OF FREEDOM FOR THE CHI-SQUARE DISTRIBUTION

.995	.99	.975	.95	.90	.75	.50	.25	.10	.05
20.3	18.5	16.0	14.1	12.0	9.0	6.4	4.3	2.8	2.2

CHI-SQUARE = 495.89

ABSOLUTE VALUES

CUM. PERCENT FREQ.	CUM. FREQ.	SLOPE ANGLE	PERCENT OF MEAN SLOPE
1.000	452.00	0.0000	0.000
0.900	406.80	2.0949	0.086
0.800	361.60	5.5358	0.228
0.700	316.40	8.9213	0.368
0.600	271.20	12.6900	0.523
0.500	226.00	17.9875	0.742
0.400	180.80	22.6006	0.932

0.300	135.60	39.2624	1.207
0.200	90.40	36.2448	1.495
0.150	67.80	45.0001	1.856
0.100	45.20	53.1833	2.194
0.050	22.60	77.3971	3.193
0.020	9.04	92.7667	3.826
0.010	4.52	111.9515	4.618
0.005	2.26	117.7562	4.857
0.002	0.90	131.7446	5.434
0.001	0.45	131.7446	5.434

THE RESULTS OF FITTING A REGRESSION LINE OF THE FORM:
 $LOG_{10}(CUM. PERCENT FREQ.) = LOG_{10}(A) + B * (CURVATURE ANGLE)$ ARE AS FOLLOWS:
 $LOG_{10}(A) = 0.0501$ $A = 1.1431$ $B = -0.0204$

THE RESULTS OF FITTING A REGRESSION LINE OF THE FORM:
 $LOG_{10}(CUM. PERCENT FREQ.) = LOG_{10}(A) + B * (PERCENT OF MEAN CURVATURE)$ ARE AS FOLLOWS:
 $LOG_{10}(A) = 0.0501$ $A = 1.1431$ $B = -0.4934$

S L O P E S T A T I S T I C S

PROFILE NUMBER = 1 DELTA L = 6.00 MMS NUMBER OF SLOPES OR CURVATURES = 452

ALGEBRAIC STATISTICS

MINIMUM	MAXIMUM	MEAN	VARIANCE	ST DEVIATION	SKEWNESS	KURTOSIS	MEDIAN
-84.97992	85.97678	3.32249	1784.43213	42.24254	0.00979	-0.91329	0.00000

ABSOLUTE STATISTICS

MINIMUM	MAXIMUM	MEAN	VARIANCE	ST DEVIATION	SKEWNESS	KURTOSIS	MEDIAN	DISP. COEFF.	ELANDT COEFF.
0.00000	85.97678	35.56265	527.98877	22.97800	0.33493	-0.97413	32.68645	1.18783	1.54768

NUMBER OF NEGATIVE VALUES = 225
 NUMBER OF POSITIVE VALUES = 219
 RATIO OF NEGATIVE VALUES TO TOTAL = 0.498
 RATIO OF POSITIVE VALUES TO TOTAL = 0.485
 NUMBER OF REVERSALS PER METER OF TRAVEKSE = 35.0295

ALGEBRAIC VALUES

CLASS	CLASS BOUNDRIES	FREQ.	CUM.	PERCENT FREQ.
1	-84.980 TO -67.884	22.0		0.0487
2	-67.884 TO -50.709	31.0		0.1173
3	-50.709 TO -33.693	33.0		0.1903
4	-33.693 TO -16.597	74.0		0.3540
5	-16.597 TO 0.498	73.0		0.5155
6	0.498 TO 17.594	50.0		0.6261
7	17.594 TO 34.690	41.0		0.7168
8	34.690 TO 51.785	52.0		0.8319
9	51.785 TO 68.881	50.0		0.9425
10	68.881 TO 85.977	26.0		1.0000

ORIGINAL PAGE IS
 OF POOR QUALITY

ORIGINAL PAGE IS
OF POOR QUALITY

CUM. PERCENT FREQ.	CUM. FREQ.	SLOPE ANGLE
0.010	4.52	-80.9440
0.020	9.04	-76.9919
0.050	22.60	-67.5164
0.100	45.20	-53.1303
0.150	67.80	-43.1268
0.200	90.40	-33.6902
0.300	135.60	-22.6199
0.400	180.80	-12.2234
0.500	226.00	0.0000
0.600	271.20	13.3173
0.700	316.40	29.8254
0.800	361.60	45.9392
0.850	384.20	54.5263
0.900	406.80	60.8998
0.950	429.40	71.0253
0.980	442.96	76.9938
0.990	447.40	81.3136
1.000	452.00	85.9768

10 PERCENT TO 90 PERCENT DISPERSION OF THE ALGEBRAIC VALUES = 104.02658

PERCENTILE VALUES FOR 7 DEGREES OF FREEDOM FOR THE CHI-SQUARE DISTRIBUTION	.99	.975	.95	.90	.75	.50	.25	.10	.05
20.3	18.5	16.0	14.1	12.0	9.0	6.4	4.3	2.8	2.2

CHI-SQUARE = 43.69

ABSOLUTE VALUES

CUM. PERCENT FREQ.	CUM. FREQ.	SLOPE ANGLE	PERCENT OF MEAN SLOPE
1.000	452.00	0.0000	0.000
0.900	406.80	7.5928	0.214
0.800	361.60	12.7710	0.359
0.700	316.40	18.7756	0.528
0.600	271.20	25.0193	0.704
0.500	226.00	32.3496	0.910
0.400	180.80	39.8057	1.119
0.300	135.60	49.3989	1.389
0.200	90.40	58.5231	1.646
0.150	67.80	62.4475	1.756
0.100	45.20	69.5137	1.955
0.050	22.60	75.8629	2.133
0.020	9.04	80.0079	2.250
0.010	4.52	84.6156	2.379
0.005	2.26	84.8569	2.386
0.002	0.90	85.9484	2.417
0.001	0.45	85.9484	2.417

THE RESULTS OF FITTING A REGRESSION LINE OF THE FORM:
 $\text{LOG}_{10}(\text{CUM. PERCENT FREQ.}) = \text{LOG}_{10}(A) + B * (\text{SLOPE ANGLE})$ ARE AS FOLLOWS:
 $\text{LOG}_{10}(A) = 0.4565$ $A = 2.8610$ $B = -0.0287$

THE RESULTS OF FITTING A REGRESSION LINE OF THE FORM:
 $\text{LOG}_{10}(\text{CUM. PERCENT FREQ.}) = \text{LOG}_{10}(A) + B * (\text{PERCENT OF MEAN SLOPE})$ ARE AS FOLLOWS:
 $\text{LOG}_{10}(A) = 0.4565$ $A = 2.8610$ $B = -1.0189$

C U R V A T U R E S T A T I S T I C S

PROFILE NUMBER = 1 DELTA L = 6.00 MMS NUMBER OF SLOPES OR CURVATURES = 451

ALGEBRAIC STATISTICS

MINIMUM	MAXIMUM	MEAN	VARIANCE	ST DEVIATION	SKEWNESS	KURTOSIS	MEDIAN
-133.00092	106.82596	0.10724	695.24365	26.36747	-0.28968	4.93699	0.00000

ABSOLUTE STATISTICS

MINIMUM	MAXIMUM	MEAN	VARIANCE	ST DEVIATION	SKEWNESS	KURTOSIS	MEDIAN	DISP. COEFF.	ELANDT COEFF.
0.00000	133.00092	17.95416	372.18701	19.29214	2.54821	9.13031	12.54291	1.46860	0.93063

NUMBER OF NEGATIVE VALUES = 219
 NUMBER OF POSITIVE VALUES = 221
 RATIO OF NEGATIVE VALUES TO TOTAL = 0.486
 RATIO OF POSITIVE VALUES TO TOTAL = 0.490
 NUMBER OF REVERSALS PER METER OF TRAVERSE = 65.0406

ALGEBRAIC VALUES

CLASS	CLASS BOUNDRIES	FREQ.	CUM. PERCENT FREQ.
1	*33.001 TO *09.018	2.0	0.0044
2	*09.018 TO -85.036	2.0	0.0089
3	-85.036 TO -61.053	4.0	0.0177
4	-61.053 TO -37.070	18.0	0.0576
5	-37.070 TO -13.088	77.0	0.2284
6	-13.088 TO 10.895	221.0	0.7184
7	10.895 TO 34.878	98.0	0.9357
8	34.878 TO 58.861	19.0	0.9778
9	58.861 TO 82.843	6.0	0.9911
10	82.843 TO 106.826	4.0	1.0000

CUM. PERCENT FREQ. SLOPE ANGLE

0.010	4.51	-90.5528
0.020	9.02	-57.8386
0.050	22.55	-38.3138
0.100	45.10	-28.9903
0.150	67.65	-21.0873
0.200	90.20	-15.4255

0.300	135.30	-8.9620
0.400	100.40	-3.5557
0.500	225.50	0.0000
0.600	270.60	4.1214
0.700	315.70	9.5978
0.800	360.80	16.5660
0.900	381.35	21.4095
0.950	405.90	26.5432
0.980	428.45	37.4033
0.990	441.98	61.7758
1.000	446.49	73.8043
	451.00	106.8260

10 PERCENT TO 90 PERCENT DISPERSION OF THE ALGEBRAIC VALUES = 47.63046

PERCENTILE VALUES FOR 7 DEGREES OF FREEDOM FOR THE CHI-SQUARE DISTRIBUTION

.995	.99	.95	.90	.75	.50	.25	.10	.05
20.3	18.5	16.0	14.1	12.0	9.0	6.4	4.3	2.8
								2.2

CHI-SQUARE = 3083.47

ABSOLUTE VALUES

CUM. PERCENT FREQ.	CUM. FREQ.	SLOPE ANGLE	PERCENT OF MEAN SLOPE
1.000	451.00	0.0000	0.000
0.900	405.90	1.6008	0.089
0.800	360.80	3.8164	0.213
0.700	315.70	6.6283	0.369
0.600	270.60	9.4770	0.528
0.500	225.50	12.5345	0.698
0.400	180.40	16.1049	0.897
0.300	135.30	21.0870	1.174
0.200	90.20	27.1099	1.510
0.150	67.65	33.1657	1.847
0.100	45.10	37.7287	2.101
0.050	22.55	52.6835	2.934
0.020	9.02	73.8330	4.112
0.010	4.51	102.9824	5.736
0.005	2.26	106.5894	5.937
0.002	0.90	132.4699	7.378
0.001	0.45	132.4699	7.378

THE RESULTS OF FITTING A REGRESSION LINE OF THE FORM:
 $\text{LOG}_{10}(\text{CUM. PERCENT FREQ.}) = \text{LOG}_{10}(A) + B * (\text{CURVATURE ANGLE})$ ARE AS FOLLOWS:
 $\text{LOG}_{10}(A) = -0.0655$ $A = 0.8600$ $B = -0.0210$

THE RESULTS OF FITTING A REGRESSION LINE OF THE FORM:
 $\text{LOG}_{10}(\text{CUM. PERCENT FREQ.}) = \text{LOG}_{10}(A) + B * (\text{PERCENT OF MEAN CURVATURE})$ ARE AS FOLLOWS:
 $\text{LOG}_{10}(A) = -0.0655$ $A = 0.8600$ $B = -0.3764$

REALISTIC EARTH/LAND RADAR MODELS

Andrew J. Blanchard

Remote Sensing Center
Texas A&M University
College Station, Texas

ABSTRACT

The future applications of radar remote sensing will trend toward the use of more quantitative results. Presently, the quantitative use of radar remote sensing has had some encouraging results in monitoring of soil moisture properties. However, the bulk of radar application in the past has been oriented toward qualitative use in agricultural and geologic areas. The ability to use more quantitative approaches with radar data will require the development of mathematical models which describe target/energy interaction processes. In addition, better understanding derived from developing more accurate interaction models will improve the accuracy of the qualitative interpretation of imaging radar data.

In the past, models which provided understanding of the rough surface/EM energy interaction processes dominated research and published literature. This direction was motivated in part by a preoccupation with scatter from rough sea surface. In this situation, rough surface scattering process may be the dominant mechanism. Surface scatter theories have application in earth/land radar processes; however, the more complex and more varied physical geometries of earth/land targets limit their applicability.

Vegetation, inhomogeneous subsurface properties, low loss electrical properties, etc., all contribute to make the problem more complex than a simple rough surface problem. Recently, attempts have been made to characterize the radar backscatter from inhomogeneous volumes. These theories are more appropriate for some earth/land targets. Surface and subsurface theories by themselves cannot characterize the physical situations which exist in the variety of earth/land targets; however, a combination of the two approaches may shed some light on the problems.

The paper presents a series of models which attempt to describe more accurately the physical geometry of earth/land targets. Theoretical calculations are included to illustrate model behavior. Variations with respect to various systems and target parameters are included.

I. STATEMENT OF THE PROBLEM

The quantitative use of radar data in a number of application areas is rapidly approaching. An effort has been made in recent years to quantitatively assess agricultural moisture parameters. The development of new and more reliable airborne and spaceborne systems and the availability of less expensive radar coverage made possible by the use of more efficient processing and data collection alone will generate an increased use and need for such data.

The scientific community has not arrived at the point where it can use the quantitative data in an effective manner, however. How are areas of expertise developed which will make efficient use of inexpensive, temporal quantitative radar data? Specifically, what should the radar geology scientist do to optimize his use of radar data?

First, the areas of geologic science which can be aided by the use of radar data in both point and image form must be identified. Second, once these areas have been identified we must be able to specify distinctive radar system parameters which will maximize the amount of geologic data which can be extracted from any one system configuration. Third, we must be able to interpret these radar data both qualitatively and quantitatively in order to make an accurate assessment of geologic parameters or conditions.

As might be expected, although these three items are distinct, they are interrelated. A thread which ties them all together is the understanding of what physical parameters a radar measures and how these physical parameters can be related to geologic parameters. We need to understand the interaction of active microwaves with earth/land targets.

Earth/land targets are geometrically and electrically very complex structures. We have to deal with surfaces that are rough and smooth, those which have varying permittivity, surfaces with vegetation and those without. The situations are varied and the use of a rough surface model for all cases is inappropriate.

We require a series of models which attempt to predict radar backscatter for several general configurations of earth/land targets. These targets might be classed into several general areas: (1) bare surfaces, (2) surfaces with dense, tall vegetation, (3) surfaces with light vegetation where scatter from both vegetation and the soil/air interface could be expected. These three general classes of models are the ones proposed as realistic earth/land radar models.

The balance of this paper will be structured into several basic parts to include (1) a discussion of previously developed interaction theories which have application in the proposed physical models, (2) a mathematical description of the proposed model types, and (3) the behavior of these models as a function of various target and system parameters. The paper concludes with a recommendation for future approaches.

II. BACKGROUND OF RADAR BACKSCATTER

A. Rough Surface Models

The modeling of backscatter from rough interfaces is difficult. The interaction mechanism is a complex phenomenon dependent upon a variety of physical

(target) and sensor parameters. These parameters include incident wavelength, incident angle, polarization of the incident energy, surface roughness and the electrical and structural properties of the media.

The innate complexity of the physical phenomenon requires several assumptions in order to make analytical models tractable to a usable solution. Most solutions involve assumptions of time harmonic variations and plane incident waves. Model assumptions about the target surface characteristics usually vary with the specific mathematical approach being employed. These assumptions may include surface variation; both large and small compared to a wavelength; statistically rough surfaces; infinitely conducting surface; surfaces with finite permittivity and conductivity; and both homogeneous and nonhomogeneous subsurfaces. In general, these assumptions are a consequence of the mathematical approach and may or may not represent the actual physical situation.

The following section presents the major surface scattering theories used to model radar backscatter from rough surfaces. The small perturbation, Kirchoff and composite surface theories are outlined in general. Each discussion describes the approximation used by each theory and includes a final statement regarding the results and conclusions of each approach.

B. Rayleigh-Rice Method (Technique of Small Perturbation)

Rayleigh (1) used the method of small perturbation to describe the scattering of acoustic waves from rough surfaces. The theoretical approach used a scalar technique, hence could not account for the polarization properties of EM scattering. Rice (2) extended this theory to handle the case of electromagnetic backscatter from infinitely and finitely conductive homogeneous surfaces. In addition, Rice developed the backscatter relationships from surfaces with random roughness statistics.

Rice was concerned with the scatter of electromagnetic radiation from a surface which is almost, but not quite, flat. The random deviations of the surface are described by a roughness spectrum or roughness distribution function. The function which describes the rough surface is expressed in terms of an infinite Fourier series. The random nature of the surface is introduced by allowing the coefficients of the series to be independent random variables.

Using this model for the surface description, the electric field in the space above the surface can also be expressed in terms of a Fourier series.

The coefficients in the Fourier expressions for the scattered fields are determined by application of the divergence relation for the electric field and the tangential boundary condition for the fields at this surface.

Rice presented the solution for finitely conducting surfaces. The results are mathematically complex and require a great deal of computer evaluation to come to an answer. In terms of depolarization effects, Rice's results are conclusive. The theory predicts no depolarization for a solution correct to first order. The extension of the small perturbation theory to second order solution was handled later by Valenzuela (3).

Valenzuela derived the second order field quantities for a slightly rough finitely conducting surface in a manner similar to the approach taken by Rice.

These results are used in the final development of both polarized and depolarized backscatter cross sections. From these results Valenzuela concludes the depolarization phenomena to be a second order effect in the plane of incidence.

Figure 1 presents the behavior of the depolarized cross-section as calculated from Valenzuela's theory. The behavior as a function of surface impedance is most important in the application of the theory to backscatter measurements from relatively low conductivity targets. This model predicts scattering cross-sections which increase with the magnitude of the complex dielectric constant. For earth/land measurements, the permittivity of the earth may vary (depending on frequency) from $\epsilon_c = 4$ for dry soils to $\epsilon_c = 10-j5$ for soils with 25% moisture (by weight).

C. Kirchoff Approach (Physical Optics Theory)

Bechmann and Spizzichino (4) took the approach of using the Kirchoff-Huygens principle to calculate the field backscattered from a rough surface. This technique described the backscattered field from a surface rough in one dimension and was later extended to two dimensionally rough surfaces with random surface characteristics. The scalar nature of the solution did not allow polarization effects to be incorporated.

A vector Kirchoff approach was developed by Fung (5) using the Stratton-Chu equation. This equation is the vector counterpart of the scalar Kirchoff-Huygens integral used by Beckmann. The scattered fields are calculated by finding field values on the surface of concern and substituting into the Stratton-Chu integral. These surface fields are calculated using the tangent plane approximations. The approximation uses boundary conditions that would be valid if the point under consideration were lying in an infinite plane, tangent to the rough surface at that point. The use of vector fields makes the problems complicated when the surface is not smooth.

Fung introduced a coordinate transformation which allowed the incident field vector to be decomposed into components which could be incorporated in the tangent plane calculation. Fung considered the case of both vertical and horizontal incident polarization. Polarized and depolarized backscattered field were included in the solution. Calculations using Fung's final solution were not reported.

However, Leader (6) in 1972 considered the problem of scatter within the plane of incidence. The approach used a technique similar to that introduced by Fung; however, Leader used an expansion technique which allows easy evaluation of the integral for the backscattered field. It is from Leader's results that we can draw some conclusions regarding the Kirchoff approximations. The theory generally predicts like polarized scatter with reasonable accuracy except at high grazing angles. At the far angles the assumptions of the approach are violated (shadowing, etc.). Regarding the depolarized components, Leader showed that the lowest order depolarized terms vanished. Even higher order terms may not be zero but their contribution will be negligible.

D. Composite Surface Theories

The scattering theories reviewed in the previous section all consider scatter by a rough surface whose roughness is given by a single statistical

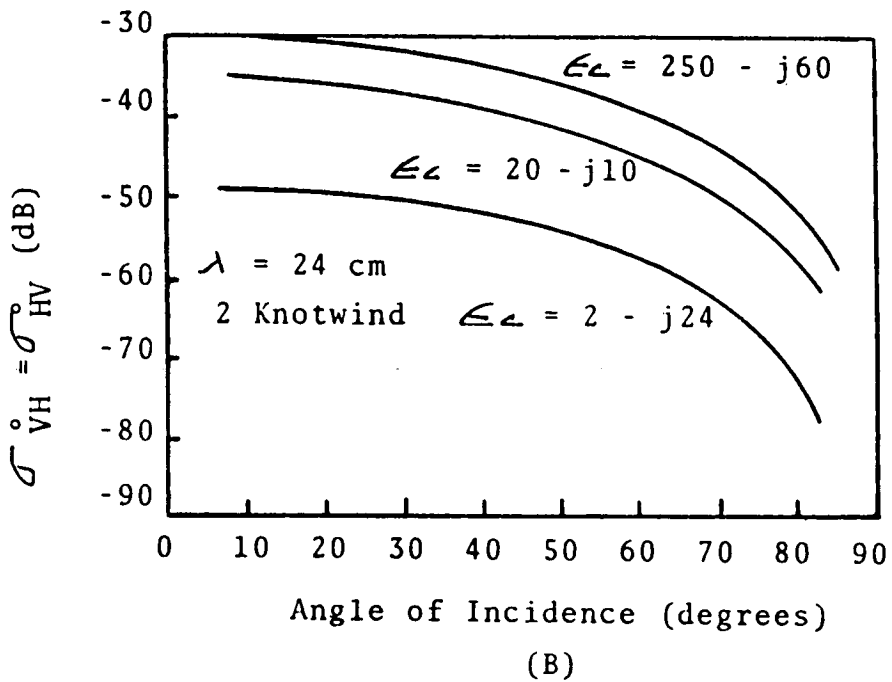
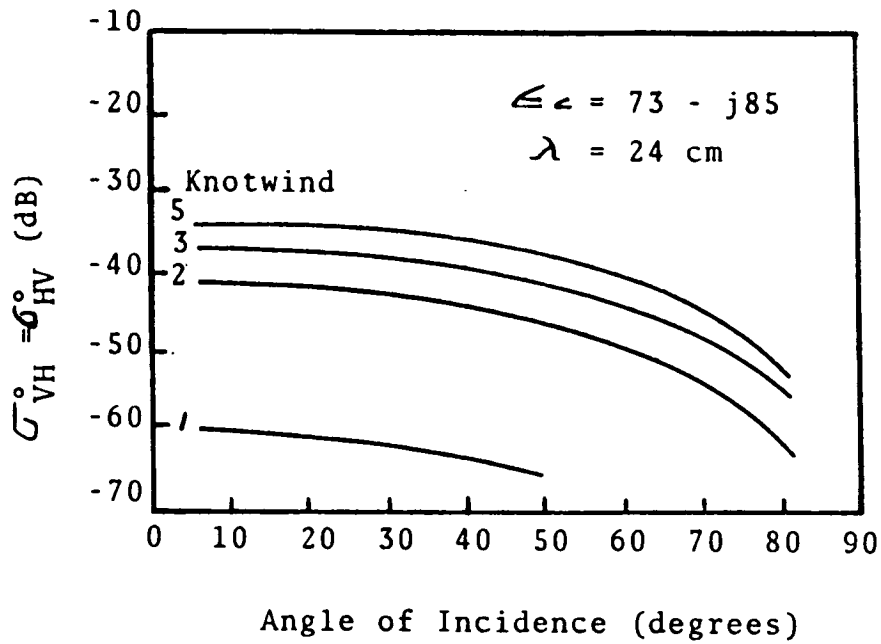


Figure 1. (a) Depolarized backscattering cross section per unit for a directive sea for various wind speeds. (b) Depolarized backscattering cross section per unit area for various complex dielectric constants (from Valenzuela).

distribution and a single correlation function. Researchers began in 1968 (7), (8), (9) to investigate scatter from surfaces with two kinds of surface statistics.

Effectively the total surface elevation

$$Y(x,y) = Z(x,y) + S(x,y)$$

is representative of the sum of two independent random processes. The first terms, $Z(x,y)$, represent the large scale undulations and must satisfy the condition that the radius of curvature is everywhere larger than a wavelength. The scatter may be computed by use of the tangent plane approximation and Kirchoff theory as previously discussed.

The second process, $S(x,y)$, represents the small scale structure and must satisfy the conditions which make the solution approachable by use of small perturbation techniques. It has been shown that the total scattered power from such a surface can be expanded as the sum of two independent terms, at least for first order calculations. One contribution is from large scale undulation alone. The second is the scattering from $S(x,y)$, referenced to some local tangent plane and averaged over the distribution of surface normals specified by the large scale roughness.

In more complex composite theories the scatters from the two types of surface roughness are not assumed to be independent processes. These solutions tend to be extremely complex.

In general, some difficulties exist in explaining experimentally measured backscatter with either the small perturbation or Kirchoff approaches. Both theories have specific regions of validity relative to the degree of surface roughness.

The Kirchoff theory is applicable when large (relative to a wavelength) scale roughness is of concern, while the small perturbation approach is applicable to small scale roughness situations. Fung et al. (10) performed an analysis to determine the areas where these approaches are valid. The results of the investigation are summarized below.

For the Kirchoff approach the condition for small and large values of σ/λ are:

$$K\lambda \leq 2.92 \cos^3 \theta \quad \sigma/\lambda \leq 0.1$$

$$K\lambda \leq 0.31 \cos \theta \quad \sigma/\lambda \geq 1.0$$

where λ is the incident wavelength; K is the curvature of the surface; θ is the incident angle; and σ the surface height. For small perturbation theory the σ/λ ratio must be less than or equal to .053. These results show that the Kirchoff theory has more applicable roughness range for natural earth/land targets.

E. Subsurface Modeling

Whereas the desire to understand the interaction of EM energy with rough sea surface directed the development of surface scattering theories, the interaction of laser light with suspended particulate matter influenced the development

of volume scattering theories. Several of these theories were developed for direct application to this problem. Their application area is broader and some results may be applied to many earth/land interaction problems.

This section will include a series of models referred to as Lead & Dalton (11), Wilhelmi et al. (12), Blanchard (13), and Rouse (14). The general approaches and assumptions of these models will be discussed in addition to limitation in application.

The physical interaction mechanism which the aforementioned approaches are attempting to model might be best illustrated by Figure 2. The physical phenomenon can be separated into two parts for purposes of discussion. The first contribution of energy backscattered toward the system consists of the energy which interacts with the rough interfaces, E_{bs} . The additional portion of the energy E_t which enters the volume through the surface must also be considered. If there exists some mechanism by which energy is backscattered toward the surface E_{bv} , then conceivably this component must be included in the total backscattered power. The following approaches attempt to model this physical phenomenon.

1. Leader and Dalton Approach. Leader and Dalton attempted to describe the volumetric scattering phenomenon. They chose to handle the volume and surface backscatter as independent processes. To this end, Leader made some assumptions about the general effects of the volume scattering mechanism. Leader did not specify the exact mechanisms involved in the volume scatter process but assumed that it was a "black box" which transformed the incident energy in a consistent manner.

Leader made an assumption that the amount of subsurface scatter was independent of scatter angle and the incident polarization. Another assumption allowed the transmission properties of the rough interface to be described by those of an average surface. Using these assumptions, calculations of polarized and depolarized backscatter coefficients were presented. Leader obtained the total backscatter cross section from the superposition of the surface and volume components. The volume scatter cross sections were found to be independent of the surface roughness statistics. This result is a direct consequence of the initial defining assumptions. The influence of the surface in the volume scatter was still not defined.

2. Wilhelmi et al. Approach. This work, performed after the introduction of Leader & Dalton results, attempted to mathematically account for the transfer of energy across the rough boundary into the subsurface.

The physical-optics approach used to describe scattering from a single scattering rough surface consists of determining the scatter of field at some point about the surface which results from currents induced on the surface by the incident electromagnetic wave. The scattered electric-field intensity at this point can be obtained using the Stratton-Chu equation as modified by Silver (15).

Wilhelmi et al. (12) used the Stratton Chu equation to determine the scattered field at some observation point above the surface and some scattering point within the inhomogeneous volume. It was assumed that the field at the subsurface point will experience multiple scattering due to the volume inhomogeneities and will be reflected back to the surface. This is the volume portion of

the field measured at the observation point. Therefore, the field measured at the observation point is due to the surface and subsurface components, which are independent because the subsurface-volume-scattering mechanism destroys the coherence of the internal and surface fields.

It is significant to note that the volumetric backscatter cross section obtained by this procedure is independent of surface roughness. There are limitations on the applicability of the Wilhelmi et al. theory to microwave measurements. The subsurface field is calculated by use of the Stratton-Chu equation, which has an inherent far field approximation. This approach effectively limits the scatterers to be much farther apart than the wavelength of interest.

To handle this problem Blanchard (13) developed a theory based on an approach Rouse (14) introduced in 1972.

3. Blanchard Approach. The theoretical model is developed by use of a physical optics method in a procedure similar to that used by Rouse. That is, the subsurface contribution is calculated by determining the surface dependent transmission coefficients of the rough surface interface in order to compute the energy entering and leaving the subsurface volume. However, the results shown here differ significantly from Rouse's results and confirm the trends of the Renau et al. (16), Leader and Dalton (11), and Wilhelmi et al. (12) measurements which show that the depolarized backscatter is independent of surface roughness.

The physical optics approach used to describe electromagnetic scattering from a single-scattering rough surface consists of determining the scattered field at the point P above the surface. These fields result from currents induced on the surface by the incident electromagnetic wave. The scattered electric field intensity at point P can be written (Silver (15)):

$$E_s(P) = K\bar{n}_2 \times \iint_s [\bar{n} \times \bar{E} - \eta \bar{n}_2 \times (\bar{n} \times \bar{H})] \cdot \exp(jk\bar{r} \cdot \bar{n}_2) ds \quad (1)$$

where \bar{n} is the local normal to the surface, \bar{r} is the position vector from the origin of the reference coordinate system to the surface element ds , \bar{n}_2 is the vector from the origin of reference coordinate system to the observation point P, k is the wave number, and η is the intrinsic impedance of the subsurface media (see Figure 3).

The procedure used to calculate the total external field is to determine the values of $\bar{n} \times \bar{E}$ and $\bar{n} \times \bar{H}$ at each point on the surface. This is done in two separate operations: one involving only surface terms and one involving only subsurface terms. The rationale for this approach is built on the assumption that the volume scattering mechanism destroys the coherence between the surface and subsurface fields.

The backscattered field due exclusively to surface scatter has been reported by Leader (6) for both horizontal and vertical incident polarization. The expression for the scattered field is given below:

$$E_{sh}(P) = ZKE_0^2 \iint_s (a + a_y z_y) \exp(-j2\bar{k}_1 \cdot \bar{r}) dx dy \quad (2)$$

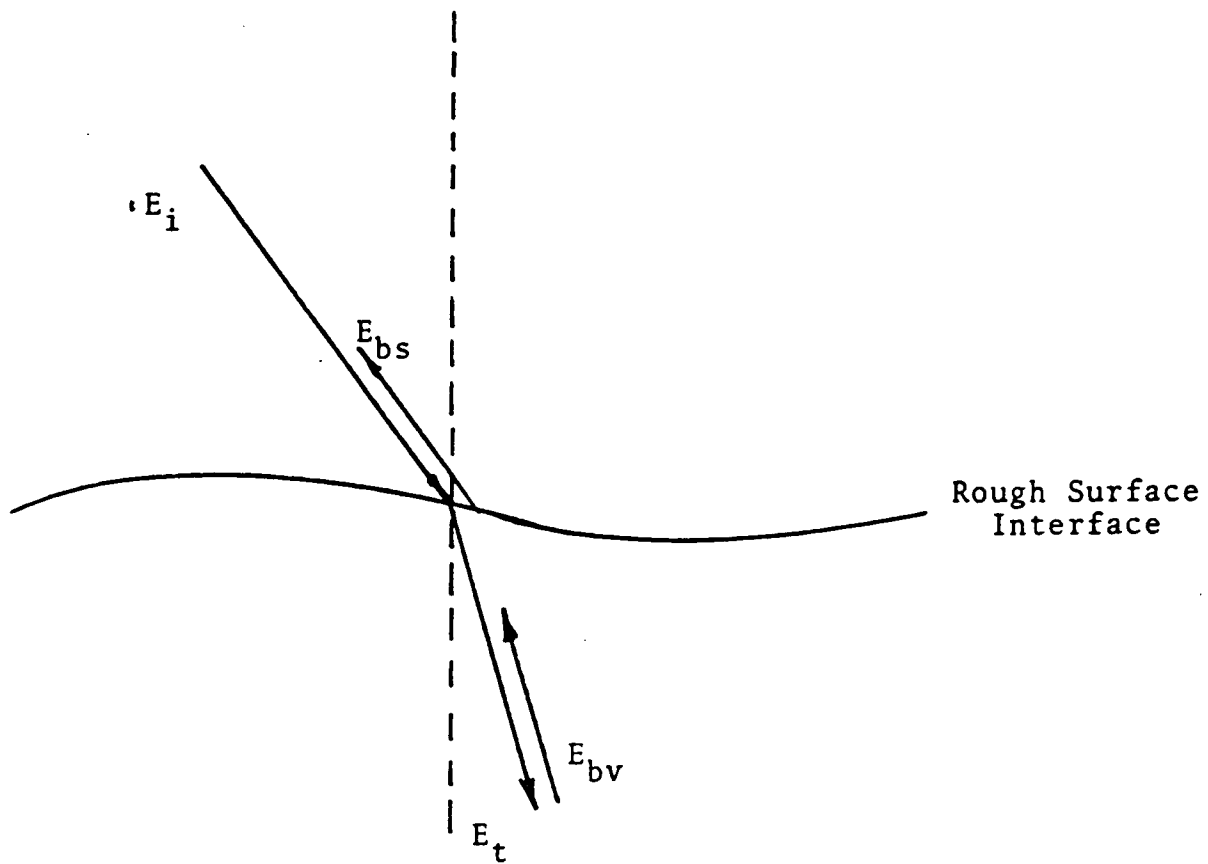


Figure 2. Subsurface scattering geometry.

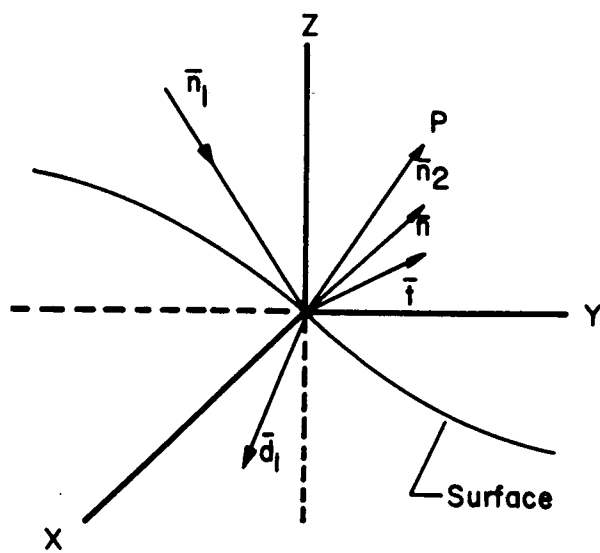


Figure 3. Scattering geometry.

and

$$E_{sv}(P) = ZKE_0 \iint_s (b + b_y z_y) \exp(-j2\bar{k}_1 \cdot \bar{r}) dx dy \quad (3)$$

where

$$a = R_1 \cos \theta$$

$$a_y = -R_1 \sin \theta - \cos \theta \left. \frac{dR_1}{dz_y} \right|_{\delta=0}$$

$$b = R_2 \cos \theta$$

$$b_y = -R_2 \sin \theta - \cos \theta \left. \frac{dR_2}{dz_y} \right|_{\delta=0}$$

and R_1 and R_2 are the reflection coefficients for horizontal and vertical polarization, respectively, Z_y is the surface slope in the y direction, θ is the angle of incidence, \bar{k}_1 is the propagation vector, and $\delta = 0$ indicates evaluation at $Z_y = 0$. Leader also showed that the depolarized cross section due to single-surface scattering is negligibly small. In the following development of the field at P due to subsurface volumetric scattering, it is shown that the depolarized component in the backscattered field is not zero for either horizontal or vertical incident polarizations.

The subsurface dependent component of the backscattered field can be calculated from Equation (1) in a manner similar to the surface dependent component. The wave which penetrates the surface is assumed to experience volumetric scatter. It is assumed that a backscattered wave will exist, which is some function of the field which entered the volume. This backscattered wave will induce surface currents of the form $\bar{n} \times \bar{E}$ and $\bar{n} \times \bar{H}$, which can then be used to calculate the field at point P due to the subsurface scatter. For horizontal polarization of the incident wave, the subsurface field that arrives at point P above the surface due to scattering within the volume has both a polarized (\bar{E}_{ssh}) and a depolarized (\bar{E}_{ssv}) component.

$$\bar{E}_{ssh}(P) = \hat{i} KE_0 (a' - \cot \theta a_y) A \quad (4)$$

and

$$E_{ssv}(P) = (\hat{j} \cos \theta + \sin \theta) KE_0 (b' - \cot \theta b_y) A \quad (5)$$

where

$$a' = -T_{11} T_{12} \gamma_1 \cos \theta$$

$$a_y' = a' \tan \theta - \gamma_1 \cos \theta \left(T_{11} \left. \frac{dT_{12}}{dz_y} \right|_{\delta=0} + T_{12} \left. \frac{dT_{11}}{dz_y} \right|_{\delta=0} \right),$$

$$b' = T_{11} T_{22} \gamma_2 \cos \theta$$

$$b_y' = b' \tan \theta + \gamma_2 \cos \theta \left(T_{11} \left. \frac{dT_{22}}{dz_y} \right|_{\delta=0} + T_{22} \left. \frac{dT_{11}}{dz_y} \right|_{\delta=0} \right),$$

and A is the surface area illuminated by the incident beam, γ is the volume reflection coefficient and T_{ij} are the electric field transmission coefficients.

By use of Leader's (6) technique for computing the backscattering cross section from the field expressions, the like polarized cross section for a perpendicularly incident wave is found to contain both surface and subsurface contributions:

$$\sigma_{hh} = \frac{A}{2} (a + \tan \theta a_y)^2 \frac{Q N_z^2}{[N_z^4 - Q N_y^2]^{3/2}} + \frac{A}{2} (a' - \cot \theta a'_y)^2 \quad (6)$$

where

$$Q = (kC'(\tau_0)\sigma_z^2)^{-2}$$

$$N_y = -2 \sin \theta$$

$$N_z = 2 \cos \theta$$

$C'(\tau_0)$ is the derivative of the surface autocorrelation function evaluated at τ_0 , and σ_z is the standard deviations of surface heights. The depolarized backscattering cross section contains only contributions from the subsurface:

$$\sigma_{hv} = \frac{A}{2} |b' - \cot \theta b'_y|^2 \quad (7)$$

It is significant to note that both the polarized and depolarized subsurface terms obtained by this procedure are independent of the surface statistics. This trend is in agreement with the results of the optical experiments of Renau et al. (16), Leader and Dalton (11), and Wilhelmi et al. (12).

Other researchers have attempted to identify the nature of the volume reflection coefficient δ (Tsang and Kong (17) Stogryn (18), Parashar et al. (19)) in terms of the geometric and electrical properties of the subsurface. However, our use of the general term δ was intended to allow identification of general model trends and behavior. Its use in the early studies of interaction of EM energy with earth/land targets is appropriate. We need to identify general classes of process before we attempt to accurately predict radar return.

III. PROPOSED REALISTIC EARTH/LAND RADAR MODELS

One approach by which all theoretical backscatter models are judged is their fit to experimental data sets. In earth/land targets the model may be inappropriately compared to a measured data set. Why compare a rough surface model and data from a physical situation which may contain parameters the model was never intended to handle? In fact, while the models which we presently have at our disposal may be valid, our application of them may be inappropriate.

The intent of this section is to propose three general classes of physical models which have some use in earth/land target description. Once proposed, an

appropriate mathematical formulation (not necessarily the only formulation) is then specified to describe the energy/target relation. The next section will present some trends in the model behavior for these classes.

Class 1: Rough Surfaces/Homogeneous Subsurface

This general class of physical targets is illustrated schematically in Figure 4. This surface model is a rather ideal case. The basis for development was for application in radar backscatter from rough seastate. It is assumed in this situation that only the surface presents itself for interaction. In only a very few earth/land situations is this the case, for example, where frequencies and permittivity values are high enough to eliminate any penetration and very little vegetation exists on the surface. Very few situations such as this will exist, although the Death Valley area does qualify. In most situations there are subsurface gradients and discontinuities which must be considered.

Class 2: Inhomogeneous Volumes

Very little is known about the contribution of subsurface effects to the overall measured scatter. However, recent evidence suggests that these effects may be significant, especially so in the case of depolarization. These volume theories are especially applicable to scatter from vegetation. When vegetation stands are tall and dense the theories presented in the previous section are particularly applicable. Some are more appropriate than others, but all have some application area. Therefore a model for this situation is proposed and is shown schematically in Figure 5. This model represents an inhomogeneous half space in general bounded by a rough surface. In its most general case this approach would model a low loss earth material such as rock or soil. The discontinuous nature of the subsurface could be attributed to the occurrence of natural voids such as are present in some volcanic tuffs or man-made voids that occur when farm lands are tilled or plowed. As previously mentioned, this concept could also be used to model scatter from vegetation. Problems will arise, however, when vegetation cover is not deep or dense enough to prevent radiation from entering and striking the soil surface.

Class 3: Layered Volumes

This measurement situation is identified as general Class 3 model. The physical model is shown schematically in Figure 6. This model consists of a vegetation layer or scattering layer superimposed on a rough and, in the general case, inhomogeneous subsurface. The layer has an average height D_1 and both the layer and subsurface have some volume scattering reflectance associated with each, denoted by δ_v & δ_s , respectively.

The next section will propose some analytical theories for the energy interaction for each of these different systems and physical parameters.

IV. MODEL DESCRIPTION AND BEHAVIOR

Mathematically several options exist to model the physical situation illustrated by the Class 1 model. As mentioned in the previous section, Kirchoff, small perturbation and composite surface theories all attempt to handle back-

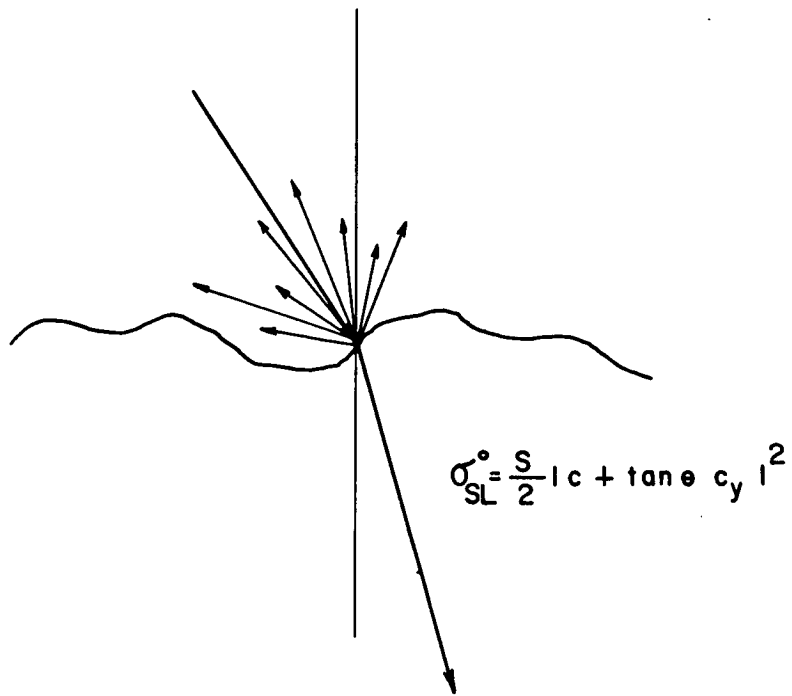


Figure 4. Surface scatter (class 1 target).

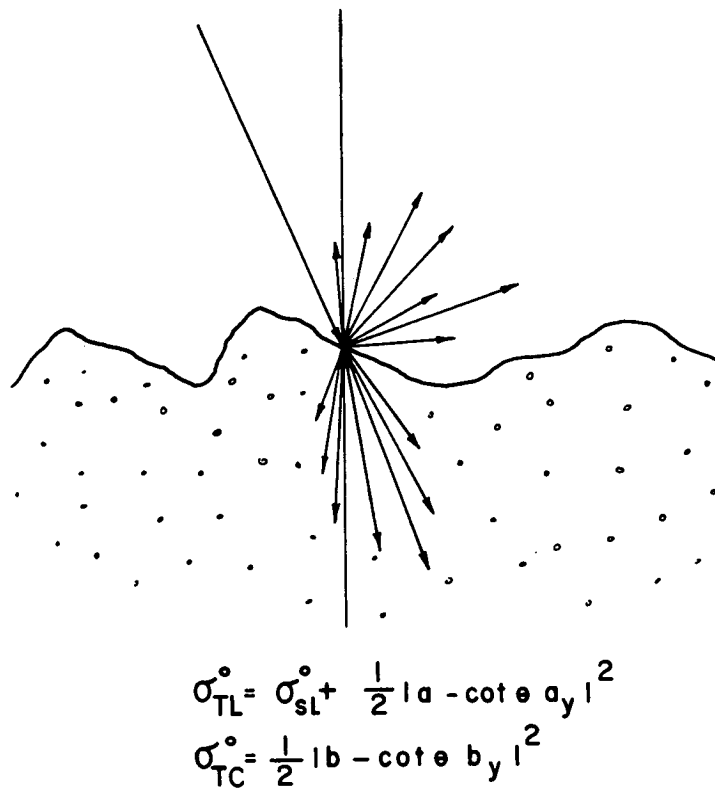


Figure 5. Volumetric scatter (class 2 target).

scatter from some form of rough surface. For purposes of comparison and ease of computation, as well as general applicability, the Kirchoff theory will be used to describe the scatter from rough surfaces.

Leader (6), following the work of Fung (5), showed that the like polarized backscatter cross section of a randomly rough surface could be expressed as (for horizontal transmit polarization):

$$\sigma_{hh} = \frac{AS}{2} |a + \tan \theta a_y|^2$$

where

$$\eta_y = -2 \sin \theta$$

$$\eta_z = 2 \cos \theta$$

$$a = 2 R_1 \cos \theta$$

$$a_y = a \tan \theta - 2 \cos \theta \left. \frac{dR_1}{dz_y} \right|_{\delta = 0}$$

A = illuminated area

$\delta = 0$ denotes evaluation @ $z_y = 0$

(for vertical transmit polarization)

$$\sigma_{vv} = \frac{AS}{2} |b + \tan \theta b_y|^2$$

where

$$b = 2 R_2 \cos \theta$$

$$b_y = b \tan \theta + 2 \cos \theta \left. \frac{dR_2}{dz_y} \right|_{\delta = 0}$$

R_1 = horizontal reflection coefficient

R_2 = vertical reflection coefficient

$$S = \frac{Q n_z^2}{(n_z^4 - Q n_y^2)^{3/2}}$$

$$\sigma_{hv} = \sigma_{vh} = 0$$

As has been previously mentioned, the Kirchoff theory predicts no appreciable depolarization due to a surface/energy interaction. The factor S in the two previous equations represents a surface roughness term related to surface statistics.

For a Class 2 series of physical models, both scatter from the surface and scatter from the volume must be taken into account.

For discussion purposes the theory proposed by Blanchard will be used to describe the interaction process.

The initial assumption of independence of the surface and subsurface back-scattered fields allows simplification of the calculation for the total backscatter contribution from both the surface and subsurface interactions. The total cross section from the surface and the subsurface can be written as

$$\sigma_t = \sigma_s + \sigma_{ss}$$

where

σ_s = cross section due to surface effects

σ_{ss} = cross section due to subsurface effects

The results for the surface effects have been previously discussed for model Class 1. Blanchard (13) has calculated the subsurface cross section as follows (for Horizontal transmit polarization)

$$\sigma_{ssh} = \frac{A}{2} |a' - \cot \theta a'_y|^2$$

$$\sigma_{sshv} = \frac{A}{2} |b' - \cot \theta b'_y|^2$$

(for Vertical transmit polarization)

$$\sigma_{ssvv} = \frac{A}{2} |b'' - \cot \theta b''_y|^2$$

$$\sigma_{ssvh} = \frac{A}{2} |a'' - \cot \theta a''_y|^2$$

These cross sections are due to volume interaction effects. The volume cross section, however, not only contains a like polarized component, it also contains a depolarized component. The surface theory contributes no depolarization. The depolarization cross section is independent of surface statistics. The complete model would be applicable in a case where both the surface and the subsurface contributed backscatter. However, in the case of scatter from vegetation only volumetric contribution would be included in the backscatter, since speaking of a rough surface for the vegetation layer is inappropriate.

The models developed for Class I and II targets were programmed on the digital computer and representative responses were calculated. The results of these calculations are presented in Figures 7 through 11. These figures present model responses as functions of surface roughness, subsurface complex permittivity and volume reflection coefficients. For purposes of comparison the model

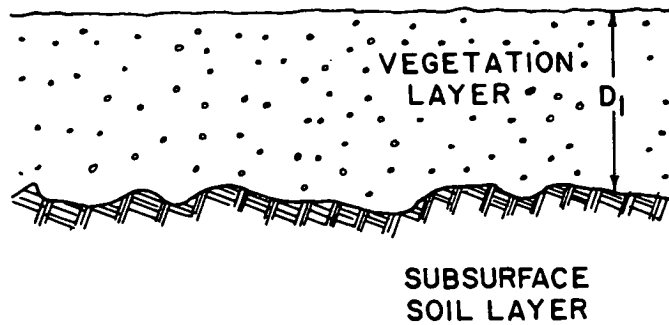


Figure 6. Layered target (class 3 target).

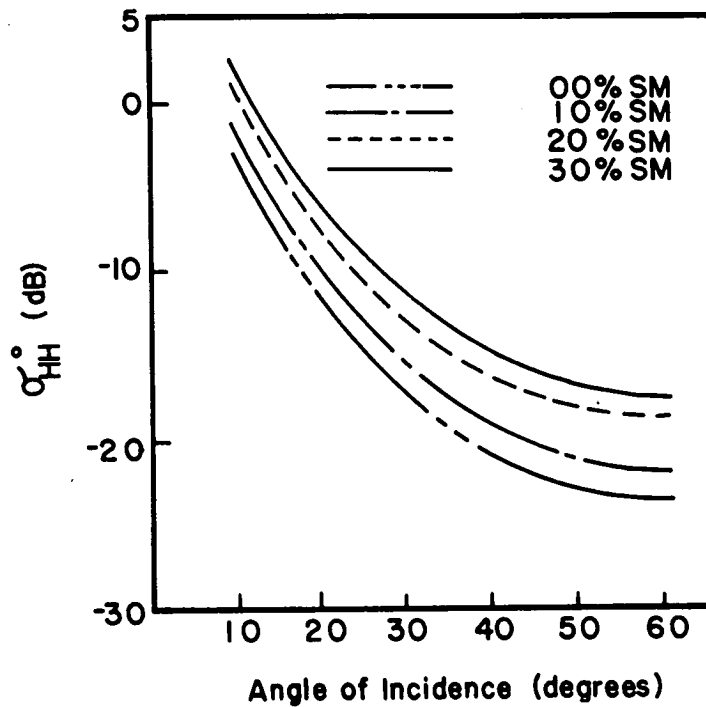


Figure 7. Variation of σ_{HH}^0 as a function of subsurface permittivity and incident angle (class 1 model).

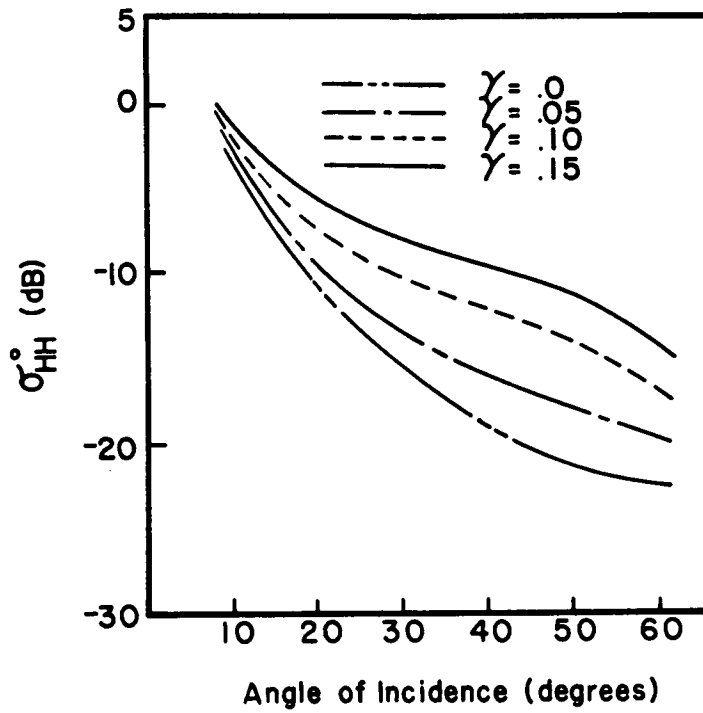


Figure 8. Variation in σ_{HH}^0 as a function of incident angle and volume reflection coefficient.

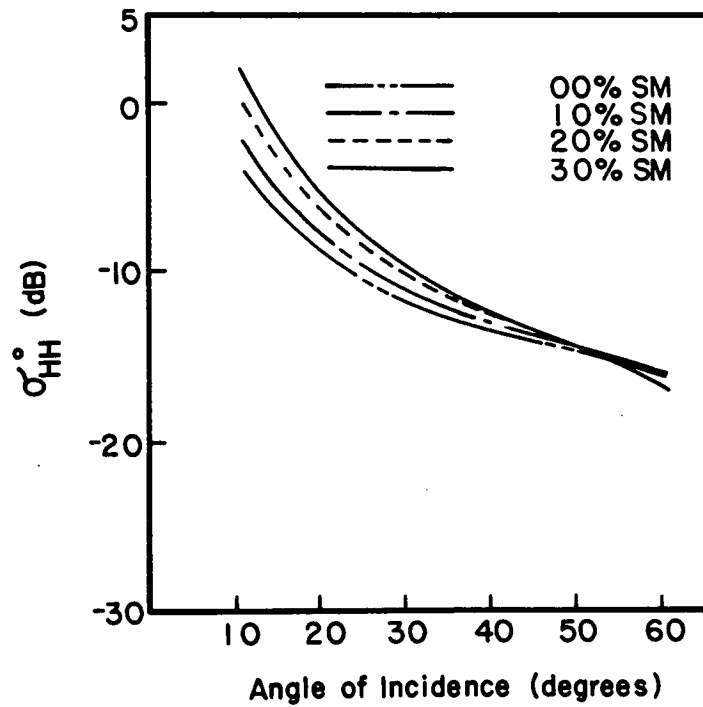


Figure 9. Variation of σ_{HH}^0 as a function of subsurface permittivity and incident angle.

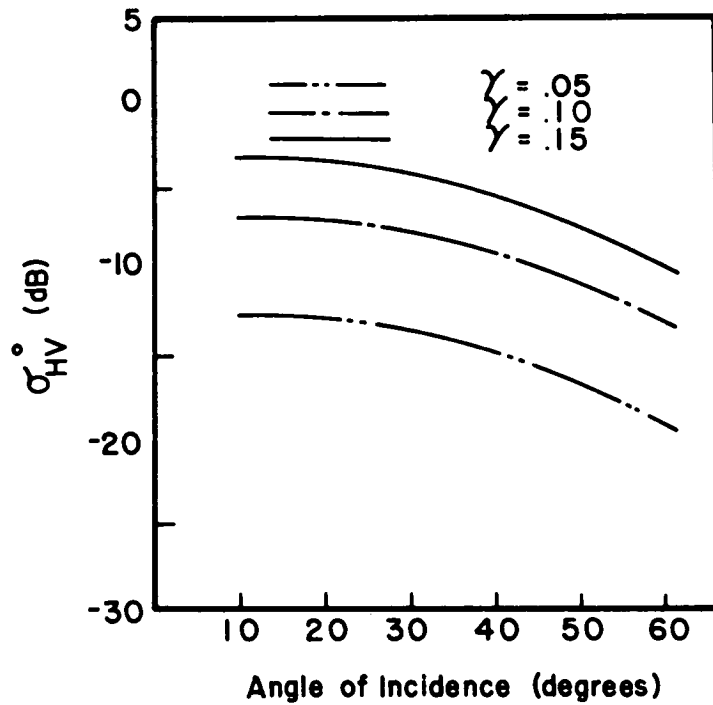


Figure 10. Variation of σ_{HH}^0 as a function of incident angle and volume reflection coefficient.

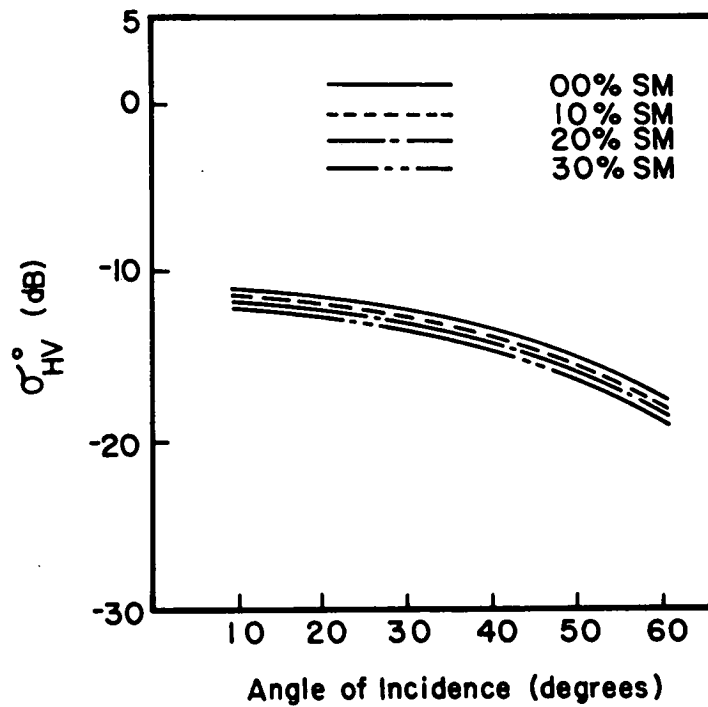


Figure 11. Variation of σ_{HV}^0 as a function of subsurface permittivity and incident angle.

predictions for both Class I and Class II targets will be included on the same graph.

Figure 7 presents the response of the backscatter cross section as a function of permittivity changes for a Class I target. The permittivity values used in these plots are those values obtained from 10-GHz measurements of soil permittivity at varying amounts of soil moisture. These curves were plotted for $Q = 1000$ for a rather smooth surface. The response vs incident angle is typical, exhibiting a rapid falloff. Also the cross section increases with increasing values of complex permittivity since the cross section is a function of the Fresnel reflection coefficient. The Kirchoff scattering theory predicts no surface-induced depolarization.

It is interesting to compare the results of the surface theories and those of the surface/volume theories. Figure 8 shows the response due to the surface term in the backscatter coefficient (i.e., when $\delta = 0$). However, as the volume reflection coefficient δ is increased, the cross section calculation is strongly influenced by the volume components. Figure 8 shows that the volumetric terms influence the cross section only for angles of incidence greater than 20° .

In general, for a Class II model, the like polarized cross section is composed of two components: a surface component which increases with increasing permittivity and a subsurface term which decreases with increasing permittivity. Figure 9 presents the like polarized cross section response as a function of incident angle for a family of permittivity values corresponding to 0, 10, 20, and 30% soil moisture. For angles less than 20° , the surface term dominates and the response trend is shown in Figure 9. However, after 20° the subsurface term begins to influence the curves by decreasing the response of the cross section to soil moisture (permittivity) variations.

Figure 10 presents the variation of the cross polarized cross sections as a function of incident angle and volume reflection coefficient. These calculations were performed for permittivity values corresponding to 10% moisture by weight and volume reflection coefficients ranging from .05 to .15. The response of the depolarized cross section is relatively flat for incident angles as great as 55° . The cross section is fairly sensitive to changes in volume reflection coefficient. Changes of 5 dB for each tenth change in volume reflection coefficient were recorded.

Figure 11 shows the depolarized cross section variation as a function of permittivity. The sensitivity of the depolarized term to moisture is significantly less than for changes in volumetric reflection due to discontinuities. These measurements are also independent of surface roughness.

The model for Class III becomes a little more complex. Scattering from several sources must be taken into account. Scatter will occur within the vegetation layer, from the soil layer, and perhaps from the subsurface layers. Figure 12 illustrates the scattering processes. The total backscattered cross section could be written as the sum of the cross section from the vegetation and a modified sum of the soil surface and subsurface cross sections.

$$\sigma_{0t} = \sigma_{0v} + M(\sigma_{0s} + \sigma_{0ss})$$

where

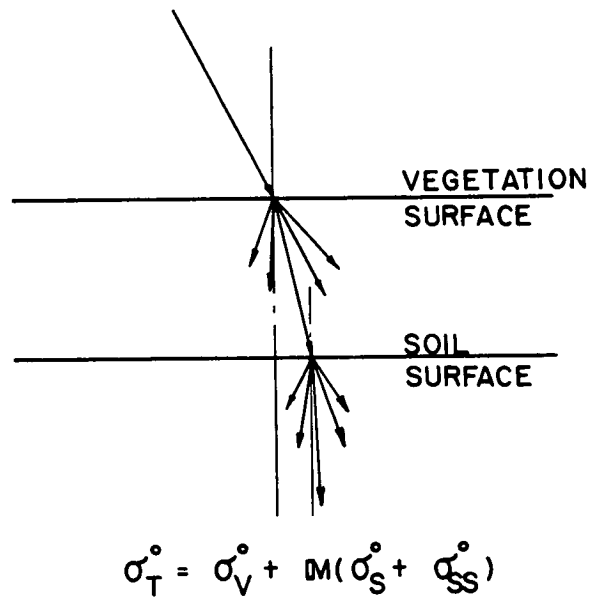


Figure 12. Scatter from a layered target.

σ_{0v} = backscatter cross section from vegetation

σ_{0s} = backscatter cross section from soil surface

σ_{0ss} = backscatter cross section from soil subsurface

$$\tilde{M} = \begin{bmatrix} \hat{\gamma}_{11} & \hat{\gamma}_{21} \\ \hat{\gamma}_{12} & \hat{\gamma}_{22} \end{bmatrix} e^{-2\alpha D_1}$$

α = loss of the vegetation layer

$\hat{\gamma}$ = vegetation backscatter polarization tensor

The like polarized return from such a target could be written:

$$\sigma_{0tL} = \sigma_{0vL} + \hat{\gamma}_{11} \sigma_{0sL} e^{-2\alpha D_1} + (\hat{\gamma}_{11} \sigma_{0ssL} + \hat{\gamma}_{21} \sigma_{0ssc}) e^{-2\alpha D_1}$$

The depolarized return becomes:

$$\sigma_{0tc} = \sigma_{0vc} + \hat{\gamma}_{12} \sigma_{0sL} e^{-2\alpha D_1} + (\hat{\gamma}_{12} \sigma_{0ssL} + \hat{\gamma}_{22} \sigma_{0ssc}) e^{-2\alpha D_1}$$

where L denotes like polarized backscatter and c denotes cross polarized backscatter.

V. RECOMMENDATIONS

Development of more realistic radar models for earth/land applications will allow the separation of system-induced errors from actual interaction effects. We can better differentiate cause and effect. That is, identify which physical parameters or combination of parameters affect radar returns. With these results one can refine qualitative interpretation methods for short term and long term use and begin to develop techniques to use radar in quantitative measurement programs. With workable physical interaction models, response to various target and system parameters can be estimated without having to physically build one or several airborne or spaceborne radar systems to make the necessary proof of concept measurements. Additionally, when the interaction processes are identified, system parameters are more easily specified and justified. But most importantly we reduce the risk of killing a potentially productive and useful remote sensing system.

We obviously have not reached the point of understanding the complex nature of radar interaction phenomena. How then does this get accomplished for earth/land targets? The following are recommendations.

- (1) Define a series of ground based measurements over real and artificial targets. These would not be application-type measurements, but more basic research. We would not look at soil moisture or roughness discrimination, but would be more concerned with factors governing permittivity responses, the responses of vegetation in radar return, and what effects of volume discontinuities have in system responses.
- (2) Couple this measurement program to a strong analytical modeling effort. I've placed the measurement program ahead of the modeling because it is in fact the more important item. The modeling effort will be more creative and more fruitful if there exists some stimulus regarding viability, direction, performance; that stimulus would be the measurements.
- (3) Examine physical parameters, such as the interaction of soil moisture with soil structure and the variability of vegetation density with vegetation moisture. These variables will influence the correlation of radar return with the physical property of the target.

REFERENCES

- Lord Rayleigh, "The Theory of Sound," 1894, Chapter 13, sec. 277a New York: Dover, 1945.
- S. O. Rice, "Reflection of Electromagnetic Waves from Slightly Rough Surfaces," Symposium on the Theory of Electromagnetic Waves, 1950.
- G. R. Valenzuela, "Scattering of Electromagnetic Waves from a Tilted Slightly Rough Surface," Radio Science, vol. 3 (New Series), no. 11, Nov. 1968.
- P. Beckmann and A. Spizzichino, "The Scattering of Electromagnetic Waves from Rough Surfaces," (The MacMillian Co., New York), 1963.
- A. K. Fung, "On Depolarization of Electromagnetic Waves Backscattered from a Rough Surface," Planetary Space Sciences, vol. 14, pp. 563-568, 1966.
- J. C. Leader, "Bidirectional Scattering of Electromagnetic Waves from Rough Surfaces," Presented at the Spring Meeting of USNC/URSI of the IEEE, April 16, 1970.
- H. L. Chan and A. K. Fung, "Backscattering from a Two-Scale Rough Surface with Application to Radar Sea Return," NASA Contract Report CR-2327, NASA Langley Research Center, 1973.
- S. T. Wu and A. K. Fung, "A Noncoherent Model for Microwave Emissions and Backscattering from the Sea Surface," Journal of Geophysical Research, vol. 77, no. 39, Oct. 20, 1972.
- P. Beckmann, "Scattering by Composite Rough Surfaces," Proceedings of IEEE, vol. 53, pp. 1012-1015, Aug. 1965.
- A. K. Fung, R. M. Axline and H. L. Chan, "Exact Scattering from a Known Randomly Rough Surface," Proceedings of the URSI, Commission II Microwave Scattering and Emission From the Earth. Berne, Switzerland, Sept. 23-26, 1974.

- J. C. Leader and W. Dalton, "Bidirectional Scattering of Electromagnetic Waves from the Volume of Dielectric Materials," Journal of Applied Physics, vol. 43, p. 3080, 1972.
- G. J. Wilhelmi, J. W. Rouse, Jr. and A. J. Blanchard, "Depolarization of Light Backscattered from Rough Dielectrics," Journal of the Optical Society of America, vol. 65, no. 9, Sept. 1975.
- A. J. Blanchard, "Volumetric Effects in the Depolarization of Electromagnetic Waves Scattered from Rough Surface," Technical Report RSC-83, Remote Sensing Center, Texas A&M University, College Station, Texas, May 1977.
- J. W. Rouse, Jr., "The Effect of the Subsurface on the Depolarization of Rough-surface Backscatter," Radio Science, vol. 7, no. 10, pp. 889-895, 1972.
- S. Silver, "Microwave Antenna Theory and Design," MIT Rad. Lab Series 1L, McGraw Hill, New York, p. 101, 1947.
- J. Renau, P. K. Cheo and H. G. Cooper, "Depolarization of Linearly Polarized EM Waves Backscattered from Rough Metals and Inhomogeneous Dielectrics," Journal of the Optical Society of America, vol. 57, p. 459, 1967.
- Tsang, L., and J. A. Kong, "Radiative Transfer Theory for Active Remote Sensing of Half-Space Random Media," Radio Science, vol. 13(5), pp. 763-773, 1978.
- A. Stogryn, "Electromagnetic Scattering by Random Dielectric Constant Fluctuations in a Bounded Medium," Radio Science, vol. 9, no. 4, pp. 509-518, May 1974.
- S. K. Parashar, A. K. Fung and R. K. Moore, "A Theory of Wave Scatter from an Inhomogeneous Medium with a Slightly Rough Boundary and Its Application and Sea Ice," CRES Technical Report 177-53, University of Kansas Center for Research, Inc. Lawrence, Dec. 1974.

SOME CONFUSION FACTORS IN RADAR
IMAGE INTERPRETATION

Bruce J. Blanchard

Remote Sensing Center
Texas A&M University
College Station, Texas

ABSTRACT

Interpretation of radar images for geologic applications is subject to confusion factors that can be caused by either system parameters or scene parameters. A number of system parameters have been found to produce misleading image anomalies. Antenna patterns, gain changes and controls, platform perturbations and image processing controls are a few of the major problems that can lead to uncertainty in interpretation. Many of the system characteristics that are of concern are minimized when using space platforms for radar systems and the remainder can be adequately handled with proper training of interpreters. The existing Seasat SAR data provides excellent examples of the improvements in imagery stability that can be achieved from space platforms.

Radar senses primarily roughness or geometric characteristics of the surface, which is generally the dominant element for geologic mapping. Radar, however, also senses the dielectric properties of the surface, which is highly dependent on soil moisture. Influences from soil moisture can be beneficial in some instances and detrimental in others when interpreting images. The influence of soil moisture for different frequency and look angle combinations is illustrated in this report. A good understanding of the radar response resulting from soil moisture difference, understanding of climatic characteristics of a region, and the use of ancillary data, can all aid in improving interpretation.

Experimental measurement of the interaction at the earth's surface when using active microwave systems has provided only a meager set of observations in relation to the many frequency/look angle/power combinations that are possible. A thorough understanding of what we are actually imaging can best be obtained by extrapolation of present results by modeling techniques because of the high costs of systems and testing over real-world terrain.

I. INTRODUCTION

Geologic interpretation of radar imagery for land use applications is dependent on classification of the radar return into categories related to some training area within the image. Such interpretation relies on the assumption that surface characteristics of areas with similar returns are truly similar. This may not always be true over water surfaces due to the influence of system parameters on the radar return. In imagery over land, both system parameters and scene parameters may lead to ambiguous returns which can ultimately lead to misinterpretation.

Unfortunately, lack of understanding of confusion factors in radar data results in condemnation of radar systems without just cause. As with any other tool used by interpreters, one must understand how the system can vary, what the effects of those variations mean in regard to the image and how the data collection and processing can influence the image. In addition, the interpreter should understand terrain conditions and the influence those conditions have on the radar return, both singly and in combination.

We have become accustomed to reliance on aircraft-mounted radar systems built for military use and have in many instances found them particularly useful in some applications. The military aircraft systems themselves are undergoing some much needed changes in regard to their data handling and processing so that imagery is improved. The wide range of possible configuration of radar systems now leads to many different types of images with which we must become familiar if we are to make full use of the available technology.

Spacecraft radar system proposals have brought forth some skeptical questioning and some criticism of our lack of fundamental knowledge concerning response from various terrain conditions. We do know that the spacecraft platforms provide many features that are beneficial such as low cost wide area repetitive coverage, reduction of look angle variation, stability of the platform, and freedom from manual operation. Although there are many data processing problems to solve on the ground, the Seasat SAR has indeed demonstrated the great advantages of spacecraft platforms for radar. These systems, however, do retain some of the same characteristics found in aircraft systems that can produce image interpretation problems. The terrain imagery from spacecraft radar may therefore contain some of the same confusion factors found in aircraft imagery.

Many of the system and terrain characteristics that are considered in this report as sources of confusion can become advantageous when well understood by the interpreter. Proper selection of system parameters for a particular application and proper timing of data collection to take advantage of changes in the surface will greatly enhance correct interpretation. Other little used techniques such as time series imagery can help improve interpretation by associating dynamic characteristics of the surface with geomorphic features.

II. CONFUSION FACTORS FROM SYSTEM PARAMETERS

An interpreter should have a general understanding of the effects on the image that are caused by changes in system parameters. The background knowledge in the past has been related to the commonly available shorter wavelength military aircraft systems. Even in these data it is wise to recognize how the image comes into being. The effects of frequency specific roughness, gain setting,

antenna patterns, polarization changes, look angle difference, platform perturbations, operator performance, data recording and data reduction can all influence the ultimate image quality and subsequently the interpretation results.

Until recent years there has been little concern with frequency-dependent roughness. With the advent of imaging systems with longer wavelengths the ability to detect small deviations in vegetation geometry may essentially be lost. Detection of this surface parameter has been traditionally used to identify changes in species of vegetation and from these changes the interpreter can infer changes in the soil type. The longer wavelengths also prove less sensitive to microroughness created by tillage patterns and thus produce much different images of agricultural scenes. Longer wavelengths, by being insensitive to minor differences in vegetation, provide an advantage in one sense because they are more reliable for estimating soil characteristics under some vegetation. Studies of the Seasat SAR data, which represent only a narrow range of look angles of the L-band like polarized system, may best demonstrate this point. The Seasat SAR data represent only one of the many options and for any change in frequency we must recognize that a change in response to surface conditions may occur.

Polarization effects on the resulting image is an area that is perhaps misunderstood due to a lack of an available supply of cross-polarized data. The reduction of return in cross-polarized data has probably created the greatest confusion by users. Some compensations for the reduced return power can be made in the image processing. Experience with some cross-polarized data from the ERIM system has indicated that much valuable terrain information is available from these data. A considerable amount of additional study and testing will be required in this area before the full value of the cross-polarized imagery can be developed. With the present state of the art it is important that the interpreter know how the processing was accomplished and use only the images where known compensation for reduced power has been incorporated in the processing.

Good automation of the gain control is another feature that would be desirable in all systems. This seems to be the one adjustment that is most frequently made by the operator on aircraft systems. Manual operation of the gain, however, has not produced as good results as the automatic gain setting on the Seasat SAR. Adequate control of the gain cannot be accomplished without a full understanding of the antenna pattern and the power being distributed. Also, most aircraft systems have not had a calibration of the antenna pattern because of a lack of funding. Our experience has shown that major differences occur as a result of antenna pattern differences between systems (Figures 1 and 2); therefore imagery between systems is difficult to compare in many instances. These two problems, gain control and antenna pattern calibration, can be overcome if the user demands are strong enough.

Look angle differences not only alter the topography expressed in the image but also have a remarkable influence on penetration of vegetation and sensitivity to soil moisture. In general, penetration and sensitivity to soil moisture can be enhanced by using look angles near nadir while roughness or topographic variations produce the predominant return at angles far from nadir. This parameter probably creates serious confusion in aircraft imagery but is essentially nonexistent in spacecraft systems. With aircraft imagery it is sometimes difficult to keep in mind that the influences of soil moisture differences are predominant in only two tenths of the near-nadir side of the image. For a system such as the Seasat SAR the change in look angle across a swath is small enough that confusion between moisture and roughness effects brought about by look angle across the image is minimized.

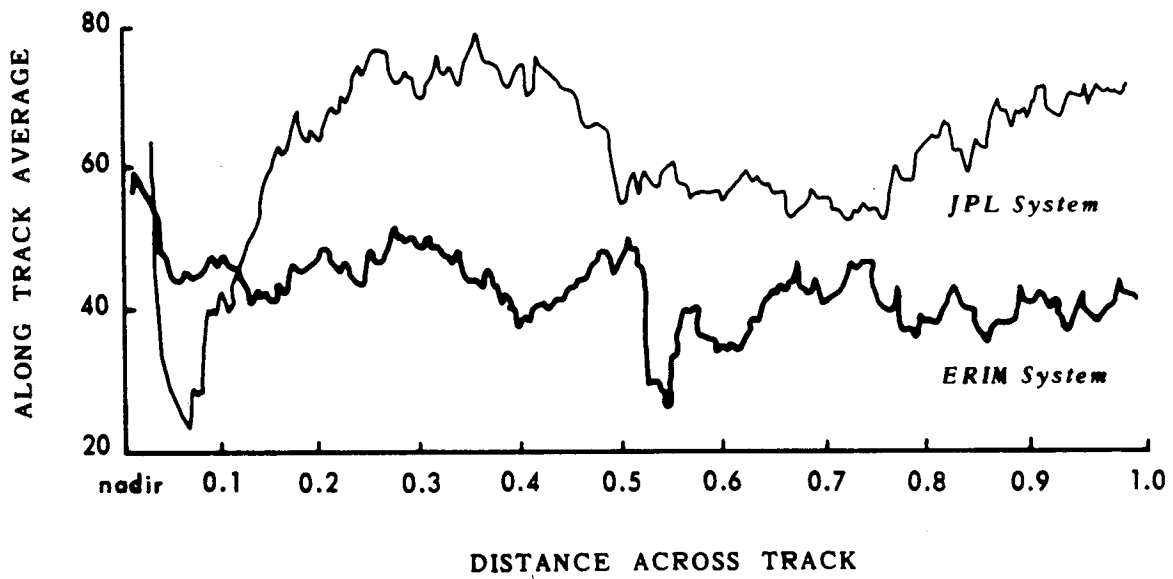
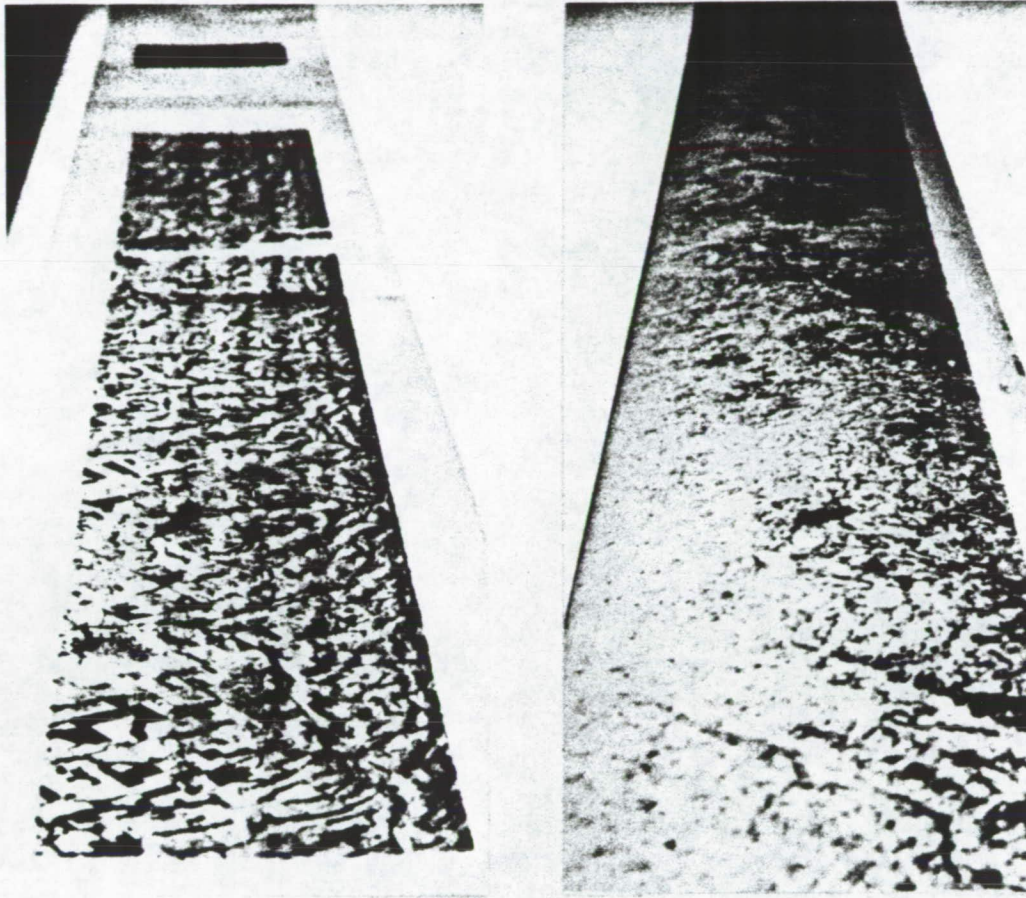


Figure 1. Effective antenna patterns from two L-band systems developed by along track averaging of digital data from imagery produced on an optical correlator.



A

B

Figure 2. Oblique photographs of (a) imagery from irregular antenna pattern and (b) imagery from Seasat SAR showing uniform change across track in the image.

ORIGINAL PAGE IS
OF POOR QUALITY

Two other system parameters that are significantly improved in spacecraft systems are the stability of the platform and the elimination of operator interference. Unstable platforms have a peculiar habit of being most erratic over a critical area being interpreted. With the existing aircraft systems, quality resulting from stability improves with operating altitude, and most operational systems are now flown relatively high to eliminate much of the instability problem. The Seasat experience has also demonstrated that getting still higher eliminates the stability problem. In regard to the operator interference on the system, probably more image quality has been decayed in the "hands on" operation than any one built-in system parameter. This is becoming less of a problem with the expenditures of sufficient funds to make aircraft systems that are essentially automated. There still remains the fascinating temptation for an operator with "hands on" control to make changes in the system during the flight or between flights, and while using imagery we should be alert to the possibility that the system may have been adjusted.

Data recording systems have been notoriously slipshod and pieced together as the radar technology has been developed. It seems the recording systems have lagged behind the development of radar, and these systems have also been victims of short funding. A poor job of recording can easily lead the interpreter to believe the radar system cannot produce the data he needs. Again, the recent development of automated recording systems has markedly reduced the opportunity for error.

Once the data have been collected with a good system, it becomes the responsibility of the user to investigate and participate in the data reduction to image products. The user should observe the operator interaction necessary in most processing systems and determine how adjustment in optical systems or in the programming of digital systems can influence the image. New users must expend the necessary time and effort to observe these procedures in order that optimum value can be realized from the data. The optical processing can require extensive participation by the optical bench operator and thus depends on this skill and the understanding of the desired results. On some optical processing systems the bench may be computer controlled, thus requiring very little operator participation. The images produced by the Jet Propulsion Laboratory from Seasat SAR data are an excellent example of the vast improvement that can be accomplished. Both the reduction of operator influence on the system and incorporation of automated correction for system parameter changes were included in this improvement.

Ultimately, the desired data processing will use computer techniques. Since no computer performs better than the programmer, it is imperative that the user of data from digital systems be aware of the program functions. All or portions of the data may be altered easily in computer processing and nonuniformity in images is as easily accomplished with the computer processing techniques as it has been by the operator of an optical system. When change detection is desired in either optical or digital processed data it is necessary to assure the user that the processor system has remained stable throughout all scenes.

III. CONFUSION FROM TERRAIN FEATURES

A large number of terrain features can interact in radar imagery in creating a very complex response. The effects of roughness and the dielectric properties of the surface are combined in most radar data to such an extent that it is difficult to isolate the effects of any one surface variable. An example of this

difficulty has been the recent attempt to collect radar returns over areas where roughness has been controlled to measure the changes brought about by change in dielectric properties. Staging these conditions in a real-world environment has indeed been difficult.

The development of a soil moisture monitoring capability with radar based on its sensitivity to dielectric properties of the surface soil is of major importance to solution of global water resources applications. Moisture distribution in the soil surface at any one time is dependent on rainfall, evaporation and transpiration rates and on the drying rate of the specific soil type. Rainfall patterns are "storm type" dependent, usually producing highly concentrated rainfall over small areas in the arid regions and widespread storms in the humid coastal regions. In some regions between these extremes, storm patterns can create linear patterns in radar return that are unrelated to the geologic and geomorphic characteristics of the surface. Higher returns created by wet soils can sometimes appear as linears, particularly when highly localized storm cells pass over dry regions. On the other hand, a time series of soil moisture response from some systems will provide a measure of drying rate that is directly related to the geomorphic development of the soils and can be used to enhance interpretation. Evaporation and transpiration are functions of the seasons and the climatic regions. The drying rates of soils will therefore vary as seasons and geographic locations change. The drying rates in one location can, therefore, only be compared with rates from the nearby areas.

Moisture measuring capability is particularly subject to frequency, and look angle and effective depth of penetration are also frequency and look angle dependent. Thus radar is sensitive to dynamic moisture and depth simultaneously. These facts will make it difficult, if not impossible, to ever remove the effects of moisture from an image, leaving only the roughness. Systems using shorter wavelengths and looking at larger angles off nadir are least influenced by moisture.

Vegetation mapping with shorter wavelengths has been recognized as a means of mapping soils and very subtle topographic features. As the angle off nadir is decreased, the value of this feature in radar images declines. Increased wavelengths also reduce the possibility of recognizing species and in fact can in some steep angles nearly negate the effects of vegetation. Massive growth of heavily fertilized native grasses on test watersheds in Oklahoma was striking on X-band while very difficult to detect on L-band imagery collected at the same look angle at the same time. Larger land cover such as brush and forest presents a greater problem to the interpreter. The penetration capability of radar in forested areas has not been adequately investigated. However, there has been some indication that standing water under timber has an effect on the return from the canopy.

Soil type differences should not be detectable in radar data, if only the dielectric constants of dry soils are considered. The interaction of soils with moisture and possibly the differences in plant root development in different soils do, however, result in a different soil-type related response. This has been observed when soils are extremely dry. A comparison of returns from two adjacent areas was made in a study of Oklahoma watersheds. One area had undisturbed native pasture and the other areas had pasture on the same geologic formation with most of the topsoil removed by erosion. Significant differences were seen in the L-band-like polarized data from both the JPL and the ERIM radars (Figure 3). X-band ERIM data over the same two areas were apparently primarily

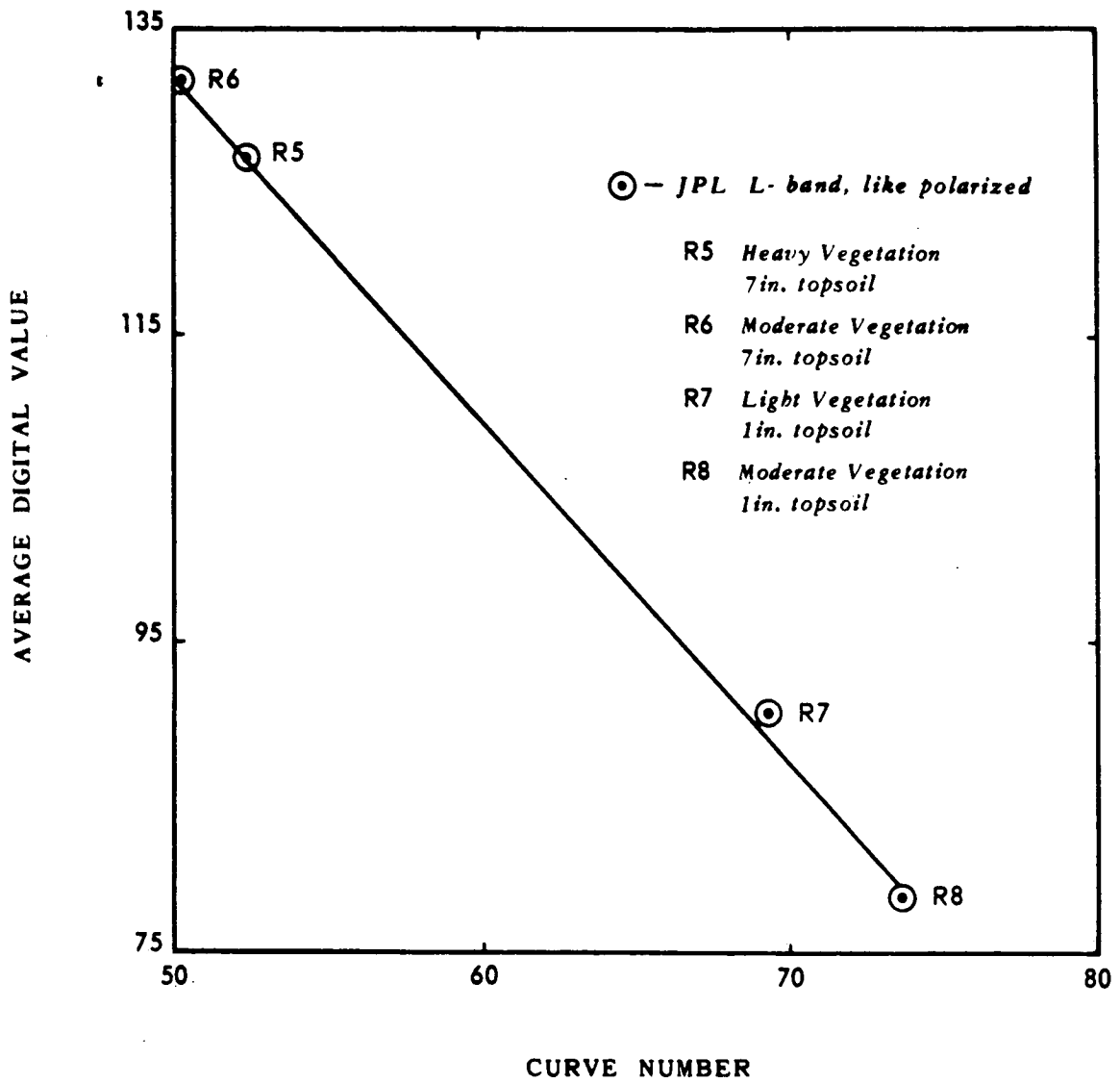


Figure 3. Differences in radar return from two pair of small watersheds having different topsoil depths.

influenced by differences in vegetation. The influence of different surface soils will then continue to confuse interpretation in agricultural lands but may be of benefit in interpretation over undisturbed soils common to rangeland in arid regions.

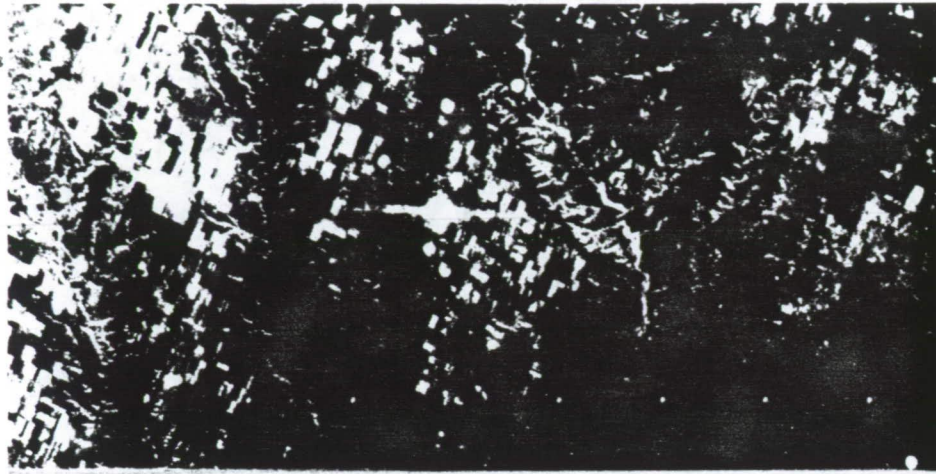
Man-made objects on the surface are the subject of many geography or land use mapping efforts, but in the interpretation for geologic investigation the same objects add confusion. This problem is especially acute when numerous bright targets are closely spaced. The effect of these bright targets may be considerably reduced by some processing techniques (Figure 4), and it may be advisable for some applications to eliminate them entirely. The current digital processing at JPL in fact clips the bright targets and sets them at one brightness level. This approach to processing appears to reduce confusion of bright targets but does hinder some approaches to calibration of the remaining data.

Other factors include look angles in reference to slope of the terrain. When we realize that such parameters as soil moisture can be best detected at steep look angles, we must also realize that response from slopes can be enhanced or degraded according to the moisture in the slopes facing the radar. This can most likely be accommodated by imaging from different directions and incorporating time series images in the analysis. The associate costs of this approach would be high and judgment must be exercised in each application to determine if the enhancement is advisable.

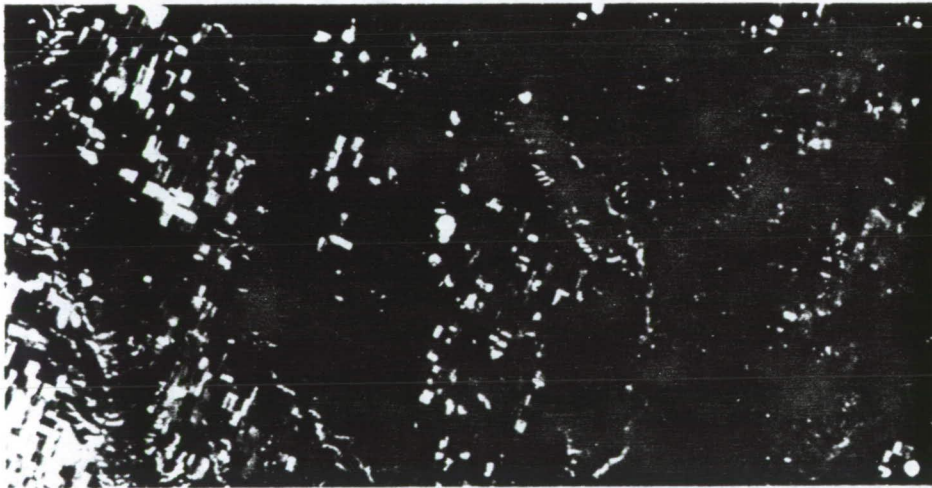
IV. DISCUSSION

With imaging radar as with other remote sensors, a multitude of users with divergent applications in mind want to use the images either in digital or in image form. There are more options in sensor parameter combinations with radar than with other sensors and it is indeed doubtful that even several configurations can satisfy all needs. To build a system that would minimize confusion factors for each application would require a single configuration for each application. Even then it may require years to determine the optimum system for each application. Demands of users for data will require that we have systems available in a time period that will not allow development of the optimum system. Hence there is a need for users to accept the fact that influences from many of the factors discussed will exist in the data and personnel will need to take these into account. If we wish to have the best of two worlds, the interpreter would need long wavelengths near nadir to get geomorphic information and shorter wavelengths far from nadir to get structural information.

It is also evident that extensive study must be done to understand some of the surface phenomena that influence radar returns. Building and flying a large number of systems to test all combinations is physically out of the question. More detailed modeling studies need to be done in cooperation with users and earth science specialists. Such studies can help us to understand the phenomena and better optimize the design parameters of our systems without the cost of actually flying them.



Optical



Digital

Figure 4. A comparison of digital and optical processing showing how effects from bright man-made targets can be substantially reduced in digital processing.

ORIGINAL PAGE IS
OF POOR QUALITY

MULTICHANNEL SAR IN GEOLOGIC INTERPRETATION:
AN APPRAISAL

Philip L. Jackson
University of Michigan*
Ann Arbor, Michigan

ABSTRACT

Multichannel SAR appears to provide advantages over single-channel SAR similar to those of multispectral (MSS) over single-channel sensing in the visible and near-visible region. Diversity of wavelengths and polarities potentially can be used for interpretation in the microwave region, where radar return is extremely sensitive to the geometry and roughness of the terrain. Although multichannel SAR imagery has been operational for some time, no thorough investigation has been made of its benefits. The advantages of multichannel SAR remain potential rather than demonstrated. Isolated illustrations indicate wide diversity of multichannel radar returns, which appear to be highly diagnostic of vegetation and lithology. However, the meaning, repeatability, and interpretability of these returns have not been thoroughly investigated. Such an investigation is desperately needed.

I. INTRODUCTION

Can the combination of synthetic aperture radar (SAR) image channels be effective for geologic interpretation in the same way that the combination of visible and near-visible multispectral scanning (MSS) channels have been? It appears that it can, but multichannel SAR has been operational for over six years without its geologic potential being thoroughly evaluated.

Single-channel SAR has proven to be extremely useful for geologic interpretation primarily because SAR discriminates subtle surface variations which indicate faults, joints, folds, domal structures, etc. These features are sensed because SAR is more sensitive to the geometry of the terrain than to its composition. The addition of SAR channels must be shown to aid in this discrimination.

MSS, which is primarily sensitive to composition rather than geometry, differs from SAR in its interaction with the terrain. While it is valid to digitally analyze multichannel SAR in precisely the same way as MSS, the interpretation of the analysis differs from that of MSS.

* Formerly with the Environmental Research Institute of Michigan

This paper is concerned with the appraisal of multichannel SAR as compared with single-channel SAR for geologic reconnaissance.

II. STATEMENT OF THE PROBLEM

Several problems for the application of multichannel radar require solutions.

- (1) Is the improvement in geologic interpretation with multichannel over single-channel SAR sufficient to justify the extra expenditure in the radar and the analysis? For example, should space SAR have frequency diversity? Studies for the space shuttle have recommended a dual-frequency system, but a single frequency is not projected. The indications are that frequency diversity would be beneficial for geologic interpretation, but the current evidence is not conclusive. Interpretation in other fields such as agriculture and ice monitoring have shown results which appear promising for geologic interpretation.
- (2) What kinds of geologic problems can multichannel imagery help solve? Broadly, two types of geologic features need defining. One is spatial distribution of lineaments or relatively abrupt changes in the surface. This type has been found to be particularly suitable for single-channel SAR. The other type is the definition of lithology or soil types over a relatively large spatial extent (similar, say, to agricultural fields), which has not been found to be particularly suitable for single-channel SAR, at least in comparison with MSS. Specifically, can the delineation and validity of lineament and structure detection be significantly improved, and can the definition of areal lithology be developed?
- (3) What are the optimal frequencies to be used for geological interpretation? We have habitually used two frequencies, X-band (~3 cm) and L-band (~24 cm), with some historical use of K-band (0.86 cm). However, other frequencies may be very valuable for geology. Unlike the case for agriculture, no continuing ground-based scatterometer investigation has been pursued for geology. For agriculture, Bradley and Ulaby (1979) have suggested C-band (3.8-7.5 cm) as being most useful. We do not know if a similar requirement would aid in geology.
- (4) How does multichannel SAR compare with other sensors such as MSS, and how can it be used most effectively with other sensors? Although some image combination has been accomplished (Jensen et al., 1977), we don't know how to exploit the great amount of information in MSS and SAR. The purposes for which one would use only SAR, only MSS, or a combination of both, and if so how combined, need investigation.
- (5) What digital analysis is required? Compared to MSS analysis, little has been accomplished with multichannel SAR. It appears that the same digital techniques can be used for SAR that have been developed for MSS because the techniques are independent of the substantially different terrain interaction mechanisms. The selection of the techniques and their interpretation will undoubtedly differ from MSS.

- (6) Can the empirical basis for interpretation be more firmly established? No continuing scatterometer investigation is currently being pursued for geologic interpretation. We are still using the nongeologic results of Cosgriff et al. (1960) for a reference to frequency and polarization. Radar scattering theory is very advanced, but of little use on terrain interaction because the surface cannot be sufficiently simplified or defined.

The above problems, each of which defines a separate area of investigation, concern applications. One problem concerning multifrequency SAR is solved: sensor development. Application lags far behind sensor development. Since 1973 the ERIM four-channel SAR has been operational and has been used to obtain imagery of ice, shipping, agriculture, oceans, wetlands, urban areas, and geology, but never in a continuing, thorough investigation. The latest development is the addition of calibration to the ERIM system.

III. BACKGROUND AND STATE OF THE ART

The application of multifrequency radar to geology was first described by Dellwig (1969) in which separately gathered imagery of the Pisgah Crater region in California was interpreted. Imagery of K-, C-, and P-band radar was gathered with different systems at different times. The sparsely vegetated Pisgah Crater region contains dry lake beds, fanglomerates, and lava beds from different flows: a variety of surfaces with different roughness characteristics. Dellwig concluded that surface roughness appears to be the parameter most strongly influencing radar return, that the long wavelengths gave a "unique" total response to terrain characteristics as compared to shorter wavelengths. He speculated on subsurface penetration by long wavelength, and stated that evaluation is needed in terms of polarization, resolution, and aspect angle. (Ten years later such evaluation is still needed.)

It should be pointed out that the Pisgah Crater region is a geologic region where the relatively large areas display different lithology, in contrast to a region where structure (as delineated by faults, etc.) is of primary importance.

Figure 1 shows a four-channel image (X- and L-bands) of Pisgah Crater gathered in 1972 on successive flights of the ERIM radar, before simultaneous imagery capability was achieved. Differentiation of areas between channels can be seen. Essentially such differentiation is the justification of multichannel SAR for both type 1 (structure) and type 2 (area) interpretation.

Vincent (in Wagner et al., 1974) and Sabins (1979) have also investigated remote sensing in the Pisgah Crater region.

From 1974 to 1977 ERIM gathered four-channel data for a number of purposes. Five of these images (two in geology) are illustrated because they have bearing on multichannel SAR for geology.

Figure 2 illustrates some digital analysis on a strip mine image gathered in eastern Kentucky in 1974. Only two of the four channels are illustrated here - X-band (3 cm) and L-band (24 cm), both like-polarized returns. In addition, computer printouts (graymaps) of the two channels and a ratio of L/X are shown. The lineament at the denotation "5" was greatly enhanced and first brought to notice by the graymap of the ratio. The lineament turned out to be an old prospecting cut which was overgrown with younger trees of the same height as the surrounding tree canopy. In this case a lineament was enhanced by the use

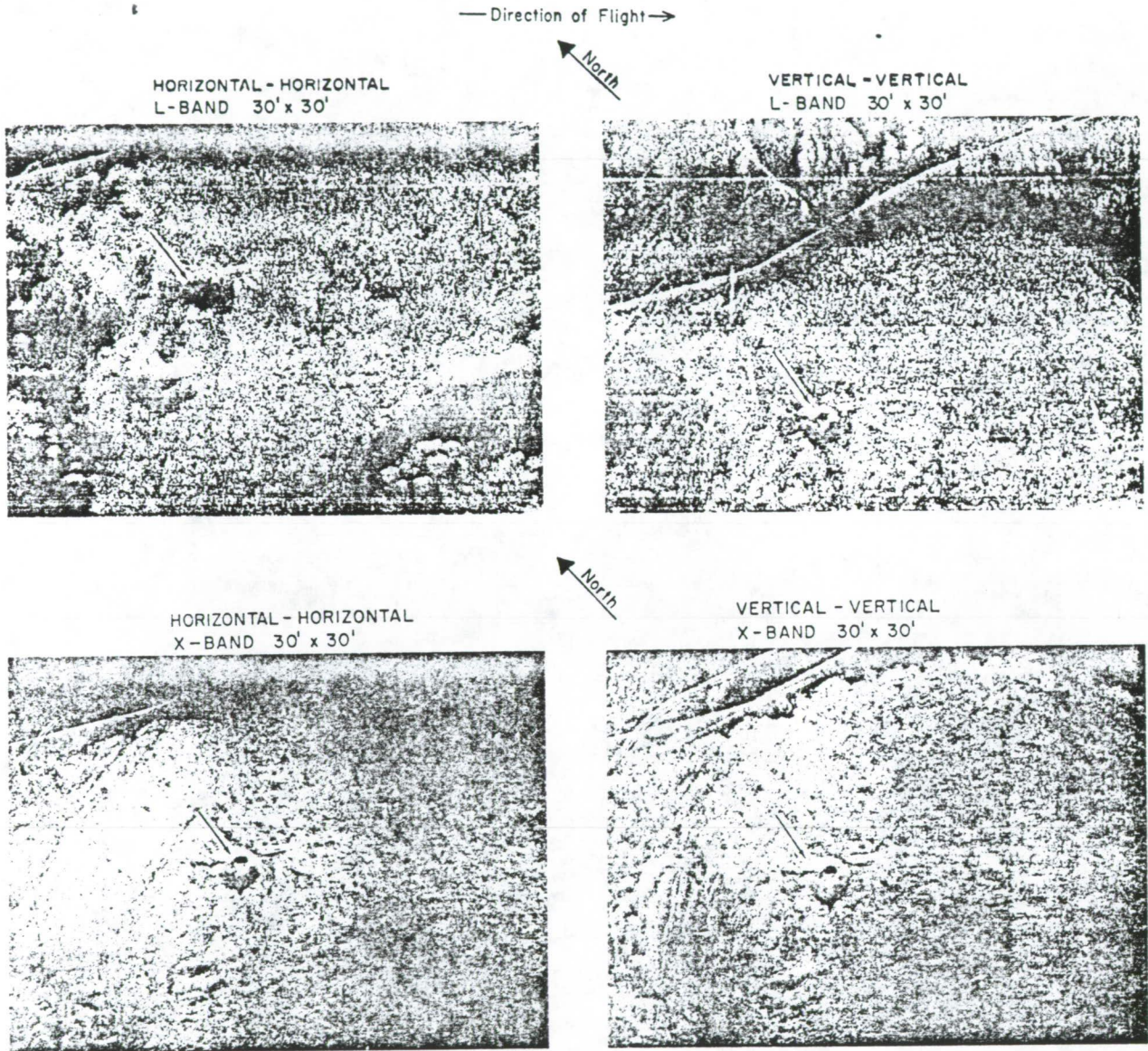


Figure 1. Four-channel radar imagery of the Pisgah Crater, California region: XXH, XHV, LHH, LHV. L-band and X-band gathered on separate flights.

ORIGINAL FROM
OF POOR QUALITY

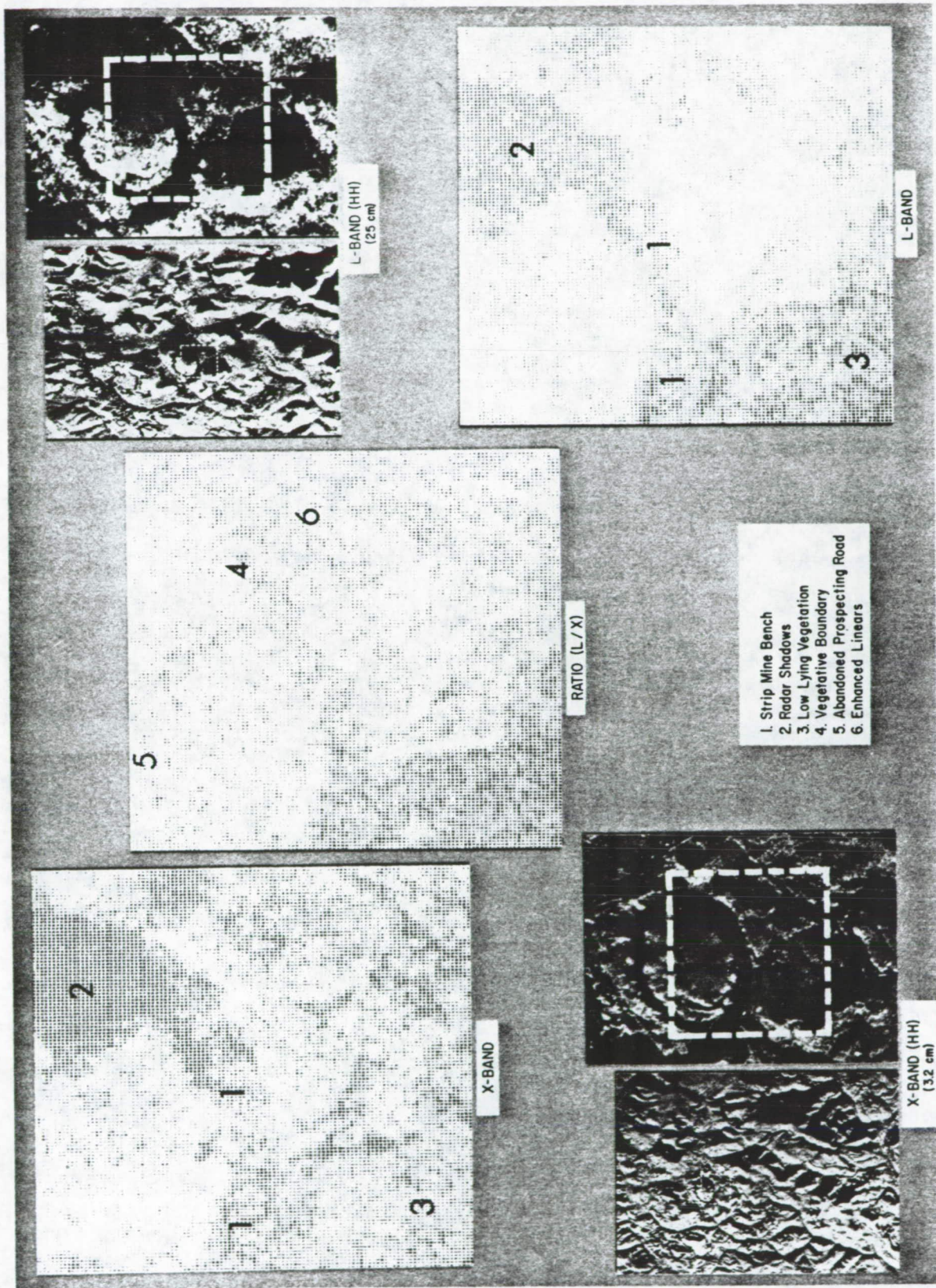


Figure 2. Imagery and graymaps of strip mine region in eastern Kentucky, and graymap of ratio of L/X, obtained in April 1974.

ORIGINAL COPY OF RECORD

of multichannel over single-channel SAR. This example is thought to be the first experiment on the ratioing of the SAR frequencies.

Figure 3 departs from geology to show the vast differential between returns over areas of different roughness. This Arizona agriculture scene graphically displays the differences in return, which should be diagnostic of the vegetation in agriculture and, by analogy, possibly of lithology in geology (although probably much more subtly). Any given field is imaged differently on the four channels, with much more variance than found with MSS. SAR can thus provide a rich basis for interchannel comparisons.

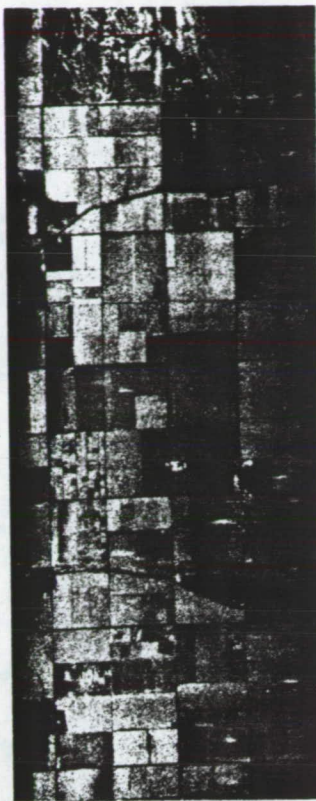
The next example (Figure 4) shows the sensitivity of SAR to roughness and the geometry of the surface. This ice imagery shows variations exclusively due to roughness, because the dielectric constant is virtually identical throughout the scene. In one portion of the scene the X-band shows very low return and the L-band significant return. This is because the L-band penetrates the ice and is reflected from the rough ice-water interface. Again by analogy the application to geology is inferred, in that most soils are similar in dielectric constant, that only the geometry produces differential returns, and that the longer wavelength may penetrate the soil to a limited extent.

A hydrologic example, from which geology can be inferred in some cases, is shown in Figure 5. This four-channel imagery was obtained in 1975 at Marineland, Florida, as an exercise for Seasat. Two features of these images should be remarked. The first is that the waves are imaged in three channels, but not in the fourth, XHV. This may be due to the waves presenting "facets" (for 3-cm wavelength) which are essentially perpendicular to the radiation path, so that no depolarization occurs. Analogous results were reported by Daily et al. (1978) and Schaber et al. (1979) for blocky, faceted rocks in Death Valley and Central Arizona, respectively, both investigations of which will be described later.

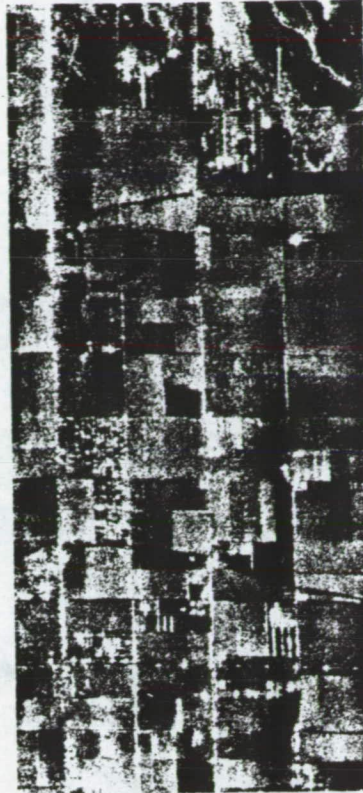
The other feature of interest in Figure 6 is the delineation of swamps. Note the channel in the lower right corners of the images. It is narrow on the 3-cm-wavelength image and wide in the 24-cm wavelength. The multifrequency system here is discriminating the height of vegetation over water, where the longer wavelength is specularly reflected from the water. This example relates to geology because vegetation often indicates underlying geology.

A geologic example is shown in Figure 6 which did not result in diagnostic information. The scene is in northwestern West Virginia near the Ohio River. It is of a mature, dissected surface that is highly vegetated. No structural features such as faults or folds have been mapped or can be seen at the surface. The purpose of imaging was to attempt to see surface manifestation of suspected fractures at 1000 m depth. The presence of heavy vegetation and the use of too large a scale prevented the imagery from being diagnostic for the purpose of detecting relatively wide lineaments. Landsat imagery, particularly color composites, was more useful for this purpose.

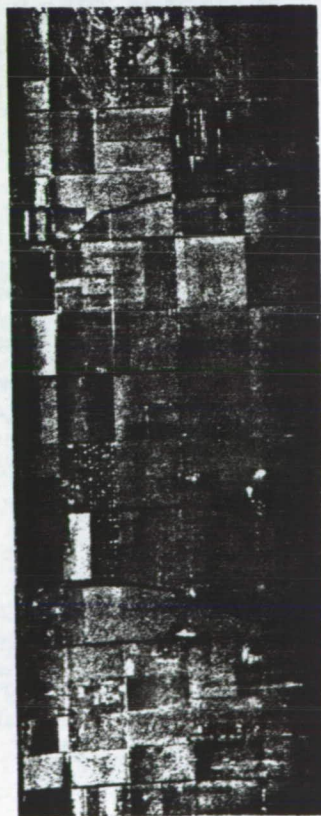
Probably the single continuing investigation of multifrequency SAR has been that of the Death Valley, California, region by the U.S. Geological Survey (Flagstaff) and JPL. This excellent investigation has furthered the understanding of radar interaction with terrain. Death Valley has series of areas with different sizes and geometry of surface rocks of homogeneous roughness within a prescribed area. From such a natural "controlled" experimental area much has



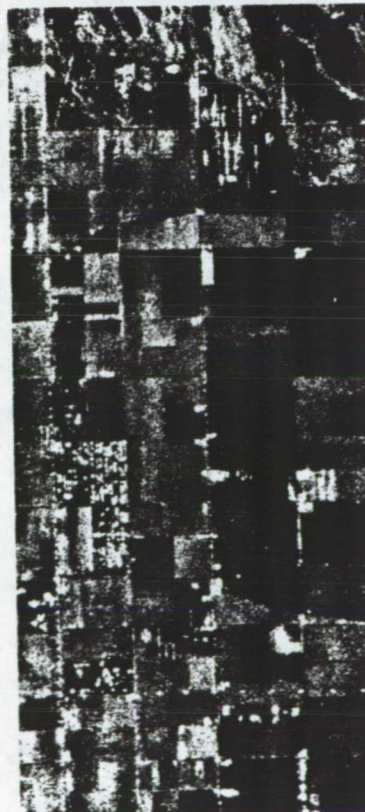
X-BAND CROSS POLARIZATION
30' x 30'



L-BAND CROSS POLARIZATION
30' x 30'



X-BAND PARALLEL POLARIZATION
30' x 30'

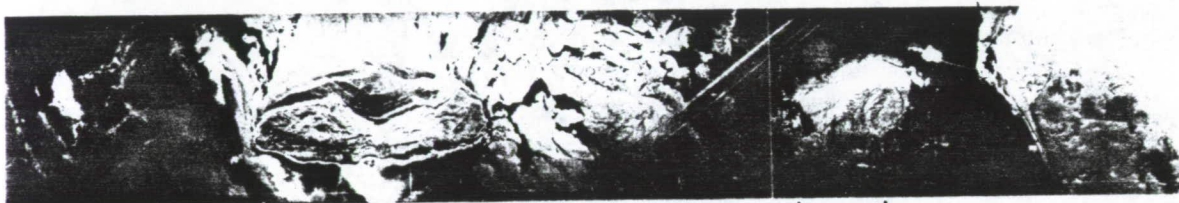


L-BAND PARALLEL POLARIZATION
30' x 30'

Figure 3. Four-channel SAR imagery of Arizona agricultural area: XHH, XHV, LHH, LHV.



X-BAND PARALLEL POLARIZATION 30' x 30'



X-BAND CROSS POLARIZATION 30' x 30'



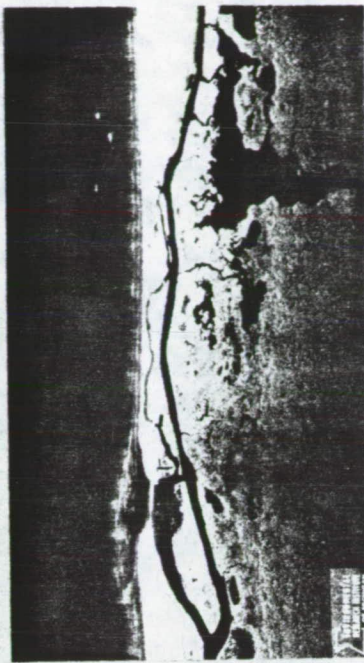
L-BAND PARALLEL POLARIZATION 30' x 30'



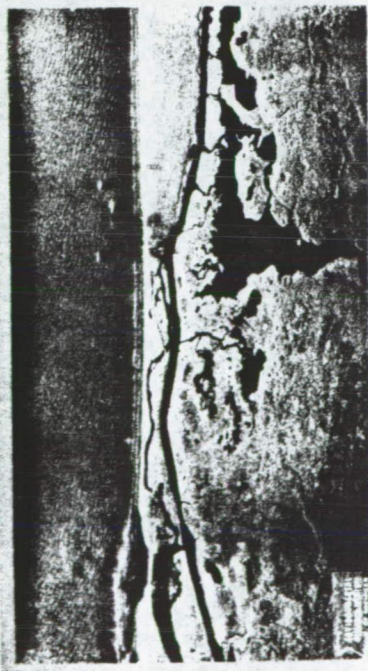
L-BAND CROSS POLARIZATION 30' x 30'

Figure 4. Multichannel SAR imagery of ice: XHH, XHV, LHH, LHV.

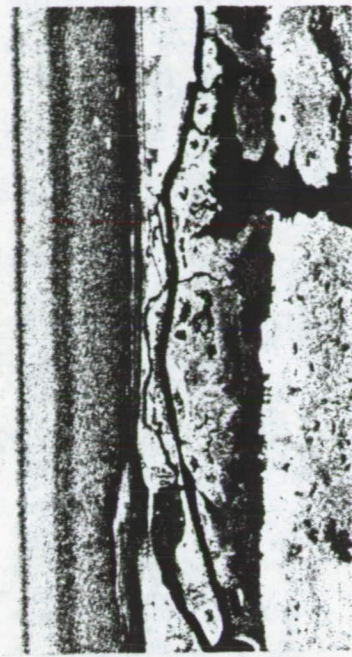
ORIGINAL PAGE IS
OF POOR QUALITY



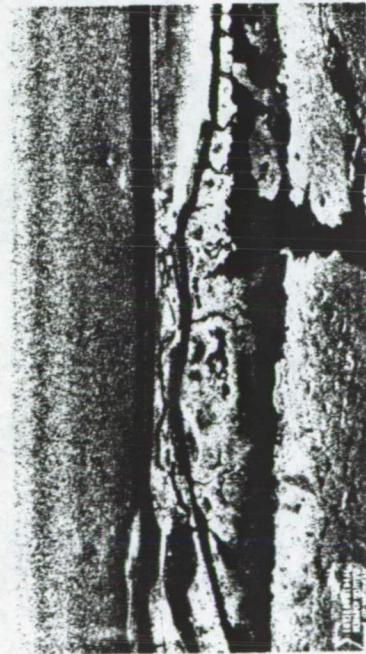
X-band HV



X-band HH



L-band HV



L-band HH

Figure 5. Multichannel imagery of ocean, shore and wetlands, XHH, XHV, LHH, LHV at Marineland, Florida.

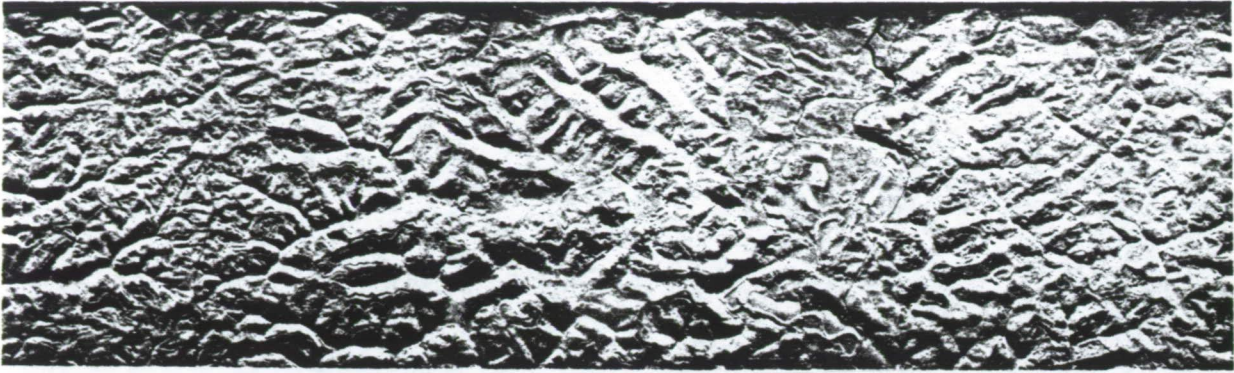


Figure 6. Four-channel SAR imagery of the Cottageville, West Virginia, shale gas field in the Appalachian Plateau. From top: XHH,LHH,XHV,LHV.

been learned about radar interaction with roughness. Schaber et al. (1976) first investigated the effect of surface roughness on 25-cm wavelength, and were able to show the dependence of returns on roughness and relate these returns to the Rayleigh roughness criterion. Daily et al. (1978), using L-band (25 cm) like and cross-polarized and X-band like-polarized returns achieved "...nearly complete discrimination of surficial geologic units." For discrimination they used three axes, a frequency ratio, a polarization ratio, and a single-channel image - and located the vectors for each surficial geologic unit in three-dimensional space. Also they found that in one unit, composed of angular blocks, few depolarized returns were observed. It was also believed that the 25 cm penetrated to the brine water table. Daily et al. have achieved probably the most advanced digital analysis on SAR data, even though such analysis is often applied to MSS data.

Recently Schaber et al. (1979) have studied lava flows in Arizona, finding that "...multifrequency, multipolarization radar image data can be of significant value in geologic and morphologic analysis of volcanic surfaces, especially when used in conjunction with visible to thermal IR and field observations." They found effects that can be explained by direct surface reflection, multiple scatter and Rayleigh scatter, but further work is required for roughness statistics and absolute cross-section measurements.

The ERIM four-channel SAR is now located in a Canadian Bureau of Mines and Resources CV-580 aircraft. Under the Canadian SURSAT program, continuing studies are being undertaken of multichannel radar applied to geological test sites as well as agriculture, wetlands, forestry, and ice test sites. The studies are just now commencing, with only preliminary results, which are inconclusive at present. An example of four-channel imagery is shown in Figure 7 by courtesy of INTERA, the prime contractor for the studies. This is a region of lakes near Yellowknife, Canada. Some lineaments are evident which may be faults. The gain in discrimination by multichannel over single-channel SAR is not evident in this form and must be evaluated with digital analysis.

The state-of-the-art of geologic interpretation with multichannel SAR can be gleaned from the description of the foregoing investigations and illustrations. The potential for effective geologic interpretation appears to be there, but a convincing, repeatable basis for its superiority over single-channel SAR is not yet demonstrated for exploration and other purposes in regions which do not have the characteristics of the distinct, definable, almost laboratory-like surfaces of Death Valley, or of the almost amorphous, densely vegetated Appalachian plateau.

State of the art of SAR sensor development is far ahead of SAR application. Reliable, high-resolution multifrequency and multipolarity SAR exists. Four channels (XHH, XHV, LHH, LHV) can be imaged simultaneously. This ERIM radar can be used with any depression angle, has 5-ft-range and 7-ft-azimuth resolution with a 6.6-km swath width. Also, it has wide swath width capability of 18 km with reduced resolution. Real-time digital readout with 1000 samples swath is installed in the aircraft.

IV. SYSTEM PARAMETERS AND DATA PRODUCTS

System parameters for SAR have been defined for some time (Rydstrom, 1959).

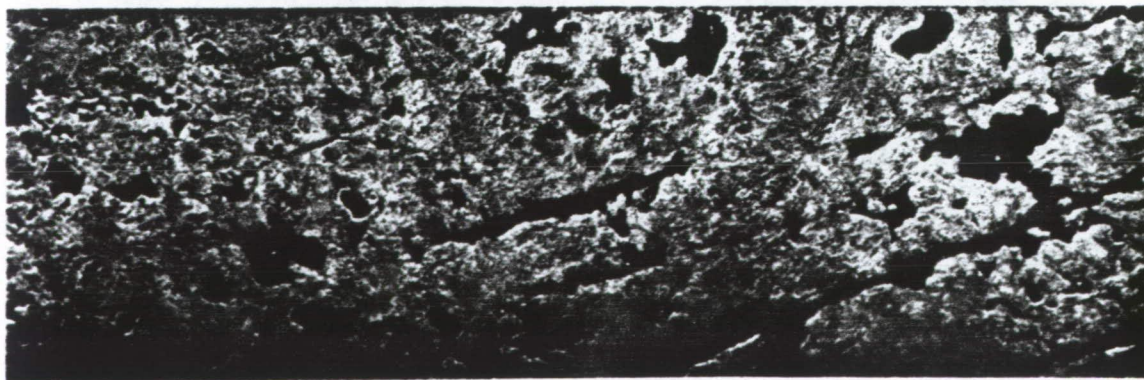
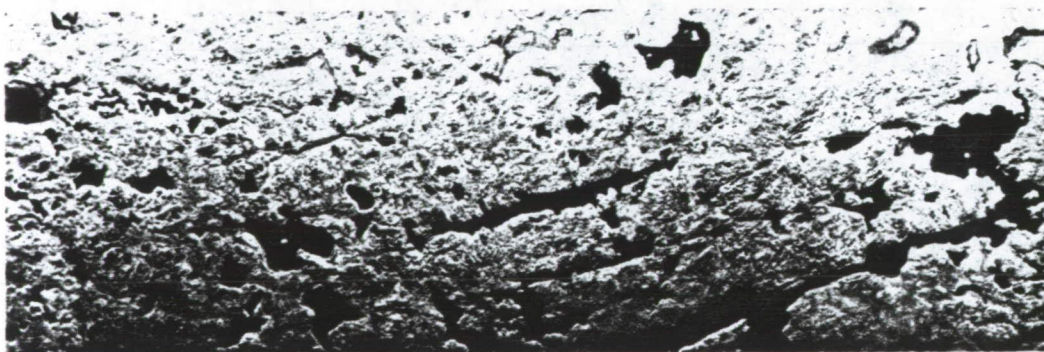
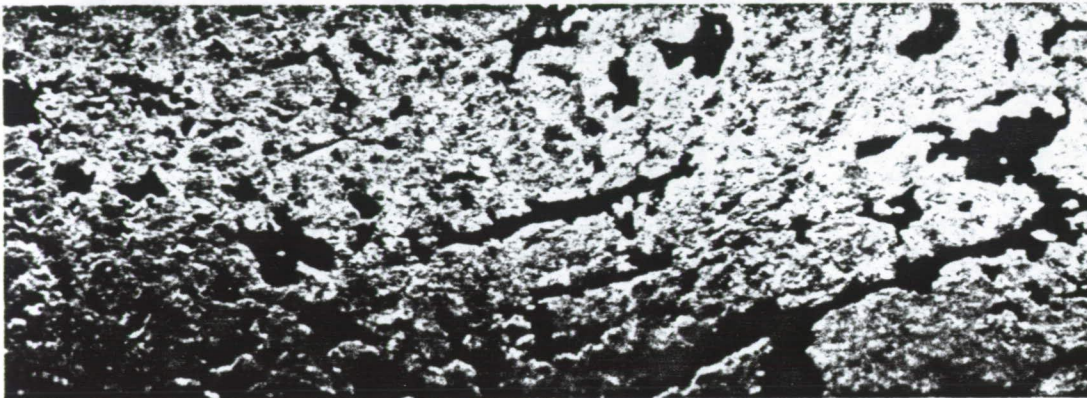
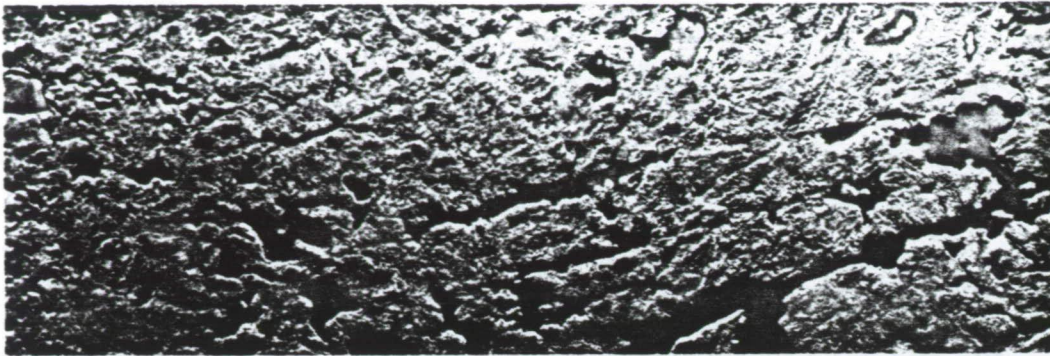


Figure 7. Four-channel SAR imagery of a region near Yellowknife, Canada: XXXH, XHV, LHH, LHV. (Courtesy of Intera, Inc.).

These include the following:

- (1) Frequency
- (2) Polarity
- (3) Incidence angle
- (4) Surface roughness
- (5) Dielectric constant

To these classically referenced parameters one might, depending on one's inclination and concept of definition, add the aspect, or azimuth angle. Certainly if one specifies orthogonal looks at a geologic feature, one is, in effect, asking for another measurement parameter.

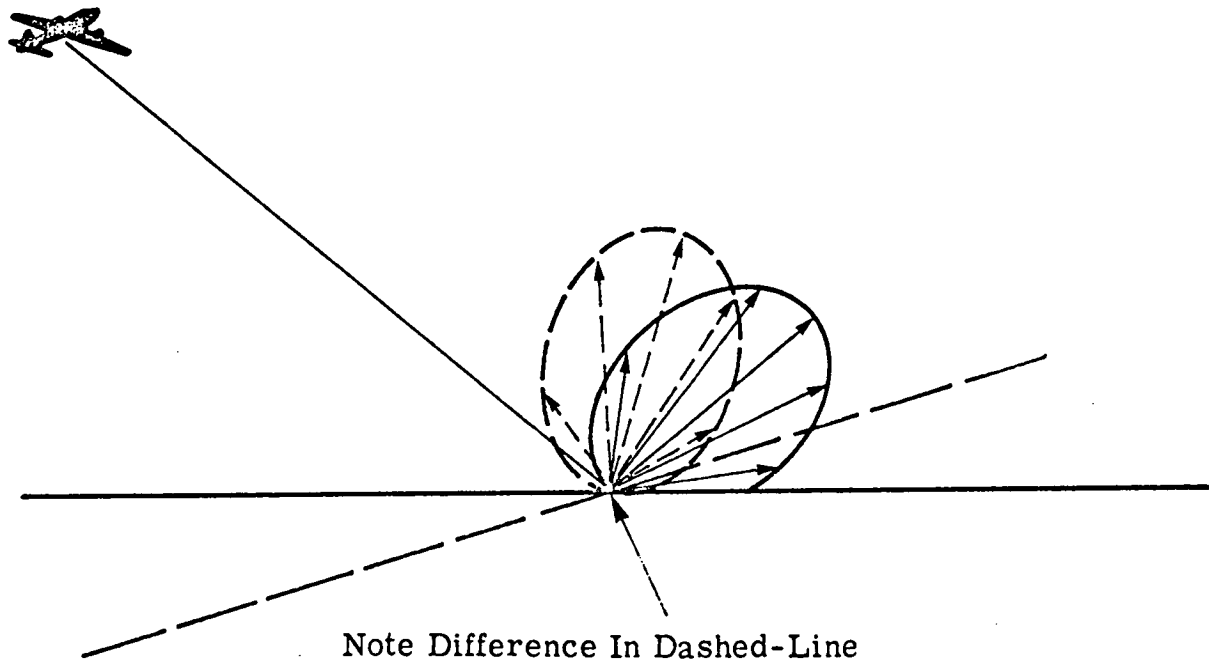
Our particular concern is that of multichannel SAR encompassing the interaction of frequency and polarity with the geometry of the terrain.

For multifrequency to be diagnostic a particular terrain geometry must affect at least two radar wavelengths differently, so that a differential return between the two wavelengths occurs. There would be, of course, no diagnostic aid if the return were the same for two wavelengths over many kinds of terrain. However, if the return were the same for one kind of terrain and different for others, that fact in itself would be diagnostic. Because the primary influence on the amount of return is surface roughness, which is defined in terms of the radar wavelength, it is almost inevitable that the amount of radar return will differ between wavelengths. If it differs in a repeatable manner for each type of lithology, frequency diversity can prove useful.

Such repeatability may be hard to come by, however, because of the high sensitivity of incidence angle, hence slope of the terrain. Figure 8 illustrates this sensitivity to slope. The solid radial diagram lies on the edge of the radar return direction. A small angular change in terrain slope (which is doubled in the radial pattern of reflection) can cause a greatly amplified change in the return to the SAR. Examining the diagram of Figure 8 leads one to easily (uneasily?) see that extricating the influence of roughness from slope or vice versa can be extremely difficult. As almost no terrain is free from slope changes, most areas will produce the combined effect of roughness and slope. The repeatability of SAR returns for lithologic surfaces must be carefully investigated.

Polarity diversity is the other discriminating feature of multichannel SAR. Except for the relatively straightforward cases where blocklike facets produce low depolarized returns (Daily et al., 1978; Schaber et al., 1979), we know little about depolarization by geologic or other materials, despite extensive theoretical work. Many cases of differences in depolarization occur (e.g., Figures 2-6) which have not been explained.

The radar system completely controls the parameter of frequency (although a purist might say that the Doppler effect from a moving object also partially controls frequency). The choice of frequency and initial angle of incidence (depression angle) can be important in obtaining data but, as stated above, the angle of incidence is modified by the local slope of the terrain.



Note Difference In Dashed-Line
Component Of Reflection To SAR

Figure 8. Diagram illustrating the sensitivity of slope to SAR. Arrows represent radial diagram of partially diffuse reflection.

Dielectric constant, which is the parameter dependent upon the composition of the reflecting material and governs the amount of reflection from the material, is a secondary effect when it comes to the actual radar return to the SAR.

The combination of frequency diversity and polarity diversity is used for multichannel SAR. The parameters governing multichannel SAR are so intertwined that isolating any one of the terrain parameters - roughness, incidence angle (slope) and dielectric constant - requires almost perfect laboratory conditions.

Data products are identical to those of MSS - separate images, composite images, digitally processed data such as ratios, digitally analyzed data for identification of areas, spatially processed data for lineament enhancement. Although different parameters of the terrain interaction mechanism are dominant in MSS and SAR, digital analysis only is applied to the differences between channels. For this reason the same analysis procedures are valid for SAR as for MSS. The interpretation, however, may differ considerably.

V. ANALYSIS AND INTERPRETATION TECHNIQUES

For geology, single-channel SAR has provided the most valuable information in structural variation of the surface (for example, defining geologic faults). This contrasts with areal classification as required for agriculture. However, areal classification is also valuable for geology in mapping lithological exposures. We therefore have defined two types of features we wish to interpret - spatial (or structural) and areal. For the former, single-channel SAR has been very useful, more so than other sensors, and for the latter it has sometimes been adequate, but often not as effective as other sensors. These two types are not exclusive. For example, structural features are often defined by abrupt changes in lithology.

We take analysis to mean the digital or optical operations upon the data to glean more information. For example, to take four channels of data and produce a color composite of various ratios is a form of analysis.

By interpretation we mean that we infer that a particular lineament is a fault, an arcuate structure is an intrusion, etc. We take the analyzed (or processed) data and infer as much as we can about the structure, composition, and geologic history of the imaged region.

I emphasize the difference between analysis and interpretation because the kinds of analysis are identical for MSS and multichannel SAR, but the interpretation can differ widely. The analysis methods which have been developed over many years for MSS can validly be applied to multiple channel SAR. The analysis methods are completely independent of the nature of the radiation-terrain interaction. Because one can measure the frequency dependence of reflectivity and emissivity of materials in the visible and near-visible range and can thus build up a series of curves has nothing to do with the analysis methods used.

Analysis only concerns the difference in return between channels. An array of responses to varied stimuli defines a physical object. If this array statistically or deterministically defines the object in a repeatable manner, then the nature of the stimuli or the theory of interaction between the stimuli and the object is moot so far as subsequent analysis is concerned.

The entire scope of MSS analysis methods is, therefore, available for multichannel SAR. These methods have been developed and proven over many years, and do not need to be enumerated here. However, SAR produces one spatial image phenomenon with no counterpart in MSS: radar speckle. This interference effect produced by the terrain is usually recognized as noise, but may have the potential of being diagnostic. New analysis methods unrelated to MSS analysis may be required to exploit (or eliminate) this phenomenon.

Because the wavelength/roughness ratio is not far from unity (unlike MSS) the radar returns are highly sensitive to small changes in surface geometry, which may be independent of geology. This may cause a wide variance between regions of the same geology, causing problems with dependable classification.

To aid in classification other types of remote sensing can be used in conjunction with SAR. If images are registered properly, multichannel SAR can be analyzed as added channels to MSS. The intermingling of MSS and SAR channels widens the scope and refines the discrimination of remote sensing data. Intermingled data can be analyzed and enhanced precisely the same way as data exclusive to either MSS or SAR.

Work by Holmes (1979) has shown the diagnostic richness of multichannel radar for agriculture. He determined the first four eigenvectors (principal components) of the four-dimensional multichannel space. He found data variability along the principal eigenvector as

62% - sum of two polarizations of L-band

21% - sum of two polarizations of X-band

14% - difference between X-band polarization

3% - difference between L-band polarization

This work of Holmes (1979) is the only investigation of multichannel radar data variability of which we are aware.

VI. VALUE OF TECHNIQUES AND RESULTS

The value of data analysis techniques of multichannel radar has not been conclusively shown for geology. The strip mining example (Figure 2), in which an old prospecting cut was enhanced and interpretively revealed, certainly illustrates the principle that multifrequency radar can be used to enhance a linear. However, isolated examples such as this do not provide a solid basis for evaluation of a technique. Results are sporadic and preliminary because investigations have been either desultorily funded or pursued with inadequate sensing instruments.

Mathematical characterization of most terrain surfaces is achievable only when unrealistic simplifications are made. Therefore, one must await thorough, continuing investigations over a number of sites until a proper evaluation can be made.

The Death Valley investigations of Schaber et al. (1976) and Daily et al. (1978) have provided excellent reference data on nontypical (so far as mineral and hydrocarbon exploration is concerned) but eminently classifiable surfaces. These investigators have provided excellent background data that indicates multifrequency and multipolarity SAR can be useful.

In another field, agriculture, the investigation of Holmes (1979) on the Ohio River floodplain shows promise and direction for application to geology.

The Canadian investigations are in a preliminary stage, so no firm conclusions can be drawn from their work.

The plain fact is that the value of techniques (gathering, analyzing, and interpreting) for multichannel SAR is not known as this time. Sporadic experimental indications and theory are, however, promising.

VII. RECOMMENDATIONS FOR INVESTIGATIONS OF MULTICHANNEL SAR APPLICATION IN GEOLOGY

The recommendations are to:

- (1) Improve the empirical and theoretical basis of terrain-multichannel SAR interaction, including ground based scatterometer investigations similar to those used for agriculture (Ulaby, 1979).
- (2) Conduct intensive and continuing investigations at test sites with mineral and hydrocarbon potential, using thorough ground truth and many analysis techniques. Do not waste time and money on "one-shot" investigations. The Geosat test sites are recommended.
- (3) Couple digital analysis development closely with geologic interpretation, again in a continuing investigation.
- (4) Exploit the use of multichannel SAR, MSS and photography for the optimal combined use, and for the determination of the suitability of each type for individual sensor use.
- (5) Investigate radar wavelengths for geologic remote sensing. Evaluate them in comparison with the presently used X- and L-bands.
- (6) Make some use of the best multichannel systems available.

REFERENCES

- Bradley, G. A. and F. T. Ulaby, 1979, SR&T Review, ASME Quarterly Report 9 March 1979, NASA/JSC Contract NAS9-14052, University of Kansas Center for Research, Inc.
- Cosgriff, R. L., W. H. Peake, and R. C. Taylor, 1960, Terrain scattering properties for sensor system design (Terrain Handbook II), Engineering Experiment Station, The Ohio State University, Vol. XXIX, No. 2.

- Daily, M., C. Elachi and T. Farr, 1978, Discrimination of geologic units in Death Valley using dual frequency and polarized radar data. Geophy. Res. Letters, 5 (10), pp. 889-892.
- Holmes, A. A., 1979, Augmentation of Landsat with synthetic aperture radar for agricultural applications, ERIM report 130100-16-F, Ann Arbor, Michigan.
- Jensen, H., L. C. Graham, L. J. Porcello and E. N. Leith, 1977, Side looking airborne radar, Scientific American, 237, No. 4, 84-95.
- Rydstrom, H. O., 1967, Interpreting local geology from radar imagery, Geol. Soc. Amer. Bull., 78, 429-436.
- Sabins, Jr. F. F., 1979 (Chevron Oil Field Research Company), personal communication.
- Schaber, G. G., C. Elachi, and T. Farr, 1979, Remote sensing data of SP mountain and SP lava flow in north-central Arizona, submitted for publication.
- Schaber, G. G., L. Berlin, and W. E. Brown, 1976, Variations in surface roughness within Death Valley, California: Geologic evaluation of 25 cm wavelength radar images, Geol. Soc. of Amer. Bull 87, 29-41.
- Wagner, T. W., R. Vincent, B. Drake, R. Mitchel, and P. Jackson, 1972, Tunnel site selection by remote sensing techniques, Willow Run Laboratory, University of Michigan report 10018-13-F.

AUTOMATIC SHADING CORRECTION AND SPECKLE NOISE
MAPPING/REMOVAL TECHNIQUES FOR RADAR IMAGE DATA

Pat S. Chavez, Jr.
U. S. Geological Survey
Flagstaff, Arizona

ABSTRACT

Images recorded by radar imaging systems are being used more frequently and are proving to be useful in mapping various geologic information. Due to the way that radar images are recorded, they have specific problems which have to be considered that are not typical of non-radar images. Techniques have been developed to correct for shading problems, and to suppress speckle noise contained in the radar images.

I. INTRODUCTION

With the launching of Seasat, the planning of the Venus Orbiter Imaging Radar (VOIR) mission, and the new improvements that have been made to the various airborne imaging radar systems, there has been an increased use of radar images. Radar images can be collected by real aperture or synthetic aperture systems and can record the output data in different formats (LaPrade, 1976). The real aperture radar systems usually go directly to a negative film while the synthetic aperture systems can go to a negative or to digital format using several different techniques. The data that are recorded directly onto film can also be put into digital format by using a photo scanning system. Once in digital format, the radar images can be processed using digital image processing techniques. This paper will discuss two techniques developed by the author, (1) a technique to correct for antenna pattern and antenna pointing problems, referred to in this paper as "shading," and (2) a technique which identifies picture elements (pixels) within the radar image that have speckle noise, removes the noise, and generates a speckle noise image or map.

II. DISCUSSION

Side-looking airborne radar (SLAR) images are being used more extensively than ever before for geologic mapping projects in a variety of environmental settings (Rydstrom, 1967; Gelnett and Gardner, 1979; Cannon). Airborne radar data have become increasingly available since the mid-1960's, and we now have limited satellite radar data from Seasat which are currently being examined by a number of scientists, representing many disciplines, to determine their potential (Gray et al., 1973; Lewis and Waite, 1973; Commission on Natural Resources Report, 1977).

Until recently, most radar backscatter was recorded directly on negative film and then processed in a photographic laboratory to increase or reduce the amount of scene contrast. Currently, however, it is possible to have the radar data converted into digital format using several techniques. The simplest and least expensive technique, which always applies to real aperture and at times to synthetic aperture radar data, is to digitize the image directly from a film transparency by using a photo-scanning system. In many cases, especially if the user is going to use radar images that were recorded by a real aperture (brute force) airborne system several years ago, this is the only option available. A second choice, appropriate for synthetic aperture radar, is to revert back to the optical correlator and use the raw signal film to again correlate the radar image, but instead of using a piece of film in the image plane of the optical correlator, use is made of an image dissector, enabling the data to be digitized directly from the optical correlator at the image plane (Rawson et al., 1978). The advantage of this technique is that a larger dynamic range can be preserved and there are no problems introduced due to the different film characteristics. The third option is to start with raw signal records in digital format and correlate the data digitally. This allows for the preservation of an even larger dynamic range and there is no film involved at all. The problem with this technique is that it takes a considerable amount of computer time and is therefore quite expensive. Perhaps at a later date, when implemented on an array processor, it will be possible to process data at a more rapid and hence a less expensive rate. To the author's knowledge, there are only two groups that currently have this capability for producing digitally correlated Seasat radar images: MacDonald, Dettwiler and Associates (MDA) in Richmond, B.C., Canada; and the Jet Propulsion Laboratory (JPL) in Pasadena, California.

Two desirable features of the three correlation techniques are geometric corrections and antenna pattern corrections. Most of the radar images that have been generated up to now, both airborne and satellite, do not fully correct for these effects or for any antenna pointing errors that may exist in the data. Therefore, it has become necessary to use digital processing techniques to correct for these problems. This paper concentrates on techniques used for shading and speckle noise corrections on selected multifrequency and multipolarization radar data. The techniques were tested on images furnished to the author by Phillip Jackson and Robert Shuchman from the Environmental Research Institute of Michigan (ERIM). The images were generated by the ERIM synthetic aperture radar system under a contract to the Department of Energy for the Morgantown Energy Technical Center in West Virginia. The ERIM system records data simultaneously in X- and L-bands and in parallel and cross polarizations, i.e., multifrequency, multipolarization (MFMP). The techniques which I developed for these radar data can also be applied to radar data collected by other systems.

One of the advantages of the MFMP radar data is that the user can apply multispectral analysis and processing similar to that accomplished with Landsat MSS data (Ahern et al., 1978). The radar backscatter of various material types can be compared, and the multispectral and multipolarization information can be used to generate color composites, color ratios, and structural enhancements and as input for digital classification techniques.

III. AUTOMATIC SHADING CORRECTION

The extreme shading problem, which often exists in radar data, does not allow the user to take full advantage of the various types of processing techniques

mentioned above. The shading effects in the radar images can be so extreme that important terrain information is suppressed and some enhancements tend to extract the shading problem more than the information of interest. The shading effects can be introduced by the antenna pattern and/or an error in the pointing of the antenna during data acquisition (Figures 1 to 4).

Due to the fact that the antenna pattern and pointing data are often not available, especially for airborne systems, the author has developed an automatic shading correction for radar images. The computer technique which is currently being used examines a set of $N \times M$ square boxes of windows, usually 101×101 pixels each, and computes the average within these windows, excluding those values below a certain NMIN and above an NMAX. The values for NMIN and NMAX can be selected from the frequency histogram of the original image or a listing of sub-scenes within the image. The NMIN and NMAX values are selected in order to eliminate the effects of radar shadows and high returns, such as those from corner reflectors or speckle noise values, from the averages for the $N \times M$ windows. This allows the averages of the windows to be a better representative example of the shading function. The author is currently experimenting with different size windows spaced at different intervals. The optimum spacing for the X-band data sets used in this study was approximately 250 pixels, which generated an array of 5×11 boxes of 101×101 pixels in the data used, but should be less if the shading problem is extreme. This was the case in the L-band data sets which required an array of 9×11 boxes of 101×101 pixels. The latter array size has been made the standard default size for both X- and L-band data.

In this technique, it is assumed that the minimum shading effect in the radar image exists at the center of the image. Therefore, the shading correction coefficients are generated by dividing the averages of the various windows ($N \times M$ windows exist) into the average of the center window. This establishes an $N \times M$ array of coefficients which can then be used to correct the data, and the value of the center coefficient will always be equal to one. For the data points that fall within the $N \times M$ array, the program uses bilinear interpolation to compute the value of the coefficient needed to correct the data point. It has been found that at times it is best to actually use the average of all the windows that are in the center column of the $N \times M$ array. This concept is more statistically sound since more values are contributing to the average, and therefore the average is more representative of the overall image. One apparent problem with relying solely on the center window is the possibility of having the window centered on a particular material type not representative of the brightness distribution of the whole area. Thus when the other windows' averages are normalized to the center window, the generated coefficients will be influenced by the material type which is predominant in the center box.

The user can increase the window size in order to eliminate some of the effects of this problem. Because the largest amounts of shading effects usually occur in the scan direction and near the edges of the image, using the average of all the center column windows should not significantly affect the result, and should produce a better average for normalization of the other window averages. A minor problem that this may introduce is that there will be no fixed or constant spatial area that will remain identical to the original input values; that is, no one set place will always be multiplied by unity as was the case in the original technique in which the coefficient at the center of the image was always unity. Figures 1 to 4 show a comparison of the automatic shading corrections on the X-

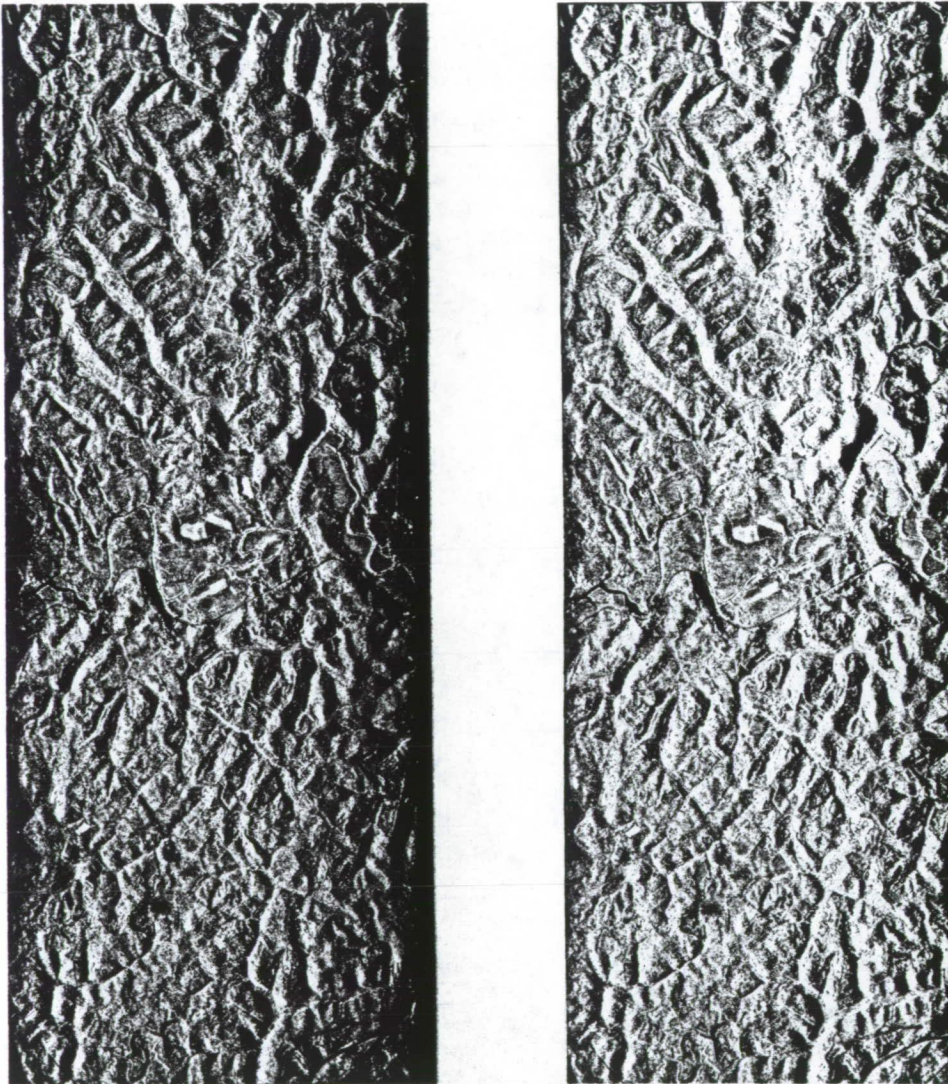


Figure 1. These two images represent the X-band parallel polarization (HH) before and after the automatic shading correction.



Figure 2. These two images represent the X-band cross polarization (HV) before and after the automatic shading correction.

ORIGINAL PAGE IS
OF POOR QUALITY

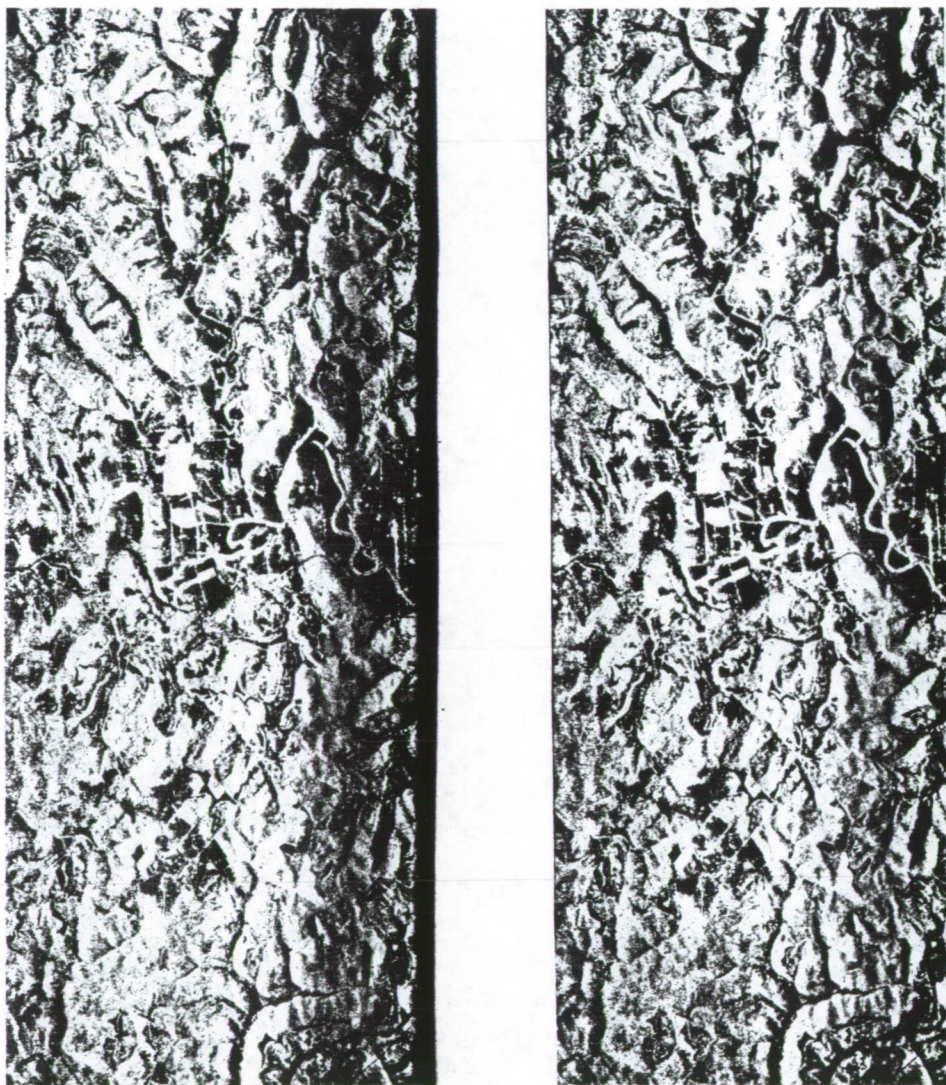


Figure 3. These two images represent the L-band parallel polarization (HH) before and after the automatic shading correction.

ORIGINAL PAGE IS
OF POOR QUALITY



Figure 4. These two images represent the L-band cross polarization (HV) before and after the automatic shading correction.

and L-bands with like and cross polarization. Figure 5 shows some examples of the ratios of the parallel to cross polarization before and after shading corrections.

IV. SPECKLE NOISE REMOVAL

The second step initiated to preprocess or clean up the radar data is the identification of the pixels containing speckle noise, and removal of speckle noise from the images. A technique similar to one perfected by the author to identify and remove bit errors from Landsat-3 band 8 (thermal infrared) data was used. Speckle noise has a resolution at a one-pixel scale, thereby creating an effect similar to bit error noise. The technique employs two steps: (1) applies a very small high-frequency spatial filter, either a 3 x 3 or a 5 x 5 pixel array to the digital data, and (2) uses the output of the filter with an appropriate tolerance to decide if a particular pixel has speckle noise (Figure 6).

The average of a 3 x 3 window subtracted from the middle pixel DN value provides information as to how much the DN differs from its neighborhood or the window that is being used. If it is assumed that, in general, there is a limit as to how much a point can vary from its close proximity, a 3 x 3 neighborhood in this case, then it can be stated that changes which occur outside this limit are caused by something other than the characteristics of the image information, which is assumed to be valid. By evaluating the histogram of the small spatial filter a tolerance can be selected that will suppress, or set to zero, all DN values in the original image which lie outside the selected limits. Once this has been done, a low-frequency spatial filter program is executed which acts as a smoothing filter and generates an average of a 3 x 3 or 5 x 5 box using only non-zero values. The program replaces only pixels of zero value with the average of the box. This results in the replacement of only the points which were identified as speckle noise and leaves unchanged the remainder of the original data. Usually, only a small percentage of the pixels are identified as speckle noise points. Therefore, it would be possible to write one program that would apply the small spatial filter, identify the noise, and smooth the data in a single operation. This would make the process more efficient, in terms of time and cost, than executing three separate programs.

Because the amount of speckle noise can be dependent upon the environmental target type or the texture of it, speckle noise might possibly be used as an interpretation parameter when mapping the various environmental targets (Phillip Jackson, personnel communication). Because of this, it may be useful to create a "speckle noise image" which shows what pixels were identified as speckle noise and removed from the original radar image (Figure 7). This type of image can then be used to check for different speckle patterns that may exist in the image and hopefully help in the mapping of the various units of interest. In addition, the speckle noise image or a spatial filter version of it could be used as input into a classification technique as a new parameter or dimension. The speckle noise image can also be used to check if any non-speckle information was removed. This can happen at times with corner reflectors or with very narrow (1-pixel-wide) linear-type targets (e.g., powerlines) that may exist in the radar image. These data can be retrieved by creating the speckle noise image.

Some of the advantages of removing the speckle noise from the image are identical to the advantages mentioned for the shading correction. One major advantage is that the user can generate larger scaled prints in the photo lab because the image will not appear blocky. The pixels within a small area will hold

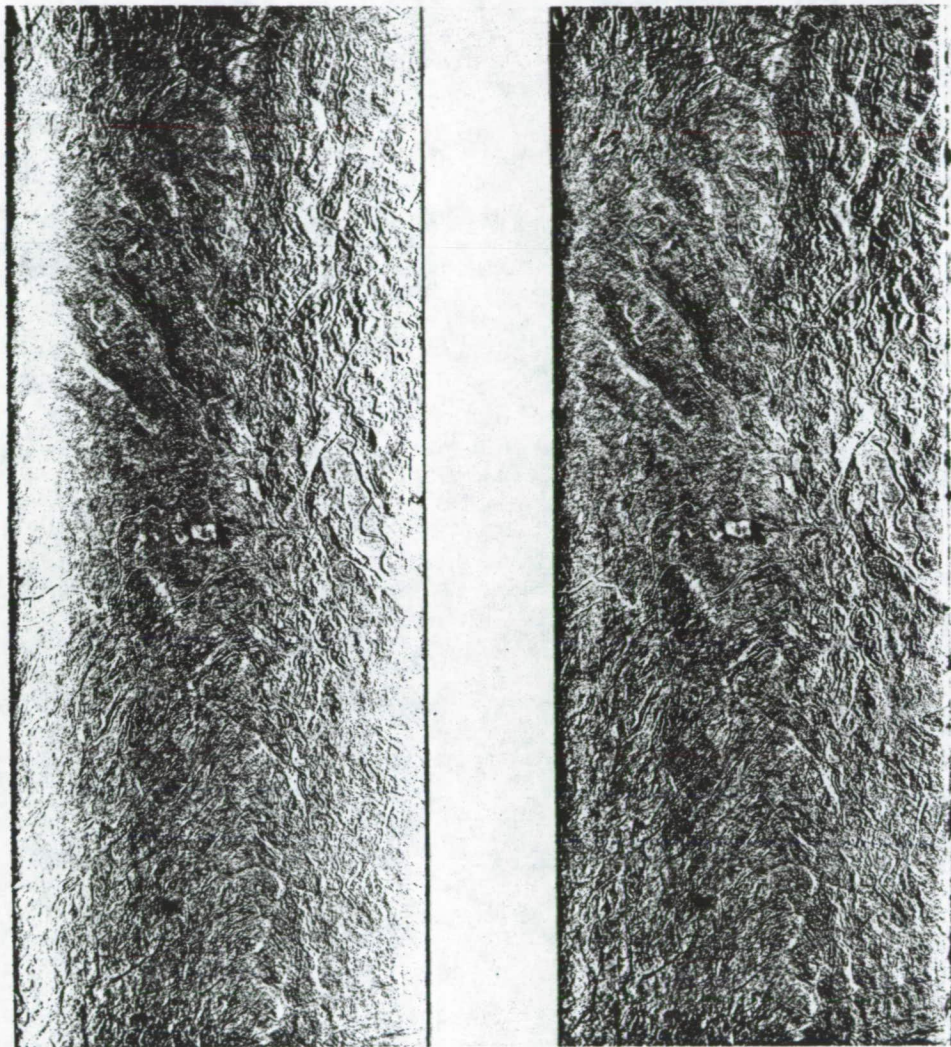


Figure 5. Shown above is the ratio of X-band HH to X-band HV (X_{HH}/X_{HV}) before and after shading corrections. The same linear contrast stretch has been applied to both ratios in order to keep the contrast differences only a function of the shading.

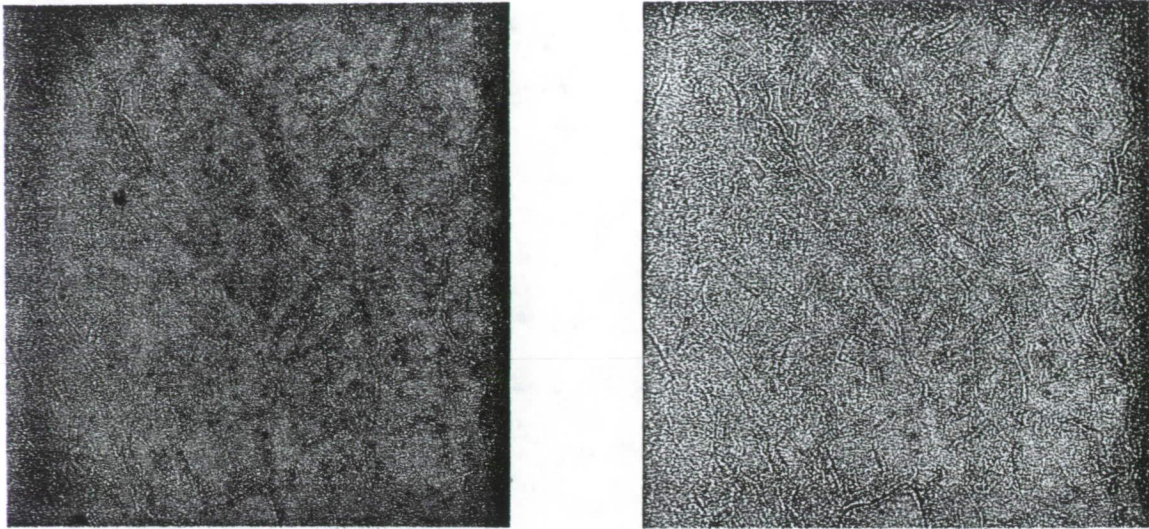


Figure 6. The two images above show the results of a 3 x 3 (left and a 5 x 5 (right) spatial filter on a portion of the X-band HH image. The results of the 3 x 3 filter with a set tolerance was used to identify pixels which have speckle noise.

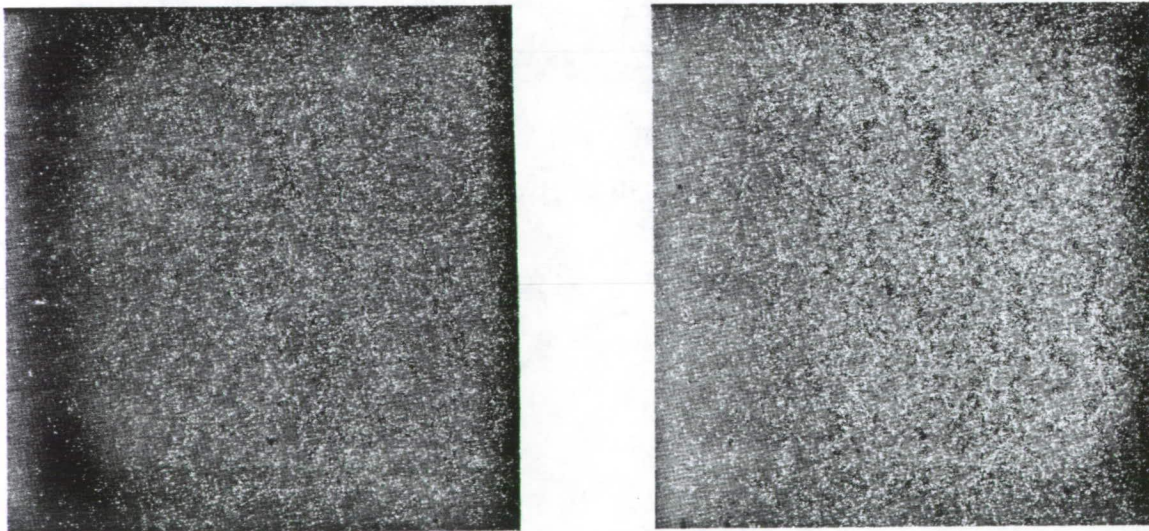


Figure 7. The two "speckle noise images" above show the pixels that have been identified as speckle noise using the results of the 3 x 3 spatial filter shown in figure 6. The left image represents speckle with a tolerance of plus and minus 25, and the right image represents the pixels with speckle with a tolerance of plus and minus 20.



Figure 8. The images above show a portion of the X-band HH before and after speckle noise removal. The image on the right was processed for speckle noise with a tolerance of plus and minus 22 DN using the 3 x 3 spatial filter shown in figure 6.



Figure 9. These two images represent the results of speckle noise removal using tolerances which are either too low (right) or too high (left). If the tolerance is too low there will still be some speckle left in the image. If the tolerance is set too high the image will be smoothed too much.

ORIGINAL VALUE
OF FOUR

together better, and the user will not be seeing individual pixels at these larger scales (see Figures 8 and 9).

ACKNOWLEDGEMENT

I would like to thank Lynda Sowers for her help in getting the data computer processed, and Lennis Berlin and Patricia Termain for the reviews of the text.

This paper presents the results of one phase of the research being done under contract W-13, 130, sponsored by the National Aeronautics and Space Administration.

REFERENCES

- Ahern, F. J., D. G. Goodenough, A. L. Gray, R. A. Ryerson, R. J. Vilbikaitis, M. Goldberg, Simultaneous Microwave and Optical Wavelength Observations of Agricultural Targets, Canadian Journal of Remote Sensing, V. 4, pp. 127-142, 1978.
- Application and Scope of Terrain Imaging Radar, Litton Aero Service Report, Goodyear Aerospace Division.
- Cannon, P. J., The Application of Radar and Infrared Imagery to Quantitative Geomorphic Investigations, Bureau of Economic Geology Publication, University of Texas.
- Gray, A. L., R. K. Hawkins, C. E. Livingstone, R. Lowry, R. Rawson, The Influence of Incidence Angle on Microwave Radar Returns of Targets in an Ocean Background, Canada Journal of Remote Sensing, 1978.
- Gelnett, R. H., J. V. Gardner, Use of Radar for Ground Water Exploration in Nigeria, West Africa. Proceeding of Thirteenth International Symposium on Remote Sensing of Environment, Ann Arbor, Michigan, April 1979.
- LaParde, G. L., Basic Concepts of Synthetic-Aperture, Side Looking Radar, Goodyear Aerospace Corporation Report, Litchfield Park, Arizona, 1976.
- Lewis, A. J., W. P. Waite, Radar Shadow Frequency, Photogrammetric Engineering, 1973.
- Microwave Remote Sensing from Space for Earth Resource Surveys, Report prepared by the Committee on Remote Sensing Programs for Earth Resource Surveys, Commission on Natural Resources, 1977.
- Rawson, R., A. Liskow, A. Klooster, R. Hamilton, Digitizing of SAR 77 Image Data, Final Report, Environmental Research Institute of Michigan, Ann Arbor, Michigan, October 1978.
- Rydstrom, H. O., Interpreting Local Geology from Radar Imagery, Geological Society of America Bulletin, V. 78, pp. 429-436, March 1967.

ENGINEERING/ENVIRONMENTAL PAPERS

Applications of Radar Imagery to Arctic and Subarctic Problems

P. Jan Cannon .

Radar Detection of Surface Oil Accumulations

John E. Estes, Peggy O'Neill, and Michael Wilson

Application of SLAR in Nuclear Power Plant Siting: A Case History

Barry S. Siegal

APPLICATIONS OF RADAR IMAGERY TO ARCTIC
AND SUBARCTIC PROBLEMS

P. Jan Cannon
Geology/Geophysics Program
University of Alaska
Fairbanks, Alaska

ABSTRACT

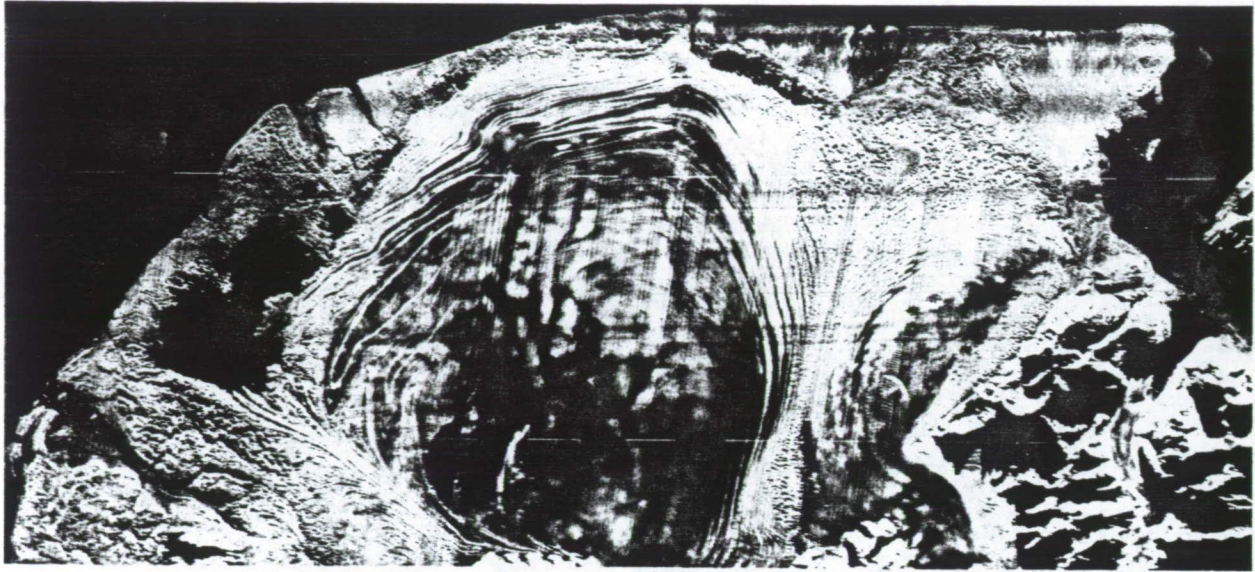
This report contains an assessment of the application of imaging radar to geologic problems in the form of a collection of 24 papers and recommendations for NASA's program in this field. The material was developed in the framework of a Workshop held in Snowmass, Colorado, from 16 through 20 July 1979, under the auspices of the Jet Propulsion Laboratory, California Institute of Technology, with sponsorship of the Resource Observation and Planetary Divisions of NASA.

I. INTRODUCTION

Radar imagery is one of the most modern techniques for collecting data which directly concerns a planetary surface. Radar imagery is important to scientists who are involved in planetary problems of a considerable range in scope. The ability of radar imagery to enhance minor landforms is important to geologic problems (Figure 1). The identification of a landform provides information which can be used to interpret the geologic processes which are shaping an area. The enhancement of landforms provides data which can be used in the following geologic problems:

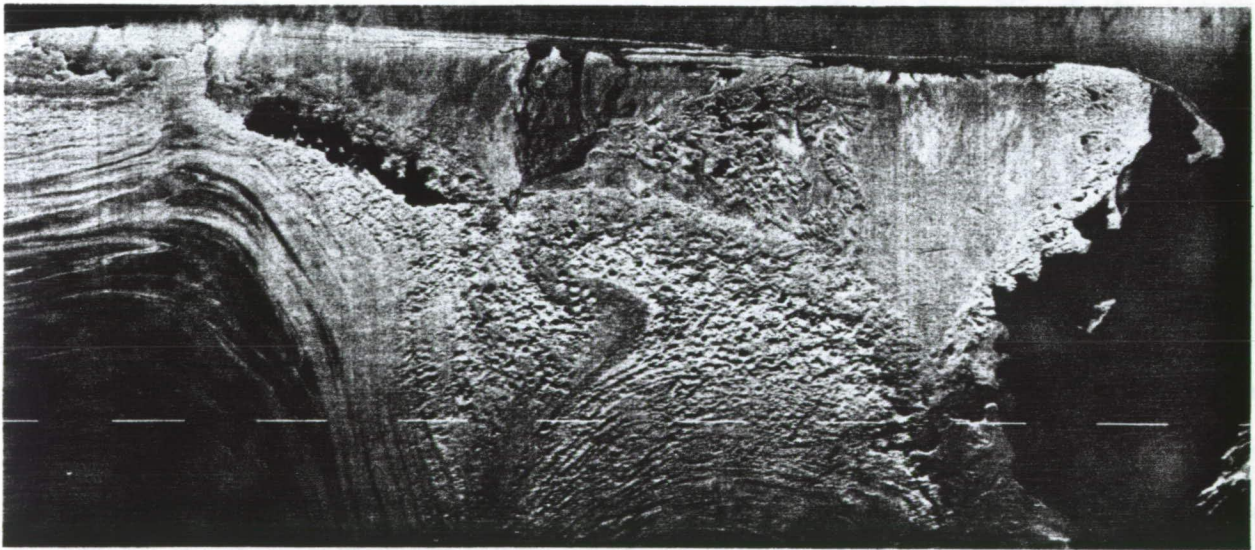
- (1) Floodplain mapping.
- (2) Ice jams during breakup.
- (3) Tectonics and related hazards.
- (4) Outburst flooding.
- (5) Regional structure.

Preceding page blank



PART A

1 _____ 10km



PART B

1 _____ 5km

Figure 1. Parts A and B are X-band, real aperture, radar imagery of the Malaspina Glacier of Alaska, taken with an APS/94D system. Part A was acquired at the scale 1:500,000. Part B was acquired at the scale 1:250,000. At both scales, the enhancement of the landforms around the margin of the glacier is apparent. Due to the differences in scale only a portion of Part A is shown in Part B. South is at the top of each part.

- (6) Rock type discrimination.
- (7) Geomorphic processes.
- (8) Gravel deposits.

Landform enhancement also provides data important to the biological problems of habitat identification and location. Since interpretation is dependent upon the scale and scope of the scene presented, there is a large information gap between the available products of aerial photography and Landsat imagery. Radar imagery can best fill this information gap.

II. ARCTIC AND SUBARCTIC RADAR IMAGERY REQUIREMENTS

In order to be applicable to geologic problems in the Arctic and Subarctic, radar imagery must meet the requirements listed in Table 1. These requirements are not unique to the Arctic and Subarctic. However, because of the climate and remoteness of the areas concerned, it is important to stress them as stringent guidelines. The requirements are to produce data useful to a geologic interpreter who is involved with a qualitative mapping problem.

The first requirement of wide dynamic range implies that sufficient levels of reflected radar energy be recorded by the radar imagery system that the resulting image can show at least 12 levels of gray. Interpretation is greatly aided by tones which are directly related to amounts of radar energy intensity which are reflected back to the receiver. The gray levels on the imagery should represent both functions of slope and surface roughness of the planetary surface. A radar imagery interpreter uses both functions along with spatial information to produce a model of the planetary surface.

Table 1. Arctic and Subarctic radar imagery requirements*

1. Wide dynamic range
2. Specific dates of acquisition
3. Moderate resolution
4. Intermediate scale
5. Variety of products
6. Look angle control
7. Look direction control
8. Timely product delivery
9. Data blocks
10. Indexes

* These are discussed in the text and are not necessarily unique to the Arctic and Subarctic.

The requirement of specific dates of acquisition is due to two things: First, when things happen in the Arctic, they happen fast, such as breakup. Second, processes and features of deep winter are poorly understood. Arctic data are needed four times a year: during deep winter, at breakup, just before freeze-up, and after freeze-up. Freeze-up sets the scene for the long Arctic winter; therefore, information about the location of water and ice at that time is needed to plan activities for the winter. Deep winter is a time when poorly understood processes are occurring and features unique to that time of year are being built by those processes. In particular are the problems associated with aufeis. Aufeis refers to sheets and lenses of ice which build up throughout the winter. It results from the freezing of ground water which is forced to the surface by hydrostatic pressure. It often dams up streams, causing flooding in winter and at breakup.

Information is needed about breakup because that is the time of year when not only the greatest changes occur in the Arctic and Subarctic, but the time when changes occur rapidly. Snow and ice, which have been accumulated over a period of several months, melt within a few weeks. This sudden melting produces running water from more than half of the year's total precipitation. The most extensive flooding occurs at this time.

Subarctic data are also needed four times a year. In addition to data during breakup, data are needed just before breakup in order to evaluate potential flooding hazards. Data are needed at the summer vegetation maximum because there is a greater abundance of vegetation types and amounts in the Subarctic than in the Arctic. Winter planning can be done with data taken after freeze-up.

Moderate resolution and intermediate scale are physical requirements needed to fill the geologic information gap for the image interpreter. Locating the area shown in an aerial photograph on a copy of Landsat imagery seems like a simple task. However, it can be an impossible task because of the large differences in resolution and scale. What an interpreter sees in one scene and uses for a reference cannot necessarily be seen in another scene. This information gap occurs in both directions, from aerial photograph to Landsat image or from Landsat image to aerial photograph. Radar imagery with a resolution of 15 to 25 meters at scales of 1:1,000,000 to 1:250,000 will fill this gap. This gap cannot be filled with photography because of limitations in photographic systems. Photographic systems do not present the extent of area in a simple contiguous view available from imaging radar systems. The spherical distortions from photographic systems are often a more serious handicap to interpretation than the geometric distortions produced by imaging systems. It is important here to stress that only by stereoscopic viewing of photography is the same amount of terrain information made available as is available from monoscopic viewing of radar imagery. Stereoscopic viewing takes time, extra training, and usually special equipment. A Landsat system cannot fill this gap because of the lack of terrain information available from such a system.

The information that is available from a remote sensing system is in some cases related to the types of format in which the data are available. For most projects that data could be made available in two steps. The first step would be negatives of graphic displays on the order of the "quick look" concept. The second step would be computer-compatible tapes for more detailed interpretation and analysis. The variety of products should be related to the timely delivery of those products - hard copy negatives first, with computer-compatible tapes a

reasonable time later. Negatives of images are very important to an interpreter. They provide a means by which positive copies can be made cheaply and rapidly. An interpreter may draw on and cut up several "working copies" until a satisfactory interpretation is attained. Then the information is transferred to a final map base of some type.

One of the great advantages of radar imagery is that its acquisition can be so constructed as to gain the maximum geologic information related to relief. During acquisition, the look angle and the look direction should be set in order to best fit the expected terrain. High incident angles of look should be used over low relief and lower incident angles of look should be used over high relief. The look direction should always be towards increasing relief such as from the shoreline landward.

The maximum interpretability of radar imagery requires that supporting data be made available. Data blocks on the radar imagery should include such things as location of some point or edge, aircraft heading and aircraft altitude. Indexes showing the centers or one edge of a flight line are also helpful. Footprint indexes are expensive and time consuming to make. Good remote sensing interpreters do not need or want footprint indexes.

III. RADAR IMAGERY OF ALASKA

Radar imagery has been acquired of portions of Alaska in order to supplement information about environmentally important geomorphic features and associated natural processes. The unique ability of radar imagery to enhance subtle geomorphic features provides information on a perceptual level that has, only recently, become available to scientists in Alaska.

The northwestern part of Alaska along the eastern shore of the Chukchi Sea is a potential source of petroleum. The largest village in the area and presently the most important for petroleum-related activities is Kotzebue. Figure 2 is X-band, real aperture, radar imagery which shows the Alaskan coast from Cape Blossom to Cape Krusenstern. This is wintertime imagery which shows the fracture patterns in the offshore ice. Wintertime radar imagery like that shown in Figure 2 could be used in designing and locating well sites.

Figure 3 is wintertime radar imagery of the central part of the Seward Peninsula. The area was covered with about one meter of dry snow when the imagery was acquired. The snow which falls from September to May does not melt until late May or early June. In this area, at the time the radar imagery was taken, the total snow accumulation was 1.2 meters, according to the 1976, NOAA Annual Weather Summary for Nome and Kotzebue. A field measurement taken by this author at the time was 0.91 meters of snow on the ground. This is the compacted accumulation. The recent lava flow west of Imuruk Lake shows distinctly, although the entire scene was snow covered. This ability to enhance landforms through a continuous snow cover is unique to radar imagery. Radar imagery can provide landform information during the darkness of the Arctic winter, through clouds, and through dry snow. No other remote sensing technique can begin to approach this capability.

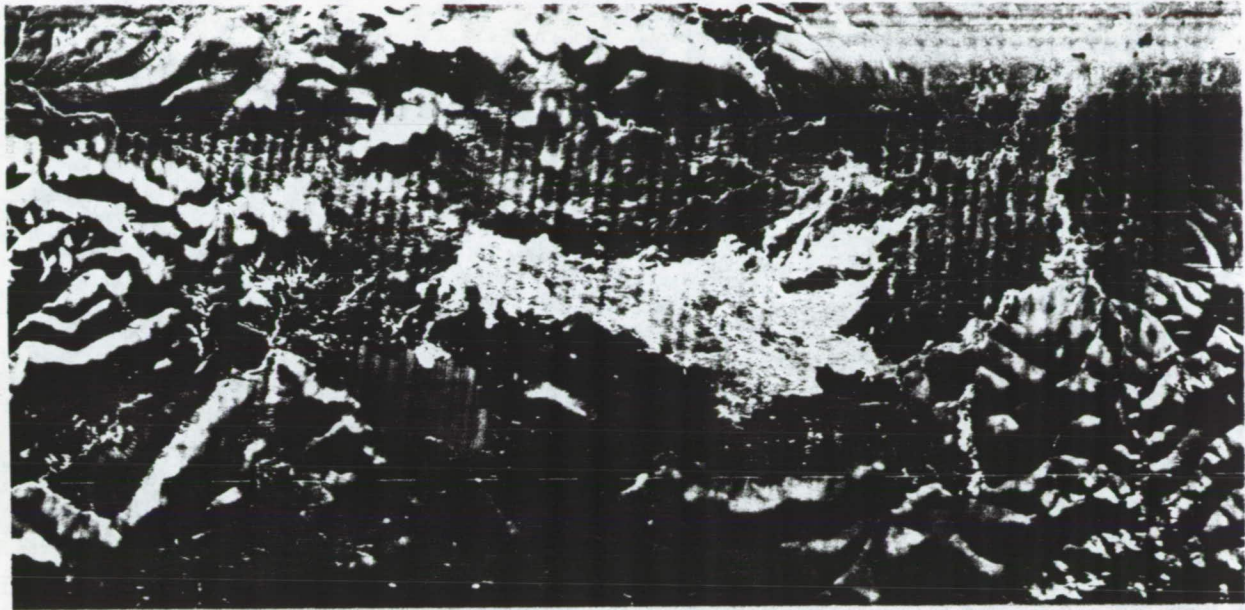
The radar imagery shown in Figure 4 is of the Amatusuk Hill, east of Cape Sabine, on the eastern shore of the Chukchi Sea. The folded geologic structures are sharply enhanced on the radar imagery. These type of structures are often



1 _____ 10km

Figure 2. X-band, real aperture, radar imagery of an area from Cape Blossom on the Baldwin Peninsula to Cape Krusenstern on the Chukchi Sea coast. The Noatak River is in the lower center of the scene. The imagery was taken during last winter. The textures and patterns in the ice are due to fracturing and surface freezing phenomenon. The short bright spike jutting out from the Baldwin Peninsula at Kotzebue is a winter time extension of the runway.

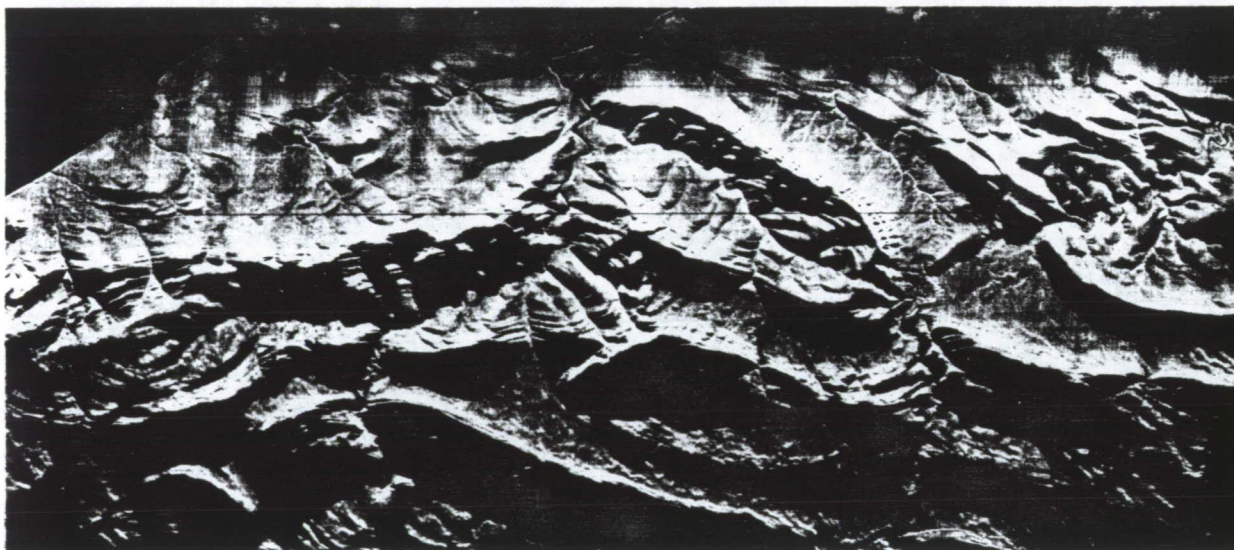
ORIGINAL PAGE IS
OF POOR QUALITY



1 10km

Figure 3. X-band, real aperture, radar imagery of the central part of the Seward Peninsula. This imagery was acquired during late winter when nearly one meter of dry snow covered the entire area. The bright area in the central part of the scene is a recent lava flow. The lava formed a delta in the frozen-over Imuruk Lake. This ability to enhance a landform, like the lava flow, through a continuous snow cover is unique to radar imagery. South is at the top.

ORIGINAL PAGE IS
OF POOR QUALITY



1 _____ 10km

Figure 4. Summer time, x-band, real aperture, radar imagery of the Amatusuk Hills, east of Cape Sabine. North is at the top of the scene. The bright lines on the sides of some slopes are individual stratum that reflect the radar energy more than the surrounding strata.

related to important petroleum deposits. Large deposits of coal are located in these hills and radar imagery could be used in planning and logistics related to the development of these coal reserves. Also, the imagery shown in Figure 4 can be used to obtain such basic geologic information as strike and dip of the sedimentary rocks and the continuity of the outcrop of a particular rock layer.

Talik lakes, formed by the loss of ground ice, occur in the Arctic and Subarctic zones of the North American and Eurasian continents. The talik lakes located on the Arctic coastal plain of Alaska are elliptical in shape and show a preferential direction of orientation. Radar imagery of parts of the Arctic coastal plain (Figures 5 and 6) shows that the orientation of the lakes is directly related to jointing or fractures in the adjacent bedrock. This enhancement of the geomorphic expressions of structure on radar imagery has provided the first real clue to the orientation of the lakes. It is anticipated that radar imagery of other parts of Alaska, when acquired, will provide similar geologic discoveries.

IV SUMMARY

Radar imagery provides year-around data acquisition of areas in the Arctic and the Subarctic. The information provided by radar imagery taken during the Arctic night is unique, and cannot be provided by any other remote sensing technique of present development.

Portions of the coastal plains of Alaska have been mapped using radar imagery as the major data source (Cannon, 1976). The foremost factor influencing the choice of radar imagery as the major data source was the demand for neoteric data. The weather is so adverse in parts of Alaska that radar imagery was the only remote sensing technique which could meet the demand. The major map products derived from radar imagery are landform maps and lineament maps. These maps are used to make environmental assessments of areas and to reconstruct the geomorphic history of certain regions or features.

Since radar imagery provides information about geologic structure and geomorphic features, it can be used to determine the relationship which exists between geologic structure and geomorphology. Important geologic information related to surface roughness can even be obtained through a dry snow cover (Figure 3). The movement and structure of sea ice is extremely important to the present biological and energy programs in the immense coastal zone of Alaska. Radar imagery is the only remote sensing technique which can provide the information needed about sea ice through a cloud cover and dry snow, during strong wind conditions, and throughout the Arctic night.

REFERENCE

- Cannon, P. J., 1976, Critical Landform mapping of Alaska using radar imagery: in 2nd Annual Pecora Symposium, Oct. 25-29, Proceedings, pages 144-160.

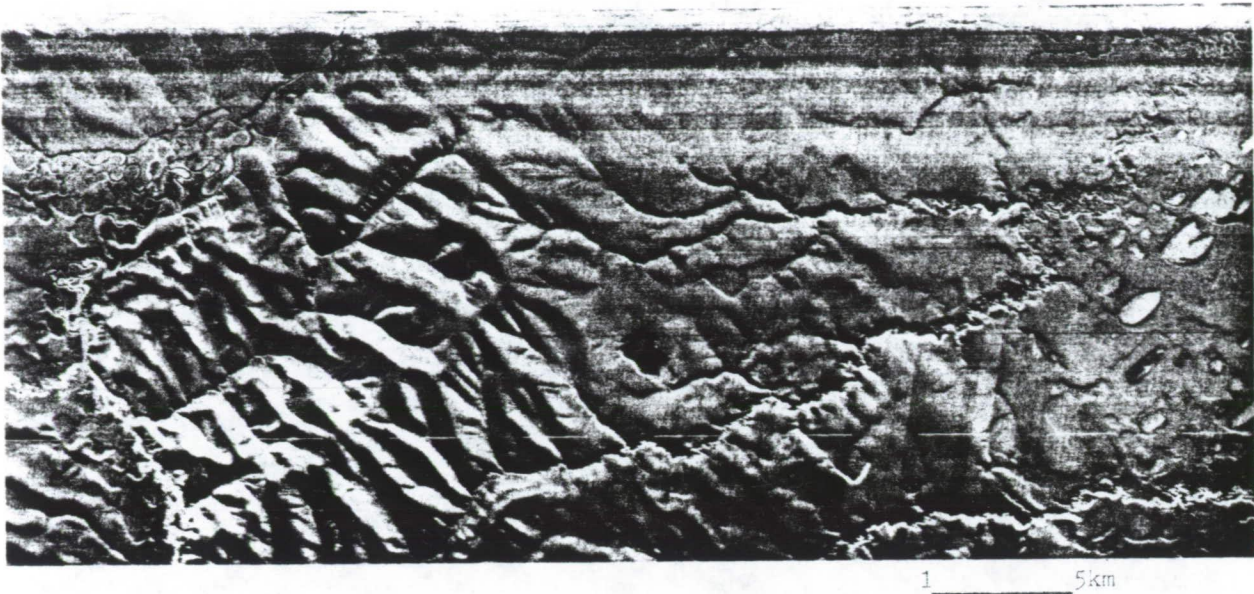


Figure 5. Late winter, x-band, real aperture, radar imagery of the margin of the Arctic coastal plain, north of the Brooks Range. The rectilinear lakes have their sides oriented parallel to the jointing in the underlying bedrock. The elliptical shaped lakes have their long axis oriented parallel to the jointing.

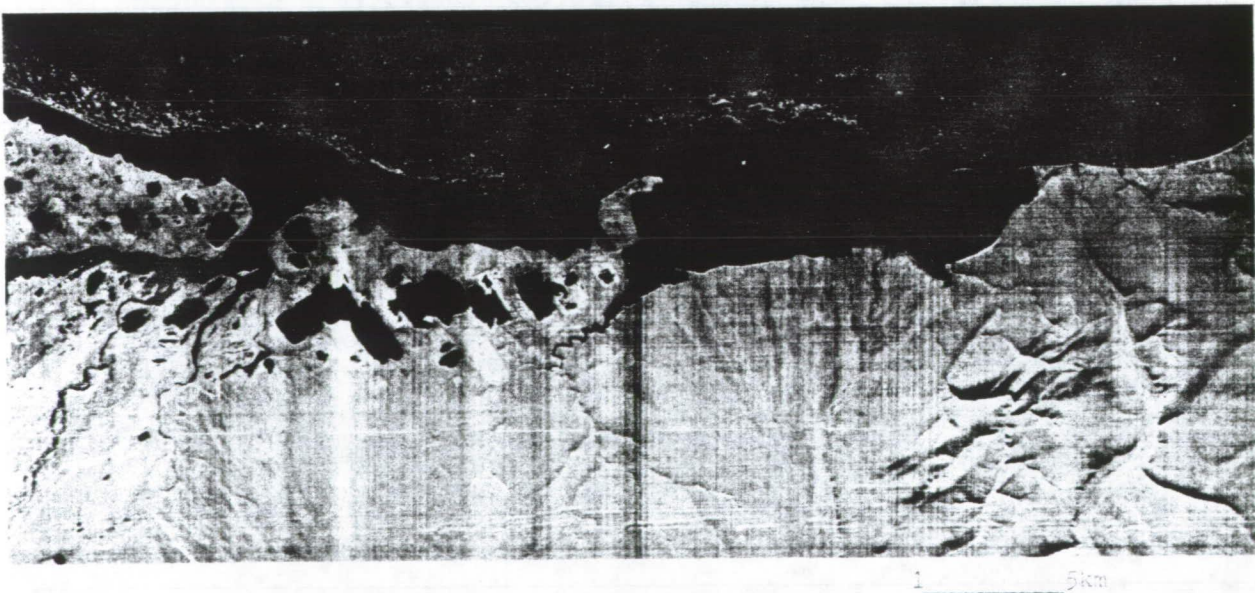


Figure 6. Mid-summer, x-band, real aperture, radar imagery of the Beaufort Sea coast east of Prudhoe Bay. The dog-leg projection near the center is Konganevik Point. The bright specks offshore are ice floes. The lakes are oriented with respect to the jointing in underlying bedrock. North is at the top of the scene. The large bright elliptical patch on the coastal plain is a drained lake.

RADAR DETECTION OF SURFACE OIL ACCUMULATIONS

John E. Estes
NASA/JPL/University of California, Santa Barbara

Peggy O'Neill and Michael Wilson
Geography Remote Sensing Unit
University of California, Santa Barbara

ABSTRACT

Researchers of the University of California, Santa Barbara Geography Remote Sensing Unit, have been studying the ability of remote sensing systems to detect, identify, measure and monitor marine oil accumulations since the early 1970's. As part of this effort, a number of experiments have been conducted on the potential of both real and synthetic aperture active microwave systems. These experiments have included work with both horizontally and vertically polarized X-band systems, as well as the Seasat synthetic aperture L-band horizontally polarized active microwave sensor.

The Santa Barbara Channel, off southern California, is an excellent test bed for conducting real world experiments on the capabilities of various remote sensor systems. Oil from natural seeps in the channel covers areas both large and small depending upon weather conditions, presenting researchers with a variety of target types in terms of both sizes and shapes. The persistent nature of these seeps also means that studies can be conducted over a range of sea surface and atmospheric conditions.

Although we at Santa Barbara are currently involved in assessing Seasat SAR data in this area, the results of an experiment conducted in May 1976 will be discussed in more detail here. The United States Coast Guard currently is developing AIREYE, an all-weather, day/night airborne surveillance system, for installation aboard future medium range surveillance (MRS) aircraft. As part of this program, a series of controlled tests were conducted off southern California to evaluate the oil slick detection capabilities of two Motorola-developed side-looking radars. The systems, a real-aperture AN/APS-94D and a synthetic-aperture coherent-on-receive (COR) were flown over the Santa Barbara Channel on May 19, 1976. Targets imaged during the coincident overflights included natural oil seepage, simulated oil spills, oil production platforms, piers, mooring buoys, commercial boats and barges at other targets. Based on an analysis of imagery from the coincident radar runs, COR provide better detection

of natural and man-made oil slicks, whereas the AN/APS-94D consistently exhibited higher surface target detection results.

This and other tests, as well as our ongoing Seasat SAR experiments for the United States Geographical Survey and the Natural Oceanic and Atmospheric Administration, have shown that active microwave systems do have considerable potential for aiding in the detection and analysis of surface oil accumulations.

I. INTRODUCTION

Oil is today simultaneously an irreplaceable resource as well as a pernicious pollutant. The need to know where and when marine oil slicks appear stems from both of these dichotomous outlooks. On one hand rapid detection and location of spills greatly facilitates efficient cleanup operations, as spreading and dispersal are thus minimized. At the same time, though they are not always linked to recoverable oil structures, naturally occurring oil slicks may provide preliminary surface evidence of undiscovered underground reserves (Halbouty, 1975). Through recent years, estimates of recoverable oil reserves in the coastal zone have consistently increased. Weeks (1965) set the world's potential offshore reserves occurring in water depths down to 1000 feet at 630×10^9 barrels, recoverable by primary production methods. Albers et al. (1973) have expanded this estimate considerably to 800×10^9 barrels for areas inside the 100 fathom line. These increases in total recoverable reserves are a continuing phenomenon which reflect a broadening definition of "recoverable," as well as the fruition of increasingly sophisticated exploration techniques (Wood, 1979). One such potential technique would employ airborne or satellite active microwave sensors for the detection of marine oil slicks.

Researchers of the University of California, Santa Barbara Geography Remote Sensing Unit (GRSU), have been studying the ability of remote sensing systems to detect, identify, measure, and monitor marine oil accumulations since the early 1970's. Recently, these experiments have focused on evaluating the oil slick imaging potential of both real and synthetic aperture as well as horizontally and vertically polarized active microwave systems. The data for these studies was obtained via low to medium altitude aircraft coverage. With the launch of Seasat-A, NASA's first dedicated ocean dynamics satellite, however, GRSU research efforts have expanded to include microwave sensors on orbital platforms. The imaging peculiarities of synthetic aperture radar (SAR) which remove absolute range to target as a limitation on resolution (Tomiyasu, 1978) have led researchers to believe that surface oil slicks might be detectable on spacecraft radar as well. With the support of the United State Geological Survey and National Oceanographic and Atmospheric Administration, GRSU personnel are currently involved in a verification test of this detection ability.

II. STUDY AREA

The test site for these, as well as several other similar imaging verification experiments (Kotlarski and Anderson, 1973; Mauer and Edgerton, 1975), has been in the area of natural oil and gas seepage found offshore at Coal Oil Point, California, in the Santa Barbara Channel. The consistent presence of these geological features has created the opportunity for a dedicated surface verification orientation to oil detection sensor performance. This area is known for

the extent and diversity of its seep activity, with observations concerning natural submarine seepage dating back to 1868 (Imray, 1868). Sandwiched between the major Santa Ynez and Santa Monica fault systems, the Santa Barbara Channel has undergone a complex sequence of faulting, folding and erosion (Vedder, Wagner and Schoellhamer, 1969; Dibble, 1966), and has all the geological prerequisites of high seepage potential (Wilson et al., 1974):

- (1) Strike-slip faulting associated with high incidence of earthquakes.
- (2) Tight compressive folding associated with high incidence of earthquakes.
- (3) Thick, geochemically mature Tertiary sediments.
- (4) Igneous activity and prolific source rocks.

The seafloor topography off Coal Oil Point consists primarily of fractured shale of the Monterey Formation, which in some areas is exposed but which in other areas is covered by a considerable overburden. The location of major oil seep activity lies within two miles directly off Coal Oil Point, with several distinct seep areas usually observable within this region (see Figure 1).

Although the rate of oil flow from natural seeps in the Coal Oil Point area is somewhat variable, oil slicks derived from natural seepage are generally noted on the ocean surface there year round. Estimates of oil flow rates as high as 900 barrels per day (Straughan and Abbot, 1971) have been made for the immediate area of Coal Oil Point; although more conservative appraisals in the 50 to 100 barrels per day range (Mikolaj, Allen and Schlueter, 1972) seem better justified on a sustained daily basis.

III. RADAR DETECTION MECHANISMS

The primary characteristic of the ocean surface which determines radar backscatter is roughness. For a perfectly smooth surface all incident radiation is specularly reflected forward and nothing returns to the receiver. At some threshold roughness levels, however, scattering tends away from purely specular towards a diffuse mode and some incident EMR is directed back at the sensor. This level of surface height variability is called the Rayleigh roughness length (h) and is dependent upon the specifics of radar wavelength (λ) and depression angle (B). The form of this relationship is

$$h = \lambda/8 \sin \beta$$

Oil on the ocean surface disrupts the distribution of wave frequency components and to some extent wave amplitudes. It depresses capillary and ultragravity waves by increasing surface tension, which is the restoring force at these wavelengths. It additionally interferes with the wind's ability to create longer period gravity waves (Barger and Garret, 1970) such that the entire high end of the ocean surface frequency spectrum is reduced in amplitude. As can be seen from the Rayleigh roughness equation, this physical damping mechanism occurs at a scale which lends itself to detection by active microwave sensors. The surface wavelengths which are selectively removed in the presence of oil are near in dimension to those wavelengths employed by the sensor itself. The microwave portion of the electromagnetic spectrum is generally regarded to run from 1 mm to 1m wavelength.

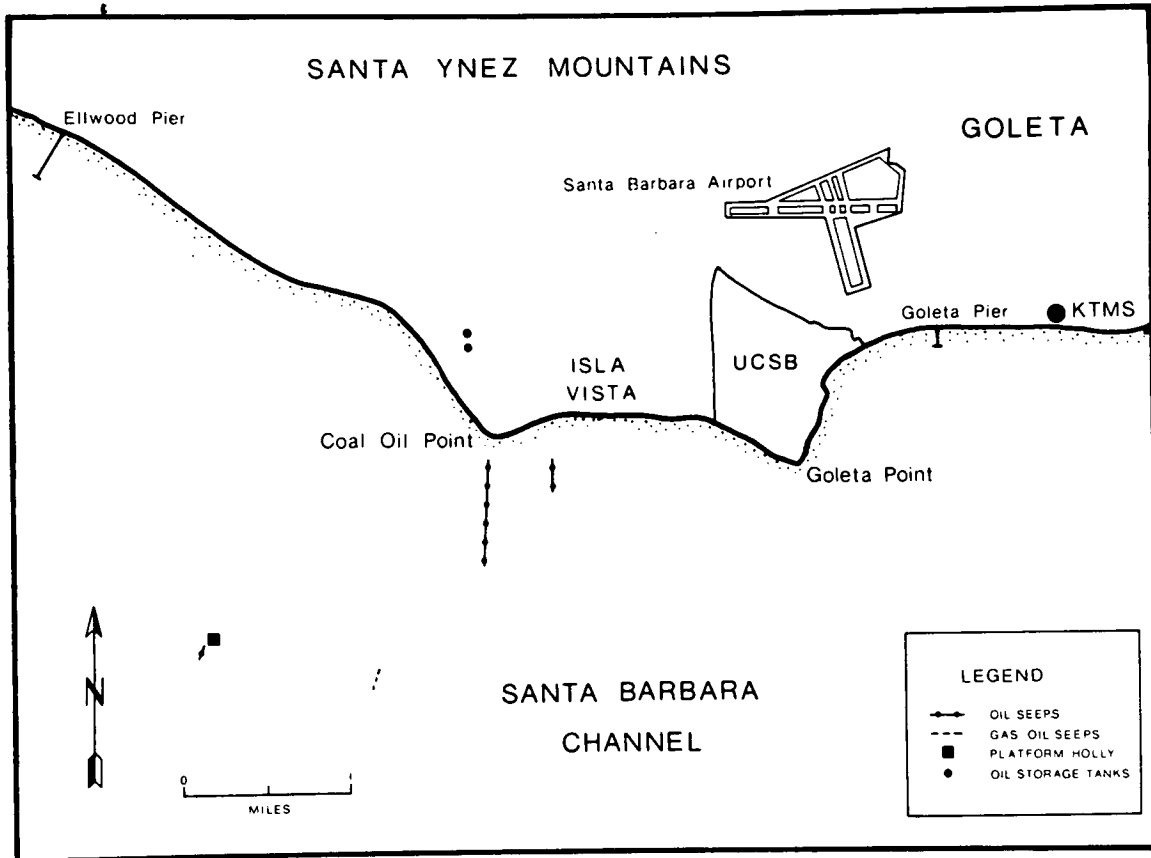


Figure 1. Map of the Coal Oil Point, California test site, showing the location of chronic natural oil and gas seeps present within two miles of shore. Note the long linear seeps between Coal Oil Point and oil production platform Holly.

An additional factor influencing the ability of radar to detect surface oil accumulations involves the backscattering criterion for an ocean surface which is somewhat altered from that of a simple dependency on Rayleigh roughness by the nature of the target. As superimposed wave fields are periodic perturbations, the opportunity exists for phase-reinforced multiple reflections from an ocean surface. This phenomenon was first observed and identified on over-the-horizon radar systems when the Doppler shift of the sea's return was observed to correspond to the phase velocity of waves with one-half the radar system wavelength (Crombie, 1955; Ingals and Stone, 1957). This reinforced reflection effect has been termed Bragg scattering (Raney and Lowry, 1978; Weissman and Thompson, 1977). It is both system wavelength and depression angle dependent with the surface wavelength being determined by

$$\text{Bragg wavelength} = \lambda / (2 \cos B)$$

(see Figure 2). For Seasat system geometry the Bragg wavelength is 34.35 cm, which is near the upper limit of the ultragravity wave spectrum (1.7 cm to approximately 25 cm). By damping in the capillary wavelength range and diminishing larger scale roughnesses by reducing boundary layer air/sea interaction, oil slicks mechanically alter ocean surface dynamics at precisely the scale which makes them most detectable by active microwave sensors.

IV. HISTORY AND STATE-OF-THE-ART

Upon examining (13.1 GHz) scatterometer data flown over open ocean oil slicks, Krishen (1972) observed 5 to 10 dB drops in the backscattered signal from that of adjacent clean surface areas. This response characteristic was studied over a wide range of conditions by van Kuilenburg (1975) in the controlled environment of a large wave tank. A fixed, dual polarization, X-band scatterometer (9.7 GHz) provided continuous backscatter readings of the water surface roughness, while a hydraulic wave ram and wind machine produced a variety of in vivo simulations. Periodically, oil of several types was introduced into the wave tank and the reduction in backscatter monitored. The result of this work is a contrast ratio table of radar backscatter for unaffected versus oil damped surfaces over a range of wind speeds, wave heights, and polarizations.

A more familiar active microwave sensor data product is the two-dimensional image format of side look airborne radar (SLAR). Analysis of this two-dimensional data is both complex and, in some instances, less than numerically exact. This latter drawback is due initially to the present inability to calibrate these imaging sensors, which limits broad application of the sort of contrast ratio analysis used by van Kuilenburg. Relative comparisons, however, can be made between datasets of varying look angles, frequency, polarization, target roughness, etc., but absolute return levels must be regarded with suspicion. There are several of these comparative studies of the response of imaging radars to oil slicks on the ocean surface: Guinard and Purves (1972), Kotlarski and Anderson (1973), Maurer and Edgerton (1975).

The desirability of a more quantitative approach to this sort of system verification research is self-evident. For any real applications task the mere presence or absence of surface oil slicks is only the initial information requirement. From either the pollution monitoring or the exploration standpoint, areal extent, thickness, chemical makeup, and persistence through time of oil slicks are all of equally vital concern. Although the detection of oil on water by active microwave sensing devices has been achieved by numerous research

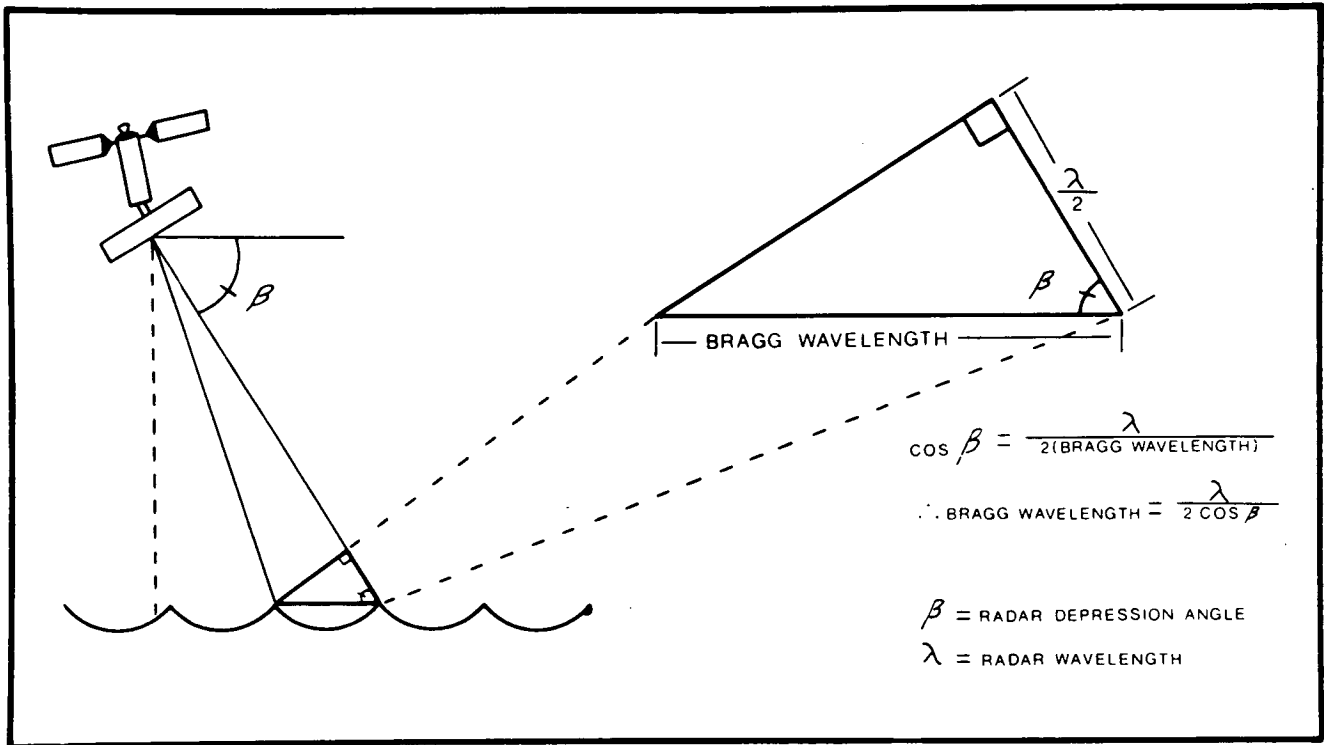


Figure 2. Of additional impact on radar return from an ocean surface is the periodic nature of superimposed wave fields. Given perfectly spaced surface waves, a phase-reinforced backscatter termed Bragg scattering occurs when the range (distance) from sensor to wave scattering surface equals one half the radar wavelength.

studies to date, more precise remotely sensed measurements of oil slick characteristics need to be forthcoming. The GRSU has moved in this direction in recent oil detection studies for the USCG, Aerojet General, USGS, and others.

V. AIRBORNE RADAR STUDIES

In April 1976 the United States Coast Guard contracted with GRSU to evaluate the oil slick and target detection capabilities of two X-band side-looking airborne radar systems being developed by Motorola to meet the service's AIREYE requirement (an all-weather, day/night airborne surveillance aircraft). Radar imagery from the two sensors, a real aperture horizontally polarized AN/APS-94D and a synthetic aperture vertically polarized coherent-on-receive (COR), was acquired during coincident overflights of the Santa Barbara Channel on May 19, 1976 (see Table 1 for system specifications). The principal objective of this test program was to document and compare overwater performance capabilities of real and synthetic aperture radars against a range of man-made and natural surface targets. As an integral part of performance documentation, GRSU provided sea truth data support and an assessment of the relative detection capabilities of the two systems.

Targets imaged during the radar overflights included natural oil seepage, simulated oil spills (oleyl alcohol), oil production platforms, piers, mooring buoys, commercial boats and barges, small pleasure craft and coastal kelp beds. The main intent of sea truth support activities conducted coincident with the AN/APS-94D and COR flights was to identify potential fixed, moving and surface pollution radar targets in each of the test areas and accurately record their locations. Sea truth data formats included low altitude aerial photographs, detailed sketch maps and extensive field notes.

Meteorological and oceanographic conditions were considered favorable for the radar tests on May 19th. Wind direction was 220° at 5 mps, and the swell direction was 270° with 1 m waves. Under such conditions the sea surface provides good radar backscatter contrast to oil-covered areas. Four distinct slicks caused by crude oil from the natural oil and gas seeps offshore at Coal Oil Point and in the western Santa Barbara Channel, as well as simulated oil slicks created by the controlled release of small quantities of oyleyl alcohol at two locations southwest of Coal Oil Point by Navy personnel, were present in the test area during the time of the coincident radar overflights and provided reliable targets for evaluating the oil detection capabilities of both systems. The four natural slicks ranged in size from 10.2 to 15.8 square kilometers, while the artificial slicks varied from a small slick estimated at 24 by 36 meters to a linear slick 3.65 kilometers long by 90 meters wide.

Radar imagery from 10 coincident APS-94D/COR overflights of the Santa Barbara Channel were compared with all sea truth information in order to determine how many of the known targets were interpreted as being present in the radar data. Based on summary results from the multiple data runs over the test area, GRSU investigators found that the horizontally polarized real aperture APS-94D consistently exhibited higher man-made surface target detection results. These results imaged 95.7% of possible targets (156 of 163) compared to 74.7% for the COR radar (121 of 162 targets) (Kraus and Estes, 1976). On the other hand, the vertically polarized synthetic aperture COR radar was significantly better at detecting natural and man-made surface oil slicks. The success rate was 65.8% (25 of 38 slicks) compared to 28.9% (11 of 38) for the APS-94D. Neither system

Table 1. System specifications

	AN/APS-94D	COR	OSDR-94	Seasat SAR
Aperture	Real	Synthetic	Real	Synthetic
Frequency	X-band	X-band	X-band	L-band
	9.1 GHz	9.315 GHz	9.3 GHz	1.275 GHz
Wavelength	3.3 cm	3.22 cm	3.2 cm	23.53 cm
Antenna size	4.9 m	2.46 m	2.46 m	11 m X 2 m
Polarization	Horizontal	Vertical	Vertical	Horizontal
Sensor platform	Grumman OV-1D aircraft (1976) HC-130B aircraft	C-47 transport plane	HC-130B aircraft	Seasat Satellite
Flight altitude	2000 m (1976) 2615 m, 770 m, 2000 m (1977)	1690 m	770 m, 2000 m, 2615 m	800 km
Actual swath	0-25, 0-50 km	0-25, 20-45 km (20 km range de- lay)	0-25, 0-50 km	100 km wide with 240 km range delay
Data format	Strip imagery/ photographic film	Real-time digit- al processing with 1, 2, or 3 looks; film imagery	Film imagery	Optically correlated film imagery. Digitally cor- related (4-look) computer compatible tapes with film writer output

detected the small oily alcohol spill. This failure was attributed to the limited surface areal expression of the slick, which was smaller than the minimum resolution cell size of the sensors. If the small artificial slick is excluded from consideration, the detection rate for surface pollution slicks is increased to 83.3% (25 of 30 slicks) for the COR and 36.7% (11 of 30) for the APS-94D (Figure 3).

In contrast to the COR, which detected surface concentrations of oil from all directions, the AN/APS-94D appeared to be very dependent on look direction for oil detection, imaging oil slicks only when the radar system was looking into the ocean swell direction. From the limited sampling data available, it was difficult to determine whether the poor performance of the APS-94D was due to the horizontal polarization of the antenna, the gain factor, or a combination of these and other factors. However, previous studies have shown that oil films reduce sea backscatter more for vertical than for horizontal polarization, with consequent improvement in oil detection capabilities for vertically polarized systems (Guinard and Purves, 1970; Krishen, 1972).

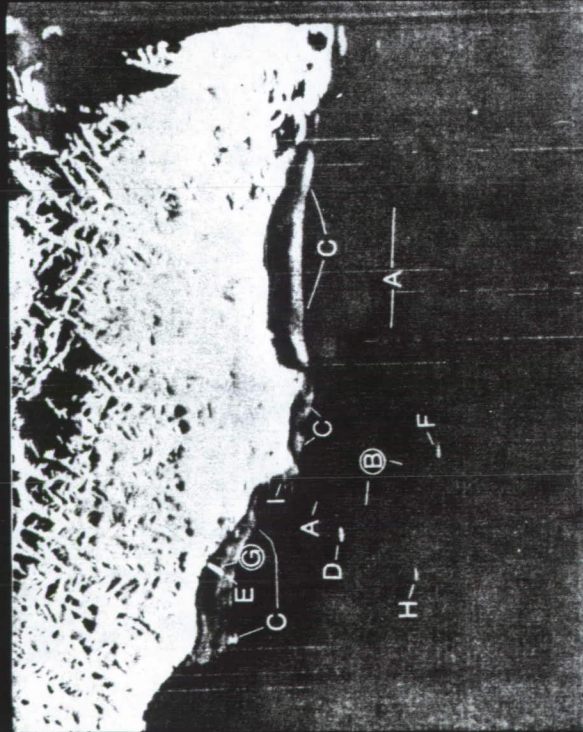
A similar microwave sensor evaluation study was conducted over the Santa Barbara Channel the following year by GRSU personnel on a different combination of sensing systems. In January 1977 the United States Coast Guard sponsored a flight test program to assess the performance of an airborne oil surveillance system (AOSS II) developed by Aerojet Electro Systems Company. The sensor package included horizontally and vertically polarized X-band real aperture side-looking airborne radars (SLAR), a passive microwave imager (PMI), a multi-spectral line scanner with ultraviolet and thermal infrared (TIR), and a KS-72 metric camera. The primary responsibilities of GRSU in support of the AOSS II evaluation program were to (1) provide comprehensive sea truth support for selected data acquisition flights over the Santa Barbara Channel, (2) verify image integrity of the data obtained with the radars, line scanner and aerial camera, and (3) assess the overwater target detection capabilities of the SLAR and the multispectral line scanning systems against man-made and natural surface targets, including oil slicks. Only the evaluation of the active microwave sensors will be discussed here; information on the remaining sensors can be found in AOSS II Systems Verification Test (Kraus et al., 1977).

Flown on an HC-130B aircraft, the AOSS II system included an X-band real aperture AN/APS-94D radar with a 4.92-m horizontally polarized antenna (identical to the system evaluated by GRSU in the 1976 Coast Guard study and an X-band real aperture Oil Slick Detection Radar (OSDR-94, a derivative of the AN/APS-94D) with an 2.46-m vertically polarized antenna. (See Table 1 for system specifications.) Multiple data runs to acquire radar imagery were conducted on March 3, 1977, March 8, 1977, and April 7, 1977, over the following targets in the Santa Barbara Channel: buoys, floats and moorings, piers and pilings, oil production platforms, ships and boats, kelp beds, and natural oil seeps. Sea truth information in the form of aerial photographs, detailed sketch maps and extensive field notes to document target types and locations was gathered coincident with each radar overflight.

Oil slicks from natural seeps in the Santa Barbara Channel were consistently present on AOSS II test flight days. Seven slicks covering an area of 11.3 square kilometers were observed off Coal Oil Point, with three other slicks measuring an additional 11.3 square kilometers found in adjacent portions of the channel. Although weather conditions were sufficiently good to permit completion

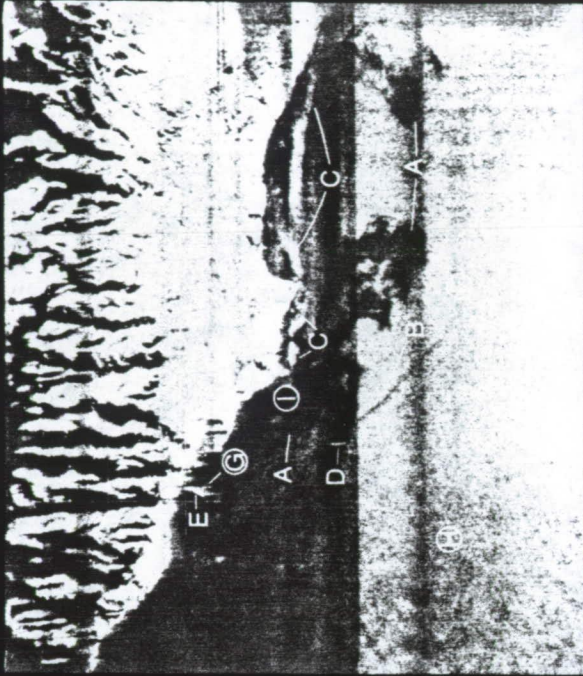
WESTERN SANTA BARBARA CHANNEL TEST AREA: MAY 19, 1976

RUN 6:
FLOWN WEST TO EAST;
LOOK DIRECTION SOUTH



- A NATURAL SEEP OIL SLICK
- B OLEYL ALCOHOL SLICK
- C KELP
- D PLATFORM HOLLY
- E OIL SUPPORT PIER (1900 feet)

RUN 7:
FLOWN NORTH TO SOUTH;
LOOK DIRECTION WEST



- F USCG CUTTER PT. JUDITH (83 feet)
- G ALUMINUM CREWBOAT (61 feet)
AND WOODEN TUG (83 feet)
- H FIBERGLASS SAILBOAT (40 feet)
- I 5-POINT MOORING AND RADAR
REFLECTOR BUOY

O INDICATES TARGET NOT DETECTED

Figure 3. Example of synthetic aperture radar imagery showing oil slick and manmade target detection capabilities of the COR system. Although some look direction dependence is evident, oil slicks are nevertheless detected in both images.

of scheduled test flights, they were somewhat rougher than the conditions encountered during the 1976 radar flights, with winds of 13 - 15.5 mps and waves 0.6 - 1.2 m in coastal waters and 1.2 - 2.1 m in midchannel on March 3, 1977.

Assessment of target detection capabilities was based on seven runs with the horizontally polarized AN/APS-94D and eight runs with the vertically polarized OSDR-94, with a total of 25 SLAR images analyzed. Although it was determined that the APS-94D exhibited slightly superior detection capabilities with respect to structural targets such as ships and oil platforms (86.9% to 83.0%), the OSDR-94 proved to be the more sensitive to marine oil slicks, imaging 40% (6 of 15) of the possible slicks compared to 0% for the APS-94D.

The 1976 and 1977 airborne radar evaluation flights presented a unique opportunity to compare real and synthetic aperture radar data, as well as horizontally and vertically polarized radar data, acquired over oil slick targets concurrently with accurate sea truth information. Based on the results of these studies, both real and synthetic aperture vertically polarized X-band airborne radars are much more successful in detecting surface oil slicks in marine waters than horizontally polarized systems. Additional work needs to be done, however, in determining the effects of frequency, look angle and sensor platform altitude on remotely sensed oil slick signatures. Current GRSU research on the oil detection capabilities of the L-band Seasat SAR represents an initial step in that direction.

VI. SEASAT SAR STUDY

Launched June 27, 1978, Seasat-A represented the National Aeronautics and Space Administration's first effort at a dedicated ocean dynamics free flyer. It was placed into a 108° - inclined circular orbit 800 kilometers above the earth's surface. Under a grant from the United States Geological Survey, GRSU personnel are now involved in a system verification study which will attempt to document a positive response of this satellite's imaging radar to the perennial oil slicks that occur off Coal Oil Point, California. The Seasat radar system is an L-band (1.275 GHz), horizontally polarized synthetic aperture radar (SAR) with a steep depression angle ($\sim 70^\circ$), a swath width of 100 km, and a theoretical resolution of 25 m. Though not specifically optimized for oil detection, this instrument may provide the first documented microwave images of oil slicks from spacecraft altitudes.

The sea surface verification phase of this study was initially patterned after previous efforts of similar focus, whereby detailed slick maps are generated from field notes, sketches, and aerial photographs gathered concurrent with actual radar imaging. On October 10, 1978, however, Seasat-A suffered catastrophic failure, before any such verification tests were conducted. As the areas extend and surface configuration of oil slicks must be reasonably known at the time of each imaging overpass in order to assess the sensor's response to these target features, Seasat's premature failure necessitated the reconstruction of this information via hindcasting techniques and ancillary data sources¹. This task became feasible upon consideration of the following: (1) the known location of major seeps within the study area, (2) an extensive collection of climatological data for the study area during the imaging period (July 15 to August 10, 1978), and (3) empirically derived response characteristics of oil to these meteorological and oceanographic parameters.

In order to create predicted oil slick trajectories, a vector addition algorithm, modeled after one originally designed by USGS, has been written which performs a resolution of forces summation on time-stepped surface wind and current input data. The input vectors are appropriately scaled (Fay, 1971; Waldman et al., 1973), converted from polar coordinate to cartesian format, and added together to produce a single resultant trajectory vector for each time step in the series (see Figure 4). Once generated, these time-stepped resultants are plotted in head-to-tail fashion away from individual points of origin (seeps), starting with the last calculated and proceeding outward to the first (see Figure 5). This procedure will give the best approximation of oil slick configurations in the study area at the instant of each Seasat imaging overpass. The output will then be compared with processed imagery in the hope of observing a similar pattern. The accuracy of the trajectory model will be assessed by comparing on-site observations of slick configuration with the output of predictive model runs driven by simultaneously observed wind and current data.

Preliminary inspection of both digitally and optically correlated imagery from Seasat revolution number 308 reveals the predicted low returns for the Coal Oil Point study area (see Figure 6). One linear seep which runs southwest for approximately 1/2 mile directly off the point seems to be depicted especially well. A problem, however, exists in that large areas of the channel exhibit a very similar diminished backscatter response, effectively masking the oil signal from simple visual identification. These areas are interpreted as zones of little or no surface wind. Such wind row features are common along the northern margin of the channel where eddies and backwinds are the rule rather than the exception.

Separation of these features in an optical processing mode seems unlikely as the SAR imagery is a single channel dataset. One possibility which will be pursued using digital data stems from an assumed difference between the wave frequency spectra associated with the oil slicks and that of the relatively smooth zones of low return from portions of the ocean surface surrounding the slicks. This assumption will obviously break down in the limit as absolute calm removes all the surface roughness driving impulse. With even a moderate breeze, however, the differential damping effect of oil's increased surface tension should produce a unique distribution of frequency components. Two-dimensional spatial frequency (Fourier) transforms of different portions of the SAR subimage (representing targets of open water, wind rows, and known oil slicks) will be compared with the hope of detecting characteristic differences in these frequency distributions, thereby isolating unique characteristic oil slick signatures on SAR imagery.

VII. CONCLUSIONS AND RECOMMENDATIONS

Based on the experience of the Geography Remote Sensing Unit in offshore sensor evaluation studies, active microwave systems on aircraft and satellite platforms appear to have great potential for oil detection activities. Although the reliability and proximity of the oil slicks originating from the natural seeps off Coal Oil Point have permitted oil detection studies under a variety of sensor and environmental conditions, additional testing and research still need to be accomplished to determine the following:

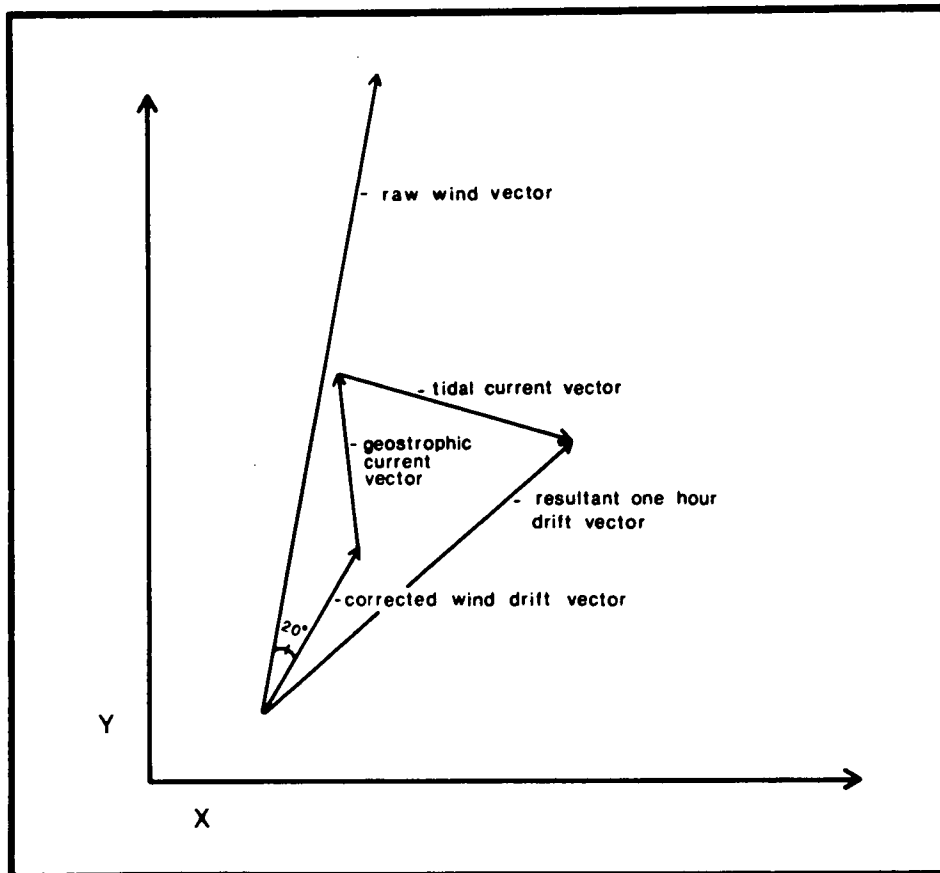


Figure 4. Oil slick hourly drift vectors are predicted using a vector addition algorithm whereby the forces which produce surface drift are scaled and summed. The resultant represents one hour of predicted drift in terms of distance and direction. Plotted head to tail away from established oil seep sources this time series of drift vectors yields a prediction of oil slick configuration at any specified instant.

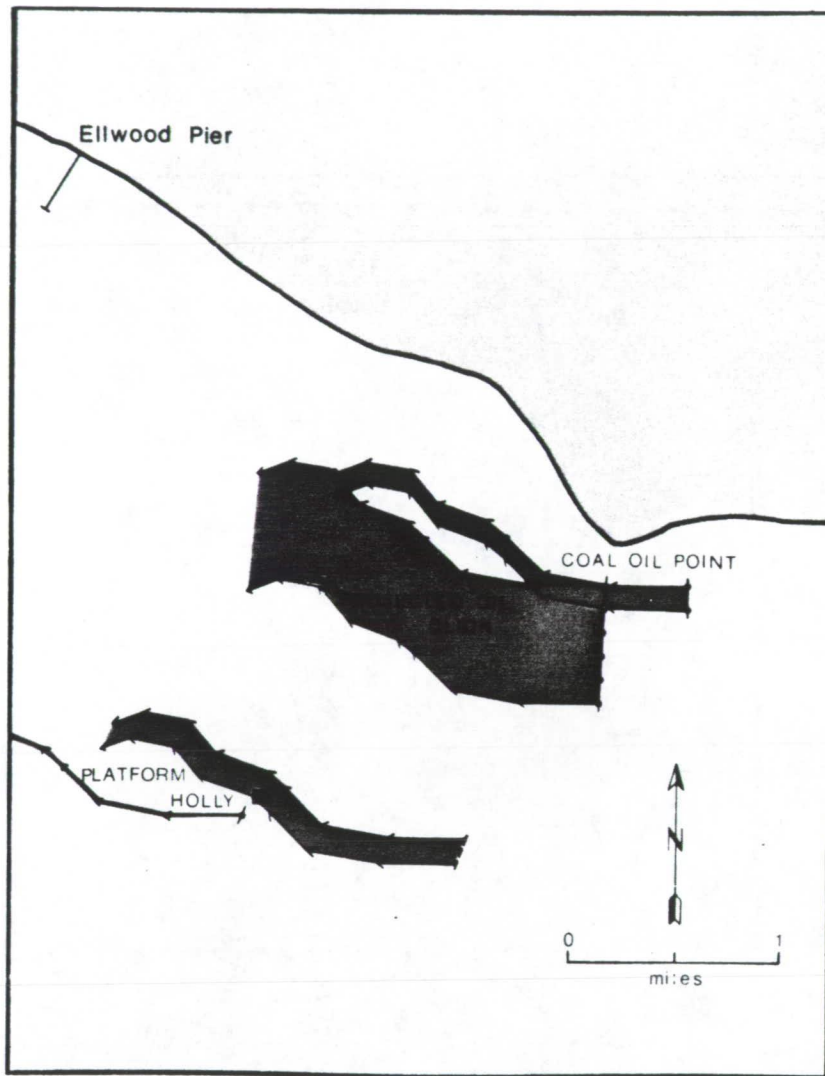


Figure 5. Example of oil slick trajectory map produced from time-stepped meteorological and oceanographic data compiled from land and water stations in the Santa Barbara Channel area. Plots of resultant vectors, in reverse series, yield a predicted oil slick configuration for a specific instant in time. These slick maps can then be compared to SAR imagery where corresponding oil slick signature patterns would be evident.

OF SEASAT DATA IS
OF POOR QUALITY



Figure 6. Film writer output of digitally correlated Seasat SAR data of the Coal Oil Point study area. An area of reduced return interpreted as surface oil accumulations can be seen offshore between Platform Holly and Coal Oil Point. This area corresponds well to the known location of natural oil seeps (see Figure 1). Note also the area of low backscatter running diagonally across the bottom of the image caused by wind rows in the Santa Barbara Channel which serve as confusion targets for oil slicks on radar imagery.

- (1) The effect of sensor frequency, polarization, look angle and platform altitude on oil slick signatures under a range of meteorological and oceanographic parameters.
- (2) The exact nature of the interactions between microwave energy and the sea surface, and the manner in which oil of various ages and thicknesses modified these interactions.
- (3) The capabilities of radar systems to measure properties of oil slicks (such as thickness and areal extent) once detection has been attained.
- (4) The role of radar in a multisensor oil detection and monitoring system.

In order to acquire information necessary to begin to deal with these issues, several specific actions are proposed:

- (1) To more feasibly measure the effects of polarization and look angle on oil detection response, permission might be obtained to mount a radar sensor on an oil production platform in the Santa Barbara Channel (such as Platform Holly at Coal Oil Point). Such placement would be cheaper than equivalent sensor aircraft overflights and would take advantage of areas of chronic natural oil seepage where effective surface truth could be obtained under a range of sea state and weather conditions.
- (2) Repeating airborne studies employing the NASA-X-, C-, and L-band radar systems should be conducted to fully test their overwater oil detection and measurement potential under diverse environmental conditions.
- (3) Existing research on orbital radars using Seasat SAR data could be supplemented by scheduling data acquisition over the Santa Barbara Channel by the Shuttle Imaging Radar (SIR-A) with appropriate coincident surface truth.
- (4) The Earth Resources Synthetic Aperture Radar Committee should consider establishing the Santa Barbara Channel oil seeps as a test site for active microwave sensor experimentation and initiating experiments to prove the potential of space imaging radars employing surface and airborne data collection in this area at the earliest possible opportunity.

The detection of oil slicks on ocean waters has importance for both pollution monitoring and resource exploration. Verification and refinement of the technology which allows weather and solar illumination independent surveillance of these marine surface features constitutes a logical objective as both the value of undiscovered petroleum reserves and the penalties associated with accidental oil spills spiral continuously higher.

REFERENCES

- Albers, J. P., M. D. Carter, A. L. Clark, A. B. Coury, and S. P. Schweinfurth, 1973, "Summary Petroleum and Selected Mineral Statistics for 120 Countries Including Offshore Areas," U. S. Geological Survey Professional Paper 817.
- Barger, W. R. and W. D. Garrett, 1970, "Effects of an Artificial Sea Slick Upon the Atmosphere and the Ocean," *Journal of Applied Meteorology*, 9(6):396-400.
- Crombie, D. D., 1955, "Doppler Spectrum of Sea Echo at $13.56 \text{ Mc sec}^{-1}$," *Nature*, 175(4):681-687.
- Dibblee, T. W., 1977, "Geology of the Santa Ynez Mountains, Santa Barbara County, California," Bulletin 186, California Division of Mines and Geology, San Francisco.
- Fay, J. A., 1971, "Physical Processes in the Spread of Oil on a Water Surface," Proc. of the Joint Conferences on Prevention and Control of Oil Spills, June, pp. 463-467.
- Guinard, N. W. and C. G. Purves, 1970, "The Remote Sensing of Oil Slicks by Radar," Naval Research Laboratory, Project No. 71404-A004, U. S. Coast Guard, Washington D. C.
- Halbouty, M. T., 1976, "Application of Landsat Imagery to Petroleum and Mineral Exploration," *Bulletin of American Association of Petroleum Geologists*, Vol. 60(5):754-793.
- Imray, J. F., 1868, "Sailing Directions for the West Coast of North America," Part 1: London, James Imray and Son.
- Ingals, R. P., and M. L. Stone, 1957, "Characteristics of Sea Clutter at High Frequency," *IRE Transactions on Antennas and Propagation*, AP-5(1):164-65.
- Kotlarski, J. R. and H. R. Anderson, 1973, "Oil Slick Detection by X-band Synthetic Aperture Radar," Hughes Aircraft Co., Environmental Research Institute of Michigan, Eds., Willow Run Laboratory, Vol. 3:1775-1790.
- Krishen, K., 1972, "Detection of Oil Spills Using a 13.1 GHz Radar Scatterometer," Proc. of the 8th International Symposium on Remote Sensing of Environment, ERIM, p. 1105-1111.
- Kraus, S. P. and J. E. Estes, 1976, "Summary Evaluation of the Offshore Target Detection Capabilities of AN/APS-94D and COR Radar System," University of California, Santa Barbara, U. S. Coast Guard Contract No. DOT-CG-63898A.
- Kraus, S. P., J. E. Estes, S. G. Atwater, J. R. Jensen, and R. R. Vollmers, 1977, "Radar Detection of Surface Oil Slicks," *Photogrammetric Engineering and Remote Sensing*, Vol. 43(12):1523-1531.
- Maurer, A., and A. T. Edgerton, 1975, "Flight Evaluation of U. S. Coast Guard Airborne Oil Surveillance System," Proceedings of Conference on Prevention and Control of Oil Spills, March 1975, San Francisco: American Petroleum Institute.

- Mikolaj, P. G., A. A. Allen, and R. S. Schlueter, 1972, "Estimates of Surface Pollution Resulting from Submarine Oil Seeps at Platform A and Coal Oil Point," American Inst. Min. Metall. Petroleum Engineers, Offshore Technology Conference, Dallas, Texas, Paper No. OTC-1549, Vol. 1: 1365-1378.
- Raney, R. K., and R. T. Lowry, 1978, "Ocean Wave Imagery and Wave Spectra Distortions by Synthetic Aperture Radar," Proceedings of the 12th International Symposium on Remote Sensing of Environment, ERIM, pp. 683-702.
- Straugham, D. and B. C. Abbott, 1971, in "Water Pollution By Oil," P. Hepple, Ed., Institute of Petroleum, London, pp. 257-262.
- Tomiyasu, K., 1978, "Tutorial Review of Synthetic Aperture Radar (SAR) With Applications to Imaging of the Ocean Surface," Proceedings of the IEEE, Vol. 66, No. 5.
- Van Kuilenburg, J., 1975, "Radar Observations of Controlled Oil Spills," Proceedings of the 10th International Symposium on Remote Sensing of Environment, ERIM, Vol. 1, pp. 243-250.
- Vedder, J. G., H. C. Wagner, and J. E. Schoellhamer, 1969, "Geologic Framework of the Santa Barbara Channel Region," Geology Petroleum Dev., and Seismicity of the Santa Barbara Channel Region, California, U. S. Geological Survey Professional Paper 679, Washington D. C.
- Waldman, G. A., R. A. Johnson, and P. C. Smith, 1973, "The Spreading and Transport of Oil Slicks in the Open Ocean in the Presence of Wind, Waves, and Currents," Final Report, Contract No. GG-D-17-73, prepared for U. S. Coast Guard, July 1973.
- Weeks, L. G., 1965, "World Offshore Petroleum Resources," Bulletin of the American Association of Petroleum Geologists, Vol. 49(10):1694.
- Weissman, D. E., and T. W. Thompson, 1977, "Detection and Interpretation of Ocean Roughness Variation Across the Gulf Stream Inferred From Radar Cross Section Observations," Marine Technology Society and IEEE, Oceans 1977, Vol. 1:14B-1 - 14B-10.
- Wilson, R. D., P. H. Monaghan, A. Osanik, L. C. Price, and M. A. Rogers, 1974, "Natural Marine Oil Seepage," Science, Vol. 184(5):857-865.
- Wood. P. W. J., 1979, "New Slant on Potential World Petroleum Resources," Ocean Industry, Vol. 14(4):59-71.

APPLICATION OF SLAR IN NUCLEAR POWER PLANT
SITING: A CASE HISTORY

Barry S. Siegal
Ebasco Services, Inc.
Greensboro, N.C.

ABSTRACT

Over 10,000 square km of Side Looking Airborne Radar imagery was obtained and analyzed for the siting of the first nuclear power plant in the Republic of the Philippines. The imagery was obtained using the Motorola APS/AN-94D (X-band) real-aperture system as part of an overall remote sensing program to site and evaluate potential site regions. Analysis of SLAR images, in conjunction with Landsat, color, black and white and thermal infrared images, provided basic information on structure, relative geochronology, stratigraphy, geomorphology, and ground water, which facilitated field operations and data synthesis.

I. STATEMENT OF THE PROBLEM

Siting investigations for nuclear power plants demand multidisciplinary phased programs that address many technical, licensing, and socioeconomic factors. Questions concerning safety, environmental impact, costs, site development requirements, and proximity to load demand must be ascertained early in the siting investigation to minimize unnecessary siting and development expenditures. Geological and seismological considerations must include factors necessary to insure that the nuclear plant can be constructed and operated at the site without undue health and safety risks. Plant design is established in accordance with seismic and geologic criteria set forth in United States Nuclear Regulatory Commission (USNRC) guidelines which have also been adopted in one form or another by many nations developing nuclear power generating facilities.

The design basis for maximum vibratory ground motion is a key factor in site selection and evaluation. The earthquake which could cause maximum vibratory ground motion at the site, designated the Safe Shutdown Earthquake (SSE), is established by determining the effect of the most severe earthquakes associated with a capable fault or within a seismotectonic province. Capable faults are defined as having moved at least once within the past 35,000 years, recurrently within the past 500,000 years, or having a record of macroseismicity. Seismotectonic provinces are regions characterized by like geologic structural features and equipotential seismicity. In establishing the SSE, it is assumed that any historical earthquakes associated with the capable fault can occur where the fault is nearest the site. The length of the fault is also important in determining possible rupture length and maximum earthquake.

Earthquakes which cannot be associated with capable faults are assumed to be "random earthquakes," and therefore likely to occur anywhere within the seismotectonic provinces. For design purposes, the epicenter of the maximum-magnitude random earthquake is assumed to occur at its closest approach to the site within its seismotectonic province.

While estimates of the SSE are crucial in the early stages of site selection, many other factors must be considered for conceptual engineering and evaluation of licensing and economic feasibility. Of course, the relative significance of these factors is dictated by the geologic setting. Siting of the first nuclear power plant in the Republic of the Philippines permitted the first detailed study in the tectonic-volcanic setting of an active island arc system to determine a safe site and address site safety from a regulatory sense. The challenging problem of assessing seismic and volcanic hazards provided a unique opportunity to use remote sensing techniques in a little studied, geologically complex region.

II. BACKGROUND

In 1965, the International Atomic Energy Agency (IAEA) and the Philippine National Power Corporation began studies related to the siting of the first nuclear power plant in the Philippines. Ebasco was contracted in 1974 to provide specific consulting services for the proposed nuclear power plant, to be located in the area of Bataan. As part of a regional assessment, three microregions within the Bataan Peninsula were selected for study on the basis of the previous studies (Figure 1). From north to south, these regions are (1) the southern tip of Zambales Peninsula, (2) the area within 10 km of the barrier of Bagac, and (3) the southern tip of Bataan Peninsula, typified by San Jose Point. The three microregions were qualitatively evaluated with respect to potential geologic and seismologic hazards, including site faulting, foundation quality, security against volcanic events, seismic history, distance to nearest credible hypocenter, and site amplification characteristics. Assessment included the planning and execution of a remote sensing mission and field and laboratory investigations. The underlying philosophy at this stage of investigation was to evaluate the relative merits of each microregion, taking into account the known conditions of each area. Microregions having unknown or poorly known conditions would be assigned low ratings in recognition that additional, possible lengthy investigations and exploration would be required to support final site selection. Of course, such added investigation would adversely affect the overall project schedule and budget.

As part of the assessment, a comprehensive remote sensing program was planned to provide baseline data for field investigations, seismology and geochemical studies, environmental assessments, and offshore geophysical programs. Specific objectives of the remote sensing study included the following:

- (1) Identifying linear features which could be the surface expressions of faults or fractures.
- (2) Locating volcanic centers.
- (3) Determining stratigraphy and relative geochronology between the volcanic and tectonic events within the Zambales-Bataan volcanic highlands.

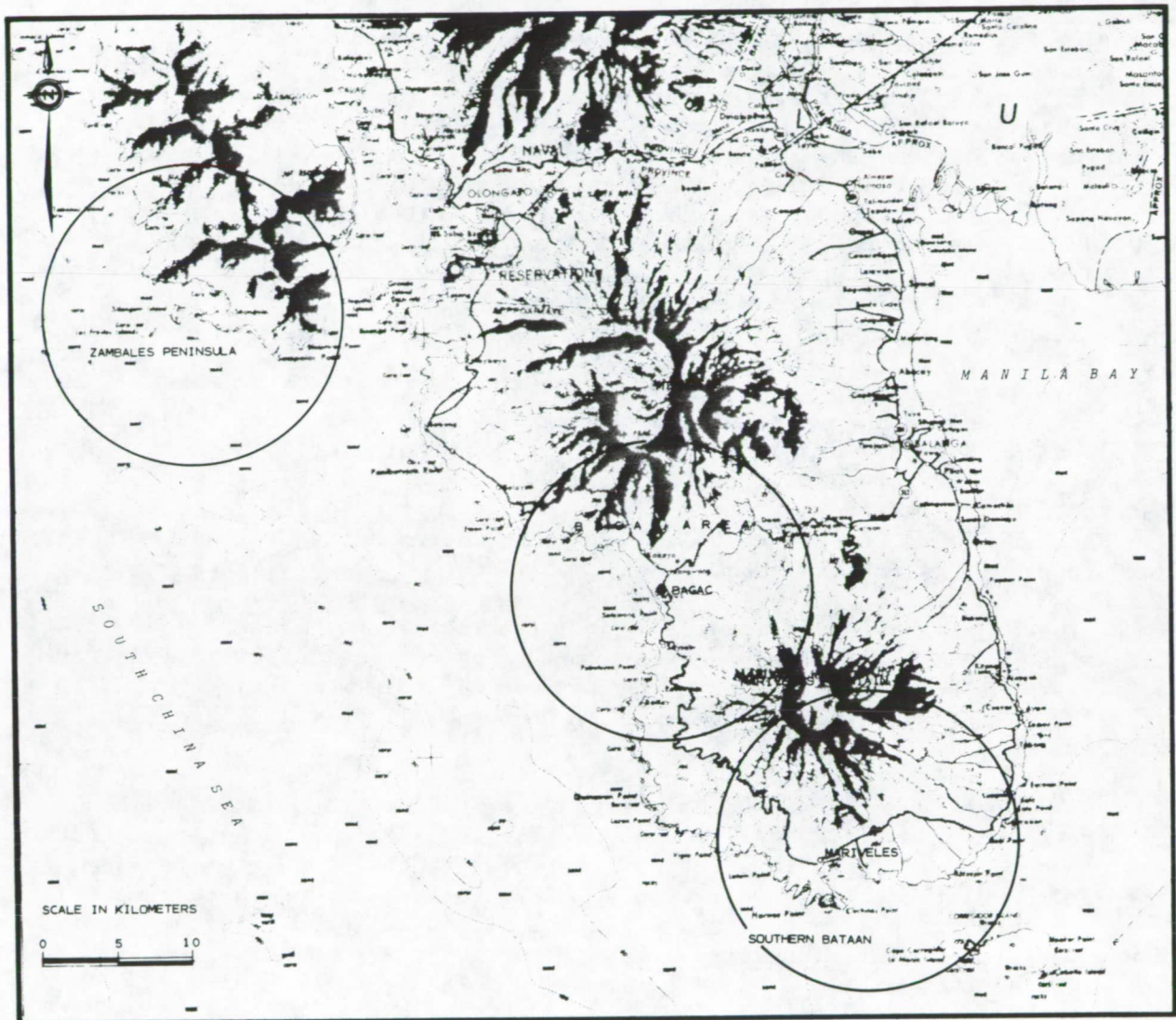


Figure 1. Potential site regions.

- (4) Locating coastal and near-shore hot springs and delineating zones of suspended offshore sediment concentration and movement.

Information from the remote sensing study and other studies was to be used to select potential sites and to prepare the required Safety Analysis Reports for licensing.

III. SYSTEM PARAMETERS AND DATA PRODUCTS

SLAR imagery, using the Motorola APS/AN94-D (X-band) real-aperture system, was obtained for 10,000 km², extending from Mt. Pinatubo, south to the Taal-Banahao volcanic area, and from the west coast of Luzon, east to Laguna de Bay (Figures 2 and 3). Flight lines were north-south with a two-look direction. Contact prints were prepared from the 1:250,000 acquisition scale, enlarged to 1:100,000 scale for more detailed study. The nominal scale of the imagery was small enough to denote regional features, yet large enough to highlight terrain relief features in relation to site-specific details. Ground resolution was approximately 20 m. Linear features such as fishpond dikes as little as one meter wide can be identified.

Color and black and white aerial photographs at a scale of 1:8000 were obtained for the Bataan Peninsula coastline from Eman Point south to Caybobo Point. Black and white aerial photographs at scales of 1:8000 and 1:15000 were obtained within a 10-km radius of Bagac; they were used to supplement existing 1:15000-scale black and white aerial photographs of the entire Bataan Peninsula and the 1:20000 photographs for the Mapalan Point region.

A predawn flight, using a Daedalus 60 thermal infrared line-scanner, 0.5-milliradian spot size, 0.1°C temperature sensitivity, acquired thermal infrared imagery for the entire coastline of the Bataan Peninsula. Because of the dense vegetation cover and extreme topographic relief, no flight was planned over the volcanic highland area.

Linear features interpreted as faults were noted on the images and considered with respect to potential site areas and available seismic data. Linear features which could be significant to a potential site area, based on established distance-length relationships, would require field verification to determine origin, age of last movement, extent, etc. Potential site areas were selected to minimize necessary linear feature investigations and further insure plant safety.

Textural boundaries on SLAR images were delineated in the early phase of study to help guide field sampling for geochronology studies. In general, SLAR images accurately portrayed the geochronological boundaries established by age dating and paleomagnetic studies.

IV. VALUE OF TECHNIQUES AND RESULTS

A. Microregion Assessment

SLAR images were used in the first phase of the siting study to evaluate the three microregions and to select potential site areas within the selected region.

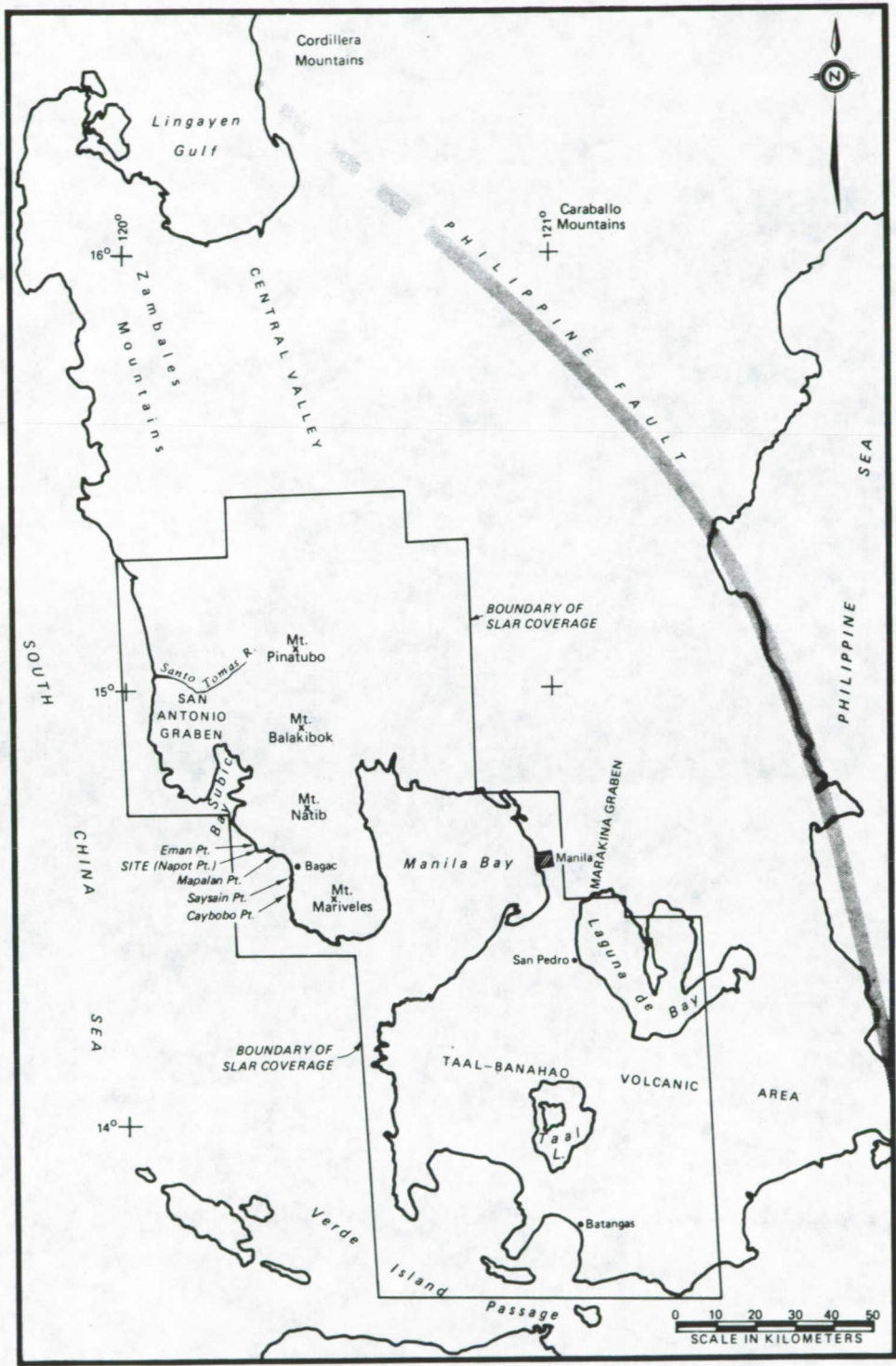


Figure 2. Reference map showing areas of SLAR coverage.

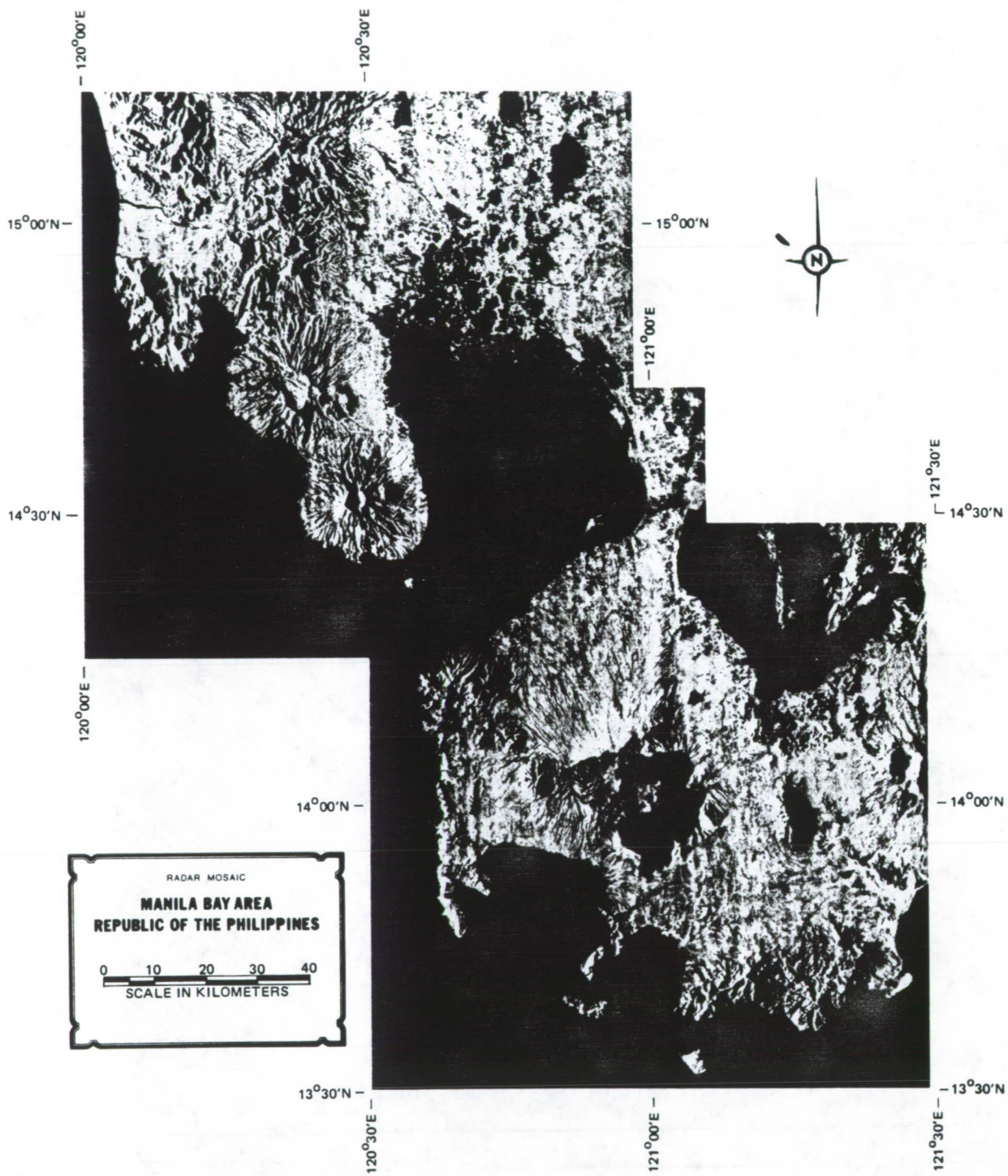


Figure 3. East-look SLAR mosaic.

Distinct pervasive fracturing, which occurs in a suite of mafic-ultramafic rocks, is evident on SLAR images of the Zambales region (Figure 4). Available information suggested that major faults are common, the closest forming the boundaries of the east-west-trending San Antonio Graben. While the areal extents of these faults were generally mapped, analysis of the SLAR images suggested their extent might be greater than indicated, conceivably resulting in a relatively high SSE value for a site in this region, and extensive field investigations to determine capability of the linear features noted.

The southern Bataan microregion can be seen on SLAR images as a broad, gently sloping fan of volcanic material originating from the summit of Mt. Mariveles. While no evidence of faulting was suggested by examination of SLAR and Landsat images, the susceptibility of a site to potential damage from even small volcanic events would make licensing difficult. In addition, magnetic maps of the area showed a possible structural feature directly offshore San Jose Point, which appeared to correlate with an area of seismic activity.

The Bagac region was found to be underlain by a thick sequence of pyroclastic rocks related to the Mt. Natib and Mt. Mariveles volcanic area. No evidence of faulting in the site region was found on the images or during field reconnaissance. In addition, there are no historical epicenters in the region, and imagery suggested that several parts of it provide excellent protection from volcanic hazards. The advantages of the Bagac region over the Zambales and Southern Bataan regions suggested it should be considered the candidate site area. Six specific sites within this region were therefore selected for detailed analysis: Napot Point, Mapalan Point, Bagac I and II, Saysain Point, and Caybobo Point. Caybobo Point was eliminated early because it lacks natural protection from volcanic activity and is too near a possible parasitic vent noticed on SLAR images. Mapalan Point was eliminated because it displayed morphological characteristics suggesting it was part of a large slide block that rotated and slid 1-2 km downslope Mt. Natib. Although the natural topography of the area provides excellent protection from volcanic hazards, existence of a possible glide plane beneath the point ended consideration of Mapalan Point as a primary site. Saysain Point was eliminated because it lacks natural protection from volcanic events and is characterized by a deep weathering profile. Both Bagac sites were eliminated because of susceptibility to river and tsunami flooding, liquefaction, and anticipated construction dewatering problems. The Napot Point site, however, afforded a high degree of natural protection from volcanic events, no threat of flooding or tsunami damage, and excellent foundation stability; therefore, it was chosen as the preliminary site.

B. Site Confirmation Studies

After selection of the primary site, extensive investigations thoroughly evaluated seismic and volcanic risks to the proposed plant and fulfilled all nuclear licensing requirements. During the site confirmation studies, analyses of SLAR images were used in a variety of ways to guide field investigations and help establish the seismological and volcanological data base. A primary activity was tracing the extent of known faults within 100 km of the site to assist in estimating and refining the SSE. The trace of the San Antonio Graben, a SSE generator, is clear on both SLAR and Landsat images (Figures 4 and 5). On Landsat images, the distinction results primarily from a tonal change due to difference in spectral reflectance between the ultramafic rocks of the Zambales Mountains and the surficial covering of Holocene sediments within the graben.

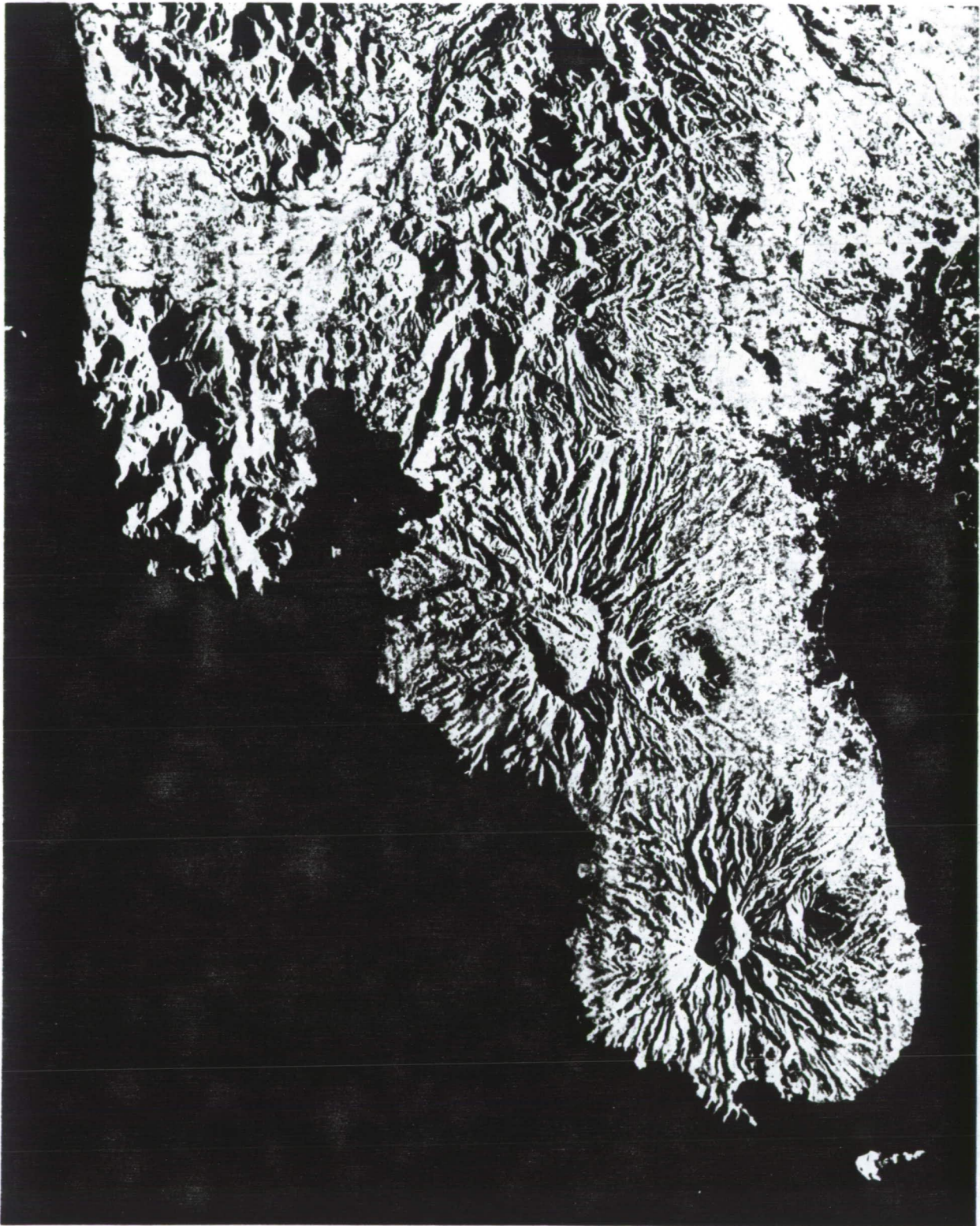


Figure 4. Enlargement of SLAR image for Bataan Peninsula.



Figure 5. Landsat image of Bataan Peninsula and surrounding area.

ORIGINAL PAGE IS
OF POOR QUALITY

The northern boundary of the graben is conspicuous topographically and is partly outlined by the Santo Tomas River; tone and topography make the southern boundary distinct on the imagery.

Topographic change across the graben is particularly distinct on SLAR images. Variations in tonal expression of the graben and the adjacent region are due to an apparent difference in the surface roughness of the ultramafics of the Zambales Mountains and the Holocene sediments of the graben.

Relatively cloud-free Landsat imagery was available for the study region at a scale of 1:1,000,000. False-color composite images were produced at a variety of scales, using a color additive viewer. Composite images of SLAR and Landsat were produced using photographic techniques.

V. ANALYSIS AND INTERPRETATION TECHNIQUES

The first phase of the remote sensing analysis was directed at identifying possible faults, landslide scars, areas of recent volcanism, and physiographic features which could channel volcanic material toward potential site areas in the event of future volcanism. Analysis was primarily by visual examination and field reconnaissance. Where appropriate, stereoscopic techniques and light-table projections were used.

Color additive techniques improved recognition of subtle textural and tonal variations, facilitating fabric delineation. During interpretation, type and amount of ground cover were considered in order to minimize geologic misinterpretation resulting from surface-roughness variations from nonspecific vegetational distribution. Black and white and color photography was analyzed with SLAR images, using standard photogeology interpretation procedures. Landslide scars and areas prone to slippage were particularly noted and checked in the field.

In all analyses the images were viewed from several directions to help identify significant, but subtle, linear features. Consideration was also given to the preferential enhancement of linear features by each of the data acquisition systems. The significance of such enhancement can be seen on the different northwest-trending linear features on the western flank of Mt. Natib (Figure 4). The apparent distinctness of these linear features appears to result primarily from "shadow" enhancement, as reported by Wise (1969) from study of raised plastic relief maps photographed from different directions, under varying illumination conditions. Analysis of deviations of the linear features from maximum enhancement conditions stipulated by Wise (1969) revealed that their distinctness primarily was a function of illumination conditions.

Stereoscopic analysis of side-lapping SLAR strips (primarily from East-Look direction) further revealed that the features are erosional channels that do not breach the rim of Mt. Natib and extend to Olongapo Bay, as might be suggested from casual observation of the SLAR mosaic. In fact, they trend westward only until they intersect a low-lying rim near Bisay River; drainage is then southwest into Bisay River. The northwestward-trending erosional channels within the Mt. Natib Crater do not lie along the same projection line as the linear features on the flank of the crater.

The San Antonio Graben, an active fracture zone and a potential Safe Shutdown Earthquake (SSE) feature is recorded on geologic maps as extending 20 km west-northwest. Westward, geophysical and seismic data suggest the fault extends through the Luzon Trough. Eastward, seismic data suggests the fault extends toward the Central Valley. This interpretation is strengthened from analysis of SLAR images that show several linear features that appear to correspond with the southernmost fault and extend toward the Central Valley. Although the San Antonio Graben is mapped as two bounding faults, its appearance on imagery and field investigations suggest a series of step faults.

SLAR images were also important in determining relative age of volcanic materials and in directing a field sampling program. A total of 52 samples from lava flows and intrusive bodies were collected within the site region and dated radiometrically. The temporal distribution was determined, using time-series analysis techniques developed by Stepp (1972) and Wickman (1966). In general, the correlation between the degree of erosion of volcanic material and its age is excellent.

VI. SUMMARY

Remote sensing techniques have proved invaluable in selecting and evaluating potential site areas for the first nuclear power plant in the Republic of the Philippines. SLAR images were extensively used for directing field investigations and in establishing tectonic provinces and temporal distribution of volcanism. Evaluation of the data obtained from the remote sensing program and all studies have shown that the only credible hazard is volcanic ash fall.

The site location and the topographic characteristics of the area would protect it from other possible hazards. Investigations in Luzon and compilations of worldwide data led to determination of a design basis ash-fall and its probability of occurrence.

ACKNOWLEDGEMENT

The author wishes to express his appreciation to the National Power Corporation (NPC) of the Republic of the Philippines for providing the opportunity to undertake the study cited and to present its results. Acknowledgement is also extended to Ebasco and NASA/JPL for support during the preparation of this paper.

REFERENCES

- Stepp, J. C., 1972, Analysis of completeness of the earthquake sample in the Puget Sound area and its effect on statistical estimates of earthquake hazard: Proceedings of the International Conference on Microzonation 2, 897-910. NTIS P. B. 219-383.
- Wickman, F. E., 1966, Repose-period patterns of volcanoes. Parts I-V, in Arkiv for Mineralogi och Geologi, v. 4, p. 291-367.
- Wise, D. U., 1969, Pseudo-radar topographic shadowing for detection of sub-continental sized fracture systems, Proc. of 6th International Symposium on Remote Sensing of the Environment, University of Michigan, p. 603-615.

MAPPING PAPERS

Application of Imaging Radar to Mapping
Franz W. Leberl

Stereo Radar for Mapping and Interpretation
L. Graham

A New Look at Togo Through the Eyes of a SLAR
Louis F. Dellwig

APPLICATION OF IMAGING RADAR TO MAPPING

Franz W. Leberl
Institute for National Surveying and Photogrammetry
Technical University, A-8010, Graz, Austria

ABSTRACT

The present state of mapping with radar is reviewed. Emphasis is on radargrammetric mapping with single images, stereo pairs and block adjustment. Applications to thematic mapping are addressed as well. Examples presented concern radar mosaicking, sea-ice study and extraterrestrial mapping (Moon, Venus).

I. INTRODUCTION

The application of side-looking radar images to topographic mapping had been studied intensively and nearly exclusively at military agencies until a few years ago. Civilian research at that time was limited. However, while the study of military radar mapping until recently seems to have been deemphasized, it is being considered for civilian tasks. A number of operational mapping projects have been carried out with radar in different regions of the world. Brazil's RADAM project is the largest of these. At the same time the importance of radar is being evaluated as a remote sensing tool to be used in conjunction with other data. This is particularly signified by considerations for radar imaging from satellites (Seasat-A, Space Shuttle and Space Lab, Venus Orbital Imaging Radar).

Simultaneously, research is taking a closer look at the capabilities and limitations of radar imaging for remote sensing of subsurface features, surface roughness, soil moisture, polarization anomalies, etc. Mapping with radar is thus a developing field of study with valuable present applications and future promise.

This short review will go over the basics of radargrammetry, addressing the projection equation, stereo-radar and image block adjustment. Then recent work will be reviewed concerning the applications of radargrammetric mapping to cartography, with references to measurements of sea-ice drift and marine mapping.

II. SINGLE IMAGE RADARGRAMMETRY

A. Mathematical Expression

Radargrammetric projection equations have been formulated on many occasions in the literature. It is essential to differentiate between real-aperture and synthetic-aperture imaging. In both cases the basic fact remains that radar

projection lines are circles concentric with respect to an antenna (Figure 1). However, with brute force radar (real-aperture) the plane of a projection circle is normal to the longitudinal antenna axis, while with synthetic-aperture radar (SAR) it is normal to the velocity vector of the antenna. From Figure 2 one may thus specify the following projection equation:

$$\underline{p} = \underline{s} + \underline{A} \cdot \underline{r} \quad (1)$$

where \underline{p} , \underline{s} are vectors in an object space coordinate system defined by unit vectors \underline{x} , \underline{y} , \underline{z} , while \underline{r} is a vector in an image space coordinate system defined by unit vectors \underline{u} , \underline{v} , \underline{w} , and \underline{A} is a rotation matrix.

The unit vectors, \underline{x} , \underline{y} , \underline{z} , are fixed to the imaged object, while the unit vectors \underline{u} , \underline{v} , \underline{w} are fixed to the radar antenna.

The vector \underline{r} is a function of slant range r , look angle Ω and a system constant ϕ (squint):

$$\underline{r} = r(\sin \phi, (\sin^2 \Omega - \sin^2 \phi)^{1/2}, \cos \phi) \quad (2)$$

The matrix \underline{A} describes the rotation of the image system \underline{u} , \underline{v} , \underline{w} into the object system (\underline{x} , \underline{y} , \underline{z}). It is defined by the classical ρ , ω , ψ angles of photogrammetry, provided however that real-aperture radar is considered. For SAR it is a function of the velocity vector \underline{s} of the antenna.

Further details may be found in the literature (Leberl, 1975e, 1978; Leberl et al., 1967a). It may be interesting to note that the radargrammetric difference between real-aperture and SAR has so far not been considered in a majority of radargrammetric studies. A recent valuable exception dealing with satellite SAR is the paper by Kratky (1979).

B. Accuracies

Single image radar mapping accuracies achieved in the past depend on a number of factors of a particular project or experiment: type of radar system, resolution, stabilization, density of ground control, type of control, mapping method, type of terrain. Therefore results of one study may not be generalized.

The term "accuracy" describes the geometric errors of mapping. In a study one can check these errors using checkpoints and computing root mean square errors m_x , m_y in the coordinate directions x and y . These error components can be combined into a single point error m_p :

$$m_p^2 = m_x^2 + m_y^2$$

Actually achieved point errors m_p are plotted in Figure 3; it is clear that accuracies can vary widely as a result of project parameters. Details have been discussed in the literature (e.g., Leberl, 1976b).

In the best cases published accuracies were of the order of the ground resolution. Such results were reported, e.g. by Gracie et al. (1970), where very high density of well identifiable ground control was available (about 10 points per 100 sq km).

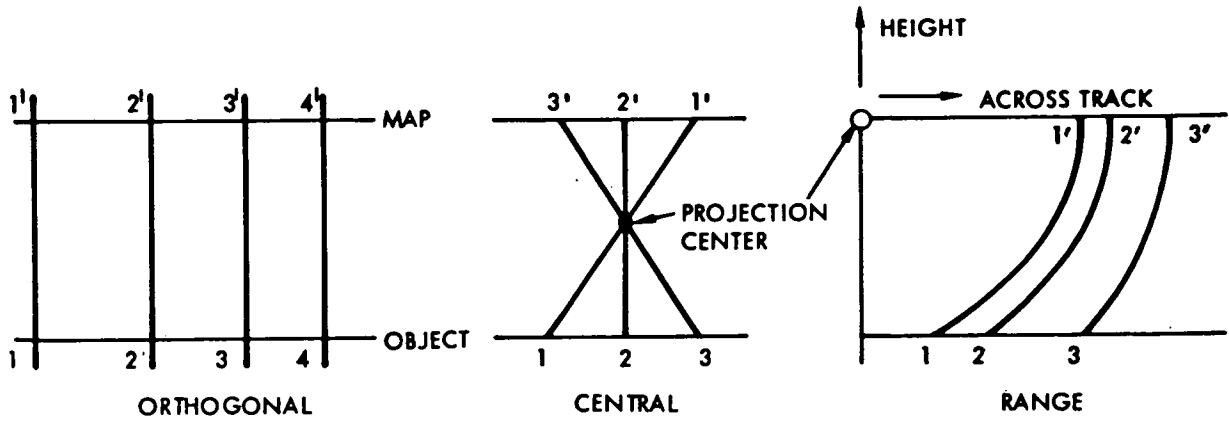


Figure 1. Projection lines for (a) the orthogonal, (b) the central and (c) the radar range projection. Note that projection lines are circles in case (c).

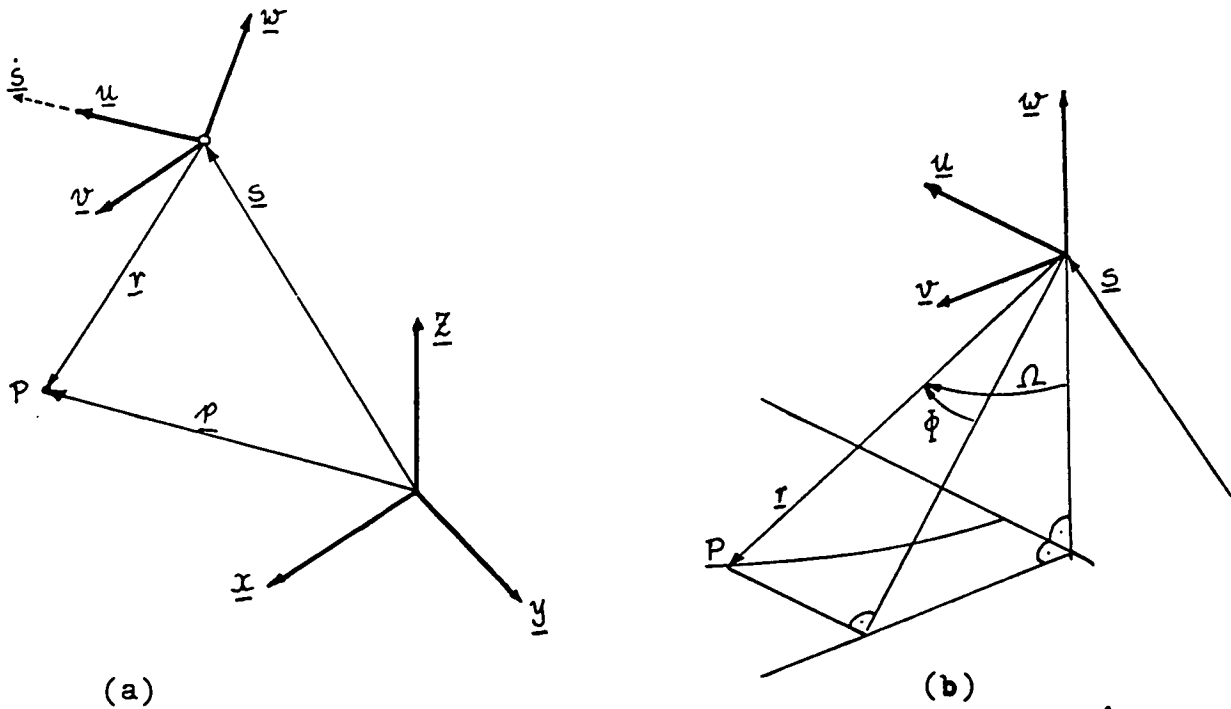


Figure 2. Definition for the radar projection equations.

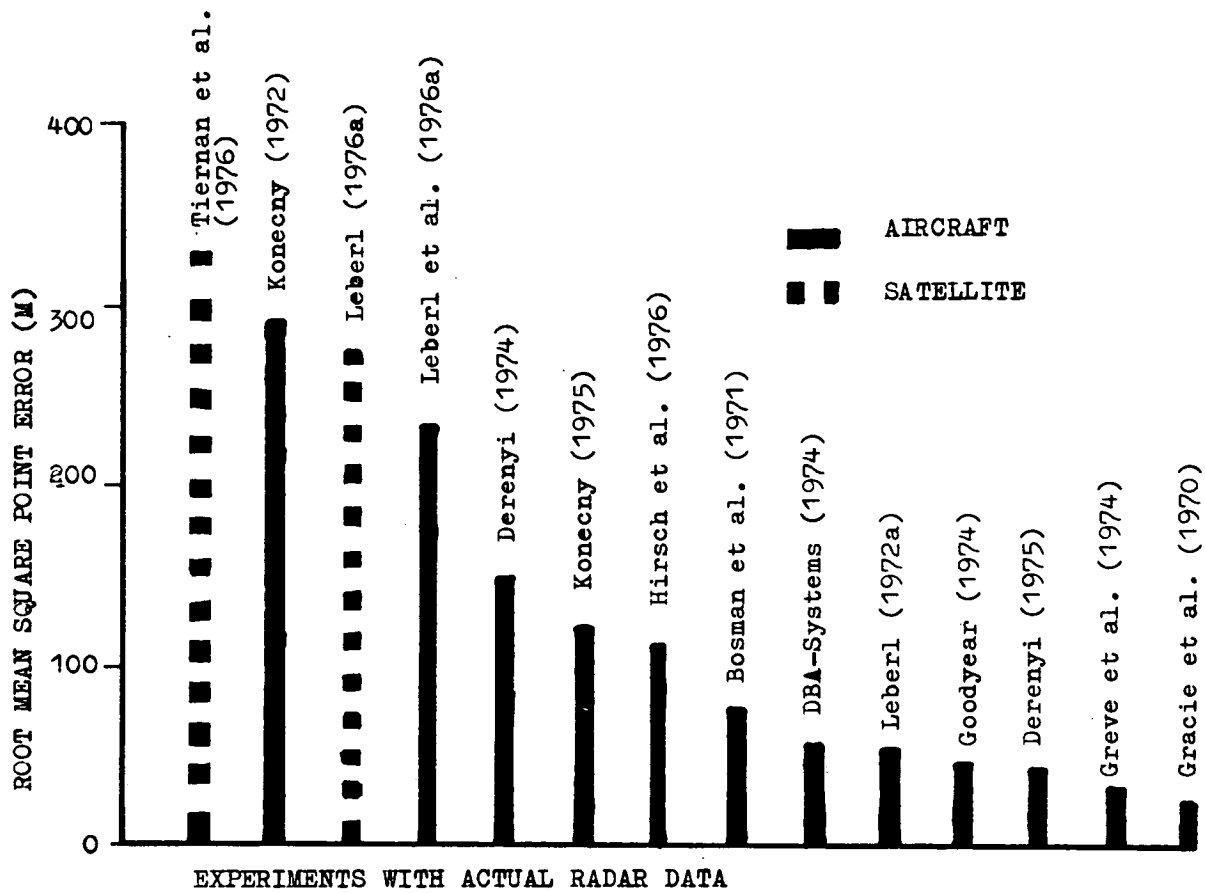


Figure 3. Accuracies achieved with single image radar mapping. Results depend strongly on specified project parameters. Satellite results are from the Apollo 17 mission to the Moon in 1972.

"Ground resolution" is here understood as the minimum distance that two reflectors must have on the ground to produce separate images. A value for the ground resolution is usually provided by the equipment operator and often is a result of confusion when comparing radar systems of different manufacturers, or when comparing radar with other imaging techniques.

C. Rectification

Rectification is the transformation of the single radar image into a map projection. The process is usually photographic, but can also be numerical or graphical or any combination of the above. Using Eqs. (1) and (2) with measured navigation data does enable one to transform a given radar image point into the map coordinate system (whereby the ground height must be known or assumed to be known). If in addition to navigation data ground control points are also available, then the set of transformed radar image points can be matched to these control points. Generally this match may be done with some sort of interpolation algorithm and many different procedures are possible and have been applied in the past.

While numerically the possibilities for rectification are boundless, they are limited in practice if the photographic image is to be reproduced with correct geometry. The technology of digital image processing permits complete flexibility for rectification (see Figure 4). All geometric corrections are possible; however, this rectification is presently expensive and tedious and therefore unsatisfactory for any large mapping effort.

Jensen (1975) described an optical rectifier for image strips that permitted changes to the along versus across track scales. The instrument employed anamorphic lenses. Its performance was such that the rectified images were of degraded quality; rectification was partial only (along track scale), and the solution was therefore unsatisfactory.

Peterson (1976) has extended the optical correlator (for SAR) to achieve correction of along track scale. The solution is straightforward and does not degrade image quality. Rectification of along track scale is achieved during the conversion of signal films to map films. The simplicity of this method makes it attractive. However, it only applies to SAR. Its implementation requires prior numerical computation to determine the amounts of image deformations. On the basis of this computation, curves can be produced for the along track scale (Figure 5).

An ortho photo-production capability for radar was developed by Leberl and Fuchs (1978) and recently applied by Leberl et al. (in press) to a series of radar images. The equipment used is the Avioplan OR-1 manufactured by Wild of Heerbrugg, Switzerland. Similar instruments exist also from other manufacturers. A result is illustrated in Figures 6a, b.

III. RADAR STEREO MAPPING

A. Visual Stereo

Stereo viewing of overlapping radar imagery can greatly enhance the interpretation of the images by providing an improved means to observe morphological details (Koopmanns, 1974), to determine slope angles and height differences and

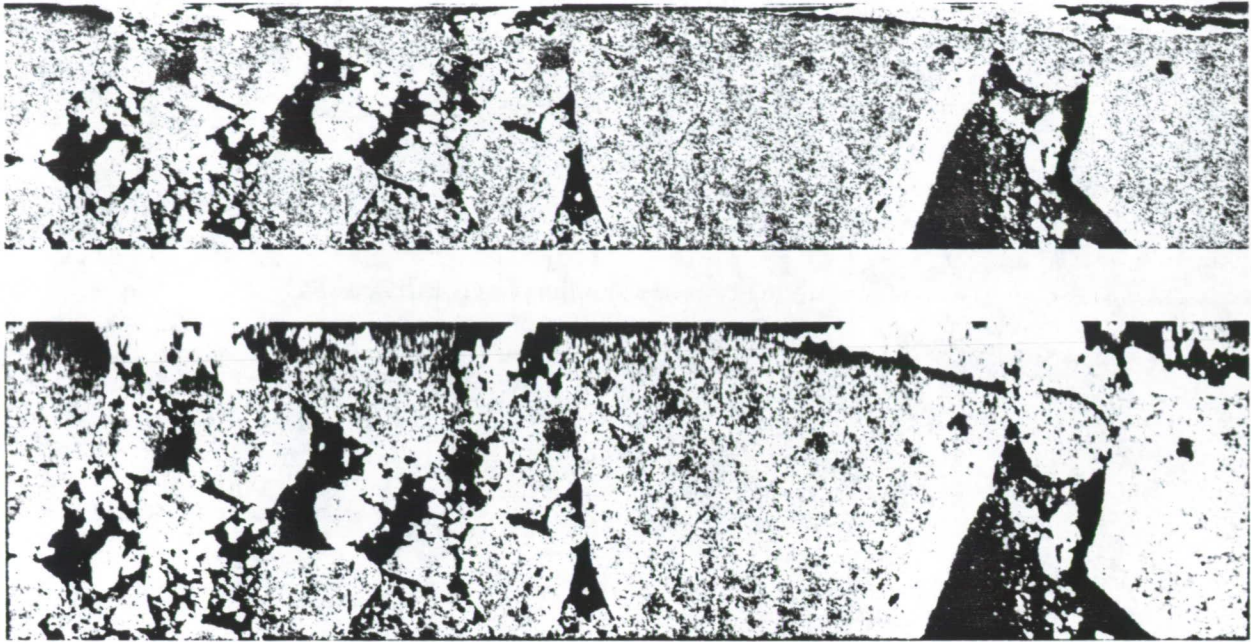


Figure 4. Example of radar image rectification using digital image processing. The distorted image (a) is in slant range presentation. Rectification is mainly a transformation to ground ranges.
 (Images courtesy Jet Propulsion Laboratory, taken with L-band synthetic aperture radar system over arctic sea ice.)

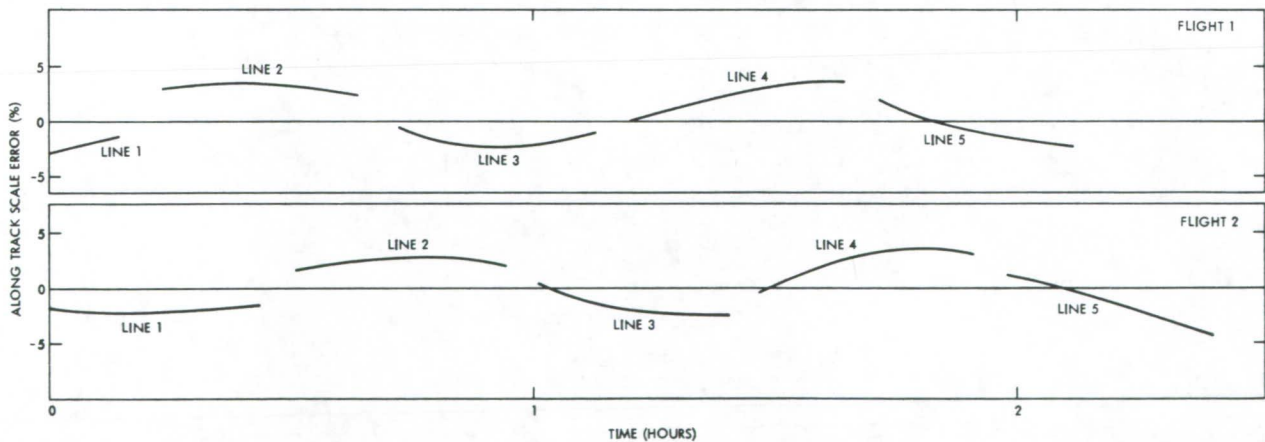


Figure 5. Scale error curves found in radar image strips (Leberl, Jensen and Kaplan, 1976). The periodicity of the along track scale errors as function of time is obvious.

ORIGINAL PAGE IS
 OF POOR QUALITY

ORIGINAL PAGE IS
OF POOR QUALITY



Figure 6. Westinghouse Ka-band image, flight height 6 km; (a) Not rectified (slant range presentation), like polarized. (b) Rectified on photogrammetric orthophoto-machine, cross-polarized.

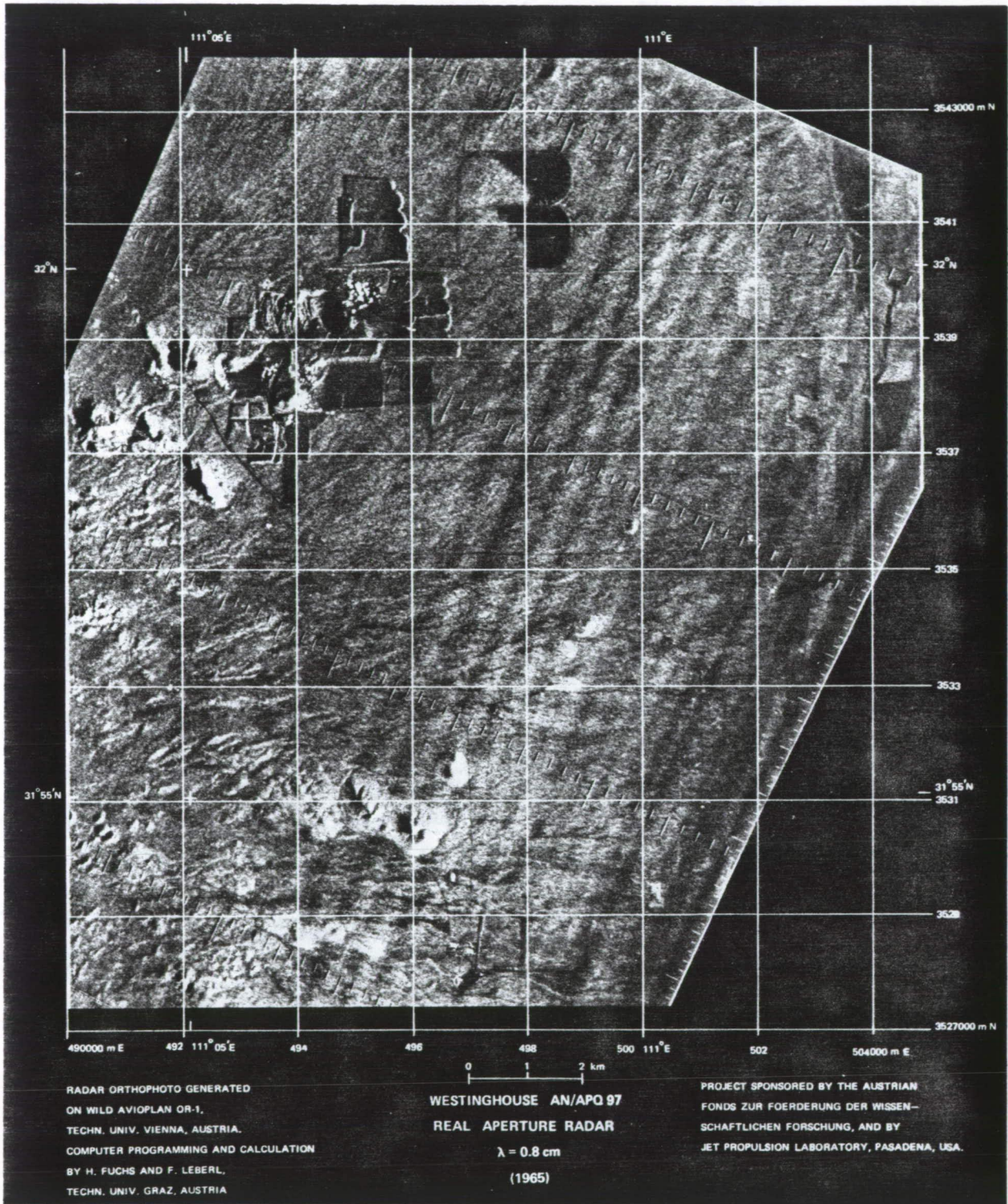


Figure 6 (Contd)

to improve cartographic mapping and point positioning accuracies. The present state of knowledge was reviewed by Leberl (1979).

A number of different schemes are conceivable to produce overlapping imagery in such a way that visual stereo is possible. Figure 7 illustrates the most common ones: same side and opposite side (La Prade, 1963; Rosenfield, 1968). These schemes are the only ones possible for synthetic aperture radar. Crosswise intersecting flight lines do not seem to produce valid visual stereo (Graham, 1975b). Other types of stereo arrangements would be possible with real aperture radar, for example, with convergent schemes using tilted antennas (Leberl, 1972b; Bair and Carlson, 1974).

In order to view a three-dimensional model the two images comprising the stereo pair must be sufficiently similar: the image quality and object illumination must be comparable and the geometric differences (parallaxes) must not exceed a certain maximum. In photography this hardly ever presents a problem since sun angles do not change drastically in overlapping photos. In radar images however the illumination angles depend on the orientation and position of the sensor and so does the appearance of the images.

Figures 8 to 11 present examples of radar stereo pairs demonstrating some of the limits to stereo viewing. Figure 8 shows part of the Estrella mountains in Arizona, U.S.A., imaged with an opposite side arrangement from an aircraft at 12 km altitude. It can be seen that slopes that reflect strongly in one image are in the radar shadow in the other image. A stereo impression can be obtained in the flat areas of this stereo pair, but becomes very difficult in the mountains. Figure 9 demonstrates with the same side stereo pair taken with the same radar system that there are no problems to stereo viewing.

Figures 10 and 11 present two Apollo 17 satellite radar stereo pairs taken of the lunar surface with same side geometry and very small stereo base. Look angles, however, are much steeper than in the examples of Figures 8 and 9. This leads to larger relief displacements and to differences of image contents in stereo mates even with small stereo bases. In the flat part of Figure 10 stereo viewing is not difficult. However, in the Apennine Mountains stereo fusion becomes nearly impossible and this is even more difficult in the image taken over the rugged Oriental region on the Moon's far side (Figure 11). From the above examples, the following factors influencing radar stereo viewing can be identified:

- Stereo arrangement (same side, opposite side).
- Look angles (angles off-nadir).
- Stereo intersection angles.
- Ruggedness of the terrain.

Exact interrelations among these factors are presently not well understood. Past experiences lead, however, to the tentative conclusion that opposite side stereo can only be applied in cases of flat or rolling surfaces, while rugged terrain requires same side imaging. Stereo viewing improves with shallower look angles (45° off-nadir and more). With steeper look angles (near nadir), the stereo base has to be reduced for successful stereo viewing, otherwise the differences of relief displacement become too large (compare Fig. 11). This smaller stereo base while improving the stereo viewability, does degrade the accuracy of the stereo

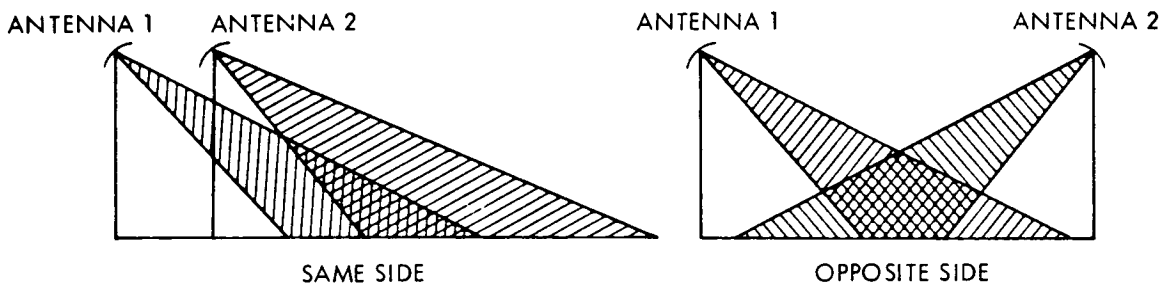


Figure 7. Basic flight configuration for stereo radar.

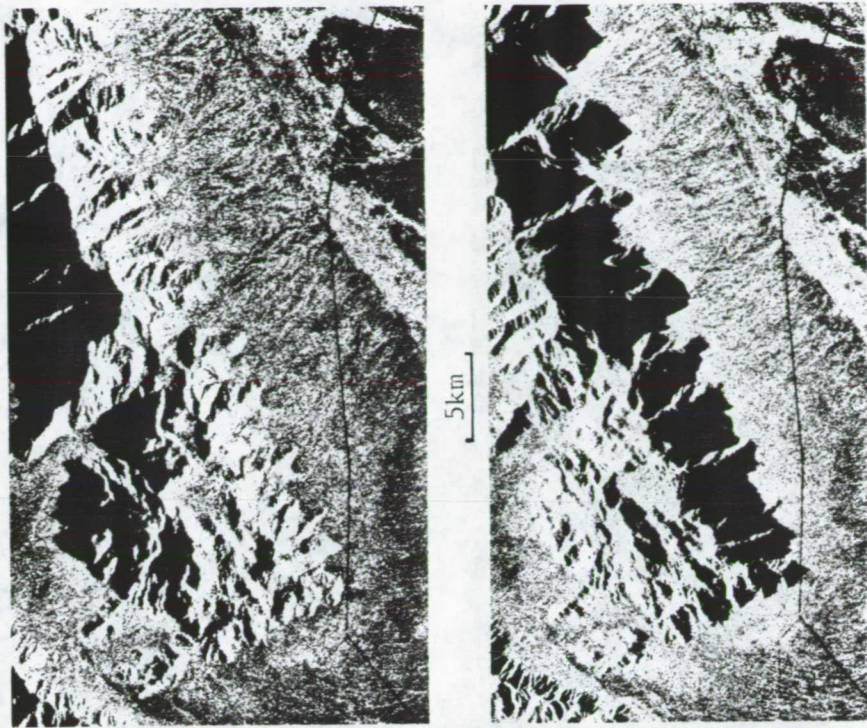


Figure 8. Aircraft stereo radar image pair, opposite side geometry. X-band, 12 km altitude; Estrella Mountains, Arizona (Courtesy of Aeroservice, Goodyear)

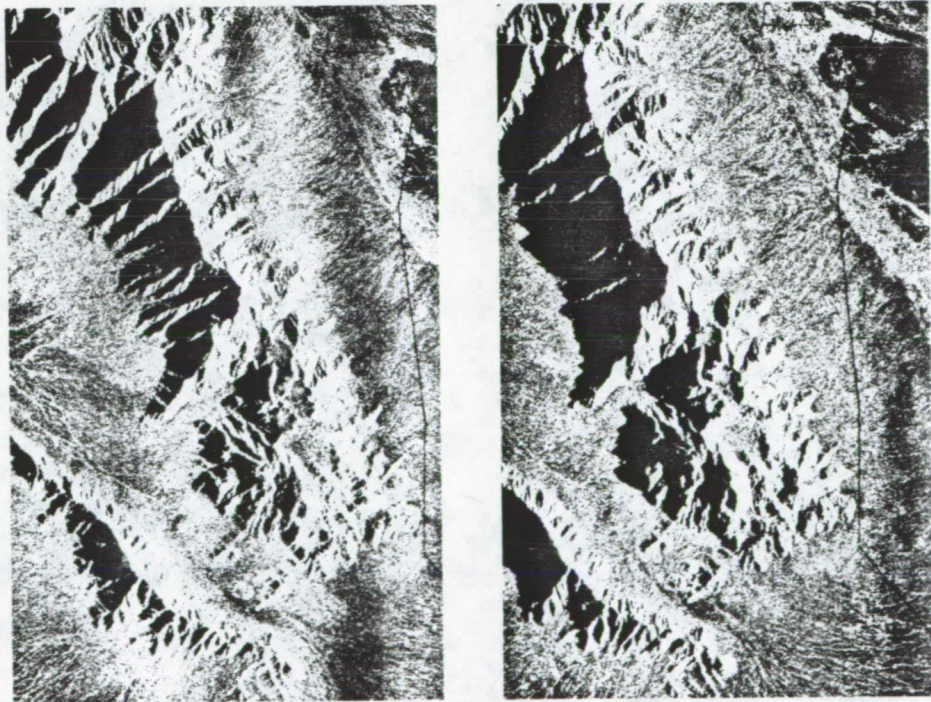


Figure 9. Aircraft stereo radar image pair, same side geometry. X-band, 12 km altitude; Estrella Mountains, Arizona (Courtesy of Aeroservice, Goodyear)

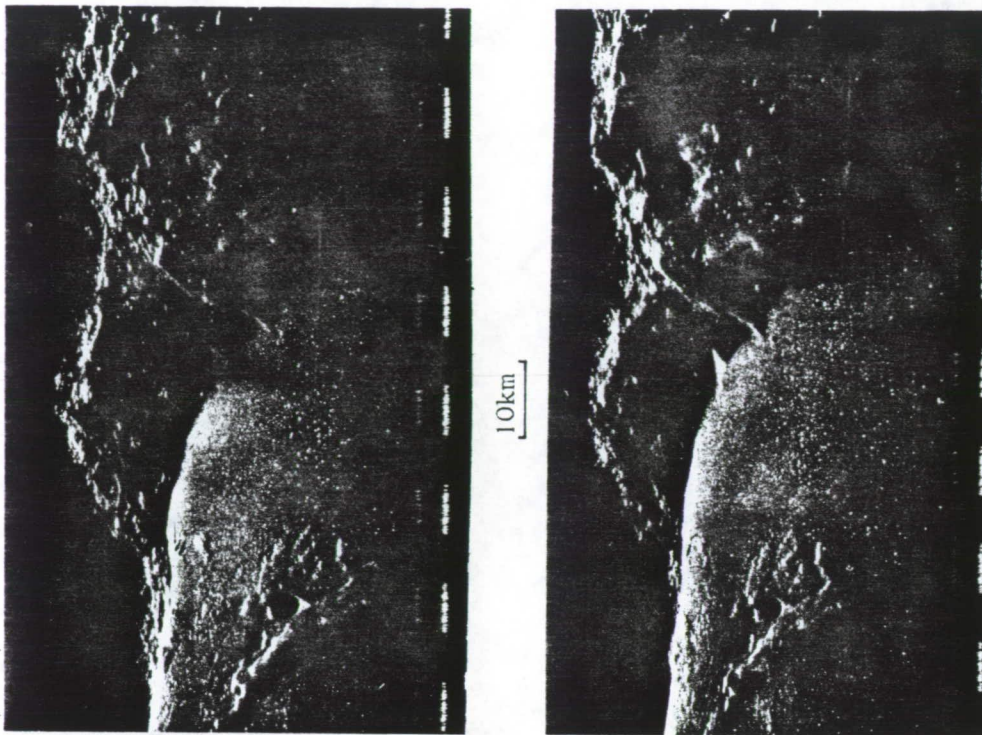


Figure 10. Satellite stereo radar, same side imaging, Apollo 17 - ALSE-VHF, Apennine Region on Moon.

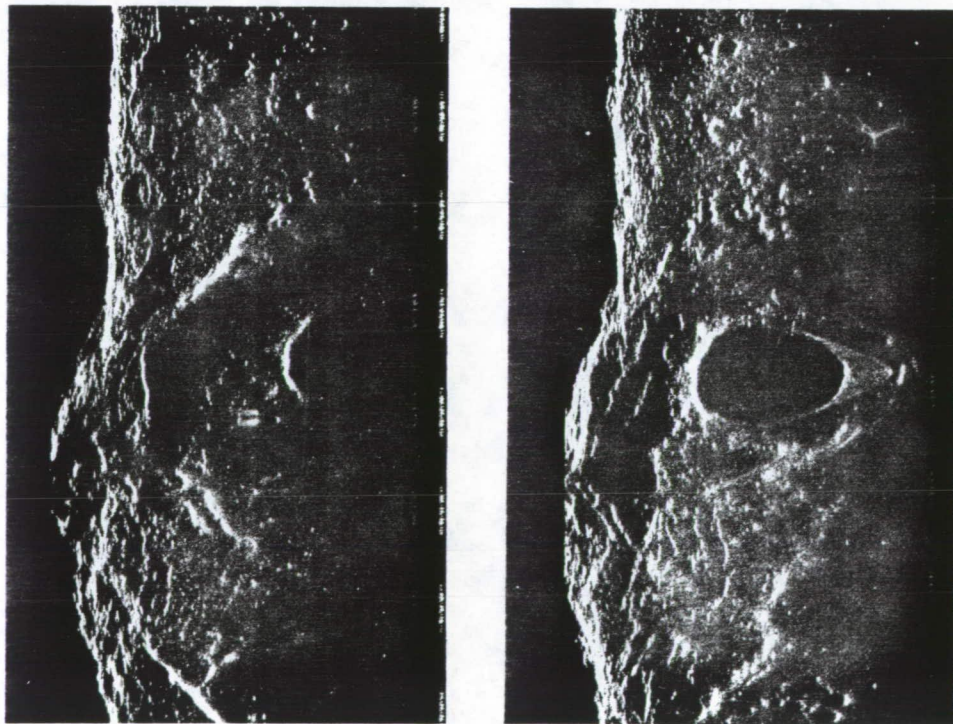


Figure 11. Satellite stereo radar, same side imaging, Apollo 17 - ALSE-VHF, Oriental Region on Moon.

model. One finds oneself in a tradeoff between stereo viewability and mapping accuracy.

B. Stereo Computation

Proper radar stereo computations may start from Equations (1) and (2), where vector \underline{p} is the unknown and to be found from:

$$\begin{aligned}\underline{p} &= \underline{s}' + \underline{A}'\underline{r}' \\ \underline{p} &= \underline{s}'' + \underline{A}''\underline{r}''\end{aligned}\tag{3}$$

where (') denotes the left and (") the right image.

A simplified formulation is obtained when one assumes a stereo pair with parallel, perfectly straight and level flight lines. Figure 12 shows that in a ground range presentation a stereo parallax Δp can be found that relates to ΔH as follows:

$$\begin{aligned}\Delta H &= p' / \tan \Omega' \\ \Delta H &= p'' / \tan \Omega'' \\ \Delta p &= p' \pm p'' = \Delta H (\tan \Omega' \pm \tan \Omega'') \\ \Delta H &= \Delta p / (\tan \Omega' + \tan \Omega'')\end{aligned}\tag{4}$$

Equation (4) is valid only if the projection circles can be approximated by straight lines (Figure 12). The plus sign applies to opposite side stereo, the minus sign to same side.

The situation for slant range geometry is slightly more complex. Even a flat ground will appear to be bowed in the radar stereo model. A discussion of this can be found in Leberl (1978, 1979).

C. Accuracies

As with single image mapping, the range of accuracies achieved so far with stereo radar is also diverse. Also here a large series of factors is of influence.

Figure 13 illustrates height accuracies obtained in the past. A conclusion may be that accuracies range from the resolution up to many tens of times the resolution in this regard. Stereo arrangement and control density are the main factors of influence. A study by Gracie et al. (1970) concluded that stereo height measurements would be accurate to within ± 13 m. However, this result applies to a density of 35 control points per 100 sq km and very well identifiable test points. Dowdell (1977) achieved a ± 25 -m root mean square height error using triple overlaps and high density of control. The computing effort was considerable. With a more modest (and realistic) density of control that corresponds to a reconnaissance-type, large area survey, say 4 points per 10,000 sq km, height accuracies may deteriorate to ± 100 to ± 200 m and more (see, for example, Derenyi, 1975; Leberl, 1977a).

The future can bring about an improved radar stereo capability from aircraft sensors if navigation and resolution improve, and from satellite sensors if look angles are varied sufficiently from one pass to the overlapping one over a given

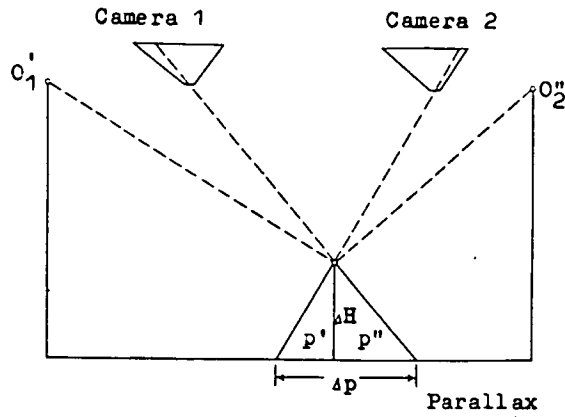


Figure 12. Definitions for the simple stereo computation with side-looking radar. The stereo base $O_1 O_2$ of radar corresponds to a camera base of camera 1 to camera 2 to produce equivalent parallaxes.

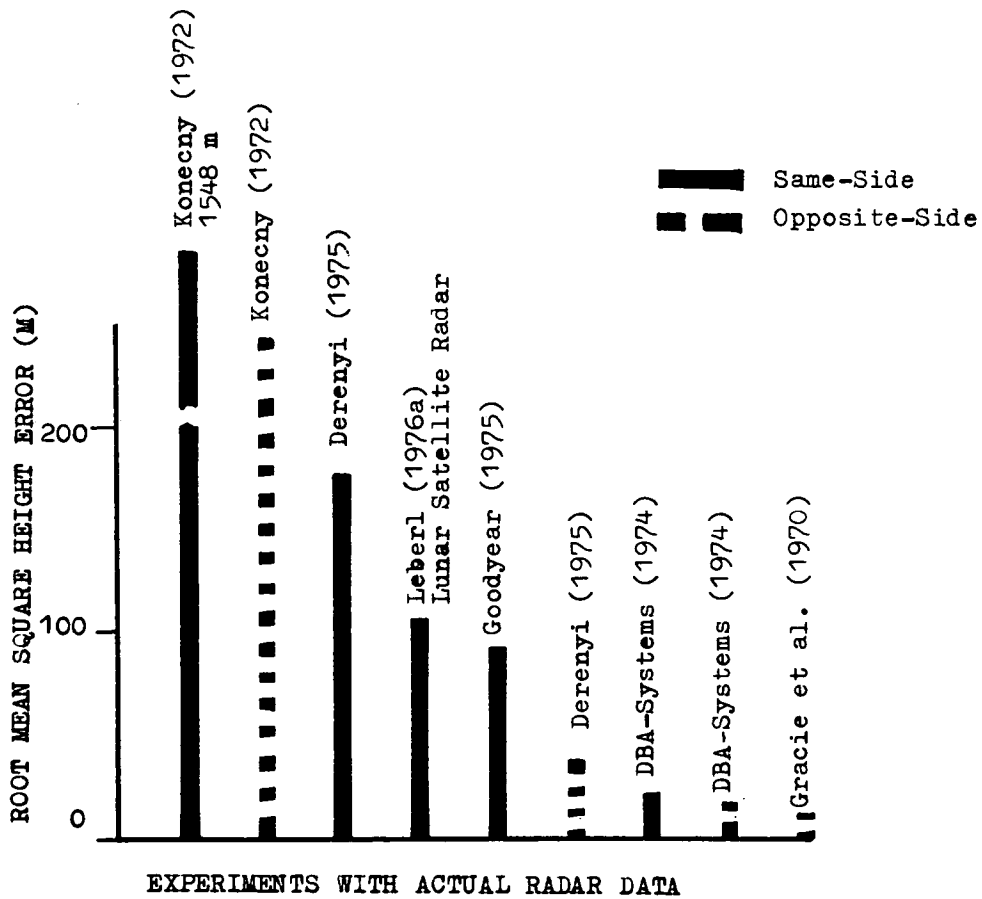


Figure 13. Accuracies achieved in experiments with radar stereo. Results strongly depend on project parameters.

area. However, the active mode of operation causes an inherent weakness of stereo: differing image contents can only be attained if look angles vary, but good visual stereo fusion requires similar look angles.

IV. BLOCK ADJUSTMENT AND MOSAICKING

A. General

Actual radar mapping projects result in blocks of overlapping image strips (Brazil's Radam: 25%, Proradam: 60%, West Virginia, U.S.A.: 25% and 60%). Mapping should thus be based on an adjustment to densify the generally sparse net of control points and to take advantage of the available redundancy in the overlaps. So far radar block adjustment has been applied to planimetry, using the original images (Leberl, 1975c; Leberl et al., 1976b). Three-dimensional radar block adjustment has been studied in a laboratory environment by DBA-Systems (1974) and by Dowideit (1977). The approaches, however, are not practical under present constraints.

Radar mosaicking has been carried out on three levels of sophistication: (a) No control points are used; the images are simply compiled to fit into mosaics. (b) Production strips are flown along parallel lines (for example north-south) and tie-lines are flown across (for example east-west); the tie-lines are controlled by ground control points or by tracking of the aircraft (e.g., Shoran) and the production lines are compiled into mosaics to fit the tie-lines. (c) All production strips are controlled by continuous tracking of the aircraft (Shoran); or a block adjustment is carried out to control all radar images for mosaicking.

Of these the most satisfactory method has been found to be a numerical block adjustment. Settings are obtained for the image correlator (SAR) to correct the scale of the image strips in a recorrelation (Peterson, 1976). Mosaicking is greatly simplified by the method as compared to other approaches.

B. Method of Block Adjustment

1. Internal Adjustment. The block adjustment is based on a fit of the radar image strips with respect to each other using tie-points in the common overlap of images (Figure 14). A coherent image block is obtained as shown in Figure 14 (b). Spline functions are used to describe image corrections Δx (along flight) and Δy (across flight). A spline consists of pieces of polynomials according to Figure 15; each of the pieces is:

$$\begin{aligned}\Delta x &= a_{i0} + a_{i1}(x-x_i) + a_{i2}(x-x_i)^2 + a_{i3}(x-x_i)^3, \\ \Delta y &= b_{i0} + b_{i1}(x-x_i) + b_{i2}(x-x_i)^2 + b_{i3}(x-x_i)^3,\end{aligned}\tag{5}$$

where a_{ij} , b_{ij} is the j th polynomial coefficient of piece i . The condition applies:

$$x_{i-1} \leq x < x_i\tag{6}$$

which implies that a polynomial piece is valid only in the range delimited by values x_{i-1} and x_i .

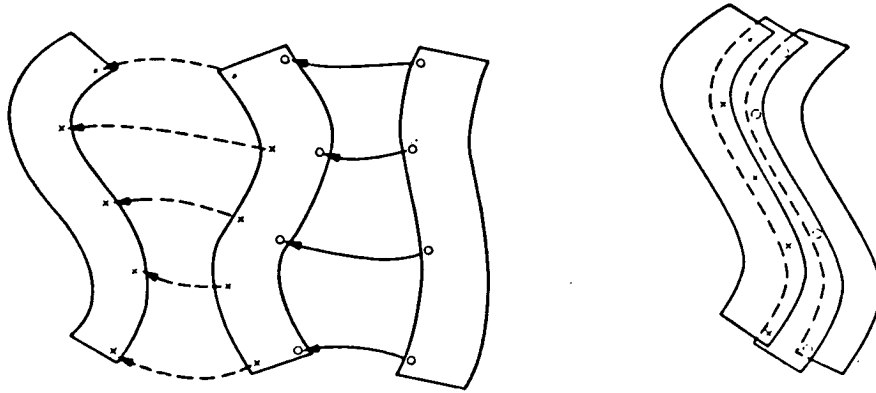


Figure 14. Principle of internal radar block adjustment. Tie-points are used to tie the strips (or stereo models) into a coherent block.

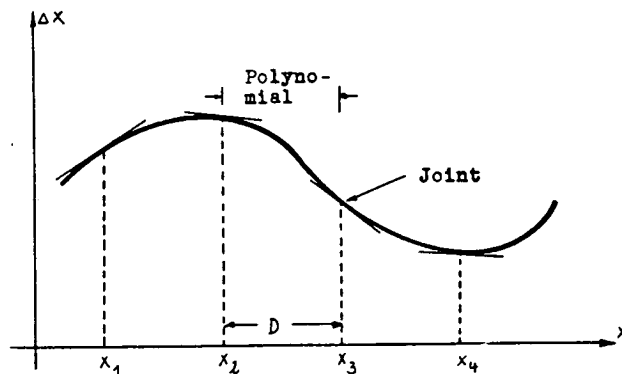


Figure 15. Spline-function or piecewise polynomial. The function is composed of polynomial pieces defined over a range D . Conditions exist at joints that adjacent polynomials are not discontinuous.

Additional conditions apply to enforce a smooth transition from one polynomial piece to the next: the derivatives of 0th, 1st, 2nd order are made identical at the joints of polynomial pieces. We find:

for the function value (0th derivative):

$$a_{i0} + a_{i1} \cdot D + a_{i2} \cdot D^2 + a_{i3} \cdot D^3 = a_{i+1,0}, \quad (7)$$

for the tangent (1st derivative):

$$a_{i1} + 2a_{i2} \cdot D + a_{i3} \cdot D^2 = a_{i+1,1}, \quad (8)$$

for the curvature (2nd derivative):

$$2a_{i2} + 6a_{i3} \cdot D = 2a_{i+1,2}, \quad (9)$$

D is the length of the polynomial piece:

$$D = x_{i+1} - x_i. \quad (10)$$

2. External Adjustment. The coherent radar image block must be transformed into the net of ground control points. The principle is illustrated by Figure 16. Any method of interpolation can be used to fit the image block to the control points. Often these methods are denoted by "warping" functions or "rubber sheet stretching."

Internal and external adjustment can be carried out sequentially or simultaneously. A sequential solution has the advantage of low programming and computational efforts. The generally limited density of ground control and dominating effect of periodical ("systematic") image errors permit the conclusion that a sequential solution does not produce results significantly inferior to a simultaneous approach (Leberl, 1975d).

C. Results

Block adjustment accuracy has been evaluated in a controlled experiment with images from the U.S.A. (Leberl, et al., 1976b). The result is shown in Figure 17. The abscissa shows the density of control, the ordinate the root mean square point errors in check points. The image had side-laps of 20%.

An equal distribution of ground control produces the best results. A point density of 15 points per 100,000 sq km can result in rms point errors of about ± 150 m (or coordinate errors of ± 100 m).

DBA-Systems (1974) and Dowideit (1977), in a more sophisticated, three-dimensional method of computation, obtained results that were about 3 X the resolution of the radar images, using however an unpractically high density of about 10 control points per 100 sq km (10,000 points per 100,000 sq km).

V. APPLICATIONS

The term mapping, as understood by the US Federal Mapping Task Force (Donelson, 1973), comprises

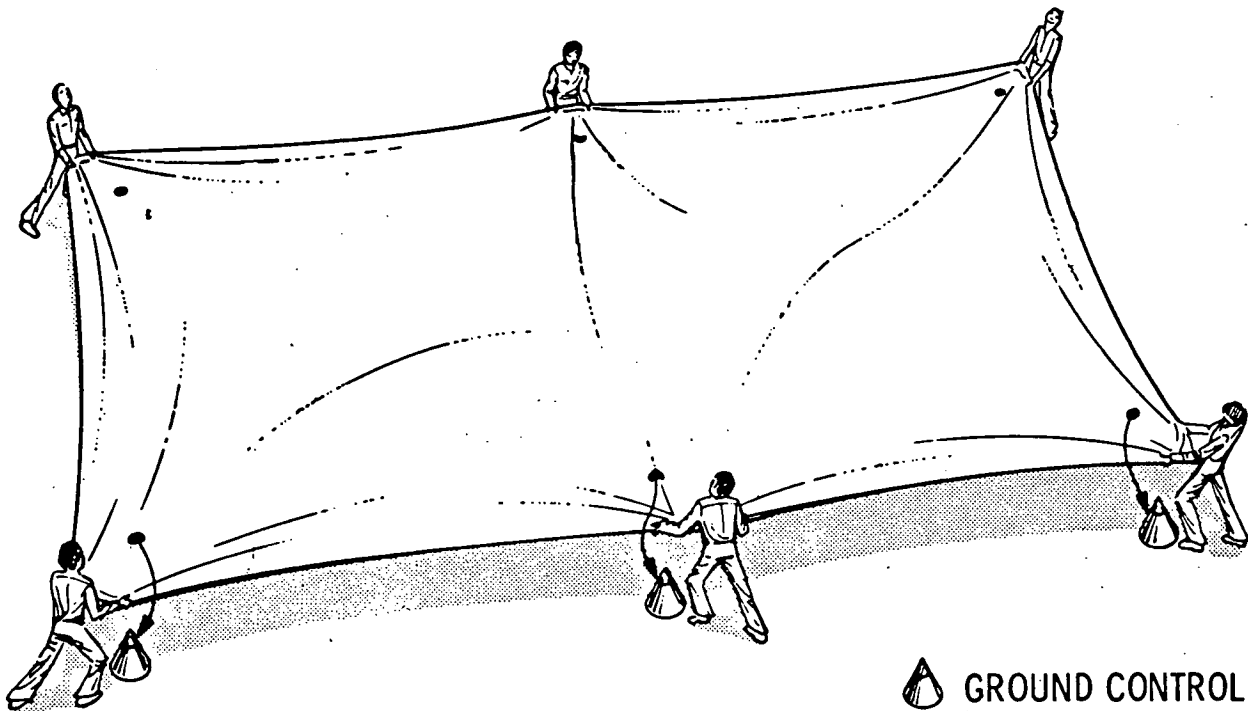


Figure 16. Principle of external radar block adjustment: the coherent block is made to fit the ground control points. Methods of fitting are numerical interpolation ("warping," "rubber sheet stretching").

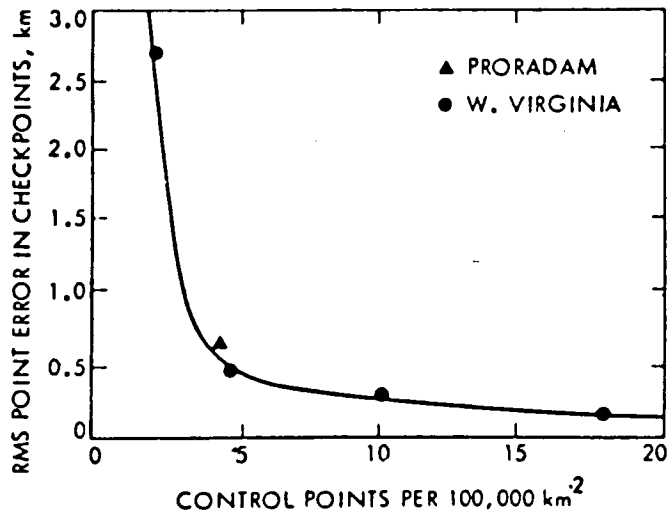


Figure 17. Accuracy of radar block adjustment for mosaicking: data are from an experimental radar block in West-Virginia (Leberl, Jensen and Kaplan, 1976) and from Colombian Proradam (Leberl, 1977a).

Land surveys (point positioning for geodesy, engineering)
 Land mapping (plainimetric, topographic, thematic),
 Marine mapping (nautical charts, bathymetry, floating aids, hazards)

Instead of focussing on some specific radar mapping applications it may be more relevant to discuss such applications in general terms. For specific applications reference is made to an extensive literature (see Bibliography). From the point of view of point positioning accuracy and of resolution of details, radar is generally no match for current methods of surveying and photogrammetry. However, timeliness and costs of mapping products are often of such an over-riding concern that radar's independence from weather and sun illumination could justify a certain spectrum of mapping applications in spite of its limited accuracy performance.

These applications, however, are only in land and marine mapping, not in point positioning tasks. These would be useful only in planetary exploration, such as on Venus, or to support mapping functions such as image rectification.

A. Land Mapping: Planimetry

Table 1 illustrates the map accuracy standards as they apply in the USA.

Table 1. Map accuracy standards in the U.S.A. in meters, expressed for planimetric point positioning

Scale	90% of coord. errors, m			Stand. deviation of coord. errors, m		
	Class			Class		
	A	B	C-1	A	B	C-1
1:250,000	90	180	359	54	110	218
1:100,000	36	72	143	22	44	87
1: 50,000	18	36	72	11	22	44

Comparison of this table with radar mapping accuracies clarifies that airborne radar mapping essentially can satisfy scales 1:250,000 at class B-level, or 1:100,000 at class C-1 level. Satellite radar can be expected to have a geometric stability superior to aircraft radar so that the potential exists for mapping errors of only in the order of magnitude of 30 m or so, provided that resolution permits such precise point identification.

B. Land Mapping: Height

For height mapping, stereo radar accuracies are generally not sufficient. Only in the context of thematic mapping (geomorphology, for example), or as a means to rectify individual images, must one see the usefulness of radar stereo. Only under very special circumstances, such as on Venus, or in arctic areas, may one find radar a tool suitable for measuring heights. However, space photography

such as the large format camera on the Space Shuttle, on Space Lab and later on a free-flying Multi-Mission Modular Spacecraft (MMS) must be expected to be superior in height accuracy.

C. Thematic Mapping

Radargrammetry is an obvious tool for preprocessing radar images for subsequent thematic analysis. Applications include merging of multitemporal data of images from different sensors and of images with maps or with topographic relief data. An example is the radar-Landsat synergism (Harris and Graham, 1976, Daily et al., 1978).

D. Marine Mapping

Nautical charts exist at the following scales in the U.S.A.:

<u>Type</u>	<u>Scale Range</u>
Sailing	< 1:600,000
General	1:100,000 to 1:600,000
Coastal	1: 50,000 to 1:100,000
Harbor	1: 50,000

Many inhospitable areas of the world with low illumination levels (polar regions) and/or cloud covers must still be served in the need for charts. Man-made point features such as ships and floating aids and nautical features such as icebergs and sea-ice can well be mapped by radar (Super and Osmer, 1975; Leberl et al., 1979). This is of particular significance because of the relative ease with which it is possible to signalize all image features on an otherwise specularly reflecting water-surface.

VI. RECOMMENDATIONS

Radargrammetry still is lacking significant efforts for technique development and for experimental performance verification. Methods of rectification of single images, stereo mapping and use of blocks of overlapping image strips must be studied to more fully understand the applicability, possibilities, and limitations of radar mapping. Investigations must include development of efficient techniques to employ modern mapping equipment such as differential rectifiers, analytical photogrammetric plotters, and digital image processing systems.

Concepts and questions can be treated using aircraft data. Such data may be of great value for themselves and for qualitative evaluation of expected results from satellite radar. They may be misleading, however, concerning quantitative conclusions on satellite radar; as a result one should use aircraft data in an initial phase of work to delimit, in general terms, the potentials of satellite radargrammetry and following such experiments with data from space. Short space missions such as those with the Space Shuttle could prove to be of singular importance to test and verify various concepts and expectations concerning merging of radar with digital terrain height files and other images, stereo mapping and point positioning for rectification using orbit data, and control points and overlapping image strips. During an experimental phase, extended space missions would not add significantly beyond the configuration that is available from short sorties.

BIBLIOGRAPHY (STATUS 1979)

- Akowetzki, W. I., 1968. On the transformation of radar coordinates into the geodetic system. Geod. Aerofotosjomka, 1968 (in Russian).
- Ambrose, W., 1967. A radar image correlation viewer. Photogramm. Eng., 33.
- Bair, G. L. and Carlson, G., 1975. Height measurement with stereo radar. Photogramm. Eng. Remote Sensing, 41.
- Bair, G. L. and Carlson, G. E., 1974. Performance comparison of techniques for obtaining stereo radar images. IEEE Trans. Geosci. Electron., GE-11.
- Berlin, G. L., 1971. Radar mosaics, Prof. Geogr., 23(1).
- Bicknell, T. et al., 1975. A study to determine the feasibility of using radar techniques for public land surveying. Jet Propulsion Laboratory Report under contract to the Bureau of Land Management, Contract No. 53500-PH3-995, Pasadena, Calif.
- Bosman, E. et al., 1971. Project Karaka - The transformation of points from side looking radar images into the map system. Final Report, Part 1, Netherlands Interdepartmental Working Community for the Application and Research of Remote Sensing Techniques (NIWARS), Delft.
- Bosman, E. R., Clerici, E., Eckhart, D. and Kubik, K., (undated). Project BEBLOKA - The transformation of points from overlapping images obtained with different sensors into the map system. Final Report, Netherlands Interdepartmental Working Community for the Application and Research of Remote Sensing Techniques (NIWARS), Delft.
- Bosman E. R., Clerici, E., Eckhart, D. and Kubik, K., 1972a. Transformation of points from side-looking radar images into the map system. Bildmessung Luftbildwesen, 42(2).
- Bosman, E. R., Clerici, E., Eckhart, D. and Kubik, K., 1972b. KARIN - A program system for the mapping of remote sensing information. Pres. Pap., 12th Congr. Int. Soc. Photogrammetry, Ottawa; also Final Report, Netherlands Interdepartmental Working Community for the Application and Research of Remote Sensing Techniques (NIWARS), Delft.
- Bryan, M. L., Stromberg, W., and Farr, T., 1976. Computer processing of SAR L-band imagery, Photo Eng. and Remote Sensing, Vol. 43. No. 10, pp. 1283 - 1294.
- Bryan, M. L., Stromberg, W., and Farr, T., 1977. Picture processing of SAR L-band imagery; Proceedings, ASP - ASCM Annual Convention, Washington, D.C.
- Carlson, G. E., 1973. An improved single flight technique for radar stereo. IEEE Trans. Geosci. Electron., GE-11(4).
- Claveloux, B. A., 1960. Sketching projector for side-looking radar photography. Photogramm. Eng., 26.

- Cohen, E. et al., 1975. An earth and ocean SAR for space shuttle-user requirements and data handling implications. Proc. Natl. Telecomm. Conf., New Orleans, La.
- Crandall, C. J., 1963. Advanced radar map compilation equipment. Photogramm. Eng., 29.
- Crandall, C. J., 1969. Radar mapping in Panama. Photogramm. Eng., 35.
- Daily, M., Elachi, C., Farr, T., Stromberg, W., Williams, S., and Schaber, A., 1978. Application of multispectral radar and Landsat imagery to geologic mapping in Death Valley, JPL Publication 78-19, Jet Propulsion Laboratory, Pasadena, California.
- Dalke, G. et al., 1968. Regional slopes with non stereo radar. Photogramm. Eng., 34.
- DBA Systems, 1974. Research studies and investigations for radar control extensions. DBA Systems Inc., Melbourne, Fla. (Defense Documentation Center Report No. 530784L).
- De Azevedo, L., 1971. Radar in the Amazon. Proc. 7th Int. Symp. Remote Sensing of the Environment. Ann Arbor, Mich.
- Derenyi, E. E., 1970. An Exploratory Investigation into the Relative Orientation of Continuous Strip Imagery. Thesis and Research Report No. 8, Univ. of New Brunswick, Fredericton, N.B.
- Derenyi, E. E., 1972. Geometric considerations in remote sensing. Proc. 1st Canadian Symp. on Remote Sensing. Ottawa.
- Derenyi, E. E., 1974a. SLAR geometric test. Photogramm. Eng., 40.
- Derenyi, E. E., 1974b. Metric evaluation of radar and infrared imageries. Proc. 2nd Canadian Symp. on Remote Sensing. Univ. of Guelph, Guelph, Ont.
- Derenyi, E. E., 1975a. Topographic accuracy of side looking radar imagery. Bildmessung Luftbildwesen, 1975 (1).
- Derenyi, E. E., 1975b. Terrain heights from SLAR Imagery. Pres. Pap. 41st Annual Conv. Am. Soc. Photogramm., Washington, D.C.
- DiCarlo, C. et al., 1968. All weather mapping. Pres. Pap. Int. Congr. of Surveyors (FIG), London.
- DiCarlo, C. et al., 1971. DoD data processing equipment for radar imagery. Pres. Pap. Int. Congr. of Surveyors, Wiesbaden.
- Donelson E. et al., 1973. Report of the Federal Task Force for Mapping, Charting, Geodesy and Surveying. Executive Office of the President, Office of Management and Budget, Washington D.C.
- Dowideit, G., 1975. A simulation system for theoretical analysis of radar restitution and a test by adjustment. Proc. Symp. Comm. III, Int. Soc Photogramm., Stuttgart. In: Deutsche Geodätische Kommission, Reihe B, Heft No. 214.

- Dowideit, G., 1977. Eine Blockausgleichung für Aufzeichnungen des Seitwärts-Radar (SCAR), Bildmessung und Luftbildwesen, Vol. 45, No. 1, pp. 17 - 23.
- Dowideit, G., 1977, Eine Blockausgleichung für Abbildungen des seitwärts-schauenden Radar (SLAR), Wissensch. Arbeiten der Lehrstühle für Geodäsie etc., Nr. 75, Techn. Universität Hannover, FRG, 185 pp.
- Egbert, E., 1969. Calculation of ground street lengths and area from radar measurements. In: D.S. Simonnett (Editor), The Utility of Radar and Other Remote Sensors in Thematic Land Use Mapping from Spacecraft. Annu. Rep. U.S. Geol. Surv., Interagency Report - NASA 140.
- Esten, R. D., 1953. Radar relief displacement and radar parallax. USAERDL-Report No. 1294, Ft. Belvoir, Va.
- Fiore, C., 1967. Side looking radar restitution, Photogramm. Eng., 33.
- Geier, F., 1971. Beitrag zur Geometrie des Radarbildes. Thesis, Techn. Univ., Graz (in German).
- Geier, F., 1972. Fundamentals of orientation for radar PPI images with approximated horizontal distances. Pres. Pap., 12th Congr., Int. Soc. Photogramm., Ottawa.
- Glushkov, V. M. et al., 1972. Toros - Side looking radar system and its application for sea ice condition study and for geologic explorations. Pres. Pap., 12th Congr., Int. Soc. Photogramm., Ottawa.
- Goodyear, 1972. Flight test report all-weather topographic mapping system AN/ASQ-142. Contract No. F 33657-70-C-0769, Goodyear Aerospace Corp., Litchfield Park, Ariz.
- Goodyear, 1974. Preliminary imagery data analysis Goodyear Electronic Mapping System (GEMS). Goodyear Aerospace Corp., Report GIB-9342, Code 99696.
- Gracie, G. et al., 1970. Stereo radar analysis. U.S. Eng. Topogr. Lab., Ft. Belvoir, Va., Report No. FTR-1339-1.
- Gracie, G. and Sewell, E. D., 1972. The Metric Quality of Stereo Radar. Proc. of the Techn. Program, Electro-Optical Systems Design Conference, New York, 12-14 Sept.
- Graham, L. C., 1970. Cartographic applications of synthetic aperture radar. Proc. Am. Soc. Photogramm., 37th Annual Meeting; and Goodyear Aerospace Corp., Report GERA-1626.
- Graham, L., 1972. An improved orthographic radar restitutor. Pres. Pap., 12th Congr., Int. Soc. Photogramm., Ottawa; also in Goodyear Aerospace Corp., Report GERA-1831.
- Graham, L. and Rydstrom, H. O., 1974. Synthetic aperture radar applications to earth resources development. Goodyear Aerospace Corp., Report GERA-2010, Code 99696.

- Graham, L. C., 1975a. Geometric problems in side-looking radar imaging. Proc. Symp. Comm. III, Int. Soc. Photogramm.; Stuttgart, W. Germany; In: Deutsche Geodätische Kommission, Reihe B, Heft No. 214.
- Graham, L., 1975b. Flight planning for stereo radar mapping. Proc. Am. Soc. Photogramm., 41st Meet., Washington, D.C.
- Greve, C. and Cooney, W., 1974. The digital rectification of side looking radar. Proc. Am. Soc. Photogramm., Annu. Conv., Wash., D.C.
- Harris, G. and Graham, L. C., 1976. LANDSAT - radar synergism. Pres. Pap., 13th Int. Congr. Soc. Photogramm., Comm. VII, Helsinki.
- Hirsch, Th. and Van Kuilenburg, J., 1976. Preliminary tests of the EMI-SLAR mapping quality. Netherlands Interdepartmental Working Community for the Appli. and Res. of Remote Sensing (NIWARS), Internal Report No. 39, Delft.
- Hockeborn, H. A., 1971. Extraction of positional information from side looking radar. Bildmessung Luftbildwesen, 39 (1).
- Hoffmann, P., 1958. Photogrammetric applications of radar scope photographs. Photogramm. Eng., 24.
- Hohenberg, F., 1950. Zur Geometrie des Funkmessbildes. Austrian Academy of Sciences, Math.-Naturwissenschaftliche Klasse, Vienna, Vol. 2-3.
- Jensen, H., 1972. Mapping with coherent-radiation focused synthetic aperture side-looking radar. In: Operational Remote Sensing: An Interactive Seminar to Evaluate Current Capabilities. Am. Soc. Photogramm.
- Jensen, H., 1975. Deformations of SLAR imagery-results from actual surveys. Proc. Symp. Comm. III, Int. Soc. Photogramm., Stuttgart. In: Deutsche Geodätische Kommission, Reihe B, Heft No. 214.
- Kober, C. L, et al., 1950. Determination of target height from radar PPI-Photographs. Air Force Tech. Rep. No. 6500, Wright Air Development Center, Ohio.
- Konecny, G. and Derenyi, E. E., 1966. Geometric considerations for mapping from scan imagery. Proc. 4th Symp. Remote Sensing of the Environment, Ann Arbor, Mich.
- Konecny, G., 1970. Metric problems in remote sensing. Publications of the International Institute for Aerial Surveying and Earth Sciences (ITC), Delft, Series A, No. 50.
- Konecny, G., 1971. Orientierungsfragen bei Streifenbildern und Aufnahmen der Infrarotabtastung. Bildmessung Luftbildwesen, 41 (1).
- Konecny, G., 1972a. Geometrical aspects of remote sensing. Arch. Int. Soc. Photogramm., Invited Paper, 12th Congr., Ottawa.
- Konecny, G., 1972b. Geometrische Probleme der Fernerkundung. Bildmessung Luftbildwesen, 42 (2).

- Konecny, G., 1975. Approach and status of geometric restitution for remote sensing imagery. Proc. Symp. Comm. III, Int. Soc. Photogramm., Stuttgart; In: Deutsche Geodätische Kommission, Reihe B, Heft No. 214.
- Koopmans, B., 1974. Should stereo SLAR imagery be preferred to single strip imagery for thematic mapping? ITC-Journal 1974-3, Enschede.
- Korneevn, I.U.N., 1975. Analytical method for photogrammetric processing of a single radar photograph. Geod. Aerofotosjomka, 1975 (2) (in Russian).
- Kratky, V., 1979. SEASAT orbit effects on imaging geometry of synthetic aperture radar, 3rd GDTA Symposium, 19 - 22 June 1979, Toulouse, France.
- LaPrade, G. L., 1963. An analytical and experimental study of stereo for radar. Photogramm. Eng. 29.
- LaPrade, G. L., et al., 1969. Elevations from radar imagery. Photogramm. Eng., 35.
- LaPrade, G. L., 1970. Subjective considerations for stereo radar. Goodyear Aerospace Corp., Report GIB-9169, and Photogramm. Eng.
- LaPrade, G. L., 1975. Radar signature of inverted catenary with equilateral triangular cross section (St. Louis Gateway Arch). Arizona Electronics Eng. Memo. No. 525, Goodyear Aerospace Corp., Arizona Div., Litchfield Park, Ariz.
- Leberl, F., 1970, Metric properties of imagery produced by side looking airborne radar and infrared line scan systems. Publications of the International Institute for Aerial Survey and Earth Sciences (ITC), Series A, No. 50, Delft.
- Leberl, F., 1971a. Vorschläge sur instrumentellen Entzerrung von Abbildungen mit Seitwärts Radar (SLAR) und Infrarotabtastsystemen. Bildmessung Luftbildwesen, 39.
- Leberl, F., 1971b. Remote Sensing - Neue Methoden zur Wahrnehmung auf Abstand. Österreichische Zeitschrift für Vermessungswesen, No. 6.
- Leberl, F., 1971c. Untersuchung über die Geometrie und Einzelbildauswertung von Radarschragäufnahmen. Thesis, Tech. Univ., Vienna.
- Leberl, F., 1972a. Evaluation of single strips of side looking radar imagery. Arch. Int. Soc. Photogrammetry, Invited Pap., 12th Congr., Ottawa.
- Leberl, F., 1972b. On model formation with remote sensing imagery. Österreichische Zeitschrift für Vermessungswesen No. 2.
- Leberl, F., 1972c. Radargrammetria para los Interpretes de Imagenes. Centro Interamericano de Fotointerpretacion, (CIAF), Bogotá, Colombia.
- Leberl, F., 1974. Evaluation of SLAR Image Quality and Geometry for PRORADAM. ITC-Journal, 2(4).

- Leberl, F., 1975a. The geometry of, and plotting from, single strips of side looking airborne radar imagery. International Institute for Aerial Survey and Earth Sciences (ITC) Technical Report No. 1, Enschede.
- Leberl, F., 1975b. Radargrammetry for Image Interpreters, ITC Tech. Rep. No. 2, Enschede.
- Leberl, F., 1975c. Radargrammetric point determination PRORADAM. Bildmessung Luftbildwesen, 45 (1).
- Leberl, F., 1975d. Sequential and simultaneous SLAR block adjustment. Photogrammetria, 31 (1).
- Leberl, F., 1975e. Lunar Radargrammetry with ALSE-VHF Imagery. Proc. Am. Soc. Photogramm., Fall Tech. Meeting, Phoenix, Ariz.
- Leberl, F., 1976a. Mapping of lunar surface from side-looking orbital radar images. The Moon, Vol. 15, pp. 329 - 342.
- Leberl, F., 1976b. Imaging radar applications to mapping and charting, Photogrammetria, Vol. 32, pp. 75 - 100.
- Leberl, F., 1977. Radar mapping applications using single images, stereo pairs and image blocks: methods and applications, Revista Brasileira de Cartografia, No. 20, pp. 16 - 26.
- Leberl, F., 1978. Satelliten-Radargrammetrie, Dtsch. Geod. Komm., Reihe C, No. 239.
- Leberl, F., 1979. Accuracy Aspects of Stereo Side Looking Radar, JPL Publication 79 - 17, Jet Propulsion Laboratory, Pasadena, USA.
- Leberl, F., Farr, T., Bryan, L. and Elachi, C., 1976a. Study of Arctic Sea Ice Drift from L-Band Side Looking Radar Imagery. Proc. Am. Soc. Photogramm., 42nd Ann. Conv., Washington, D.C.
- Leberl, F., Jensen, H. and Kaplan, J., 1976b. Side-looking radar mosaicking experiment. Photogramm. Eng. and Remote Sensing, 42.
- Leberl, F., and Elachi, C., 1977. Mapping with satellite side-looking radar, Proceedings, 2nd GDTA Symposium St. Mandé, France, pp. 451-465.
- Leberl, F., and Fuchs, H., 1978. Photogrammetric differential rectification of radar images, Proceedings Symp. of Comm. III of the Intl. Soc. Photogrammetry, 29 July - 5 August, Moscow, USSR, pp. 434 - 455.
- Leberl, F., et al., 1979. Mapping of sea-ice and measurement of its drift using aircraft synthetic aperture radar images, J. Geophysical Research, Vol. 84, No. C4, pp. 1827 - 1835.
- Leberl, F., Fuchs, H. and Ford, J. (in press). A Radar Image Time Series. Intl Journal of Remote Sensing.
- Leonardo, E., 1959. An application of photogrammetry to radar research. Photogramm. Eng., 25.

- Leonardo, E., 1963. Comparison of imaging geometry for radar and photographs. Photogramm. Eng., 29.
- Leonardo, E., 1964. Capabilities and limitations of remote sensors. Photogramm. Eng., 30.
- Levine, D., 1960. Radargrammetry. McGraw-Hill, New York, N.Y.
- Levine, D., 1963. Principles of stereoscopic instrumentation for PPI-photographs. Photogramm. Eng., 30.
- Levine, G., 1965. Automatic production of contour maps from radar interferometric data. Pres. Pap., Fall Tech. Meet., Am. Soc. Photogramm., Dayton, Ohio.
- Lewis, A. J., and MacDonald, H. C., 1970. Interpretive and Mosaicking Problems of SLAR Imagery. Remote Sensing Environ., 1(4).
- Ling, C., Rasmussen, L., and Campbell, W., 1978. Flight path curvature distortion in side-looking airborne radar imagery, Photogramm. Eng. and Remote Sensing, Vol. 44, No. 10, pp. 1255 - 1260.
- Loelkes, G. L., 1965. Radar mapping imagery - Its enhancements and extraction for map construction. Pres. Pap., Fall Tech. Meet., Am. Soc. Photogramm., Dayton, Ohio..
- Loshchilov, U. S., and Voyevodin, U. A., 1972. Determining elements of drift of the ice cover and movement of the ice-edge by the aid of the TOROS aircraft lateral scan radar station, Problemi Artiki, Antartiki, No. 40, pp. 23-30.
- Luchininov, V. S., 1975. Contactless radar mapping of warm valley glaciers - Transformation of radar coordinates. Transl. from Russian in Sov. Phys. Tech. Phys., 20(4).
- Macchia, R. P., 1957. Radar presentation restitutor. Photogramm. Eng., 23.
- Manual of Photogrammetry, 1966. Combinations of Photogrammetric and Radargrammetric Techniques, Chapter XXI, Author-Editor: D. Levine, 3rd edition.
- Masry, S. E., Derenyi, E. E., and Crawley, B. G., 1976. Photomaps from non-conventional imagery. Photogramm. Eng. Remote Sensing, 42(4).
- Miranda, A., 1970. Radar stereo equipment. Goodyear Aerospace Corporation, Report GIB-9198.
- Moore, R. K., 1969. Heights from simultaneous radar and infrared. Photogramm. Eng., 35.
- Moreira, H. F., 1973. Project RADAM - Remote sensing application to environment analysis of Amazon region. 2nd Annual Remote Sensing of Earth Resources Conference, Univ. of Tennessee Space Inst., Tullahoma, Tennessee.
- Norvelle, F. R., 1972. AS-11-A Radar Program. Photogramm. Eng., 38.

- Peterson, R. K., 1976. The correction of anamorphic scale errors in holographic radar imagery. Goodyear Aerospace Report, Code 99696, Litchfield Park, Ariz., Pres. Pap., 13th Congr. Int. Soc. Photogramm., Helsinki.
- Phillips, R., et al., 1973. Apollo lunar sounder experiment. Apollo-17 Preliminary Science Report, NASA-SP 330, Washington, D.C.
- Protherse, W. M., et al., 1950. The geometry of the radarscope. Tech. Paper, No. 107, Mapping and Charting Laboratory, Ohio State Univ., Ohio.
- Raytheon Co., 1973. Digital rectification of side-looking radar (DRESLER). Final Report, Raytheon Co, Autometric Operation, Prep. for U.S. Army Engineer Topographic Laboratories, Fort Belvoir, Va., 22060, Rep. No ETL-CR-73-18.
- Rinner, K., 1948. Die Geometrie des Funkmessbildes. Austrian Academy of Sciences, Math. Naturwiss. Klasse; also in: Handbuch der Vermessungskunde. Jordan-Eggert-Kneissl, Vol. VI, Metzlersche Verlagsbuchhandlung, Stuttgart, 1966.
- Roessel, J. Van and De Godoy, R., 1974. SLAR mosaics for Project RADAM. Photogramm. Eng., 40.
- Rose, J. and Friedman, L., 1974. A design for a Venus orbital imaging radar mission. Am. Inst. Aeronaut. Astronaut., AIAA-Pap. No. 74-222.
- Rosenfield, G. H., 1968. Stereo Radar Techniques. Photogramm. Eng., 34.
- Rydstrom, H. C., 1968. Radargrammetric Applications of the Right Angle Solution Nomogram. Goodyear Aerospace Corp., Report GIB 9124, Litchfield Park, Ariz.
- Scheps, B. B., 1960. To Measure is to know - Geometric fidelity and interpretation in radar mapping. Photogramm. Eng., 26.
- Schertler, R. J., et al., 1975. Great Lakes all-weather ice information system. Proc. 10th Symp. Remote Sensing of the Environment, Ann Arbor, Mich.
- Schreiter, J. B., 1950. Strip projection for radar charting. Tech. Paper No. 130, Mapping and Charting Laboratory, Ohio State Univ., Ohio.
- Shakine, A., and Le Toan, T., 1978. A Study of Digitized Radar Images, Intl. Symp. on Remote Sensing of Environment, Ann Arbor, U.S.A.
- Smith, H. P., 1948. Mapping by radar - The Procedures and possibilities of a new and revolutionary method of mapping and charting. U.S. Air Force, Randolph Field, Texas.
- Stilwell, J. E., 1963. Radar network adjustment. Photogramm. Eng., 29.
- Super, A. D., et al., 1975. Remote sensing applied to the international ice patrol. Proc. 10th Symp. on Remote Sensing of the Environment, Ann Arbor, Mich.
- Tiernan, M., et al., 1976. Lunar Cartography with the Apollo 17 ALSE Radar Imagery. The Moon, 15(1/2).

- Thomann, G. C., 1969. Acoustic simulation of stereo radar. Tech. Mem. No. 133-8, CRES, Univ. of Kansas, Lawrence, Kansas.
- Thomann, G., 1969. Distance computation on radar film. In: D. G. Simonnett (Editor), The Utility of Radar and Other Remote Sensors in Thematic Land Use Mapping from Spacecraft. Annu. Rep., U. S. Geol. Surv., Interagency Report, NASA-140.
- Thompson, T. W., et al., 1972. Progress report on 25cm radar observations of the 1971 AIDJEX studies. Arctic Ice Dynamics Joint Experiment (AIDJEX) Bulletin, No. 12, Univ. of Wash., Seattle, Wash.
- Yoritomo, K., 1965. All weather mapping. Pres. Pap., Fall Tech. Meet., Soc. Photogramm., Dayton, Ohio.
- Yoritomo, K., 1972. Methods and instruments for the restitution of radar pictures. Arch. Int. Soc. Photogramm., Inv. Pap., 12th Congr., Ottawa.
- Zhurkin, I. G., and Kornegev, N. 1974. Relationship between the coordinates of terrain points and the coordinates of image points in side-looking radar systems with an antenna along the fuselage. Geodesy, Mapping, Photogrammetry, Vol. 16, No. 3, pp. 140 - 146.

STEREO RADAR FOR MAPPING
AND INTERPRETATIONL. Graham
Goodyear Aerospace Corporation
Arizona Division

ABSTRACT

This paper discusses the use of terrain imaging radar to extract elevation information by stereo viewing and measurement. Either a 3-D visual model or elevation measurements may be obtained by simultaneous viewing or differential measurement of images obtained by a side-looking radar from two different flightpaths. Expressions describing radar image geometry, model vertical exaggeration, and stereo measurement accuracy are derived. The dependence of the exaggeration and accuracy on system parameters and key system errors is derived, discussed, and illustrated by application to several airborne and spaceborne systems and system concepts, and the results of some preliminary measurements of imagery from two airborne and one spaceborne system are given.

I. STATEMENT OF THE PROBLEM

Side-looking, terrain-imaging radar systems have been used for terrain analysis for at least a decade. Most applications have used monoscopic imaging. Stereo mode operation for photointerpretation and terrain elevation measurement has been recognized as a useful extension and used with some success, but only sporadically. As a result, the relationships between radar engineering parameters such as resolution, postdetection integration, and geometric fidelity on the one hand, and application utility such as accuracy of terrain analysis and accuracy of elevation measurement on the other hand are not well understood nor widely known.

The requirement for better understanding and quantification of radar stereo capabilities is becoming more important because systems having more nearly optimum stereo viewing parameters than previously used are becoming available to geologic and terrain surface analysts. The critical parameter in this context is the radar stereo convergence angle and its variation over the stereo model. This angle determines the vertical exaggeration of the model and, in combination with system resolution, determines the measurement accuracy. For a given sensor coverage, the ability to achieve an optimum convergence angle and approximate it over the imaged swath improves with sensor altitude above terrain. For example, the NASA JSC AN/APQ-102A radar installed in a high-flying B-57 aircraft achieves optimum angles over a significantly wider swath than previous radars. Satellite

borne systems such as the Seasat radar and the proposed Venus orbital imaging radar have, or can have, even more advantageous convergence angles, although their resolution is considerably poorer. Full realization of the potential of these and other systems cannot be achieved until the variables are quantified and understood.

II. BACKGROUND

A. Image Geometry

Side-looking radars (SLRs) direct a beam of energy at right angles to the flightpath of the aircraft in which they are installed as shown in Figure 1. A short burst, or pulse, of microwave energy is directed from a high-powered transmitter along a vertical fan-shaped beam by a directional antenna. As the resulting wave train impinges on the terrain, it becomes scattered, and a portion of it is sent back to the aircraft, where it is intercepted by the same antenna and sent to a sensitive radio receiver.

A signal is created whose amplitude depends on the magnitude of microwave energy received at any instant. This detected, or video, signal controls the brightness of a moving spot of light. The moving spot is imaged on photographic film, thus forming a latent image which, when chemically processed, exhibits at any point a photographic density corresponding to the microwave reflectivity of a part of the corresponding strip of terrain in the antenna beam.

As the aircraft advances along the flightpath, the vertical beam is moved to new positions so that succeeding pulses sense adjacent strips of terrain. The film advance is synchronized with aircraft motion to record these adjacent terrain strips on adjacent film strips, with returns recorded from like distances in alignment. The resulting radar imagery of terrain reflectivity is like a microwave photograph of the terrain, except that the measurable distance to features in the image corresponds to distances along the flight track Y and from the flight track R . Limiting image resolution is determined by the length of the transmitted pulse (quantitatively equal to $\delta_R = c\tau/2$, where c = velocity of propagation and τ = time duration of pulse) in the range direction and by antenna beamwidth and range ($\delta_Y = R\beta = R\lambda/L_p$, where β = antenna beamwidth, λ = wavelength, and L_p = antenna length) in the along-track direction.

In synthetic aperture radar (SAR) systems, fine resolution in the along-track direction is achieved by storing and processing the radar returns prior to forming the image. This results in forming a long synthetic antenna along the flight track which has a corresponding by narrow effective antenna beam, $\beta_S = \lambda/2L_S$, and thus fine along-track resolution. In SAR systems, δ_R is usually made about equal to δ_Y , and one can think in terms of an image resolution cell or pixel of dimension δ_R by δ_Y . Except for the provision of finer resolution, however, the basic image geometry is the same as for the rudimentary radar of Figure 1.

By solving the triangle formed by the altitude, Z , the slant range, R , and the across-track distance from the flight track, X , and noting that Y is proportional to y , the transformation from the cylindrical coordinate system, R, Y, θ to the rectangular coordinate system x, y, z can be obtained:

$$\left. \begin{aligned}
 (a) \quad y &= kY \\
 (b) \quad x &= kR \cos \theta \\
 (c) \quad z &= kR \sin \theta
 \end{aligned} \right\} \quad (1)$$

and these may be solved simultaneously for the inverse transformation:

$$\left. \begin{aligned}
 (a) \quad y &= y/k \\
 (b) \quad R &= (x^2/k^2 + z^2/k^2)^{1/2} \\
 (c) \quad \theta &= \tan^{-1} z/x
 \end{aligned} \right\} \quad (2)$$

where x , y , and z are the cartesian coordinates of a point in the image scale and k is the image scale factor.

B. Ground Range Images

In earth resources applications, the display across-track coordinate is usually nonlinear (hyperbolic with R or time) in such a manner that objects in a datum plane at some reference elevation are recorded as a linear function of distance from the aircraft ground track, X , in the datum plane, as shown in Figure 2. Without this correction, the image is referred to as a slant range image and with it, as a ground range image.

Figure 2 shows arbitrary terrain points P_1 through P_6 , and their relative positions in a slant range sweep image as compared to their relative positions in a ground range sweep image. The required motion of the recording spot to obtain a ground range image in a particular datum may be obtained by letting $R = ct/2$ and $z = kh$ in Equation (2)(b) and solving for x . Thus,

$$x = k \left(\frac{c^2 t^2}{4} - h^2 \right)^{1/2} \quad (3)$$

where

h = altitude of radar above datum

t = transmission time of radar pulse from
radar to terrain point and back

c = velocity of propagation

This hyperbolic sweep, which causes the points to vary in spacing across the image also, of course, causes an image resolution variation, which might be thought of as a variation in pixel size.

C. Elevation Displacement

Points lying at elevations other than the datum plane are recorded at across-track positions different from their true orthonormal positions, as illustrated in Figure 3.

Figure 3 depicts an aircraft flying at point a, a distance h above a datum, imaging in ground range a point at p, a distance h - z above the datum, and a distance R from the aircraft. The true horizontal position of the imaged point with respect to the aircraft is X. The point is displaced in the image by an amount δX to the point X - δX .

The amount of displacement may be calculated by equating the hypotenuse of triangle a-o-b to that of a-p-c with the result

$$\delta X = X - (X^2 - h^2 + z^2)^{1/2} \quad (4)$$

If the terrain relief is known, either by radar stereo measurements or from some other source, the displacements may be calculated and removed and a radar "ortho-photo" prepared.

D. Stereo Vertical Exaggeration

When two images obtained from different sensor positions are viewed stereoscopically, a three-dimensional model of the imaged scene can be observed. If the images are made by cameras whose focal planes are parallel, and if the ratio between the spacing of the two cameras and the distance from them to the scene is approximately the same as the ratio between the interocular spacing of an observer and his normal viewing distance for detailed scrutiny of an object, then the observed scene or object will have the same proportions as the original object. That is, the ratio between the observed dimensions along the line of sight to the observed dimensions normal to the line of sight will be the same. For most observers, the ratio of observing distance to interocular distance is approximately five. If the cameras are placed further apart, the dimension along the line of sight will be increased proportionally to the dimensions normal to it. The proportional increase is called the "vertical exaggeration." Therefore, if one forms the ratio between camera spacing, B, and distance to the scene, h, the vertical exaggeration q will be approximately $q = 5B/h$. Experiments have shown this approximate relationship to also be true for typical conventional stereo viewers.¹

Magnification of the individual images magnifies observed dimensions both along and across the line of sight equally. If the scene is magnified so that the image resolution matches the observer's visual acuity, then the vertical exaggeration is a measure of the observer's ability to interpret three-dimensional effects with the resolution available from the camera.

¹GERA-2120: Stereoscopy, LaPrade, G. L., et. al., Litchfield Park, Arizona, Goodyear Aerospace Corporation, 15 September 1975.

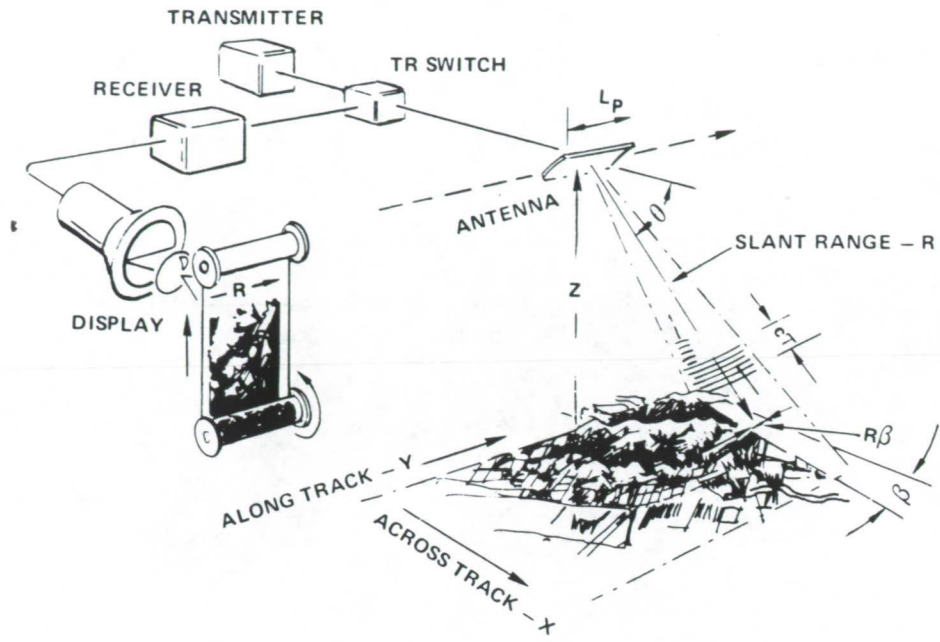


Figure 1. Side-looking radar geometry.

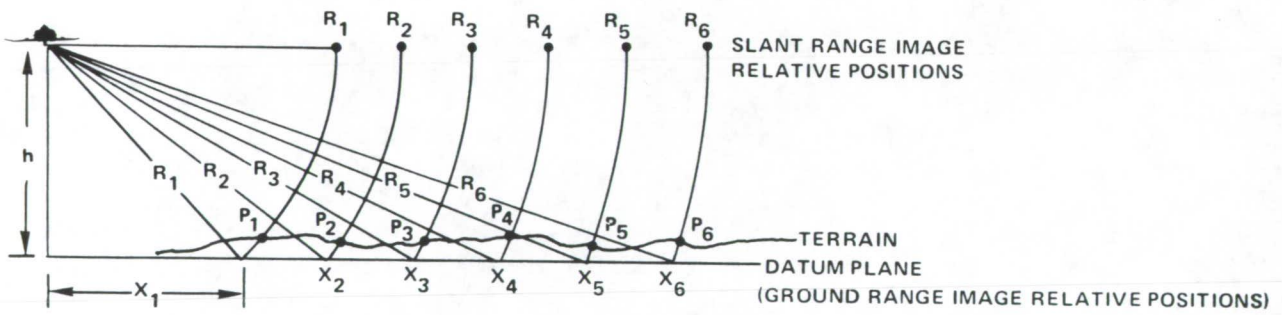


Figure 2. Ground range sweep.

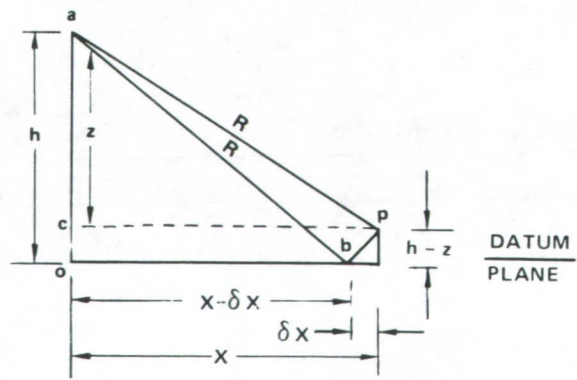


Figure 3. Elevation displacement, ground sweep range.

The differences between the two stereoscopic scenes are caused by differing elevation displacements in the two scenes. Figure 4 shows two cameras imaging a scene and illustrates the elevation displacements, d_1 and d_2 , and the difference between them, Δp , the parallax to a particular elevated point, p .

If two radar images are made from flightpaths arranged so that a radar line of sight to the point p is normal to a camera line of sight, then the elevation displacements for the radar images and those for the camera images will be the same. Furthermore, the vertical exaggeration for the radar images will be the same as that for the equivalent positions. This is illustrated in Figure 5.

Now,

$$\begin{aligned}
 q &\approx \frac{5B}{h} = \frac{\Delta p}{e} \\
 &= 5 \left(\frac{d_2 - d_1}{e} \right) \\
 &= 5 \left(\frac{e \tan \theta_2 - e \tan \theta_1}{e} \right) \\
 &= 5 (\tan \theta_2 - \tan \theta_1) \quad \text{(a)} \\
 &= 5 \left[\frac{\sin (\theta_2 - \theta_1)}{\cos \theta_2 \cos \theta_1} \right] \quad \text{(b)}
 \end{aligned} \tag{5}$$

Equation (5)(a) shows that the vertical exaggeration of a radar stereo pair with a ground range sweep depends on the difference between the tangents of the two depression angles at any point. Equation (5)(b) shows the dependence on convergence angle, $(\theta_2 - \theta_1)/2$. A similar derivation for slant range imagery yields

$$\begin{aligned}
 q &= 5 (\sin \theta_2 - \sin \theta_1) \\
 &= 10 \sin \frac{(\theta_2 - \theta_1)}{2} \cos \frac{(\theta_2 + \theta_1)}{2}
 \end{aligned} \tag{6}$$

This illustrates the dependence on convergence angle and on average depression angle $(\theta_2 + \theta_1)/2$.

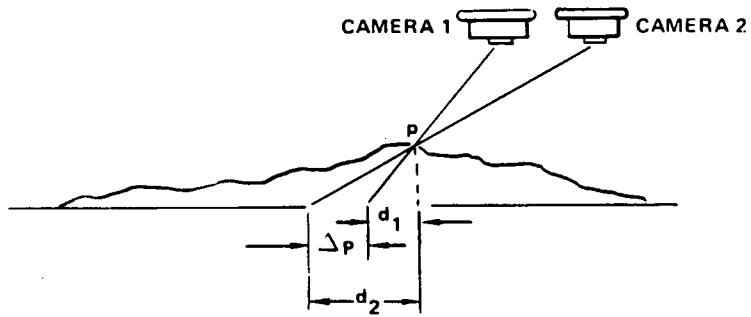


Figure 4. Stereo elevation displacement.

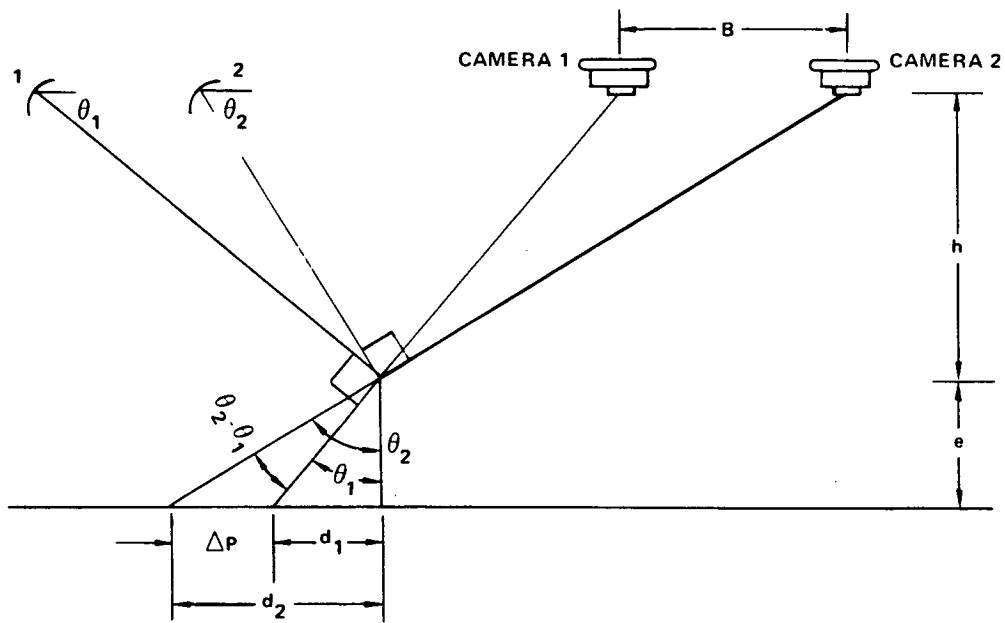


Figure 5. Radar vertical exaggeration.

E. Stereo Measurement Accuracy

Although related, the accuracy with which measurements may be made in the stereo mode does not depend only on the geometry that defines vertical exaggeration, but must include a number of other factors. If one writes Equation (2)(b) in the form

$$R^2 = x^2 + z^2 \quad (7)$$

for two different flightpaths displaced from a coordinate system by a_1 and a_2 in the x direction and b_1 and b_2 in the y direction, then one obtains

$$\left. \begin{aligned} R_1^2 &= (x - a_1)^2 + (z - b_1)^2 & (a) \\ R_2^2 &= (x - a_2)^2 + (z - b_2)^2 & (b) \end{aligned} \right\} \quad (8)$$

Equations (8)(a) and (b) may be solved by simultaneous solution to obtain x and z as a function of flightpath positions a_1b_1 and a_2b_2 , and range R_1 and R_2 . Errors in x and z as functions of uncertainties in these components can be found by implicit differentiation of Equations (8)(a) and (b) before simultaneous solutions.

Thus,

$$\left. \begin{aligned} dx &= \frac{(z - b_2) R_1 dR_1 - (z - b_1) R_2 dR_2}{(x - a_1)(z - b_2) - (x - a_2)(z - b_1)} = \frac{h_2 R_1 dR_1 - h_1 R_2 dR_2}{h_2 G_1 - h_1 G_2} & (a) \\ dz &= \frac{(x - a_1) R_2 dR_2 - (x - a_2) R_1 dR_1}{(x - a_1)(z - b_2) - (x - a_2)(z - b_1)} = \frac{G_1 R_2 dR_2 - G_2 R_1 dR_1}{h_2 G_1 - h_1 G_2} & (b) \end{aligned} \right\} \quad (9)$$

where

h = elevation of terrain with respect to aircraft

G = horizontal position of terrain with respect to aircraft

Or, letting differentials represent errors and assuming independence between the range measurements,

$$\left. \begin{aligned} \sigma_x^2 &\approx \frac{h_2^2 R_1^2}{(h_2 G_1 - h_1 G_2)^2} \sigma_{R_1}^2 + \frac{h_1^2 R_2^2}{(h_2 G_1 - h_1 G_2)^2} \sigma_{R_2}^2 & (a) \\ \sigma_z^2 &\approx \frac{G_1^2 R_2^2}{(G_1 h_2 - h_1 G_2)^2} \sigma_{R_2}^2 + \frac{G_2^2 R_1^2}{(G_1 h_2 - h_1 G_2)^2} \sigma_{R_1}^2 & (b) \end{aligned} \right\} (10)$$

Hence, the slant-range elevation measurements in combination with instrumentation and aircraft position measurement errors can be transformed by Equation (10) into across-track and measurement errors as illustrated in Figure 6. Along-track error may be determined by Equation (1a) in combination with instrumentation, aircraft position, and aircraft orientation errors. In the special case where the altitudes and range accuracies are equal, so that $h_1 = h_2 = h$; $\sigma_{R_1} = \sigma_{R_2} = \sigma_R$,

$$\left. \begin{aligned} \sigma_x &\approx \frac{(R_1^2 + R_2^2)^{1/2}}{G_1 - G_2} \sigma_R & (a) \\ \sigma_z &\approx \frac{(G_1^2 R_2^2 + G_2^2 R_1^2)^{1/2}}{h(G_1 - G_2)} \sigma_R & (b) \end{aligned} \right\} (11)$$

An appropriate representation of limiting system measurement error is the area of the approximate rhombus defined by the intersection of the cylindrical sections of thickness $\sigma_{R_1} = \sigma_{R_2} = \sigma_R$ in Figure 6. The condition for maximum accuracy could be obtained from Equation (11) by minimizing this area, which is $\sigma_x \times \sigma_z / 2$, but an examination of Figure 6 leads to the conclusion that it is minimized when the convergence angle at the terrain is 90 degrees. This does not maximize vertical accuracy nor vertical exaggeration, but is probably the best compromise for most cases. It should also be noted that this optimum can be obtained only at one point within the overlapping images. However, as the distances become larger with respect to swath coverage, as in satellite operation, it is possible to approximate a given convergence angle more closely over the stereo swath.

III. SYSTEM PARAMETERS

From the foregoing discussion, it is apparent that the important parameters in stereo analysis are system resolution and the various combinations of viewing angles or equivalent distance measurements. The vertical viewing angle used in earlier discussions was defined as the radar depression angle because it is equal to the terrain grazing angle for a flat earth. In the satellite case, the grazing angle must be computed separately. This angle and the off-nadir angle can be related to satellite imaging parameters directly from the geometry of Figure 7 as

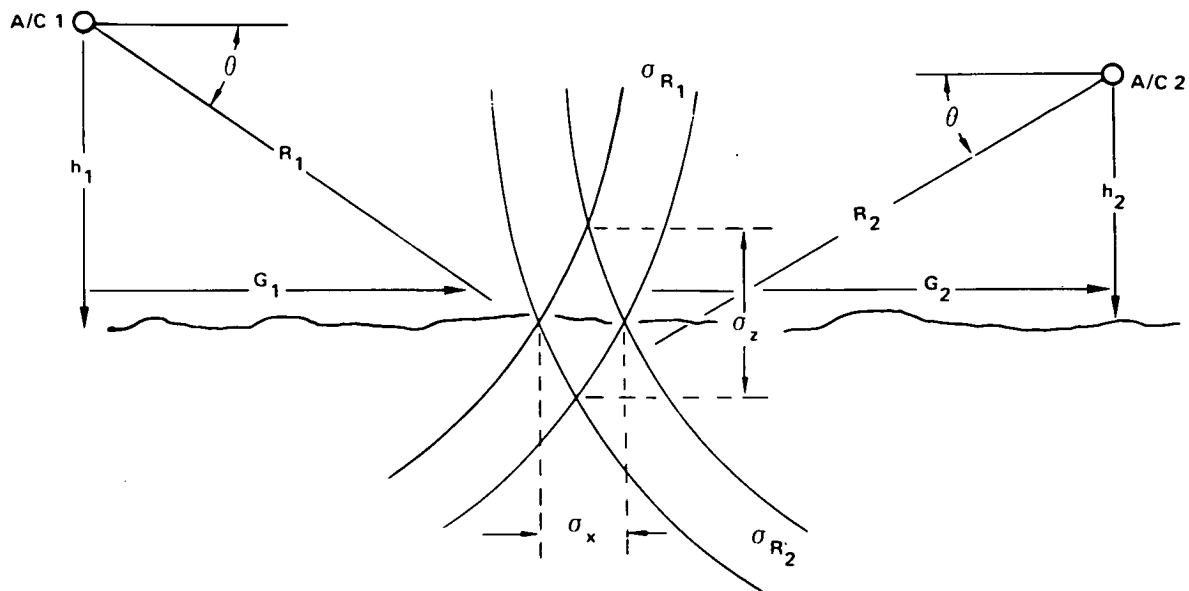


Figure 6. Stereo measurement accuracy.

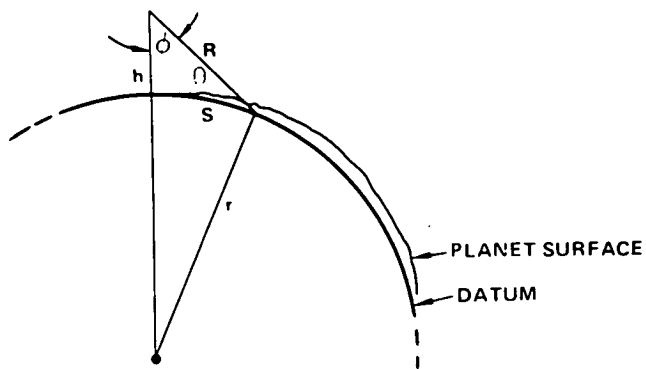


Figure 7. Orbital imaging parameters.

$$\theta = \tan^{-1} \frac{h + r \left(1 - \cos \frac{s}{r}\right)}{r \sin \frac{s}{r}} - \frac{s}{r} \quad (12)$$

$$\phi = \frac{\pi}{2} - \frac{s}{r} - \theta \quad (13)$$

$$R = \frac{r \sin \frac{s}{r}}{\sin \phi} \quad (14)$$

where

θ = grazing angle

h = altitude above datum

r = radius of planet

s = distance from nadir to point on terrain

ϕ = angle off nadir to point on terrain

R = slant range from radar to point on terrain as defined in Figure 7.

The previous equations defining vertical exaggeration, measurement accuracy, and imaging parameters are summarized as follows, with the parameters uniformly defined as in Figure 8, where a flat earth is shown. In the following paragraphs, several specific systems are analyzed, using flat earth formulas for airborne systems and curved earth formulas for orbital systems, except for measurement accuracy where curved earth formulas are used to calculate parameters and flat earth formulas to calculate accuracy. Opposite side imaging is included by observing the sign conventions of Figure 8. Equation summary:

$$\begin{aligned} q_{\text{ground range imaging}} &= 5 (\tan \theta_2 - \tan \theta_1) & (a) \\ &= 5 \left[\frac{\sin (\theta_2 - \theta_1)}{\cos \theta_2 \cos \theta_1} \right] & (b) \\ q_{\text{slant range imaging}} &= 5 (\sin \theta_2 - \sin \theta_1) & (c) \\ &= 10 \sin \frac{\theta_2 - \theta_1}{2} \cos \frac{\theta_2 + \theta_1}{2} & (d) \end{aligned} \quad (15)$$

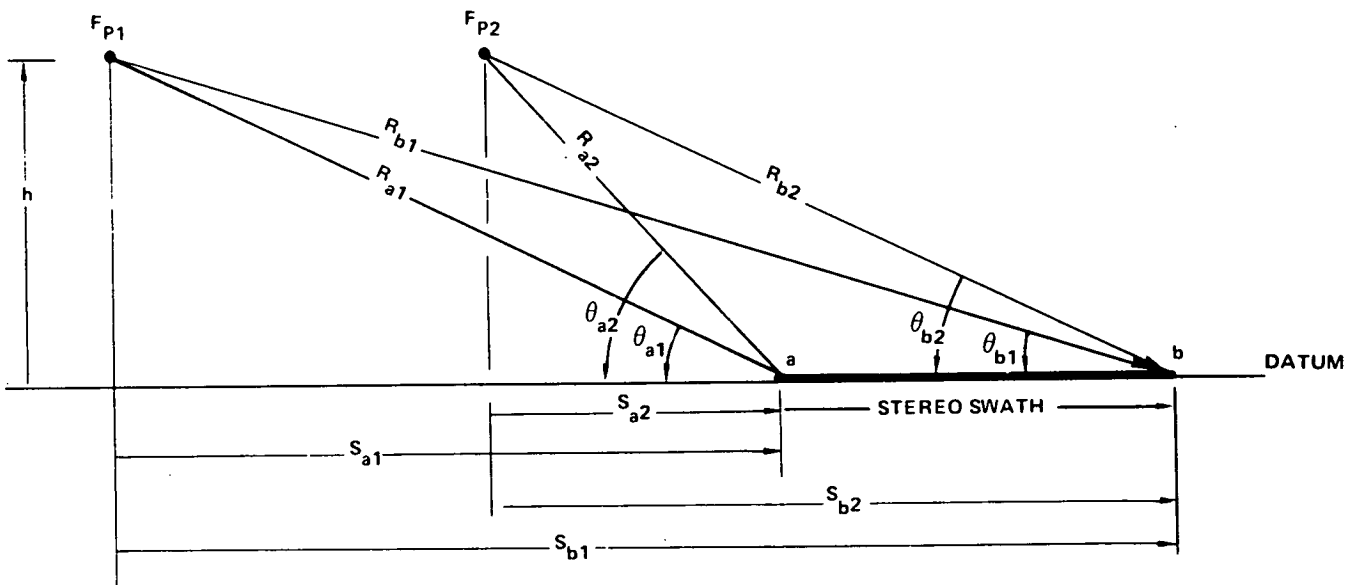


Figure 8. Definition of terms for system comparison.

$$\sigma_x = \frac{(R_1^2 + R_2^2)^{1/2}}{s_1 - s_2} \sigma_R \quad (e)$$

$$\sigma_z = \frac{(s_1^2 R_2^2 + s_2^2 R_1^2)^{1/2}}{h(s_1 - s_2)} \sigma_R \quad (f)$$

$$\theta = \tan^{-1} \left[\frac{h + r \left(1 - \cos \frac{s}{r}\right)}{r \sin \frac{s}{r}} \right] - \frac{s}{r} \quad (\text{curved earth}) \quad (g) \quad (15)$$

$$R = \frac{r \sin \frac{s}{r}}{\sin \left(\frac{\pi}{2} - \frac{s}{r} - \theta \right)} \quad (\text{curved earth}) \quad (h)$$

$$R = \frac{h}{\sin \theta} \quad (\text{flat earth}) \quad (i)$$

IV. ANALYSIS, SPECIFIC SYSTEMS

Stereo imagery of several specific radar systems is, or will be, available. The salient imaging parameters, vertical exaggeration, and basic measurement accuracy as defined in the previous sections are given in Table 1.

Calculations of some appropriate systems (the Johnson Space Center (JSC) 102A and the VOIR) are made for both same-side and opposite-side geometries showing the advantages of opposite-side optimization in vertical exaggeration and measurement accuracy. Little experimental data exists to quantify the estimates made here.

For completeness, some recently obtained preliminary vertical accuracy results obtained from GEMS, JSC-102A, and SEASAT are given in the last line of Table 1. The data given are the results of only a few measurements made with a simple mirror stereoscope and a parallax bar. Measured elevations were compared with topographic maps. In each case, the average error was removed to represent the case with adequate ground control and to show only errors in the actual stereo measurement. Individual deviations between the radar stereo measurement and the topographic map sheet were averaged in the GEMS case and the root mean square found in the others. No opposite side measurements were made.

Table 1. Stereo parameters of specific systems

Parameter	GEMS		JSC-102A		AN/UPD-4	SEASAT	VOIR - Low Res		VOIR - Hi Res	
		S.S. ^a	O.S. ^b				S.S.	O.S.	S.S.	O.S.
h^c , km	10	16	12	10	800	300	300	300	300	300
S_{a1} , km	24	18.53	4.633	37.06	290	410	255	448	280	280
S_{a2} , km	9	4.633	-23.16	18.532	240	140	-305	140	-292	-292
S_{b1} , km	46	37.06	23.16	55.60	340	460	305	460	292	292
S_{b2} , km	31	23.16	-4.633	37.06	290	190	-255	152	-280	-280
θ_{a1} , deg	22.62	40.81	69.00	15.10	70.0	33	46.87	31	45	45
θ_{a2} , deg	48.01	73.85	-27.39	28.35	73.3	65	-41.52	65	-44	-44
θ_{b1} , deg	12.26	23.35	27.39	10.20	66.97	30	41.52	30	44	44
θ_{b2} , deg	17.88	34.64	-69.00	15.10	70.0	56	-46.87	63	-45	-45
R_{a1} , km	26.0	24.48	12.86	38.39	851	511	390	546	415	415
R_{a2} , km	13.45	16.66	26.08	21.05	835	347	425.9	347	425	425
R_{b1} , km	47.09	40.37	-26.08	56.47	869	555	-425.9	555	-425	-425
R_{b2} , km	32.57	28.75	-12.86	38.39	851	358	-390	351	-415	-415
γ , km	-	-	-	-	6378	6310	6310	6310	6310	6310
σ_R^d , m	10	10	10	3	8	230	230	38	38	38
q_a	3.47	12.95	15.6	1.07	2.93	7.47	9.76	7.72	9.8	9.8
q_b	0.5	1.29	15.6	0.42	1.97	4.52	9.76	6.93	9.8	9.8
σ_{xa}^e , m	19.52	21	10.4	7.1	190	369	237	80	39	39
σ_{xb}^e , m	38.17	35	10.4	11.0	194	423	237	106	39	39
σ_{za}^e , m	26.60	15	10.3	5.70	63.4	452	230	64	38	38
σ_{zb}^e , m	139.45	62	10.3	48.37	76.7	555	230	75	38	38
σ_z measured, m	40	8			60					
		20								
		27								

^aSame side ^dAssumed here equal to range resolution

^bOpposite side ^eFor flat earth

^cAssuming 2 km average terrain elevation above datum

V. VALUE OF TECHNIQUES AND RESULTS

Stereo measurements and interpretation techniques are expected to be of extreme value in cases where radar is the only remote sensor capable of economically imaging a particular surface. Other papers will discuss past applications in geologic interpretation.

VI. RECOMMENDATIONS

Radar stereo imagery should be collected with varying parameters to quantify calculations and estimates of the type presented here. In particular, opposite-side imagery having convergence angles near 90 degrees, probably using 45-degree depression angles, should be collected to quantify the optimum geometric imaging parameters. Both vertical exaggeration and overall measurement accuracy are enhanced by using geometry that results in a convergence angle of approximately 90 degrees, and this is most conveniently obtained by using opposite-side stereo imagery with approximately 45-degree depression angles. In the past, little success has been achieved with opposite-side operation because shadows and highlights are reversed in the two stereo images, making fusion difficult. However, radars operating in steep angle modes, 45 degrees and better, have not been readily available. These steep angles minimize both shadows and highlighting, so that adequate fusion at near 90-degree convergence angles may be possible, and a well-planned experiment should be carried out to explore the possible use of optimum opposite-side stereo for both interpretation and measurement.

A NEW LOOK AT TOGO THROUGH THE EYES OF A SLAR

Louis F. Dellwig
University of Kansas Center for Research, Inc.
Remote Sensing Laboratory
Lawrence, Kansas 66045

ABSTRACT

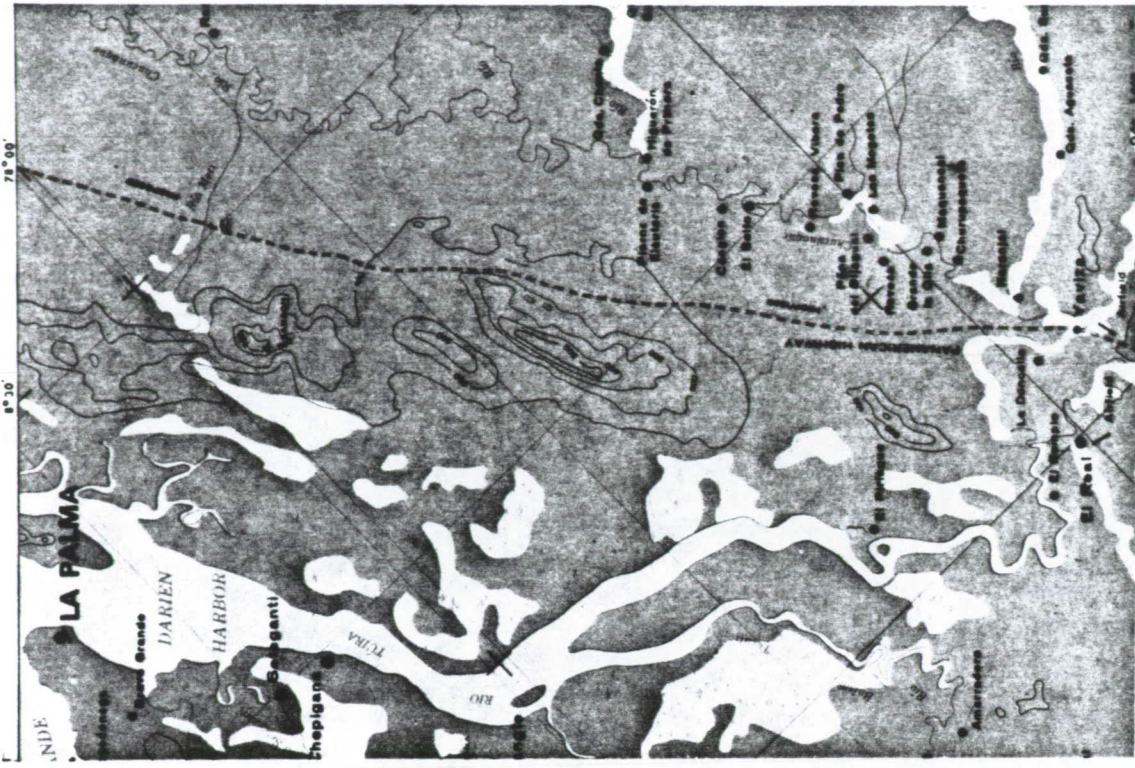
Imaging of Togo in 1977 with SLAR provided the data required for the production of map-controlled radar mosaics at a scale of 1:200,000 with 95% of all control points at that scale within ± 4.0 millimeters of true positions. The mosaics served as the base for the generation of a new geologic map of Togo. Aided by two looks, numerous revisions resulted, not only with the addition of previously unknown structural features, a revision of age relationships and the refinement of unit boundaries, but also with the repositioning of rock units and the reorientation of major faults.

Geologic mapping of Togo was initiated as early as 1905. That numerous investigators with diverse interests have participated in revision without apparent rectification of major errors in position and orientation suggests that modification in detail was effected in large part on the original map base. That such is the case is further emphasized by the lack of congruity between major topographically expressed rock units and their well-defined counterparts on the radar maps. Furthermore, it suggests the seriousness of the error of geologic map revision utilizing a previously published map as a base without verification of its geometric fidelity.

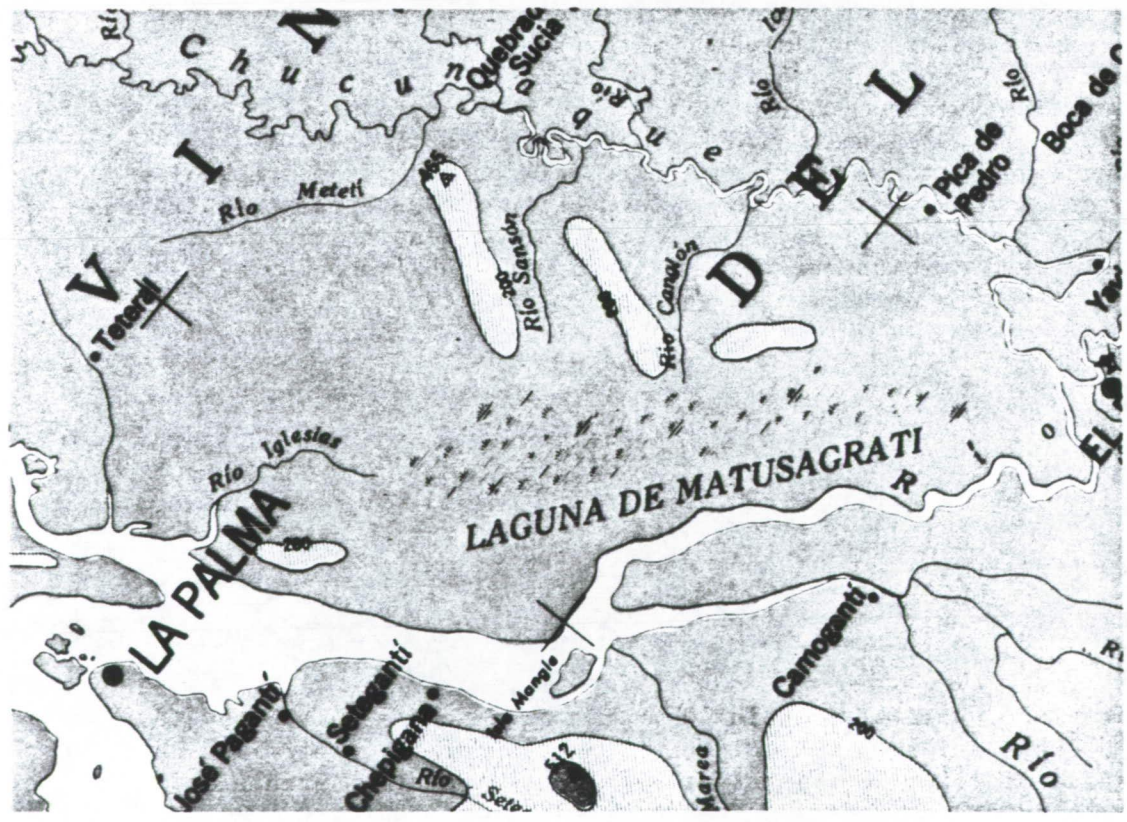
I. INTRODUCTION

The publication of the geologic map of Darien Province, Panama (MacDonald, 1969), emphatically demonstrated the value of SLARs as geologic mapping tools. Not to be overlooked, however, was the significant repositioning and rotation of up to 60° of a series of hills east of La Palma (Figure 1a, 1b). Although the value of the synoptic view and low illumination angle in detecting geologic features has been clearly demonstrated by many other investigators, the value of a SLAR survey for rectifying the location and orientation of such features has not received sufficient attention.

Imaging of Togo, West Africa, in 1977 with Side-Looking Airborne Radar (SLAR) provided such data required for the production of semicontrolled radar mosaics at a scale of 1:200,000. Analysis of first-generation prints and positive transparencies and transfer of the derived data to mosaics revealed



(b)



(a)

Figure 1. (a) Area east of La Palma, Republic of Panama, Special Map No. 2. Produced by USARCARIB. Undated (pre-1967). Because of problems of cloud cover control was at a minimum. Error in orientation of hills east of La Palma has been corrected in the map produced from radar imagery in 1968. (b) Topographic map east of La Palma constructed from interferometer data obtained during the SLAR (AN/APQ-97) survey of Panama.

significant errors in the existing geologic and topographic maps of Togo. Aided by two opposing radar look directions, numerous revisions resulted, including identification of previously unknown structural features, redefinition of age relationships, refinement of unit boundaries, and the repositioning of structural features and lithologic units. Positional errors in some cases were as much as 12 kilometers and orientation errors of major faults by as much as 22 degrees.

Geologic mapping of Togo was initiated at least as early as 1905 by Koert with the first comprehensive outline of the geology of what is now Togo being published in *Das Deutsche Kolonialreich* (Meyer, 1910). Since that time, contributions to the geologic knowledge of the country have been made by geologists of diverse national origins. Prior to the independence of Togo the greatest contributions were made initially by the Germans and later by the French. Although modification of the earliest map has been a continually ongoing process in an effort to refine lithologic and structural relationships, a great diversity of opinion concerning major rock and structural relationships as well as a lack of geometric fidelity is frequently observed.

Mapping in the Gold Coast while under British trusteeship was extensive and continuity of units in some instances could be maintained across the border into Togo. However, contrasting structural style and facies changes eastward from the Gold Coast across the Togo Range and general poor accessibility to terrain in the border areas precluded the elimination of "state line faults."

It becomes immediately obvious that a geometrically accurate base on which stratigraphic units and major structural features can be identified and accurately delineated is necessary for the resolution of such problems. The initial effort thus requires utilization of aerial survey techniques. Landsat imagery was evaluated but because of both coarse resolution and extensive cloud cover (which in fact has prevented any coverage being acquired in some areas as of this writing) provided no significant contribution to the solution of these problems (Gelnett, Dellwig and Bare, 1978). However, SLAR imagery was generated without disruption or attenuation by conditions adverse to acquisition of imagery in the visible portion of the spectrum. Such imagery when mosaicked provided the necessary geometric fidelity and offered a synoptic view at a scale of 1:200,000.

A. Generation of the Base

The survey covered an area of approximately 56,000 square kilometers, which was surveyed in 33 calendar days between mid October and mid November 1977. Sixty flight lines provided for complete coverage of the area. Because the system "looks" to both sides of the aircraft simultaneously, there was complete north and south "look" coverage. The strips were utilized to develop 24 1° x 1° radar mosaics which conformed to the existing IGN topographic map series at a scale of 1:200,000.

The flight plan used for the Togo SLAR survey provided sufficient sidelap between strips such that 60 percent of control points were common to any two adjacent strips and 20 percent common to any three adjacent strips. Control points consisted of recognizable man-made (bridges, etc.) and natural (isolated hills, etc.) features which could be accurately identified and located. On strip negatives control points common to adjacent strips were identified and scale differences, where present, rectified and adjusted to a master UTM (Universal

Transverse Mercator) grid and a corrected topographic base map, i.e., 1° x 1°, 1:200,000 scale IGN topographic maps and 1° x 1.5°, 1:250,000 scale JOG topographic maps. A specially designed SLAR strip printer featuring a high resolution process lens was used to scale rectify SLAR strips of approximately 4 x 40 inch format. The process insures (1) the best possible registration of SLAR strips-UTM grid-IGN topographic base maps, and (2) that position errors of features on the maps can be easily identified and corrected in the laying of the mosaic.

B. Accuracy of the Base

The resulting mosaic should not be construed to be a precise geodetic product. The accuracy of the radar mosaics is proportional to the accuracy of the existing topographic base map control and, as such, can only be stated in terms of discrepancies between the map and the radar mosaic. Positional errors in the topographic base maps were frequently detected by matching control points on sidelapping SLAR strips which had been registered to the corrected UTM grid. A statistical analysis of mosaics constructed in this manner for Nigeria (Motorola Aerial Remote Sensing, Inc. 1978) indicated a degree of accuracy of location of control points as follows:

All control points	Error, mm	Error, m
68% are within	±1.09	273
95% are within	±2.18	546
99% are within	±3.28	819

Since the same constructional techniques were used in the preparation of the Togo mosaics, the same degree of accuracy is assumed. Position errors may well have been a fraction of those stated above if all control points on the existing base-map series were absolutely correct, which is unlikely by virtue of how they are compiled and in view of practiced drafting standards (± 0.5 millimeters or ± 127 meters at a scale of 1:250,000). At the scale of mapping positional errors of 12 kilometers and orientation alignments of 22 degrees far exceed maximum possible.

II. MAPPING TECHNIQUE

Interpretation was done on acquisition scale (1:250,000) prints, which were roughly laid to correspond with the semicontrolled radar maps, and the interpreted data were transferred to the mosaics. By using the original strips we were able to define any target signatures in a near, intermediate and far range position and thus extend geologic and vegetation boundaries more accurately from one strip to those adjacent to it. In the event that a boundary or feature problem remained unresolved after examining such items in all range positions on north and south look images, stereoscopic or first generation positive transparency examination provided additional insight to the problem. Landsat imagery was available for all of Togo with the exception of the coastal area, but no significant data for geologic mapping and only very limited data for vegetation mapping, and that only in areas of high relief, were revealed.

A. Mapping Guidelines

In mapping Togo, guidelines were established as follows:

- (1) Because of the reduction of large areas to near peneplanation and an apparent development of a thick soil cover, unless a rock unit has a sufficiently unique chemical composition to enable the development of a unique vegetation community, the tone-texture-topographic signature of that unit may not be sufficiently distinct to permit its isolation. Thus, no unit on the existing geologic map would be incorporated unless it was clearly expressed on the radar image. This does not imply that the unit is not sufficiently unique in composition to be identified on the ground.
- (2) Age relationships among geologic units were initially assumed to be correct as previously mapped by Lawson (1973). Modifications were made (a) where there is a clear relationship between intrusives and host rocks, (b) in areas of sedimentary rocks in which bedding can be used to document an unconformity, (c) in areas where relative vertical movement along faults between units of different ages can be documented, and (d) in areas where fold patterns can be accurately defined and can be used to demonstrate relative ages.
- (3) Because of numerous discrepancies in the orientation and positioning of faults on published maps, the only faults shown on the interpretation overlays were those identified from the radar imagery.
- (4) In the identification of lithologic units, particularly intrusives, if the tone-texture signature on the radar suggested a lithology which contrasts with published information the change was made to conform with the evidence interpreted from the radar.

These decisions having been made, characteristic tone-texture signatures were selected from areas which appeared to accurately relate to mapped units. Allowing for variations due to topographic relief, facies variations within a unit, partial masking by transported mantle and structural variations within the unit, such signatures (Figures 2, 3) were used as guides for the determination of the areal extent of each unit. Other criteria were called upon in several instances to define unit contacts which were not expressed by an apparent contrast in bedrock signatures. Farming patterns or densities were assumed to be indicative of soil composition and, if not determined to be related to alluvial deposits, were considered to be potentially suggestive of changes in bedrock composition. Abrupt changes in drainage patterns were also assumed to be suggestive of changes in composition or structure of the underlying bedrock and were mapped as lithologic contacts. In one instance the boundary between an area marked by isolated inselbergs and that in which inselbergs were essentially absent was considered to represent a boundary between two units of similar composition, in the one of which concentrations of resistant minerals were characteristic. Thus, map units are essentially rock-stratigraphic in nature and their vertical extent may contrast to some degree with that as originally defined. Utilizing such guidelines resulted in several significant changes in age relationship (Figure 4).

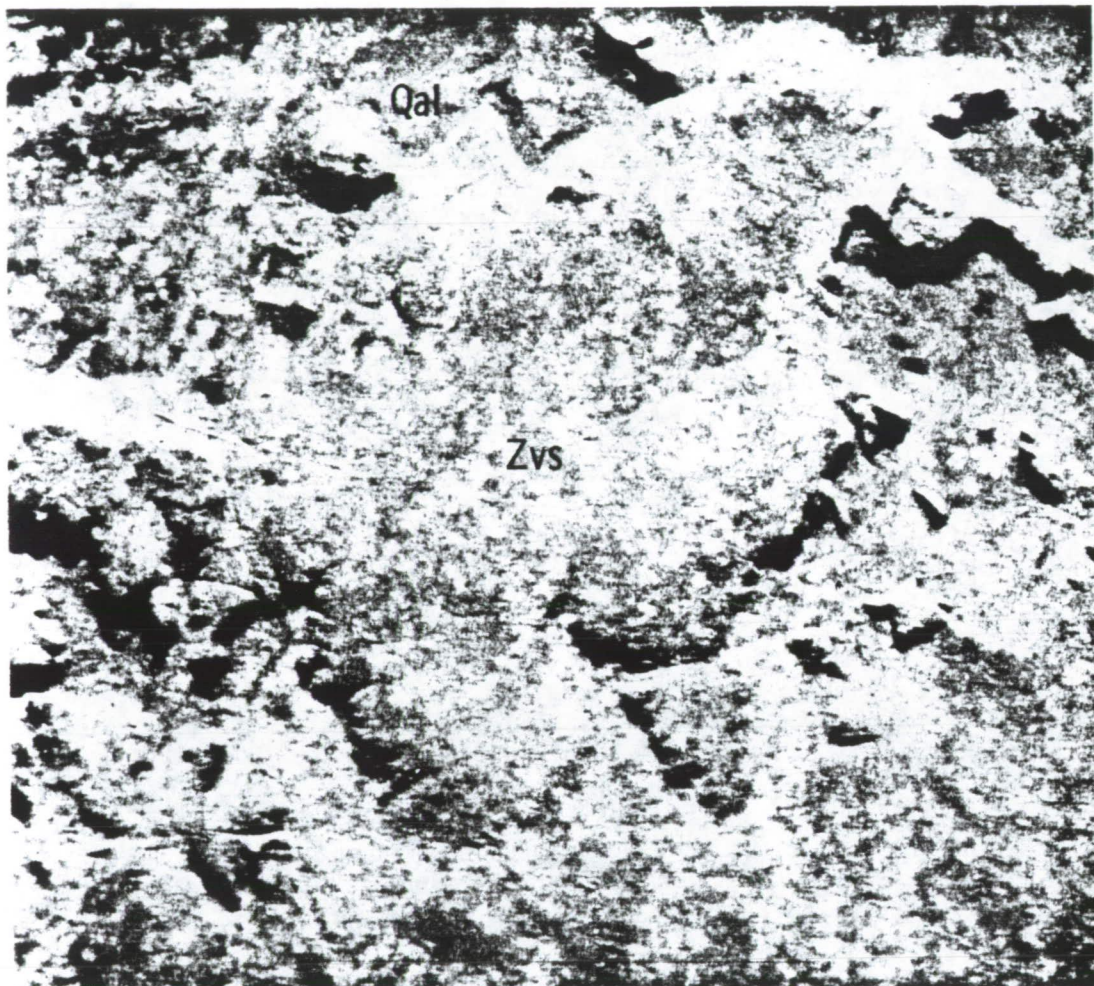


Figure 2. Tone-texture SLAR signature established for Qal (Recent Alluvium) and Zvs (Infracambrian, Voltaien) in northern Togo.

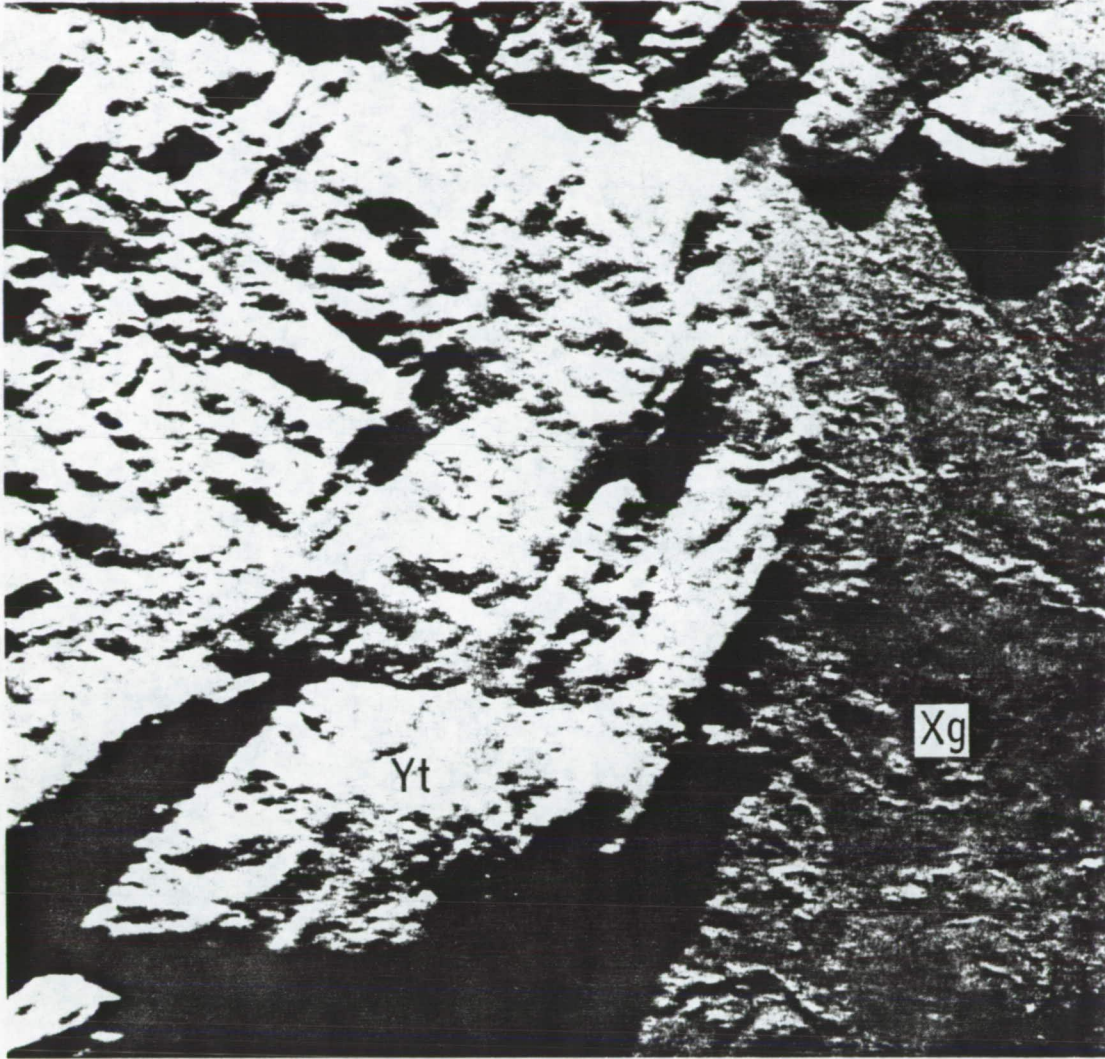


Figure 3. Tone-texture SLAR signatures of Yt (Togo Formation) and the unit to the east of the Togo Range Xg (Precambrien, Inferiean, Dahomeyer) between Palime and Atakpame. The Togo Formation provides the most distinctive radar signature of all units mapped in Togo.

ORIGINAL PAGE IS
OF POOR QUALITY

1973
Lawson

1978

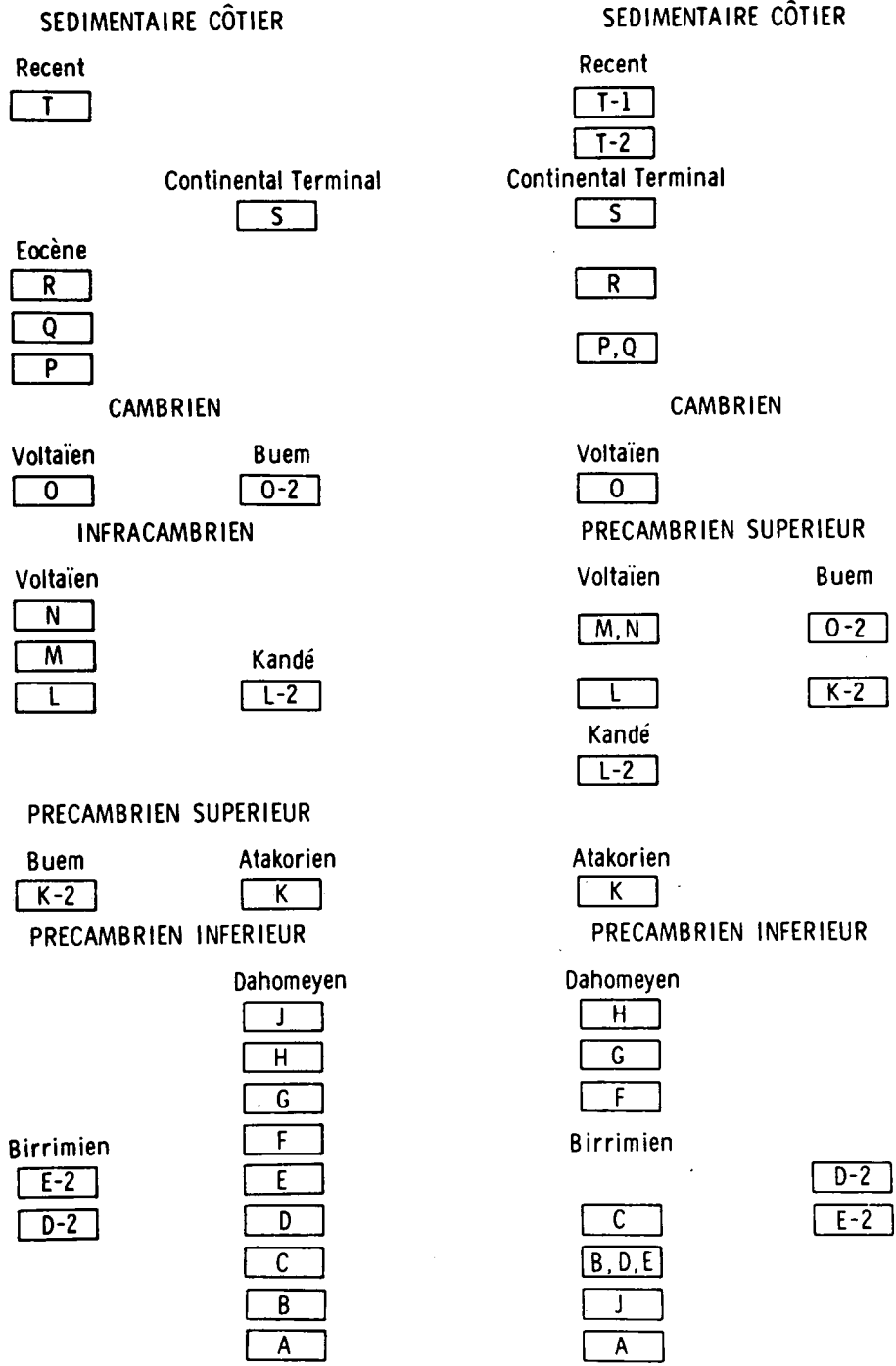


Figure 4. Comparison of geologic columns: 1973 map of Togo (Lawson) and map produced from radar imagery (1978).

B. Map Modifications

That the original map of Koert is gross in aspect and has been the subject of considerable modification is not unexpected. At the time of the mapping, 21 tribes speaking a variety of dialects occupied the area. The only major highway in what is now Togo extended north from Lome to Sodoke. This four-year study actually represented an outstanding scientific achievement. Although north of latitude 10°N (Figure 5a-d) the map of 1973 shows subdivision of units and re- refinement of contacts, several contacts mapped by Koert have undergone only minor repositioning. However, a comparison of the map generated from radar data and the 1973 map suggests that little or no modification of drainage and adjacent floodplain position has been effected in recent years. Furthermore, although modified from the earlier interpretation by Koert, judging from topographic expression the western limit of the Togo Formation as defined by Lawson at the Togo-Benin border appears to be misplaced by approximately 45 kilometers.

Southward in the Togo Range, previously published maps contrast in many aspects with the map generated from radar imagery (Figure 6a-6d). Although the map of Grant (1969) is intentionally simple, the area indicated as being underlain by the Togo Formation shows only nominal correlation with the topographic expression of that unit between Atakpame and Palime and, having been drawn from other sources, suggests an earlier error of position. Additionally, correlation north of Atakpame with the map of Lawson as well as the map generated through analysis of radar imagery is essentially nonexistent. Although the interpretation of structure and lithology southeast of the outcrop of the Togo Formation between Atakpame and Palime provided through radar imagery interpretation is subject to question, the lack of correlation of rock unit distribution as proposed by Lawson with tone-texture signatures and topography as expressed on the radar image at very least identifies areas in need of additional field evaluation.

The indicated faults are not all-inclusive; smaller features were eliminated to improve clarity of presentation at this published scale. However important the detection of numerous previously unidentified sutures, the reorientation aided by the synoptic view provides important data particularly if the potential for mineral exploration arises. That better definition of orientation can be realized with the synoptic view of SLAR has long been understood (Wing, Overbey and Dellwig, 1970). Additionally, hogbacks or cuestas properly oriented with respect to the direction of illumination enable the identification of changes in dip and consequently the shifting of position of axes of folds.

III. CONCLUSIONS

That numerous investigators with diverse interests have participated in revision without apparent rectification of major errors in position and orientation suggests that the refinement of the geologic map of Togo was effected on a base which was generated prior to the availability of precise geodetic data. That such is the case is emphasized by the lack of congruity of major topographically expressed rock units and structures in recently published small-scale maps with their well-defined counterparts on the radar imagery. Furthermore, it suggests the seriousness of the error of geologic map revision utilizing a previously published map as a base without verification of its geometric fidelity and raises the question of the potential of such error elsewhere, especially in those countries where cloud cover has prohibited the acquisition of

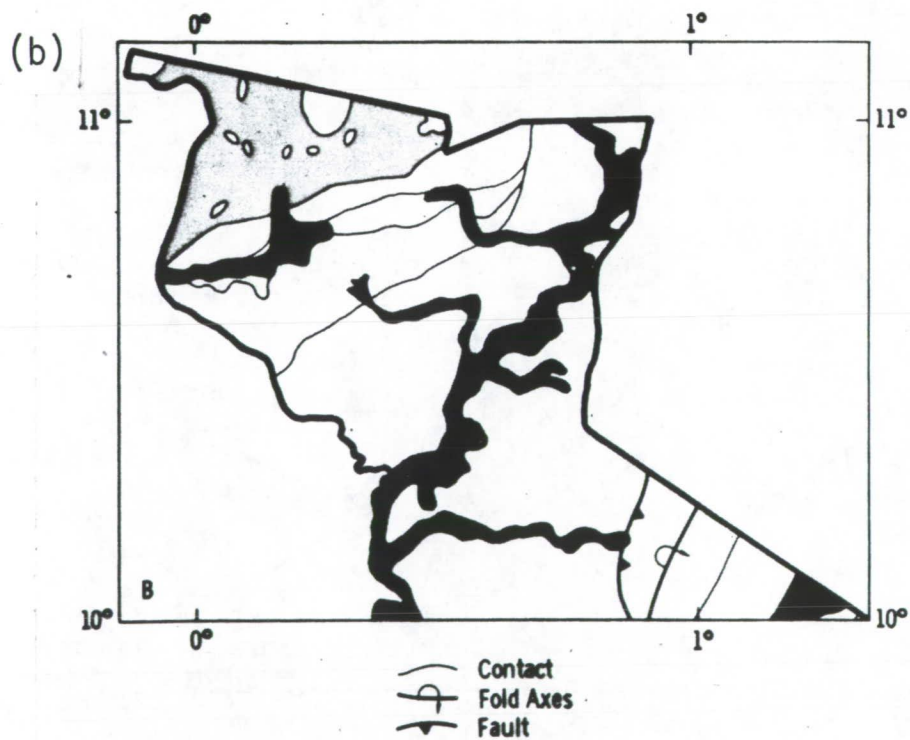
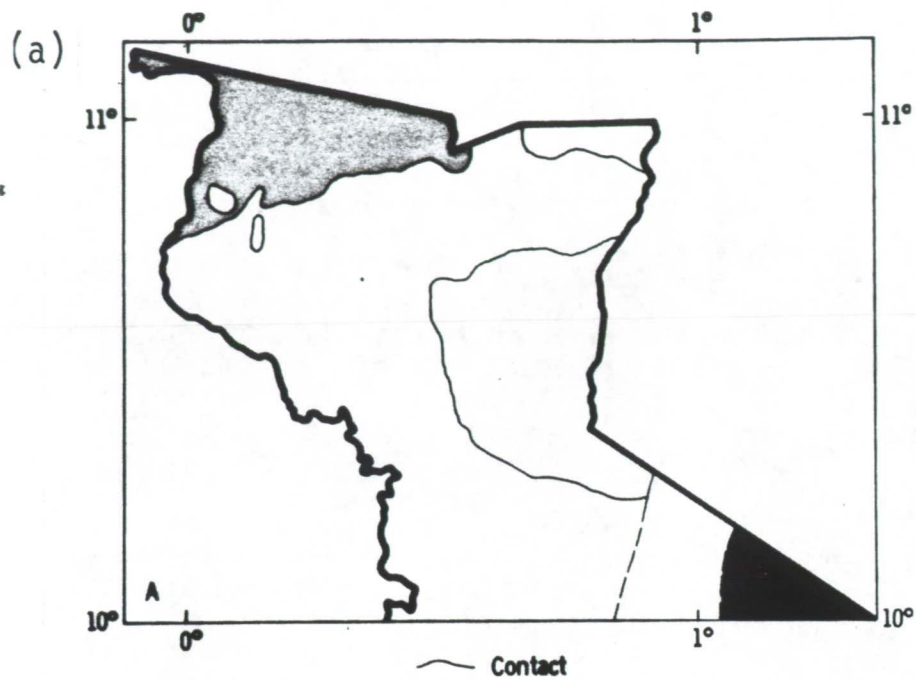


Figure 5. Comparison of distribution of selected geologic units north of latitude 11° N, Togo, West Africa. (a) Koert, 1910; (b) Lawson, 1973; (c) MARS, 1978; and (d) radar imagery.

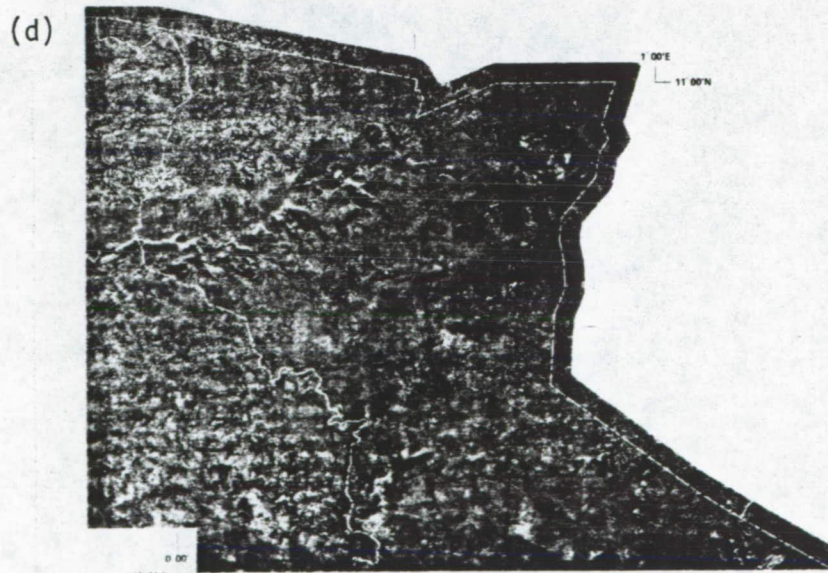
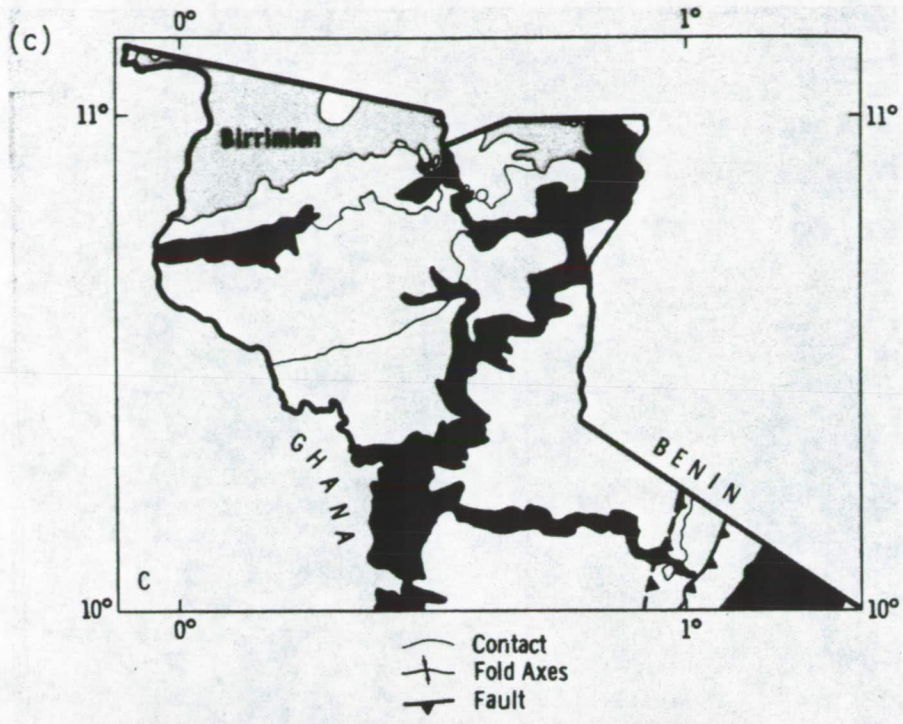


Figure 5 (Contd)

ORIGINAL PAGE IS
OF POOR QUALITY



(a)

(b)

Figure 6. Comparison of distribution of Togo Formation in the Togo Range, latitude 6-9°N. (a) Grant, 1969; (b) Lawson, 1973; (c) MARS, 1978; and (d) radar imagery.



(c)



(d)

Figure 6 (Contd)

ORIGINAL PAGE IS
POOR QUALITY

conventional aerial photography. At a scale of 1:200,000 point displacement on radar imagery (except in instances at extreme layover or foreshortening) is of considerably less magnitude than the latitude normally encountered in defining rock unit contacts. This would be especially true in deeply weathered terrain such as that encountered in Togo. The well known capabilities of the sensor (i.e., presentation of a synoptic view and selective and differential shadowing) along with the demonstrated attainment of geometric fidelity more than adequate for geologic mapping define SLAR's as valuable tools for modification as well as original map generation, and in areas where tone-texture signatures conflict sharply with map data provided by field or other sensor study identify a need for further study.

ACKNOWLEDGMENTS

The geologic map of Togo was prepared in conjunction with Dr. Joe Gardner, MARS Aerial Remote Sensing, Inc. and Dr. James McCauley, Kansas Geological Survey. Dr. Gardner's participation, review of this manuscript, and his suggestions are gratefully acknowledged. The cooperation of MARS Aerial Remote Sensing, Inc. in supplying the imagery is appreciated. A research grant from the Mobil Foundation, Inc. provided funds for drafting and preparation of illustrations and, to the Foundation, I express my sincere appreciation.

REFERENCES

- Gelnett, R. H., L. F. Dellwig and J. E. Bare, 1978. "Increased Visibility from the Invisible," Proceedings of the Twelfth International Symposium on Remote Sensing of Environment, Manila, Republic of the Philippines, April, 3:2205-2216.
- Grant, N. K., 1969. "The late Precambrian to early Paleozoic Pan-African Orogeny in Ghana, Togo, Dahomey, and Nigeria," Geol. Soc. America Bull., 80:45-56.
- Koert, W., 1910. Begleitworte zur geologischen Karte von Togo, in Meyer, Hans, Editor, Das Deutsche Kolonialreich, 2, Leipzig and Vienna.
- Lawson, D. T., 1973. Carte Geologique du Togo.
- MacDonald, Harold C., 1969. "Geologic Evaluation of Radar Imagery from Darien Province, Panama," Modern Geology, 1:1-62.
- Motorola Aerial Remote Sensing, Inc., 1978, "Final Report, Side-Looking Airborne Radar Survey of Nigeria," Motorola Aerial Remote Sensing, Inc., Phoenix Ariz., 77p.
- Wing, R. S., W. K. Overbey, Jr. and L. F. Dellwig, 1970. "Lineament Analysis. Burning Springs Area, West Virginia - An Aid in the Definition of Appalachian Plateau Thrusts," Geol. Soc. America Bull., 81:3437-3444.

EXPLORATION PAPERS

The Use of Radar and Landsat Data for Mineral and Petroleum
Exploration in the Los Andes Region, Venezuela

Robert K. Vincent

Geological Mapping in the Amazon Jungle - A Challenge to Side-
Looking Radar

Aderbal C. Correa

Side-Looking Airborne Radar Image Interpretation and Geological
Mapping: Problems and Results

J-Y. Scanvic and E. H. Soubari

The Evaluation of 3-cm-Wavelength Radar for Mapping Surface
Deposits in the Bristol Lake/Granite Mountain Area, Mohave Desert,
California

Ray Sugiura and Floyd Sabins

Radar, an Optimum Remote Sensing Tool for Detailed Plate Tectonic
Analysis and Its Application to Hydrocarbon Exploration (An
Example in Irian Jaya, Indonesia)

Claude M. Froidevaux

Fracture Trace Expression and Analysis in Radar Imagery of
Rain Forest (Peru)

P.H. A. Martin-Kaye, J. W. Norman, and M. J. Skidmore

THE USE OF RADAR AND LANDSAT DATA
FOR MINERAL AND PETROLEUM EXPLORATION
IN THE LOS ANDES REGION, VENEZUELA

Robert K. Vincent.
Geospectra Corporation
Ann Arbor, Michigan

ABSTRACT

A geological study of a 27,500-km² area in the Los Andes region of northwestern Venezuela was performed which employed both X-band radar mosaics and computer-processed Landsat images. The 3.12-cm-wavelength radar data were collected with horizontal-horizontal polarization and 10-meter spatial resolution by an Aeroservices SAR system at an altitude of 12,000 meters. The radar images increased the number of observable suspected fractures by 27% over what could be mapped by Landsat alone, owing mostly to the cloud-cover penetration capabilities of radar. The approximate eight-fold greater spatial resolution of the radar images made possible the identification of shorter, narrower fractures than could be detected with Landsat data alone, resulting in the discovery of a low-relief anticline that could not be observed in Landsat data. Exploration targets for petroleum, copper, and uranium were identified for further geophysical work.

I. INTRODUCTION

In 1978 a geological study was conducted by Geospectra Corporation for the Environmental Research Institute of Michigan (ERIM) dealing with mineral and petroleum exploration in and around the state of Tachira, Venezuela. ERIM had been subcontracted by Bendix, which in turn was under contract to the Venezuela Ministry of Energy and Mines. In January 1979, ERIM published a report (McKeon, 1979) on the Venezuela project, which in addition to geology also included land use, forestry, water resources, urban/transportation, and agricultural remote sensing tasks. The report referred to above is not available for public dissemination, but the Venezuelan Ministry of Mines graciously permitted the geological task to be reported in an oral paper presented earlier this year at the American Society for Photogrammetry meeting in Washington, D.C. (Vincent and McKeon, 1979). This paper closely follows the written account of the geological tasks given in the report (McKeon, 1979).

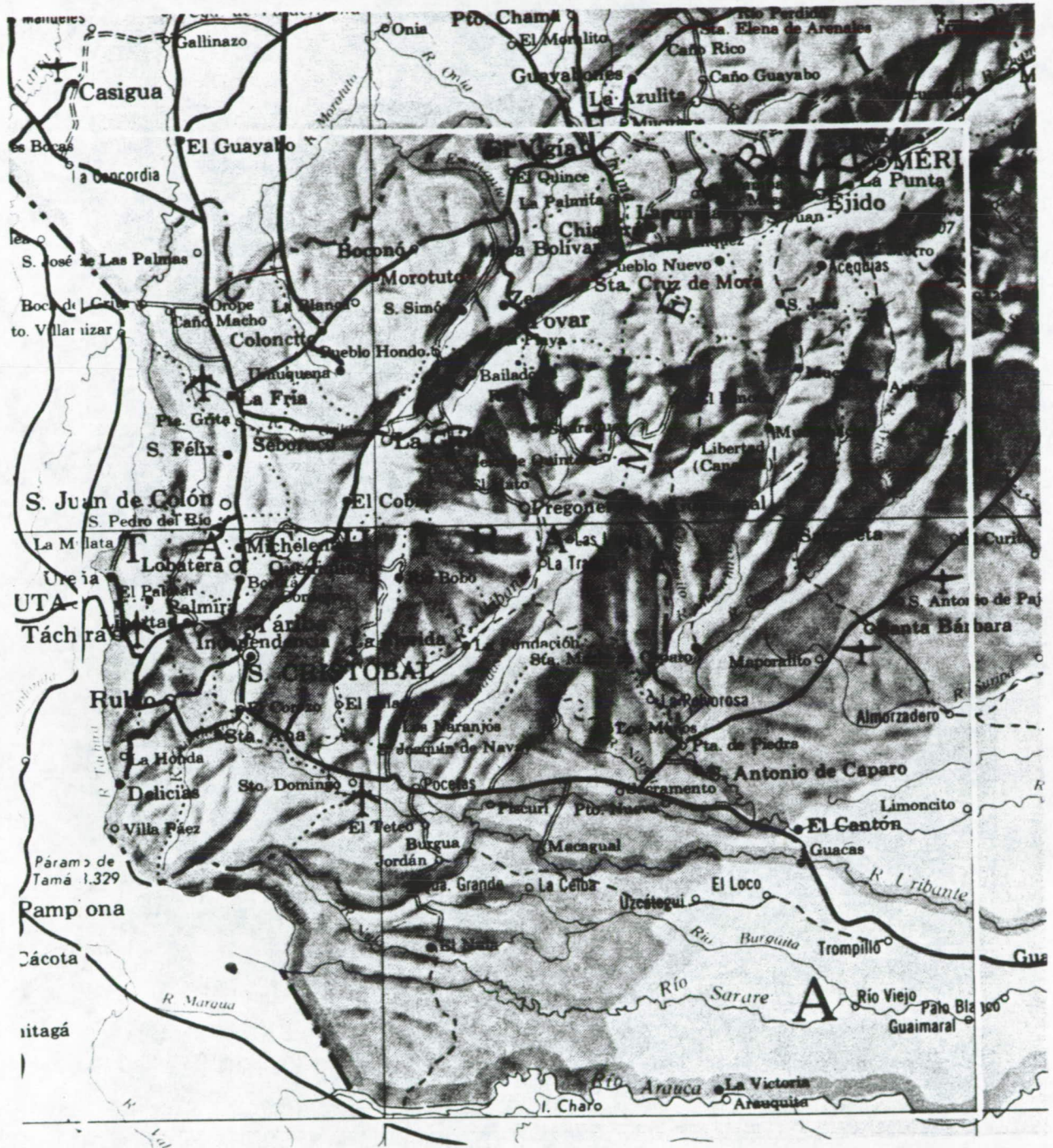
The Venezuelan government contracted Litton Aeroservices to map the Los Andes region around the Venezuelan state of Tachira in 1972, with the Aeroservices SAR system, which employs a GEM-1000 radar data collection system built by Goodyear. From 1972-1977, the entire country was covered, resulting in 1:250,000 scale mosaics of high quality. The Aeroservices SAR system integrates a GEM-1000 with a precision navigated French-built Caravelle aircraft (comparable to a DC9), such that radar observations can be made out of either side of the aircraft. The Venezuelan data were collected at a 12,000-meter altitude on north-south and south-north flight lines, but the look direction was always west. Thus, the whole project area was covered with the same look direction, greatly simplifying the interpretation tasks. The radar wavelength was 3.12 cm (X-band), with an apparent ground resolution of 10 m and horizontal polarization for both transmitter and receiver. Unfortunately, all mosaics were returned to Venezuela at the project end, and no figures displaying the radar images were available for this paper. Only the results of the investigation are given here.

Landsat 1:250,000 scale color composites of bands 4, 5, and 7 for four frames and black and white 1:400,000 scale R4/5 (band 4 divided by band 5) ratio images of three subframe areas were provided by ERIM for the study. The Landsat and radar data were studied together for two types of geological phenomena: Faulting caused by the collision of two continental plates and ferric oxides in exposed rocks and soils caused both by primary sedimentation and by secondary geochemical alteration. A one-week field trip followed the interpretive phase.

The project area, shown in Figure 1, covered a region which included the entire state of Tachira.

II. MAPPING OF LINEAMENTS

Lineaments suspected of being fractures (faults or joints) were mapped from both the Landsat false color composites and the radar mosaics at a scale of 1:250,000; all are shown at a reduced scale in Figure 2. All lineaments were digitized and plotted by a Calcomp plotter to produce Figure 2. The lineaments were first mapped from Landsat alone (Figure 3). Most of the large blank areas in Figure 3 were cloudy areas, even though these were the best Landsat frames available for the area. In a separate task, lineaments were then mapped from the radar data and the resulting map was compared with those mapped from Landsat. Only those lineaments identified from the radar data but not found in Landsat data were digitized and plotted as Figure 4. Note that these additional lineaments derived from radar data were located not just in cloud-covered areas in the Landsat data, but also in many cloud-free areas as well. As a guide for future remote sensing experiments, it should be noted that the radar data added 27% to the number of lineaments mapped from Landsat scenes in this perennially cloudy study area. After the lineaments shown in Figure 2 were digitized and entered into a computer file, a moving "window," with dimensions of 11.25 by 11.25 km, was automatically scanned across the file with a 66% overlap at sides and bottom, so as to record the total length in km of lineaments per km² occurring in the moving "window." This created a grid of data points such that any one point was separated by 3.75 km in all four directions from its nearest neighbor. From the grid, a contour map of lineament length density was produced for the entire program area, with contour lines showing the amount of line kilometers of lineaments per km² (Figure 5). As a further interpretive aid, all 4795 lineaments shown in Figure 2 were grouped and plotted by 10° azimuth ranges to show directional trends. Figure 6 is an example of such a plot for the range 10° - 20° (clockwise from north) and contains subset of 407 lineaments.



REPUBLICA DE VENEZUELA

ESCALA 1:1.000.000



Figure 1. Study area at 1:1,000,000 scale, including the state of Tachira. North is upward.

ORIGINAL PAGE IS
OF POOR QUALITY



Figure 2. Lineaments mapped from Landsat and radar. The north and west boundaries of Los Andes program area are indicated by the top and left edge of this and the next four figures.

VENEZUELA LINEARS
LANDSAT IMAGERY ONLY



Figure 3. Lineaments mapped from Landsat.

VENEZUELA LINEARS
RADAR IMAGERY ONLY



Figure 4. Lineaments mapped from radar.

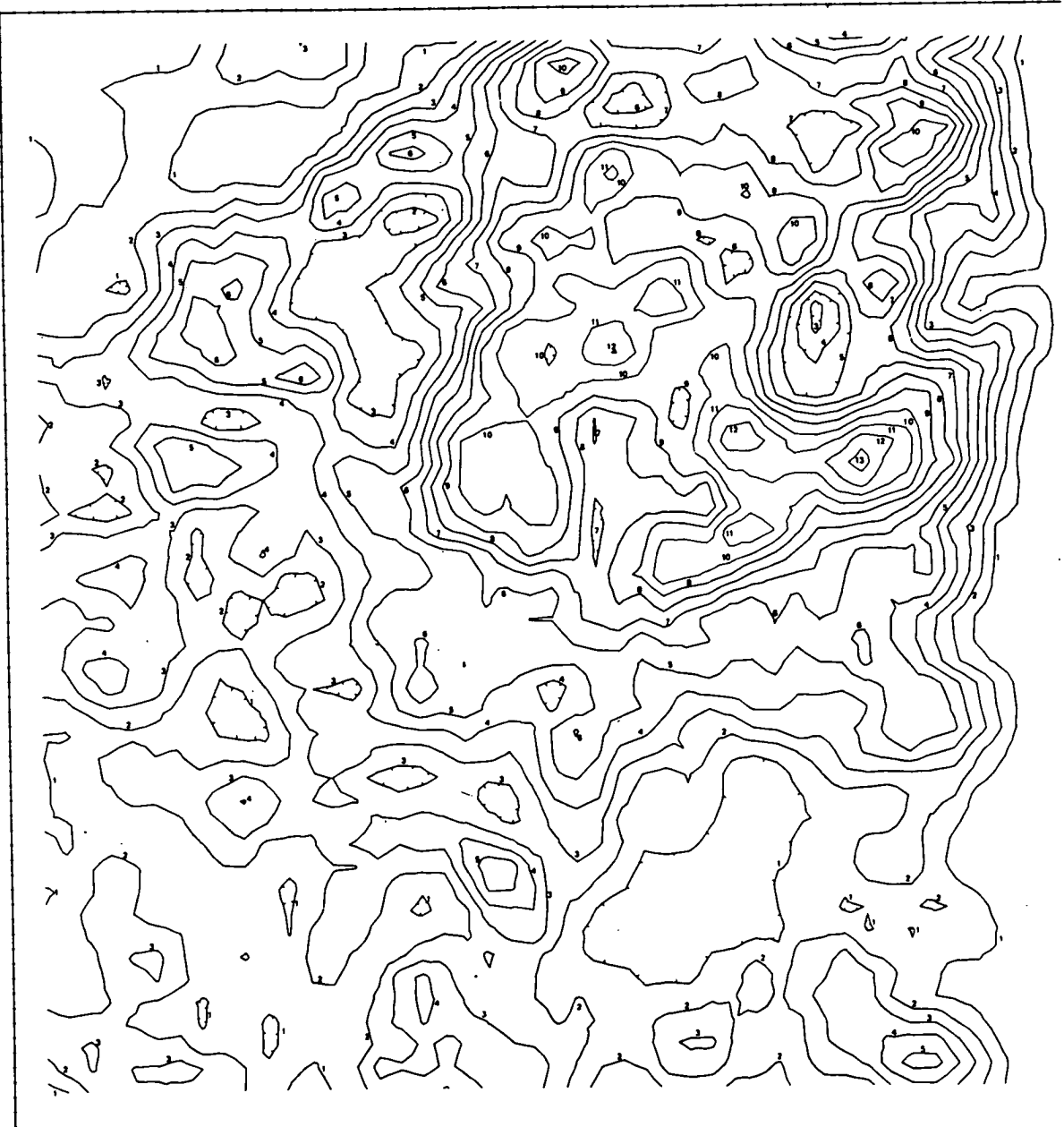


Figure 5. Contour map of lineament length density contours are labeled in intervals of 0.1 km of lineaments per km².

10° - 20°

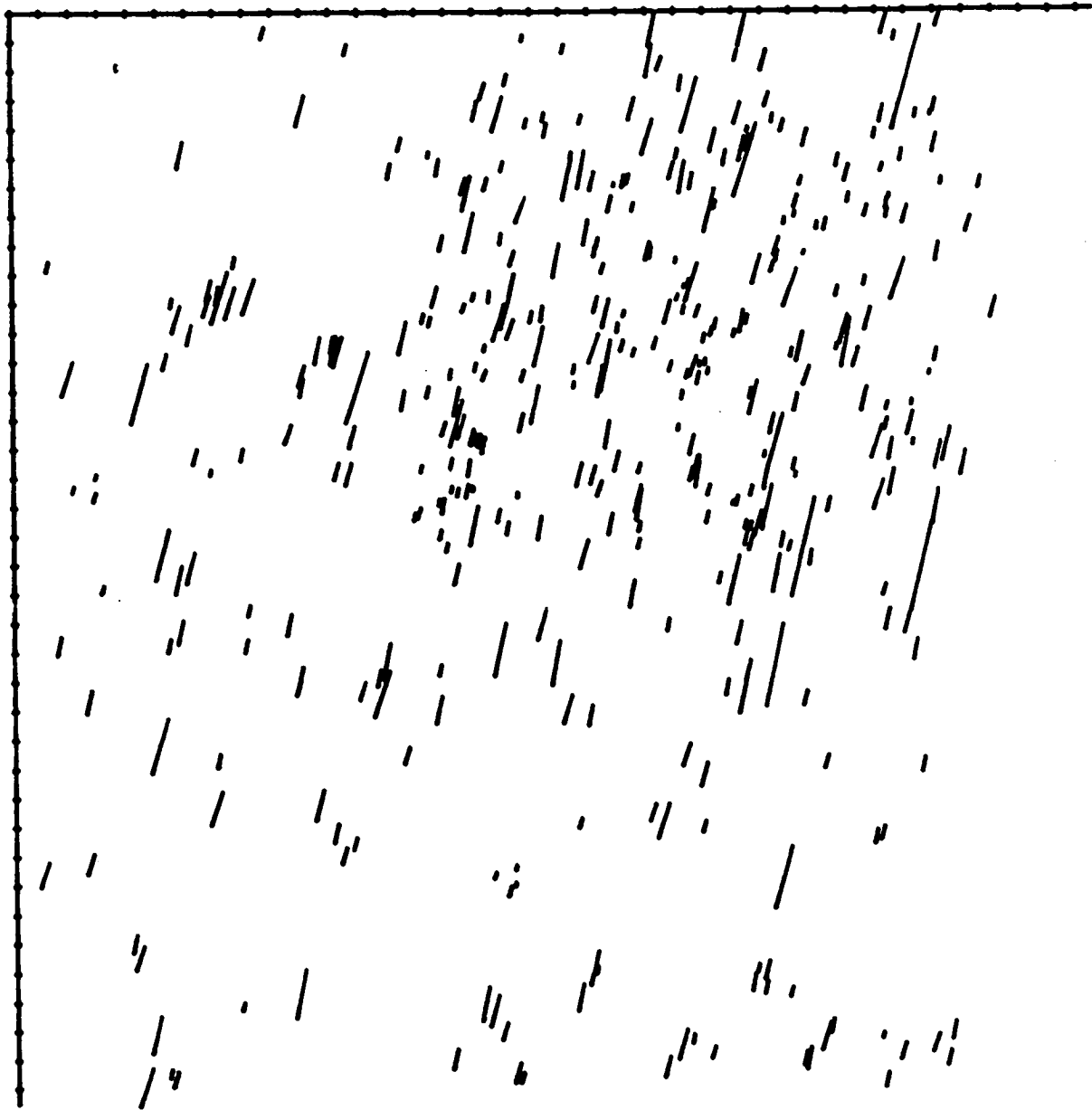


Figure 6. Example of lineament plot by 10° azimuth range. The north and west boundaries of Los Andes program area are indicated by the top and left edge of this figure.

Eighteen such azimuthal classes were plotted for the study. Finally, Figure 7 was prepared by John McKeon (McKeon, 1979; Vincent and McKeon, 1979) to show the regional trend of all the lineaments within Los Andes. Figures 2 and 5 were studied for unusual fault patterns that may have associations with mineralization.

III. MAPPING OF FERRIC OXIDES

Ferric oxides have unusual reflectance properties, in that the reflectance of ferric oxides increases more with increasing wavelength from the visible green to the visible red than practically any other natural terrain feature. This reflectance property, which makes ferric oxides colorful (reds, pinks, oranges, and yellows) to the human eye, causes the ratio of band 4 to band 5 reflectances (R4/5) to be lower for ferric oxides than for almost anything else in nature, even though they do not stand out as brightest or darkest in either band 4 or band 5 alone. R4/5 ratio images of the three subscene areas were produced at 1:400,000 scale for subscenes including the cities of Merida, Tovar, and San Cristobal. For the sake of brevity, these ratio images are not shown here. The Merida subscene was located in the north-western corner of Figure 1. The Tovar and San Cristobal subscenes were in the north-central and west-central parts of Figure 1, respectively.

It is practically impossible, in most cases, to separate secondary (geochemical alteration) ferric oxides from primary (syngenetic) ferric oxides on the sole basis of spectral reflectances detected from Landsat bands 4, 5, 6, and 7 or ratio images derived from these channels. Future Landsat satellites with channels in the 1.5 μm and 2.0 μm wavelength regions may make such spectral discriminations possible. In the meantime, Landsat ratio images are used to separate ferric oxides from other terrain elements. Those lithologic units that are known to have little or no primary ferric oxides are singled out for further study. Spatial patterns in ferric oxide exposures that might associate the ferric oxides with a structural feature, where faulting may have provided escape routes for geochemically active fluids from greater depth, were also investigated. Such fluids can produce bleaching and oxidation, which discolor rocks and their residual soils.

IV. INTERPRETIVE RESULTS

Figure 8 was derived from analysis of Figure 2, Figure 5, and the azimuthal plots (like Figure 6) to show sites of interesting structural features. Sites 1, 2, and 3 in Figure 8 show the areas of highest lineament length density (> 12 km of lineaments per km^2) in the study area. Sites 4-12 show areas where lineament patterns may indicate the nature of the predominant tectonic force which produced them. Sites 4, 6, 7, 9, 10, and 12 display lineament patterns that were most likely produced by compressional forces. They are characterized by numerous fault intersections with an intersection angle of approximately 60° . The compressional force vector is assumed to bisect the approximately 60° angle of intersection. Sites 8 and 11 have lineament patterns that suggest they were caused by tensional forces at right angles to the enechelon lineaments. The lineament pattern in Site 5 appears to have been caused by orthogonal compressional and tensional forces. Site 13 in Figure 8 appears to be an anticline. The locally high fracture length density plus the occurrence of Tertiary outcrops completely surrounded by Quaternary sediments as shown on existing geologic maps indicates that this area has probably been uplifted since Tertiary time.

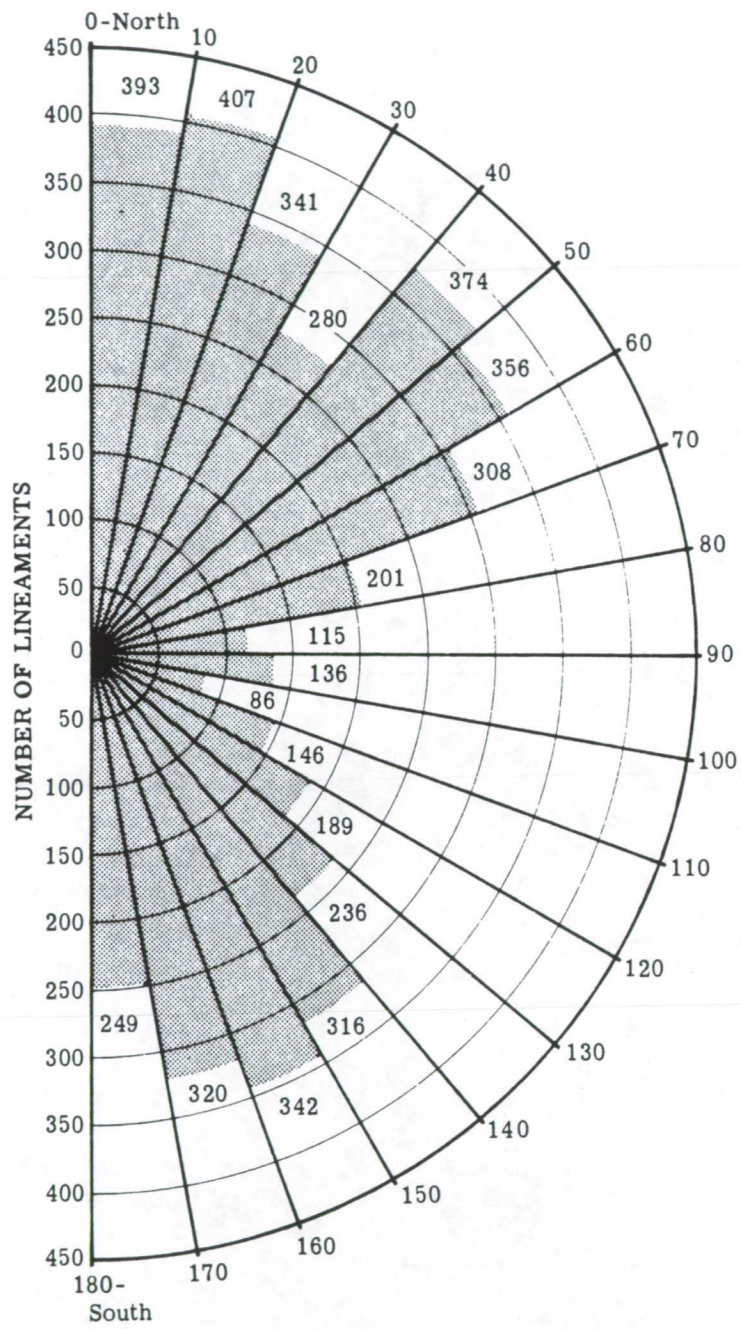


Figure 7. Rose diagram showing trend of 4796 lineaments mapped from Landsat and radar, Los Andes, Venezuela.

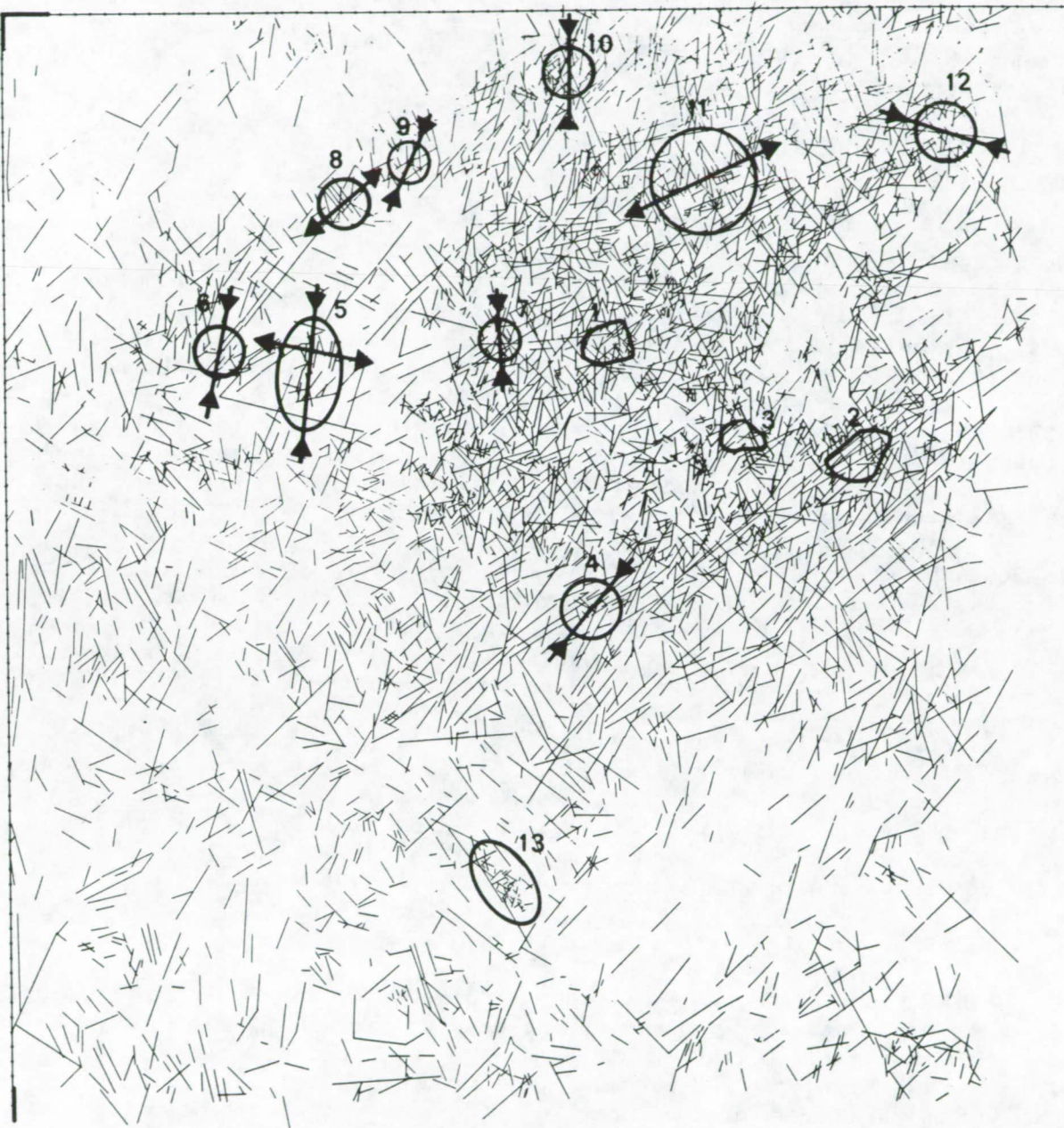


Figure 8. Structural interpretations shown on the map of Landsat radar derived lineaments.

ORIGINAL PAGE IS
OF POOR QUALITY

The rose diagram in Figure 7 shows by the regional trend of the lineaments that, taken as a group, the lineaments appear to reflect the regional tectonic forces. Note that there are three directional modes: NNE to SSW, ENE to WSW, and NNW to SSE. One possible interpretation by McKeon (McKeon, 1979; Vincent and McKeon, 1979) of this trend is that compressional forces exerted along the NNE to SSW direction could account for the two modes at the 70° intersection angle formed by the ENE to WSW and NNW to SSE trends. The third mode of lineaments at NNE to SSW may be caused by regional tensional forces that are orthogonal to the regional compressional forces.

Interpretation results of ferric oxide patterns noted in the R4/5 ratio images will only be highlighted and summarized here. In the Merida subscene an oval pattern of ferric oxides occurs in the southwestern quarter of Site 11 in Figure 8. The oval occurs chiefly in what the geological map shows as Carboniferous-Permian sediments of the Mucuchaci, Rio Momboy, and El Aquila Formations and partly in Precambrian granite. Just off the western edge of the oval, a semicircle of what is mapped as Carboniferous-Permian igneous intrusive occurs. The oval could be a collapsed volcanic feature or a collapsed magma chamber of a hypabyssal intrusive. It was recommended that the area should be remapped, with close attention to the possibility that previously unmapped, extrusive rocks may occur in that area and copper or other metal occurrences may accompany them, especially since this area appears to have been faulted by tensional forces. No field work was done there as part of this project due to time limitations.

Just above Site 7 in Figure 8, some ferric oxide exposures were noted in the Tovar subscene that could be primary iron oxides similar to the La Quinta Formation, in which copper is known to occur, although the area is mapped as Carboniferous-Permian rocks, which supposedly have no redbeds. This area likewise was not checked in the field, due to time limitations.

A circular ferric oxide pattern was noted in the San Cristobal subscene just west of Hato de La Virgen (near Lobatera in Figure 1, just north of San Cristobal). It occurs in what the geologic map shows to be the Carbonera Formation of Tertiary age. This area was field checked for secondary ferric oxides in Tertiary-aged sandstones, which would bode well for uranium exploration. The field results are given in the following sections.

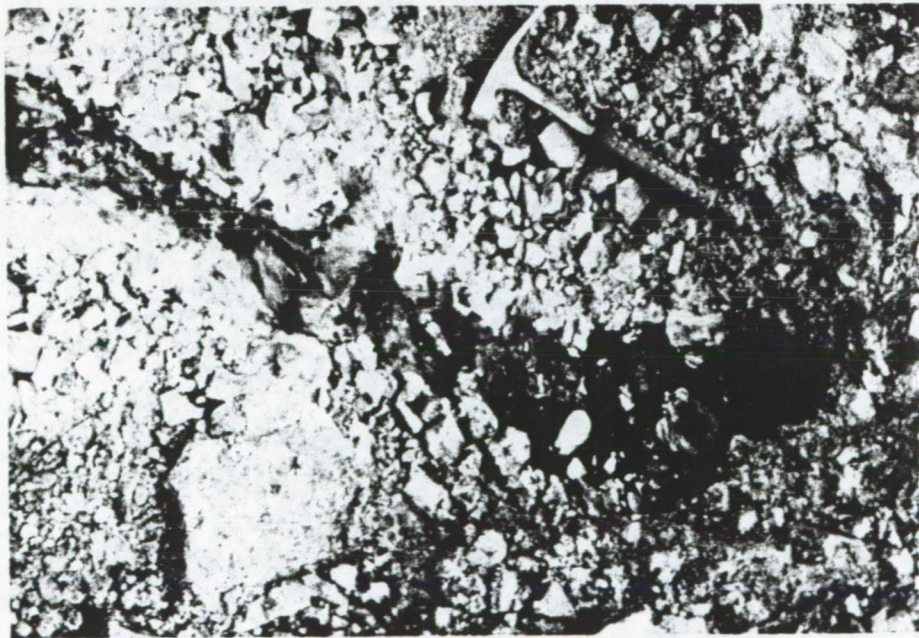
V. FIELD RESULTS

J. B. McKeon (ERIM), R. K. Vincent (Geospectra), and Venezuelan geologists A. Useche and J. Furnaguera conducted one week of field checking in the region around San Cristobal. Logistical support, two jeeps and one helicopter, was provided by the Ministry of Mines. No helicopter flights could be safely made in the mountains because of their high altitudes (sometimes greater than 3000 meters). Figures 9 and 10 show some field photos of areas in western and southwestern areas of the study area (shown in Figure 1), but mostly in the San Cristobal subscene. Only highlights of this field trip will be summarized here.

Photo 1 in Figure 9 and Photos 2 and 3 of Figure 10 show the Hato de La Virgen area. Secondary iron oxides (limonitic soil) were found in Tertiary-aged sandstones of the Carbonera Formation in this region, coinciding with the circular ferric oxide pattern described in the previous section. The similarities of age, oxidation-reduction products, carbonaceous trash, and present climate



(1) Fault scarp northwest of Hato de La Virgen; view is to the southwest. The fault trends NNE to SSW. (November 15, 1978)



(2) One of numerous hot mineral springs at Aguas Calientes. (November 15, 1978).

Figure 9. Field photos from Venezuela.

U.S. GEOLOGICAL SURVEY
WATER RESOURCES DIVISION
FEDERAL BUREAU OF INVESTIGATION



(3) Example of copper mineralization in La Quinta Formation, near Seboruco. (November 14, 1978)



(4) Bleached sandstones of the stratigraphic section where thin coal seams were found, northeast of San Joaquin de Navay. (November 16, 1978)

Figure 9 (Contd)



(1) The site near Hato de La Virgen showing limonitic residual soils; view is to the northeast.
(November 15, 1978)

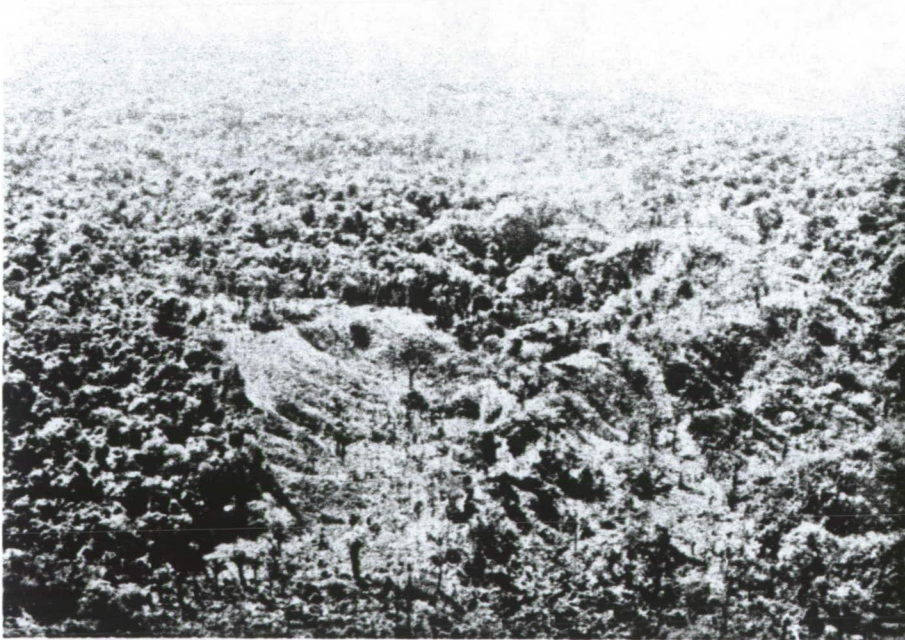


(2) View to the southwest of the Hato de La Virgen site, which appears favorable for uranium mineralization.
(November 15, 1978)

Figure 10. Field photos from Venezuela.



(3) Examples of gravel removal from river bank alluvium, Rio Torbes south of San Cristobal; view is to the south.
(July 27, 1978)



(4) Anticlinal structure (Site 13), within the forests of San Camilo, that is favorable for oil and gas accumulation (November 16, 1978)

Figure 10 (Contd)

(semi-arid, due to high elevations) between these and uranium-producing sandstones in Wyoming and New Mexico in the U.S. make this an attractive area for uranium exploration. Ground scintillometer and radar track-etch surveys were recommended, since the area is too undulating and high above sea level for safe airborne gamma-ray surveys.

The copper mineralization shown in Photo 3 of Figure 9 was found near Seburoco and El Cobre in Site 5 of Figure 8. No ferric oxide patterns could be viewed in the R4/5 ratio image because clouds obscured this area, though the mineralization occurred in the La Quinta Formation redbeds, which were discolored only over subpixel (less than 79 meters) areas and likely could not have been detected by ferric oxide mapping from Landsat ratio images anyway. However, Site 5 was one of the three sites (with Sites 8 and 11) which appeared to have been fractured by tensional forces (see Figure 8). Tensile fractures are readily opened by invading fluids under high pressure, and some of them eventually come to be occupied by dikes or mineral veins. Sites 5, 8, and 11 were recommended for copper exploration.

Photo 4 of Figure 10 shows a helicopter photo of the suspected anticline in Site 13 of Figure 8, near La Ceiba. Sandstones of probable Tertiary age are surrounded by Quaternary sediments in this area. It has slightly greater topographic relief than the surrounding sediments, and this slight relief is what the radar data probably detected. The Mirador Formation of Tertiary age contains a massive sandstone which would provide excellent reservoir potential for petroleum. The area was recommended for a seismic survey, which the Ministry of Energy and Mines is now conducting.

VI CONCLUSIONS

The principal effect of employing X-band radar images and Landsat images together was a 27% increase in the number of suspected fractures which could be mapped in the 27,500-km² study area, as compared to fractures mapped from Landsat images alone. Another advantage offered by the inclusion of radar data was that fractures of smaller length could be mapped than could otherwise be seen in Landsat images of grosser spatial resolution. A suspected anticline was mapped that probably would have been missed were it not for the shorter lineations mapped from the radar images. One look direction for the entire study area was a great help for interpretation of the radar mosaics.

Interesting structural features found from the radar and Landsat images have provided good exploration targets for oil, gas, and copper in the study area. Ferric oxide mapping and comparative geology have provided a good exploration target area for uranium. The study has been partially confirmed by field checking, and geophysical followups are now being made by the Venezuelan Ministry of Energy and Mines.

ACKNOWLEDGEMENTS

Thanks are due to the monitoring official for the study, Dr. Luis A. Gonzales S., and the Venezuelan Ministry of Energy and Mines for permission to publish the geological portions of this study and to John B. McKeon and ERIM for providing slides and photos for this presentation, as well as for technical consultations.

REFERENCES

- McKeon, J. B., Remote Sensing of the Resources of Los Andes Region, Venezuela, Final Report - Volume 1, Environmental Research Institute of Michigan Report 305200-7-F, Ann Arbor, Michigan, January, 1979.
- Vincent, R. K., J. B. McKeon, and George N. Scott, "Mineral Exploration with Landsat and Radar Data in the Los Andes Region, Venezuela," Abstract Only, Proceedings of the American Society for Photogrammetry 45th Annual Meeting, Washington, D. C., March, 1979.

GEOLOGICAL MAPPING IN THE AMAZON JUNGLE -
A CHALLENGE TO SIDE-LOOKING RADAR

Aderbal C. Correa
Conoco Inc.
Exploration Research Division
Ponca City, Oklahoma

ABSTRACT

Acquisition of geological information in the less well known, heavily forested areas of the world has benefited tremendously from the use of side-looking radar (SLAR) images. The largest, continuous coverage of this type over jungle terrain is available today for 5 million-square kilometers (approximately 50 percent of the area of the U.S.) of the Amazon Jungle in Brazil. This coverage was acquired by a synthetic aperture radar system operating in the X-band (3-cm wavelength) and provided spatial resolution quoted as better than 20 m throughout the images.

The objectives of this study are to present some of the characteristics of the images generated by the radar system, the basic physical interaction model used during interpretation, and outline the procedure followed for geological mapping with radar images in heavily forested terrain.

Anomalous features found in radar images that are not related to any attributes of vegetation, soils, or rocks in the area are classified into four classes according to their cause: (1) imaging system characteristics, (2) images processing, (3) aircraft flight stability, and (4) local weather. Any of these features may cause or contribute to misinterpretation of the data.

A brief outline of the physical environment and vegetation characteristics peculiar to the Amazon Jungle is given to provide the background for the discussion of energy target interaction models. Examples of radar images of the central part of the jungle are used to illustrate a common approach to geologic mapping in this environment. During the initial phase of interpretation, the interaction phenomenon is evaluated and textural and tonal characteristics of the radar image are observed. Field checking of selected areas is the next phase of a geologic mapping program. Reinterpretation of radar images and auxiliary data (aerial photographs, Landsat images, and field data) is the last phase of geologic mapping.

The use of radar images for more detailed, follow-up studies of small areas, however, requires an in-depth appreciation of the characteristics of radar systems used, a more complete understanding of the physical interaction phenomenon, and the use of more refined interpretation models in radar geology.

I. INTRODUCTION

The Amazon Jungle in northern Brazil has always attracted the interest of the most diversified types of people because of its mysteries and potential for natural resources in such a large region. Radar coverage now provides a new data set to evaluate its resources as well as providing an excellent mapping base for the area.

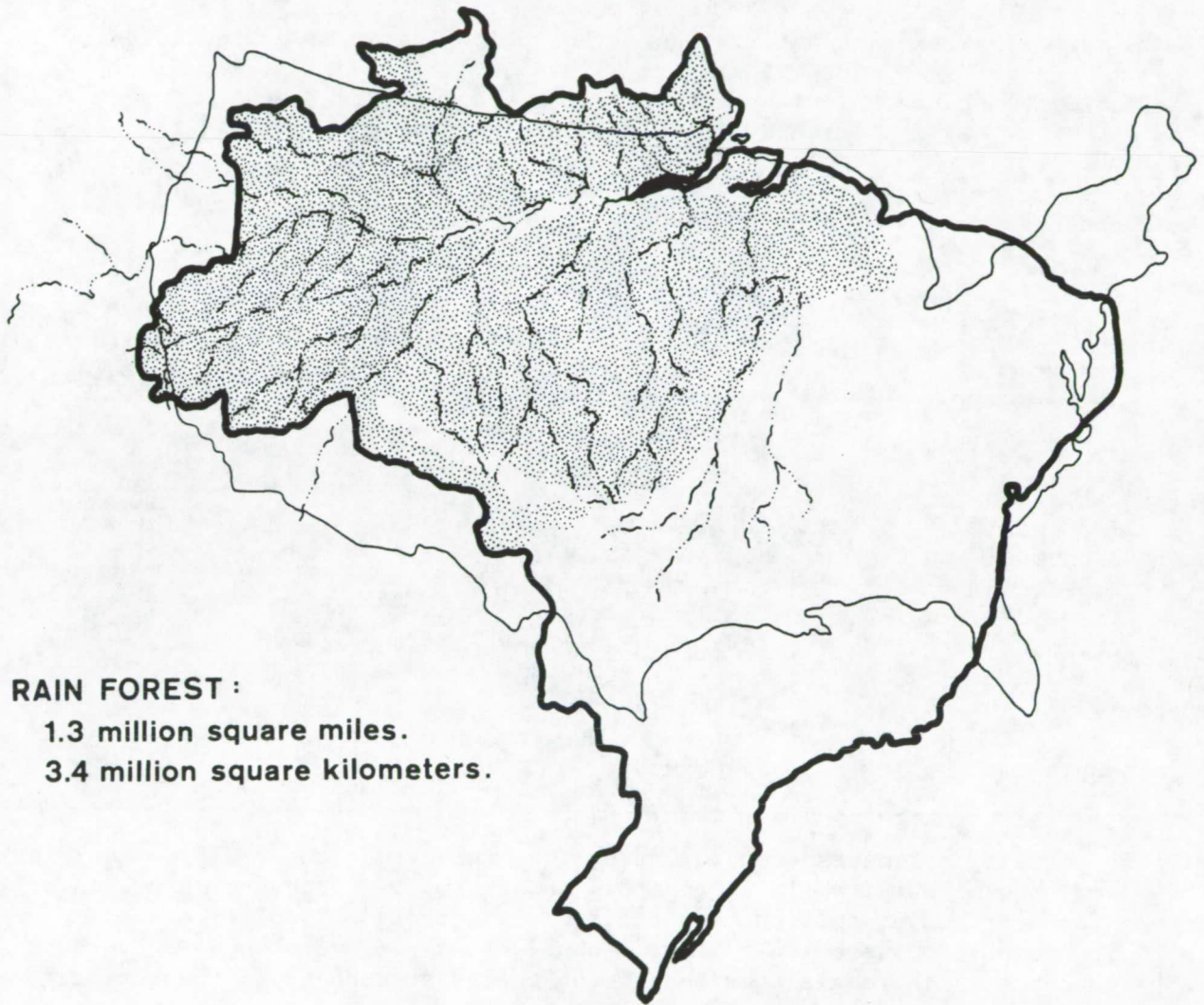
The radar mapping of the Amazon is the result of a Brazilian government project started in 1971 that has been known as RADAM Project. During its initial phase, an area of almost 5 million km² (1.9 million mi² or approximately 50 percent of the area of the United States) was mapped. Most of this area is occupied by the Amazon tropical rain forest (Figure 1) and, because of frequently widespread cloud cover, has had inadequate air photo coverage. The radar mapping project, renamed RADAMBRASIL, was extended to the remainder of Brazil and completed in March 1976.

In this paper, side-looking radar data collected over the Amazon region will be discussed with respect to (1) characteristics of the images generated by the radar system used, (2) energy-target interaction model adopted for interpretation, and (3) procedures followed during geological mapping. Radar images, mostly of the central part of the Amazon Jungle, are used to illustrate this discussion.

II. RADAR MAPPING OF THE AMAZON

Several requirements had to be met by the data generated for the RADAM Project. The most important, perhaps, after image quality, was positional accuracy for individual radar strips as they were to be mosaicked and ultimately serve as a cartographic base. Moreover, radar images were acquired during north-south flights in a westward looking direction to generate shadows in the terrain similar to those observed in Landsat images for the region. The satellite for a large part of the Amazon acquires images under a sun elevation in the 40° to 50° range and 50° to 60° azimuth, while the depression angle of the radar beam ranged from 45° in the near range to 13° in the far range.

The radar system chosen for this survey was a synthetic aperture radar, operating in the X-band (9,600 MHz), built by Goodyear Aerospace Corporation. This system, installed in a high-performance twin-jet Caravelle belonging to the Aeroservice Division of Western Geophysical Company, was flown at 700 km/h and at an altitude of 11,000 m (36,000 ft). The survey craft also acquired aerial photographs over selected areas (cloud cover conditions permitting) with both a Zeiss mapping camera with super-wide-angle lens and color infrared film, and a multi-spectral camera. These vertical aerial photos at the 1:130,000 and 1:73,000 scales, respectively, provided auxiliary data to interpret radar images. They were also very useful in checking location and linearity of flight lines.



RAIN FOREST :
1.3 million square miles.
3.4 million square kilometers.

Figure 1. Amazon rain forest.

The inertial navigation system of the aircraft was used in combination with position information provided by a network of shoran radio-positional stations throughout the region. The position of these shoran stations was surveyed with an accuracy of approximately 10 meters (30 feet) using the TRANSIT satellite positioning system. During the later phases of the survey, it was observed that location accuracy for radar images was still very high when north-south flight lines were combined with a few east-west flight lines. These east-west tie lines were located over distinctive ground features that had their geographic coordinates defined with help of the TRANSIT system. This procedure replaced the use of the shoran system for the remainder of radar coverage for the project.

A summary of the characteristics of the radar system is given in Table 1.

Table 1. Characteristics of the radar system used in the RADAM project (Azevedo, 1971; Moreira, 1973)

Radar system	GEMS 1000, Goodyear Mapping System
Band	X (9,600 MHz)
Antenna	Synthetic aperture with capability to acquire data from either side of aircraft. Antenna stabilized for yaw, roll, and pitch of the aircraft.
Polarization	HH
Depression angle	Near range: 45° Far range: 13°
Ground resolution	16-m (52.5-foot) range and azimuth directions.
Image swath	37 km (23 miles)
Data acquisition scale	1:400,000

The quality of images acquired during the survey was analyzed routinely by RADAM personnel. Moreira (1973) reported on some of the problems observed in a very informative paper that unfortunately had restricted circulation. The following discussion based on Moreira's observations illustrates some of the problems observed in images acquired during the radar mapping of the Amazon.

Anomalous features found in radar images that are not related to any of the terrain types present in a region can be classified into four groups according to their cause: (1) imaging system characteristics, (2) image processing, (3) aircraft flight stability, and (4) local weather. Any of these may be responsible or contribute to interpretation errors if one is not familiar with them.

Radar images with slight quality degradation due to any of the problems discussed below that was not serious enough to be an obstacle to interpretation, were accepted by the RADAM Project. An additional requirement, however, was that the problems could not occur in more than 5 percent of the total area mapped

(Moreira, 1973).

A. Imaging System Characteristics

In situations when the antenna pattern does not provide uniform illumination of the terrain, longitudinal dark and light banding is observed in the images (Figure 2). This problem is substantially minimized by additional processing of the image.

The additional processing required by images with the longitudinal banding described above may be responsible for strong tonal contrast between adjacent strips in a mosaic. Another source of tonal and textural variations in mosaics is the change of backscattering level from the terrain in the near and far ranges of a radar strip. In flat terrain with relatively homogeneous vegetation cover, the incident energy with a small depression angle (13°) is associated with a rougher texture and lighter gray tones on the far range image relative to those on the near range image (Figure 3).

In situations where there is a sudden change in topographic relief from a flat horizontal surface, such as in a river or lake, to the vertical face of a cliff, or tall dense vegetation, the strong backscattering is observed on the radar image as a well defined white strip. The automatic gain control of the system, however, may not compensate for unusually high return signal levels, resulting in an abnormally wide bright zone along the area of relief change (Figure 4). The position of the vegetated land/water interface in relation to the scanning direction is a major factor determining the presence of these bright edges on the radar image. If this interface in jungle terrain is oriented approximately parallel to the scanning direction, the gain adjustment problem may never arise. In other positions of the interface, the backscattering level is also a function of the type of vegetation, soil moisture content, and depression angle.

B. Image Processing

Images with very fine lines along the azimuth direction (parallel to the ground track) indicate that the data film was scratched during processing (Figure 5). In general, this is not a major problem during interpretation.

When the image generated for interpretation is defocused because of processing problems, it is necessary that an interpreter be aware of that fact. The apparent textural change on the image resulting from defocusing may be difficult to detect along a radar strip, but it is more obvious in mosaics (Figure 6).

Moreira (1973) describes other types of image degradation that are associated with photographic processing. These are not discussed here because they were not found by the author in images used to generate mosaics for the RADAM Project. Images showing these processing defects (e.g., large scratches, fingerprints, etc.) were rejected during the quality control evaluation of the radar data.¹

C. Aircraft Flight Stability

Optimum flight conditions for a side-looking radar survey dictate that the aircraft fly smoothly and in a straight line. Sometimes this is not the case because of zones of turbulence and/or strong winds. A limited amount of

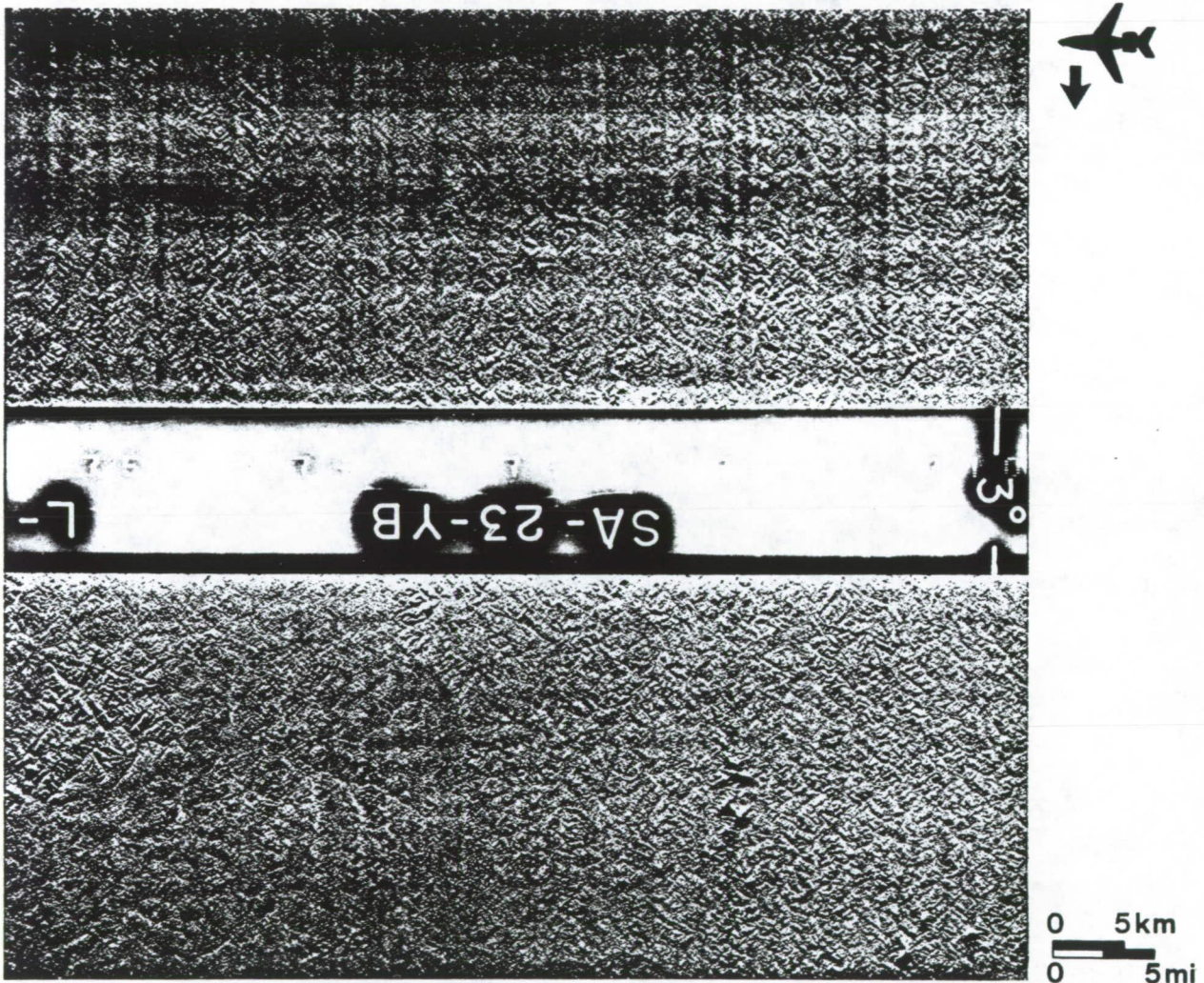


Figure 2. Longitudinal dark and light banding (parallel to flight direction) in radar image which is observed when the antenna pattern does not provide uniform illumination of the terrain. This image defect, known as side-lobe banding, is usually more noticeable in the near-range portion of the radar image.

ORIGINAL PAGE IS
OF POOR QUALITY

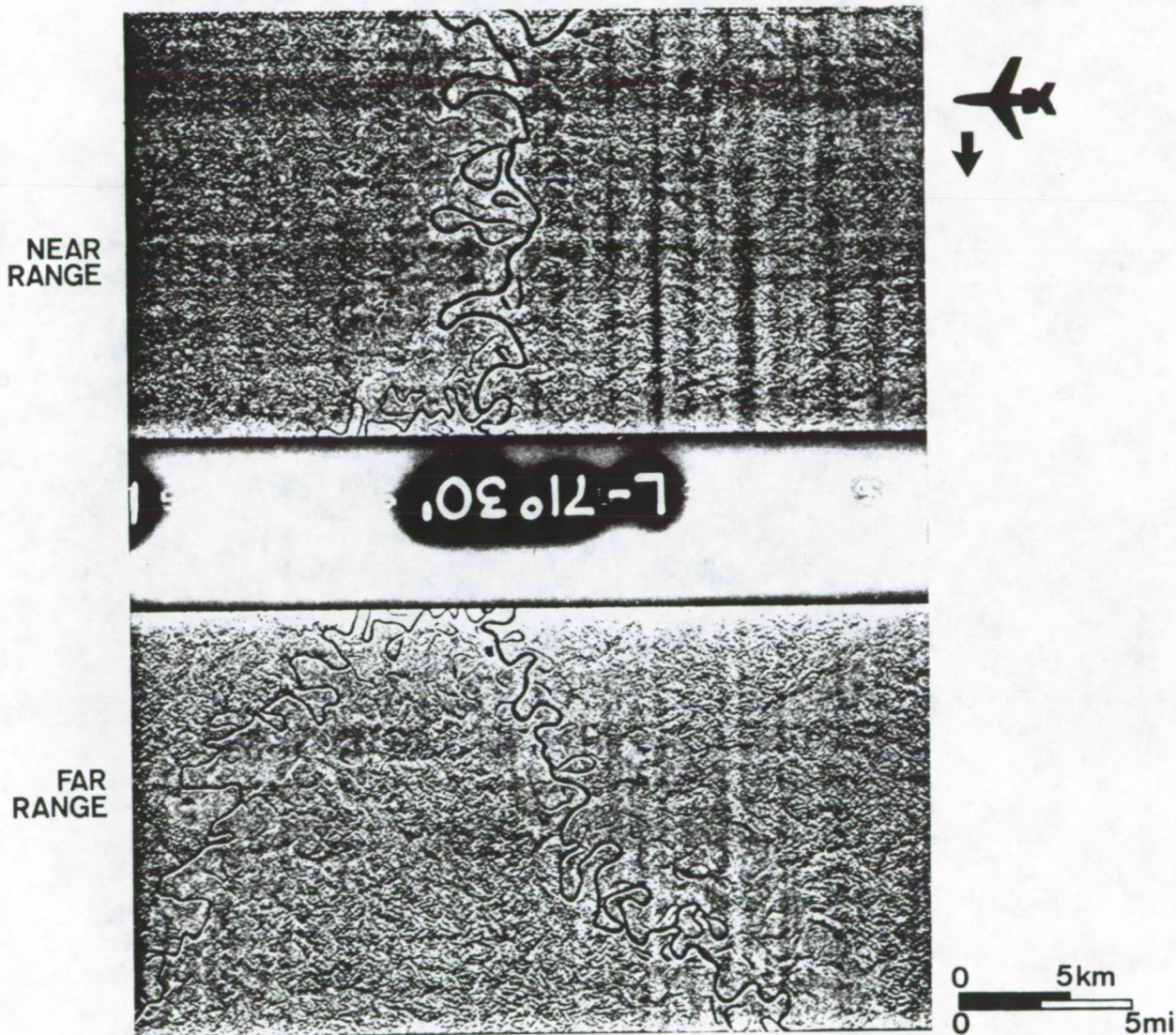


Figure 3. Segment of radar strip acquired over a flat terrain with relatively homogeneous vegetation showing a rougher texture and lighter gray tone on the far-range image relative to the near-range.

ORIGINAL PAGE IS
OF POOR QUALITY

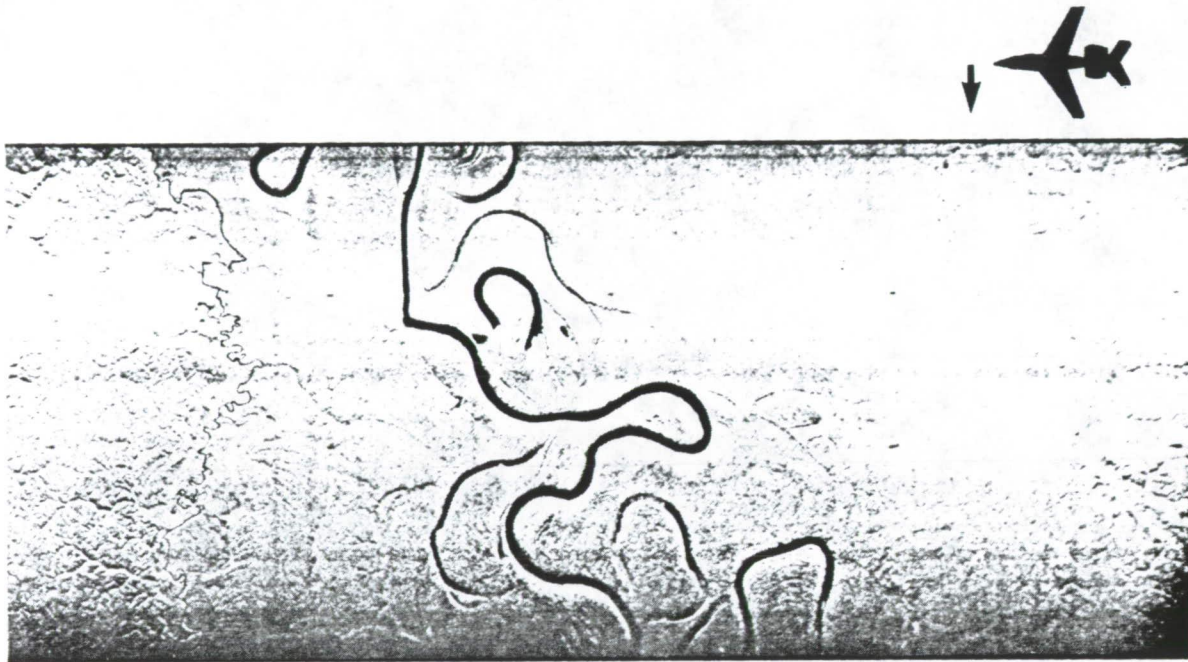


Figure 4. Abnormally bright zones observed along river margins where high return signal levels were not compensated by the automatic gain control of the radar system.

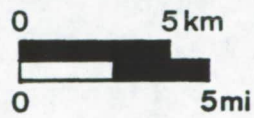
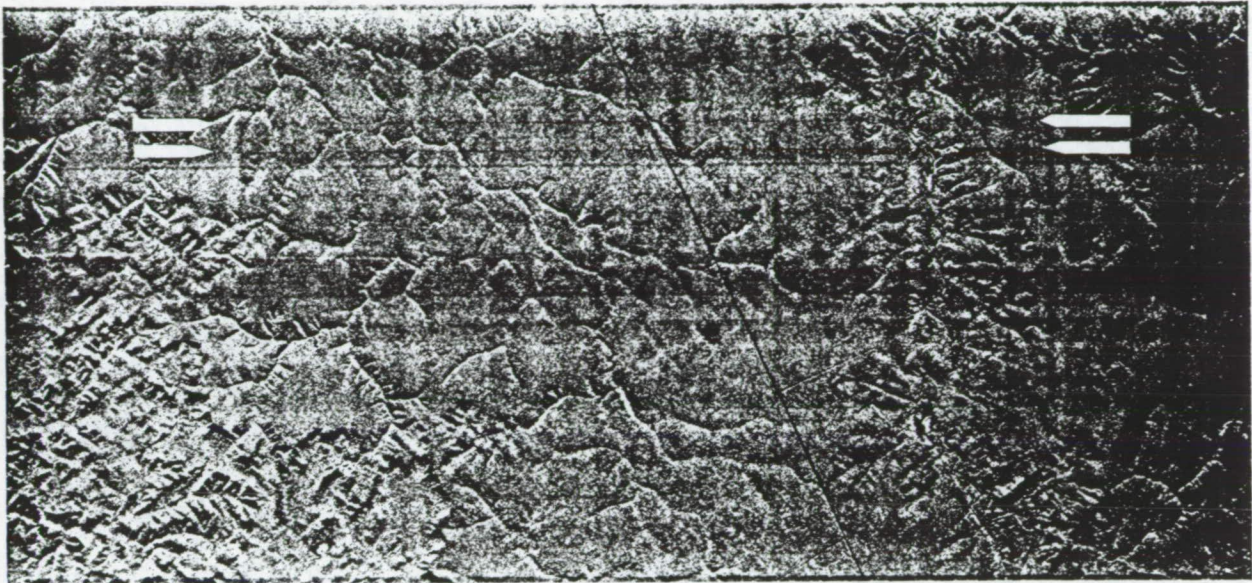


Figure 5. Fine lines along the azimuth direction (shown by marks) indicate that the data film was scratched during processing.



Figure 6. Part of mosaic showing two radar strips separated by horizontal line. Apparent change in texture from the upper to lower part of figure is due to defocusing the image during optical correlation of the radar data.

compensation is provided by the mapping system for aircraft perturbation (roll, pitch, yaw, and variations of speed). When the limits of the system are exceeded, radar images show strong banding along the range (normal-to-ground track) direction and distortion of terrain features (Figure 7).

D. Local Weather

Side-looking radar systems are well known for their "all-weather" capability which permits their use in areas often covered by clouds. The systems, however, do not perform well when there is rain in the area being mapped. Strong rainstorms can backscatter the radar signal, creating a light zone on the image. Also, the terrain behind the rain clouds, in relation to the flight path, is covered by shadows and, therefore, becomes a zone without information (Figure 8).

III. ENERGY-TARGET INTERACTION AND GEOLOGICAL MAPPING

Geological interpretation of radar images requires a theoretical knowledge of system and target parameters affecting the radar return to the receiver, and an evaluation of how these parameters are dependent on the characteristics of the natural environment. A prior familiarity with vegetation and terrain characteristics of the Amazon region, therefore, is a requirement to image interpretation. Once this is established, radar images may be utilized more effectively in geological mapping.

A. Physical Environment and Vegetation

The Amazon Jungle has some general characteristics, such as predominance of broadleaved trees with an average height of 20 to 30 m (65 to 98 ft), wide canopies spreading from the upper part of the trunk, and straight stems and trunks, that may create the false idea that no major variations are to be expected. The uniformity of the vegetation is also apparent when the jungle is seen from an airplane. However, when the vegetation is observed in more detail, the presence of a strong correlation of vegetation with the physical environment becomes obvious. This correlation has served as the basis for vegetation classification schemes (e.g., Azevedo, 1950, 1972).

After radar images became available for study, the need for a better appreciation for the relationships between vegetation and the physical environment became apparent. Based on the concept that the presence of a given vegetation group may identify an ecological system where biological conditions are in balance with the physical environment (climate, soil, and geological settings), RADAM scientists developed a classification system for the Amazon Jungle (Veloso et al., 1975). Some of the common vegetation types and their ecological environments are described below.

1. Tropical Rain Forest. This forest is characterized by dense tree distribution and multistory vegetation cover. The uniformity in tree height may be broken by a few tree species that stand above the average tree population. The rain forest is present in the most diverse environments including mountains and deeply eroded igneous and metamorphic terrain with altitudes above 1,000 m (3,200 ft) and alluvial plains (Figure 9).

2. Woodland Forest. This forest is typified by tree density smaller than that in a rain forest, and an occurrence in different environments. Two subtypes have been recognized, however, that indicate special climate and soil conditions

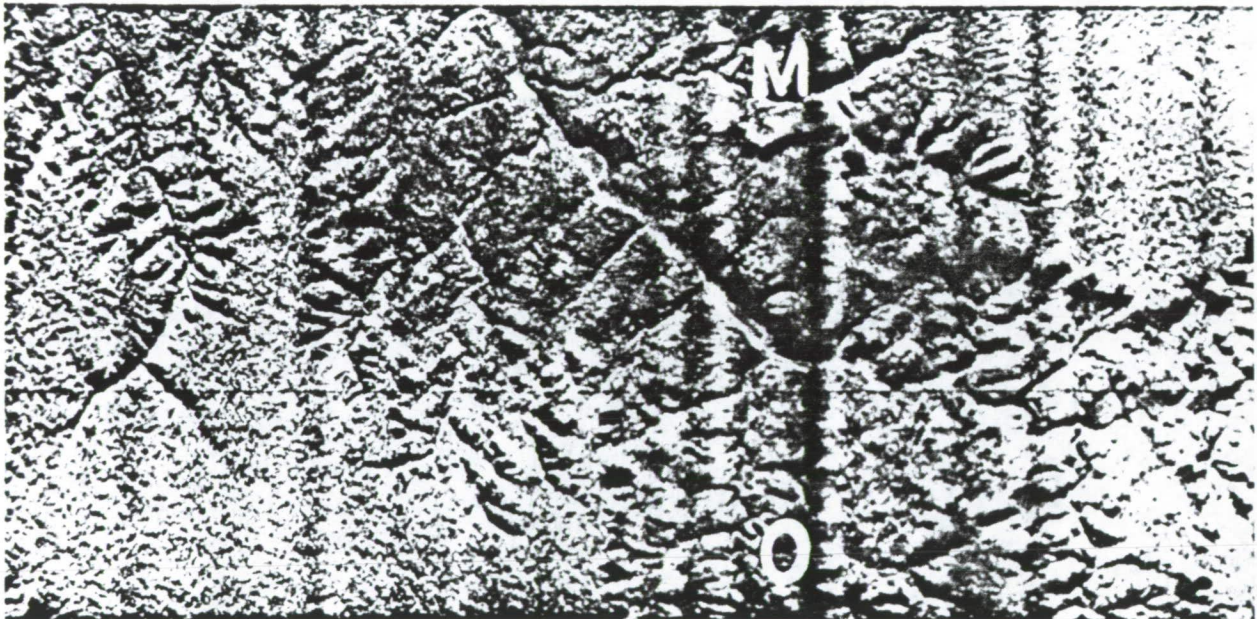


Figure 7. Strong banding and distortion of terrain features normal to ground track direction observed when the radar system did not compensate for excessive aircraft instability.

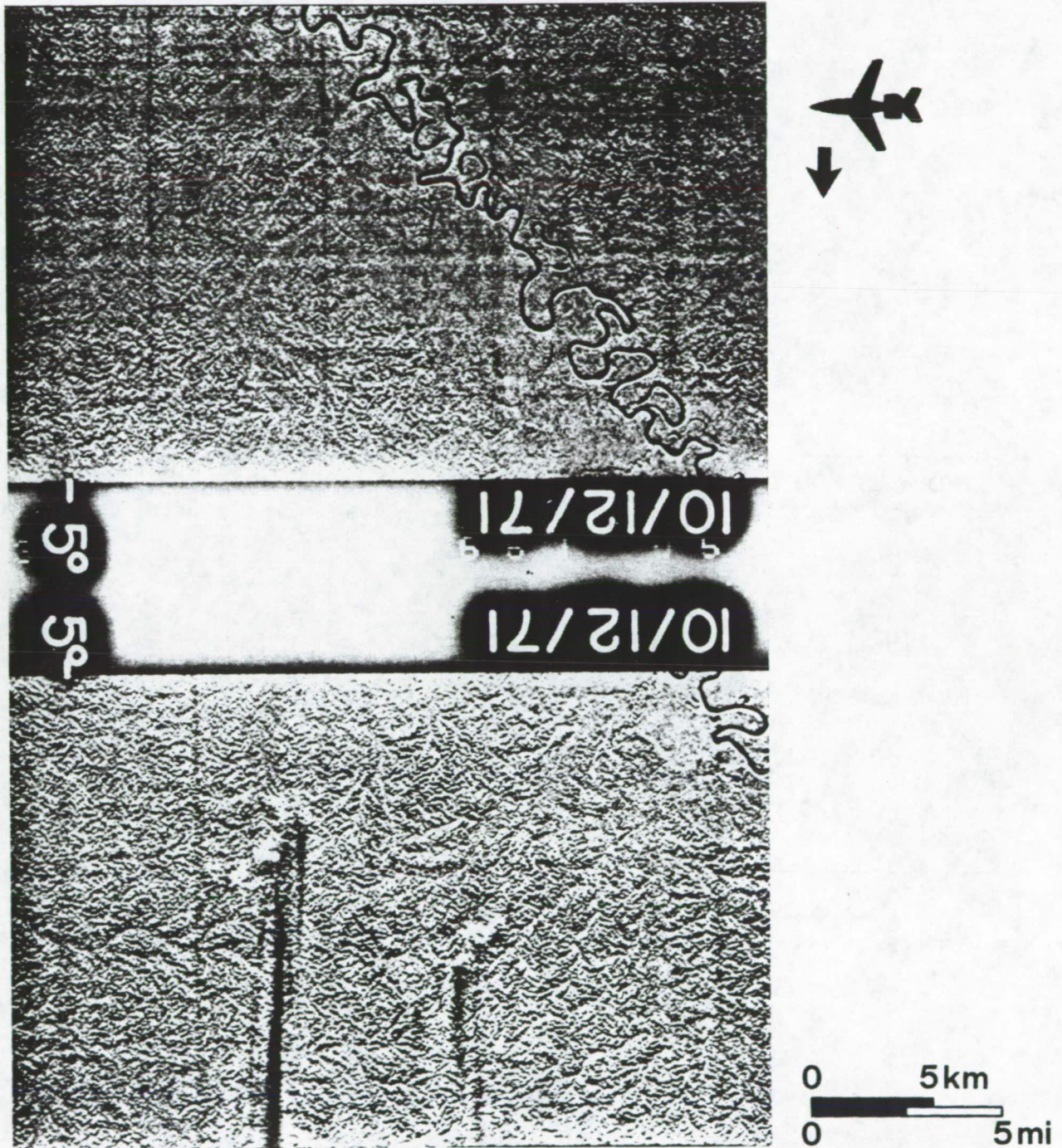
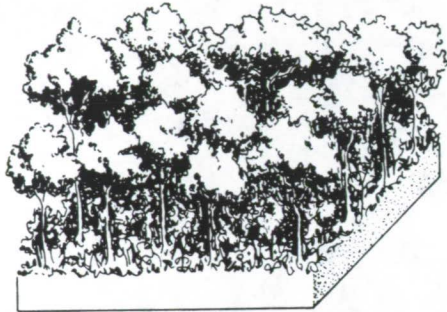
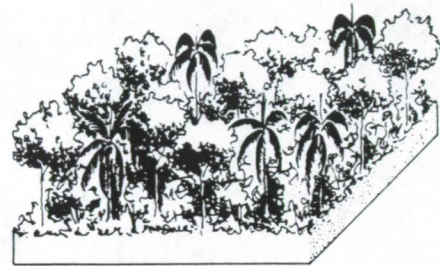


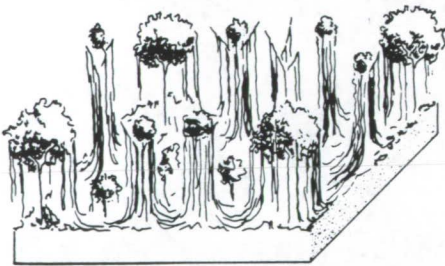
Figure 8. Light zones in radar image (lower part of figure) due to backscattering of radar signals by strong rainstorms. The terrain behind the rain clouds, in relation to the flight paths, is obscured by long shadows.



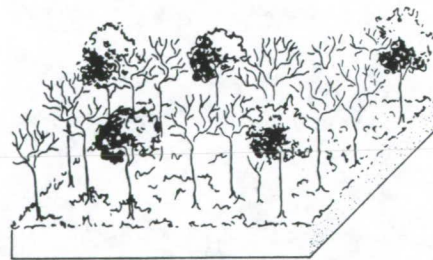
TROPICAL RAIN FOREST
(Floresta Tropical Densa)



WOODLAND FOREST WITH PALM TREES
(Floresta Aberta com Palmeiras-Cocal)



LIANA FOREST
(Floresta Aberta sem Palmeiras-Cipoal)



SEMIDECIDUOUS FOREST
(Floresta Estacional)

Figure 9. Amazon vegetation types.

(Veloso et al., 1975). One of them, the woodland forest with palm trees, is usually present in valleys and gently undulating terrain where the soil is fertile and well developed (Figure 9). The other is the so-called liana forest, which is usually present in mountain slopes and hilltops, where the terrain has been deeply eroded. The growth and expansion of lianas in the forest leads to their eventual distribution over tree canopies in the competition for sunlight (Figure 9). Host trees deprived of sunlight in many cases die. A possible consequence of natural forest decay is increased soil leaching and the development of laterites covered by shrubs and grass.

3. Semideciduous Woodland Forest. This forest occurs in low mountains and deeply eroded igneous, metamorphic, and sedimentary terrains. In general, the average tree height is small as compared to the forest types described previously, tree trunks and branches are not straight, and many species loose their leaves during the dry season (Figure 9).

4. Savanna Vegetation. This growth is present in areas where dry and rainy seasons are well defined and the relief is undulating, crystalline basement outcrops, and the soil is relatively thin and sandy to clayey. Trees are usually small, have large evergreen leaves and contorted trunks with rough bark, and are distributed sparsely over a terrain covered by grass. According to tree distribution patterns several subtypes can be defined (Figure 10).

5. Floodplain Vegetation. This growth occupies alluvial plains periodically covered by water during river flood stages. The alluvial forest typically occupies areas with well-developed soils. Shrubs and grass dominate river margins where the soil is sandy (Figure 10).

B. Geologic Mapping on Radar Images

Interpretation of side-looking radar images is based on the interpreter's ability to infer geological features from the radar return - that part of the transmitted energy that is intercepted by the radar receiver. Major parameters that influence radar return may be grouped into those that are characteristic of the imaging system and those that are properties of the terrain or target (Table 2).

Table 2. Major parameters controlling radar return (mod. from Moore, 1976)

Properties of imaging system:	Depression angle
	Polarization
	Wavelength (frequency)
	Ground resolution
Properties of the terrain:	Surface roughness
	Slope
	Complex dielectric constant
	(permittivity and conductivity)

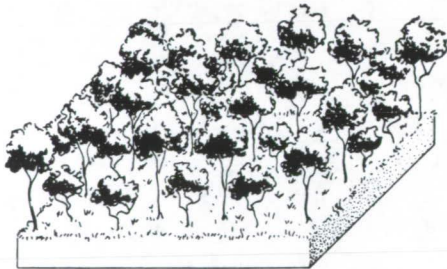
Parameters characterizing a radar system usually are kept constant for a given data acquisition survey. Depression angles, polarization, wavelength (frequency), and ground resolution for the RADAR Project are listed in Table 1.



ALLUVIAL FOREST
(Vegetação Arborea com Palmeiras)



SHRUBLAND
(Vegetação Aluvial Arbustiva)



WOODLAND SAVANNA
(Savana Arborea Densa)



PARKLAND SAVANNA
(Parque de Savana)

Figure 10. Amazon vegetation types.

Properties of the terrain, however, are quite variable. Surface roughness expresses roughness of the terrain in relation to the radar wavelength used. In those situations where surface roughness is responsible for the magnitude of the radar return, it controls the extent of the scattering process, which, in turn, determines the reradiation pattern. Scattering observed for surface roughness on the order of a wavelength or more is responsible for an isotropic reradiation pattern that results in a rough texture on radar images. When surface roughness is much less than a wavelength ($\lambda/10$), the reradiation pattern is approximately specular and the surface appears smooth on radar images (Waite and MacDonald, 1971).

In flat horizontal terrain, a constant depression angle for a side-looking radar system corresponds to a constant incidence angle of the energy beam on the ground surface. Changes of ground slope in the natural environment result in a variation of the incidence angle for a constant depression angle. In his analysis of the effect of terrain slope on incidence angle, MacDonald (1969) has shown that there is an increase of reradiation when the slope is inclined at an angle towards the imaging radar and a decrease is observed when the slope is away from the energy source.

The complex dielectric constant is a property of the target that accounts for its permittivity (dielectric constant) and conductivity and affects radar return. Dielectric properties of most materials are relatively small and differ very little from each other unless water, which has high permittivity, is present (MacDonald, 1969; Moore, 1976). Changes in moisture content for any given material, therefore, are responsible for changes in reradiation patterns.

The energy-target interaction characteristics and radar system parameters outlined above are combined with photogeologic interpretation techniques during qualitative analysis of radar images. The Amazon Jungle, as well as other tropical rain forests, is a special case in radar geology for the interpreter because the ground surface is seldom without a dense vegetation cover. The most common situation is where geological data is inferred from the analysis of vegetation (type, distribution, etc.) and of the physical environment (drainage pattern, landforms, etc.). Three areas in the Amazon region were selected to illustrate a possible approach to geologic mapping in heavily forested terrain (Figure 11).

C. Area A - Amazon Floodplain

A radar mosaic of the area east of the town of Santarem shows typical images acquired over the Amazon floodplain (Figure 12). A schematic cross section of the vegetation in this area is shown in Figure 13.

Along the margin of the major rivers, sand beaches and levees are usually associated with grassland vegetation. Radar return from these areas is controlled mostly by ground surface roughness and moisture content. Abandoned meanders and levees are usually well defined on the far range portion of radar strips.

Permanently flooded terrain dominates the so-called "igapo" (swamp) forest with relatively dense multistory vegetation, tree height usually below 20 m (65 ft), and lianas. Plant population includes palm trees and is quite diversified.

Tree canopies, long stems and trunks, and lianas provide for a large scattering volume for incident energy. Radar return from this environment is almost

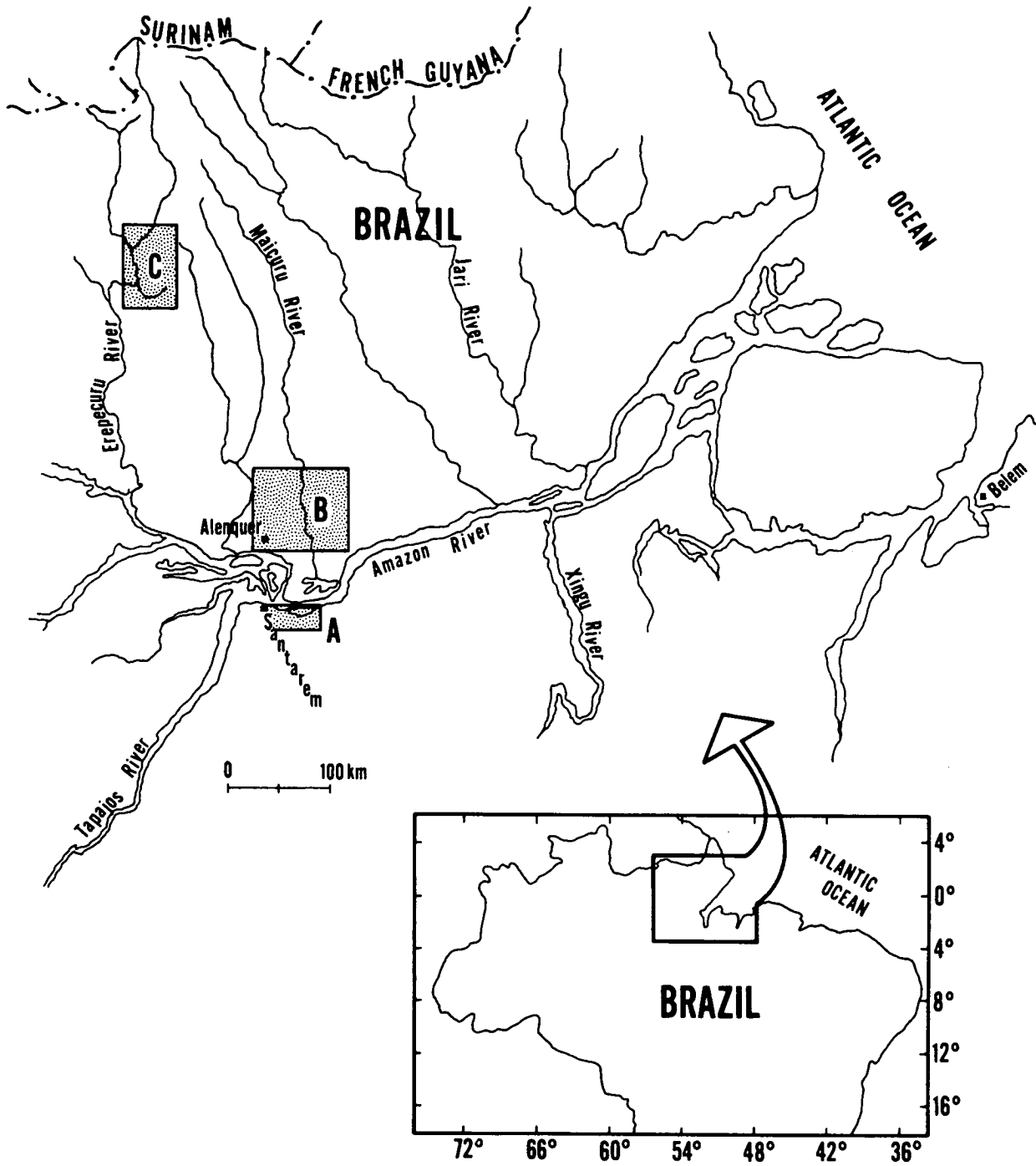


Figure 11. Location map.

AREA A



Figure 12. Radar mosaic of an area in the Amazon floodplain. The town of Santarem is on the left side of the mosaic. The Amazon (Amazonas) River is shown along the central part of the image.

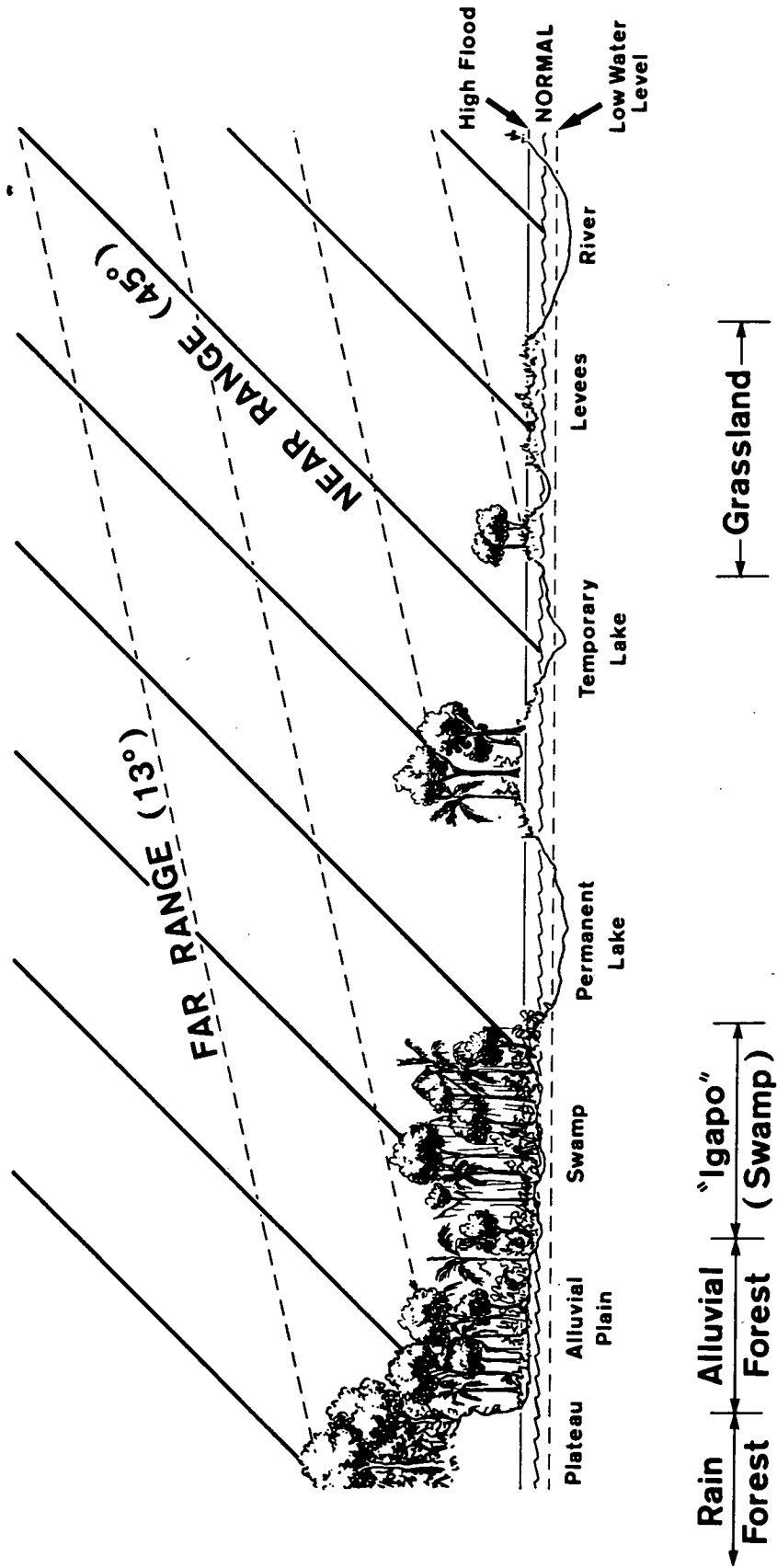


Figure 13. Vegetation cross section, Amazon floodplain.

exclusively a function of vegetation surface roughness. In the near-range portion of radar images, however, high depression angles may account for some penetration of microwave energy through light vegetation cover. No field study has been conducted yet to verify this assumption, but tonal contrasts assumed to be related to water and soil moisture are observed mainly in the near-range portion of radar strips.

The alluvial forest occupies areas that are flooded periodically by rivers. Vegetation in this forest is not as diversified as in the "igapo" forest, and consists mostly of tall trees such as rubber trees (Hevea brasiliensis), palm trees, and lianas. Because of relatively large individual canopies and multistory vegetation, it is likely that incident energy is continuously attenuated and scattered, probably never reaching the ground surface. Similar gray tones and rough texture on both near- and far-range portions of radar images support this conclusion.

Tropical rain forests in many areas occupy the plateau areas that are not flooded at any time. Some of the tallest tree species of the Amazon Jungle, including Brazil nut trees (Bertholletia excelsa, H.B.K.), occur in this habitat. The transition from the "igapo" and alluvial forest to the rain forest indicates also the contact between Quaternary alluvial sediments and older formations (Figure 14). Radar return from the rain forest is not likely to be influenced by the properties of soils or rocks because incident energy must be scattered and attenuated by the vegetation cover alone.

D. Area B - Sedimentary Terrain

A radar mosaic of the area northeast of the town of Alenquer shows a typical coverage available for the sedimentary sequence of the Amazon Basin (Figure 15). A schematic cross section illustrates a possible distribution of vegetation along a north-south direction (Figure 16). The generalized stratigraphic section for the area is in Figure 17. Most of the units mapped on radar images for the area, however, do not correspond with formations shown in the section. The contact between "radar units" is more representative of gross lithologic packages indicated by changes in landforms. This approach to geologic mapping can be taken whenever the vegetation canopy conforms to the relief of the underlying ground surface.

In the tropical rain forest, the dense, multistory vegetation causes attenuation and diffuse scattering of microwave energy within the forest. Greater penetration of the incident energy into the vegetation may be possible in the woodland savanna and liana forests, but special terrain and high-depression angles are required for this. The fact that diabase dikes can be mapped without difficulty in both sedimentary and crystalline terrain may indicate some edaphic control of a unique vegetation assemblage or conformation of tree canopy to topographic relief. Possibly both situations contribute to enhancing the detection of the dikes. An extensive diabase sill mapped in the central part of the area is characterized by a relatively uniform fine texture and gray tone on radar images (Figure 18).

E. Area C - Igneous and Metamorphic Terrain

Igneous, metamorphic, and volcanic rocks in the Precambrian Basement Complex are detected on radar images by characteristic landforms, drainage and structural patterns, and distribution of vegetation (Figure 19). The igneous and metamorphic complex in the Amazon is covered to a great extent by deep rain forest. Deep erosion of the complex results in a hilly topography and V-type valleys controlled

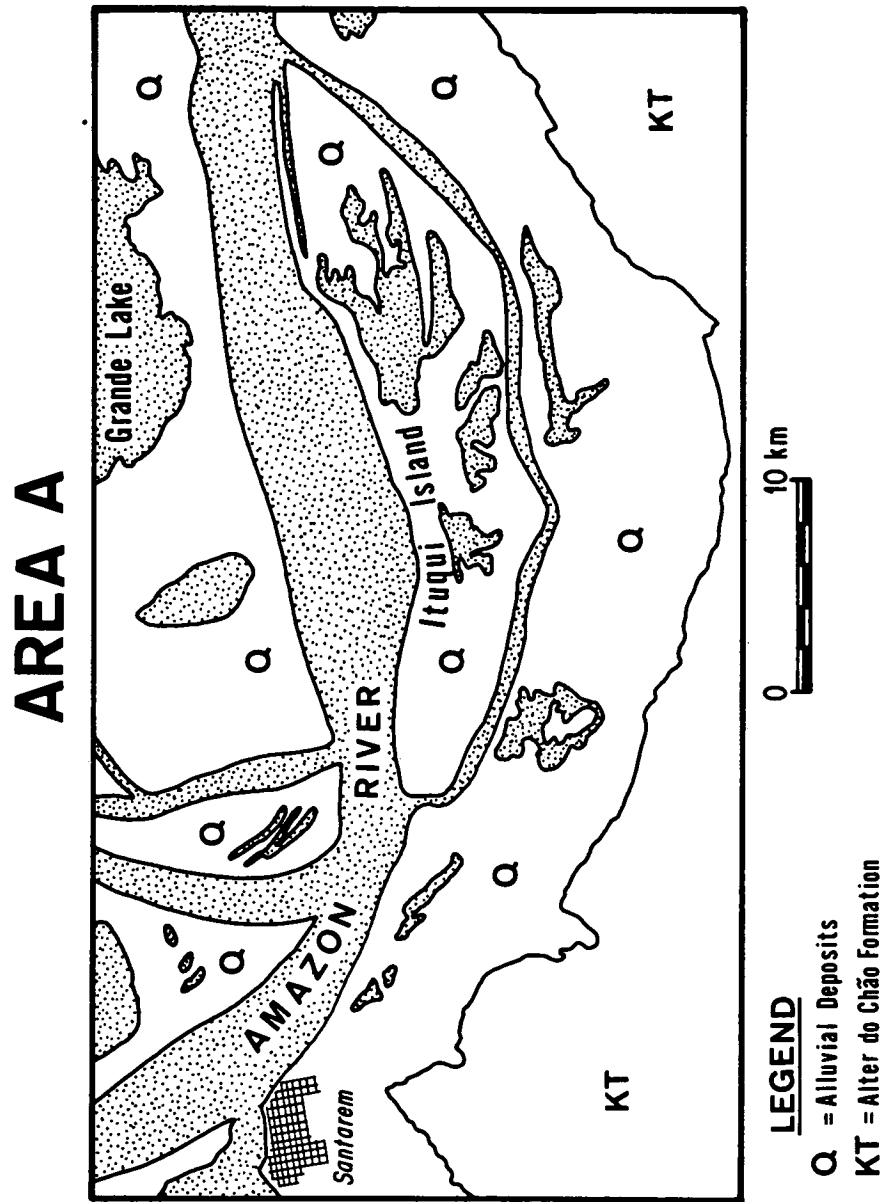


Figure 14. Generalized geologic map of the area in the Amazon floodplain corresponding to radar mosaic in Figure 12.

AREA B

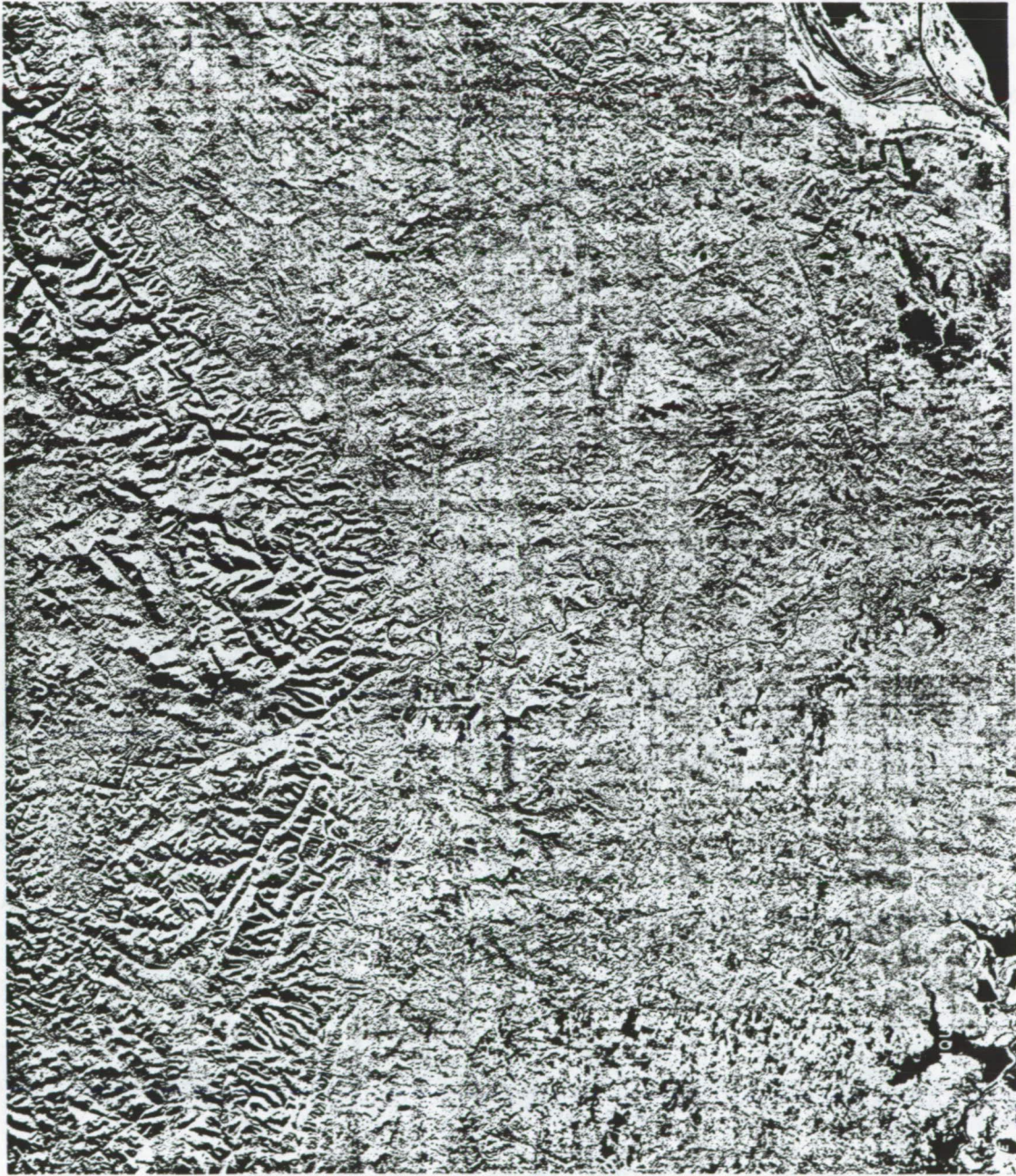


Figure 15. Radar mosaic of an area in the Amazon Basin. The town of Alenquer is shown in the lower left.

ORIGINAL PAGE IS
OF POOR QUALITY

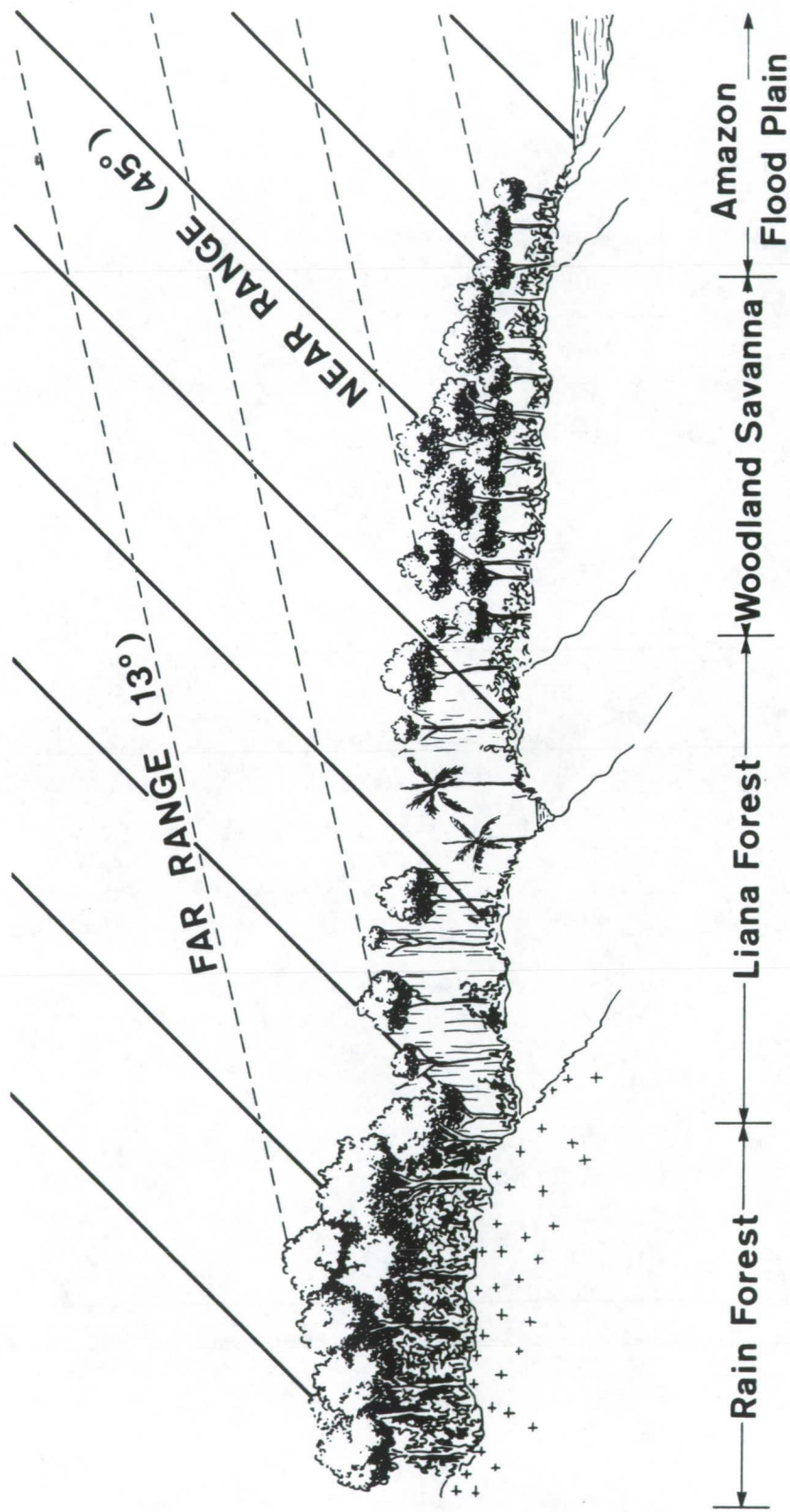


Figure 16. Vegetation cross section, sedimentary terrain.

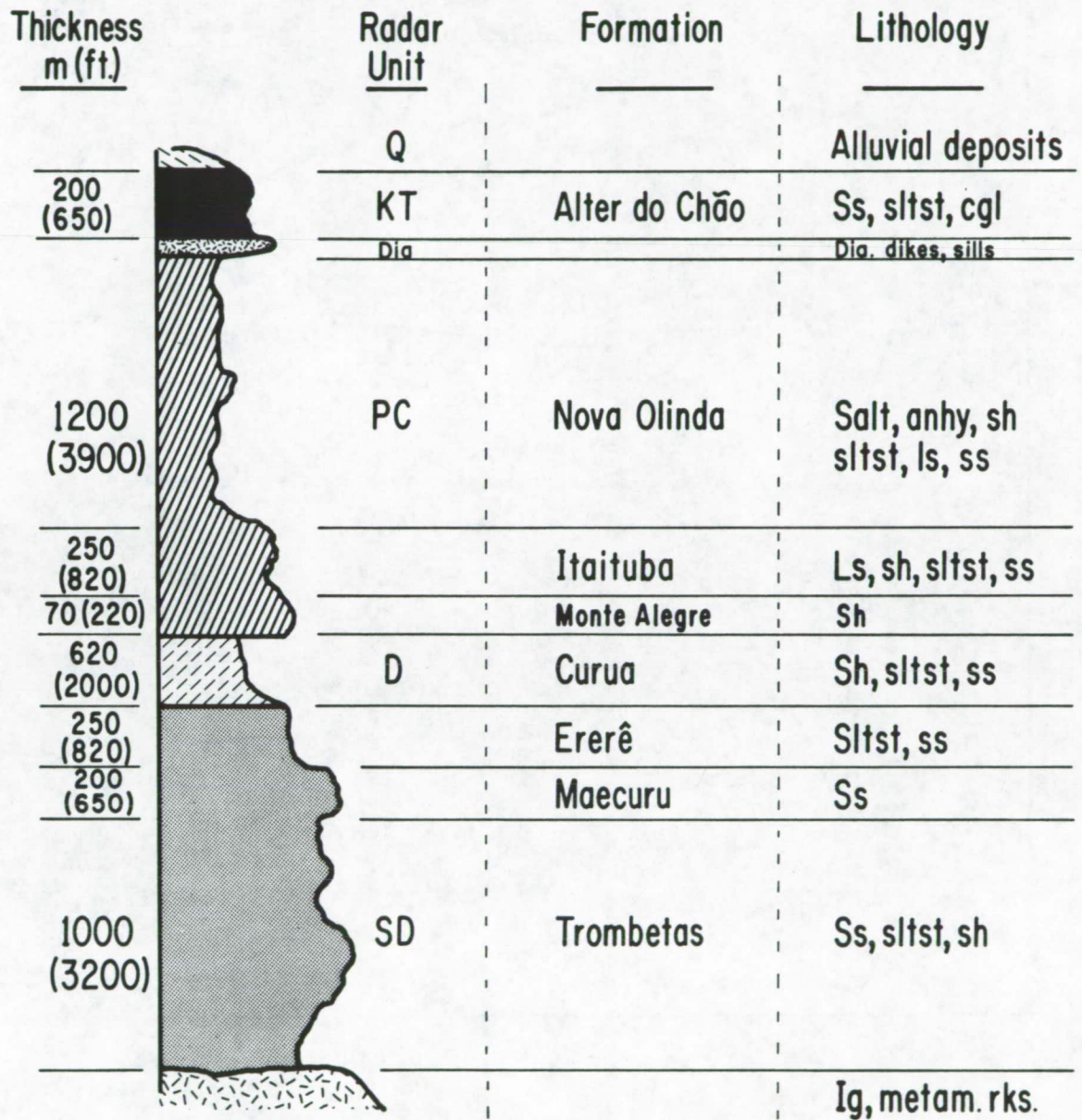


Figure 17. Stratigraphic section, Amazon Basin.

AREA B

Legend

- Q Alluvial deposits
- KT Alter do Chão Fm
- Dia Diabase Sill
- PC Mt. Alegre, Itaituba and N. Olinda Fm
- D Curua Fm
- SD Trombetas, Maecuru and Erere Fm
- PE Igneous and metamorphic Complex
- Diabase Dike
- Fault
- Lithologic Contact
- - - - Possible Lithologic Contact

Scale
0 10 km

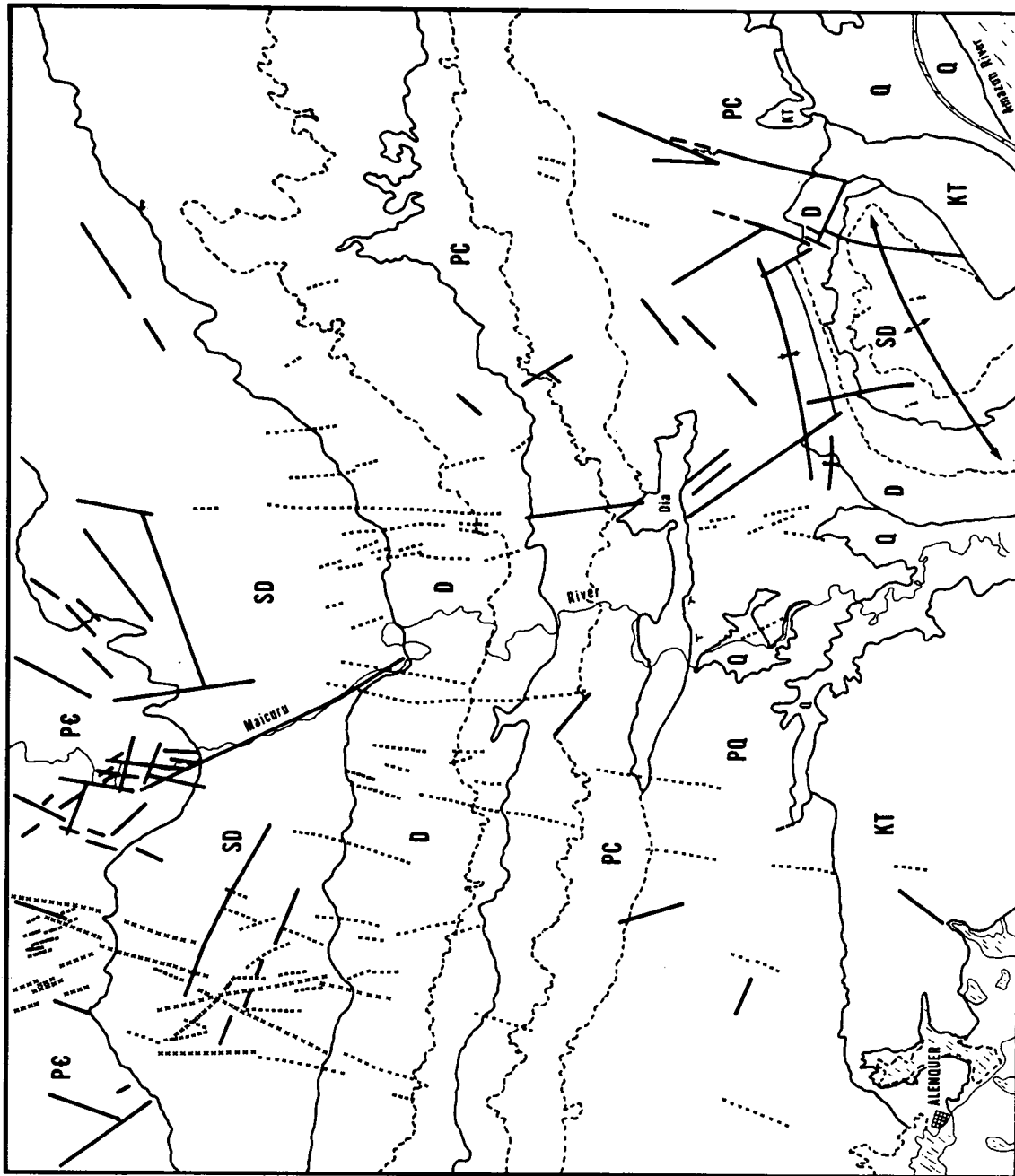
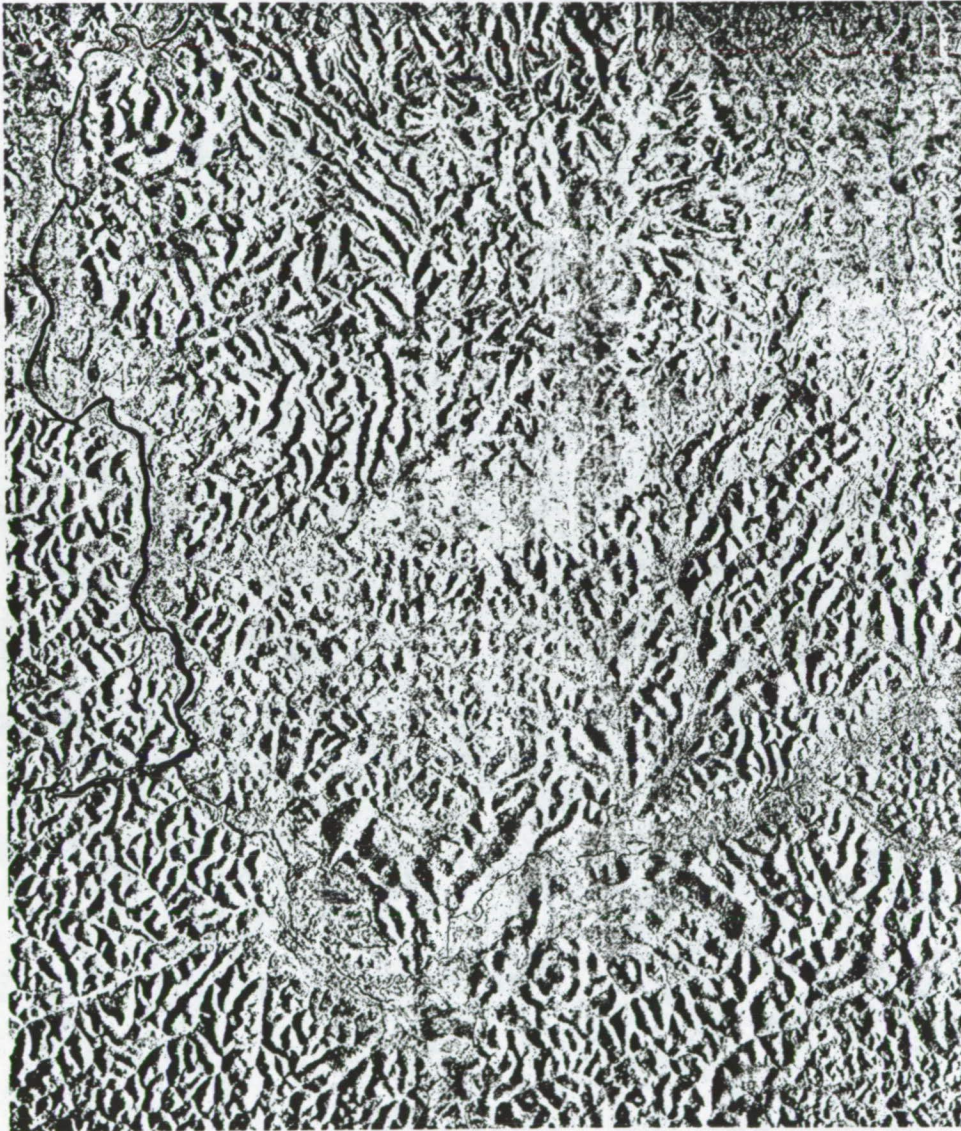


Figure 18. Generalized geologic map of the area in the Amazon Basin corresponding to radar mosaic in Figure 15.



AREA C



Figure 19. Radar mosaic for an area in the Precambrian Basement Complex of northern Brazil. The Paru do Oeste River, one of the tributaries of the Amazon, lies along the left side of this mosaic.

ORIGINAL PAGE IS
OF POOR QUALITY

in part by fracture patterns. Field examination has shown that the coarse texture observed on radar images over the basement is associated mostly with granites and gneisses.

Three landforms have been observed in volcanic terrain. One of them has typical elongate inselberg-type hills with flat tops and savanna-type vegetation (Costa et al., 1975). A much flatter terrain, which shows a smooth texture on radar images, has the same type of vegetation described previously. A denser vegetation covers the hilly area that has been mapped (Oliveira, et al., 1975) as underlain by volcanic rocks different from the other two (Figures 19 and 21).

A schematic cross section of the vegetation over Area C shows energy-target interaction expected in near- and far-range radar strips (Figure 20).

F. Procedures for Geological Mapping

Reconnaissance geological mapping in the Amazon Jungle may be regarded as a three-step procedure. The first phase consists of interpreting radar images over the area of interest. Other remote sensing data such as Landsat and aerial photographs can be effectively used to supplement the interpretation. The next step entails field checking of selected areas. The final step in the program involves reinterpretation of remote sensing data to incorporate information acquired during the preceding phase.

IV. FUTURE RESEARCH NEEDS

Radar image interpretation appears to be adequate for reconnaissance mapping programs even though it still is a qualitative procedure. Its limitations for usefulness, however, are reached when a detailed evaluation of the geologic information in radar images is required, or when follow-up studies of small areas are desired. Some of the present obstacles to a quantitative approach to data analysis are a function of the photographic procedure taken to generate images. For example, it presently is difficult to correlate tonal information between individual radar strips because of the differences in photographic processing they may have undergone.

The value of side-looking radar as a tool to detect geological structures and to study structural patterns and trends is widely known (Cameron, 1965; Dellwig, et al., 1966; Hackman, 1966; Wing, 1971; Reeves, 1975), although its use as a lithological identification tool remains questionable, particularly in the jungle environment. As observed by MacDonald (1969) in his evaluation of side-looking radar data over Panama, gross lithologic determinations can be made on regional scale if lithologies are expressed by landforms. A more complex evaluation of the usefulness of radar images in geological mapping is expected as a result of controlled studies of the energy-target interaction phenomenon. Additional research is needed to investigate the contribution of surface roughness of vegetation, soil, and rocks, as well as of the dielectric properties of vegetation and ground surface materials to the radar return from jungle terrain.

The penetration of vegetation by radar energy with multifrequency and multi-polarization systems is another needed topic of research. Waite and MacDonald (1971) report that for defoliated vegetation, K-band radar energy at the proper incidence angle may penetrate what is still considered to be a dense volume of tree boughs. A similar situation is believed to be observed on X-band radar images

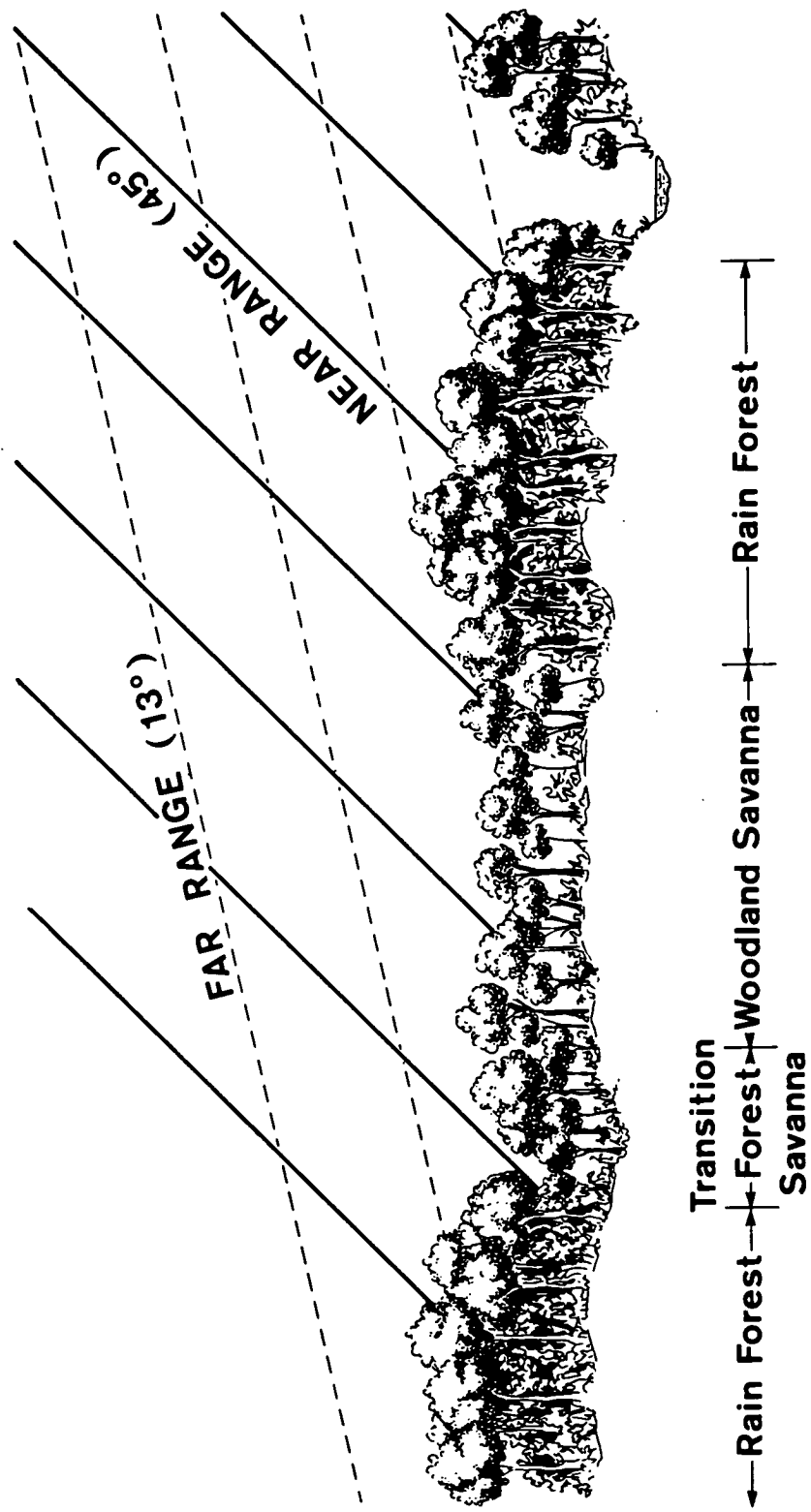


Figure 20. Vegetation cross section, igneous/metamorphic terrain.

AREA C

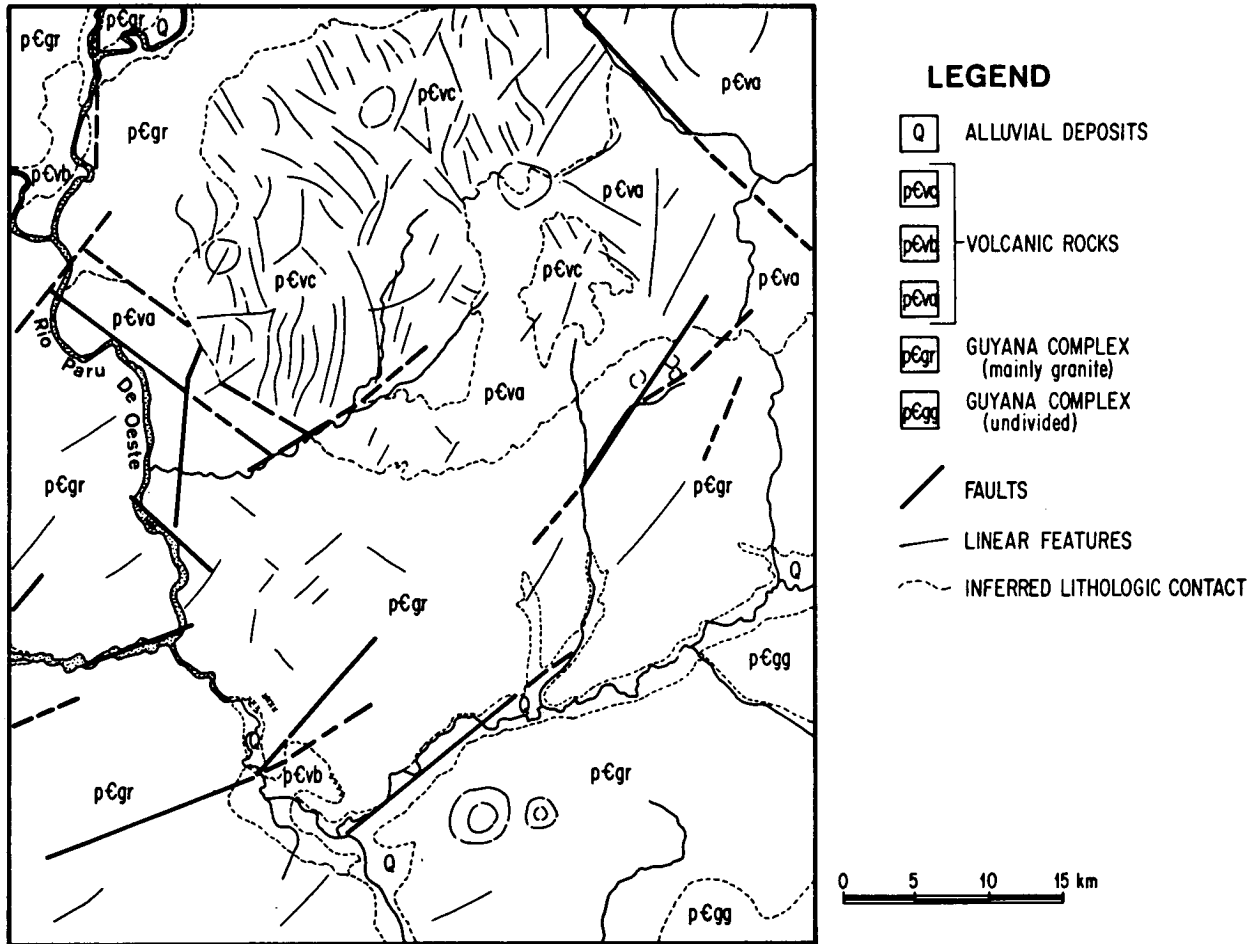


Figure 21. Generalized geologic map of the area corresponding to radar mosaic in Figure 19.

acquired over the Amazon Jungle when the right combination of low incidence angle and vegetation type is present. On the far-range portion of radar images (high incidence angle), it is unlikely that any penetration of vegetation will be observed unless shrubs and grassland are the vegetation cover (Dellwig and Bare, 1978).

V. SUMMARY

The Amazon Jungle may be an excellent test site for further research on the use of radar as a geologic mapping tool in heavily forested areas. Side-looking radar images are already available for the whole area, and representative sites can be selected on the basis of dominant vegetation types and geological settings. This paper is an attempt to examine the problems of radar geologic-mapping in the jungle environment. The unique data set generated by the X-band imaging radar system used in Brazil becomes more useful to the geologist when combined with Landsat images, aerial photographs, airborne geophysical data, and field information. However, without additional development of radar systems, without a more complete understanding of the energy-terrain interaction phenomenon, and without more refined interpretation models, it is possible that the Amazon Jungle will remain a challenge to geological mapping by side-looking radar.

ACKNOWLEDGEMENTS

I thank D. C. Jacobs, who provided criticism and editing of the manuscript; O. Bittencourt-Netzo, who kindly kept me up-to-date on the progress of the RADAM Project; and A. J. Blanchard, with whom I have discussed many of these ideas. Conoco, Inc., has provided the time and services to prepare this paper. W. E. Rigsby, D. L. Beall, P. L. Barnett, J. C. Elliot, J. A. Storrusten, and W. D. Harris III drafted the illustrations; V. H. Treat did the photographic work; and Conoco's Secretarial Services typed the manuscript.

REFERENCES

- Azevedo, A. de, 1950, Regiões climato-botânicas do Brasil: Bol. Paulista de Geografia, No. 6, pp. 32 - 43.
- _____, 1972, Brasil--a terra e o homem, 2nd ed.: São Paulo, Cia. Editora Nacional, v. 1, 622 pp.
- Azevedo, Luiz H. A., 1971, Radar in the Amazon: Proc. 7th Symp. Remote Sensing Environment, v. 3, pp. 2303 - 2306.
- Cameron, H. L., 1965, Radar as a surveying instrument in hydrology and geology: Proc. 3rd Symp. Remote Sensing Environment, Univ. Michigan, Ann Arbor, pp. 441 - 452.
- Costa, R. C. R., and Melo, D. P., 1975, Geomorfologia de Folha NA. 21 Tumucumaque e parte de Folha NB. 21, in Projeto RADAMBRASIL: Brasil, Dept. Nacional Produção Mineral, v. 9, pp. 121 - 153.
- Dellwig, Louis F., and Bare, Janet E., 1978, A radar investigation of north Louisiana salt domes: Photogram. Eng. Remote Sensing, v. 44, No. 11, pp. 1411 - 1419.

- Dellwig, L. F.; Kirk, J. N.; and Walters, R. L., 1966, The potential of low resolution radar imagery in regional geologic studies: Journ. Geophys. Research, v. 71, No. 20, pp. 4995 - 4998.
- Hackman, R. J., 1966, Geologic evaluation of radar imagery in southern Utah: U.S. Geol. Survey Prof. Paper 527-D, pp. D135 - 142.
- MacDonald, Harold C., 1969, Geologic evaluation of radar imagery from Darien Province, Panama: Modern Geology, v. 1, pp. 1 - 63.
- Moore, Richard K., 1976, Active microwave systems in Remote Sensing of Environment, J. Limtz, Jr., and D. S. Simonett, ed.: Reading Mass., Addison-Wesley Publ. Co., 694 pp.
- Moreira, Helion F., 1973, Controle de qualidade de imagens de radar: Brasil, Dept. Nacional Produção Mineral, Projeto RADAM, Tech. Rept., 57 pp.
- Oliveria, A. S.; Fernandes, C. A. C.; Issler, R. S.; Abreu, A. S.; Montalvão, R. M. G.; Teixeira, W., 1975, Geologia da Folha NA. 21 Tumucumaque e parte da Folha NB. 21 in Projeto RADAMBRASIL, Brasil, Dept. Nacional Produção Mineral, v. 9, pp. 17 - 118.
- Reeves, Robert G. (ed), 1975, Manual of remote sensing: Falls Church, Virginia, Am. Soc. Photogrammetry, 2 vols., 2144 pp.
- Veloso, H. P.; Goes-Filho, L.; Leite, P. F.; Barros-Silva, S.; Ferreira, H. C.; Loureiro, R. L.; Terezo, E. F. M., 1975, Vegetação da Folha NA. 20 Boa Vista e parte das folhas NA. 21 Tumucumaque, NB. 20 Roraima e NB. 21 in Projeto RADAMBRASIL: Brasil, Dept. Nacional Produção Mineral, v. 8, pp. 307 - 404.
- Waite, W. P., and MacDonald, H. C., 1971, "Vegetation penetration" with K-band imaging radars: IEEE Transactions on Geoscience Electronics, v. GE-9, No. 3, pp. 147 - 155.
- Wing, R. S., 1971, Structural analysis from radar imagery of the eastern Panamanian Isthmus, Part I: Modern Geology, v. 2, No. 1, pp. 1 - 21.

SIDE-LOOKING AIRBORNE RADAR IMAGE INTERPRETATION
AND GEOLOGICAL MAPPING : PROBLEMS AND RESULTS

J-Y. Scanvic and E. H. Soubari
Office of Geologic and Mining Research
National Geological Service

ABSTRACT

This paper summarizes geological experiments and surveys conducted by BRGM and GDTA members to evaluate interest in SLAR image interpretation. Two surveys have been selected for presentation : Les Vans (Massif central, France) and Guyana (South America). They have permitted a comparison between different types of SLAR : Goodyear, Motorola, JPL and Vigie in term of lithological and structural applications. On the Les Vans test-site conclusions reached concern radiometry, which is better on L-band imagery, polarization, HV being more useful than HH for geological mapping in an L-band system, wavelength and illuminations.

Over Guyana, a French department in South America, the use of Goodyear X-band SLAR enables satisfactory geological and structural mapping under heavy equatorial forest with cloud cover conditions. A differentiation program has been developed for fracture filtering and image enhancement with a coherent light laser, and significant results have been obtained.

Finally, the main experiments conducted in France, with SLAR, by Institut francais du Pétrole, Laboratoire de Physique de Grenoble, Institut national de la recherche agronomique et Centre d'étude spatiale des rayonnements are briefly described. Results obtained on sea and vegetation are very significant.

I. INTRODUCTION

During the past four years BRGM and GDTA members have made several geological surveys, in and outside France, including preliminary mapping using side looking radar imagery. The aim of these applied and experimental surveys was to (1) evaluate over a selected test-site SLAR mapping ability (X-band), by comparing published geological mapping and radar image interpretation, (2) produce in equatorial countries, where cloud cover makes it difficult to obtain good aerial photograph coverage, a preliminary geological map which can be compared to the one obtained by photogeology, and (3) test two experimental SLAR

systems, the Vigie-Thomson and the JPL.

II. BACKGROUND

General SLAR experience was acquired by a remote sensing BRGM team in 1974, with Goodyear 3-centimeter-wavelength images acquired* over a test site located in the southern part of the Massif central (Les Vans, France). This test site is covered by:

Aerial photographs, different scales, black and white, color and infrared color.

Thermal imagery, 3 to 5 μ , 8 to 14 μ .

Geological mapping at 1/80,000, in progress at 1/50,000.

Geophysical data, mainly aeromagnetism.

Landsat good quality imagery, taken at different times.

Vigie-Thomson X-band SLAR images.

JPL L-band, two polarization images.

Seasat images, which are expected soon.

During this time BRGM has been involved in several geological mapping and mineral exploration surveys using SLAR images to prepare base maps or complementary maps. They are located in:

Brazil, with Goodyear 3-centimeter wavelength, HH polarization.

Guyana, with Goodyear 3-centimeter wavelength, HH polarization.

Nigeria, with Motorola 3-centimeter wavelength, HH polarization.

These experiments and surveys have permitted BRGM to get an idea of some SLAR characteristics:

Wavelength, 3 and 25 centimeters.

Polarization, HH and HV.

Resolution, 10 to 35 meters.

Illumination, north and south.

The following different types of SLAR were tested:

Goodyear, Motorola, JPL and Vigie-Thomson.

*By the "Club de télédétection" formed by IFP, oil companies and BRGM.

III. SYSTEM PARAMETERS AND DATA PRODUCTS

The three American SLAR we have tested are currently in use and their system parameters are well known. The Vigie SLAR, operated by GDTA, is an experimental French system built by:

Thomson C.S.F. company (antenna and SLAR system).

Centre national des études spatiales (digital system processing).

Institut géographique national (plane and flight).

GDTA is the operator; BRGM and IFP have geological mapping and interpretation techniques experience.

Vigie system parameters are mentioned in Table 1.

In general, the data products we have studied are black and white paper films, one strip alone sometimes, mosaics where possible. For two areas north and south illumination images have been interpreted : for the first one the images were acquired in two flights (Les Vans, Goodyear); for the second they were acquired in one flight (Nigeria, Motorola).

With Vigie, SLAR images have been obtained by generating a film from the digital tape, using the Visumat image processor. In this way images can be geometrically corrected (Figure 1 IGN) with very good accuracy. On some images (Goodyear) enhanced products have been generated with a laser system (Figure 2).

IV. ANALYSIS AND INTERPRETATION TECHNIQUES

Two of the surveys have been selected for presentation because they reach valuable conclusions. They concern the Les Vans test-site and a survey in Guyana, where BRGM geologists are mapping the country to prepare for mineral exploration.

A. Geology

Les Vans is located in the southeastern part of the Massif Central (France), one of the main basement areas of France (see index Figure 7). Les Vans were chosen as a test site in imaging radar for the following reasons :

Various rocks crop out extensively, ranging from granite to marly limestones, including schists, limestones and quaternary sand or gravels.

The density of vegetation varies with rock lithology.

Wide range of roughness units, which correlate well with geological units, as distinguished on a geological map.

Various topographic situations.

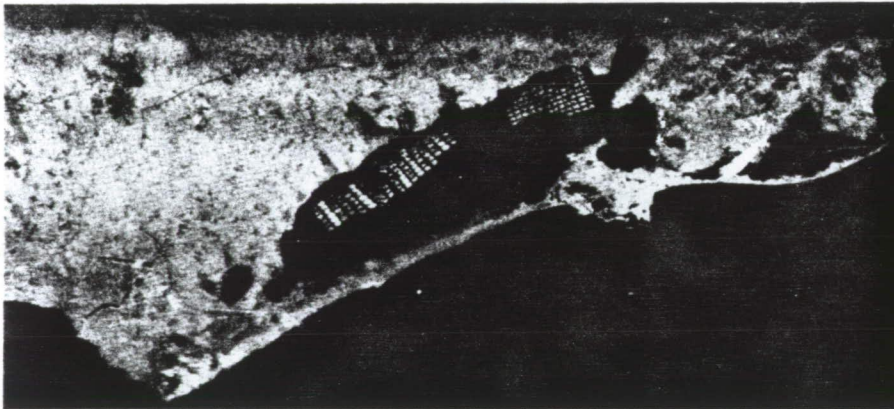
Cartographic utilisation

VIGIE SLAR

Localisation



A - SLAR corrected image , Cap d'Agde area (France)
1/250 000



B - Same image with cartographic superposition

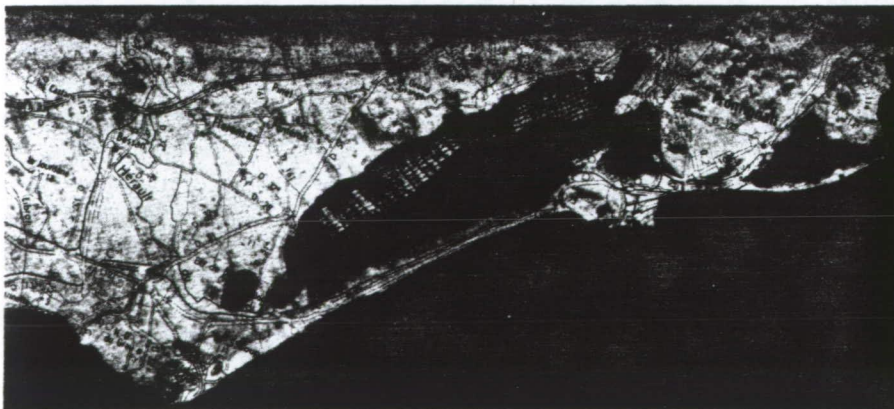


Figure 1. Corrected Vigie image.

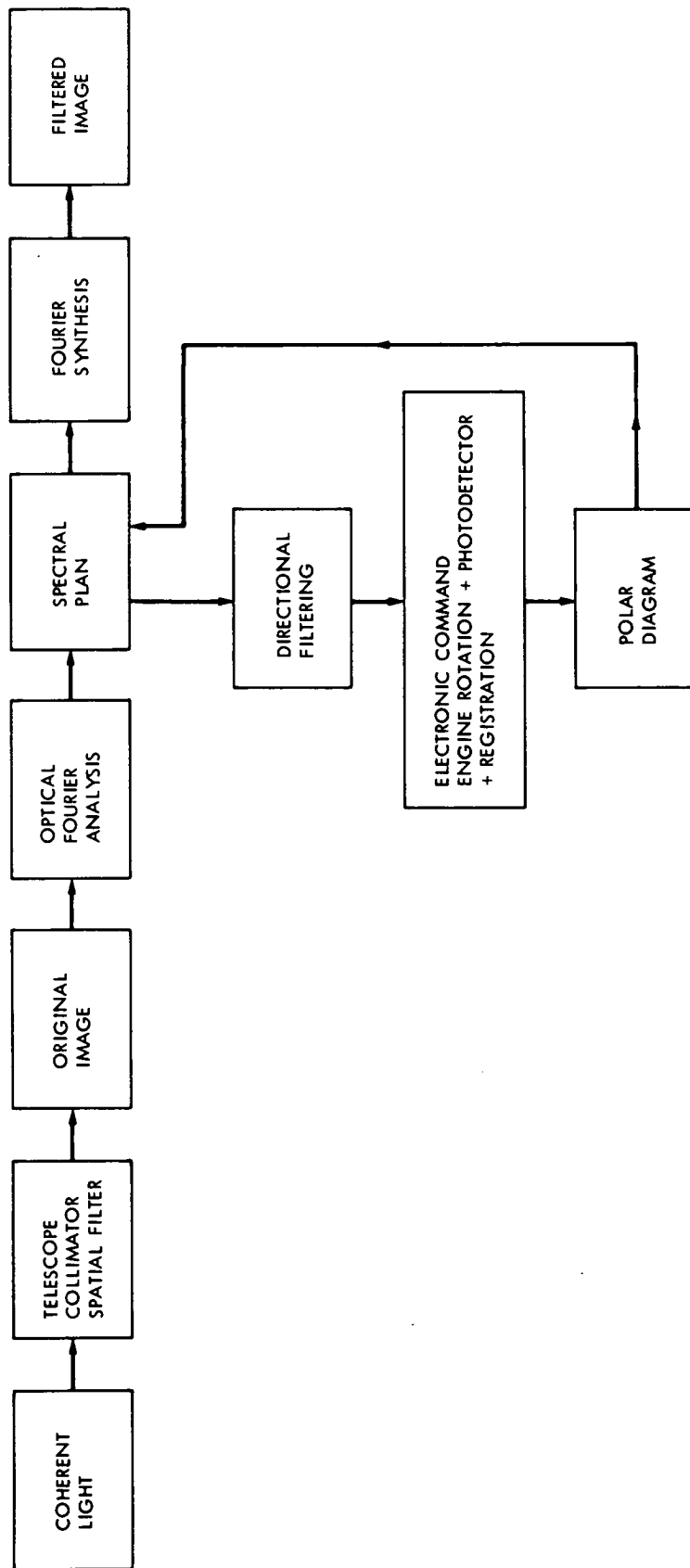


Figure 2. Laser coherent light system.

Table 1. Vigie system: technical characteristics

<p><u>Radar</u></p> <p>Pulse length, 0,2 μs</p> <p>GVT for 1000 to 7000 m altitude</p> <p>Frequency band X = 3, 22 cm</p> <p><u>Antenna</u></p> <p>Length, 4</p> <p>Horizontal polarization</p> <p><u>Quality Image</u></p> <p>Observed area, 21 km</p> <p>useful observed area, 13-15 km</p> <p>Sampling, 30 x 15 m</p> <p>Calibration \pm 1 dB</p> <p><u>Navigation</u></p> <p>Registration of navigation</p> <p>Parameters and attitude</p> <p>IRIG clock</p>	<p><u>Plane</u></p> <p>B 17</p> <p>300 km/h</p> <p>Flight altitude, 1000 to 7000 m</p> <p>Flight duration, 10 h</p> <p><u>Coverage</u></p> <p>4000 km²/h</p> <p><u>Digital Registration</u></p> <p><u>Visualization</u></p> <p>On board : 1/300 000 scale</p> <p>On ground</p> <p><u>Processing (on the ground)</u></p> <p>Geometric correction</p> <p>Radiometric correction</p> <p>Mosaic</p> <p>All processing</p> <p><u>Data Products</u></p> <p>CCT digital tape</p> <p>Visumat or Vizir (image processor) film</p> <p>Calcomp</p>
--	--

B. Interpretation of Results

Three SLAR systems have been used on the test site :

Goodyear, 3-centimeter wavelength, north and south illuminations, HH polarization.

Vigie, 3-centimeter wavelength, digital registration, HH polarization.

JPL 25-centimeter wavelength, HH and HV polarization.

1. Goodyear Interpretation of Significant Results. Image scale is 1/100,000. North and south illumination flights have been carried out and interpretations compared :

a. Referring to published geological maps, granites, schists and limestones have a distinct SLAR signature, mainly due to roughness. Note that schists correspond to a vegetated area with distinct topographic differences; limestone is a flat, unvegetated area, granite is an intermediate type (low vegetation and medium relief) area.

North and south illuminations make it possible to improve interpretation : the Mount Lozere granite, for instance, is better viewed on a north illumination image. If one refers to the survey performed in Nigeria, opposite illuminations are very useful in mountain areas, where shadows limit lithological distinctions.

b. Over two selected zones (areas A and B), the effect of illumination on fracture interpretation has been especially studied. Some differences exist, as shown by diagrams (Figure 3), but they are not important.

c. Over the same selected area automatic processing has been done directly on the radarimagery (zone A1).

To establish a fracturing polar diagram the Fourier transform has been used, obtained by an optical technique (laser source). Two mathematical operators have been developed to differentiate contours on the computer by digitalized holography. This processing allows enhancement and restitution of image contours, allowing easier interpretation, detection and localization of linears.

c1. Spatial (directional) filtering. The optical correlator is a double diffraction optical system in which one can visualize the bidimensional Fourier spectrum of a linear spatial distribution in the Fraun Hoffer plane first objective focal plan image system 1. By inserting a spatial directional filter one can perform linear filtering or explore the spectrum by rotation scanning to establish a diagram. When the main directional trend is known one can restore a filtered image with an inverse Fourier transform. Optical directional filtering allows the elimination on the original image of the linear features having certain directions and the outline of features having complementary orientations. This operation makes it possible to select lineaments oriented between $\theta^\circ - \Delta\theta$, $\theta^\circ + \Delta\theta$, θ being the measured angle (or indicated by the diagrams) and $\Delta\theta$ the directional filter aperture ($\approx 20^\circ$).

CEVENNES

ILLUMINATION EFFECT ON LINEAMENTS INTERPRETATION ON SLAR IMAGES

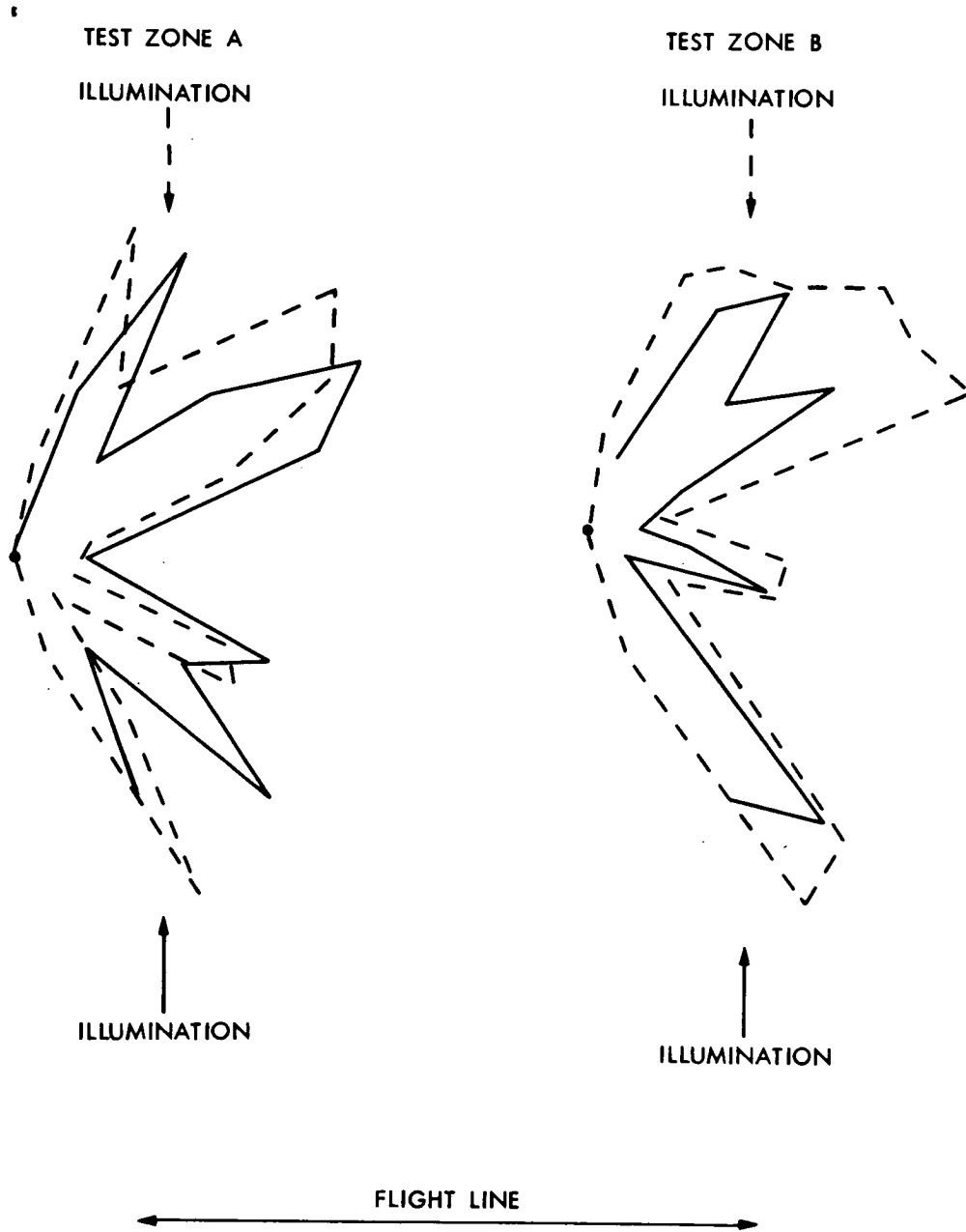


Figure 3. North and south illumination polar fracture diagram.

The exploitation of the spectral analysis obtained by optical techniques allows the extraction of some qualitative and quantitative data from different types of images or maps: photolineament map, radarimagery, etc. Also lineament directional trend or periodical structures frequency may be detected (Reference 2).

c2. Spatial filtering by digitalized holography. We have experimented on one side looking radar image the differentiation mathematical operators in an attempt to enhance data such as lineaments and contours: the omnidirectional differentiation has been used (References 3,4). On a computer using the Lohmann and Paris method (References 5,6), we have synthesized optical operators with a binary digital hologram. First and second order mathematical operators are the following :

$$\text{First order} \quad : \quad \text{gradient} \quad \vec{\nabla} \quad \frac{\delta}{\delta x} + j \frac{\delta}{\delta y} \quad \text{with} \quad j = \sqrt{-1}$$

$$\text{Second order} \quad : \quad \text{Laplacian} \quad \Delta \quad \frac{\delta^2}{\delta x^2} + \frac{\delta^2}{\delta y^2}$$

The differentiation program is very useful in image enhancement, first of contours but also of non-obvious features.

Figure 4 illustrates orientation filtering and Figure 5 represents polar diagram obtained in this way. Comparison between polar diagrams determined from optical interpretation or directly on radarimagery shows they are similar, outlining the same trends. Comparison between fracturing selected by interpreters and optical fracturing selection along the North 75° orientation demonstrates the ability of the laser system for direct filtering on radar-imagery, even with higher density.

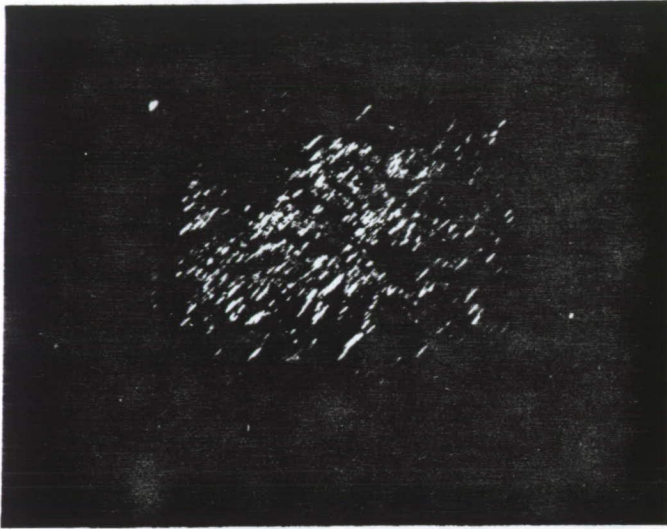
On test zone A1 laser enhancement ability has been tested. On this enhanced image (Figure 6) results are significant enough to follow up this first attempt.

2. Vigie Interpretation of Significant Results. Image scale is 1/200,000. Two altitudes have been selected : 5000 and 3000 meters; on both images, lithology is differentiated (Figure 7) granites, schists and limestones, but navigation problems strongly disturb the signature (Reference 7).

Roughness is better viewed than radiometric differences. At a 5000 m altitude results are better than at 3000 m. Vigie digital data have not yet been processed and this ability will have to be explored to improve interpretation. Note that this flight is a one strip only, there is no possibility of mosaicking and, at that scale, SLAR does not permit to obtain the synoptic view necessary for geological purposes to be obtained; it is a disadvantage for interpretation.

3. JPL Interpretation of Significant Results. Image scale is about 1/500,000. Two polarization images have been studied, HH and HV, and results are distinct. On HH polarization (Figure 8) the main lithologies can be differentiated : granites, schists and limestones. The fracture pattern is not very dense, compared to HV polarization or to HH Goodyear and Vigie SLAR images. On HV polarization subtle differences can be made in the Cretaceous limestones area where Carboniferous can be delineated (Figure 9). Compared with geological

S L A R optical filtering

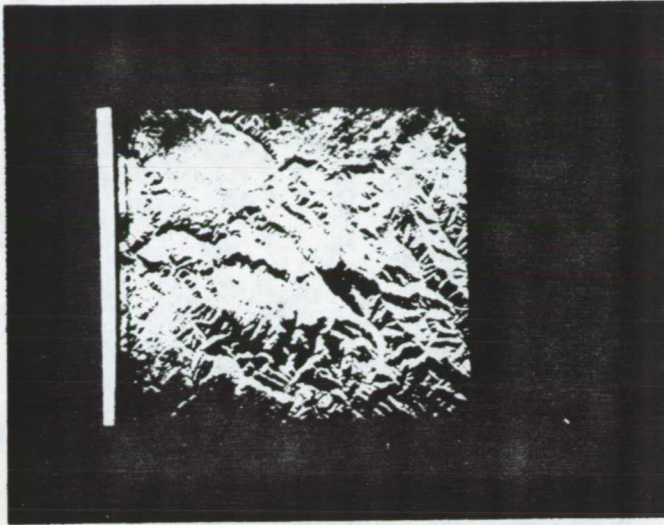


Zone A :
North 75° trend
visualisation

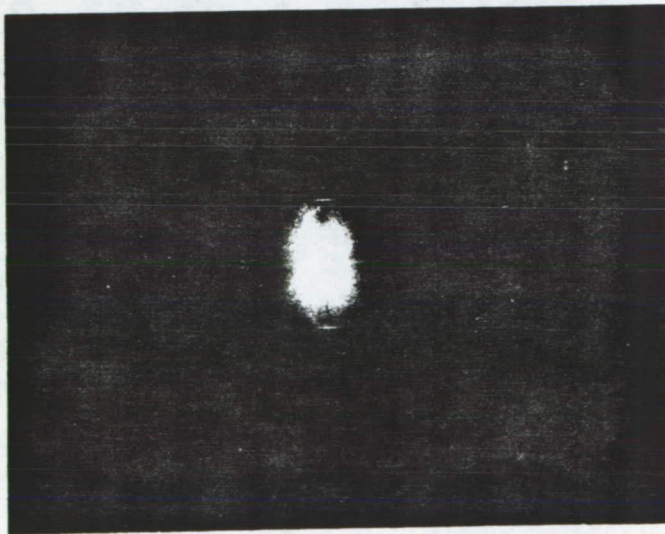


Figure 4. Al zone laser fracture filtering.

S L A R optical filtering



SLAR image
A 1 zone



Optical Fourier spectrum
oriented to 90°

Figure 5. A1 zone laser polar fracture diagram.

ORIGINAL PAGE IS
OF POOR QUALITY

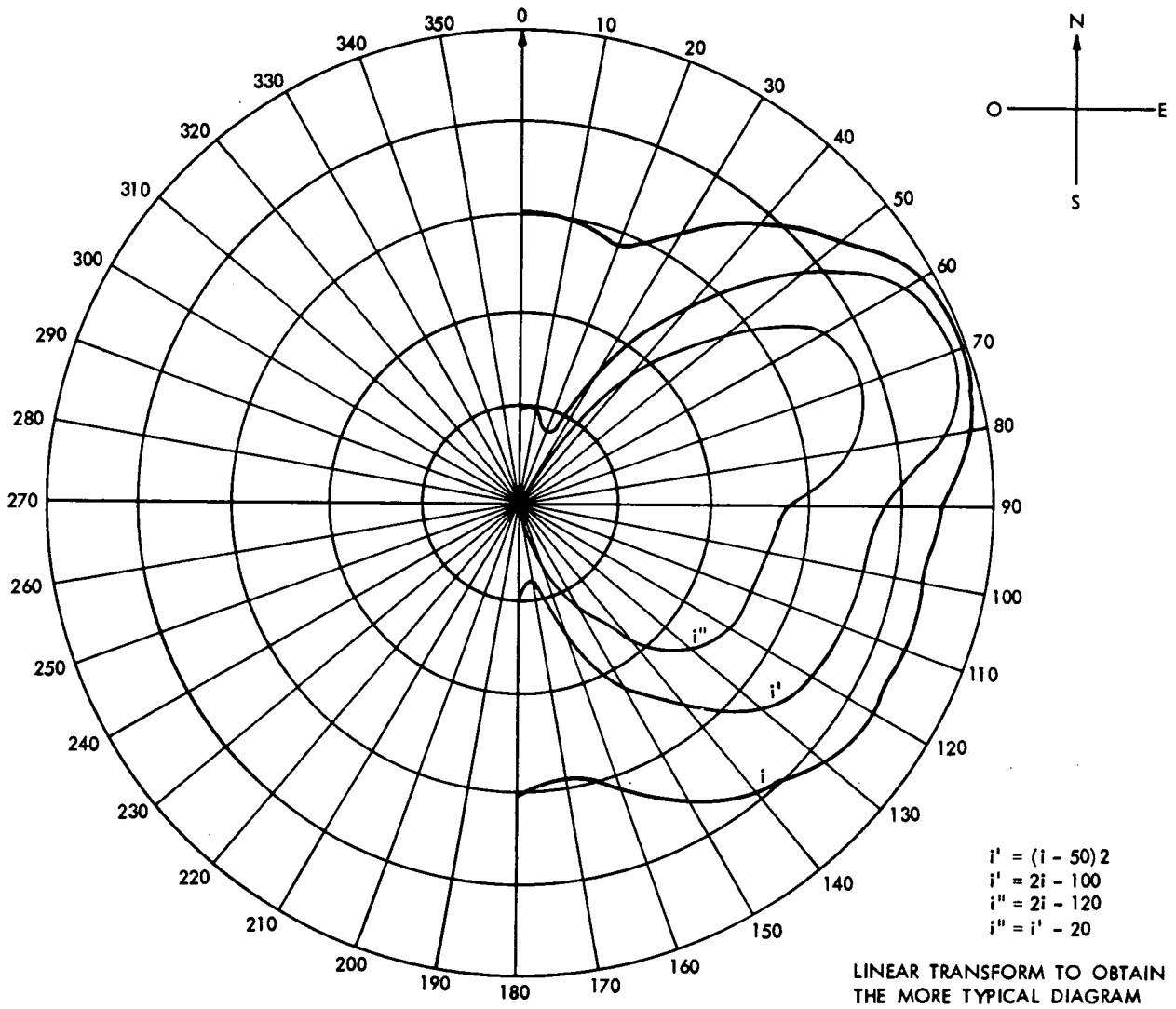
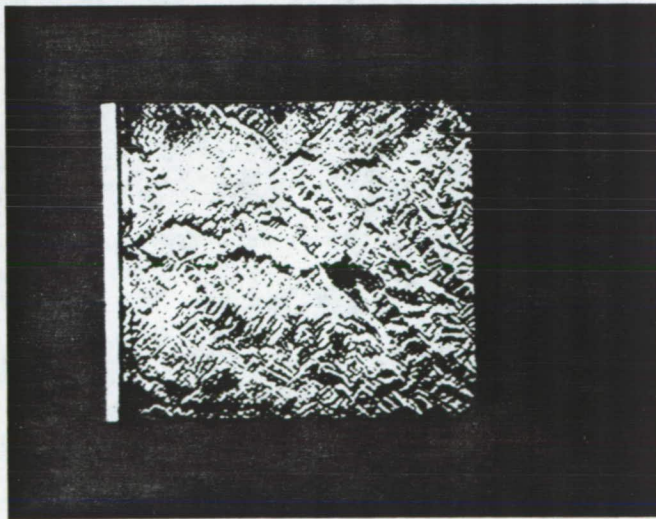


Figure 5 (Cont)

S L A R optical contrast enhancement



Zone A 1 :
first order transform



Zone A 2 :
second order transform

Figure 6. Laser enhancement image.

ORIGINAL PAGES
OF POOR QUALITY

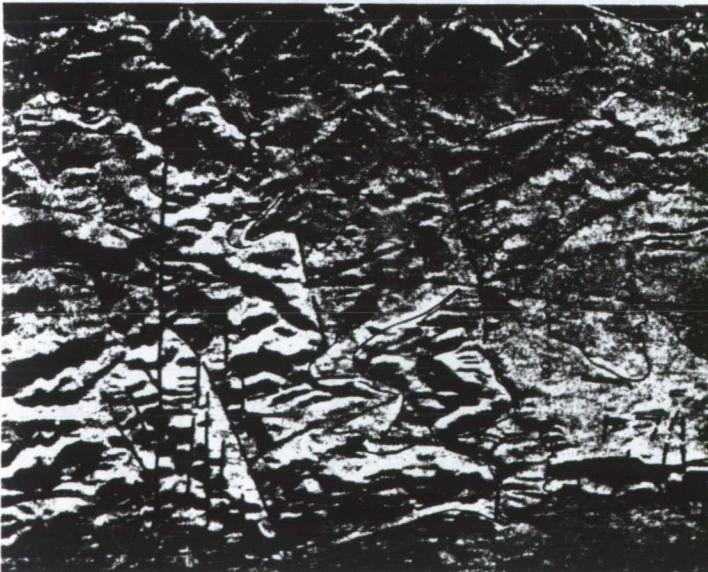
S L A R geological interpretation

VIGIE

Les Vans area (France)

Approximate scale 1/200 000

Localisation



LEGEND

Tectonic :

- Villefort fault (1)
- Vialas vein (2)
- Ales fault (3)
- Vialas vein extension (4)

Lithology :

- Granit (5)
- Schistes (6)
- Cretaceous limestones (7)
- Jurassic limestones (8)
- Marly limestones (Miocène) (9)
- Carboniferous (10)

Figure 7. Vigie geological interpretation (Les Vans, France).

J.P.L. SIDE LOOKING RADAR "LES VANS" - FRANCE

H.V. Polarisation

H.H. Polarisation

Legend



→ North

1 - Granite (Mt Lozere)

2 - Schistes (Ardèche)

3 - Schistes boundarie

4 - Limestones (Cretaceous)

5 - Marly limestones (Miocene)

6 - Ceze (river)

Figures 8-9. HH and HV images polarization (Les Vans, France).

map lithology and fractures are fairly well mapped.

In general one can say interpretation of JPL HV polarization images gives more significant results than HH polarization, mainly based upon radiometric differences.

Ph. Giraudin (IFP) has performed a general study on these same SLAR images. He reaches the conclusion that JPL images, especially HV polarization, give a good signature for vegetation : if the vegetation changes with lithology, as happens over Les Vans, JPL HV polarization image enables better geological mapping.

4. Goodyear, Vigie, JPL-Comparison of Results. In three main geological units mapped over the Les Vans area, granites, schists and limestones are differently interpreted on the different SLAR images. If one compares HH image polarization, Goodyear seems the best, probably because of its better resolution; Vigie images are strongly disturbed by navigation problems which are now partly solved. JPL HH image polarization gives poorer results and interpretation is not evident. But note that mosaicking, an important factor for interpretation, is missing at this experimental stage and degrades JPL and Vigie images. The JPL HV polarization image allows an improved interpretation, compared with the three others and with the geological map.

Geometric characteristics of each SLAR have been examined by Ph. Giraudin (Reference 8). For JPL images, where distortions are visible, accurate measurements have not been made: topographic details visible both on maps and images have been used as a reference. For Goodyear images a detailed analysis has been used as a reference. For Goodyear images a detailed analysis has been performed. Conclusions reached by Giraudin are the following:

JPL: along the flight line difference with the theoretical location is about 1 millimeter a 1/100,000 scale. Perpendicular to the flight line the difference is more important, 1 cm,

Goodyear: the scale is 1/101,000 and 1/97,100, (along the flight line). The difference is about 1,4 millimeter,

Vigie: On Figure 2 one can see the good geometrical accuracy which can be obtained with this digital registered data.

C. Guyana

1. Geology. The survey is located in Guyana, a French department in South America, north of Brazil (Figure 10) on the Regina and Baie d'Oyapock 1/100,000 map. Referring to a published geological map (1/500,000) the following units are present (Reference 9):

Recent quaternary formations, laterites.

Metamorphic rocks, schists, quartzites, conglomerate, lavas.

Cristalline rocks, dolerite, granites.

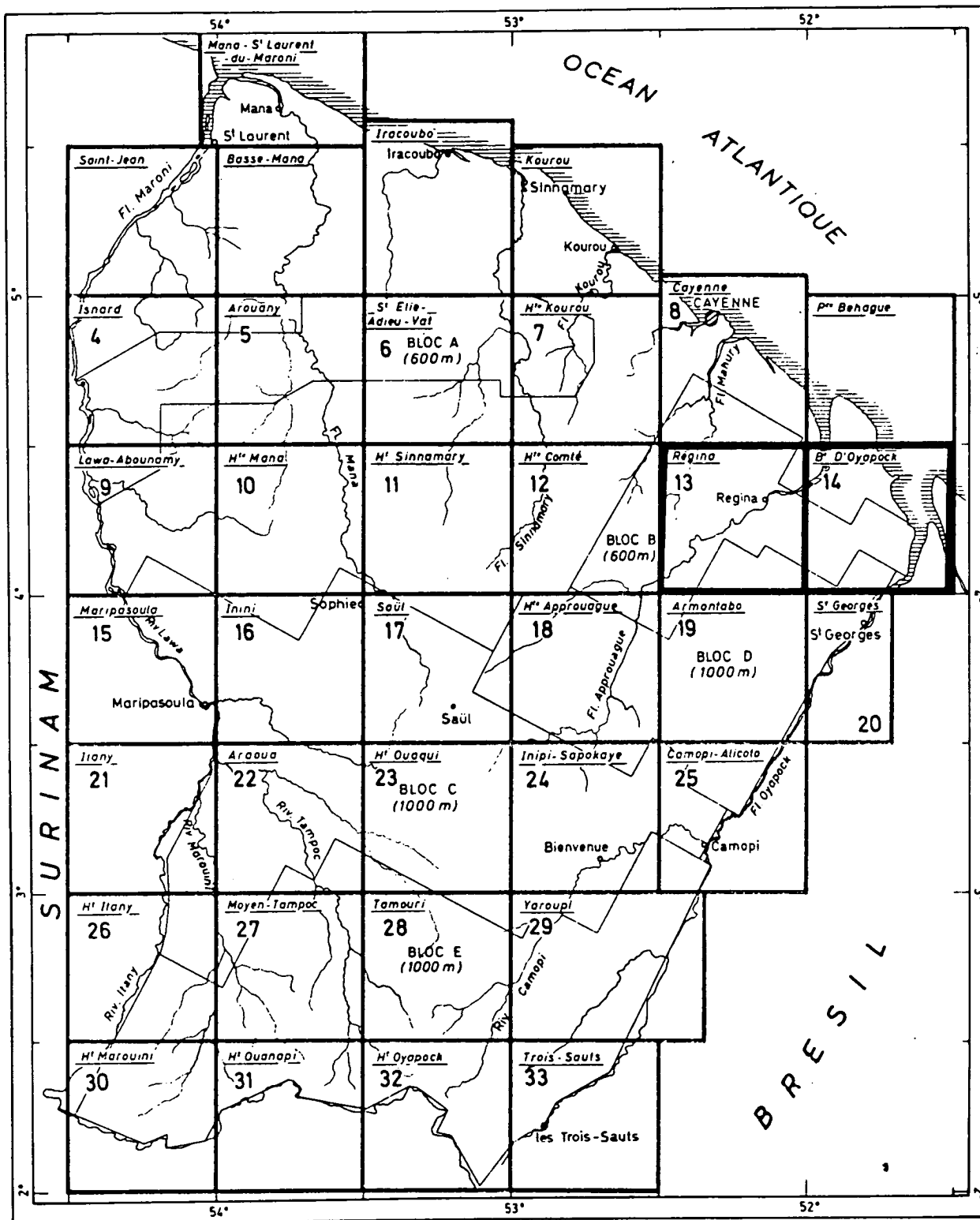


Figure 10. Guyana survey location.

The area is covered with a very dense equatorial forest, except along the coast.

2. Interpretation of Data. The survey has been done to prepare geological mapping and mineral exploration over Guyana, on SLAR images obtained from the "Ministerio des Minas y energia" Brazil. These images have been taken during the Radar project, in 1971 with the Goodyear GEMS 1000 X-band synthetic aperture. Mosaics at a 1/250,000 have been constructed by the project. During flight time cloud cover was very important.

On the selected area the following are available : geological map, photogeological map, and aeromagnetism.

We have reduced all these documents to the SLAR scale, 1/250,000, to make comparison easier.

3. Interpretation of Results.

a. Recent quaternary. Sand dunes, terraces and alluvial deposits are differentiated on SLAR images by their brightness (medium grey).

Laterites are only visible when they have a certain extent. They are distinguished by morphology and brightness (dark grey). This can be important for mineral exploration, some of them being bauxitic.

b. Metamorphic rocks. Four units have been differentiated on the geological map. One unit has a small extent but can be differentiated by a subtle morphology. The three other units are composed of schists and quartzites and only two of them have a typical signature, mainly due to morphology and fracturing.

c. Eruptives and crystalline rocks. A Dikes have a clear SLAR signature.

Granite A has a distinct pattern, scattered relief inside a mountain mass. Granite B can be differentiated from granite A (shape). Compared with the photogeological map constructed from black and white 1/50,000 scale aerial photographs, mapping obtained from SLAR images gives a correct picture, even if not so detailed. Locally geological features are enhanced or extended by correlation.

Comparison with aeromagnetic interpretation does not bring out any significant details but confirms existence of north-south fractures.

Finally, SLAR HH polarization over Guyana gives a correct idea of what can be done in equatorial forested area, during a cloudy season. SLAR is an all-weather remote sensing system which allows one to prepare a photogeological type map.

D. Miscellaneous

One aim of this paper is to present the main experiments conducted by French remote sensing scientists in the SLAR domain. Significant results can be summarized in three sections.

1. SLAR Image and Sea Surface Survey. In his report Ph. Giraudin presents results obtained by the Institut français du pétrole, which is involved in a sea state survey at the request of oil companies working offshore. This survey concerns platform security problems and hydrocarbon pollution and brings out significant conclusions.

2. SLAR Image and Geological Mapping. Ph. Giraudin and, before him, Ph. Rebillard (Reference 10) present reports on their investigations using SLAR (JPL, Goodyear). Rebillard's conclusions bring out significant results on fracturing (5 on Figure 11), new details being found and then checked on the field. He also mentioned the interest of HV polarization (JPL) in detecting alluvial deposits and ancient meanders which do not appear on HH polarization image.

3. SLAR Images and Vegetation. Conclusions carried out by the INRA, CESR remote sensing team are significant. Using JPL HH and HV polarizations taken over the Landes forest (France) during the Galileo II flight (Reference 11) they demonstrate JPL ability to classify trees, as a function of their age, with a very good accuracy.

V. CONCLUSIONS

In the Guyana site Goodyear SLAR provides geological information correlated with previous geological maps and photogeological maps. This good agreement indicates the real ability of SLAR as a true all-weather system, images being acquired during the cloudy season, opening the way to photogeological type interpretation in forested areas. In the Les Vans test site different types of SLAR have been tested. Results concern :

A. Radiometry

X band SLAR gives an image on which one can mainly interpret morphology. L-band SLAR opens the way to a second type of interpretation where brightness can be related to surface roughness and geological differences.

B. Polarization

X-band SLAR HH polarization images enable satisfactory geological and structural mapping. L-band SLAR, HH polarization images contain less information than X-band HH polarization images, and less than L-band HV polarization images. L-band SLAR, HV polarization offers important mapping possibilities but geometry has to be improved.

C. Wavelength

If HH polarization images are compared, X-band seems, at this time, to allow a better interpretation in geology but L-band, because of its ability to differentiate vegetation, enables results in geology which have to be explored.

Optical filtering can be used directly on SLAR images to prepare fracture analysis : orientations can be selected and rose diagrams constructed automatically. Since SLAR data generally are not recorded digitally, image enhancement by laser has to be improved.



PLANCHE IV



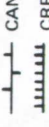
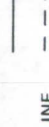
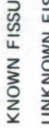
-  WATER COURSE
 -  ALLUVIAL ZONE
 -  OLD MEANDERS
 -  CANAL
 -  CREST LINE
 -  KNOWN FISSURE
 -  UNKNOWN FISSURE
- CIRCLED NUMBERS REFER TO THE TEXT

Figure 11. JPL interpretation (the Alps, France).

ORIGINAL PAGE IS
OF POOR QUALITY

A more general conclusion concerns interest in mosaicking, which gives a synoptic view, for geological mapping, and type of illumination which brings out complementary details.

Finally, as far as mineral exploration is concerned, SLAR opens the way to photogeological type interpretation in cloudy area and for that reason can be considered as a technique which makes it possible to select targets for prospecting for ores.

REFERENCES

1. Goodman, J. W., 1972, Introduction à l'optique de Fourier et à l'holographie, Masson, Paris.
2. Soubari, E. H., 1977, Nouvelle méthode de traitement des cartes de champs géomagnétiques et géogravimétriques par voie optique. D. I. université de Strasbourg, France.
3. Reinhardt, E. R., and Bloss, W. H., 1978, Optical differential operation processor, Optical Engineering Jan. 1978, Vol. 17, No. 1, pp. 69-72.
4. Hazan, J. P., 1975, Les applications de Titus et de Phototitus au traitement d'images et de données, Acta Electronica, 18, 3, 1975 pp. 201-219.
5. Lohmann, A. W., and Paris, D. P., 1967, Binary Fraunhofer hologram generated by computer, Applied Optics, 6 : 10, 1967.
6. Lohmann, A. W., and Paris, D. P., 1968, Computer generated spatial filters for coherent optical data processing. Applied Optics, 7, 4, 1968.
7. Scanvic, J. Y., 1979, Commentaires sur les radargraphies des Vans - Ardèche (Radar, Vigie bande X) Jan. 1979, BRGM report.
8. Giraudin, Ph., 1978, Les images du radar latéral, IFP report, Oct. 1978.
9. Division photogéologie et télédétection du BRGM, 1979, Rapport sur les interprétation des images radar de Guyane, 1979, BRGM.
10. Rebillard, Ph., 1977, Programme Radar JPL, 1977, Analyse des clinchés de l'axe de vol n°3 Diois - Baronnies (France), Laboratoire d'applications spéciales de la physique.
11. INRA, CESR, International report.

DEFINITIONS

INRA	Institut national de la recherche agronomique (National Institute for Agronomic Research) (M. Boissard)
IGN	Institut géographique national (National Geographic Institute)
IFP	Institut français du pétrole (French Petroleum Institute)

CESR Centre d'études spatiales des rayonnements (Center for Space Radiation Studies) (M. Riom, Mme Le Taon)

BRGM Bureau de recherches géologiques et minières (Office of Geologic and Mining Research)

GDTA Groupement pour le développement de la télédétection aérospatiale (Group for the Development of Aerospace Remote Sensing)(CNES, IGN, IFP, BRGM, BDPA)

CNES Centre national d'études spatiales (National Center for Space Studies)

BDPA Bureau de développement pour l'agriculture (Office of Agricultural Development)

THE EVALUATION OF 3-CM-WAVELENGTH
RADAR FOR MAPPING SURFACE DEPOSITS
IN THE BRISTOL LAKE/GRANITE MOUNTAIN
AREA, MOJAVE DESERT, CALIFORNIA

Ray Sugiura
Woodward-Clyde Consultants
and
Floyd Sabins
Chevron Oil Field Research Co.

ABSTRACT

Surface deposits in the Bristol Lake/Granite Mountains area, Mojave Desert, California were mapped using high resolution 3-cm-wavelength radar images. The surface deposits range from silt to boulders in size and were separated into six radar-rock units on the basis of radar return signatures (brightness and texture) and geomorphic expression. Field reconnaissance of the six units showed that the brightness of the radar signatures on the images correlates with the surface roughness of each unit.

Two major radar signature anomalies were noted during the study. A dark radar signature for the large sand ridges in the Kelso Dunes area and a distinct northwest trending contrast boundary between bright and dark radar signatures in the Bristol Dry Lake area. Field reconnaissance of the two areas indicated that near surface moisture may be the cause of dark signatures. Further work, however, is needed to determine the exact cause for the anomalous signature.

The effect of vegetation on the radar signature from a uniform surface material is clearly illustrated in the Kelso Dunes area. Dune areas with little to no vegetation produce a dark signature, whereas areas with sparse to moderate vegetation produce an intermediate to dark signature.

I. INTRODUCTION

Applications of SLAR imagery for geologic studies have been described in the literature. Studies by Barr (1968), MacDonald (1969, 1976), MacDonald and Waite (1972), Schaber (1976), Daily and others (1978) and Sabins (1978) have shown that there are subtle variations in surface roughness, recorded by tonal variations on radar imagery, that can be used to delineate many types of geologic surfaces. The objective of this study was to evaluate the use of SLAR imagery of the Bristol Lake Granite Mountains area for mapping surface deposits. Additional studies are in progress to analyze lineaments expressed on the imagery.

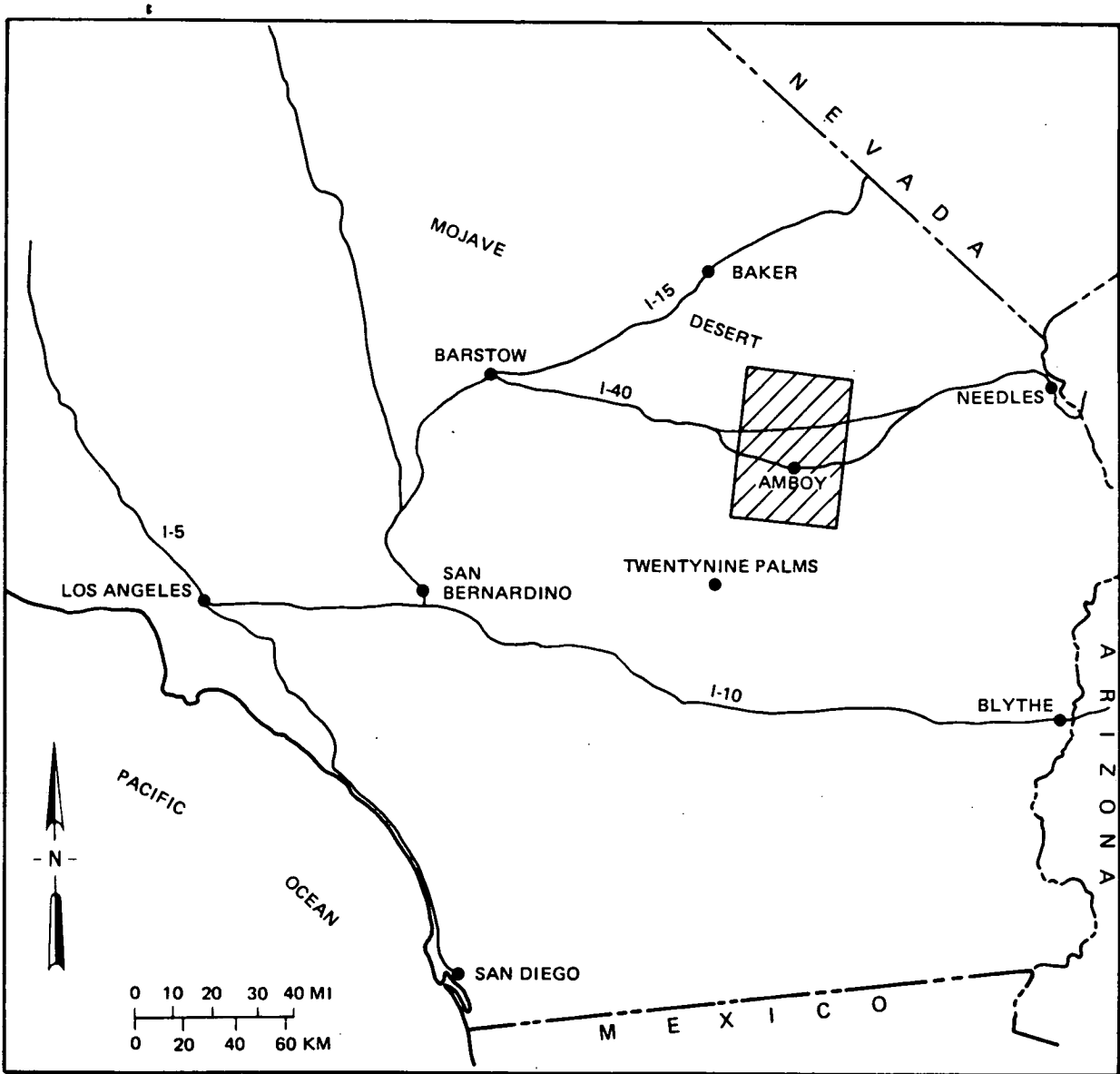


Figure 1. Index map showing location of radar mosaic (Figure 4).

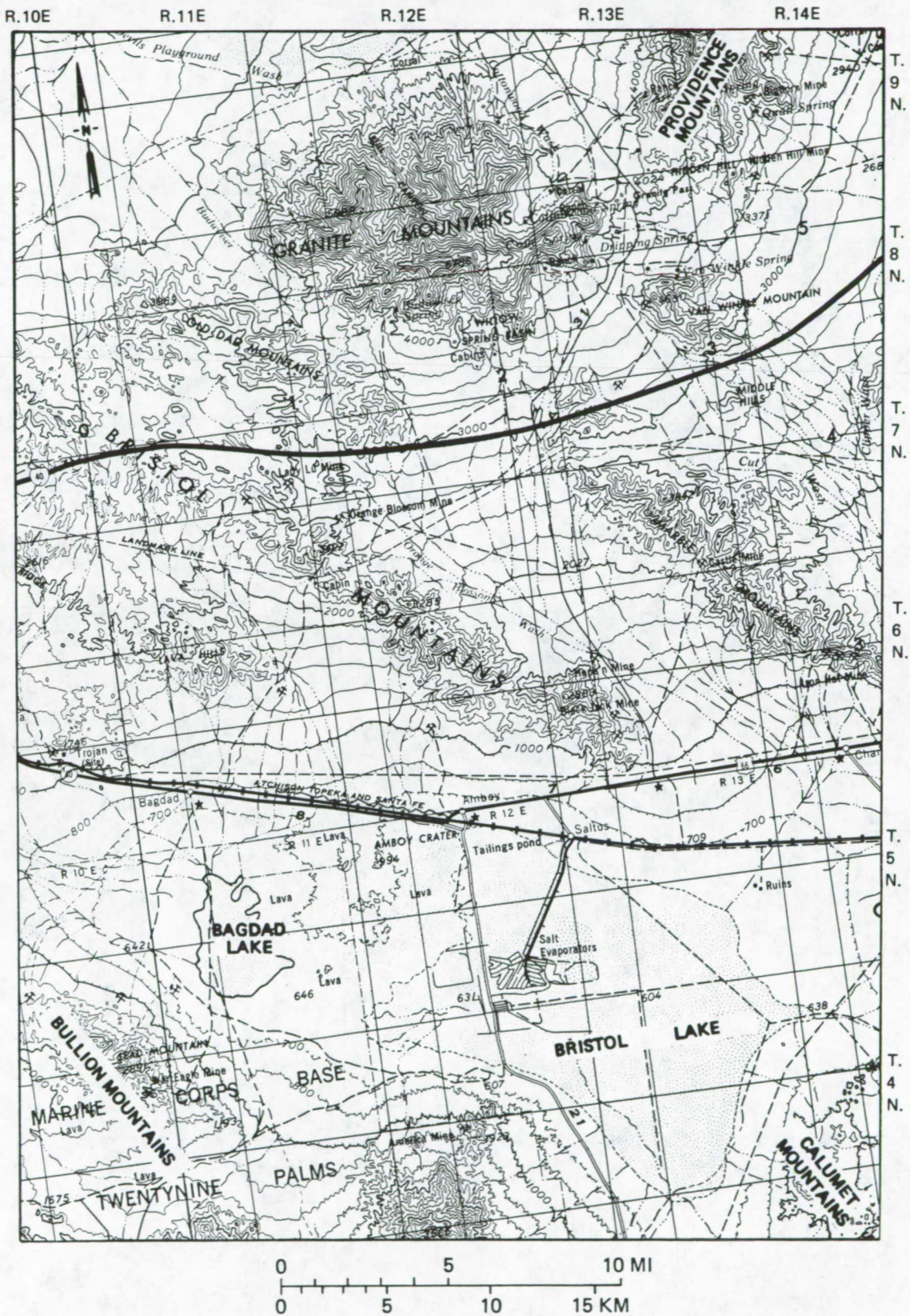
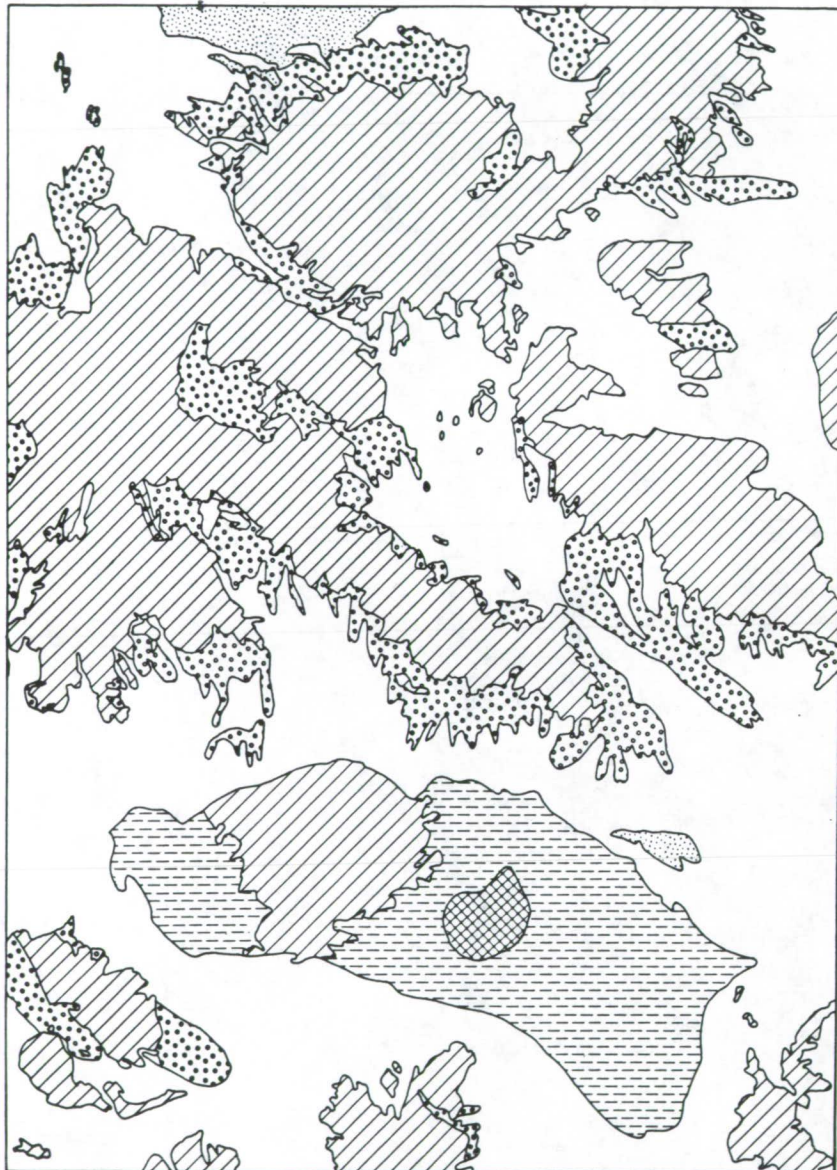


Figure 2. Topographic map of Bristol Lake - Granite Mountains study area, San Bernardino County, California. Contour interval (200 feet).



EXPLANATION

-  Younger alluvium
-  Eolian sand
-  Salt deposits
-  Playa deposits
-  Older alluvium
-  Crystalline and pre-Quaternary sedimentary rocks

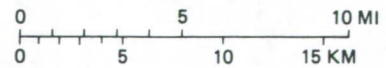


Figure 3. Generalized geologic map of the Bristol Lake - Granite Mountain area, California (modified from Bishop, 1963).

The study area covers approximately 2500 square km (940 square mi) and is located in the eastern Mojave Desert, California, about 270 km (170 mi) east of Los Angeles (Figure 1). The area was selected for study primarily because of the availability of high-resolution SLAR images. In addition, it is reasonably accessible from Interstate Highway I-40, Highway 66, county roads, and jeep trails. The topography of the region is typical of the Mojave Desert physiographic province; it consists of rugged, moderately dissected northwest-trending mountain ranges separated by alluvial covered slopes and basins; the basins commonly contain playas (Figure 2).

The mountains primarily consist of pre-Tertiary crystalline rocks and Tertiary volcanic flows and tuffs. Quaternary basalts and cinder cones, and late-Tertiary to early-Quaternary fanglomerates that are tilted and dissected form low to moderate hills along the flanks of the mountains. The intervening areas between mountain ranges consist of late Quaternary alluvium, eolian sand, and playa deposits (Figure 3).

The climate is semiarid to arid; average annual rainfall is 10 cm (4 in.) (Bassett and Kupfer, 1964). Vegetation is sparse on the mountain slopes, moderate to sparse on the pediments and alluvial fans, and generally absent on the playas and active portions of the sand dunes. Creosote bush is the most common vegetation and is present almost everywhere except on the playas and active sand dunes. Small desert shrubs, bushes, and native grasses are also relatively common. Larger plants, such as Joshua trees, are present around the base of the Granite Mountains: juniper and pinyon pine occur at higher elevations. Palo verde and tamarisk trees are common in the populated areas and locally in patches along major drainages and Highway 66.

II. RADAR IMAGERY

Radar imagery used in this study was acquired in July 1975 by Goodyear Aerospace with a 3-cm-wavelength (X-band) synthetic aperture SLAR system. The imagery was flown at an altitude of 10,200 m (33,500 ft) along a flight path oriented N14°E. The look direction was to the west, with a depression angle of 30° for the near range and 10° for the far range. The swath width of individual image strips is approximately 36 km (22.5mi). The parallel-polarized images record energy that was transmitted and received in the horizontal mode. The original imagery was recorded in a ground-range format at a scale of 1:400,000 with a spatial resolution of 12 m (40 ft).

III. INTERPRETATION AND ANALYSIS

Interpretations were made on a 1:250,000 scale uncontrolled radar mosaic (Figure 4) and individual image strips at a scale of 1:200,000. Individual image strips, photographically enlarged to a scale of 1:80,000, were used to interpret specific features that were not clearly distinguishable on the smaller scale images. Field studies were conducted to verify the interpretations of the radar imagery and to identify the features responsible for the radar signatures from selected areas.

A. Discrimination of Surface Deposits

The surface deposits in the Bristol Lake/Granite Mountains area were separated into six radar-rock units, based on a combination of their radar signature (brightness), physiographic setting, and drainage texture and pattern.

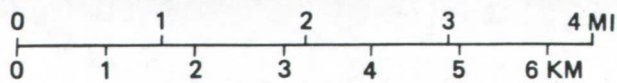
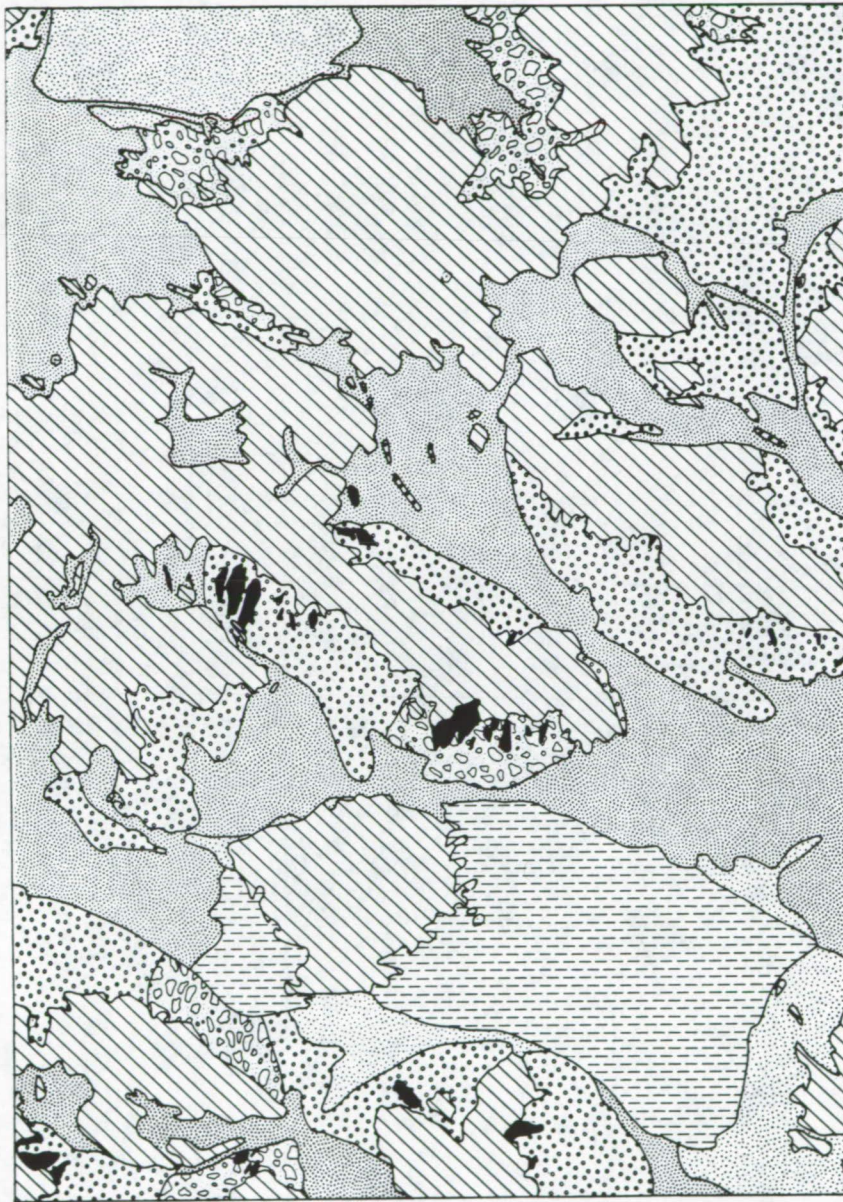


Figure 4. X-band radar mosaic of the Bristol Lake - Granite Mountain area, California. Letters refer to typical localities.



EXPLANATION

-  Cobble-boulder fan deposits
-  Gravel-cobble fan deposits
-  Sand-gravel fan deposits
-  Desert pavement surfaces
-  Eolian sand deposits
-  Playa deposits
-  Crystalline and pre-Quaternary sedimentary rocks

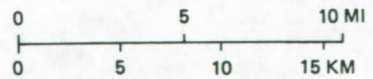


Figure 5. Interpretation of surface deposits from the radar mosaic (Figure 4).

Table 1. Radar-rock unit characteristics

Radar-rock unit	Measured surface roughness, h (average)	Radar signature Predicted	Radar signature Observed	Physiographic setting	Typical locality ¹
Cobble-boulder fan deposit	30 cm	Bright	Bright	Adjacent to bedrock outcrops and upper fan areas; generally dissected by drainage channels.	A
Gravel-cobble fan deposits	10 cm	Bright	Bright to intermediate	Adjacent to bedrock outcrops and midfan areas.	B
Sand-gravel fan deposits	0.5 cm	Intermediate	Dark to intermediate	Upper to lower fan areas; and valleys between mountain ranges.	C
Desert pavement	1 cm	Dark	Dark	Adjacent to bedrock outcrops and upper to midfan areas.	D
Eolian sand deposits	<.05 cm	Dark	Dark to intermediate	Lower fan areas and along margins of the playas.	E
Playa deposits	<.01 cm	Dark	Dark	Enclosed basin areas.	F

¹Refers to locations shown on the radar mosaic, Figure 4, and ground photographs, Figure 6.

The smooth-and-rough criteria of Peake and Oliver (described in Sabins, 1978) were calculated for a typical locality of each radar-rock unit using the depression angle at which that locality was imaged. The calculated criteria express the limiting values of average surface roughness in centimeters (h) at which a surface will appear smooth (dark radar signature), intermediate (gray), or rough (bright). The characteristic radar signatures for the units are listed in Table 1 and the distribution of the units is shown in Figure 5.

B. Characteristics of the Radar-Rock Units

1. Cobble-Boulder Fan Deposits. This radar-rock unit has the brightest return of all the surface deposits delineated in the study area (Figure 4). The unit corresponds to the rough alluvial fan surfaces adjacent to bedrock areas and consists of cobbles and boulders. Adjacent to the Granite and Providence Mountains, Figure 2, the diameter of the sediments ranges from 0.15 m (0.5 ft) to 1.2 m (4 ft), averaging about 0.3 m (1 ft) (Figure 6A). At other localities, such as near the southeast end of the Bullion Mountains, the cobbles and boulders average about 15 cm (6 in.) in diameter. The surface of this unit is generally incised by deep, steep-sided gullies and washes. Farther down the fan slopes, the surface topography is irregular because of accumulations of cobbles and boulders on the sides and top of interfluves. Vertical relief between the washes and interfluves ranges from 0.3 m (1.0 ft) to 3 m (10.0 ft). The combination of coarse fragments with irregular and bouldery topography produces the bright tone that constitutes the radar signature of this unit.

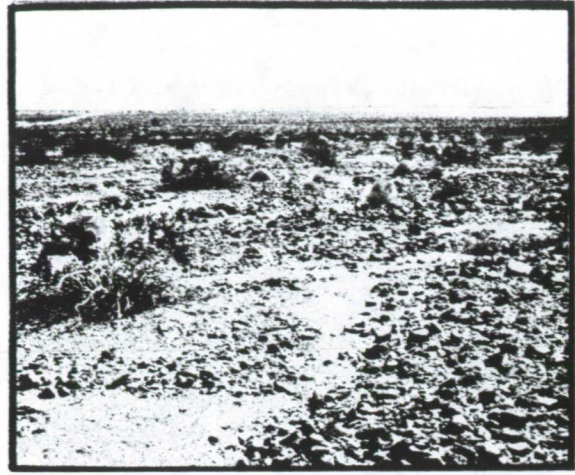
2. Gravel-Cobble Fan Deposits. This unit consists of channel bars separated by relatively minor swales or channels. Vertical relief from the top of the bars to the bottom of the swales ranges from 0.3 m (1 ft) to 1.5 m (5.0 ft). The bars consist of gravel, cobbles, and scattered small boulders ranging in diameter from 4 cm (1.5 in.) to 30 cm (1 ft) and averaging 10 cm (4 in.) (Figure 6B). The sand and gravel deposits in the swales are distinctly finer grained than the material of the channel bars. The predominance of coarse sediments and the irregular bar-and-swale topography produces the bright to intermediate radar signature.

3. Sand-Gravel Fan Deposits. This unit consists primarily of coarse sand with minor amounts of gravel and scattered cobbles (Figure 6C). The diameter of the gravel ranges from 0.5 cm (0.2 in.) to 2.5 cm (1 in.). The surface is nearly level, but gentle undulation results from elongate narrow fluvial gravel bars and small mounds of sand around the base of bushes. The gravel bars are caused by sheetflow down the fan surface during periods of intense precipitation. The heights of the bars and mounds range from 5 cm (2.5 in.) to 30 cm (12 in.) above the adjacent surfaces. Vegetation is sparse to moderate and consists of small creosote shrubs and other small bushes. Based on the field observations, the dark to intermediate radar signature of this unit is produced by the combination of (1) the gravel bars, (2) the small mounds around the base of the bushes, and (3) the vegetation.

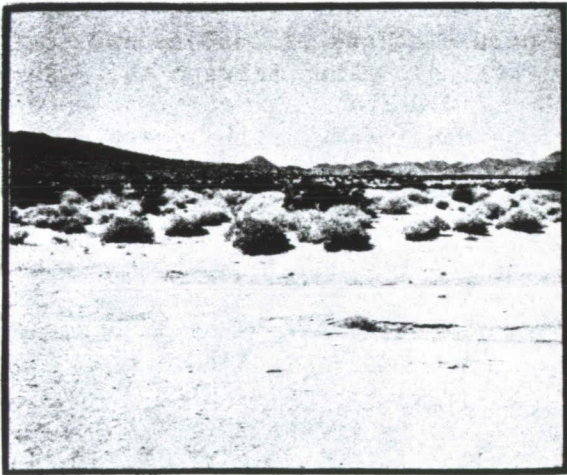
4. Desert Pavement. This unit occurs adjacent to bedrock outcrops, on the upper slopes of alluvial fans and consists of gravel, cobbles and scattered boulders that are aligned or fitted together to form a desert pavement (Figure 6D). The exposed surfaces of the fragments that compose the pavement surface are coated with dark-brown desert varnish. As the name implies, the desert pavement surfaces are smooth. Specular reflection of radar energy from the smooth desert



A. COBBLE-BOULDER FAN DEPOSITS



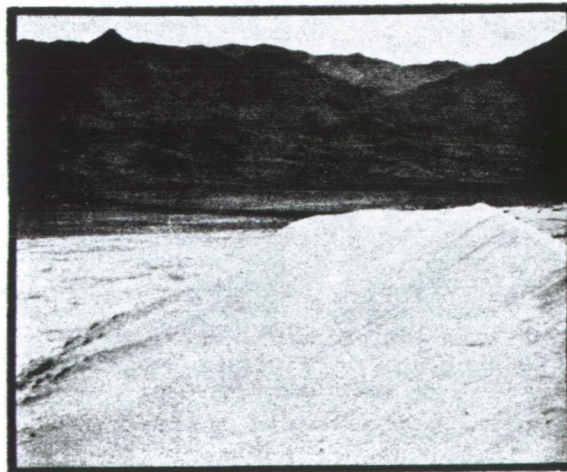
B. GRAVEL-COBBLE FAN DEPOSITS



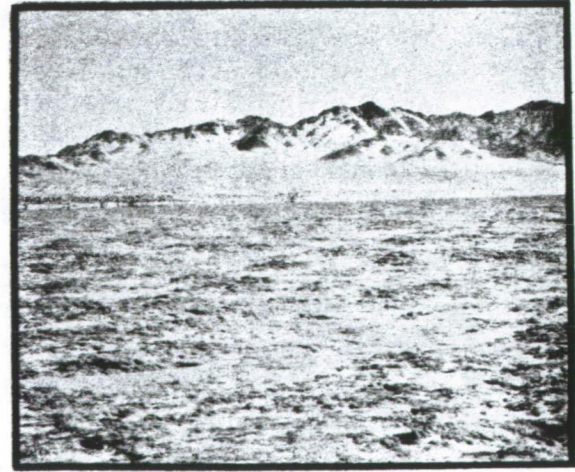
C. SAND-GRAVEL FAN DEPOSITS



D. DESERT PAVEMENT SURFACE



E. EOLIAN SAND DEPOSITS



F. PLAYA DEPOSITS

Figure 6. Ground photographs of the radar rock units.

pavement surface produces a distinctive dark radar signature. On the radar image (Figure 4), the dark desert pavement areas are crossed by bright lines that represent drainages. The drainages contain coarse gravel and boulders and local concentrations of vegetation, which cause the bright signature. Corner reflections from suitably oriented drainage walls also contribute to the bright signature.

5. Eolian Sand Deposits. Eolian sand deposits occur along the margins of Bristol and Bagdad playas and at the Kelso Dunes, north of the Granite Mountains. The eolian sand adjacent to the two playas has a dark radar signature. These deposits consist of fine-grained sands that form a thin cover over alluvium. Locally, the sands form small- to moderate-size dunes, such as along the south side of the Bristol playa. On the image, these dunes are marked by bright streaks aligned parallel with the playa margin; the streaks appear to be caused by vegetation along dune edges and along the boundary between the playa and the sand.

The Kelso Dunes are the largest body of sand in the study area (Figure 6E). The dunes consist of sand averaging 0.05 cm (0.02 in.) in diameter and have generally smooth surfaces (Sharp, 1966). Although the surfaces are dry, the sands are relatively moist two to three centimeters (1 in.) below the surface. On the enlarged radar image, dunes are readily separated into four subdivisions on the basis of radar signatures (Figure 7). These subdivisions are listed in Table 2, together with their radar signatures and field descriptions. The distribution of the subdivisions is shown in Figure 8. Figure 9 is a high-altitude aerial photograph of the Kelso Dunes.

a. Longitudinal Dunes. Longitudinal dunes occur along the western margin of the Kelso Dunes and in the northeastern portion of the dune field (Figure 8). The dunes have a subdued form, range up to about 12 m (40 ft) in height, and have a moderate to sparse vegetation cover. On the radar image (Figure 7), the dunes have a distinct pattern of alternating dark and bright strips that match the trends of the dunes shown on the aerial photograph (Figure 9). Factors contributing to the alternating dark and bright strips on the radar image include highlights and shadows caused by interaction between dune morphology and the radar beam and the relative concentration of vegetation in the linear depressions between dunes.

b. Irregular or Rounded Dunes. Irregular or rounded dunes occur in the northeastern portion of the Kelso Dunes and as smaller areas in the central and southern sections of the field (Figure 8). These dunes have an intermediate to dark radar signature (Figure 7). The dunes in this subdivision are subdued, have a rounded mound form, and commonly surround hollows that range in depth from a few meters to 7 m (25 ft). Vegetation cover is sparse to moderate, averaging 25 to 35 percent (Sharp, 1966). The vegetation cover appears to be the controlling factor that produces the intermediate to dark radar signature.

c. Transverse Dunes. The transverse dunes are located on the flanks of the four main sand ridges (Figure 8) and have a generally dark signature, with discrete bright tones on the radar image (Figure 7). These dunes have a smooth, gently sloping windward side and a steeper lee side, generally with a distinct slip face. The inclination of the slip face ranges from 25° to 30°. Heights of these dunes are variable but average between 6 m (20 ft) and 9 m (30 ft). The dark signature appears to correspond to the smooth, windward side of the dunes, whereas the discrete bright tones are produced by the steep slip faces.

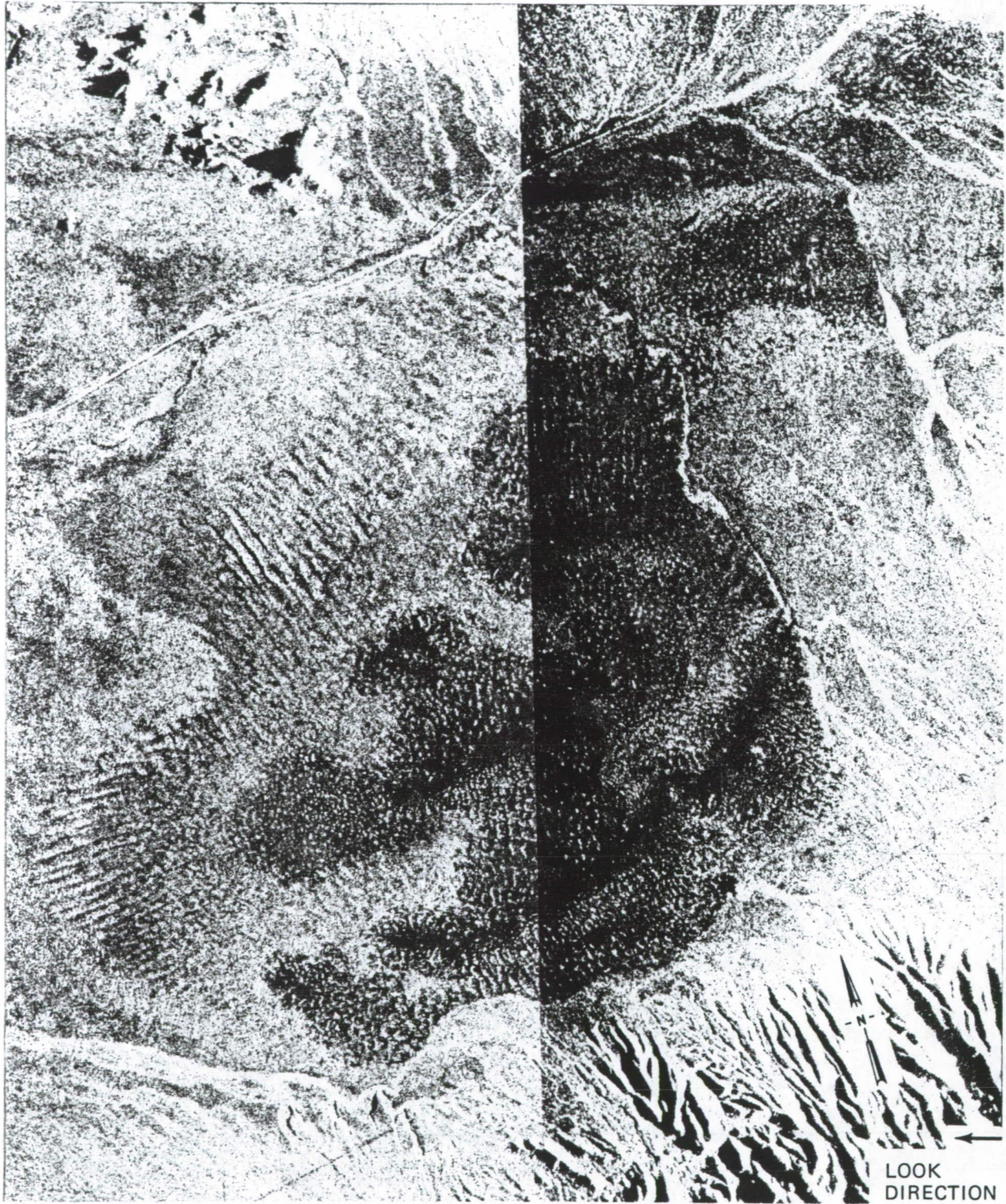


Figure 7. Radar image of the Kelso Dunes area.

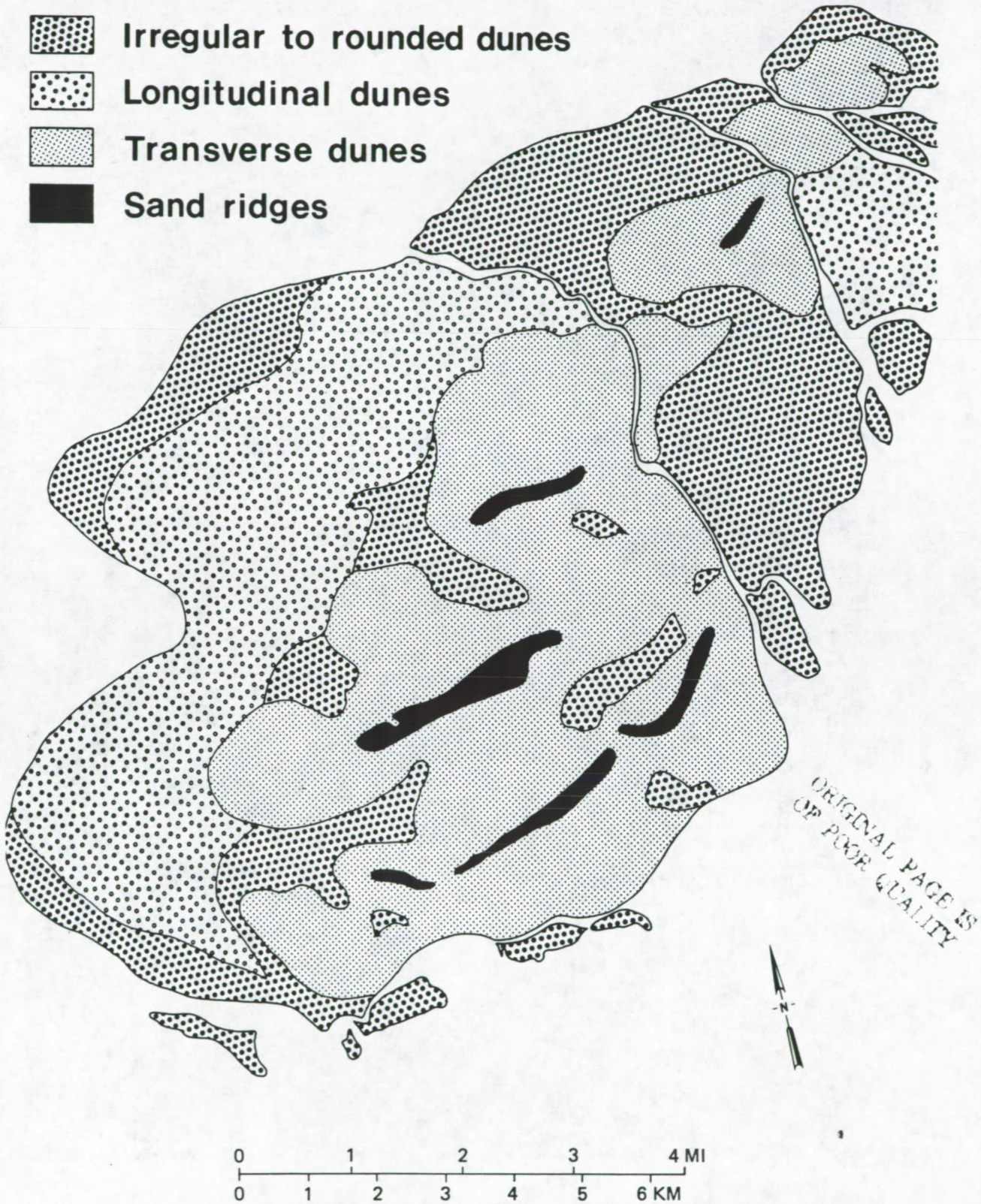


Figure 8. Radar interpretation map of the Kelso Dunes area, showing distribution of subdivisions.



Figure 9. High altitude aerial photograph of the Kelso Dunes area.

d. Sand Ridges. The elongated sand ridges have the darkest radar signatures in the Kelso Dunes. These ridges are located in the central and north-eastern portion of the dune field (Figure 8). The sand ridges vary in size as follows: length, 1.6 to 6.4 km (1 to 4 mi); width, 300 to 600 m (1000 to 2000 ft); and height, 45 to 167 m (150 to 550 ft). Examination of the largest of the sand ridges showed that the ridge narrows abruptly upward from its base toward its angular peak. The slopes of the ridges range from 30° to 33° for the upper portions and from 20° to 25° for the lower portion (Sharp, 1966). Vegetation consists of sparse grass around the ridge base and locally on the steep slopes.

The dark radar signature for the sand ridges is surprising. For their size and geometry with respect to the radar look direction, a brighter radar signature similar to the bright signatures observed from other ridges on the radar mosaic (Figure 4) is expected. The lack of a brighter radar signature and general lack of expression of the sand ridges on the images may be related to the difference in dielectric constant between the dry surface and the moist underlying sand. Although radar waves generally are reflected from a surface, they may have penetrated the thin surface layer of loose sand on the ridges. If this was the case, the radar energy could be partially absorbed by the underlying moist sand, with its higher dielectric constant. This would explain the anomalously dark signature of the sand ridges.

6. Playa Deposits. This unit, found at Bristol and Bagdad playas, has the darkest radar signature within the study area (Figure 4). The two playas are essentially flat, with little or no vertical relief, except for the salt work excavations and spoil piles in the western portion of Bristol playa. The playa

Table 2. Subdivision of Kelso dunes characteristics

Dune area	Radar signature	Field description
Longitudinal dunes	Intermediate	Subdued longitudinal dunes; vegetation sparse to moderate
Irregular to rounded dunes	Intermediate to dark	Irregular to rounded subdued dunes; dunes often separated by nearly flat areas; vegetation sparse to moderate
Transverse dunes	Dark with discrete bright tones	Transverse dunes with gentle windward slopes and steep lee slopes; dune heights up to 10 m (30 ft); vegetation absent to sparse
Sand ridges	Dark	Large linear sand ridges with steep slopes, heights range from 45 m (150 ft) to 167 m (550 ft); vegetation absent to sparse

sediments consist of silt, clay, salt, and minor amounts of fine sand (Figure 6F). The playa surfaces have a puffy appearance and are covered by a dry crust less than 1 cm (0.5 in.) thick. The sediments underlying the crust are moist to locally wet. The small puffy mounds, 4 to 7.5 cm (1.5-3 in.) high and 15 to 60 cm (6-24 in.) in diameter, form a microrelief on the playa surfaces.

Although the unit is characterized by its dark radar signature, there are areas within the Bristol playa that have bright to intermediate signatures which correspond to areas with small mounds. These mounds also occur in other parts of the playa where the radar return signature is dark; an example of this is the area south of the northwest-trending lineament across the southern half of the playa (Figure 4).

The lineament across Bristol playa appears as a distinct tonal contrast on the radar image and extends from the salt work excavations to the southeastern margin of the playa (Figure 4). On 1:80,000 aerial photographs (not shown here), the lineament is expressed as a subtle tonal contrast and is not as distinct a feature as on the radar image. Field reconnaissance of the playa surface on both sides of the lineament revealed no major differences in sediment type or in appearance of the surface. It did, however, indicate that the sediments south of the lineament had a relatively higher moisture content.

As was the case with the sand ridges, the dark radar signature from the sediments on the south side of the lineament may be related to the higher moisture content of the material below the thin dry crust. If the radar waves penetrate the crust, they may be partially absorbed by the underlying moist material. This reasoning provides a logical explanation for anomalously low backscatter recorded for the playa surface on the southside of the lineament.

Field investigation of the lineament consisted of (1) a limited seismic refraction survey across lineament and (2) examination of the bedrock outcrops in the Calumet Mountains, located along the projected trace of the lineament. These methods revealed no evidence of faulting of the playa sediments.

Nonetheless, as discussed previously, the playa sediments below the thin crust on the southern side of the lineament were more moist than the sediments across the lineament. This suggests that the lineament may be the surface expression of a buried fault that controls ground water movement beneath the playa.

IV. SUMMARY

This study shows that X-band radar imagery can be used to delineate surface deposits that have different surface roughness characteristics. It is also possible to estimate the relative average surface roughness of the gravel to cobble and finer-grained materials using Peake and Oliver's smooth and rough criteria.

Features associated with the various radar-rock units can also be delineated on the X-band images. These include drainage channels, the pattern of large fluvial gravel bars, desert pavement area, and dune forms.

The effect of vegetation on the radar return from a uniform surface material is clearly illustrated in the Kelso Dunes area. Areas with sparse or no vegetation produce dark return, whereas areas with sparse to moderate vegetation have an intermediate to dark return.

REFERENCES

- Barr, D. J., 1968, Use of side-looking airborne radar imagery for engineering soil studies: Final Technical Report, Geography Science Division, U. S. Army Engineer Topographic Lab., Ft. Belvoir, Virginia, 90 p.
- Bassett, A. M., and Kupfer, D. H., 1964, A geologic reconnaissance in the southeastern Mojave Desert, California: California Division of Mines and Geology Special Report 83, 42 p.
- Bishop, C. C., et al., 1963, Geological map of California, Needle sheet, Scale 1-250,000, published by California Division of Mines and Geology. Compiled by Charles Bishop.
- Daily, M., Elachi, C., and others, 1978, Application of multispectral radar and landsat imagery to geologic mapping in Death Valley, JPL Publication 78-19, Jet Propulsion Laboratory, Pasadena, California, 47 p.
- Dellwig, L. F., Hanson, B. C., Hardy, N. F., Holtzman, J. C., Hulen, P. L., McCauley, J. R., Moore, R. K., 1975, A demonstration and evaluation of the utilization of side-looking airborne radar for military terrain analysis: ETL report-0023, U.S. Army Engineer Topographic Lab., Ft. Belvoir, Virginia, 31 p.
- MacDonald, H. B., 1969, Geologic evaluation of radar imagery, Darien Province, Panama, *Modern Geology*, v. 1. pp. 1-63.
- MacDonald, H. C., 1976, Use of radar in geology, *in* Geoscience Application of Imaging Radar Systems, Lewis, A. J. ed., *Remote Sensing of the Electro Magnetic Spectrum*, v 3, p. 93-104.
- MacDonald, H. C., and Waite, W. P., 1972, Terrain roughness and surface discrimination with SLAR in arid environment, RSL technical report 177-25, University of Kansas Center for Research, Inc., Lawrence, Kansas, 37 p.
- MacDonald, H. C., and Waite, W. P., 1971 Optimum radar depression angles for geological analysis, *Modern Geology*, v. 2; p. 179-193.
- MacCavley, J. R., 1973, Surface configuration as an explanation for lithology-related cross-polarized radar image anomalies, RSL Technical Report 177-36, University of Kansas Space Technology Laboratories, Lawrence, Kansas, 54 p.
- Sabins, F. F., Jr., 1978, *Remote sensing principles and interpretation*: W. H. Freeman and Co., San Francisco, California, 426 p.
- Schaber, G. C., Berlin, G. L., and Brown, W. E., Jr., 1976. Variation in surface roughness within Death Valley, California: Geologic evaluation of 25-cm-wavelength radar images: *Geological Society of America Bulletin*, v. 87, p. 29-41.
- Schaber, G. C., and Brown, W. E., Jr., 1972, Long-wavelength radar images of Northern Arizona - a geological evaluation, U.S. Geological Survey Professional Paper 800-B, p. B175-B181.

Sharp, R. P., 1966, Kelso Dunes, Mojave Desert, California, Geological Society of American Bulletin, v. 77, p. 1045-1074.

RADAR, AN OPTIMUM REMOTE-SENSING TOOL FOR DETAILED PLATE
TECTONIC ANALYSIS AND ITS APPLICATION TO HYDROCARBON
EXPLORATION (AN EXAMPLE IN IRIAN JAYA, INDONESIA.)

Claude M. Froidevaux
Phillips Petroleum Company
Bartlesville, Oklahoma 74004

ABSTRACT

**ORIGINAL CONTAINS
COLOR ILLUSTRATIONS**

In many parts of the planet, a general dynamic pattern of plate motion is accepted, but the geologic details of plate boundaries are not examined closely enough to be fitted into the scheme.

Radar images, because of their intermediate scale, geomorphic definition, and synoptic quality, appear to be optimum tools for detailed testing of the plate tectonics model. At the same time, the critical elements for the four-dimensional analysis of local or regional hydrocarbon history so essential in improving our predictability in exploration are provided. The method is the best available in areas of prevailing cloud and vegetal cover.

Radar was a useful tool in deciphering the evolution of the Salawati area, a province of oil-producing Miocene reefs located at the western extremity of Irian Jaya, Indonesia (Figures 1 and 2). The Salawati area lies in the complex area of interaction of four major crustal plates: the Pacific oceanic plate on the north, the Australian continental plate on the southeast, the Asian continental plate on the west, and the Indian oceanic plate on the southwest.

Geometric, geomorphic, and structural information derived from the examination of radar imagery and combined with geologic and geophysical evidences strongly indicates that Salawati Island was attached to the Irian Jaya mainland during the time of Miocene lower-Pliocene reef development, and that it was separated in middle Pliocene to Pleistocene time, opening the Sele Strait rift zone. The island moved 17.5 km southwestward after an initial counterclockwise rotation of 13°.

The rift zone is subsequent to the creation of the large left-lateral Sorong fault zone that is part of the transitional area separating the westward-moving Pacific plate from the relatively stable Australian plate. The motion was triggered during a widespread magmatic intrusion of the Sorong fault zone, when the basalt infiltrated a right-lateral fault system in the area of the present Sele Strait.

Rifting along three parallel major left-lateral strike-slip faults can be traced from the Sele Strait to the southern part of Salawati Island. The amount of relative displacement increases from the southeast fault to the northwest fault. These faults later become the site of important down-to-the northwest normal faulting to accommodate the subsidence resulting from the load of Pliocene-Pleistocene deposits derived from the high northern basaltic mountains.

Pliocene-Pleistocene diastrophism thus has defined several zones of varied structural character: the Sele Strait, the Irian Jaya mainland, Salawati Island, and their respective surroundings. An understanding of the dynamic character of the area was essential to successfully study hydrocarbon migration and accumulation:

- (1) When the paleogeography is restored to a predrift position, the distribution of oil-bearing Miocene reefs is different from the present arrangement.
- (2) The changing nature of structural unit boundaries implies that a given fault could have acted both as a barrier or an avenue for hydrocarbon migration at different times.

I. INTRODUCTION

The purpose of this presentation is to illustrate the important and useful role played by radar imagery in a comprehensive study of a prospective hydrocarbon-bearing province located within a complex area of crustal plate interaction.

II. POTENTIAL OF RADAR IMAGERY

The most useful ability of radar sensing is to emphasize morphology. This is illustrated by the example shown on Figures 3 to 5. Figure 3 is an enlargement of a portion of the radar mosaic represented on Figure 6. It shows the obvious presence of fish traps around elongated islets in the form of small white arrows. One of these structures is seen on Figure 4.

Figure 5 is a reproduction of an aerial photograph of the same area, showing a great abundance of detail hidden to radar sensing. Corals can be identified under several feet of water, the depth of the sea could be estimated from the change in color, and different species of trees are recognizable along the beach. But the fish traps remain very hard to detect. The same difficulty subsists even when comparing the original aerial photograph (scale 1:20,000) with the original radar mosaic (scale 1:100,000), which is 25 times smaller in area.

The morphologic characters enhanced by radar sensing are:

- (1) Shape. Radar imagery expresses clearly and objectively the outline of the land. Relationships of shapes provided the original intuition of the thesis developed in this study: mainly, that Salawati Island appears to have been detached by rifting from the mainland.

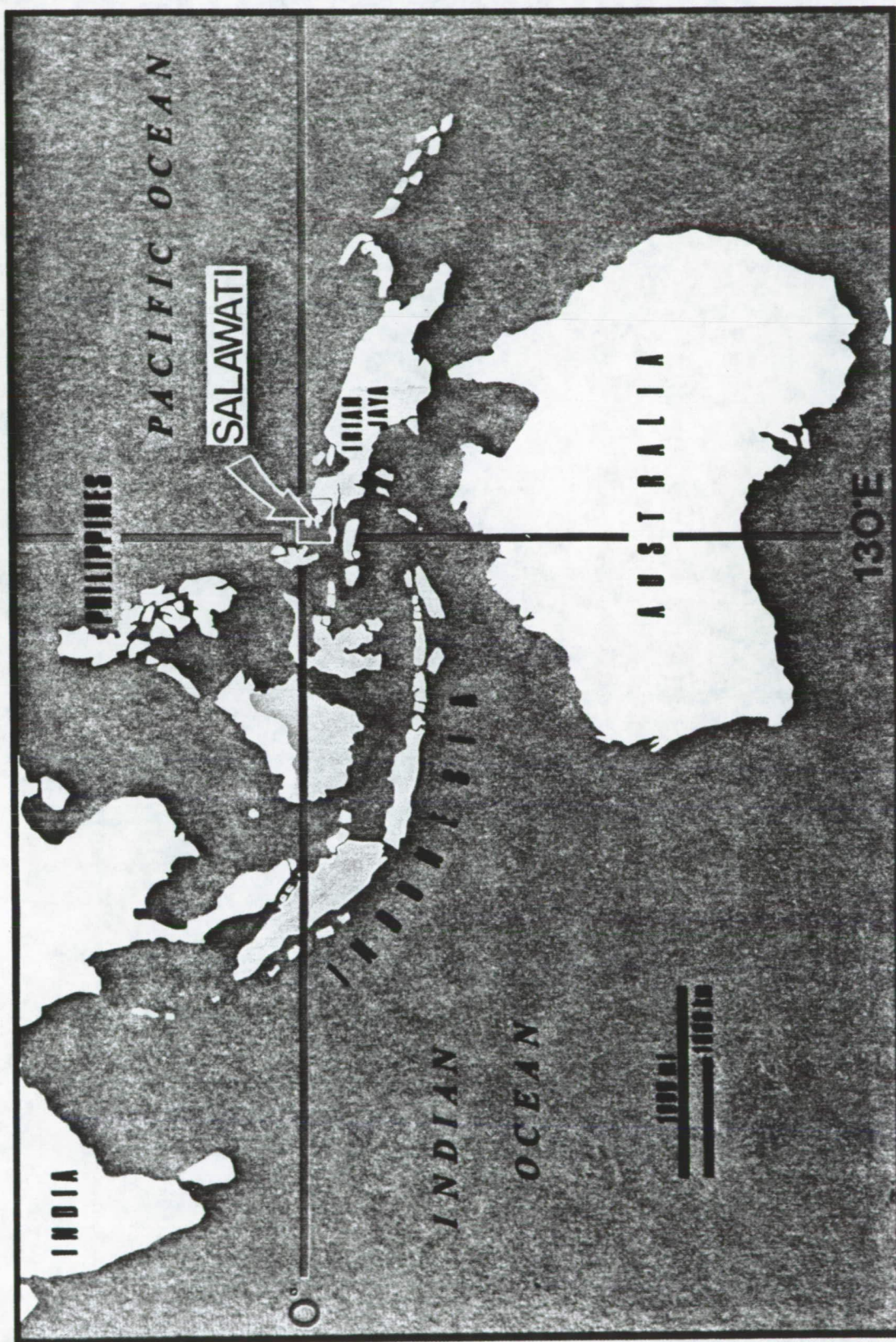


Figure 1. Location. The red rectangle represents the example area.

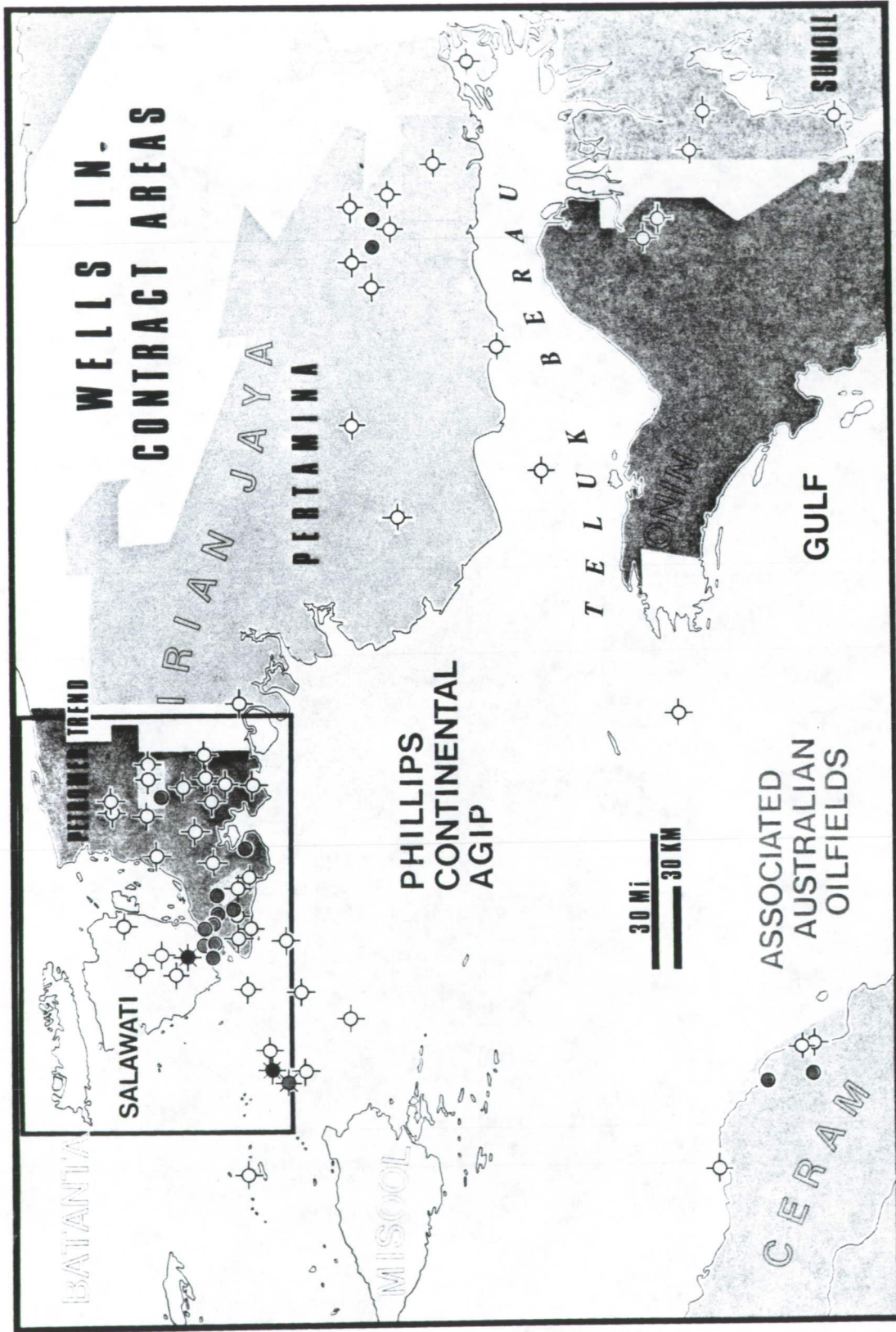


Figure 2. Hydrocarbon exploration in Western Irian Jaya, as of 1977. Salawati area is in rectangle.



Figure 3. Enlargement of the upper center part of radar mosaic, Figure 6, showing the sharp signature of fish traps as white arrows. South is on top.



Figure 4. Oblique aerial view of the same fish traps as shown in Figure 3.
View is to the South.



Figure 5. Aerial photograph of the elongated island shown in Figures 3 and 4. Fish traps are very hard to detect, although a much greater amount of detail is available on this picture than on the radar image.



Figure 6. Radar mosaic of the Salawati area, from a 1974 survey by Aero Service - Goodyear, flown in north-south strips with synthetic aperture. White bar represents 10 km.

- (2) Linears. Radar imagery enhances a large amount of linear features, such as coastline segments, textural change boundaries, and thin, contiguous shadow and bright zones, which cannot be seen easily in the field, but which can nevertheless be identified by analogy as faults, fractures and/or eroded fold ridges when compared to the relatively rare ground data. Radar linears can be assembled into comprehensive structural maps (two-dimensional), which can serve as excellent bases for three-dimensional geometric analysis substantiated by subsurface data.
- (3) Patterns. Arrangements of linears in patterns are clues to tectonic analysis (four-dimensional), because their geometric properties reflect the orientation of the stresses, and indirectly the forces, exerted on the deformed body of rock. The coexistence of different patterns in the same rock and at the same location implies successive tectonic events, and therefore calls for the analyst to decipher the geologic history of an area.
- (4) Texture. Texture is mostly useful in two-dimensional analysis (as is tone) for the making of geologic maps emphasizing lithology rather than structure. However, in some cases, a change in texture can be the expression of a fault (see Figure 7).

The following is an example of the application of Radar data analysis to detail plate tectonic study related to hydrocarbon exploration.

III. GENERAL TECTONIC SETTING OF SALAWATI AREA

The oil-producing Salawati area is located at the western extremity of the island of New Guinea. The main elements of the general tectonic framework are represented in Figure 8.

A. Sorong Fault Zone

The dominant tectonic feature of the Salawati area is the Sorong fault zone that comprises the northern part of the island. The fault is part of a large global transcurrent zone that can be traced from eastern Papua New Guinea to the vicinity of Celebes (Sulawesi). It separates the westward-moving Pacific oceanic plate from the relatively stable Australian continental plate. As a result, the Sorong fault is a left-lateral strike-slip fault zone. The exact amount of relative motion along this zone is unknown: Some workers (Hamilton, 1973) believe that it may be as much as 1000 km. This may be excessive, but the displacement probably is of the order of tens of miles at least. The fault zone is 8 to 13 km wide in the Salawati area, where mixtures of rocks of all kinds have been recognized in a disordered assemblage.

B. Tarera-Aiduna Fault Zone

This is a large-scale tectonic feature similar to the Sorong fault, but of lesser extent. It can be traced from the southern coast of Irian Jaya to possibly the south flank of Ceram Island. Left lateral motion was recognized early by Dutch geologists southeast of the Lengguru foldbelt. It was confirmed later, offshore on the west, by the study of seismic records. The horizontal displacement on this zone may be of the order of 60 km at the longitude of the



Figure 7. Radar image of the northern part of the Salawati Island showing: (1) the southern border of the Soron fault zone as to textural change from the coarse basalt signature on the north to the fine grain of the clastic sediments on the south, (2) ridges of eroded gravity folds that were derived from the northern elevated area. (Enlarged from radar mosaic of Figure 6).

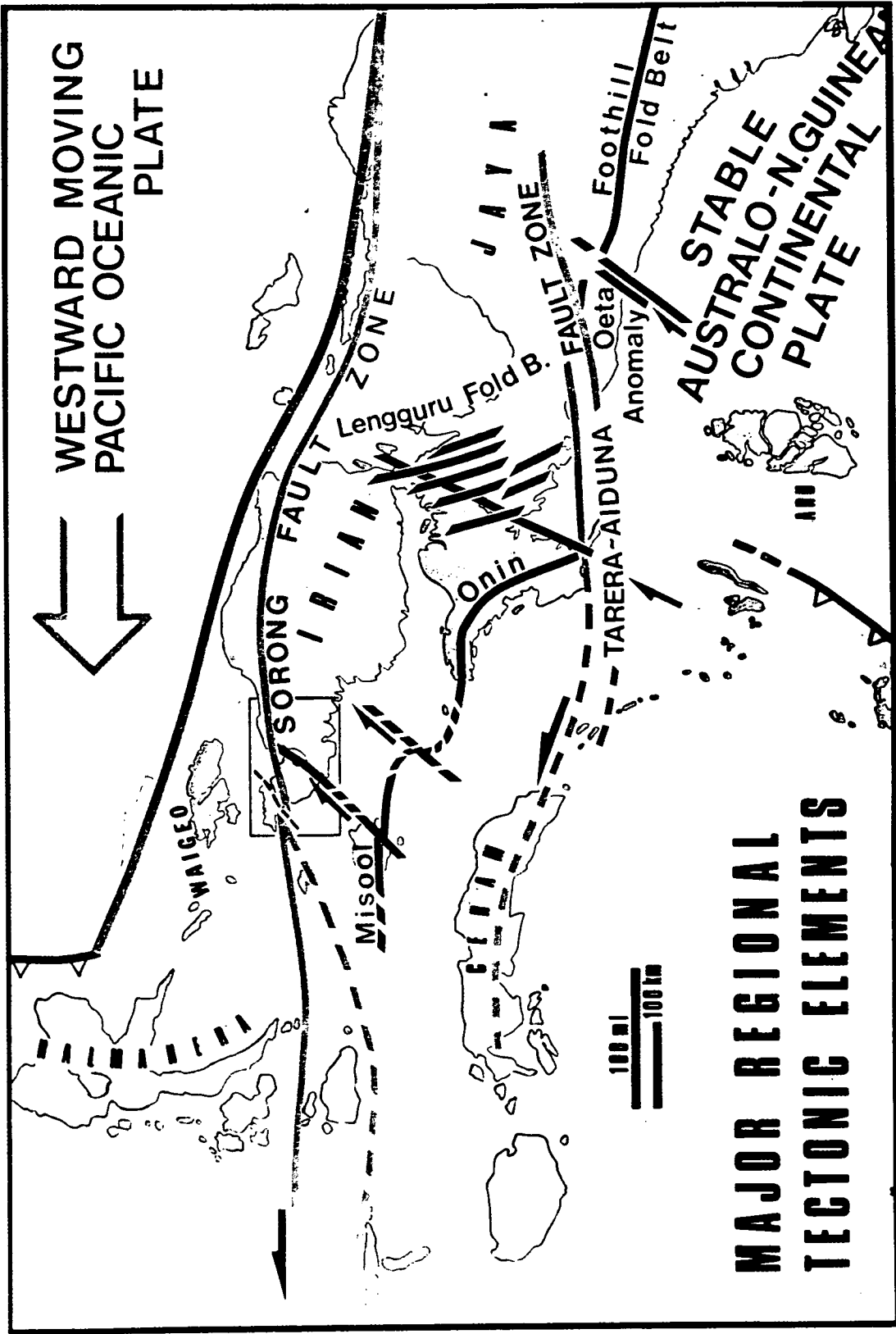


Figure 8. Irian Jaya is dominated by large E-W, left-lateral fault zones (blue) and associated right-lateral NE-SW faults (red). Salawati area is in red rectangle.

Salawati area, according to field observations made in southern Ceram on shifted drainage and offset outcrops of metamorphic rocks (Tjia, 1973).

C. Oblique Zones of Right-Lateral Motion

The two previously mentioned left-lateral fault zones delimit a broad area in which secondary large-scale features have been generated by coupling effect. They are the high-angle right-lateral motion zones expected in a left-lateral wrench system. From east to west these features are the Oeta anomaly, Lengguru foldbelt, Misool-Onin anticlinorium flexure, and Sel Strait-Misool fault.

1. Oeta Anomaly. This zone was recognized as a longitudinal high in early New Guinea gravimetric exploration (Visser and Hermes, 1962). The Oeta feature is a folded structure on the west side of a steep west-dipping, right-lateral fault that borders the anomaly. The fold is the result of upthrust drag along the fault which is the probable cause of the anomaly. The effect of both the fold and fault can be seen at the intersection of the Oeta anomaly with the foothill foldbelt: the other east-west trending fold system (related to the time of southward subduction of the Pacific plate) was bent right laterally by the fault. The Triassic anticlinal core at the intersection assumed a domal shape as a result of superposition of the younger Oeta upthrust fold, which is related to the time of westward motion of the Pacific plate (Figure 8).

2. Lengguru Foldbelt. This is a right-lateral bend of the generally east-west-trending New Guinea mountain system. The folds have been reoriented into a typical right-lateral en echelon pattern. The direction of faulting is outlined by a long and narrow bay.

3. Misool-Onin Anticlinorium Flexure. The eastern end of Misool Island is a mirror image of the western end of the Onin Peninsula. Both terminate as four narrow plunging anticlines, strongly indicating that they belong to the same folded ridge. However, the opposite plunging directions are not oriented exactly toward each other and suggest, rather, that the ridge is displaced right-laterally somewhere under the sea.

4. Sele Strait-Misool Fault. The Sele Strait longitudinal axis is aligned with a right-lateral fault that shaped the straight east coast of Misool Island, which can be seen on radar imagery offsetting the prominent ridge of Eocene limestone of the north flank of the anticlinorium (Figure 9).

IV. STRUCTURAL ANALYSIS BASED ON RADAR IMAGERY

A. Radar Survey

The study area was surveyed in 1974 by Goodyear-Aero Service in north-south flight strips, using a synthetic aperture radar. A copy of a semicontrolled mosaic is represented on Figure 6. The geomorphologic emphasis of this radar picture can be appreciated by comparison with the best false color Landsat image of the same area (Figure 10), which mainly reflects healthy vegetation (red) and cloud cover, two characters of little use for our study.

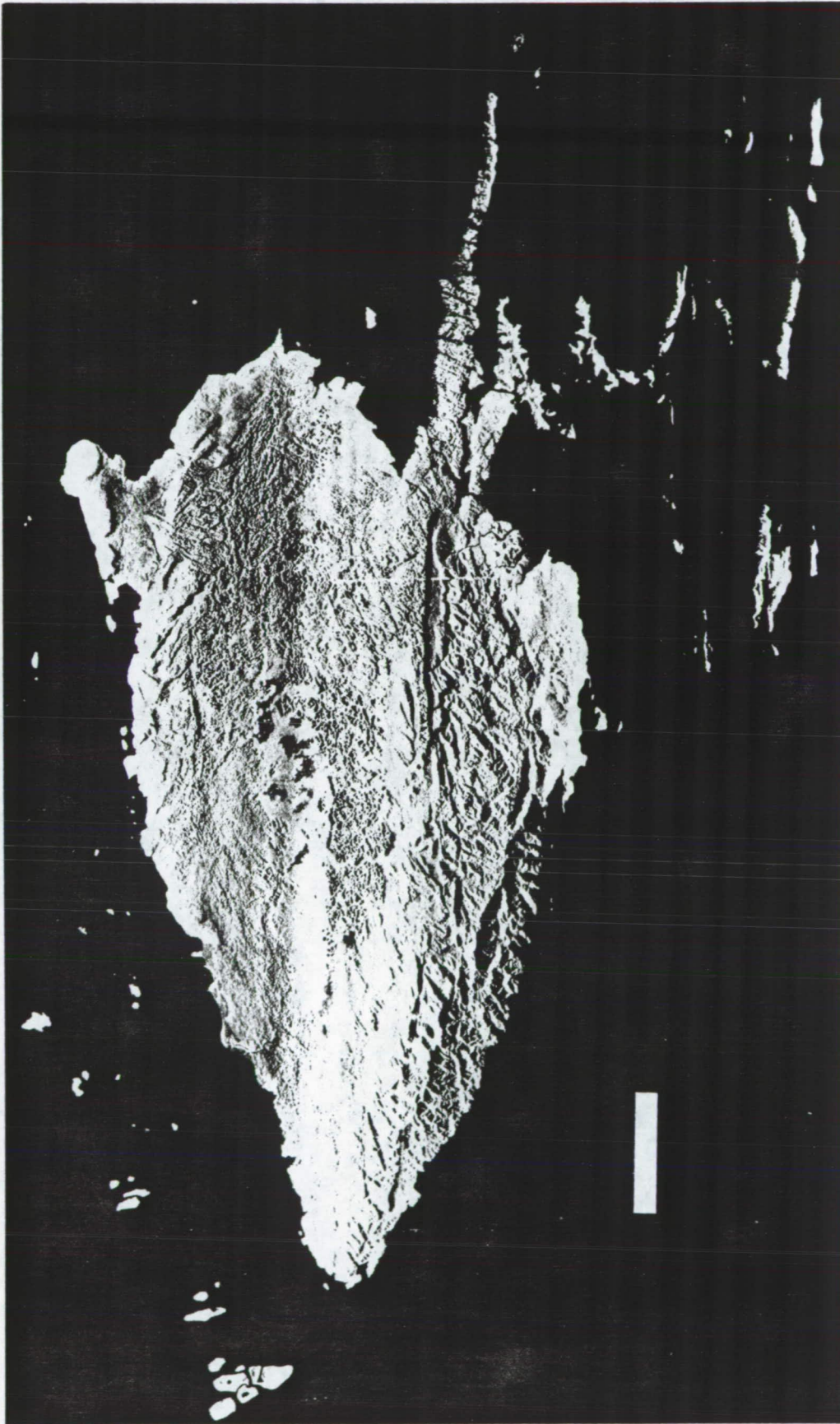


Figure 9. Radar image of Misool Island. North is at the top. A SW-NE trending, right-lateral fault, visibly offsetting the Eocene limestone on the east coast, is in line with the Sele Strait that separates Salawati Island from the mainland (see Figures 8 and 14 for location). The coexistence of elevated Pleistocene reefs in the northwestern islets, with drowned karst in the southeast (expressed by jagged coastlines) suggests a recent east southeastward tilting of Misool Island (see Recent Tectonics). White bar represents 10 km.



Figure 10. Color additive Landsat image of the same area as shown in Figure 6. Two unwanted characters are emphasized: A healthy vegetation (red) and cloud cover. White bar represents 10 km.

B. Shape

A glance at the radar mosaic of the Salawati area (Figure 6), which is the best cartographic unbiased expression of its land shapes, suggests that Salawati Island was detached from the Irian Jaya mainland and drifted away, opening the gap of the Sele Strait. Furthermore, if the island is placed in its proposed original position, the northern elevated area will fit perfectly between the mountainous Batanta Island and the high coastal ridge of the mainland. The Sele Strait will be closed almost completely by its islets. Warir Island (see Figure 11) is, however, too big to be enclosed completely between the two present shores, and the northwest corner of Salawati corresponds almost exactly to the eastern bay of Batanta, although the closing southern part of the bay seems to be in the way (Figure 12). These three spatial problems can be solved when considering data from surface geology (see below).

C. Linears and Patterns

Linears and patterns derived from radar imagery are represented on Figure 13.

1. Sorong Fault System. The southern edge of the fault zone (blue line) roughly parallels the southern foot of the basaltic mountains of the mainland and Salawati. On the west, a modification of the current interpretation is proposed. The fault trace can be carried from the Kofiau Island (Figure 14) area to the deep channel located just south of Batanta Island, instead of being traced directly to Salawati. This interpretation is supported by both seismic and geomorphologic data (see below). The Batanta part of the fault trace is believed to end near the eastern extremity of the island, at the contact of the basalt and clastic rocks, by an offsetting fault. The basic geometric elements of the Sorong fault zone are an approximate east-west direction and left-lateral strike-slip motion, with a dynamic compartment on the north side (related to the Pacific plate), and a relatively static compartment on the south side (related to the Australian-New Guinean plate).

The direction of the fault must be measured on the fixed mainland block, where it is about N80 to 85°E. (The trace of the fault on Salawati assumed a more southwesterly direction after rotation of the island.)

2. Sele Strait Fault System. The original direction of the fault (red line) is probably roughly parallel with the stable east side of the strait, making an angle of about 60° with the Sorong fault, which corresponds to the theoretical direction of an antithetic set of strike-slip faults in a left-lateral wrench system. This possibility is corroborated by the Sele Strait gap being aligned with the right-lateral fault of eastern Misool (Figure 14).

a. Strain Ellipsoid. The hypothesis that the Sele Strait was initially a right-lateral system can be checked by a study of its internal geometric properties, which can be measured directly on radar imagery (Figure 11). The geometric elements are plotted on Figure 13. A right-lateral fault should have developed a conjugate set with approximately the same angular relations as the one initiated by the Sorong fault, because the rock material is the same. This is exactly what can be seen in the group of islands on the south side of the Sele Strait near the mainland (green lines). The trapezoidal shape of several islets is modeled after a conjugate set of fractures related to the main

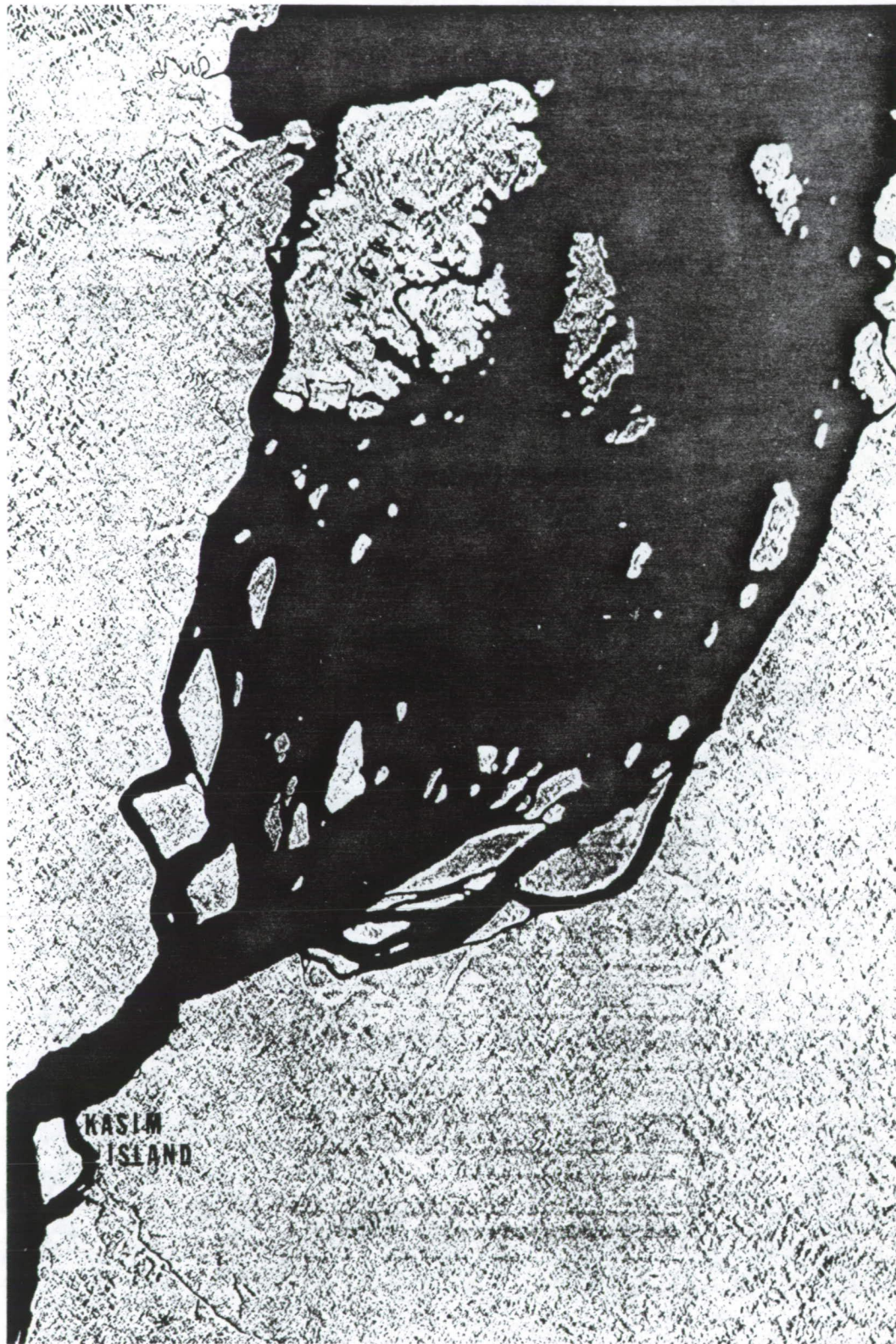


Figure 11. Enlargement of a portion of the radar mosaic of Figure 6, showing the sharply defined shapes of the islets in Sele Strait, used in structural analysis for the construction of strain ellipsoids (see Figures 13 and 24). North is on top.

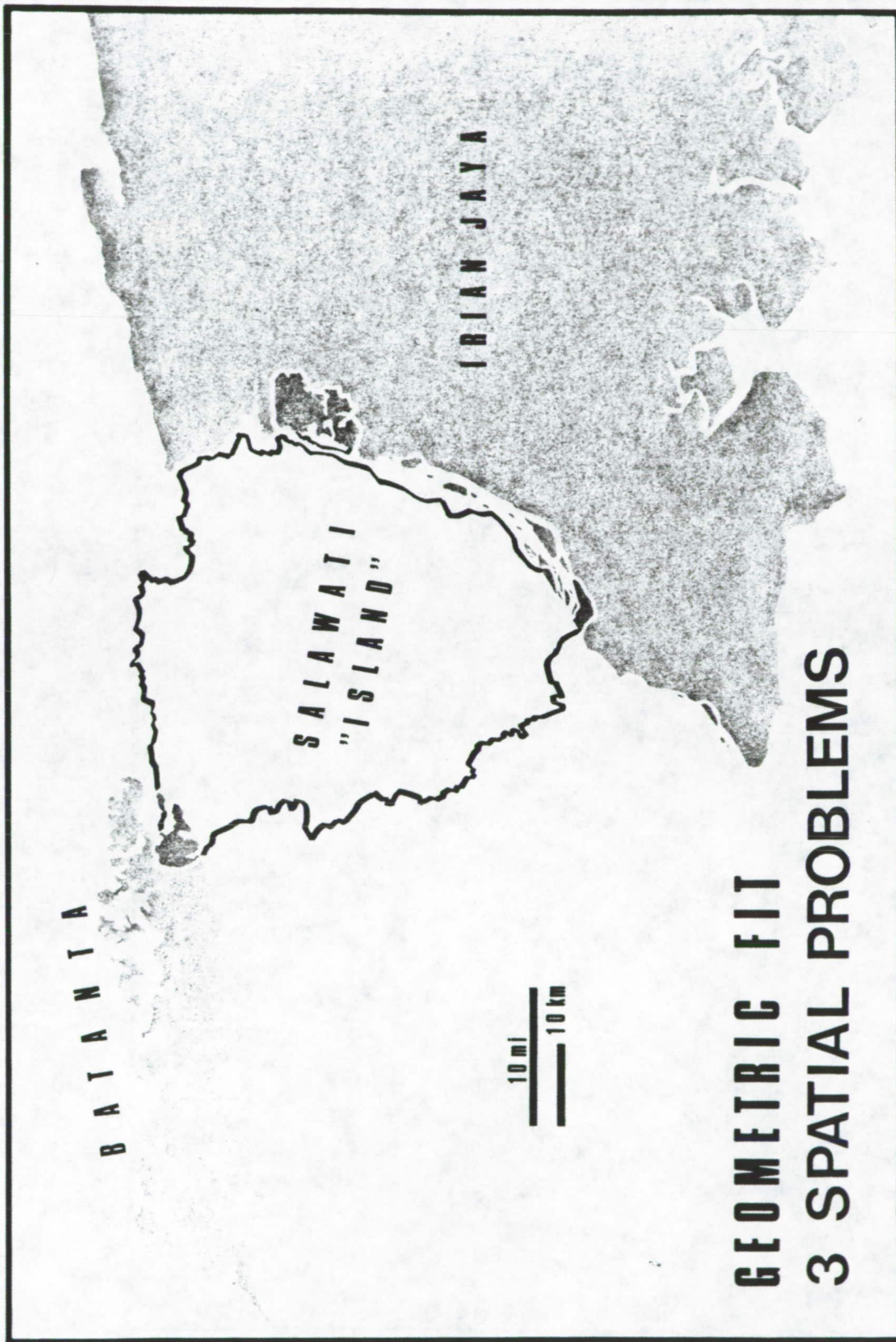


Figure 12. When the Salawati block is placed back in its alleged original position, three areas overlap the surrounding lands (red). These spatial problems can be solved when considering geological data (see Figure 15).

ORIGINAL PAGE IS
OF POOR QUALITY

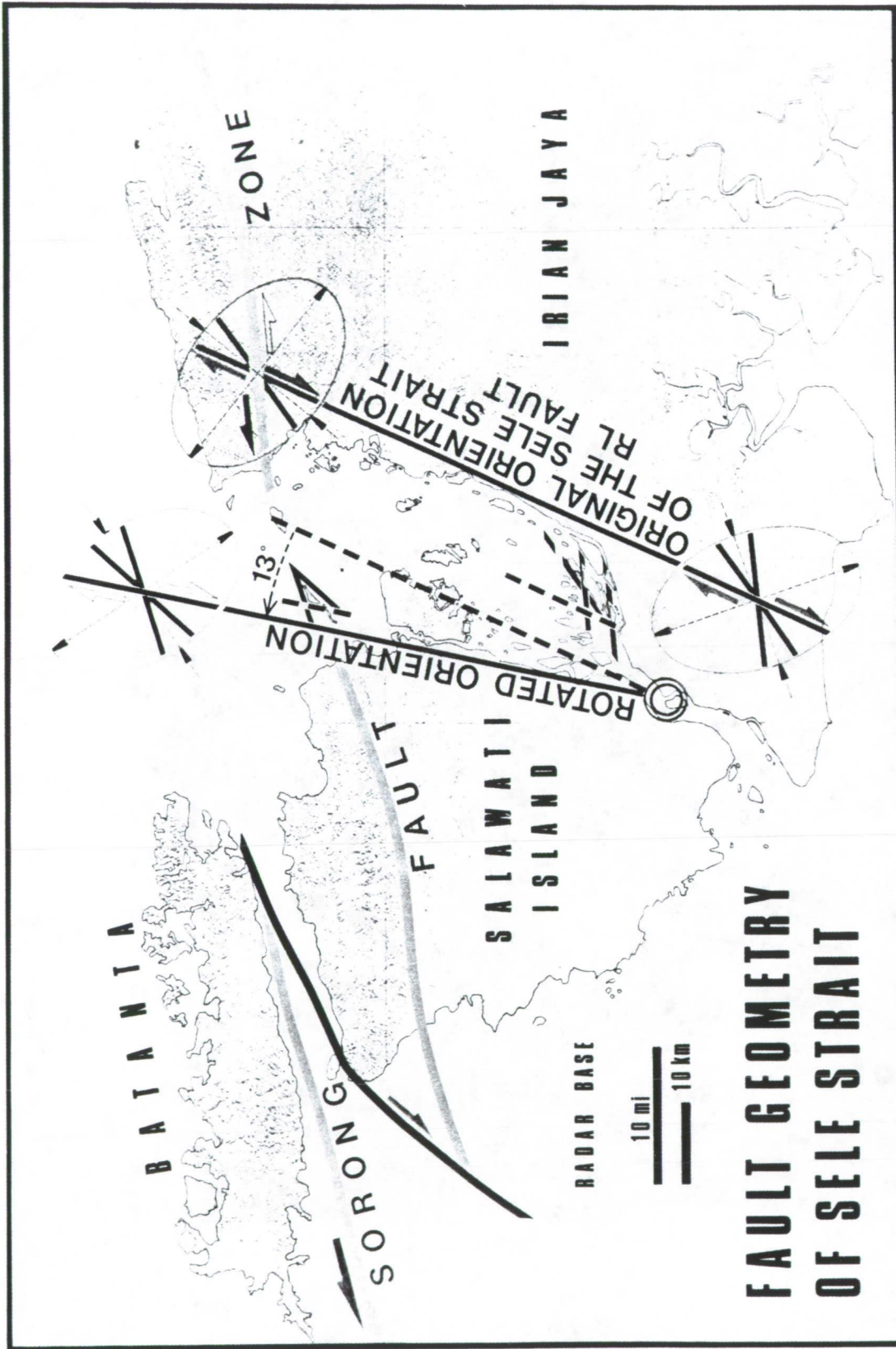


Figure 13. Rectilinear west coast of strait appears to be rotated 13° CCW with respect to east coast. Orientation of east coast corresponds to that of antithetic right-lateral fault in conjugate set (red) defined by left-lateral system of Sorong fault (blue). Orientation of fracture-controlled shape (green) of Sele Strait islets corresponds to the expected conjugate set of the right-lateral system of the strait. Furthermore, it is also rotated 13° CCW on the Salawati side (upper center).

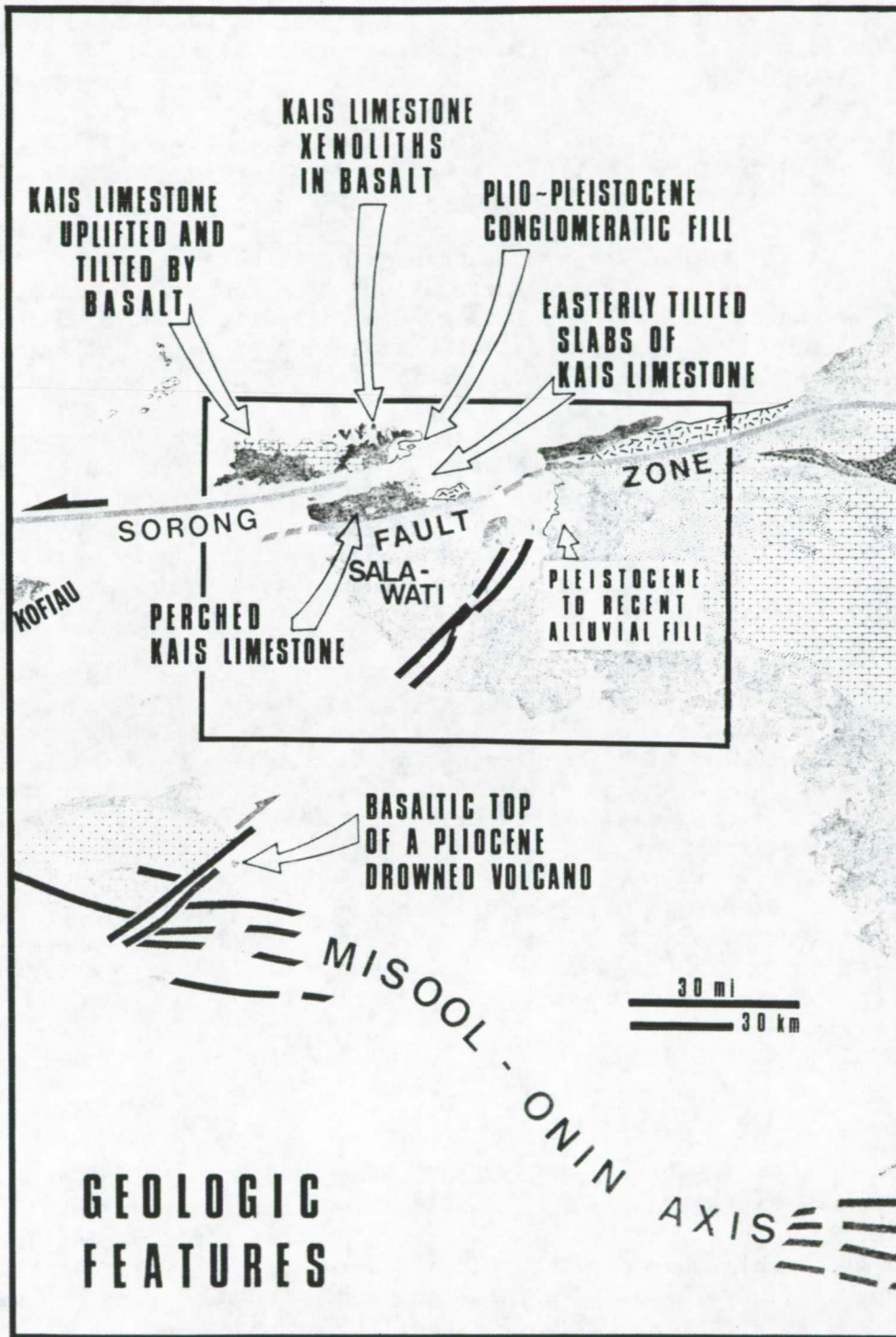


Figure 14. The right-lateral fault of Misool (red) is in line with the Sele Strait, that separates Salawati Island from the mainland. Red rectangle corresponds to Salawati area of Figures 10 and 11. Dark green = basalt, red = granite, patterned white = tectonic breccia, brown and yellow = Plio-Pleistocene, patterned blue = Eocene - Oligocene, pale green = Mesozoic, dark blue = Paleozoic.

direction of right-lateral faulting of the Sele Strait. The ellipsoid thus defined has the same geometric properties as the one along the Sorong fault, but in reverse, because here the main axis of wrenching is right-lateral. The high-angle conjugate set amounts also to 60° .

b. Rotation. On the west side of the Sele Strait, the conjugate set of fractures is the same, but it appears to have been rotated counterclockwise. The east coast of Salawati Island can be taken as a reference for the rotated direction of the Sele Strait right-lateral fault. The strain ellipsoid is outlined at Warir Island, where the north coast is parallel with the high-angle conjugate set, also making an angle of 60° with the narrow straight channel that separates Warir from Salawati. The airstrip islet of Jefman (Figures 3 to 5), which underwent the greatest amount of rotation, is shaped according to the elements of the strain ellipsoid, rotated 13° counterclockwise.

The counterclockwise rotation indicated by the study of the strain ellipsoid can be checked by other means. A reference line can be chosen and traced between two points on Salawati Island. Its measured direction can be compared to the direction of the same line in the initial prerotated position of the block. It is preferable to pick two points that are easily recognizable such as the southwest tip and northeast corner of the island. The method shows a counterclockwise angle of rotation of 13° also.

c. Translation. Rotation alone can account for a large part of the opening of Sele Strait but is not sufficient to explain the present position of Salawati Island. A comparison of the position of the island after its 13° counterclockwise rotation with its present location indicates a subsequent southwestward translation of the block of 17.5 km. This translation was measured by comparing pairs of displaced points picked on the island in their position before and after translation.

It should be noted that the "translation" is in the strict sense also a rotation because any displacement on the spherical surface of the earth can only be described as such. In the present case, the arc of 17.5 km corresponds to a rotation of less than 10 minutes along a great circle.

V. TESTING OF RIFT HYPOTHESIS

A. Data from Surface Geology

A look at the geology (Figure 14) confirms the alleged fit of the Salawati block in its former mainland frame, and even allows for a better match (Figure 15). The distribution of the geologic elements becomes simpler. All the mountains appear as a continuous basaltic ridge (characterized by a coarse texture on radar imagery, Figure 6) parallel and contiguous to the Sorong fault. Some granite outcrops in northeast Salawati match similar exposures near the northwest corner of the mainland.

The spatial problems raised by the northwest corner of Salawati and the Island of Warir are easily explained. The islet in the bay of eastern Batanta and the promontories closing the bay on its south side are made of an accumulation of coarse Pliocene to Pleistocene conglomerates containing mostly limestone and basaltic boulders. Once this young mass of rock is removed, it leaves a larger gap that can accommodate the northwest corner of Salawati almost perfectly.

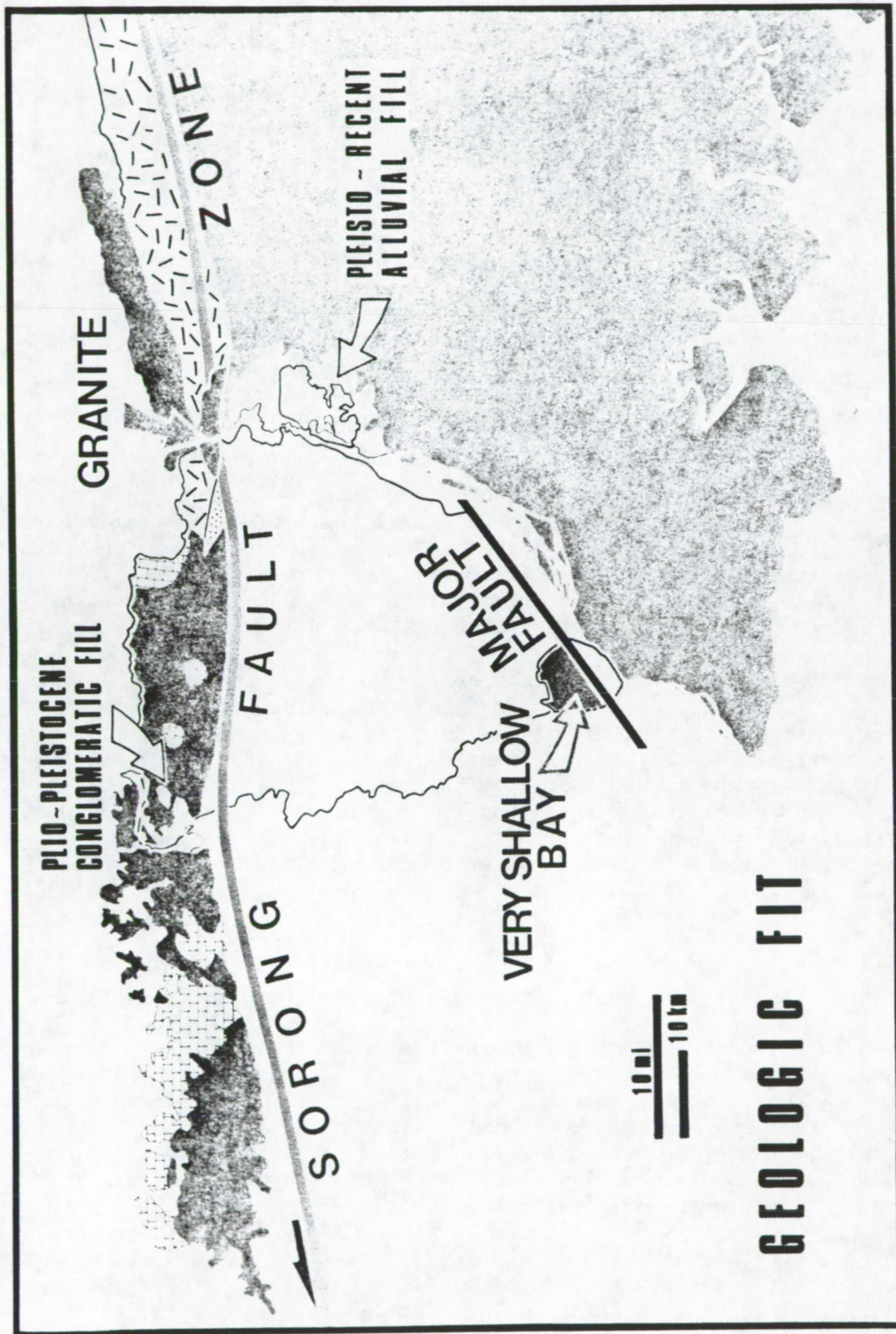


Figure 15. The NW and SE geometric overlaps coincide with areas of deposits younger than the time of rifting. The southern tip of Salawati can be slipped along a known major fault to provide a perfect geometric fit. Good geologic fit is further emphasized by the linear arrangement of the basalt (green) and the matching of granite outcrops (red).

ORIGINAL PAGE IS
OF POOR QUALITY

Just across the Sele Strait from Warir Island, the mainland rivers have filled a gap on the coast with Pleistocene alluvial deposits. The outline of the coastal alluvial plain corresponds to the shape of the drifted island.

If the south tip of Salawati is moved southwestward along a known major fault (Figure 15), so that its present shallow bay shore becomes aligned with the west coast of Salawati, the block closes the Sele gap with the best possible fit. In that position, the present south tip of Salawati Island would adjoin the north end of Kasim Island (Figure 11).

B. More Data from Radar

In western Irian Jaya, the eastern exposures of Miocene limestone (Figure 14) clearly display on radar imagery a conjugate set of fractures, enhanced by karstic solution (Figure 16). The two systems intersect at approximately 60° , symmetrically with respect to a meridian. This arrangement is typical of a north-south compressional stress field, and thus suggests its relation to an ancestral tectonic model developed at the time of the birth of New Guinea, when the Pacific plate was being subducted southward under the Australian continental plate.

The stream pattern in the lower land of Pleistocene to recent exposures west of the Miocene limestone outcrops geometrically resembles the fracture system (Figure 17). The coincidence of the old fracture system with the present drainage pattern suggests that western Irian Jaya has remained tectonically quiet for a long time, probably since its creation, and supports the interpretation that the area was a relatively fixed block when Salawati was rifting away.

On Salawati, where no limestone rocks crop out, there is no clear surface expression of the fracture pattern. The most obvious geomorphic features related to structure in Salawati are anticlinal ridges carved in Pliocene-Pleistocene sandstones that were folded at a later stage of the deformation. The folds seem to have been formed by gravity sliding from the northern high mountains. They are confined to and parallel with the mountain front, asymmetric to the south, partly thrust, shallow, and abut against the first major normal fault in the central part of the island. Their signature on radar imagery is outstanding (Figures 6 and 7).

C. Data from Seismic

Figure 18 represents the fault patterns interpreted from seismic data.

The subsurface fault pattern of western Irian Jaya (Redmond and Koesoemadinata, 1977) presents the same geometric arrangement as the pattern exposed at the surface on radar imagery (Figure 16). The fractures are distributed in the same two prevailing directions 30° apart from a meridian. The same properties apply to the area south offshore. This general compatibility is an expected condition for a structurally stable area where no drastic tectonic event occurred to disturb the original configuration.

The faults mapped at the level of the granite basement in Salawati Island show a pattern slightly different from the mainland, with more right-angle fault intersections. This angular relation may be a reflection (and is typical) of the original tensional fractures developed during the cooling period of an intrusion, especially since the characteristic is confined largely to the older faults.

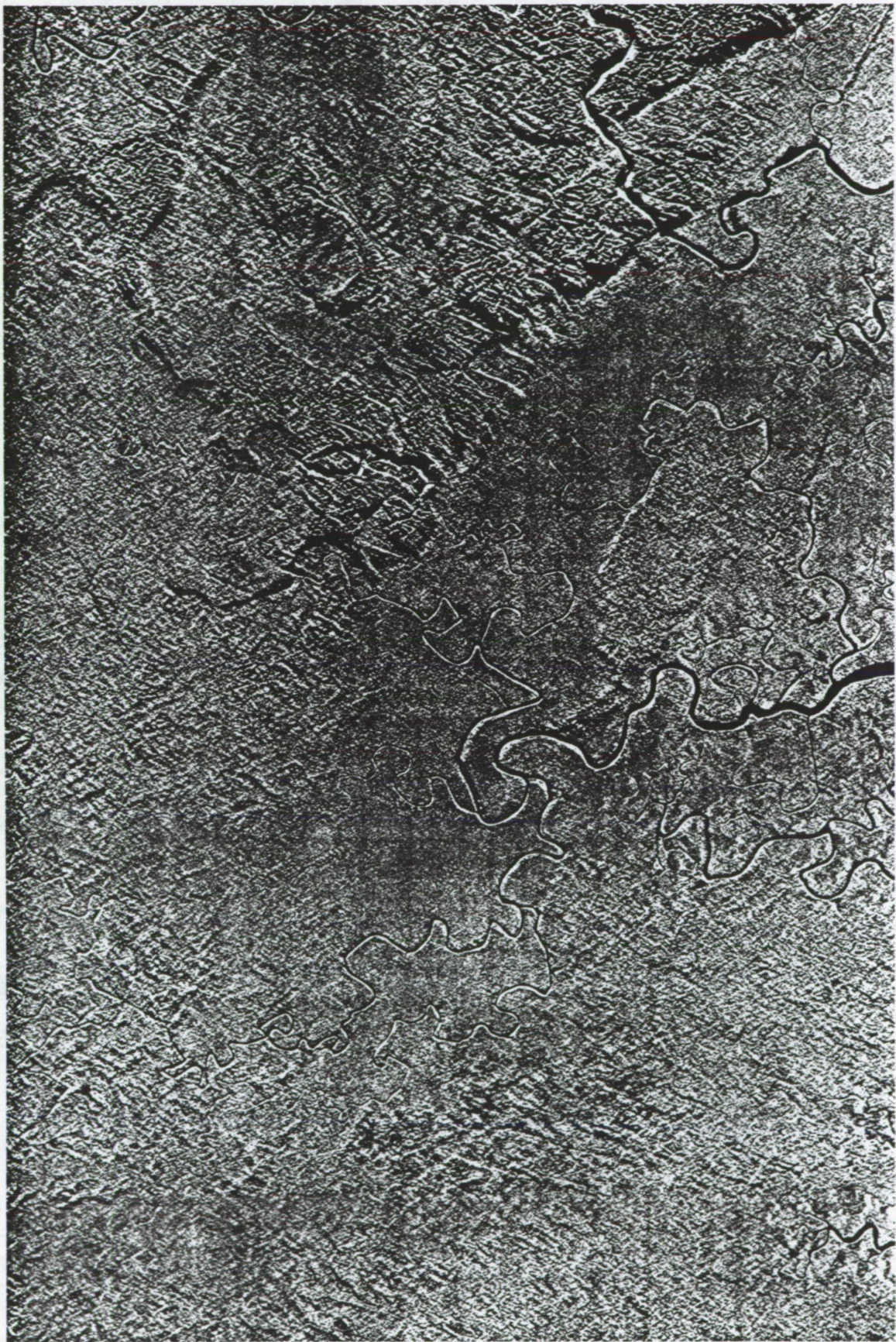


Figure 16. Enlargement of the SE portion of the radar mosaic of Figure 6, showing fracture and river patterns in the mainland, used in the construction of Figure 17. North is on top.

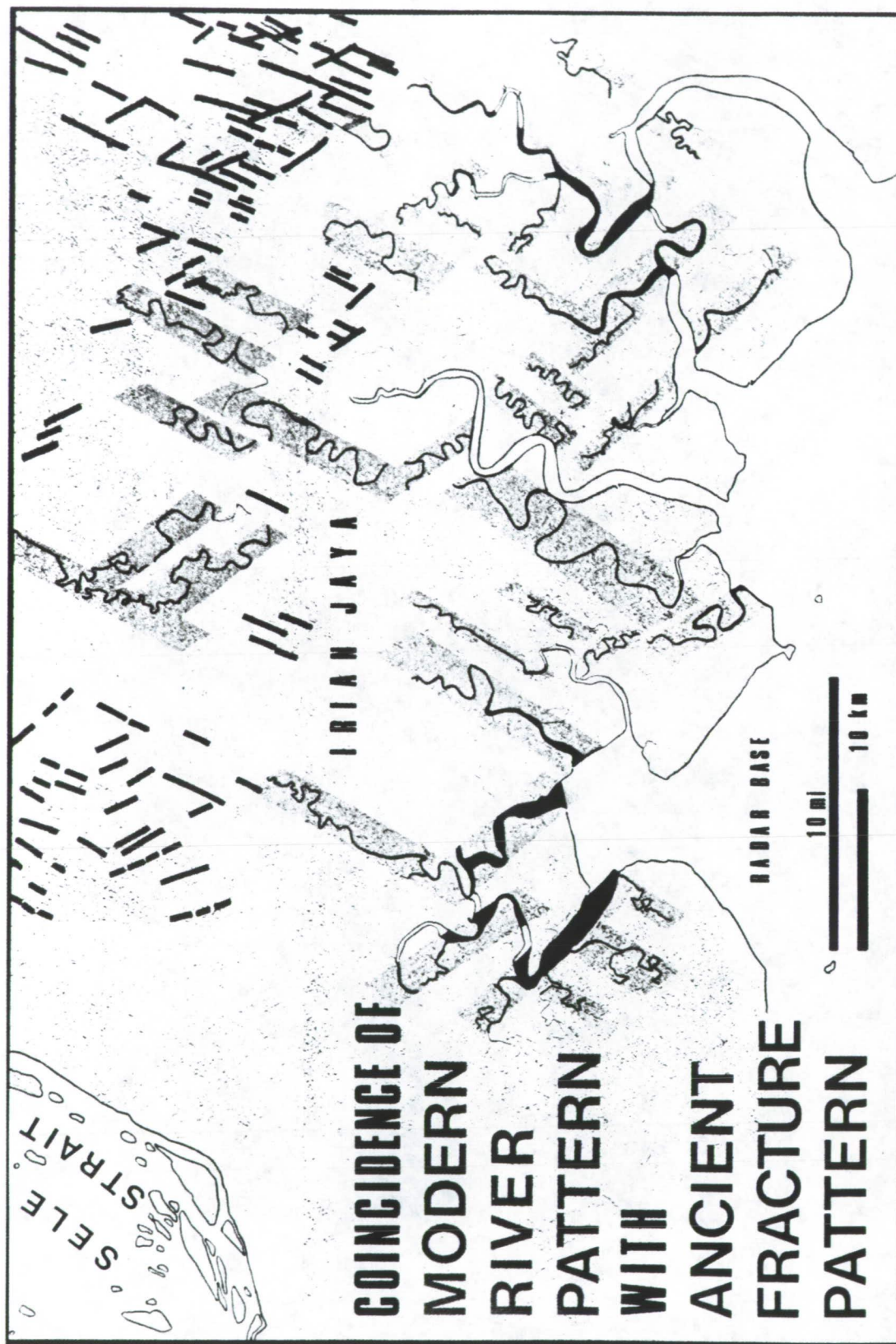


Figure 17. Coincidence of modern drainage pattern with ancient fracture pattern in the mainland suggests that this area remained tectonically stable during rifting of Salawati Island. Radar patterns are shown on Figure 16. North is on top.

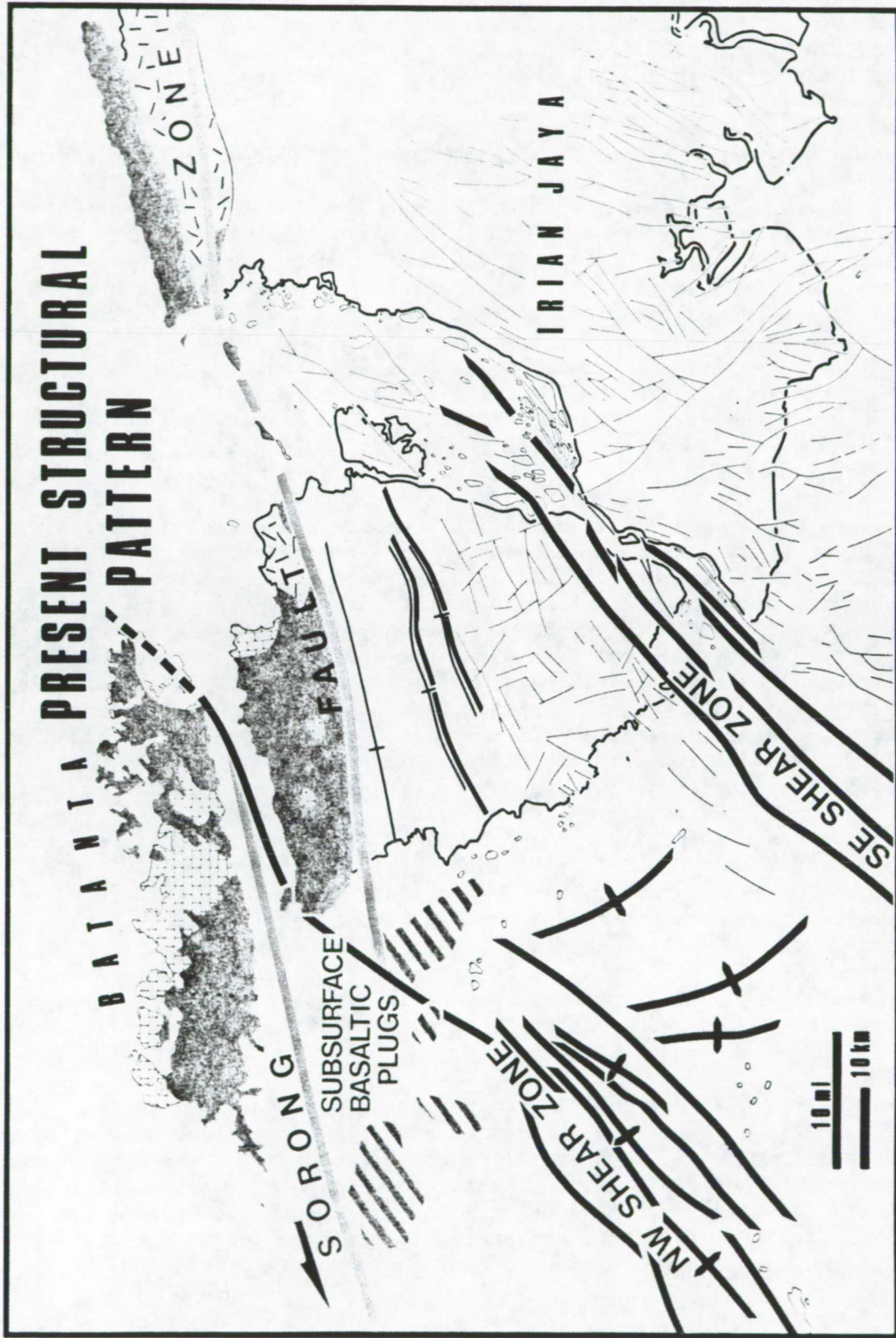


Figure 18. Fault patterns derived from seismic data. Two shear zones (red) bound the moving island. Expected compressional folds are present between them in front of the block. Other folds are located within the NW shear zone and are oriented in contradiction to the compression due to the block motion. Their possible origin is explained on Figure 19.

Offshore Salawati Island, from the southern entrance of the Sele Strait toward the direction of eastern Misool Island, a series of seismic discontinuities can be mapped as a set of parallel, southwest trending faults. They are interpreted as the southeast left-lateral shear zone that bounded the Salawati block during rifting. No evidence of compression is present along this zone outside Sele Strait.

Offshore, northwest of Salawati, a major zone of disturbance extends from the eastern end of Batanta Island, southwestward through the bordering strait and beyond to the vicinity of Misool Island. This zone, called the northwest shear zone, originated during the drift as a right-lateral system with a maximum relative displacement of about 30 km near Batanta (larger than on the southeast shear zone because of the additional greater effect of the initial counterclockwise rotation of the Salawati block).

The area offshore Salawati Island on the southwest, between the two shear zones described previously, was the logical place for compressional strain to have developed under the effect of the drifting block. Gravity and seismic work suggests that the edge of the underlying central Salawati granite mass corresponds approximately to the west coast of Salawati. The expected effect of a moving rigid block is to induce folding and/or thrusting in the softer material in front of it, perpendicular to its motion. The detected pattern, however, is not so simple. Only a few monoclinial flexures and large but low-amplitude folds, with axes approximately parallel with the front edge of Salawati Island, can be interpreted in the relatively undisturbed offshore area bounded by the two shear zones. The alignment of islets parallel with the west coast of Salawati suggests a geomorphic relation with this deformation. These folds seem more intense toward the north. This phenomenon may be caused by the increasing amount of displacement in the north compared to that in the south owing to the initial counterclockwise rotation and distance away from the center of rotation at Kasim Island. Most of the compressional strain can be seen clearly along the bounding northwest shear zone. The faults themselves indicate evidence of thrusting between slightly folded sheets. This apparently contradictory orientation of the folds can be explained by the combined effect of the shear zone and the push exerted by the moving Salawati block. Folds may have been initiated along the shear zone as drag folds which, at an incipient stage, would have been oriented more nearly diagonal to the shear zone, and also more nearly parallel with the western edge of the Salawati block (Figure 19). Once started, the folds would have defined the weak area, where further strain could develop. Then, under continuous coupling effect, they would progressively arrange themselves more nearly parallel with the shear zone, finally to assume their present orientation.

The stress field also was complicated by vertical intrusions near the northern outside edge of the shear zone. They are probably of volcanic nature, as suggested by their proximity to the basaltic source. These intrusions may have overshadowed in part the effect of compression related to the southwestward movement of Salawati Island by introducing a southeast stress component into the deformation. Thus, tectonic features detected in the extended vicinity of Salawati Island appear to be in harmony with the hypothesis of rifting.

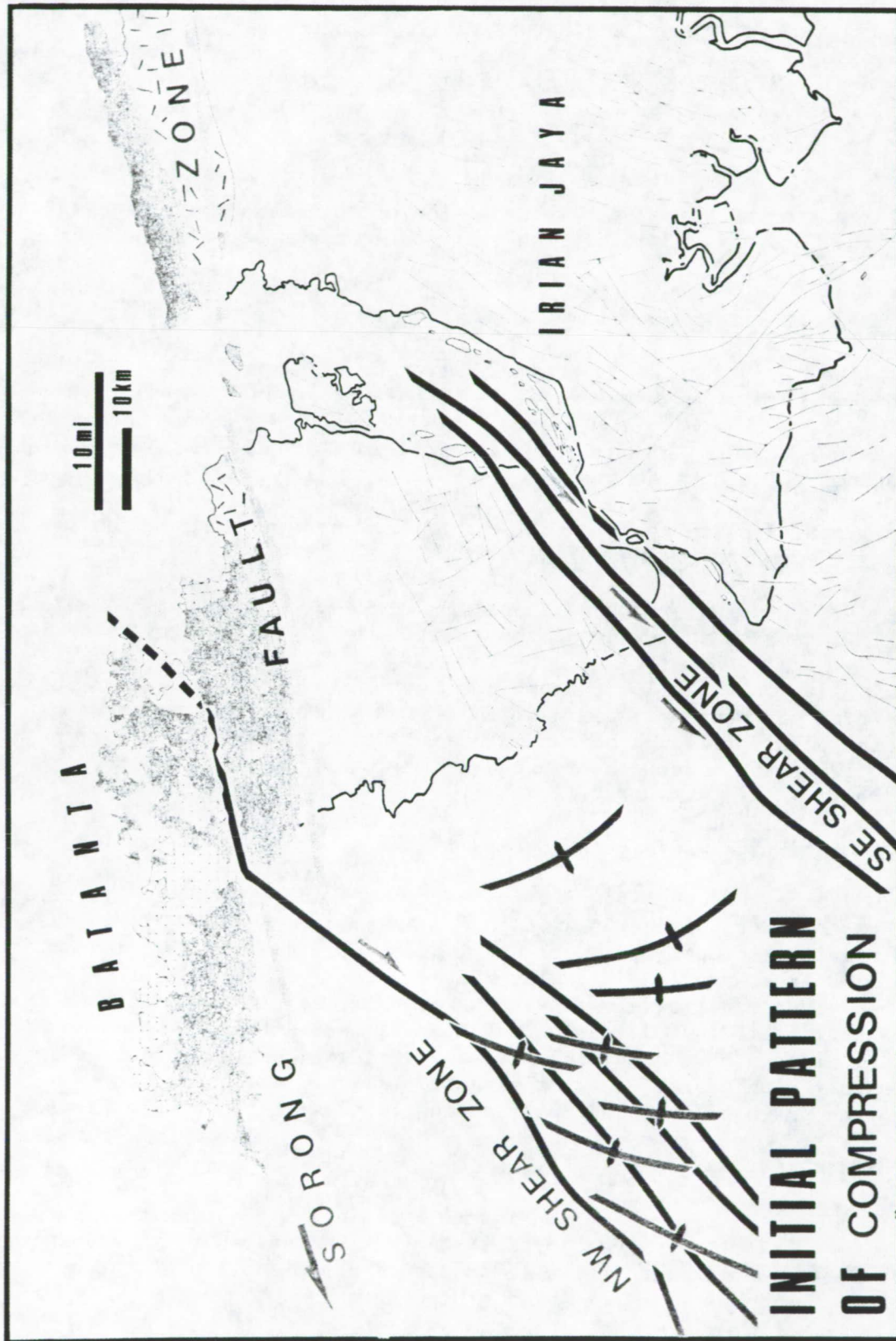


Figure 19. The folds located within the NW shear zone may have been echelon folds at an earlier tectonic stage, oriented more in harmony with the compressional direction of the moving block. Further shearing stretched them parallel to the shear zone.

D. Data from Gravimetry

Four areas of high positive Bouguer anomalies (Figure 20) were recognized by early Dutch surveys (Visser and Hermes, 1962). In decreasing order of magnitude, they are (1) a bulging nose in the northern part of Sele Strait plunging southward along the axis of the strait, (2) a high centered around the Kalamono oil field, (3) the Sele dome centered around the Sele-Walio oil fields, and (4) the significantly lower Salawati dome centered near the middle part of Salawati Island.

The largest anomaly may be the expression of the basalt intrusion into the strait from the Sorong fault zone. The other three highs seems to be related to the shape of the granitic basement.

E. Data from Submarine Morphology

The morphology of the sea bottom illustrated on Figure 21 provides several elements in good harmony with the geometry of our rift model:

- (1) A 300-ft (90 m) break in slope coinciding with the northwest shear zone detected by seismic.
- (2) Two parallel furrows in the Sele Strait corresponding to fault traces of the southeast shear zone.
- (3) A deep underwater channel bordering the edge of a very shallow shelf in line with the trace of the major fault of the strait.
- (4) A relatively shallow bottom in the northern part of the Sele Strait, which can best be explained by basaltic invasion. If it were not for the basalt filling, one would expect the strait to be deeper in the north than in the south, because of a larger amount of rift displacement.

VI. CHRONOLOGY OF TERTIARY TECTONIC EVENTS

The coherence and consistency of geometric properties and dynamic relation in the fracture pattern of the Salawati area, as seen on radar imagery, suggest that the present structural framework was initiated by the major westward motion of the Pacific plate, expressed locally by the left-lateral Sorong fault zone. Successive events are relatively easy to trace from the time of incipient motion along the Sorong fault zone. Previous events are more difficult to decipher because their effects have been obliterated by the younger large-scale diastrophism. A stratigraphic sketch summarizing the geologic evolution of the Salawati area before the phase of major normal faulting is represented on Figure 22.

A. Pre-Miocene Tertiary

We know from well records and radioactive dating that a granite was emplaced, probably in Late Cretaceous time, in the Salawati area and that its sedimentary cover was uplifted and eroded until almost mature peneplanation of the granite surface before the invasion of the middle Miocene sea.

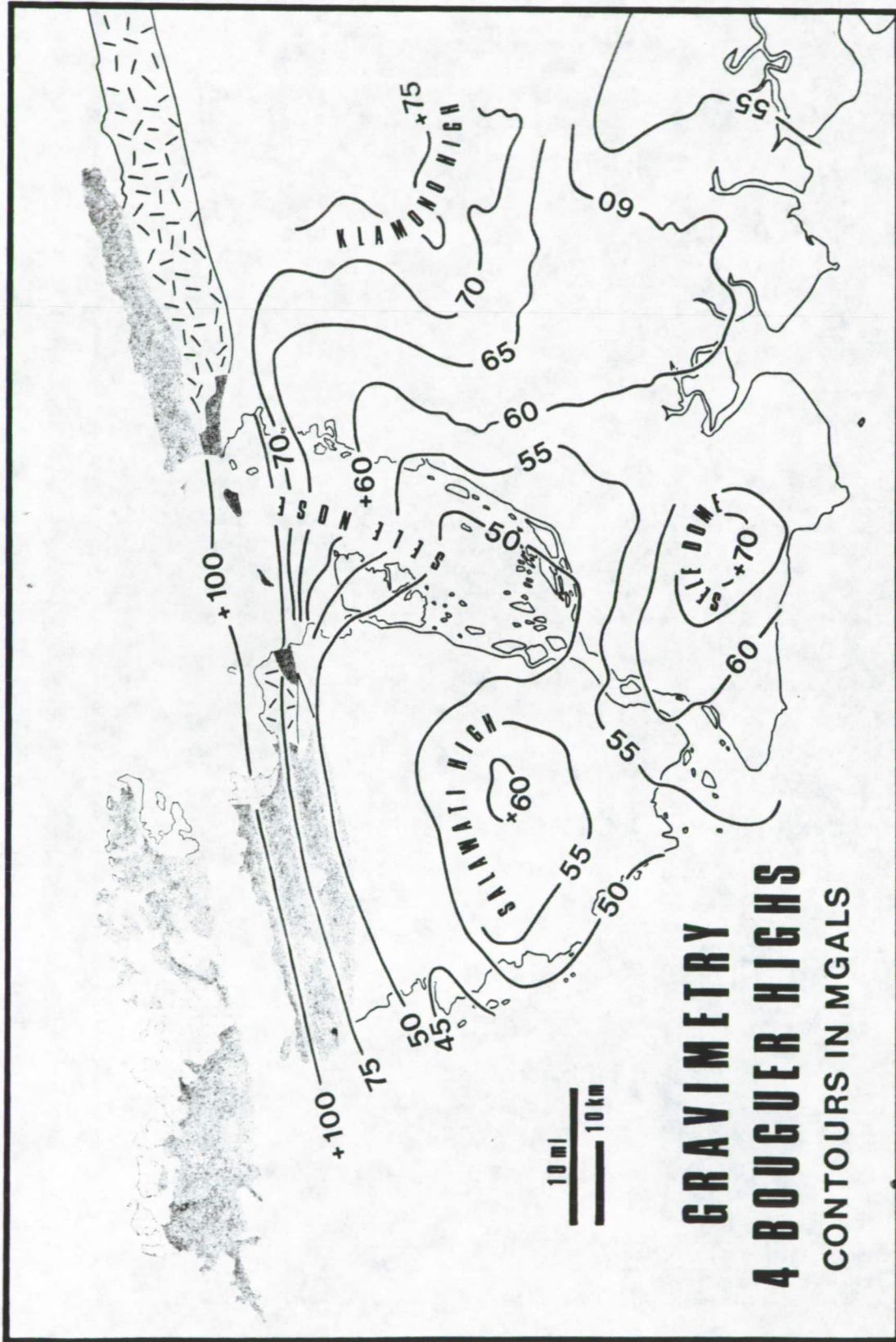


Figure 20. The largest positive gravity anomaly is probably related to an infiltration of basalt in the northern part of Sele Strait. The other anomalies reflect the shape of the granitic basement.

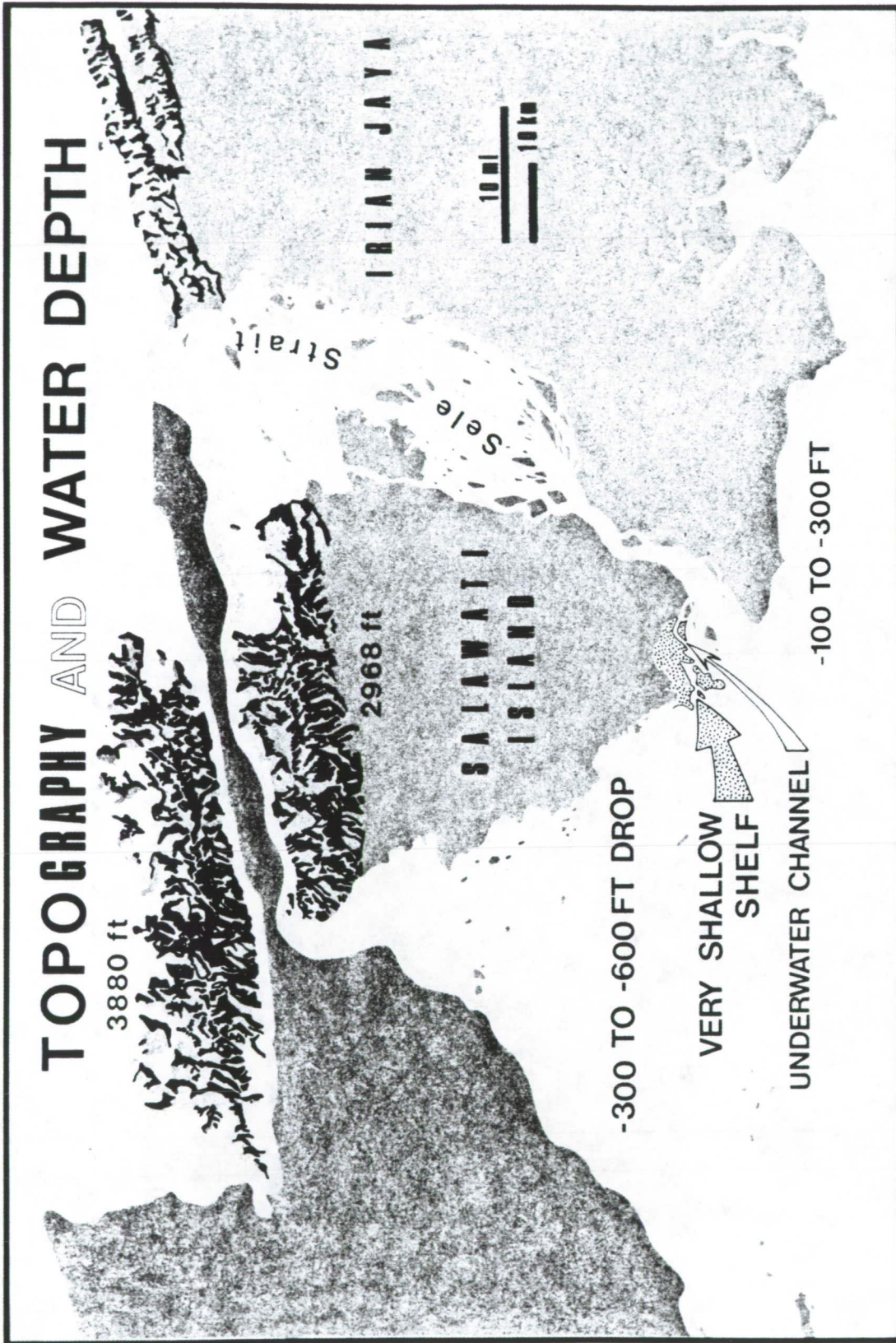


Figure 21. The two shear zones are expressed in the submarine morphology. Compare with Figure 18.

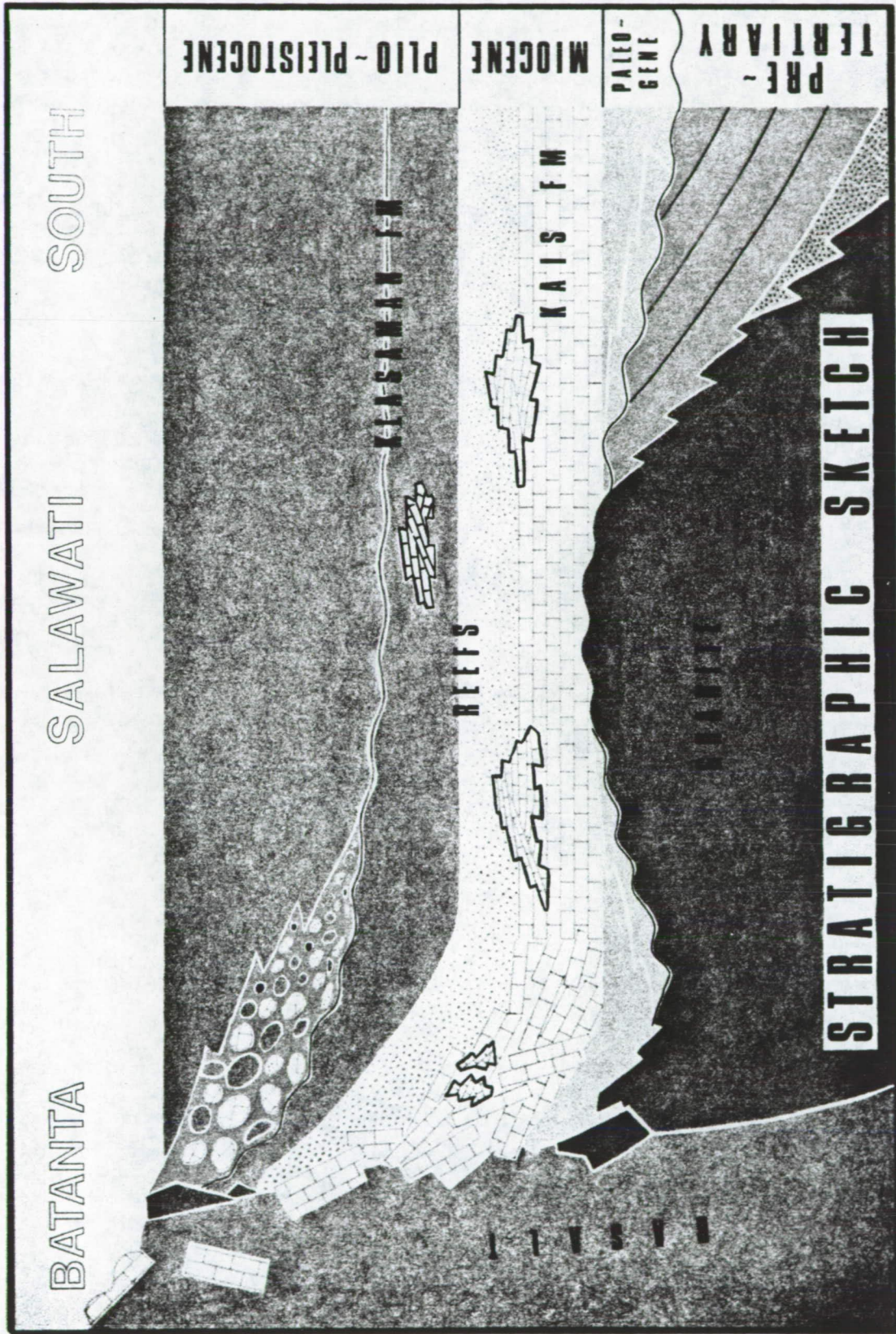


Figure 22. The emplacement of the Late Cretaceous granite was followed by 65 m.y. period of peneplanation ending with a Miocene marine invasion, which initiated reef development. During Middle Pliocene (after the formation of the last reefs), basalt erupted along the Sorong fault zone, creating a high mountain ridge in the north, that became the source of voluminous Plio-Pleistocene clastics.

The early Tertiary (Paleocene to Oligocene) apparently was locally a time of continental environment. The lower Eocene of Misool Island is characterized by wood-bearing near-shore sandstones. The Pliocene offshore of Onin (Figure 14) is unconformable on the Cretaceous. Thus a landmass is outlined stratigraphically from an area north of Misool to the Onin Peninsula area. It included Salawati and probably the western part of the mainland as far as the northern and eastern edge of the Miocene limestone outcrop area where a continuous lower Tertiary section is exposed. The present expression of this ancient crustal high may be the positive Bouguer anomalies of the Salawati, Sele dome, and Klamono areas (Figure 20). If the Salawati block is placed in its initial, pre-Pliocene position, the continuity of the anomaly is more striking (Figure 28).

Volcanic activity occurred in very early Eocene time as testified by K-Ar dating of a basalt from a well located east of Misool Island (Figure 2).

B. Miocene

At the beginning of Miocene time, the area became the site of widespread marine transgression, initiating the phase of carbonate deposition and reef development. The sea extended northward beyond the present line of the Sorong fault zone, which was formed later. The configuration of the shallow crystalline and metamorphic (?) basement certainly was determinant in the distribution of reefal activity.

The fracture pattern or erosional shape of the Miocene basement surface remains unknown. From structural analysis most of the present framework appears to be the result of Pliocene diastrophism.

C. Post-Miocene

Since the inception of the Pliocene strike-slip motion along the Sorong fault, the tectonic evolution of the Salawati area is easier to deduce. The following succession of events is believed to have taken place:

1. Formation of Sorong Fault. The Pacific oceanic plate had begun its westward motion, after a Miocene phase of southward subduction, during which the backbone of New Guinea already was roughly outlined.
2. Right-Lateral Wrenching in Sele Strait Area. A conjugate set of strike-slip faults was developed concurrently. The direction of tensional stress expressed by the geometric properties of the set (as seen in the present geomorphology of the Sele Strait islands) is oriented across the axis of the strait (Figure 24).
3. Basaltic Intrusion Along Sorong Fault Zone. The Salawati block was still a part of the Irian Jaya mainland, closing the gap of the present strait and defining a continuous zone of volcanic activity (Figure 15). The amount of left-lateral motion along the Sorong fault may already have been as much as 100 km, the present distance between the Miocene reefs of Kofiau Island (located on the westward moving compartment) and Salawati. Such a displacement would bring the Batanta Kais reefs (Miocene: Figure 14) approximately 30 km east of the northwest corner of mainland New Guinea. It is not unreasonable to imagine that the Salawati bioherms were thriving at the edge of a landmass represented by ancient Irian Jaya, facing an open sea on the west, somewhat as at present,

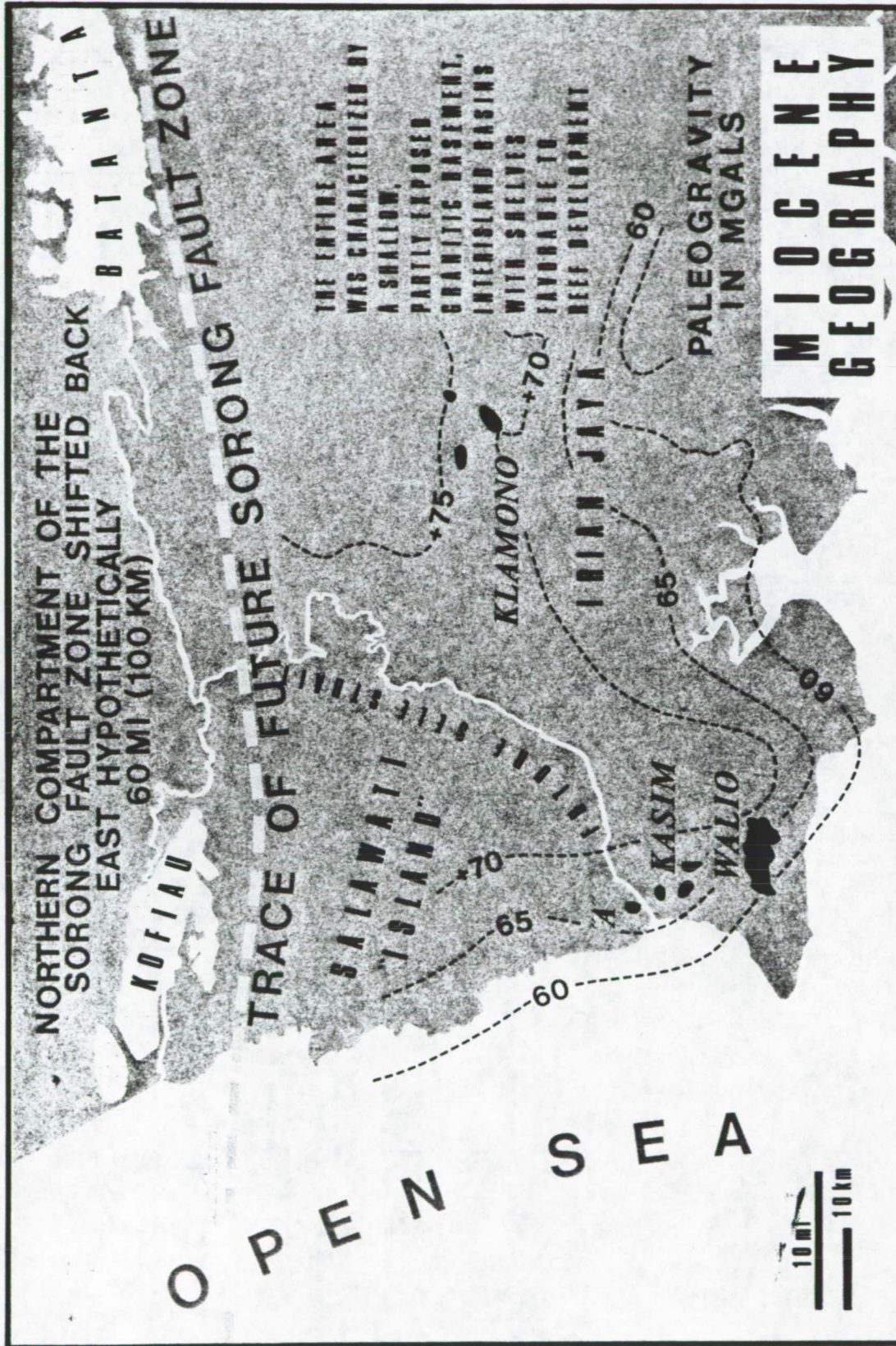


Figure 23. Before Plio-Pleistocene rifting, Salawati Island and the mainland formed a solid block underlain by granitic basement, outlined here by reconstructed gravity contours (compare with Figure 20). The "A" oil field appears to have been located north of Kasim oil field, instead of SW as today (compare with Figure 28), outlining a north-south reef trend facing an open sea to the west. Later effect of left-lateral Sorong fault zone has been removed by sliding Batanta and Kofiau islands back east about 100 km.

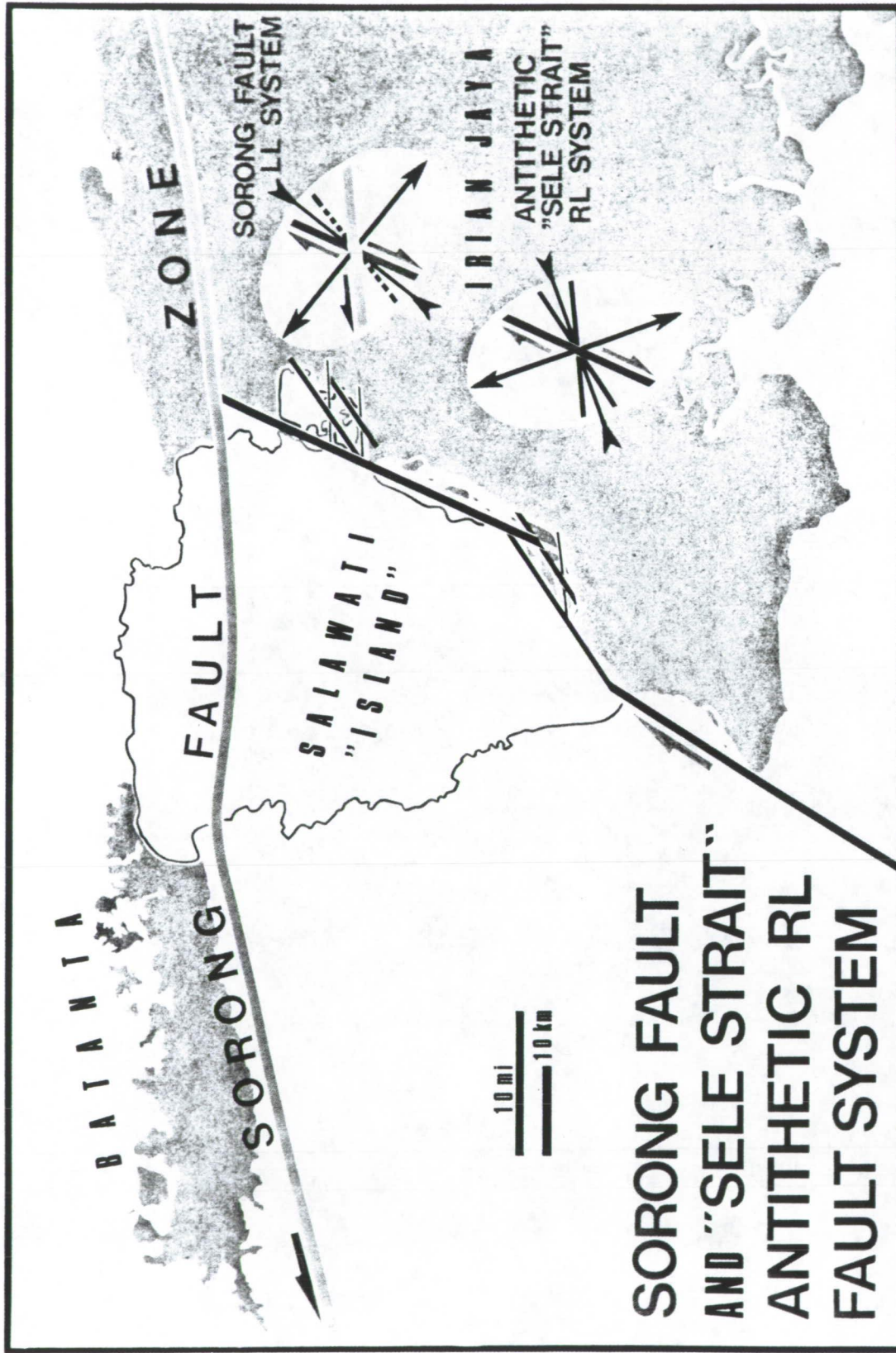


Figure 24. Reconstruction of strain ellipsoid characteristics before rifting, based on the examination of radar imagery (See Figures 6, 11, and 13).

because the large island of New Guinea was already largely defined during Miocene time. The rising basalt lifted the Miocene carbonate cover now tilted on the north coast of Batanta. The basalt partly digested the limestone, now floating as xenoliths, and filled fractures. Isolated blocks of Kais limestone are perched in the Salawati Mountains. The north Salawati mountain ridge became the source of the Klasaman Formation sediments. The downward decreases in volcanic content and increase in calcareous character of the Klasaman correlate with the progressive erosion of a carbonate-covered basaltic mass. At an early stage, most of the mountain tops probably were still carved in uplifted Miocene limestone.

4. Opening of Sele Strait by Westward Rifting of Salawati Island. The basaltic intrusion probably triggered the process already outlined by the direction of extension of the local stress field. The rifting proceeded in two phases: first rotation, then translation.

a. Initial 13° Counterclockwise Rotation (Figure 25). The rotation of the Salawati block may have been caused mainly by the wedging effect of the basaltic intrusion from the Sorong fault zone. For that reason, it may have been a rapid event of near-volcanic speed with the magma ripping through the right-lateral fracture system of Sele Strait.

The presence of a southward-bulging gravimetric high in the northern shallow part of the Sele Strait strongly suggests that the basalt partly invaded the strait (Figure 20). The possibility of a basement wedge rather than an intrusive body as a cause of the gravity anomaly is unlikely, for it would act in opposite direction to the stress field of the general fault system.

This suggestion is supported further by the presence of a small basaltic dike in a fracture of the Upper Cretaceous limestone, parallel with and near the right-lateral fault zone of eastern Misool. The exposed dike is only a few miles long but it is in line, through intermediate karstic channels, with an islet on the north, which is believed to be the emergent top of a drowned Pliocene volcano (Figure 14). The basalt in a nearby well originated during a very early Eocene volcanic event (K-Ar dating) unrelated to the Pliocene intrusion.

Figure 25 indicates a large bay on the north side of the basaltic ridge at the intersection of the right-lateral Sele fault. This bay is interpreted to be a gap left by the part of the Sorong fault basalt that was flushed into the Sele Strait, as if the basalt first rose along the Sorong fault to a certain height, and then collapsed by leaking into the Sele Strait. The present west coast of the bay is characterized by slabs of Kais limestone steeply tilted east-southeast (Hermes, 1959), as though they fell toward the opening gap. The rotation also caused the basaltic prism to break right-laterally in the area now occupied by the eastern extremity of Batanta Island. At this stage, the Salawati block became detached from Batanta and Irian Jaya and ready to move freely.

In the initial phase of rifting, the conjugate set of the original right-lateral fault system of the Sele Strait became the site of tensional faulting to accommodate the loss of volume. Horsts and grabens were created in the rift zone. These now are well expressed on radar imagery by the geomorphology of the straight—the islands are horsts separated by drowned grabens. The pivot point of

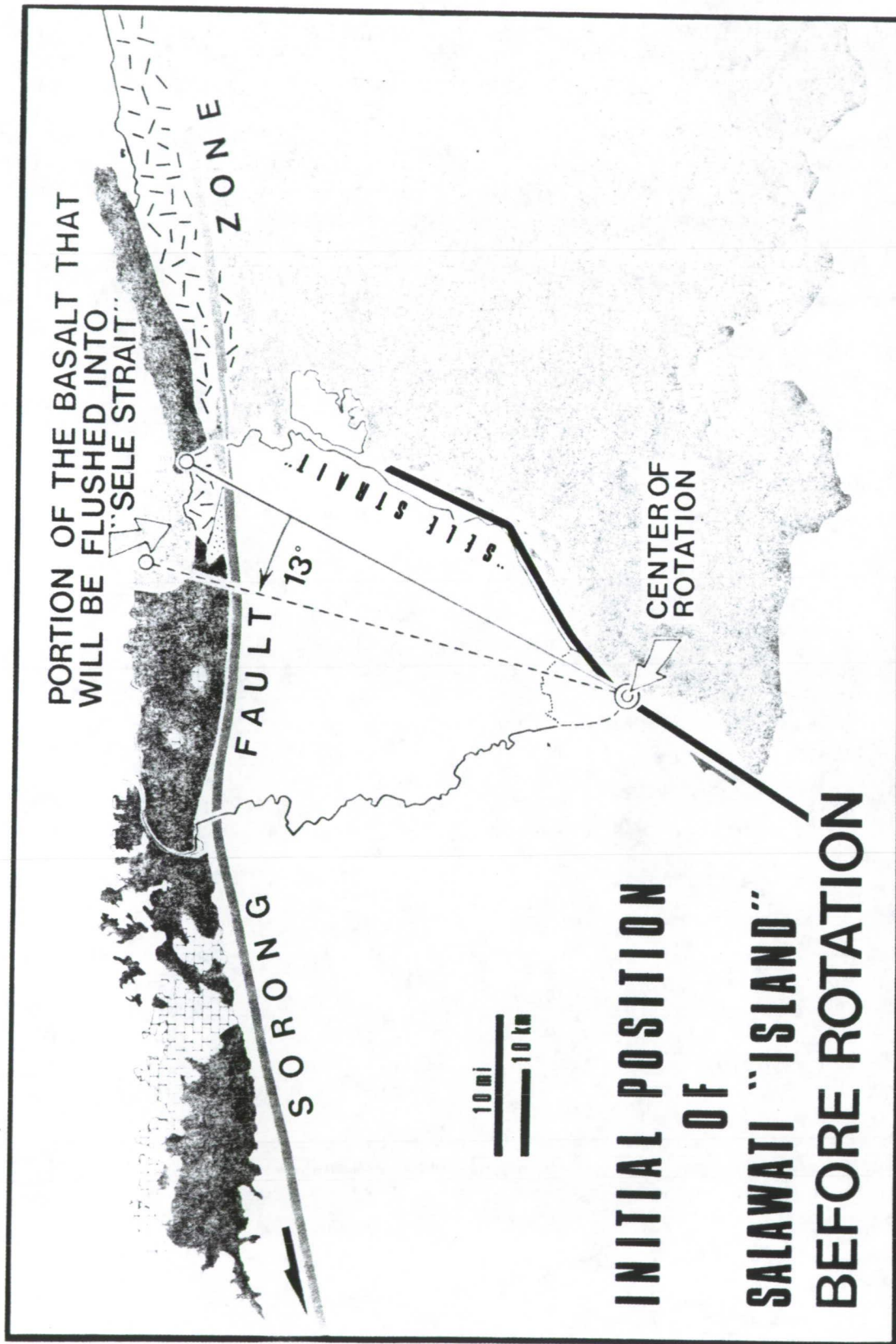


Figure 25. Geometric considerations suggest that the center of rotation of the Salawati block was located near the present Kasim Island (see Figure 28). A gap (pale green) in the northern basaltic ridge suggests that the basalt withdrew when infiltrating the Sele Strait right-lateral fault, initiating Salawati rotation by wedging effect.



Figure 26. After a 13° CCW rotation, the Salawati block was in a proper position to move freely to the SW.

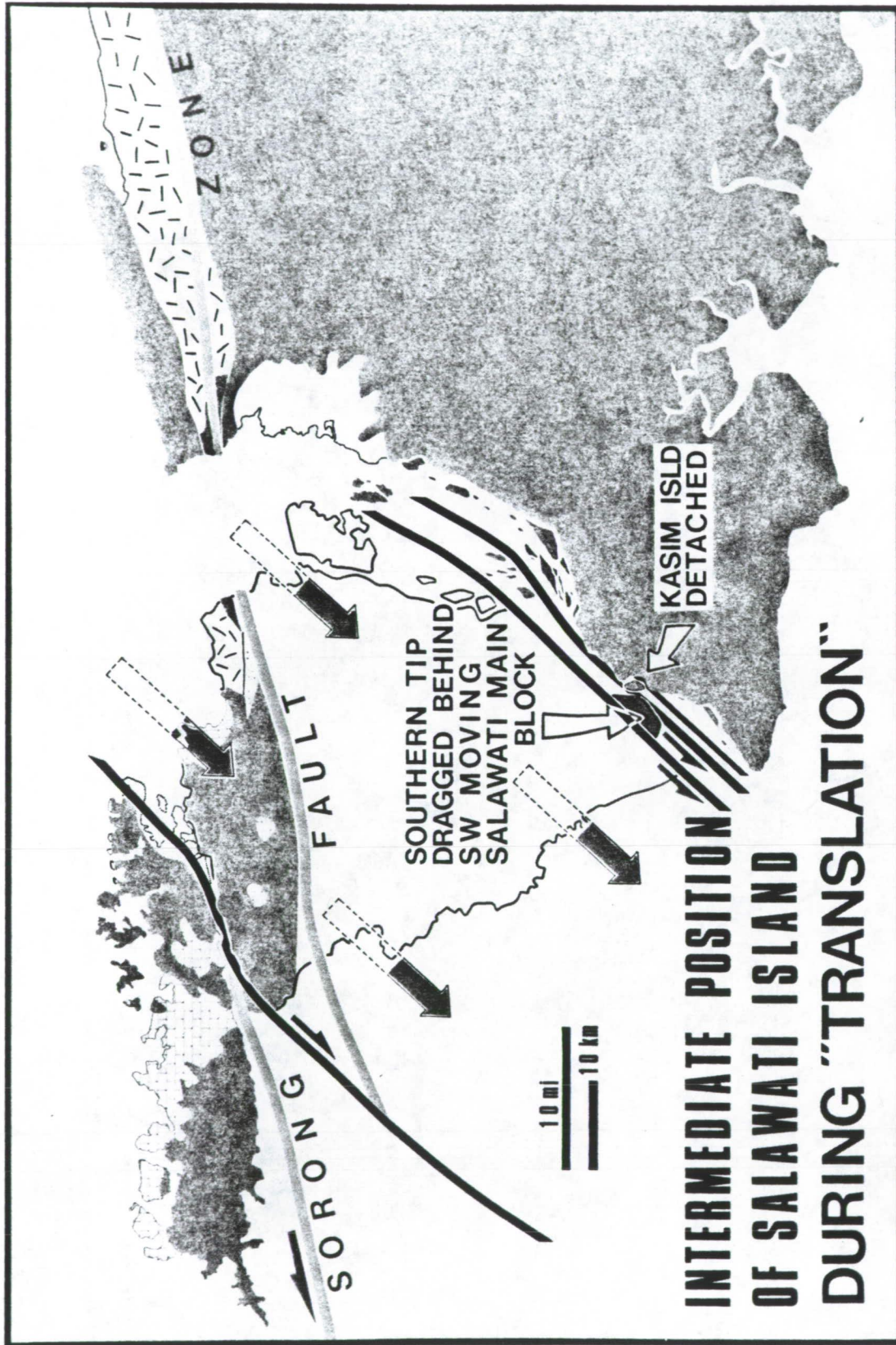


Figure 27. Intermediate stage of translation showing the separation of the southern tip of Salawati from the main block, and the creation of Kasim Island as a broken corner of the mainland, at the former center of rotation.

the rotating block was located near the southern tip of Salawati previously located just north of Kasim Island (Figure 25). The density of islands (horsts) is greater in the southern part than in the northern part of the Sele Strait, as expected near the center of rotation where less lateral displacement occurred. The fact that the western end of the Pliocene landmass broke off instead of being bent supports the interpretation of a generalized crystalline basement in the area. It is also significant that the area is the extremity of the world's second largest island.

b. Final 17.5-km Southwestward Translation. After its 13° counterclockwise rotation, the Salawati block was in a favorable position to assume a southwestward motion (Figure 23). Its east side became aligned with the present narrow part of the Sele Strait, along which it was able to slip left laterally under the continuing push exerted on its northeast corner by the progressively cooling basaltic wedge. When the basaltic wedge had hardened, the block continued its left-lateral slip motion by the slow westward push of the northern compartment of the Sorong fault. Without the initial rotation, this linear displacement would have been impeded by the resistance offered by the Sele dome (Figure 20).

The new left-lateral friction zone developed generally within the original zone of right-lateral motion of the Misool-Sele fault system. However, the slippage was exerted on two main subparallel fault planes, about 3 km apart, roughly aligned with the new general southwest direction of motion and extending into the Sele Strait, where they are expressed by two furrows on the sea bottom (Figure 21). They were the Salawati main fault and the original right-lateral fault of Sele Strait. The Salawati main fault is expressed at the surface by the straight coast northwest of Kasim Island and extends southwest to the parallel edge of a very shallow bay (Figure 21) bordered by a deep underwater channel; on the northeast, the fault corresponds to one of the sea-bottom furrows of Sele Strait. The original right-lateral fault of Sele Strait is represented at the surface by the narrow and deepest zone (120+ m) of the entire strait.

The two fault planes defined a sliver of transitional left-lateral motion that absorbed most of the strain due to the friction of the moving Salawati block along the fixed mainland. This intermediate narrow block comprises the southern tip of Salawati Island and neighboring islets. A third minor plane of friction is located between Kasim Island and the mainland.

The total amount of slippage (17.5 km) is distributed along these three planes of left-lateral motion in southern Salawati. In the strait itself, most of the slippage occurred along the extension of the plane of the main Salawati fault. The first effect of southwest translation was the breakoff of the tip of Salawati from its former location at the south edge of the shallow bay. The extremity of the block remained at the center of rotation, which was the main point of resistance (the least affected by rifting). The slippage started along the main Salawati fault plane, probably as soon as rotation was carried far enough to orient the block in a position favorable to lateral displacement. The south tip later moved left-laterally along the Sele Strait fault, slipping away from the center of rotation, and finally tearing off a corner of the mainland block, thus creating Kasim Island. Kasim Island slid along the third minor strike-slip fault (Figure 27). The amount of relative left-lateral motion decreased from 8.5 km at the northwest fault (main Salawati fault), to 8 km at

the middle fault, and 1 km at the southeast fault (Kasim Island). The northwest block moved 17.5 km; the middle sliver, 9 km; and Kasim Island, 1 km. Thus it appears that the total left-lateral motion of 17.5 km was distributed on these three fault planes. The mainland remained immobile. No horizontal slippage seems to have taken place along the northernmost major fault of Salawati, which moved with the central block. Figure 28 shows the present position of Salawati.

c. Rate of Separation. The rate of separation after the initial phase of rapid rotation can be estimated. It is known that the motion started in Pliocene time, therefore not earlier than 5.5 m.y. ago, and probably later because it reasonably can be assumed that rifting occurred after the quiet period of carbonate deposition that ended with the development of Lower Pliocene Klasaman reefs. The subsequent thick clastic Pliocene section was derived from the northern basaltic mountains that were formed shortly before the rifting of Sele Strait. Consideration of the Klasaman rate of sedimentation (to be discussed later) indirectly suggests that separation started about 2.7 m.y. ago. If it is still active today, the average velocity of southwestward motion is therefore of the order of 7 mm/year.

5. Major Normal Faulting in Salawati Island. A basement structural map indicates a general downdropping of northern compartments along the southwest-northeast fault system during a later phase of deformation. The balance of the amount of upward and downward motion recorded along the faults located between the southern and northernmost wells is comparable to the present difference in elevation between the top of a Miocene reef on the south and the top of a Pliocene reef on the north. Because during their lifetime both reefs were practically at sea level, it can be concluded that the downward motion occurred after the development of the Klasaman reefs, sometime during the Pliocene. The phase of large-scale normal faulting probably was initiated by rapid deposition of the Klasaman Formation, supplied by the high mountain ridge on the north. The marked northward thickening of the Pliocene section indicates that the source was in that area.

There is a possibility that normal faulting started during the phase of southwestward movement of Salawati away from the mainland. However, it could not have been before sufficient erosion of the basalt mountains had supplied the required load for the subsidence of the downfaulted blocks. The rate of sedimentation was fast enough to cause adjustment by normal faulting along the previously outlined zones of shear. The northernmost measured total thickness of Pliocene-Pleistocene section amounts to 3200 m and corresponds to a time span of 5.5 m.y., representing a fast average rate of sedimentation of 56 cm/1000 years. This value is a minimum because the computation includes the lower fifth of the section (up to the top of the Klasaman reef), which corresponds to a time of quiet and slow deposition favorable to reef development. If we assume, for example, that the slow rate was about 2.5 times slower than the later fast rate, the rate of clastic deposition was 93 cm/1000 years. This rate is also a minimum because it is not even measured near the mountain source.

6. Recent Tectonics. The map of earthquake epicenters by Hamilton (1974) shows three zones of activity in western Irian Jaya (Figure 8): (a) on the north, the Sorong fault zone; (b) on the south, the Ceram area, as a possible western extension of the Tarera-Aiduna fault zone; and (c) on the east, the right-lateral fault zone underlying the Lengguru foldbelt.

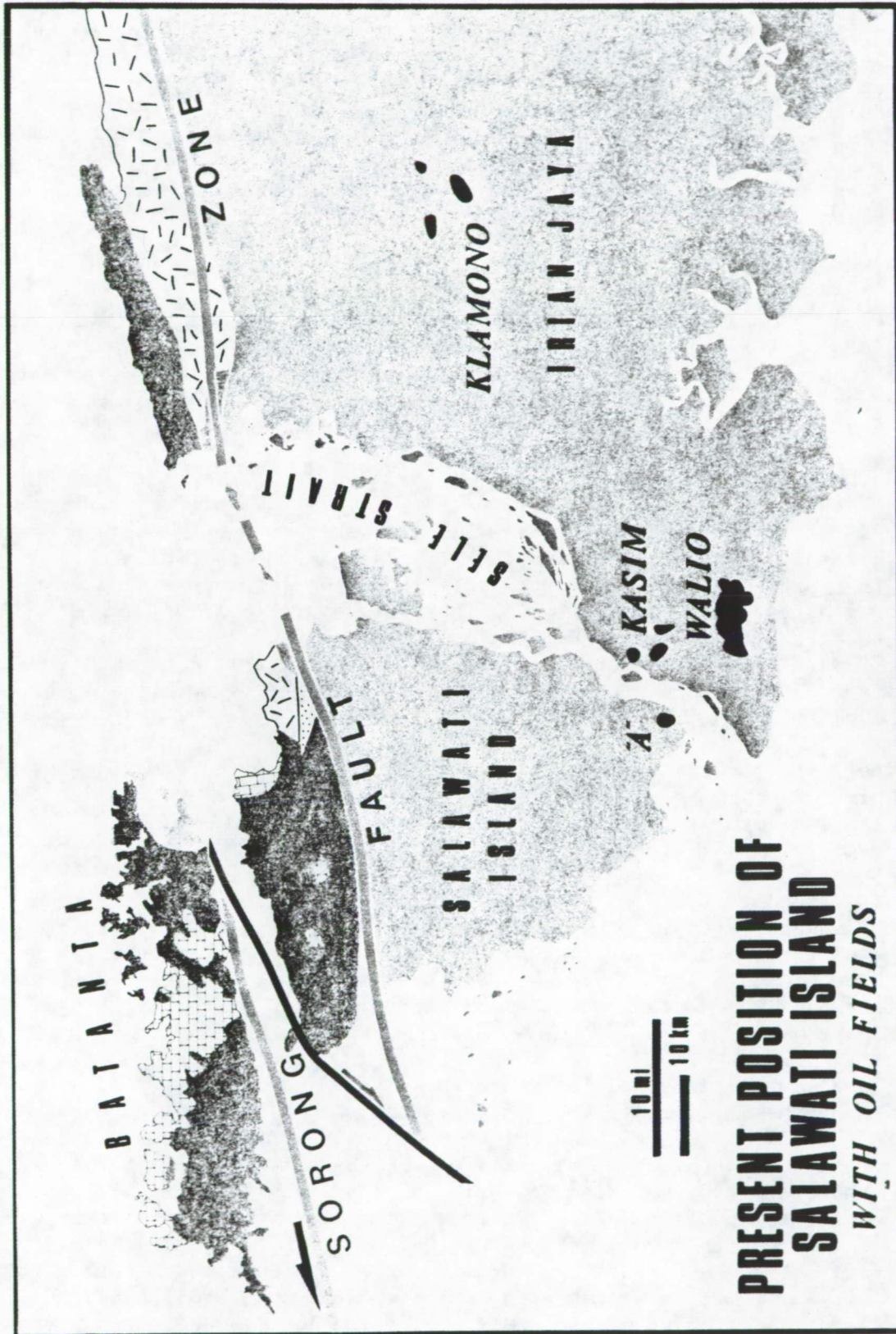


Figure 28. Salawati Island today. Oil fields are shown in black.

The presence of these zones suggests that the Salawati area is still under the effect of a general east-west left-lateral fault system.

Recent tectonic unrest is evidenced at Misool Island by several geomorphic features (Figure 9). An east-southeastward tilting of the island is shown by elevated Pleistocene reefs and meanders encased within Pliocene rocks on the northwest, and drowned karst on the east (Froidevaux, 1975). The southwestward movement of Salawati Island relative to Irian Jaya may be the force behind the tilt. Since the beginning of oil exploration in the Salawati area, at least two earth tremors have been reported by the rig and seismic crews. The island still may be moving westward away from Irian Jaya together with, but separate from, the Pacific oceanic plate.

VII. ECONOMIC IMPLICATIONS

Knowledge of the paleogeography at the time of reservoir and source rocks development, and of the successive diastrophic phases that affected them, is essential to successful hydrocarbon exploration. It is not possible, for proprietary reasons, to expose in detail all the economic implications of the proposed model, but two guiding conclusions can be offered:

A. Miocene Landscape

Figure 23 is a representation of the Salawati area before the time of Pliocene diastrophism. Salawati Island the Irian Jaya mainland formed one solid block that probably extended northward slightly beyond the present trace of the Sorong fault, toward the latitude of the Waigeo archipelago (Figure 8). The Miocene sea transgressed over the area and the carbonate development was initiated. The landscape was characterized by a shallow granitic basement, partly exposed as low-relief islands with shelves favorable to reef growth and separated by small basins.

Kais reefs are exposed on Batanta Island and appear offshore on the north on correlatable seismic lines. Some are perched in the Salawati Mountains. Bioherms of the same age are exposed in Kofiau Island on the west and in the Waigeo Island group.

The Kais carbonate rocks on the north side of the Sorong fault must be shifted back eastward to restore the Miocene picture properly. This suggests that the edge of the old Miocene Irian Jaya shelf extended farther north than today, and that it was facing an open sea on the west. On the south, the edge of the landmass was located approximately along a line joining Misool Island and the Onin Peninsula.

Once the Salawati block and its southern sliver are placed in their initial Irian Jaya frame, the Miocene position of the reefs shows that the old coastal area of reef development was oriented more nearly north-south, suggesting an open basin on the west and southwest. The reefs on the east side of Sele Strait were in the same position during the Miocene, being part of the fixed land. The bioherms on the intermediate fault sliver were farther northeast, so that they were partly north of, rather than west of, the Kasim field. The reefs of the central part of Salawati shifted even farther, having been at the longitude of the Walio field. They typically are arranged circularly around an old, erosion and/or structural basement high, that was probably one of the last islands to support reefal life in the central Salawati area in early Pliocene time just before the rapid terminal subsidence.

B. Prospective Quality of Structural Elements

Understanding the tectonic history of an area that has undergone drastic structural modification provides useful guidelines for the study of hydrocarbon migration and accumulation. Figure 29 illustrates in a simplified manner the distribution of structural units of basically different characters that were acquired during the Tertiary evolution of the Salawati area as a result of the rift and possibly drift event. The changing nature of the faults through time, as unit boundaries acting either as permeability barriers or avenues, can be integrated into a synthesis of hydrocarbon history.

VIII. CONCLUSION

The significant contributions made by the radar images in this plate tectonics study are tied initially to the ability of the radar to define a clear land-water interface. This was extremely important in that it enabled the author to closely and accurately examine shorelines of the islands involved. This initial examination provided a basis for a working hypothesis. Secondly, radar images provided, together with internal features, the geometric elements (linears and patterns) for structural analysis, from the construction of a comprehensive map (2-dimensional) to the reconstruction of a tectonic history (4-dimensional).

The intermediate scale of radar imagery provides the advantageous synoptic view of Landsat, while at the same time eliminating the unnecessary details of aerial photography. The tool suppresses the disadvantages by removing the effect of vegetal and cloud cover.

The combination of synoptic view and sharply defined patterns is particularly suited to detailed 4-dimensional analysis of mobilistic models, such as proposed by plate tectonics.

In our example, the radar geomorphic framework permitted the fitting of a great abundance of scattered, and seemingly unrelated subsurface data, into a coherent geologic story, which is always the key to sound economic exploration.

ACKNOWLEDGMENT

The author is grateful to the American Association of Petroleum Geologists for permission to reprint the parts of this article that previously appeared in its 1978 bulletin, Vol. 62, No. 7. He is also thankful to the management of Phillips Petroleum Company for authorization to publish this information.

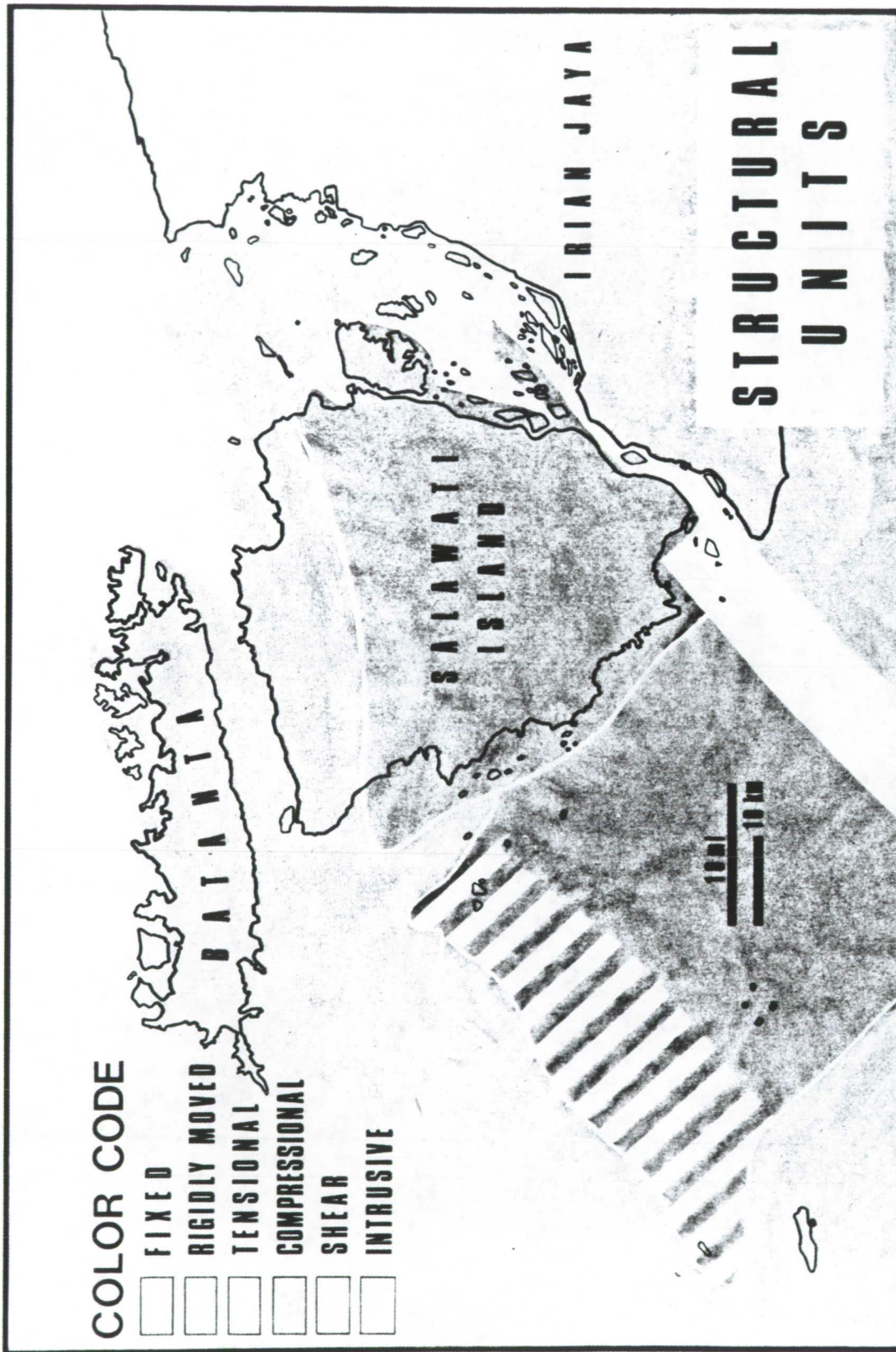


Figure 29. Rifting of Salawati Island created several structural units and boundaries of different and changing permeability characters important in deciphering hydrocarbon history.

REFERENCES

- Froidevaux, C. M., 1975, Geology of Misool Island (Irian Jaya): Indonesian Petroleum Assoc. 3rd Ann. Conv., 1979, Proc., No. 3, pp. 189-196.
- _____, 1978, Tertiary Tectonic History of Salawati Area, Irian Jaya, Indonesia: AAPG Bull., Vol. 62, No. 7, pp. 1127-1150, 14 Figs.
- Hamilton, W., 1973, Tectonics of the Indonesian Region, in Regional Conference on the Geology of Southeast Asia, Proc.: Geol. Soc. Malaysia Bull., No. 6, p. 3-10.
- _____, 1974, Earthquake Map of the Indonesian Region: U. S. Geol. Survey Misc. Inv. Ser. I-875-C, seismic map, scale 1:5,000,000.
- Hermes, J. J., 1959, Geology of the Radja Ampat Islands and North Coast of the West Vogelkop: Nederlansche Nieuw Guinee Petroleum Maatschappij (NNGPM) Geol. Rept. 477.
- Redmond, J. L., and R. P. Koesoemadinata, 1977, Walio Oil Field and the Miocene Carbonates of Salawati Basin, Irian Jaya, Indonesia: Indonesian Petroleum Assoc. 5th Ann. Conv., 1976, Proc., Vol. 1, pp. 41-57.
- Tjia, H. D., 1973, Displacement Patterns of Strike-Slip Faults in Malaysia-Indonesia-Philippines: Geol. en Mijnbouw, Vol. 52, pp. 21-30.
- Vincelette, R. R., and R. A. Soeparjadi, 1976, Oil-Bearing Reefs in Salawati Basin of Irian Jaya, Indonesia: AAPG Bull., Vol. 60. pp. 1448-1462.
- Visser, W. A., and J. J. Hermes, 1962, Geological Results of the Exploration for Oil in Netherlands New Guinea: Koninkl. Nederlands Geol. Mijnbouwkundig, Genoot. Seol. Ser., Vol. 20, 265 p.

FRACTURE TRACE EXPRESSION AND ANALYSIS IN
RADAR IMAGERY OF RAIN FOREST TERRAIN (PERU)

P.H.A. Martin-Kaye
Hunting Geology and Geophysics Ltd,
Elstree, England

J.W. Norman
Imperial College of Science and Technology,
London, England

M.J. Skidmore
National Coal Board,
United Kingdom

ABSTRACT

Mapping of minor lineaments from radar imagery of the rain forest in southeast Peru is biased due to the selective suppression of some topography which results from the observation geometry of the imaging radar system and the varied perception of lineaments on the imagery by different interpreters. Team analysis of the imagery compensates for several of the sources of bias, and results in the clear recognition of differing regimes within the regional fracture field in the study area.

I. INTRODUCTION

Analysis of faulting is an essential part of geological interpretation of any suitable imagery; statistical fracture analysis is a well-established technique in oil and mineral exploration. In oil exploration the purpose is elucidation of concealed structure and depends upon the facts that (a) folding and fracturing are interrelated and inferences about one can be drawn from the other, and (b) pre-existent fracturing can be expressed through overlying beds by joint systems and reactivated faults. Analysis of these consequential patterns can allow inference upon the structure below.

Fracture traces are often excellently expressed in radar imagery, as has long been noted. The facing and reverse slopes of even slight declivities are cast into relative highlight and shade by the oblique illumination of mapping radars; the linearity of these features catches the eye of the interpreter. It follows that radar imagery should lend itself to fracture trace studies and it is the case that numbers of these have been carried out for oil, mineral, and water exploration and engineering geological purposes.

The authors and colleagues have maintained an interest in the expression of radar lineaments in rain forest since work on the Westinghouse AN/APQ 97 imagery of Nicaragua in 1972. This interest was enlivened during the interpretation of some 312,000 square kilometers of Goodyear/Aero Service Comparison imagery of S.E. Peru, undertaken for Petroleos del Peru. That major fault lines are often readily delineable even in rain forest from radar imagery has been apparent from the time of Darien radar survey and from Amazonian imagery of Venezuela and Brazil. The ground morphology is reflected in the forest canopy and faults are expressed in linear features, sometimes corroborated by different textural characteristics in the terrain on either side.

In the Peruvian imagery, much of which is over more or less flatland rain forest of the upper Amazon Basin, very numerous minor lineaments, additional to the major fault lines, are to be seen in certain sectors, despite the young blanket geology, tropical weathering and forest cover. These traces are of shorter length than the major faults and have no recognizable displacement. They are presumed to result from minor relief controlled by master joint systems but doubtless include many small-movement faults. Elder, Jeran and Keck (1974) have shown that radar lineaments in lightly vegetated terrain correlate well with joint systems and it now seems, although ground verification is awaited, that the same can apply in heavily forested areas. Norman (1976) noted that fault lineaments interpreted from air photography could be used for fracture pattern analysis in this type of environment. Statistical analysis of radar fracture trace data for exploration purposes in rain forest appears therefore as a potentially valuable technique. This could be particularly important as international exploration companies have tended to avoid rain forest whenever there is a satisfactory alternative owing to the severe logistical problems and expense of operations.

Oil exploration ordinarily moves at early stage of seismic survey and, where logistics present no problem, there may be only limited argument for fracture trace analysis. In the case of S.E. Peru there are many thousands of square kilometers of interesting but operationally severely adverse terrain. Fracture trace analysis based on the existing radar imagery appears to present a means of indicating concealed structure even in these difficult circumstances and hence enables guidance of seismic programs. In order to check this surmise, identify pitfalls, and establish optimum procedures, various aspects of radar fracture analysis were considered by us.

II. GEOLOGIC VALIDITY OF THE MINOR LINEAMENTS

While numerous of the minor lineaments are clearly of geologic origin, swarms of others occur which are not so well expressed as to permit acceptance of this assumption without question. Although not thought to be the case it was conceived as possible that some might be due to some instrumental or processing effect. When examined stereoscopically, SLAR imagery sometimes imparts spurious rolling, corrugated or ridged effect to the terrain, supposedly induced in the correlation processing. It is not discernible in monoscopic work. Some such or other effect might possibly impose spurious linear artifacts.

The first evidence against this possibility is seen in that the youngest geological formations (young alluvium, fans, etc.) ordinarily do not show lineaments; i.e., distribution is presumably related to geology. By way of further check of the validity of the minor lineaments a test area was selected between

two major parallel rivers and interpreted at 1:100,000 scale. The directional frequency of straight sectors within these rivers was measured, it being taken that the straight sectors were under structural control. The results compared well with directional frequency data obtained from measurements on the minor lineaments between the rivers, suggesting that the same structural control was being exercised.

III. RADAR BIAS

A glance at a fracture trace interpretation of radar imagery invariably shows the majority of lineaments lying somewhere between the look direction and the swath direction. Histogram plots ordinarily have a pronounced low coincident with the look and another, of less a degree, in the direction at right angles.

The reduction of linear data in the look direction has long been recognized although not always acknowledged in radar lineament papers. The reason for the shortage of information is readily understood: each side of the linear declivity is equally illuminated; there is no contrast to make it stand out. The same effect is seen in low sun angle photography and Landsat imagery in respect of the sun direction.

The reason for reduction of information at right angles to the look in SLAR is less clear but may be due to the disruption of linearity by side relief.

It was at first thought that radar bias could be overcome by careful interpretation that paid particular attention to inconspicuous lineaments in the affected directions. Only for more substantial lineaments does this seem the case. The problem could be overcome by flying surveys with two look directions at an angle, perhaps ideally at 135° between them. This is rarely done. Reciprocal look directions have virtue but in this particular context provide no likely advantage.

Radar bias is clearly a limitation to statistical analysis. Some directional data will be absent. The sector mostly affected may be in the order of 20° . Nevertheless there is compensation in the good level of information readily extractable over the remainder of arc.

In addition to directional bias, some attention was given to the expression of lineaments in relation to position on the swath. It was thought that subtle lineaments might not receive the same emphasis at different incident angles of beam. Over four test strips, each worked by two observers, 6% more lineaments were recorded on far than for near range. This is as might be expected, the more grazing angles giving more data. Spatial frequency (i.e., number of fracture traces per unit area) is an inexact technique and the indicated increase is well within possible error. However, some support for increase in data at distance is given in that both observers also reported a small increase in the proportion of longer fractures.

IV. INTERPRETER BIAS

Interpreter bias is a potentially more serious matter than radar bias. The subject has received some notice in published papers but the extent of the problem is probably not widely recognized.

In the Peruvian imagery the minor lineaments range from clearly evident into imperceptible, and with increasing subtlety of expression it becomes a very subjective matter as to what constitutes an acceptable feature. Different interpreters are apt to take different views.

It might be thought that this problem can be overcome on the basis of experience of the interpreter but this is only partly true. It is indeed necessary to use experienced interpreters in fracture trace data extraction since only these people can effectively make the repeated decision as to what constitutes a fracture trace. This very experience poses its own difficulty. The interpreter's normal task is to establish a coherent geological picture and subconsciously tends to place greatest emphasis on features that he can rationalize. Recognition of this tendency can lead to overcompensation.

A series of tests was carried out in which the data extracted by a number of interpreters were compared. It was quickly shown that:

- (1) It is virtually impossible for any two different interpreters to produce maps in which the majority of minor lineaments coincide. Statistically this may not matter.
- (2) The personality of the interpreter clearly emerges in the meticulousness or boldness of drafted detail. Some do not hesitate to be schematic, others are finicky. Provided that the interpretation is uniform this again may not be critical.
- (3) The eye, brain or drawing arm often prefer particular directions when numerous subtle linears are handled. Some experienced men have difficulty in observing lineament directions that appear apparent to others.
- (4) In dealing with large format sheets of data equivalent attention may not be given to all parts of each.

Production of histograms showed that all interpreters invariably agreed on the shortage of lineament data in the look direction and reduction of information at right angles. It also exposed occasional omission of specific direction data. Discounting major lineaments it was found that the length ascribed to minor lineaments by any particular observer did not greatly vary. The range was 6% to 16% amongst three interpreters. This is to say that all tended to be schematic to some degree. The average length of linear depicted between these three persons differed by a factor of approximately 2; i.e., there was no consensus as to how long continuities actually were.

These and other observers tended to vary slightly the length of interpreted linears according to the direction in which they were drawn, but the favored directions were not the same in each case. Further tests showed that different observers took significantly different time to establish a fracture pattern picture for any given area; after this had been developed little change was introduced into the shape of the histogram.

All these observations underline Seigal's comment of 1977 that extreme caution must be taken before using lineament data from different investigators. The combination of interpreter with radar bias further complicates the matter. However, recognition of a problem is the first step in combatting it.

For small area projects a single interpreter of detail, aware of the pitfalls, might best be used, with another having a monitoring role. In this way a uniform approach will be obtained, and such errors and biases as inevitable likely to be systematic. The results might be manually manageable (i.e., not computerized) to a modestly satisfactory extent, particularly where the results are monitored against regionally verifiable models.

Where numerous data and large areas are involved, such as the case in the S.E. Oriente, the task would be far too laborious for one man and, in any event, manual handling of data only permits crude interpretation.

The author's conclusions are that for such projects:

- (1) Data extraction should be carried out by a small team working to a fixed invaried routine whereby all examine all imagery.
- (2) Imagery is considered on two bases: systematic examination cell by cell and, separately, "globally" in order to identify major continuities.
- (3) Data extraction is on a time basis to ensure that excessive attention is not given to any particular segment.
- (4) Results are digitized and computerized.
- (5) Results are monitored for validity against ground truth wherever available, against regional conventional interpretation, and against regional and, wherever practical, local stress models.
- (6) Results are monitored by other technique, i.e., optical and/or image processing procedures.

V. OPTICAL AND MACHINE AIDED ANALYSIS

A test of optical analysis was made from a 1:1,000,000 scale photoreduction negative of a 1:250,000 scale mosaic, i.e., of degraded quality compared with primary imagery. The procedure utilized a laser beam fourier transform device (Barnett and Harnett 1975). The resultant "rosette" pattern displayed a number of features in common with interpretation rosettes and clearly depicted diminished information around the radar look direction.

This process applied to a regular grid promises to be a useful check on changes in regional stress patterns and then could be adapted to help test for local related fold structures. However, its uncritical acceptance of all linear features without classification makes it a useful additional tool to the fracture trace analyst rather than a replacement of the photo interpreter. Moreover, the resolution is limited to the size of the statistical cell.

Experiments were also made with computerized image processors. These techniques are already used in various industrial and research applications requiring quantification of directional data. Enhancement of lineaments can be effected by pixel shift, density stretches, filtering and edge enhancement techniques. Directional and density data can then be extracted by nearest neighbor and similar analysis. The potential seems to exist for substantial degrees of automated analysis under favorable circumstances, or for the supply of data against which the validity of manually extracted lineament data can be monitored.

VI. LARGER TEST AREAS

In the test studies upon bias only small areas of Petroperu imagery were utilized. While the results were information about the problems involved they said little upon the effectiveness of statistical fracture trace study in elucidating concealed structure for this particular region. Two pilot studies of larger areas were consequently initiated: (a) over the exposed Contaya Dome and vicinity and, on the basis of encouraging results, (b) over a substantially larger area. The latter work had to be set aside for other preoccupations and remains in this status.

Despite the deficiencies of spatial density work it was decided to apply the technique over the Contaya Dome and immediately surrounding country. The data were manually handled. The result clearly showed differing regimes within the regional fracture field, in part similar to the exposed dome pattern. The differing styles appear to be separated by structural breaks which in part coincide with features recognized in conventional interpretation of the imagery, elsewhere not.

VII. CONCLUSION

This work was taken to satisfactorily demonstrate the potential value of statistical fracture trace analysis upon radar imagery in this rain forest environment. With digitized data and computer program analysis important guidance to oil exploration seems certain. The same could equally apply for other styles of exploration in appropriate circumstances. It must be said, however, that out of a considerable quantity of rain forest imagery from various sources examined, the S.E. Oriente has so far been unique in the extent to which minor lineaments in blanket sediments are expressed.

REFERENCES

- Barnett, M. E., and Harnett, P. R., 1975, Diffraction pattern sampling and its application to directional enhancement of geological image transparencies, Trans. Instn. Min. Metall. (Sect. B: Appl. earth, Sci) B53-B55.
- Elder, C. H., Jeran, P. W., and Keck, D. A, 1974, Geologic Structure Analysis Using Radar Imagery of the Coal Mining Area of Buchanan County, Va., Report of Investigations 7869, U. S. Bureau of Mines.
- Norman, J. W., 1976, Photogeological fracture trace analysis as a subsurface exploration technique, Trans. Instn. Mining and Metallurgy.

APPENDIX A

NASA/JPL RADAR GEOLOGY WORKSHOP
July 16-20, 1979
Snowmass, Colorado

List of Attendees

Arden L. Albee
Jet Propulsion Laboratory 180-904
4800 Oak Grove Drive
Pasadena, CA 91103

Frank T. Barath
Jet Propulsion Laboratory 186-118
4800 Oak Grove Drive
Pasadena, CA 91103

Andrew J. Blanchard
Texas A&M University
Remote Sensing Center
326 Teague Building
College Station, TX 77843

Bruce J. Blanchard
Texas A&M University
Remote Sensing Center
326 Teague Building
College Station, TX 77843

P. Jan Cannon
Dept. of Geology & Geophysics
University of Alaska
Fairbanks, Alaska 99701

Alfred T. Chang
Code 913
NASA/Goddard Space Flight Center
Greenbelt, MD 20771

Pat Chavez, Jr.
U.S. Geological Survey
2255 North Gemini Drive
Flagstaff, AZ 86001

Aderbal C. Correa
Exploration Research
CONOCO, Inc. MS 102 NT
1000 South Pine
Ponca City, OK 74601

Louis F. Dellwig
Space Technology Center
University of Kansas
2291 Irving Hill Drive
Lawrence, Kansas 66045

Michael B. Duke
Code SN
NASA/Johnson Space Center
Houston, TX 77058

Charles Elachi
Jet Propulsion Laboratory 183-701
4800 Oak Grove Drive
Pasadena, CA 91103

A. W. England
Code CB
NASA/Johnson Space Center
Houston, TX 77058

John Estes
Code ERL-2
NASA Headquarters
Washington, DC 20546

Richard G. Fenner
Code ED6
NASA/Johnson Space Center
Houston, TX 77058

John P. Ford
Jet Propulsion Laboratory 183-701
4800 Oak Grove Drive
Pasadena, CA 91103

Claude Froidevaux
Research & Exploration
Phillips Petroleum Co.
Bartlesville, OK 74004

R. H. Gelnett
MARS, Inc.
4350 E. Camelback Road
Phoenix, AZ 85018

Alex Goetz
Jet Propulsion Laboratory 183-501
4800 Oak Grove Drive
Pasadena, CA 91103

LeRoy C. Graham
Goodyear Aerospace Corp. Bldg. 13-15
Litchfield Park, AZ 85340

Paul G. Harrison
Cities Service Company
Energy Resources Group
Box 50408
Tulsa, OK 74150

Philip L. Jackson
ERIM
P. O. Box 8618
Ann Arbor, MI 48107

John J. Kowatch
Columbia Gas System Service Corp.
1600 Dublin Road
Columbus, Ohio 43212

Dennis Krohn
Code 906
U.S. Geological Survey
Reston, VA 22092

Franz Leberl
Institut für Landesvermessung und
Photogrammetrie Rechbauestrasse 12
A-8010 Graz, AUSTRIA

Robert B. MacDonald
Code SA
NASA/Johnson Space Center
Houston, TX 77058

Harold C. MacDonald
Department of Geology
University of Arkansas
Fayetteville, Arkansas 72701

Peter Martin-Kay
Hunting Geology & Geophysics, Ltd.
Elstree Way
Borehamwood, Hertfordshire
ENGLAND WD6 1SB

Harold Masursky
Astrogeological Studies
U.S. Geological Survey
2255 North Gemini Drive
Flagstaff, AZ 86001

Ken Meehan
Code 923
NASA/Goddard Space Flight Center
Greenbelt, MD 20771

Roger J. Phillips
Jet Propulsion Laboratory 183-501
4800 Oak Grove Drive
Pasadena, CA 91103

Harry Press
Jet Propulsion Laboratory 180-703
4800 Oak Grove Drive
Pasadena, CA 91103

Donald G. Rea
Jet Propulsion Laboratory 180-300
4800 Oak Grove Drive
Pasadena, CA 91103

W. H. Roberts, III
Gulf Research & Development Co.
P. O. Box 36506
Houston, TX 77036

Floyd F. Sabins, Jr.
Chevron Oil Field Research Co.
P.O. Box 446
La Habra, CA 90631

Steve Saunders
Jet Propulsion Laboratory 183-501
4800 Oak Grove Drive
Pasadena, CA 91103

Jean-Yves Scanvic
B.R.G.M.
Boite Postal 6009
45018 Orleans Cedex
FRANCE

Gerald C. Schaber
U. S. Geological Survey
2255 North Gemini Drive
Flagstaff, AZ 86001

Dan Schneiderman
Jet Propulsion Laboratory 180-701
4800 Oak Grove Drive
Pasadena, CA 91103

Barry Siegal
EBASCO
2211 W. Meadow View Road
Greensborough, NC 27407

Harry E. Stewart
Jet Propulsion Laboratory 183-501
4800 Oak Grove Drive
Pasadena, CA 91103

Ray Sugiura
Woodward-Clyde Consultants
P.O. Box 1149
Orange, CA 92668

James V. Taranik
Code ERS-2
NASA Headquarters
Washington, DC 20546

Paul G. Teleki
Mail Stop 915
U. S. Geological Survey
Reston, VA 22092

Robert K. Vincent
Geospectra Corp., Suite 301
320 N. Main Street
Ann Arbor, MI 48104

Conference Coordinator

Carol Snyder
Jet Propulsion Laboratory 180-704
4800 Oak Grove Drive
Pasadena, CA 91103

Conference Secretary

Charlotte Schieffelin
Jet Propulsion Laboratory 180-300
4800 Oak Grove Drive
Pasadena, CA 91103

APPENDIX B

RADAR GEOLOGY WORKSHOP

July 16-20, 1979
Snowmass, Colorado

Program Agenda

Monday, July 16

- AM - Welcome and Introduction D. G. Rea, JPL
- Workshop Logistics C. L. Snyder, JPL
- Workshop Objectives and Organization P. G. Harrison, Citco
- Keynote Address: Historical H. McDonald, U. of Ark.
Background and State-of-the-art
- Technology and Programmatic Overview F. T. Barath, JPL
- PM - Technique Development - Chm: H. Masursky, USGS
- "Planetary Radar" H. Masursky
 - "Simulation of Spaceborne Radar Images:
Optimization of Parameters for Geomor-
phology" S. Saunders, JPL
 - "Expression of San Andreas Fault on
Seasat Radar Image" F. Sabins, Chevron
 - "Analysis and Assessment of Optically
Correlated Seasat Radar Imagery taken
over Appalachian Valley and Ridge
Province, Tennessee-Kentucky-Virginia" J. Ford, JPL
 - "Airborne and Spaceborne Radar Study of
Volcanic and Sand Fields" C. Elachi, JPL
 - "Rock Type Discrimination and Structural
Analysis with Landsat and Seasat Data:
San Rafael Swell, Utah" H. Stewart, JPL

Tuesday, July 17

- AM - Technique Development (cont'd) - Chm: R. Phillips, JPL
- "Saltpan, Gravels, and Blocky Lava Flows: G. Schaber, USGS
A status report on Radar Backscatter
Research"
 - "Realistic Earth/Land Radar Models" A. Blanchard, TAMU
 - "Some Confusion Factors in Radar Image B. Blanchard, TAMU
Interpretation"
 - "Potential Application of Multichannel P. Jackson, ERIM
Radar to Geology"
 - "Automatic Shading Correction and Speckle P. Chavez, USGS
Noise Mapping Removal Techniques for
Radar Image Data"

Tuesday, July 17

PM - Engineering/Environmental - Chm: P. Teleki, USGS

- "Engineering Applications of Radar" R. Gelnett, MARS, Inc.
- "Applications of Radar Imagery to Arctic and Subarctic Problems" J. Cannon, U. of Alaska
- "Radar Detection of Surface Oil Accumulations" J. Estes, NASA/JPL/U. of California, Santa Barbara
- "Remote Sensing of the Virginia Piedmont and Coastal Plain" D. Krohn, USGS
- "Remote Sensing in Nuclear Power Plant Siting" B. Siegal, EBASCO

- Mapping - Chm: F. Leberl, U. of Graz

- "Application of Imaging Radar to Mapping" F. Leberl
- "Radar Stereo for Mapping and Interpretation" L. Graham, Goodyear
- "A New Look at Togo through the Eyes of a SLAR" L. Dellwig, U. of Kansas

Wednesday, July 18

AM - Exploration - Chm: F. Sabins, Chevron

- "Mineral Exploration with Landsat and Radar Data in the Los Andes Region, Venezuela" B. Vincent, GeoSpectra
- "Application of SLAR to Exploration in the Appalachian Region" J. Kowatch, Columbia Gas
- "Geological Mapping in the Amazon Jungle - A Challenge to Side-Looking Radar" A. Correa, CONOCO
- "Ability of SLAR Imagery in Preliminary Geological Mapping: A Review of B.R.G.M. Surveys and Experiments" J. Y. Scanvic, BRGM
- "Evaluation of Radar Imagery for use in Geologic Mapping in the Amboy-Bristol Dry Lake Area, Mojave Desert, California" R. Sugiura, Woodward-Clyde
- "SLAR, an Optimum Remote Sensing Tool for Detailed Plate Tectonic Analysis: An example of application to oil exploration in West Irian, Indonesia" C. Froidevaux, Phillips Pet.
- "The Design and Function of Oil and Gas Traps" B. Roberts, Gulf
- P. Martin-Kaye, Hunting Geology & Geophysics

Wednesday, July 18

PM - Free Time

Thursday, July 19

AM - Working Groups: generation of recommendations

PM - Working Group Chairmen: generation of integrated Workshop recommendations

Friday, July 20

AM - Plenary Session: review of integrated recommendations

NTIS does not permit return of items for credit or refund. A replacement will be provided if an error is made in filling your order, if the item was received in damaged condition, or if the item is defective.

Reproduced by NTIS
National Technical Information Service
U.S. Department of Commerce
Springfield, VA 22161

This report was printed specifically for your order from our collection of more than 2 million technical reports.

For economy and efficiency, NTIS does not maintain stock of its vast collection of technical reports. Rather, most documents are printed for each order. Your copy is the best possible reproduction available from our master archive. If you have any questions concerning this document or any order you placed with NTIS, please call our Customer Services Department at (703)487-4660.

Always think of NTIS when you want:

- Access to the technical, scientific, and engineering results generated by the ongoing multibillion dollar R&D program of the U.S. Government.
- R&D results from Japan, West Germany, Great Britain, and some 20 other countries, most of it reported in English.

NTIS also operates two centers that can provide you with valuable information:

- The Federal Computer Products Center - offers software and datafiles produced by Federal agencies.
- The Center for the Utilization of Federal Technology - gives you access to the best of Federal technologies and laboratory resources.

For more information about NTIS, send for our FREE *NTIS Products and Services Catalog* which describes how you can access this U.S. and foreign Government technology. Call (703)487-4650 or send this sheet to NTIS, U.S. Department of Commerce, Springfield, VA 22161. Ask for catalog, PR-827.

Name _____
Address _____

Telephone _____

- Your Source to U.S. and Foreign Government
Research and Technology.